

Lecture Notes in Civil Engineering

Yang Yang *Editor*

Advances in Frontier Research on Engineering Structures

OPEN ACCESS

 Springer

Lecture Notes in Civil Engineering

Volume 286

Series Editors

Marco di Prisco, Politecnico di Milano, Milano, Italy

Sheng-Hong Chen, School of Water Resources and Hydropower Engineering,
Wuhan University, Wuhan, China

Ioannis Vayas, Institute of Steel Structures, National Technical University of
Athens, Athens, Greece

Sanjay Kumar Shukla, School of Engineering, Edith Cowan University, Joondalup,
WA, Australia

Anuj Sharma, Iowa State University, Ames, IA, USA

Nagesh Kumar, Department of Civil Engineering, Indian Institute of Science
Bangalore, Bengaluru, Karnataka, India

Chien Ming Wang, School of Civil Engineering, The University of Queensland,
Brisbane, QLD, Australia

Lecture Notes in Civil Engineering (LNCE) publishes the latest developments in Civil Engineering—quickly, informally and in top quality. Though original research reported in proceedings and post-proceedings represents the core of LNCE, edited volumes of exceptionally high quality and interest may also be considered for publication. Volumes published in LNCE embrace all aspects and subfields of, as well as new challenges in, Civil Engineering. Topics in the series include:

- Construction and Structural Mechanics
- Building Materials
- Concrete, Steel and Timber Structures
- Geotechnical Engineering
- Earthquake Engineering
- Coastal Engineering
- Ocean and Offshore Engineering; Ships and Floating Structures
- Hydraulics, Hydrology and Water Resources Engineering
- Environmental Engineering and Sustainability
- Structural Health and Monitoring
- Surveying and Geographical Information Systems
- Indoor Environments
- Transportation and Traffic
- Risk Analysis
- Safety and Security

To submit a proposal or request further information, please contact the appropriate Springer Editor:

- Pierpaolo Riva at pierpaolo.riva@springer.com (Europe and Americas);
- Swati Meherishi at swati.meherishi@springer.com (Asia—except China, Australia, and New Zealand);
- Wayne Hu at wayne.hu@springer.com (China).

All books in the series now indexed by Scopus and EI Compendex database!

Yang Yang
Editor

Advances in Frontier Research on Engineering Structures

 Springer

Editor
Yang Yang
School of Civil Engineering
Chongqing University
Chongqing, China



ISSN 2366-2557 ISSN 2366-2565 (electronic)
Lecture Notes in Civil Engineering
ISBN 978-981-19-8656-7 ISBN 978-981-19-8657-4 (eBook)
<https://doi.org/10.1007/978-981-19-8657-4>

© The Editor(s) (if applicable) and The Author(s) 2023, corrected publication 2023. This book is an open access publication.

Open Access This book is licensed under the terms of the Creative Commons Attribution 4.0 International License (<http://creativecommons.org/licenses/by/4.0/>), which permits use, sharing, adaptation, distribution and reproduction in any medium or format, as long as you give appropriate credit to the original author(s) and the source, provide a link to the Creative Commons license and indicate if changes were made.

The images or other third party material in this book are included in the book's Creative Commons license, unless indicated otherwise in a credit line to the material. If material is not included in the book's Creative Commons license and your intended use is not permitted by statutory regulation or exceeds the permitted use, you will need to obtain permission directly from the copyright holder.

The use of general descriptive names, registered names, trademarks, service marks, etc. in this publication does not imply, even in the absence of a specific statement, that such names are exempt from the relevant protective laws and regulations and therefore free for general use.

The publisher, the authors, and the editors are safe to assume that the advice and information in this book are believed to be true and accurate at the date of publication. Neither the publisher nor the authors or the editors give a warranty, expressed or implied, with respect to the material contained herein or for any errors or omissions that may have been made. The publisher remains neutral with regard to jurisdictional claims in published maps and institutional affiliations.

This Springer imprint is published by the registered company Springer Nature Singapore Pte Ltd. The registered company address is: 152 Beach Road, #21-01/04 Gateway East, Singapore 189721, Singapore

Editorial Board Members

Sudharshan N. Raman, School of Engineering, Monash University Malaysia, Subang Jaya, Malaysia

Bingxiang Yuan, School of Civil and Transportation Engineering, Guangdong University of Technology, Guangzhou, China

Zhijun Xu, Henan University of Technology, Zhengzhou, China

Contents

Analytical and Numerical Analysis for the Vibrational Response of Timber-Concrete Composite Floor	1
MingYu Liu	
Research on the Integration Technology of Structural Performance Evaluation and 3D Design for Spatial Steel Structure Bridges	9
Kewei Zhu and Bing Li	
Aseismic Design of an Out-of-Code High-Rise Building in Shanghai	21
Hongmei Ren, Jianping Zhu, Yanyan Lv, and Weiwei Qin	
Finite Element Analysis of Reinforced Concrete Slab-Rectangular Column Connections Using ABAQUS	33
Yueqiao Jia and Jeffrey Chiang Choong Luin	
Rail Surface Defect Detection Method Based on Deep Learning Method with 3D Range Image	45
Geng Ming, Bo Zhou, Xiaohua Luo, Ren Ling, and Mingxiang Zhou	
Research on Damage Mechanism and Structural Optimization of Joints in Cavity Shear Wall Structure	61
Yong Tian, Guanghui Shi, Bo Zhang, Kun Guo, Fajiang Luo, Shengjie Chen, and Yibo Bai	
Theoretical Study on Natural Vibration Frequency of Externally Prestressed Simply Supported Steel Beams	71
Zhengyu Wang, Hongming Li, and Huibin Chen	
Finite Element Analysis of Punching Shear of Reinforced Concrete Mushroom Slab-Column Connections Using ABAQUS	83
Yueqiao Jia and Jeffrey Choong Luin Chiang	
Research on Restoring Force Model of Built-in Steel Tube Reinforced STRC Column Joints	93
Jiahao Zhang and Qiuwei Wang	

Study on Frost Resistance of Steel-PVA Hybrid Fiber Concrete	105
Ditao Niu, Siyu Gong, Bingbing Guo, Zhiyuan Cao, and Yan Wang	
Experimental and Numerical Investigation of Weak-Axis Connected Steel Plate Shear Wall with Non-slotted and Partially Slotted Infill Plates	113
Jiping Hao, Xinghuang Wu, Weifeng Tian, Shenghui Li, and Rong Wang	
Full-Permeability Analysis of Normal Amplitude and Variable Amplitude Fracture of M24 High Strength Bolts	131
Rong Xing, Junjie Zhang, and Honggang Lei	
Research on Health Assessment Model and Data Analysis Method of Steel-Concrete Composite Girder Bridge	141
Jizhuang Hui, Haobo Zhang, Nima Zhaxi, Duojie Cidan, Yongjian Liu, Gao Cheng, and He Shi	
Finite Element Analysis of Anchor Length Detection Method Based on Parallel Seismic Methods	153
Yi Hu, Hong Lin Cao, Qiang Liu, and Xian Li	
Numerical Simulation of Rockburst Characteristics of Tunnel Surrounding Rock Under Dilatancy Effect	163
Jian-qiang Yu, Qi Li, Yong-lu Wang, and Shuai Tao	
Credibility of Estimating the Hysteretic Energy Demands of Concentrically Braced Steel Frames	175
Cuiling Ma	
Analysis of Key Points of Steel Structure Construction Technology in Film Engineering Projects	185
M. Alashoub Turki Sulaiman and Chunyu Liang	
Analysis of the Influence of Foundation Pit Excavation on the Surrounding Surface Settlement and Retaining Structure	197
LingChao Shou, HeQuan Zhao, XiaoBo Sun, Jin Pang, Ting Bao, and LiFeng Wang	
Numerical Simulation with FLAC^{3D} on Excavation Process of Underground Powerhouse of Kaluma Hydropower Station	211
An Liu, Hua Li, Fei Lu, and Meifeng Niu	
Study on Sound Insulation of Integrated Composite Wallboard Made of ALC and Rock Wool Panel	219
Renjie Shang, Zhaoxin Hou, Zhenlong Mao, and Yundong Liang	
Study on the Properties of Concrete with Different Admixtures in Acid Corrosive Environment	231
Lei Yu, Tianyuan Zhao, and Zhi Wang	

Monitoring and Analysis of Dam Deformation in Yuankou Reservoir 241
 Ming Xu

Experimental Study on Mix Ratio Design of High Coal Gangue Content Concrete 249
 Yingran Liu, Yu Sun, Jian Gong, Yafeng Zhang, and Zhewei Sun

Analysis on Reinforcement of Statically Indeterminate Truss 261
 Ziyi Liang, Mingjun Wei, and Long Yu

Measurement of Velocity and Particle Size in Shock Wave Area Generated by Experimental Granular Flow Impacting on a Cylinder Based on Image Processing Methods 275
 Jing Xu, Jian Wang, Dongpo Wang, and Zheng Chen

Analysis on Fatigue Crack of Orthotropic Steel Bridge Decks 287
 Rui Ma, Peng Dong, and Zigang Xv

Research on Mechanical Properties of Steel Shell Concrete Immersed Tube Shear Connectors 295
 Guoping Xu, Qingfei Huang, Shenyong Song, Hai Ji, Bin Deng, and Tian Song

Research on Dam Deformation Monitoring Model Based on BP + SVM Optimal Weighted Combination 313
 Shuangping Li, Yonghua Li, Min Zheng, Jun Geng, Zuqiang Liu, and Bo Shi

Equivalent Standard Axle Load Analysis Considering Dynamic Load Based on Vehicle Axle-Tire Vertical Acceleration Field Testing ... 325
 Wei Jiang, Wei Wang, Zhichao Song, Changqing Jiang, Chenglong Zhang, and Yijian Yuan

Slope Reliability Analysis Based on Nonlinear Stochastic Finite Element Method 337
 Jing Cheng, Ziyao He, Zhong Liu, and Lei Zhang

Basic Research on Automatic Tying Equipment for Reinforced Steel Skeletons of Precast Shear Walls 355
 Zhenlei Guo, Zhijie Gao, Zhongjian Duan, and Jiayang Zhang

Bridge Comparison of Erection Solutions for Steel Box Girders Spanning from Anchorage in the Sea on Shenzhen-Zhongshan Bridge 365
 Zhi-Wu Xue and Qiang Guo

Analysis on Migration Mechanism of Chloride Ions in Concrete Close-End Pipe Piles 379
 Bo. Yang

Numerical Simulation Research for Rock Stability of Ventilation and Safety Tunnel of Karuma Hydropower Plant 391
Hua Li, An Liu, Ting Shi, and Meifeng Niu

Experimental Study on Mechanical Properties of the Damaged Hoop Head Mortise-Tenon Joint 397
Chengwei Peng and Wenlong Lv

Experimental Study on the Self-Repair Properties of Shape Memory Alloy Concrete Beam 409
Yue Zhang and Xian Cui

Application of ABAQUS by Using Python in Concrete-Filled Steel Tube 419
Zhishuo Yang, Mingxia Chen, Feixin Chen, Zuorong Dong, and Yiman Zhong

Establishment of Community Earthquake Vulnerability Assessment System 427
Xiao Wang, Qi Zhang, Guowei Zhang, Lihui Dong, and Qiuyu Zheng

Research on Deformation Characteristics of SCP Foundation for HKZM Bridge 435
Bin Li, Jiaying Zhang, Xuelei Zhang, and Zhongke Tian

Research on Vibration Design of Large Compressor Foundation 445
Xiaoshuai Qiao, Chao Sun, Yanzheng Hu, and Congbin Jiang

Analysis of the Impact of Earthquakes on the Stability of Overlying Fill Slopes 459
Bin li and Wensheng Hou

Theoretical Study of the Reinforcement of Pre-stressed Concrete Cylinder Pipes with External Pre-stressed Strands 467
Lijun Zhao and Tiesheng Dou

Structural Seismic Performance of Prefabricated Steel Plate Shear Wall with High Energy Dissipation 475
Xiaofei Ma, Yinquan Yu, and Zhe Wang

Sensor Fault Diagnosis Method of Bridge Monitoring System Based on FS-LSTM 487
Lili Li, Hao Luo, He Qi, and Feiyu Wang

Experimental Study on Inclination Test of Fiber Bragg Grating 503
Kang Tan, Ping Dong, Wanchun Gou, Qi Guo, and Yi Li

The External Prestress Effect of Curved Tendons on the Natural Vibration Characteristics of Steel Beams 517
Zhi-wei Xu, Li-xia Lin, Nan-hong Ding, and Lei Chen

Transverse Vibration Characteristics of Clamped-Elastic Pinned Beam Under Compressive Axial Loads 527
 Jianxun Zhang, Pengchong Zhang, Huicun Song, and Lei Zhu

Correction to: Experimental Study on the Self-Repair Properties of Shape Memory Alloy Concrete Beam C1
 Yue Zhang and Xian Cui

Analytical and Numerical Analysis for the Vibrational Response of Timber-Concrete Composite Floor



MingYu Liu

Abstract This study investigates the vibration characteristics of composite timber-concrete floor systems to provide a reliable benchmark for optimizing composite floor system designs. This paper uses the numerical and analytical methods for evaluation to support more detailed study results and to build a comprehensive model for future research. Through Strand7 and ABAQUS numerical finite element analysis, geometrical layout and beam material effects on the timber-concrete composite floor are thoroughly explored. Meanwhile, the analytical results are further compared with the analytical solution based on the Dunkerley method and AISC. Then 15 kinds of timber-concrete composite floor designs are simulated and numerically tested. It was found that the dimensions of the timber beams and their composition might affect the natural frequencies of the floors. On this basis, this paper proposes future design schemes to provide reliable suggestions for further research.

Keywords Analytical · Numerical · Natural Frequency · Timber-concrete composite floor

1 Introduction

The wood laminate flooring is a cost-effective structural solution that combines wood beams with concrete slabs and easily meets strength and deflection standards. The composite timber concrete floor technology may offer longer span floors with shorter sections and higher stiffness [1]. Wood is a renewable resource in Australia, reducing the use of steel in construction. Therefore, high-rise buildings can optimize material consumption. Human kinetic motion causes floor vibration, resulting in occupant discomfort and structural damage [2]. Living load affects the design of lighter, longer composite flooring, especially under ultra-low vibration settings. Although numerous studies have focused on the natural frequencies of composite floor systems, they are not reliable benchmarks for optimizing the structural design

M. Liu (✉)
Civil Engineering, The University of Sydney, Sydney 2006, Australia
e-mail: mliu8214@uni.sydney.edu.au

This is a U.S. government work and not under copyright protection in the U.S.; foreign copyright protection may apply 2023

Y. Yang (ed.), *Advances in Frontier Research on Engineering Structures*, Lecture Notes in Civil Engineering 286, https://doi.org/10.1007/978-981-19-8657-4_1

of wood-concrete composite floor systems (floor system geometry layout, beam dimension, slab thickness and timber material selection). To improve the structural safety design, it is necessary to analyze the vibration characteristics of wood-concrete composite floor system. To control composite floor serviceability and understand its changeable behaviour, simulations are run using finite element analysis with an analytical solution to simulate the floor's natural frequency. This paper examines a pin-supported timber-concrete floor, and the natural frequency of composite floor slab is discussed by numerical analysis and analytical method. On this basis, Strand7 and ABAQUS software are used to study the geometric arrangement of wood-concrete composite floor and the influence of beam materials. The findings are compared to Dunkerley and AISC [3].

Modeling strategies include simulating the natural frequencies of a wood-concrete composite floor system. The natural frequencies are calculated according to the design specifications, the numerical and analytical solutions of Strand7 and ABAQUS are compared, and some suggestions are made for the arrangement of composite floors and material sections. Strand7 and ABAQUS are used to model numerical solutions. The beam components simplify main and secondary beams in Strand7, and the slab is a shell element. The connections are at common nodes only. ABAQUS employs solid elements to replicate beam and slab elements, and element interaction may be simulated. Strand7 is supposed to provide more precise solutions than ABAQUS.

2 Model Stargey

2.1 Model

This paper uses a composite floor model to study the self-weight vibration response of wood-concrete floor system. The model is 4×3.2 m. The concrete slab was supported by $160 \text{ mm} \times 200 \text{ mm}$ beams, and the calculation is aided by rigid connections. Simulating and analysing Strand7 and ABAQUS models are early steps. Strand7 employs beam and shell components for main and subsidiary beams, and the standard nodes use support connections. ABAQUS uses solid pieces with tie connections to depict beams and slabs.

2.2 Material

AS3600-1994 [3] requires $f'c = 32$ mpa concrete for slabs. According to the Queensland Business Report, Radiata pine, Jarrah and redwood are the most widely used commercial timber resources in Australian construction [4]. The following tables illustrate composite floor geometry.

Table 1 Primary beam length effects on fundamental frequencies

Category		Frequency (Hz)		
Model	Length	STRAND7	ABAQUS	Analytical
1	4000	17.0028	23.3240	22.9225
2	5000	12.7354	18.2437	17.2749
3	6000	8.6568	13.0291	11.1132

Table 2 Secondary beam length effects on fundamental frequencies

Category		Frequency (Hz)		
Model	Width	STRAND7	ABAQUS	Analytical
4	2200	22.2431	28.8541	24.9495
5	3200	16.9028	23.3243	22.0223
6	4200	12.6713	19.9291	19.1546

2.3 ABAQUS Modeling Approach Explanation

The full structure is discretized using a 40 mm 40 mm 40 mm mesh, and each neighbouring element is linked to reduce computational error. For the connection between the primary and secondary beams and the concrete slab, a tie rod connection model is used, with both solid and uniform sections, and a four-pin supporting boundary is established. Tables 1 and 2 provide characteristics. To analyse the composite floor's natural frequencies, a Lanczos eigen solver is utilised.

2.4 STRAND7 Modeling Approach Explanation

Floor slab and beam are modelled using Strand7's Quad8 plate and Beam2 parts. The section of the beam is as described. Strand7 connected the slab and beam with common nodes, causing the slab to rest on the beam's mid-flange. To reduce the impact, beam components were offset by 0.01 m. Simulated edge pin connections prevent edge movement. Strand7's natural frequency solver determines the composite floor's fundamental frequency and vibrational response. Tables 1 and 2 provide characteristics, and the simulated model is as shown in Fig. 1.

3 Analytical Solution to Calculate Fundamental Frequency

According to the recommendation of Hicks [5], the governing equation to calculate the natural frequency of free elastic beam or uniform section vibration can be derived

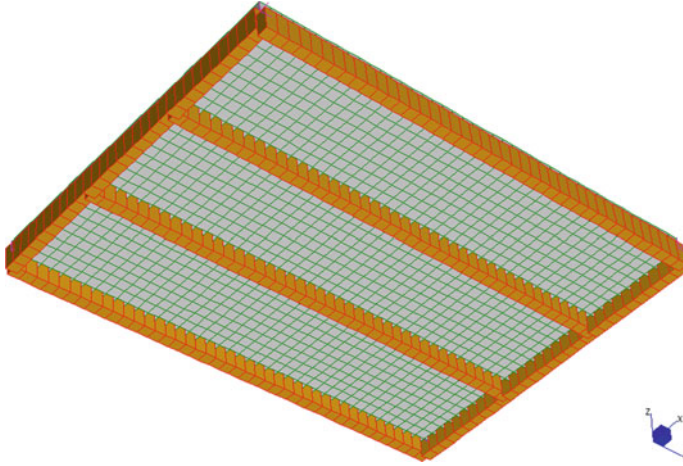


Fig. 1 Reference model in STRAND7

under bending.

$$f_n = \frac{k_n}{2\pi} \times \sqrt{\frac{EI}{m \times L^4}} \quad (1)$$

where:

EI = Dynamic flexural rigidity of the member

m = Distributed mass

L = member span

k_n = Coefficients of beam support. For the simply support element under distributed load, $k_n = \pi^2$

The maximum displacement equation for simply supported beam is:

$$\delta = \frac{5mgL^4}{384EI} \quad (2)$$

where, g is the acceleration of gravity, 9.81 m/s^2 .

Thus, rearranging the above Eq. (2) and (3), the natural frequency of individual members can be determined under maximum displacement.

$$f = \frac{17.8}{\delta} \approx \frac{18}{\delta} \quad (3)$$

Moreover, according to the Design Guide 11 by AISC [3], which shows the equation of the natural frequency of a simply supported beam under UDL.

$$f_n = \frac{\pi}{2} \left[\frac{E_t I_t}{\omega L^4} \right] \quad (4)$$

where:

f_n = Natural frequency

g = Gravitational acceleration (9.81 m/s²)

E_t = Modulus of elasticity of steel

I_t = The moment of inertia

ω = Uniform weight per unit length

L = Member span.

3.1 Boundary Condition

The condition of pin support is applied to the primary beam and the fixed support is used for the secondary beam and concrete slab. The main beams are locked in translation and free rotation, while the sub-beams and concrete slabs are locked in translation and rotation, taking into account the effects of the primary and secondary moment zones.

4 Numerical and Analytical Results Analysis

The first 15 models were simulated using ABAQUS and Strand7 and compared with the analytical solutions. The effect of timber-concrete composite floor geometry layout and beam material on the natural frequency are investigated.

4.1 Primary Beam Length Effect

Table 3 and Fig. 3 show the natural frequencies of models with different girder lengths. Strand7 and ABAQUS experiments show fundamental frequencies drop with primary beam length. The same trend is found in the analysis method, and the results are in good agreement with ABAQUS (Fig. 2).

Table 3 Number of bays effects on fundamental frequencies

Category		Frequency (Hz)		
Model	No. bays	STRAND7	ABAUS	Analytical
7	3	16.9011	23.9242	21.3359
8	4	17.7246	24.3022	21.3359
9	5	18.2253	24.9733	21.3359

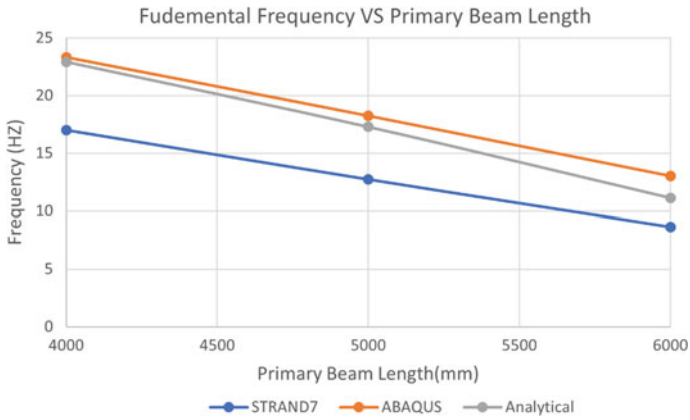


Fig. 2 Fundamental frequency versus primary beam length

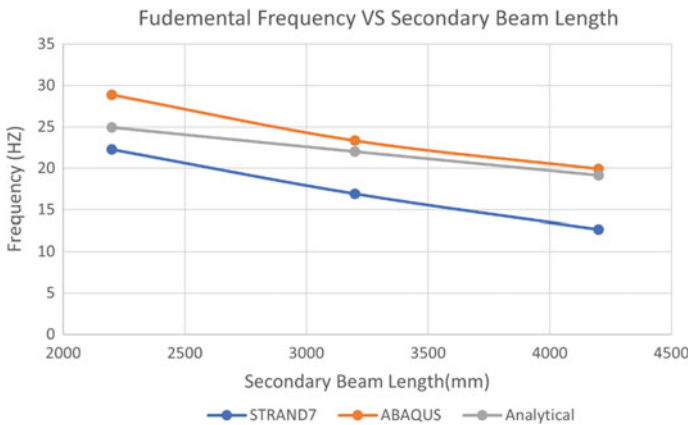


Fig. 3 Fundamental frequency versus secondary beam length

Table 4 Natural frequencies with varying slab thickness

Category		Frequency (Hz)		
Model	Slab t	STRAND7	ABAUS	Analytical
10	200	18.3022	25.3341	23.7251
11	400	26.7761	32.5902	23.7565
12	600	33.2432	37.2467	23.9161

4.2 Secondary Beam Length Effect

Table 4 shows the natural frequencies of models with different sub-beam lengths, and Fig. 4 provides the numerical and analytical results. Both Strand7 and ABAQUS fundamental frequencies diminish as secondary beam length increases. The analytical solution is more accurate than Strand7 because the findings are more like ABAQUS.

4.3 Number of Bays Effect

Table 5 shows natural frequencies for models with different bay counts. Both Strand7 and ABAQUS tests found that the fundamental frequency rose somewhat as the number of bays increased, but the analytical results remained consistent.

4.4 Concrete Slab Thickness Effect

Table 6 provides natural frequencies for models with different slab thicknesses. The results of Strand7 and ABAQUS show that the slab depth has little effect on the fundamental frequency. Even if ignoring the change, the analytical solution shows the same trend.

5 Error Analysing

Despite the offset function, Strand7 has computational issues since the node can only build the beam and plate, resulting in a lack of slab-to-beam connections when simulating models. The analytical solution ignores the connection of plate and beam, leading to the discovery of error. In the simulation, the boundary condition is pin support. However, the performance of the floor is affected by the connections between the floor and the beams.

6 Conclusion

This paper uses STRAND7 and ABAQUS to determine the natural frequencies of wood composite flooring. Analytical solutions based on Dunkerley and AISC are simulated to confirm finite element model results accuracy.

The longer the beam, the lower the base frequency of the floor system. Number of bays affects flooring frequency, although less than beam length. As the compartment expands, the frequency of the composite floor increases, and the thicker concrete slab increases the fundamental frequency. Beam composition affects results. The E/m term influences the rise or decrease of the floor's fundamental frequency, so a material with a higher E/m term may raise the frequency.

The span of the beams has the largest impact on the fundamental frequency of a wood composite floor. Consequently, it should be carefully adjusted to minimize resonance with human activity. Pine beams are recommended.

Regarding the dynamic behaviour of the composite floor, a force-induced vibration test is recommended since most harmful vibrations are created by subject forces.

References

1. Du H, Hu X, Xie Z, Wang H (2019) Study on shear behavior of inclined cross lag screws for glulam-concrete composite beams. *Constr Build Mater* 224:132–143
2. Feldmann M, Heinemeyer C, Butz C, Caetano E, Cunha A, Galanti F, Goldack A, Hechler O, Hicks S, Keil A et al (2009) Design of floor structures for human induced vibrations. EUR: Luxembourg
3. Lenzen KH (1966) Vibration of steel joist-concrete slab floors. *AISC Eng. J.* 3:133–136
4. Rijal R, Samali B, Shrestha R, Crews K (2015) Experimental and analytical study on dynamic performance of timber-concrete composite beams. *Build Mater* 75:46–53
5. Hicks S (2004) Vibration characteristics of steel-concrete composite floor systems. *Prog Struct Eng Mater* 6:21–38

Open Access This chapter is licensed under the terms of the Creative Commons Attribution 4.0 International License (<http://creativecommons.org/licenses/by/4.0/>), which permits use, sharing, adaptation, distribution and reproduction in any medium or format, as long as you give appropriate credit to the original author(s) and the source, provide a link to the Creative Commons license and indicate if changes were made.

The images or other third party material in this chapter are included in the chapter's Creative Commons license, unless indicated otherwise in a credit line to the material. If material is not included in the chapter's Creative Commons license and your intended use is not permitted by statutory regulation or exceeds the permitted use, you will need to obtain permission directly from the copyright holder.



Research on the Integration Technology of Structural Performance Evaluation and 3D Design for Spatial Steel Structure Bridges



Kewei Zhu and Bing Li

Abstract With the increase of steel structure bridges, the design of steel structure bridges begin to evolve in the direction of high quality, high precision, and short design period. In order to improve the design quality and efficiency of spatial steel structure bridges, the integration technology of structural performance evaluation and 3D design of spatial steel structure bridges is studied. Firstly, the 3D design is carried out based on the rapid design method, and then the finite element simulation is conducted by software to analyze its structural performance and optimize the 3D design model. The research results link the rapid design and structural analysis software systematically, so as to realize the integrated design of spatial irregular bridge components with BIM and FEM technology.

Keywords Spatial steel structure bridge · Performance evaluation · 3D design · BIM/FEM system · Integrated design

1 Introduction

Since China's reform and opening up, the construction of roads and bridges has developed rapidly at an amazing scale and speed, and various bridges have been built. Nowadays, different types of bridges grow up anywhere, which shows the glory of China's traffic construction. With the increase of steel structure bridges, the design of steel structure bridges begin to evolve in the direction of high quality, high precision, and short design period.

In order to improve the design quality of steel bridges with spatial shape, scholars put forward the method of using finite element simulation technology to analyze its structural performance combined with 3D design. For the spatial shape bridge

K. Zhu · B. Li (✉)

School of Civil Engineering, Fujian Chuanzheng Communications College, Fuzhou 350007, China

e-mail: 331424696@qq.com; libing841995@163.com

K. Zhu

e-mail: libing5132022@163.com

© Crown 2023

Y. Yang (ed.), *Advances in Frontier Research on Engineering Structures*, Lecture Notes in Civil Engineering 286, https://doi.org/10.1007/978-981-19-8657-4_2

structure, because of its special shape and complex alignment, Ying [1] introduced a 3D design, which effectively improved the fineness of the design and solved the drawbacks of traditional 2D design. According to the structural characteristics of the cable-stayed bridge, Hu et al. [2] adopted the parametric method to build the 3D model of the cable-stayed bridge, and realized the 3D visualization of the cable-stayed bridge. The advantages of CATIA software “template + skeleton” modeling form were clarified, and the modeling process was expounded from two aspects: skeleton building and simply supported T-beam model building. Lu et al. [3] used the 3D CATIA software to more accurately design the detailed structure of the auxiliary tower and the steel anchor box structural members in the auxiliary tower, which provides a technical reference for the detailed structural design of large complex bridges and special members. Chen et al. [4] used the parametric modeling method based on knowledge to study the parametric modeling of bridges, and put forward the bridge design knowledge expression model, knowledge acquisition method, bridge structure assembly algorithm, and bridge intelligent change algorithm. The scanning method and parametric feature modeling are the main modeling methods of the bridge model, Lu et al [5] adopted with half the data structure as the data structure of the model. Wu et al. [6] deeply discussed the process of parametric modeling of 3D geometry and studied the 3D parametric modeling of bridge components and the overall splicing of bridges in combination with the characteristics of bridges. Combined with a bridge project in the charge of Zhe [7] the specific application of CATIA software in this project was discussed. However, the above research processes split the connection between BIM and FEM in the design of spatial steel structure bridges. Experienced technicians are required to predict a structural parameter in advance, and there is a lack of direct use of FEM software to guide the design results.

In order to improve the design quality and efficiency of spatial special-shaped bridge components, the integration technology of structural performance evaluation and three-dimensional design of the spatial special-shaped bridge is the objective of the study. According to the design requirements of the spatial steel structure bridge, this paper evaluates and optimizes its mechanical properties based on finite element theory. Combined with the demand, the integrated design of BIM and FEM can improve the design quality and efficiency of products, shorten the design cycle and improve the competitiveness of products.

2 3D Design of Steel Bridge Components of Spatial Shape by Plate Design Method

2.1 Steel Structure Bridge Plate Design Method

3D design should take full account of the characteristics of downstream industries, so the steel structure design should be combined with the characteristics of steel

processing. When steel is processed by the manufacturer, the construction section is not used as the classification basis, but the thickness and size of the plate are used as the classification standards. After the plates are classified, they need to be cut twice according to the conditions of transportation and welding equipment to meet the corresponding size requirements. Based on the characteristics of steel processing, this paper puts forward the idea of the “plate design method” for the 3D design of steel structures, characterized by “designing with the entire plate and cutting at the end”.

When the plate design method is adopted, the task decomposition mode is changed at first. Instead of taking the construction section as the basis of project task decomposition, the task is divided by the main plates that make up the steel box girder (Fig. 1). The whole slab bridge design is adopted, and continuous members such as stiffening ribs are also arranged, not allowing for the disconnection between construction segments. The same type of main board is designed by one designer.

This task decomposition mode can minimize the association points of models among different designers. When the task decomposition is carried out according to the construction segments, there are many related points among the products designed by different designers, and the corresponding risk of modification is also high. However, by dividing the tasks according to the functions of the plates, there

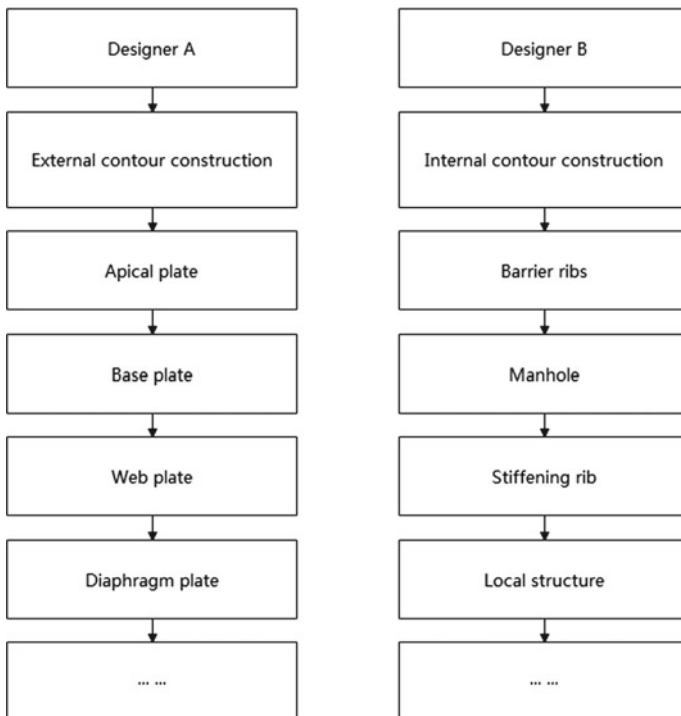


Fig. 1 Task decomposition according to main plates

are few correlation points between products designed by different designers, and the main plates all belong to the same designer. There is only one design idea for the same type of plate, which ensures the continuity and uniqueness of the same plate in the design and later modification process, and also avoids the reverse work caused by the unified design rules in the later period. When a modification is needed, the workload of modification is concentrated in a single designer, which avoids the untimely update caused by the communication of designers and reduces the risk of large-scale modification. A single designer of the same kind of plate embodies the overall design idea of the “plate design method”.

After dividing the design tasks according to the functions of plates, the 3D forward design of the bridge steel structure is carried out with reference to the mature ship design theory in 3DE.

The 3D design process of bridge steel structure is divided into two links: fundamental design of steel structure (hereinafter referred to as SFD design) and detailed design of steel structure (hereinafter referred to as SDD design). In these two links, the models are interrelated and independent.

SFD design is applied to the early and middle sections of bridge design, i.e., the period when the bridge structure may change greatly. The design content of this stage includes the main stressed plates, stiffeners, diaphragms, and large openings. At this stage, the form of the slab is a flat or curved slab with thickness, and the division of construction segments is not considered. The model at this stage is mainly used for the statistics of the whole bridge engineering quantity, finite element model analysis, construction segment planning, etc.

SFD design is applied to the middle and late stages of bridge design, which refers to the period when the bridge structure is no longer greatly changed. The main work of this stage is as follows: 1. Divide the model generated by SFD design into segments; 2. Add the detailed structures to various plates; 3. Divide the whole model into independent parts according to the construction segments. The model of the SFD stage is mainly used for the simulation of the construction scheme, the processing and blanking of plates, the drawing of final drawings, etc. The construction segments are divided only in the middle and later stages of design, which embodies the idea of the “plate design method”.

2.2 The Application of the “Plate Design Method”

The steel box girder is taken as an example. Firstly, different designers are assigned to the inner and outer contour structures of the steel box girder based on the plate. After receiving the task, each designer draws the supporting surface of each plate in turn. The top plate, bottom plate, and web plate of the steel box girder can be sketched at first, and the supporting surfaces of the top plate, bottom plate, and web plate can be obtained by sequentially stretching and sweeping along the bridge direction according to the profile of the section. According to its position, the transverse diaphragm can get its position by offsetting the mid-span section plane or fulcrum

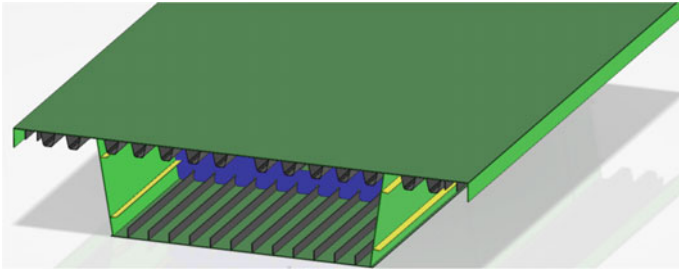


Fig. 2 Structural tree and model of steel structure plate design method

section plane of the box girder. After the supporting surface of each plate is obtained, the outline of each plate can be drawn on the supporting surface. The supporting surfaces of the main outline of the box girder, such as the top, bottom and web, are the same as the actual outline of the plate. It is sufficient to pay attention to the welding relationship and select the corresponding limiting surface. On its supporting surface, the transverse diaphragm selects the outer contour plate of the box girder, in turn, to restrict it to form the corresponding shape. The 3D design structure tree and model are shown in Fig. 8. After the main stress plate of the box girder is formed, details such as stiffening ribs, through holes, local reinforcing ribs, and welding holes can be set on it. Usually, in the scheme design stage, Stiffeners, through holes, local stiffeners, and other structures are designed.

After completing the SFD model and passing the joint review at all levels, the designer can start the design of the SDD stage. Through the plate cutting function of 3DE, the whole bridge plate will be cut according to the proposed construction section, as shown in Fig. 2. The cut plates are arranged with respect to the types of plates to form the final construction drawings. Drawing arrangements in accordance with the plate type can also facilitate the processing and blanking of steel structures.

3 Finite Element Simulation and Optimization of 3D Design of Spatial Steel Structure Bridge Components

3.1 Finite Element Simulation Analysis

Finite element theory originated from solid mechanics. It involves dividing a large whole into several small units, then solving for these units, and finally reorganizing them. In the finite element theory, the accuracy of the overall division is directly proportional to the accuracy of the obtained solution. Such an analysis mode is extremely practical in many fields, and it is an extremely important research and analysis method in steel structure bridge engineering. The main calculation formula is as follows:

According to the selected displacement mode, the displacement of any point in the cell is represented by the node displacement:

$$\{f\} = [N]\{\delta\}^e \quad (1)$$

In the formula: $\{f\}$ is the displacement array of any point in the unit, $\{\delta\}^e$ is the node displacement array of the unit, $[N]$ is the shape function matrix, and its elements are functions of position coordinates. The relationship between node force and node displacement is as follows:

$$\{R\}^e = [K]\{\delta\}^e \quad (2)$$

In the formula: $\{R\}^e$ the force of each node of the unit, $\{\delta\}^e$ is the displacement of each node of the unit, and $[K]$ is the stiffness matrix of the unit.

$$[K] = \iiint [B]^T [D] [B] dx dy dz \quad (3)$$

In the formula: $[B]$ is the strain matrix of the element, and $[D]$ is the elastic matrix related to the element material. According to the Virtual Work Equivalence Principle, the equivalent nodal force is used to replace the force acting on the element.

The total stiffness matrix $[K]$ of the whole structure is assembled by the stiffness matrix of each unit, and the equivalent nodal forces acting on each unit are assembled into the load matrix of the structure $\{R\}$ to form the total stiffness equation of the whole structure.

$$[K]\{\Delta\} = \{R\} \quad (4)$$

The total stiffness equation is restrained and solved, the element stress is calculated, and the calculation results are adjusted, thereby completing the finite element simulation analysis.

In engineering practice, due to the complexity of shape and the same magnitude of dimensions in three directions, the structures must be treated as space problems. The principle, idea, and solution of the spatial finite element method are completely similar to the planar finite element method, but it has 3D characteristics. Compared with complex spatial problems, computer storage capacity and computer cost may bring challenges. In order to solve the above problems, the former can be overcome by looking for rules and building grids to automatically generate pre-processing programs, while the latter can use higher-order elements to improve the accuracy of the elements, thus reducing the unknown quantity and saving the running time of the machine.

3.2 Simulation Optimization of 3D Design

Based on finite element simulation analysis, the overall structure and local structure of the structure are analyzed in detail. According to the analysis results and the requirements, the structure is modified and reassembled with 3D digital components, and the finite element analysis is performed until the analysis results meet the requirements. The workflow of the optimized 3D design is shown in Fig. 3.

4 BIM and FEM Integrated Technology of Spatial Steel Structure Bridge Components

In the structural performance analysis and digital design of spatial shape steel bridge components, product design and analysis are more focused on the independent application of technology. With the development and application of design technology and the increasing improvement of industry specifications and contents, there is an urgent need to adopt BIM/FEM integrated design technology to enhance the innovative design ability of traditional industries, so as to improve the design quality and

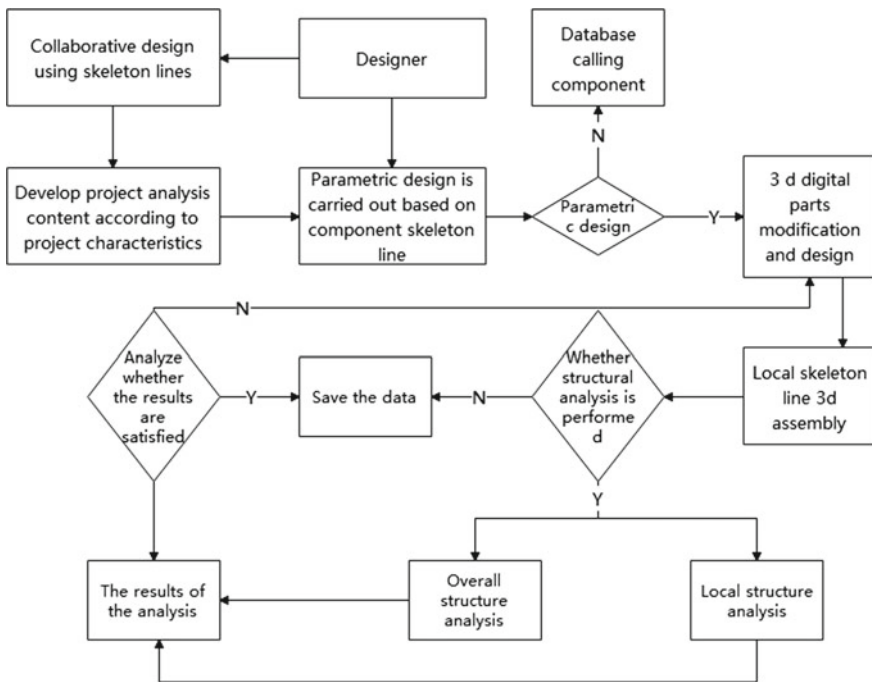


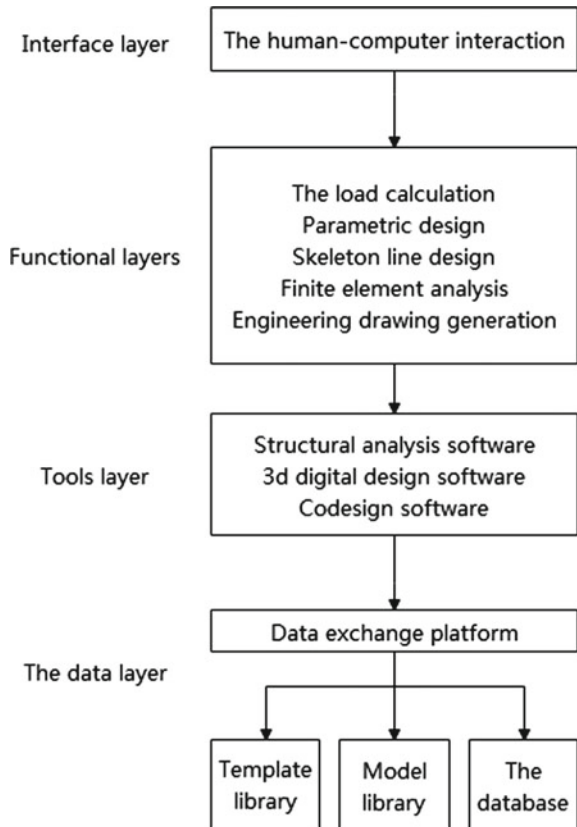
Fig. 3 Workflow chart of simulation optimization 3D design

efficiency of products, shorten the research and development cycle and improve the competitiveness of products.

4.1 Integration Technology Process

Based on the 3D design method and the structural finite element analysis system, the Building Information Modeling design (BIM) and Finite Element Method (FEM) are combined into an integration technology system. The effective integration of BIM and FEM systems can make the structure design and analysis better integrated, thus improving the product design quality and shortening the research and development cycle. The workflow of integration with BIM FEM technology is shown in Fig. 4.

Fig. 4 Workflow of BIM and FEM technology integration



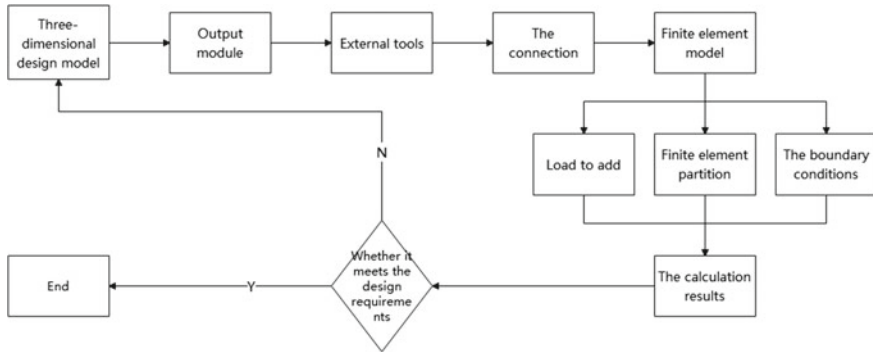


Fig. 5 Workflow of integrated design

4.2 Integrated Design Method

BIM and FEM models should be linked based on external tools. Firstly, the parametric model based on the skeleton line is established by using 3D design software. When the parametric model is established, the relationships among the main parameters are established in the variable table. Then, the link environment set in the external tool software is used, which mainly refers to the 3D design software model. It is needed to set the link interface, establish the link with the finite element analysis software, extract the variable table, and parameterize the model to be optimized, so as to update the 3D design model and finite element calculation model. The workflow of integrated design is shown in Fig. 5.

4.3 Examples of Integrated Design

The local calculation of the segment main arch adopts the integrated design of 3D design and finite element analysis. First, the segmented 3D parametric model takes a hexahedron with a 200 mm side length as a whole by meshing. The arch is Q345qD, the steel plate is simulated by a solid element, and the plate thickness is set according to the design drawing. Consolidation constraint is adopted at the joint surface between the segment and the lower segment, and the integrated design results are shown in Fig. 6.

For the first time, some stress concentration exists in the calculated structure, and the 3D design is used for parametric modification. The optimal plate thickness is obtained by iterative calculation. The overall result of the model meets the expectation and the production needs of engineering projects.

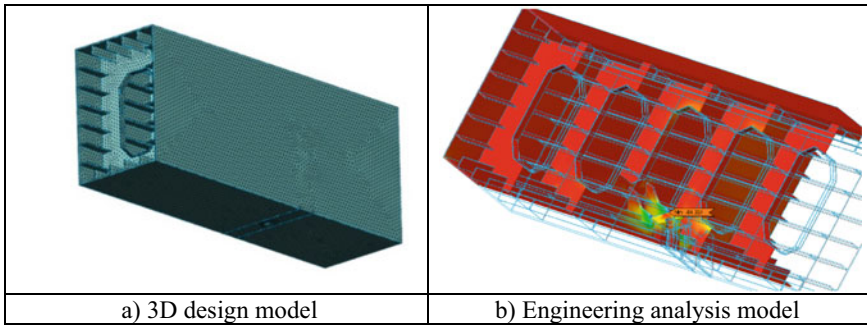


Fig. 6 Integrated design of arch rib of spatial shape bridge

5 Conclusion

In this paper, the integrated design technology is applied to the spatial shape steel bridge structure for the first time for analysis and study. The mechanical properties of spatial shape steel bridge are studied, the design flow of spatial shape steel bridge is determined, the design difficulty of steel bridge is optimized, and the integrated design scheme is designed. Then, based on the external program, the finite element analysis, optimization, and 3D design are linked together, and an integrated design scheme based on parameterization is designed. A digital design of a spatial steel structure bridge in conjunction with BIM and FEM is formed. This integrated design technology is applicable to a variety of design software and works well, which provides reference and support for the deep integration of BIM and FEM. The integration of three-dimensional design and structural analysis is not only a research goal of the bridge structure but also exists in many engineering and mechanical industries. Future research will unify 3D design and structural analysis into one platform. A set of models will break the barriers of design and analysis and improve the design efficiency of the engineering and machinery industry as a whole.

Acknowledgements Research on Modeling of Deviation Correction and Application of Coordinated Design of Railway Steel Girder (2020 Fujian Provincial Transportation Science and Technology Project 202029).

References

1. Ying A (2021) Comparative analysis of 2D CAD and 3D BIM design. *Inf Recording Mater* 22(4):3
2. Chunxia H, Wang Z (2008) Research on 3D visualization of parametric cable-stayed bridge based on OpenGL. *J Jiangnan Univ (Nat Sci En)* 36(2):47–49
3. Fei L, Ren Y, Li Y (2014) Application of 3D CATIA software in bridge engineering design. *Northwest Hydropower* 4:100–103

4. Chen M, Shide H (2011) Parametric modeling of bridges based on knowledge. *J Eng Graph* 32(5):9
5. Tiejian L et al (2005) Three-dimensional modeling of bridges and its visual simulation. *J Central South Univ (Nat Sci Ed)* 36(3):501–505
6. Xueyi W, Liu J, Yin H (2013) Construction of 3D bridge model based on parametric design. *J Graph Sci* 34(2):7
7. Wang Z (2020) 3D modeling design of conventional bridges based on CATIA. *Traffic World* 17:3

Open Access This chapter is licensed under the terms of the Creative Commons Attribution 4.0 International License (<http://creativecommons.org/licenses/by/4.0/>), which permits use, sharing, adaptation, distribution and reproduction in any medium or format, as long as you give appropriate credit to the original author(s) and the source, provide a link to the Creative Commons license and indicate if changes were made.

The images or other third party material in this chapter are included in the chapter's Creative Commons license, unless indicated otherwise in a credit line to the material. If material is not included in the chapter's Creative Commons license and your intended use is not permitted by statutory regulation or exceeds the permitted use, you will need to obtain permission directly from the copyright holder.



Aseismic Design of an Out-of-Code High-Rise Building in Shanghai



Hongmei Ren, Jianping Zhu, Yanyan Lv, and Weiwei Qin

Abstract Proper structural system and performance-based seismic design are the key issues in designing high-rise building structures. This project has unique building facade shape and complex plane function layout, and the structural plane and vertical layout are irregular. The superstructure adopts assembled integral concrete frame-shear wall structure, which is judged as out-of-code high-rise building by seismic review. Firstly, the site conditions, foundation design and structural form selection are introduced. Then, YJK software is used to calculate and analyze the seismic force of the superstructure, and the seismic performance indexes of the structure can meet the requirements of the code. Finally, the regularity of each structural unit of the superstructure is judged, and the corresponding main seismic strengthening measures are put forward.

Keywords Assembled integral frame-shear wall structure · Structural regularity · Seismic fortification measures · Out-of-code high-rise building

1 Introduction

AN out-of-code high-rise building in Shanghai is located in Pudong New District, Shanghai. It is a high-rise building with 1 basement and 3 8-story towers (including 3 podium floors). The total construction area is 45,570 m², including 38,990 m² above the ground and 6580 m² underground (Fig. 1). The superstructure is divided into three structural units by setting aseismic joints: unit A, B and C of 8 floors (Fig. 2). Integrated concrete frame-shear wall structure is adopted in the ground building and cast-in-place concrete frame structure is adopted in the basement.

The design service life of the building structure is 50 years, and the structural safety grade is grade II. The seismic fortification intensity of Pudong New District is

H. Ren · J. Zhu · Y. Lv · W. Qin (✉)
Shanghai Urban Construction Vocational College, Shanghai, China
e-mail: qinweiwei@succ.edu.cn

H. Ren
e-mail: renhongmei208@163.com

This is a U.S. government work and not under copyright protection in the U.S.; foreign copyright protection may apply 2023

Y. Yang (ed.), *Advances in Frontier Research on Engineering Structures*, Lecture Notes in Civil Engineering 286, https://doi.org/10.1007/978-981-19-8657-4_3



Fig. 1 Architectural renderings

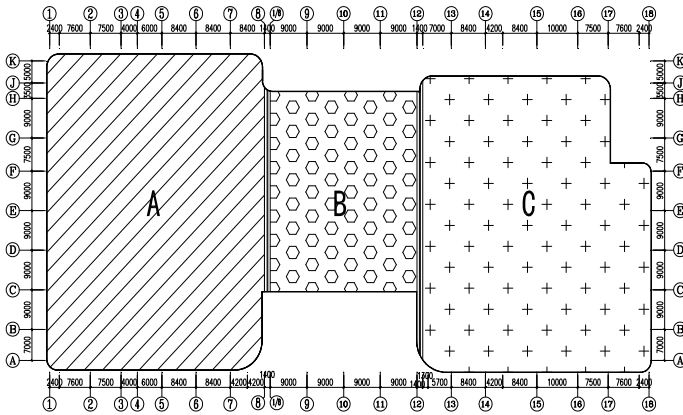


Fig. 2 Schematic diagram of building layout (Unit A, B and C)

7° and the design basic seismic acceleration is 0.10 g. The design earthquake group is group II, the site category is class IV, the design characteristic period is 0.9 s, and the seismic fortification category of the building is class C. The seismic grade of the shear wall is grade two, the seismic grade of the frame is grade three, and the seismic grade of basement frame is grade three. The maximum horizontal seismic influence coefficient under the action of frequent earthquakes is 0.08. The maximum horizontal seismic influence coefficient under the action of rare earthquakes is 0.45, the basic wind pressure is 0.55 kN/m² (return period of 50 years), and the ground roughness is class A [1–4]. The basement roof is used as the embedded part of the superstructure, and the lateral stiffness of the basement floor is 1.5 times higher than that of the first floor. The first floor adopts cast-in-situ concrete beam slab structure. The floor thickness of the superstructure is 250 mm, and double-layer bi-directional connection configuration of the rebar is adopted, which meets the requirements of embedding [5].

2 Foundation and Basement Structure Design

The design grade of the project foundation is grade B, and the waterproof grade of the basement is grade one [6]. According to the geotechnical engineering investigation report of the project, the proposed site is an unfavorable seismic site. According to the characteristics of the project and the actual distribution of the foundation soil layer on the site, the foundation adopts the pile foundation of bearing platform under column (wall) + raft. The thickness of raft is 600 mm and the strength grade of raft concrete is C35. The Φ 500 mm PHC prestressed concrete pipe pile is selected and the pile length is 28 m. The load bearing layer was not less than 4.2 m. The design value of vertical compressive bearing capacity of single pile is 1680 kN. The total number of piles is 266 and the load bearing layer of pile tip is ⑦-1 layer sandy silt.

The plane outsourcing size of the basement is about 148 m \times 69.2 m, which belongs to super-long basement structure (Fig. 3). In order to reduce harmful cracks caused by concrete shrinkage cracks and temperature cracks, the following measures are taken in the design: (1) Set post-construction pouring belt (width: 0.8 m ~ 1 m) or expansion reinforcing belt (width: 2 m), and use micro-expansion concrete to compensate for concrete shrinkage. (2) The reinforcement ratio of the basement roof is not less than 0.25%. The spacing between the basement roof reinforcement and the horizontal reinforcement of the basement exterior wall is well controlled so as to enhance the shrinkage resistance of the basement concrete. (3) Cement with low shrinkage heat of hydration is used to avoid using high grade concrete. (4) Maintenance is strengthened during construction.

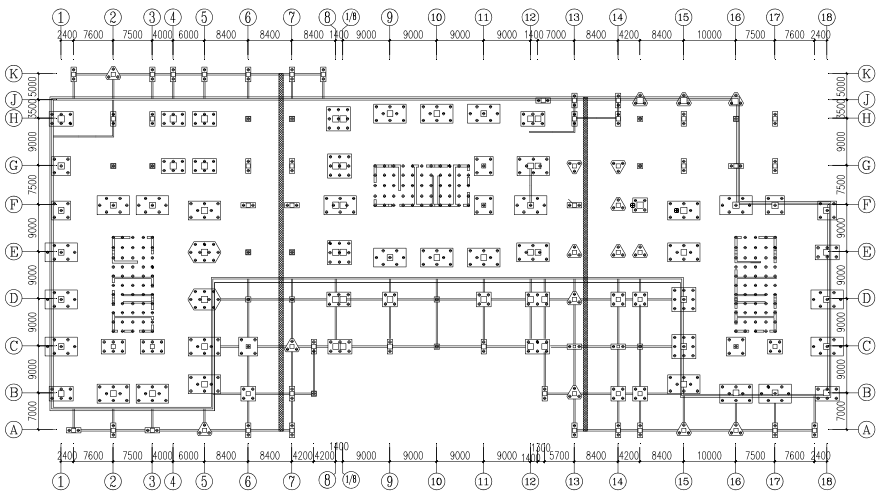


Fig. 3 Basement foundation layout plan

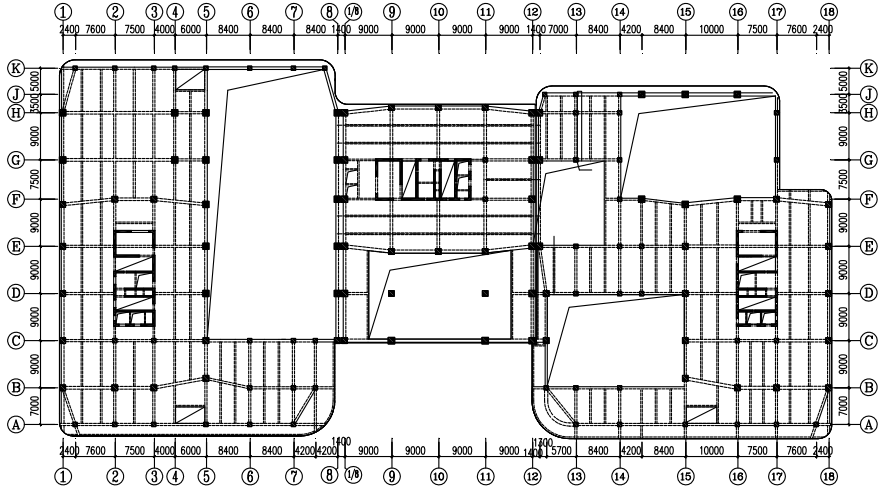


Fig. 4 Structural plan of the 2nd floor

3 Superstructure Design

3.1 Lateral Force Resistant Structural System

The main column spacing of the superstructure is 9.0 m. After setting seismic joints at axis 3 and axis 12, the superstructure is divided into three structural units, namely unit A (①~⑧ axis/A axis ~ K axis), unit B (⑧ axis ~ ⑫ axis/C axis ~ H axis) and unit C (⑫ axis ~ ⑱ axis/A axis ~ K axis). Each layer height: the first layer is 8.0 m, the second layer is 5.4 m, the third layer is 7.2 m, 4 ~ 8 layer is 4.8 m. The indoor and outdoor height difference is 0.30 m and the main roof height is 44.9 m, which is a class A high-rise building [7]. The main structure adopts assembled integral frame shear wall structure and composite floor slab.

Based on the principle of seismic conceptual design, combined with the characteristics of structural plane and the demand of the building use function, the shear wall is arranged symmetrically in two directions in stairwell, elevator, end compartment and partition wall. The stiffness shall be evenly distributed in the plane layout to reduce the torsional effect under the earthquake. Typical floor plans are shown in Figs. 4, 5, 6 and 7.

3.2 Structural Calculation and Analysis

Considering the torsional coupling effect, the YJK software is used for structural analysis and seismic internal force calculation of the building. The floor stiffness

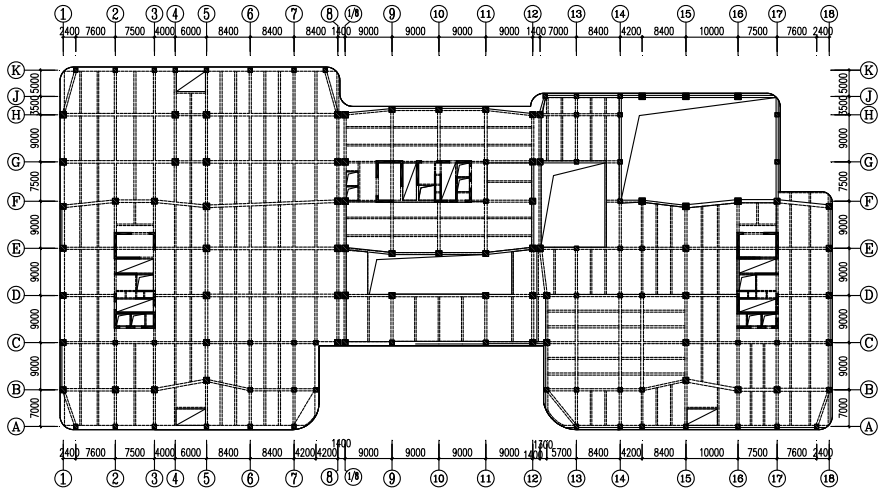


Fig. 5 Structural plan of the 3rd floor

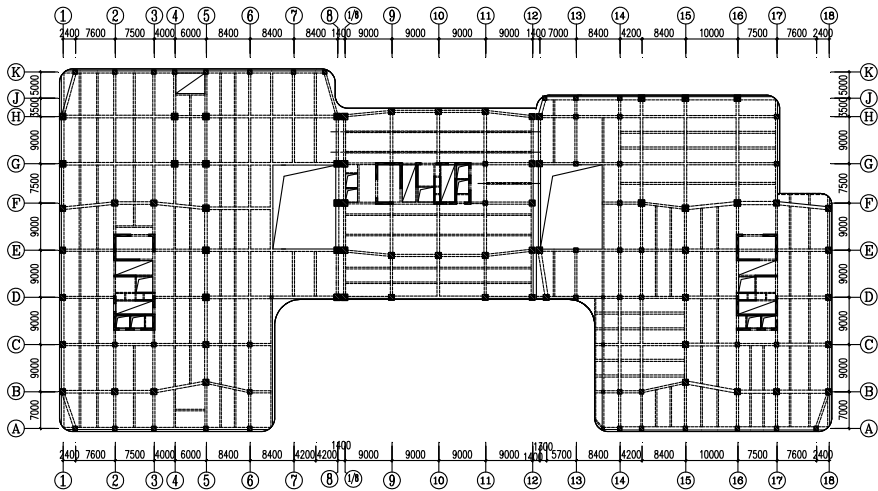


Fig. 6 Structural plan of the 4th floor

adopts the shear stiffness algorithm and 21 vibration modes are calculated. The calculation results of structural vibration characteristics of unit A, B and C are shown in Table 1 respectively. The ratio of the first natural vibration period T_3 dominated by torsion to the first natural vibration period T_1 dominated by translation is less than 0.90, which meets the specification requirements [7].

Other main calculation results such as inter story displacement angle, torsional displacement ratio, shear weight ratio and other indicators meet the specification requirements, as shown in Table 2. Stiffness ratio refers to the ratio of the lateral

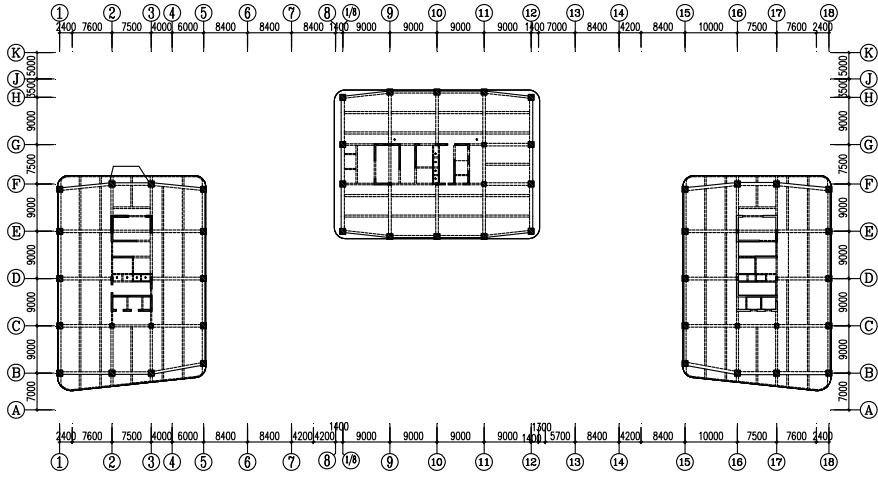


Fig. 7 Structural plan of the 5th floor ~ roof

Table 1 Vibration characteristic index

Structural element	Vibration model No.	Natural vibration period (s)	Translation coefficient	Torsion coefficient
Unit A	1	1.0415	0.07(X) + 0.85(Y)	0.08
	2	0.9892	0.90(X) + 0.09(Y)	0.01
	3	0.8736	0.07(X) + 0.10(Y)	0.83
	T3/T1 = 0.8736/1.0415 = 0.84 ≤ 0.90			
Unit B	1	1.0534	0.93(X) + 0.01(Y)	0.07
	2	1.0356	0.01(X) + 0.99(Y)	0.00
	3	0.9166	0.07(X) + 0.00(Y)	0.93
	T3/T1 = 0.9166/1.0534 = 0.87 ≤ 0.90			
Unit C	1	1.0121	0.67(X) + 0.25(Y)	0.07
	2	0.9703	0.32(X) + 0.63(Y)	0.05
	3	0.8174	0.02(X) + 0.15(Y)	0.82
	T3/T1 = 0.8174 / 1.0121 = 0.81 ≤ 0.90			

stiffness of this floor to 70% of the lateral stiffness of the adjacent upper floor or 80% of the average lateral stiffness of the three adjacent floors above it. The calculation results show that there is no soft layer in the superstructure.

Table 2 Main calculation indexes of structure

Calculation results	Structural element					
	Unit A		Unit B		Unit C	
	X direction	Y direction	X direction	Y direction	X direction	Y direction
Floor minimum shear weight ratio	4.89%	4.62%	5.08%	5.45%	5.08%	4.61%
Effective mass coefficient	98.72%	99.52%	97.62%	97.81%	92.10%	91.88%
The maximum ratio of the maximum horizontal displacement to the average value of the floor under earthquake	1.38 (3rd floor)	1.25 (3rd floor)	1.38 (1st floor)	1.27 (1st floor)	1.37 (1st floor)	1.36 (3rd floor)
Seismic base shear (kN)	16,610.40	15,685.00	11,673.70	12,513.72	15,925.72	14,467.11
Minimum shear capacity ratio of floor	0.83 (1st floor)	0.86 (1st floor)	0.94 (3rd floor)	0.94 (3rd floor)	0.87 (2nd floor)	0.91 (2nd floor)
Lateral stiffness of bottom embedded layer (>1.5)	6.7320	6.4724	9.8043	3.4956	7.2437	6.8209
Maximum axial compression ratio of frame column/shear wall limb	0.86/0.31		0.87/0.31		0.71/0.25	
Stiffness weight ratio of structural overall stability calculation (≥ 1.4)	9.44	8.55	10.18	10.78	10.00	10.52

4 Determination of Structural Regularity and Main Seismic Strengthening Measures

The structural height of the project is 44.9 m < 120 m and the height width ratio is 1.75 < 6, which meet the requirements of the code. According to the technical regulations of the Ministry of construction and Shanghai Municipality on the regularity judgment of out-of-code high-rise buildings [8, 9], the regularity judgment of structural unit A, B and C is conducted respectively.

4.1 Rule Judgment of Unit A and Unit C

- (1) Torsional irregularity: when considering the specified horizontal force of accidental eccentricity, the maximum elastic horizontal displacement of the floor is greater than 1.2 times the average value of horizontal displacement at both ends of the floor.
- (2) Eccentric arrangement: the eccentricity between the mass center and the stiffness center of floors 1~3 is greater than 0.15.
- (3) Local discontinuity of floor slab: the effective width of floor slab after opening is less than 50% of the typical width of floor slab in the Y direction of ⑤ axis ~ ⑥ axis on the second floor of unit A, the X direction of ④ axis/F axis ~ J axis on the second floor, the Y direction of ② axis ~ ④ axis on the second floor, and the X direction of ② axis ~ ④ axis/F axis ~ G axis on the third floor of unit C.
- (4) Irregular lateral stiffness: the local retraction size of the fourth floor is greater than 25% of the adjacent lower floor.

Among them, (1) and (2) do not double calculate the irregular items, so there are three irregularities in unit A and unit C, which belong to out-of-code high-rise buildings.

4.2 Main Seismic Strengthening Measures of Unit A and Unit C

- (1) Torsional irregular and eccentric arrangement: the spatial calculation model is adopted, the torsional coupling effect is included and the accidental eccentricity and two-way seismic effect are considered. The structural quality participation coefficient is controlled to be no less than 90%. Adjust the structural stiffness to make the torsional period ratio within 0.9 and control the structural torsional displacement ratio within 1.4. Properly increase the structural stiffness and reduce the inter story displacement angle of the structure under earthquake.

- (2) Local discontinuity of floor slab: the slab thickness around the opening is not less than 140 mm, and two-way and double-layer reinforcement is provided. And the reinforcement ratio is not less than 0.25%. At the same time, the calculation model in line with the actual stiffness change in the plane is adopted. During YJK calculation, the floor slab type is set as elastic membrane, the floor slab stress analysis is carried out for 2~4 floor, and the reinforcement design is checked according to the results.
- (3) Irregular lateral stiffness: The 4-storey floor slab at the sudden change of vertical shape is thickened to 150 mm. The floor slab thickness of adjacent 3 and 5 floors is not less than 130 mm, 3~5 double-layer two-way reinforcement, and the reinforcement ratio is not less than 0.25%. The calculation model for reviewing the actual stiffness change in the plane is adopted. During YJK calculation, the floor type is set as elastic membrane, the floor stress of 3~5 floors is analyzed, and the reinforcement design is verified according to the results.

Measures are taken to reduce the change of structural stiffness at the body retraction. The displacement angle between 4 layers of the bottom floor of the upper retraction structure is not greater than 1.15 times of the maximum displacement angle between layers of adjacent lower sections.

The seismic level of the vertical components around the tower of 2~5 stories is increased by one level, that is, the seismic level of the column is increased to two levels, and the seismic level of the shear wall is increased to one level.

4.3 Rule Judgment of Unit B

- (1) Torsional irregularity: when considering the specified horizontal force of accidental eccentricity, the maximum elastic horizontal displacement of the floor is greater than 1.2 times the average value of horizontal displacement at both ends of the floor.
- (2) Eccentric arrangement: the eccentricity between the mass center and the stiffness center of floors 1~3 is greater than 0.15.
- (3) Local discontinuity of floor slab: the effective width in X direction after opening of 2-story C-axis ~ E-axis and 3-story D-axis ~ E-axis floor slab is less than 50% of the typical width of floor slab.

Among them, (1) and (2) do not double calculate the irregular items, so there are two irregularities in unit B, which does not belong to out-of-code high-rise building.

4.4 Main Seismic Strengthening Measures of Unit B

- (1) Torsional irregular and eccentric arrangement: the spatial calculation model is adopted, the torsional coupling effect is included and the accidental eccentricity

and two-way seismic effect are considered. The structural quality participation coefficient is controlled to be no less than 90%. Adjust the structural stiffness so that the torsional period ratio is within 0.9, and control the structural torsional displacement ratio within 1.4 to ensure that the torsional stiffness of the structure is large enough.

- (2) Local discontinuity of floor slab: the slab thickness around the opening is not less than 140 mm, and two-way and double-layer reinforcement is provided. The reinforcement ratio is not less than 0.25% to strengthen the integrity of the floor slab. At the same time, the calculation model in line with the actual stiffness change in the plane is adopted. During YJK calculation, the floor slab type is set as elastic membrane and the floor slab stress is analyzed. The reinforcement design is checked according to the results to avoid shear failure of weak floor under large earthquake.

5 Conclusion

Based on the principle of seismic conceptual design and on the premise of meeting the building use function, the structural plane and facade layout of the structure are optimized. The reasonable structural system and calculation assumptions are adopted. The seismic strengthening measures for the weak parts of the structure are taken to ensure the bearing capacity and deformation capacity of the structure and meet the design requirements of safety, applicability and economy.

References

1. MOHURD (2004) Standard for classification of seismic protection of building constructions: GB 50223-2004. China Architecture & Building Press, Beijing
2. MOHURD (2012) Load code for the design of building structures: GB 50009-2012. China Architecture & Building Press, Beijing
3. MOHURD (2016) Code for seismic design of buildings: GB 50011-2010. China Architecture & Building Press, Beijing
4. MOHURD (2016) Technical standard for assembled buildings with concrete structure: GB/T 51231-2016. China Architecture & Building Press, Beijing
5. Tongji University (2013) Code for seismic design of buildings: DGJ 08-9-2013. Tongji University Press, Shanghai
6. ECADI (2018) Foundation design code: DGJ 08-11-2018. Tongji University Press, Shanghai
7. MOHURD (2010) Technical specification for concrete structures of tall buildings: JGJ 3-2010. China Architecture & Building Press, Beijing
8. MOHURD (2006) Technical points for special review of seismic fortification of out of gauge high-rise buildings: JZ [2006] No. 220. Ministry of Housing and Urban-Rural Development, PRC, Beijing
9. SMHUCAC (2014) Detailed rules for the implementation of seismic fortification management of transfinite high-rise buildings in Shanghai: HJG [2014] No. 954. Shanghai Municipal Housing and Urban-rural Construction Administration Commission, Shanghai

Open Access This chapter is licensed under the terms of the Creative Commons Attribution 4.0 International License (<http://creativecommons.org/licenses/by/4.0/>), which permits use, sharing, adaptation, distribution and reproduction in any medium or format, as long as you give appropriate credit to the original author(s) and the source, provide a link to the Creative Commons license and indicate if changes were made.

The images or other third party material in this chapter are included in the chapter's Creative Commons license, unless indicated otherwise in a credit line to the material. If material is not included in the chapter's Creative Commons license and your intended use is not permitted by statutory regulation or exceeds the permitted use, you will need to obtain permission directly from the copyright holder.



Finite Element Analysis of Reinforced Concrete Slab-Rectangular Column Connections Using ABAQUS



Yueqiao Jia and Jeffrey Chiang Choong Luin

Abstract Rectangular columns used in flat-slab structures run the risk of punching shear damage due to stress concentrations, especially when bending moments and vertical forces act together at the connections. Using the finite element analysis method, the existing experiments are numerically simulated using the 3D modeling software ABAQUS, and describe the cracking behavior of concrete using the concrete damaged plasticity model. The accuracy of the numerical simulation was calibrated by load–displacement curves and crack patterns using the experimental results. The study of the model was set up with different moment-to-shear ratios and outputs the trend of the average shear stress on the eccentric force side of the slab. The moment transfer coefficients are derived through the equation of ACI-318 and compared with the code values. A safe range of side length ratios is proposed to reduce the risk of punching shear damage from the use of rectangular columns. This provides a reference for practical design, but more experiments are needed to support the proposed recommendations.

Keywords Finite element method · Rectangular column · Moment transfer · Punching shear

1 Introduction

Flat-slab structures supported by rectangular columns are very common. Due to the high stresses near the columns, the slab-column connection may cause punching shear damage at the joint. Unlike square columns, the stresses around columns are uniformly distributed when the nodes are subjected to concentric forces. However, in the case of rectangular columns, the larger the column side length ratio (C_{\max}/C_{\min}),

Y. Jia (✉) · J. C. C. Luin

Faculty of Engineering, Built Environment and Information Technology, SEGi University, Kota Damansara, Kuala Lumpur, PJ, Selangor, Malaysia
e-mail: Yueqiao1993@gmail.com

J. C. C. Luin

e-mail: jeffreychiang@segi.edu.my

This is a U.S. government work and not under copyright protection in the U.S.; foreign copyright protection may apply 2023

Y. Yang (ed.), *Advances in Frontier Research on Engineering Structures*, Lecture Notes in Civil Engineering 286, https://doi.org/10.1007/978-981-19-8657-4_4

the more the stresses are concentrated near the short side of the column, as stated by Sagasetta et al. [1] and Oliveira et al. [2]. When the slab-column connection suffers the bending moment, the transmission of the moment in the slab increases the shear stress in the vicinity of the column. This will increase the risk of punching shear damage to the connection and make the slab less resistant to punching shear. This may result in the collapse of the structure, threatening human life and property.

In ACI-318 [3], when the connection is subjected to the combined action of vertical force and bending moment, the formula for calculating the shear stress on the critical section is Eq. (1). The critical section is specified as the perimeter position at one-half of the effective thickness of the slab from the surface of the column.

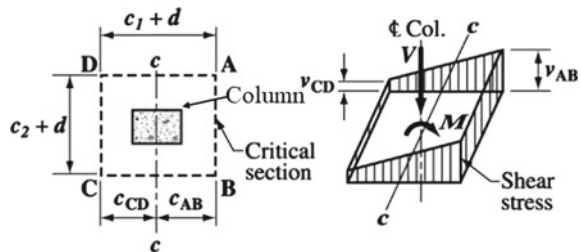
$$V_u = \frac{V}{b_0 d} + \frac{\gamma_v M x}{J_c} \tag{1}$$

where, V is the vertical shear force. b_0 is perimeter of the critical section, d is the effective depth of slab. M is the unbalanced bending moment, x is the distance from the centroid to the critical sections, and J_c is the polar moment of inertia. γ_v is the ratio of the bending moment transferred by the eccentric shear force to the total unbalanced bending moment, and calculated by Eq. (2). c_1 and c_2 are the side length of the column, as shown in Fig. 1.

$$\gamma_v = 1 - \frac{1}{1 + \frac{2}{3} \sqrt{\frac{c_1+d}{c_2+d}}} \tag{2}$$

In this paper, numerical simulation of the experiment of Teng et al. [4] with a slab-rectangular column connection was carried out using the finite element method. Three-dimensional modeling was performed using the commercial finite element analysis program ABAQUS. Taking the moment transfer coefficient specified in ACI-318 as the safe value, the safe range of the side-length ratio of the rectangular column was explored by changing the moment-to-shear ratio (M/V). According to the simulation results, it can provide a reference for the actual structural design, to reduce the risk of punching shear failure of rectangular column flat slab structure.

Fig. 1 Assumed distribution of shear stress from ACI-318



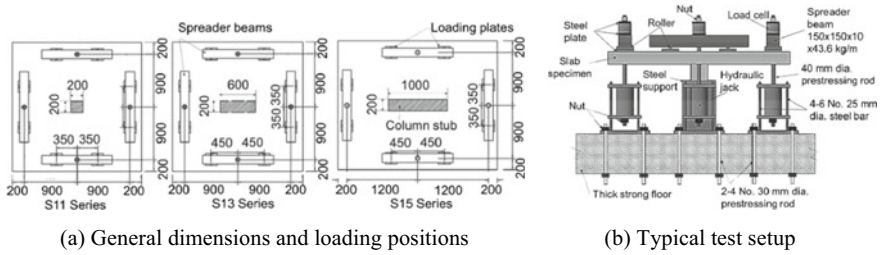


Fig. 2 Experimental settings of Teng S et al. test slabs

Table 1 Characteristics of the Teng S et al. test slabs

Specimen	Concrete	Flexural reinforcement			Dimensions	
	f_{cu}^a (MPa)	f_y (MPa)	ρ (%)	Layout of tensile reinforcement	Slab (m)	Column (m)
S11-139	140	501	1.39	$\Phi 16@118$	$2.2 \times 2.2 \times 0.15$	0.2×0.2
S13-143	142		1.43		$2.2 \times 2.2 \times 0.15$	0.2×0.6
S15-143	121		1.43		$2.7 \times 2.2 \times 0.15$	0.2×1.0

^a f_{cu} is the concrete cubic compressive strength

2 Test Specimens

Teng et al. [4] tested slab-rectangular column connections with three different column side length ratios, 1:1, 1:3, and 1:5 respectively. The center of the slab is fixed and the jack applies vertical forces on all four sides of the plate. As shown in Fig. 2b. The height of the column for all specimens is 200 mm. The concrete cover is 20 mm. The arrangement of all specimens with compressive reinforcement is $\Phi 10@260$. The geometry of the three slabs is shown in Fig. 2a. The specific information of specimens is shown in Table 1.

3 Finite Element Simulations

3.1 Modeling in ABAQUS

According to the experimental setup, the four sides of the slab are applied with vertical force by four jacks through the spreader beam. Therefore, eight shims are set on the slab through TIE, and the force application points are set on them by coupling. Figure 3 shows the boundary conditions for the connection of the column

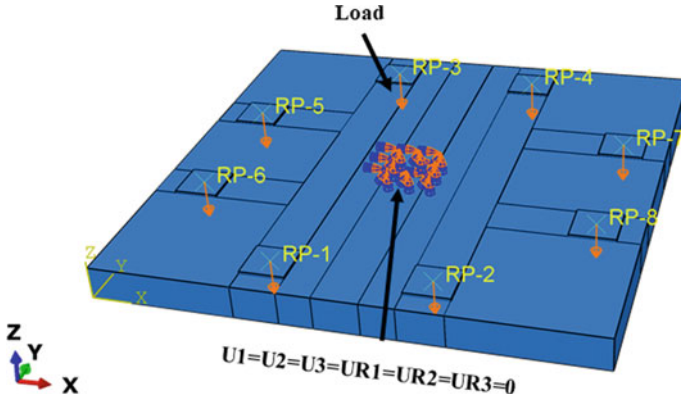


Fig. 3 Load and boundary conditions of the Teng S et al. specimen in ABAQUS

with an aspect ratio of 1. $U1 = 0$ means that the degree of freedom in the x-direction is restricted, $UR1 = 0$ represents that the degree of freedom of rotation in the x-direction is restricted, and 2 and 3 indicate the y and z-directions [5].

The concrete is simulated with an 8-node hexahedral linear reduction integral element (C3D8R) and the reinforcement is simulated with a 2-node truss unit (T3D2). The combination of the two is embedded, i.e., there is no relative slip. One of the most important steps in the finite element is to divide the mesh. To prevent hourglassing problems, the maximum size of the mesh is one-quarter of the slab thickness [5]. And the mesh size of this model is 37.5 (Fig. 6).

The experimental setup is to apply the concentric force to the specimens, while the purpose of this paper is to study the shear stress of the plate on the critical section of the rectangular column for different moment-to-shear ratios. Therefore, different M/V can be achieved by controlling the displacements applied at the force application points on the four sides of the slab.

3.2 Concrete Damage Plasticity Model

The ABAQUS finite element software used in this paper permits the user to use the concrete damage plasticity (CDP) model which can simulate the nonlinear behavior of concrete relatively accurately. The CDP model was first put forward by Lubliner et al. [6] and revised by Lee and Fenves [7]. The yield function, which describes the size of the yield surface shape, is represented by Eq. (3).

$$F = \frac{1}{1 - \alpha} \left(\bar{q} - 3\alpha\bar{p} + \beta(\epsilon^{pl}) \left\langle \hat{\sigma}_{\max} \right\rangle - \gamma - \left\langle \hat{\sigma}_{\max} \right\rangle \right) - \bar{\sigma}_c(\epsilon_c^{pl}) \quad (3)$$

where,

$$\alpha = \frac{(\sigma_{b0}/\sigma_{c0}) - 1}{2(\sigma_{b0}/\sigma_{c0}) - 1}, \quad 0 \leq \alpha \leq 0.5 \quad (4)$$

$$\beta(\varepsilon^{pl}) = \frac{\bar{\sigma}_c(\varepsilon_c^{pl})}{\bar{\sigma}_t(\varepsilon_t^{pl})}(1 - \alpha) - (1 + \alpha) \quad (5)$$

$$\gamma = \frac{3(1 - K_c)}{2K_c - 1}, \quad 0.5 < K_c \leq 1 \quad (6)$$

In Eq. (3), \bar{q} is the Mises equivalent effective stress, and \bar{p} is the hydrostatic pressure stress. α is given by Eq. (4), where $(\sigma_{b0}/\sigma_{c0})$ is the ratio of the concrete biaxial compressive strength and the uniaxial compressive strength. This ratio of different concrete types and strengths is different. The ratio made by Shang et al. [8] at the laboratory of the Dalian University of Technology in China is probably in the range of 1.06–1.48. ABAQUS set it to the default value of 1.16. The function $\beta(\varepsilon^{pl})$ is expressed by Eq. (5), which exists when the algebraically maximum principal effective stress ($\hat{\sigma}_{max}$) is positive. In the CDP model, the effective stress is $\bar{\sigma}_c = E_0\gamma(\varepsilon - \varepsilon^{pl})$. The Macauley bracket $\langle \bullet \rangle$ is calculated as $x = \frac{1}{2}(|x| + x)$. In this equation, $\bar{\sigma}_c(\varepsilon_c^{pl})$ and $\bar{\sigma}_t(\varepsilon_t^{pl})$ is the effective compressive and tensile cohesion stresses, respectively. The parameter γ is influence the shape of the yield surface. It appears when the maximum principal effective stress ($\hat{\sigma}_{max}$) is negative. K_c defines the shape of the yield surface in the deviatoric plane and it is the ratio of the tensile to the compressive meridian. The difference in its value has little effect on the simulation results as verified by Genikomsou [9]. ABAQUS set it to the default value of 2/3.

The flow rule expresses the direction of the plastic strain increment. In the CDP model, the flow potential function is defined by Eq. (7).

$$G(\sigma) = \sqrt{(\varepsilon\sigma_{t0} \tan \psi)^2 + \bar{q}^2} - \bar{p} \tan \psi \quad (7)$$

where ε represents the ratio of the plastic potential function close to the asymptote, that is, the eccentricity. It defaults to 0.1 in ABAQUS. The σ_{t0} is uniaxial tensile stress in concrete. ψ is the dilation angle that expresses the direction of the plastic strain increment vector. The larger the dilation angle, the more brittle the concrete. The recommended values in the ABAQUS user manual are 30–45°. The value of the dilation angle in this paper needs trial calculation and was finally determined to be 40°, the calibration results are presented in Sect. 4. \bar{q} and \bar{p} are introduced in Eq. (3).

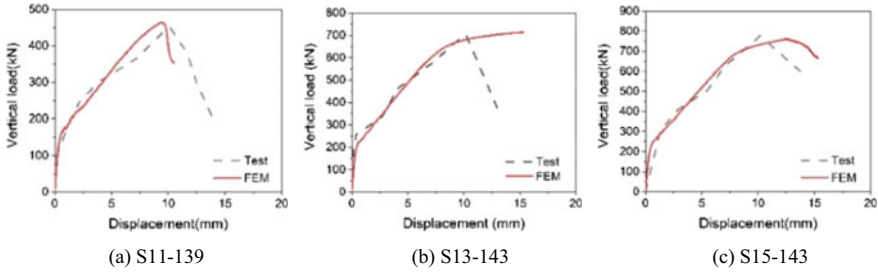


Fig. 4 Load–displacement response for experimental versus FEM of Teng S et al. slabs

4 Finite Element Analyses Results

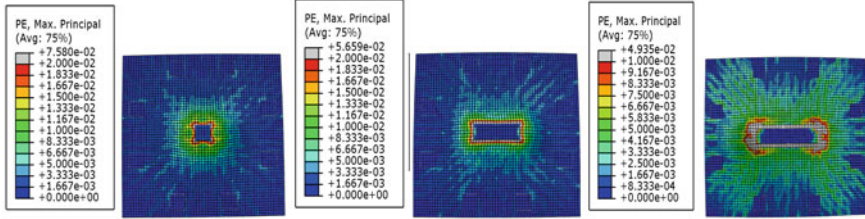
4.1 Load–Deflection Response

Figure 4 shows the load–displacement curves of the results of the three simulated specimens compared with the test results. The finite element model (FEM) results match the experimental values, both for stiffness and ultimate load. The experimental values of ultimate loads for the three samples S11-139, S13-143, and S15-143 are 454 kN, 718 kN, and 776 kN, respectively, and the numerical simulation results are 463 kN, 712 kN, and 757 kN, respectively. The ratios of experimental to simulated values are 0.98, 1.00, and 1.09, respectively. Therefore, the numerical simulation results are desirable.

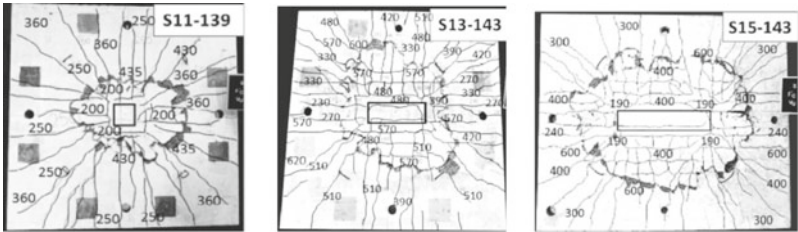
4.2 Crack Pattern

Figure 5 shows the ABAQUS post-processed crack images and experimental photos. Since the numerical simulation is an ideal state, the cracks are symmetrical patterns when the same size of the load is applied to all four sides of the slab. However, the experimental specimens may show the randomness of cracks due to errors in equipment or inhomogeneity of concrete. Therefore, the comparison of the results will not match exactly, but the direction of crack development is the same for all.

From the comparison results of the load–displacement curves with the crack patterns, it can be concluded that the accuracy of this numerical simulation is satisfactory. Therefore, the magnitude of the load applied to the four sides of the plate can be varied so that the study of the shear stress of the plate under different moment-to-shear ratios can be carried out.



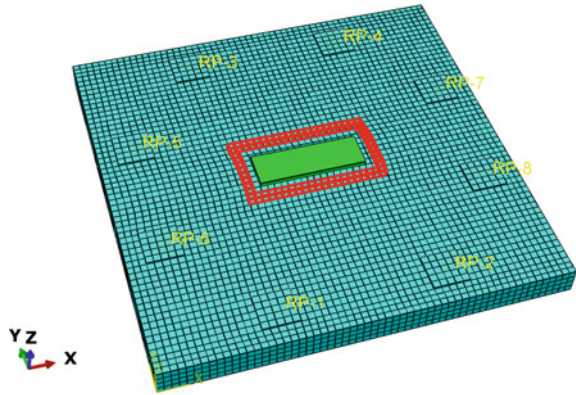
(a) Simulation results in ABAQUS



(b) Experiment photo

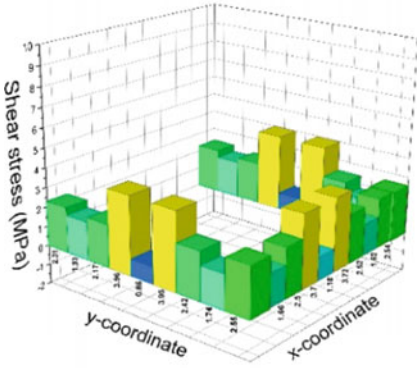
Fig. 5 Comparison of cracks patterns of S11-139, S13-143 and S15-143 between experiment and ABAQUS cloud image of Teng S et al. slabs

Fig. 6 Location of the output shear stress in ABAQUS

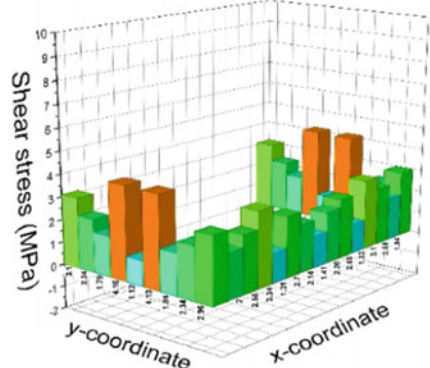


4.3 Average Shear Stress in the Critical Section

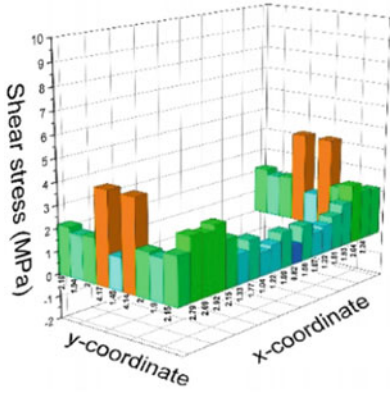
The shear stress used in ACI-318 is in the critical section. For a clear view, the red part of Fig. 6 shows the location of the critical section, i.e., half the effective plate thickness from the column (green part). Figure 7 displays the distribution of shear stress in the critical section. For a more complete comparison, a simulation of the slab with a column side length ratio of 1:2 is added (Fig. 7b). From Fig. 7, it can be seen that the larger the ratio of the column side length (C_{max}/C_{min}), the more the stress is concentrated near the short side, which again confirms the results of previous studies.



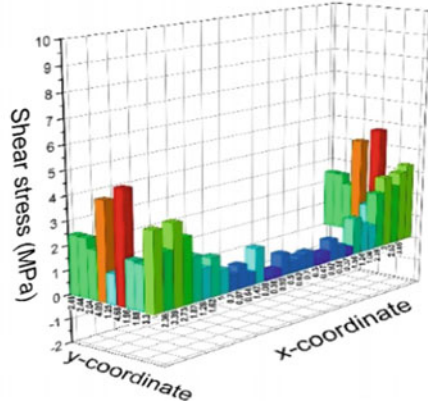
(a) S11-139



(b) S12-143



(c) S13-143



(d) S15-143

Fig. 7 Shear stress in the critical section of the slabs by Teng et al.

Relatively large loads are applied to one side of the plate and small loads of the same size are applied to the other three sides to achieve different M/V effects. The shear stress on the critical section on the eccentric force side is recorded, resulting in the trend diagram shown in Fig. 8. When M/C_{min} , the shear stress is positively correlated with M/V . When $M \perp C_{min}$, the shear stress has a slightly decreasing trend with the increase of M/V . The average shear stress on the critical section of the slab-square column connection on the eccentric force side has an approximately constant trend.

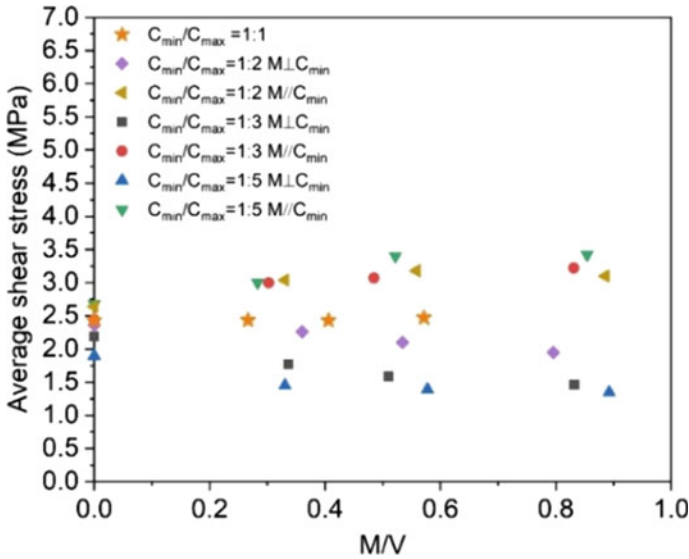


Fig. 8 Average shear stress versus M/V for columns with different side length ratios

4.4 Coefficient of the Bending Moment Transferred by Eccentric Shear

The case of different column side length ratio

Substituting the shear stress in Fig. 8 into Eq. (1) and deriving the value of γ_v , and summarizing it into Fig. 9. When $M \perp C_{min}$, the moment transfer coefficients of slabs with different column side length ratios have a similar trend with the increase of M/V. The code values calculated from Eq. (2) of ACI-318 for the cases of column side length ratios of 2, 3, and 5 are 0.34, 0.31, and 0.26, respectively. Therefore, it can be seen from Fig. 9a that none of the simulation results exceed the code values, so in the actual design, the moment transfer coefficient in the case where the bending moment is perpendicular to the short side of the column can follow the value calculated by the code formula.

When $M // C_{min}$, as can be seen in Fig. 9b, they all show an increasing trend with the increase of M/V. The dashed lines indicate the code values, and the dashed lines of the same color correspond to the dots for the same case. Thus only the slab with a column side length ratio of 2 does not exceed the code value. The simulation results for the case of the column's $C_{max}/C_{min} = 5$ are out of range and therefore not shown here.

The case of different reinforcement ratio of S13

Because when M/V is relatively small, the γ_v of the slab with column side length ratio of 3 and reinforcement ratio of 1.43% are within the specification value, as in Fig. 9b. Therefore, the reinforcement ratio of the S13 slab is changed, resulting in the

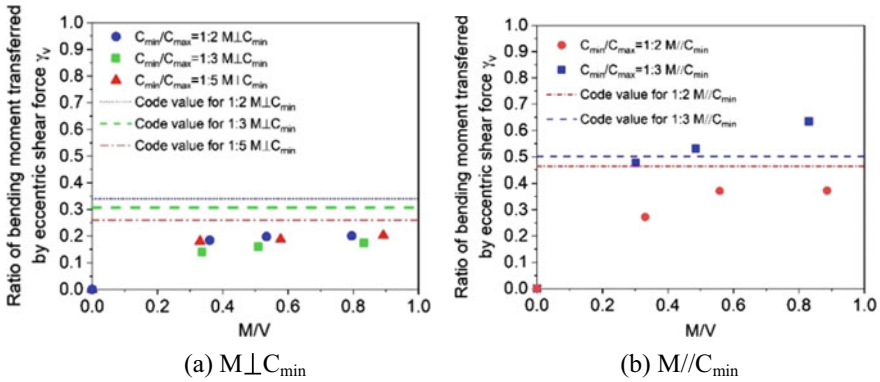
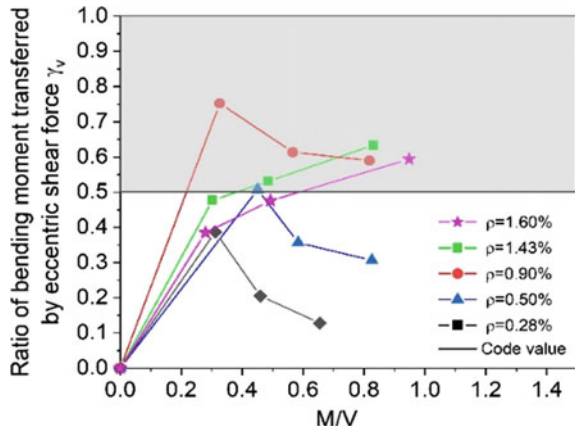


Fig. 9 M/V versus moment transfer coefficient for different column side length ratio slabs

results shown in Fig. 10. Except for the slab with $\rho = 1.6\%$ which is a supplementary model to this paper, the other four S13 slabs with different reinforcement ratios are the experiment specimens of Teng et al. The moment transfer coefficient trends were derived by simulating these five slabs at different M/V . For the case of column side ratio of 3, the ACI formula (Eq. (2)) calculates γ_v as 0.5. Therefore, the gray part in Fig. 10 is the region where the code value is exceeded. It can be seen that only the slabs with reinforcement ratios less than 0.5% are within the specification values at any M/V .

Fig. 10 M/V versus moment transfer coefficient for S13 slabs with different reinforcement ratios



5 Conclusions

The finite element model created in ABAQUS was used to analyze the punching shear resistance of the slab-rectangular column connection based on the setup of the existing experiments. The concrete damage plasticity model was used to simulate the nonlinear characteristics of concrete. The accuracy of the simulation can be demonstrated by comparing the experimental and simulated load–displacement curves and crack patterns. The shear stress on the critical section is output by post-processing with ABAQUS to obtain the distribution law of shear stress when the plate is subjected to concentric forces. As the ratio of the long and short sides of the column increases, the more the shear stress is concentrated near the short side of the column. By controlling the loads on the four sides of the slab to achieve different M/V , the results calculated using the equation of ACI-318 summarize the trend of shear stress on the eccentric force side, and the magnitude of the moment transfer coefficient for comparison with the code value.

According to the results, as shown in Sect. 4.4, for the designers' reference, the side length ratio of the columns used should preferably not exceed 2. When columns with a side length ratio of 3 have to be used due to practical conditions, the reinforcement ratio of the slab should not exceed 0.5%. Since only one experiment is simulated in this paper, more experiments are needed to support this proposal. The experiments on the rectangular column in the database are yet to be supplemented, and more experiments on it should be designed in the future to improve the study of the performance of rectangular columns.

References

1. Sagaseta J, Tassinari L, Fernández RM, Muttoni A (2014) Punching of flat slabs supported on rectangular columns. *Eng Struct* 77:17–33
2. Oliveira DR, Regan PE, Melo GS (2004) Punching resistance of RC slabs with rectangular columns. *Mag Concr Res* 56(3):123–138
3. ACI Committee 318 (2019) Building code requirements for structural concrete and commentary. American Concrete Institute, Farmington Hills, MI
4. Teng S, Chanthabouala K, Lim DTY, Hidayat R (2018) Punching shear strength of slabs and influence of low reinforcement ratio. *ACI Struct J* 115(1):139–150
5. ABAQUS Analysis user's manual 6.10-EF (2010) Dassault systems Simulia corp., Providence, RI, USA
6. Lubliner J, Oliver J, Oller S, Onate E (1989) A plastic-damage model for concrete. *Int J Solids Struct* 25(3):299–326
7. Lee J, Fenves GL (1998) Plastic-Damage model for cyclic loading of concrete structures. *J Eng Mech* 124(8):892–900
8. Huaishai S, Yupu S, Lusheng Y, Haiming S (2012) Summary of research on the biaxial compressive strength of different types of concrete. *Spec Struct* 05:18–22
9. Genikomsou A (2015) Nonlinear finite element analysis of punching shear of reinforced concrete slab-column connections. PHD Thesis, University of Waterloo, Canada

Open Access This chapter is licensed under the terms of the Creative Commons Attribution 4.0 International License (<http://creativecommons.org/licenses/by/4.0/>), which permits use, sharing, adaptation, distribution and reproduction in any medium or format, as long as you give appropriate credit to the original author(s) and the source, provide a link to the Creative Commons license and indicate if changes were made.

The images or other third party material in this chapter are included in the chapter's Creative Commons license, unless indicated otherwise in a credit line to the material. If material is not included in the chapter's Creative Commons license and your intended use is not permitted by statutory regulation or exceeds the permitted use, you will need to obtain permission directly from the copyright holder.



Rail Surface Defect Detection Method Based on Deep Learning Method with 3D Range Image



Geng Ming, Bo Zhou, Xiaohua Luo, Ren Ling, and Mingxiang Zhou

Abstract In the methods of using images for detecting surface defects of rails, the interaction such as light, stains, and water stains will cause false alarms. This paper proposals a method to detect surface defects of rails using 3D range line scan cameras combined with deep learning. By using the 3D range camera to acquire the information and 2D image information, and optimizing The original internet neural network structure, combined with the channel attention mechanism, a twin unet & 3D+ neural network model is proposed. First, the required database was established by using the 3D range camera, and then the comparison experts provided that the neural network proposed in this paper can effectually eliminate false alarms caused by light, Stains and water stains compared with other neural networks, and effectually promoted the rail surface. The correct rate of default detection.

Keywords Rail surface defects · 3D line scan camera · Twin Unet & 3D+ neural network

1 Introduction

Rail surface defects mainly refer to, Due to the wheel-rail pressure and centrifugal force of high-speed trains, the rail contact surface will be scratched, fallen off, blocks and other problems. If it is not rectified and polished at this time, after further wear, it may cause vicious time such as rail breakage, which will eventually lead to train safety accidents.

The traditional rail defect detection method is mainly through ultrasonic detection method, through the probe as the medium to detect the rail surface and internal defects [1]. Although the inspection items of rail include the defects on the rail surface and

G. Ming (✉) · B. Zhou · X. Luo · M. Zhou
China Railway Siyuan Survey and Design Group Co. LTD., Wuhan, China
e-mail: mynameisdc@yeah.net

R. Ling
Ningbo Rail Transit Group Co., Ltd. Smart Operation Branch, Ningbo, China
e-mail: sclead315@yeah.net

This is a U.S. government work and not under copyright protection in the U.S.; foreign copyright protection may apply 2023

Y. Yang (ed.), *Advances in Frontier Research on Engineering Structures*, Lecture Notes in Civil Engineering 286, https://doi.org/10.1007/978-981-19-8657-4_5

inside the rail, the inspection efficiency is greatly discounted because of the need for the probe to move for inspection. At the same time, due to the limitation of the probe, the speed is often slow in the inspection process.

Compared with the traditional ultrasonic method to detect rail defects in service, Chen et al. [2] proposed to use image method to detect rail surface defects, and locate the defect position by finding the relatively large change area in the image pixel histogram. However, this method has higher requirements for illumination environment, and it requires that the refraction and reflection of rail surface are basically consistent and will not change too much, so it is difficult to meet the requirements of engineering application. Jin et al. [3] In order to solve the problems of inconsistent reflection on rail surface and large change of illumination in rail shooting environment, a special line scanning camera was used for shooting. At the same time, deep learning method is used for detection. Compared with the previous histogram image method, this method has higher accuracy, and can better adapt to different ambient light and rails with different reflection and refractive index. However, in order to ensure that the image will not appear jitter and other problems, and also to ensure the location and recognition effect of rail surface defects by neural network, its detection speed is relatively slower and its efficiency is poor. Among them, the most important thing is that there are many stains, dirt and other attachments on the surface of in-service rails due to the site environment, which often leads to false positives in this way.

In order to solve the problem of false alarm caused by rail surface stains and slow processing speed caused by neural network method, this paper proposes to use 3D camera to photograph rail surface, and at the same time, use the optimized neural network structure to detect rail surface defects.

2 Background

2.1 Defect Detection Based on Deep Learning Method

Under the background of using deep learning method to solve practical engineering problems, many successful deep learning frameworks have been put forward one after another, and have been applied to vehicle defect detection [4], pantograph wear detection [5], railway bridge bolt loss detection and railway irregularity, etc. Through the above engineering practice, it has been proved that compared with the manual detection method or the original detection method, the defect detection based on deep learning method has a more obvious improvement in detection accuracy.

The work of others has completely verified that the neural network method of continuous deep learning has a relatively good detection effect on rail surface defects, However, there is a large consumption of time and cost, and there may be some false positives. Therefore, further improvement is needed to improve the detection

accuracy, and further reduce the time and cost required for rail surface defect detection and improve the detection efficiency.

2.2 3D Images

Compared with 2D images, 3D images are imaged in the form of structured ray scanning. In addition to the normal 2D image, the output of the 3D camera also contains data in the depth direction. Not only that, The 3D camera uses a laser transmitter with a specific band as the light source in image acquisition, It effectively avoids the interference of external ambient light, can effectively adapt to different illumination environments, and ensures that rail surface images with good imaging effect and relatively stable image quality can be obtained, which lays a good image foundation for rail surface defect detection.

2.3 Net Network Architecture

Unet [6] network structure was originally used for segmentation of lesions in medical images, and the whole network structure adopted encoding–decoding [7] network structure. Experiments show that the network structure of Unet neural network coding and decoding can extract the structural information and spatial information of objects in images relatively effectively. At the same time, because the network structure is relatively simple, the network parameters are relatively few. Therefore, compared with some complex networks such as DeepLabV3 [8], DeepLabV3+ [9] and other neural network structures, the Unet network structure needs less processing time and higher efficiency, and has the value of engineering implementation.

But for rail surface defect detection, not only the types of defects are different, but also the morphological characteristics of the same defect are different, and there is a big gap between classes. Therefore, based on the analysis of rail surface defects and the images and depth data taken by 3D camera, this paper proposes a twin Unet-3D+ neural network framework to extract and alarm rail surface defects. Finally, compared with the previous rail surface defect detection methods, the neural network framework proposed in this paper has better accuracy and higher efficiency, and has stronger engineering practicability.

3 Twin Unet & 3D+ Neural Network

In order to solve the problems of rail surface defect recognition, such as leak recognition, long processing time and difficulty in real-time detection, twin Unet-3D+ neural network is proposed in this paper. In this network, the original image data collected by

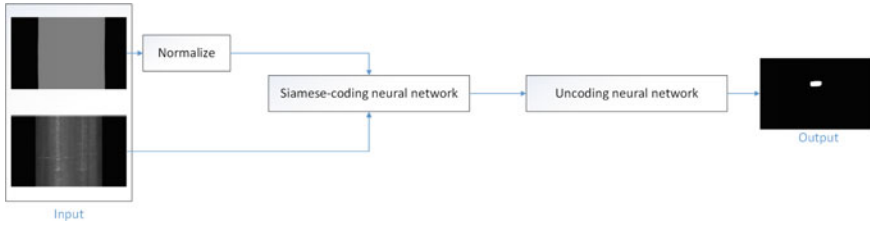


Fig. 1 Flow chart of overall algorithm

3D camera and the depth direction data are jointly input into the network. Compared with 2D cameras, 3D cameras have the following characteristics:

- (1) Collected data, such as stripping, falling block, crushing and other rail surface defects, will not only be reflected in 2D images, but also show differences with normal rail surface in depth direction. But for the surface water stains, stains and other differences, although the 2D image with other rail surface area there is a big difference, but in the depth direction of the 3D image with the normal rail surface area there is no obvious difference.
- (2) 3D cameras can only sense the specific band of light emitted by their lasers, so they can avoid the spot area formed on the image by the reflected light caused by external ambient light and smooth rail surface. Like stains and water stains, if we only rely on 2D images for recognition, it will often cause false recognition of defects and lead to false alarms. For 3D cameras, the external ambient light will not have a great impact on the image quality, whether it is for 2D images or images in depth direction, so as to ensure that real and reliable rail surface data can be obtained.

Based on the above input mode through the combination of original 2D image information and depth image information, not only the defect part can be effectively located, but also the light spot, water stain, dust and the like that may cause false alarm can be effectively eliminated, and more accurate rail surface defect alarm information can be obtained. The overall flow chart of the algorithm is shown in Fig. 1.

3.1 Overall Network Framework

Aiming at the problems existing in rail surface defect detection, this paper proposes to use twin Unet-3D+ neural network framework to solve them. The overall network framework is shown in Fig. 2.

As far as the original input image depth information is concerned, it mainly reflects the relative distance information between the photographed object and the camera position. At the same time, even if there are defects such as peeling and falling off the rail surface, its depth will not have a huge deviation, so it is necessary to

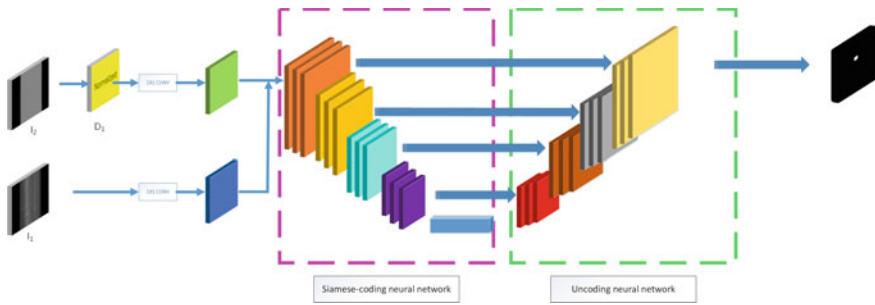


Fig. 2 Overall network framework

carry out preliminary normalization before inputting into the neural network, and the normalization method is shown in Sect. 2.2.1.

At the same time, in order to ensure the high unity of 2D image information and depth information, the encoder extraction information module at the front end of UNET is modified to be a twin [10] coding information module, which ensures that the feature information of 2D information and depth information extracted by the network has a high degree of consistency and reduces the discrete degree of 2D feature information and depth feature information as much as possible.

For the decoding information module, besides the information extracted by the preceding twin coding information module, it is necessary to further enhance the difference between depth information and 2D image information in the whole network. Therefore, in this layer, in addition to the feature information extracted by the previous twin coding information module, the extracted 2D feature information and depth information are further differentiated and input into the decoding network at the same level. The specific method is shown in Sect. 2.3.

As far as the loss function is concerned, You can't simply cross-bar the difference between the output image and Ground Truth, Instead, we should further improve the difference and unity between beam depth image and 2D image and the relationship between input and output to further optimize the back propagation link of the network, so as to improve the defect segmentation effect of the network and accelerate the convergence and training speed of the network.

3.2 Twin Coded Information Module

The network structure of twin coded information modules is shown in Fig. 3.

In addition to the normal 2D information, depth information is also used as the input of the whole module into the twin coded information module. But before input to the network, it needs to be normalized through Batch-Normalized layer to ensure that the depth information can be fully applied in the network, and at the same time,

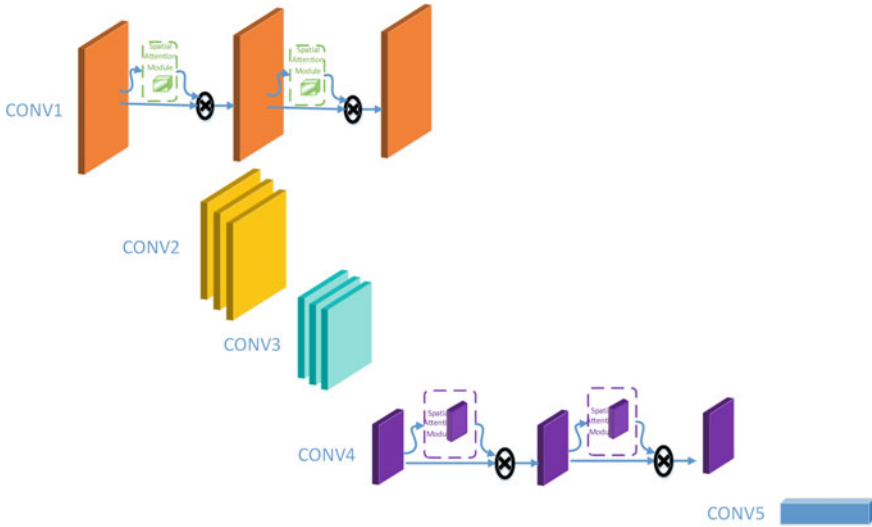


Fig. 3 Twin coding information module

the original depth value will not be far larger than the pixel value of the 2D image, which will lead to the coverage of the 2D image information.

As shown in Fig. 3, in order to ensure that the convolution network can extract consistent information content in the spatial position and object structure in I1 and D1 images, the twin network structure is mainly used for information extraction in the preceding network CONV1-CONV3 network structure. At the same time, in order to further emphasize the spatial position information and object structure information, the spatial attention mechanism is further adopted in the twin network structure of this level to extract its spatial information.

On the basis of the consistent extraction of image spatial position information and object structure information by the network in the preceding item, CONV4 to CONV5 in the latter item mainly extract feature information, so twin network structure is no longer used. On the premise that the spatial position information is consistent with the object structure information, the neural network with channel attention mechanism [11] is mainly used to extract the information. It can effectively ensure that the depth information and the original 2D image information can be fully fused and applied.

Depth information normalization layer

Depth information normalization layer is mainly used to normalize the original depth information image input into neural network and extract simple information. In this layer network, firstly, the normalized information matrix of depth information images needs to be obtained by the following formula 1.

$$f_{\text{Normalize}}(x, y) = \frac{f_{\text{org}}(x, y) - f_{\text{min}}}{f_{\text{max}} - f_{\text{min}}} \tag{1}$$

where X and Y represent the horizontal and vertical coordinates of depth information and $f_{\text{org}}(x, y)$ represent the size of its original depth information. f_{max} and f_{min} represents the maximum and minimum value of depth information in the whole depth information image; $f_{\text{Normalize}}(x, y)$ represents the normalized depth information.

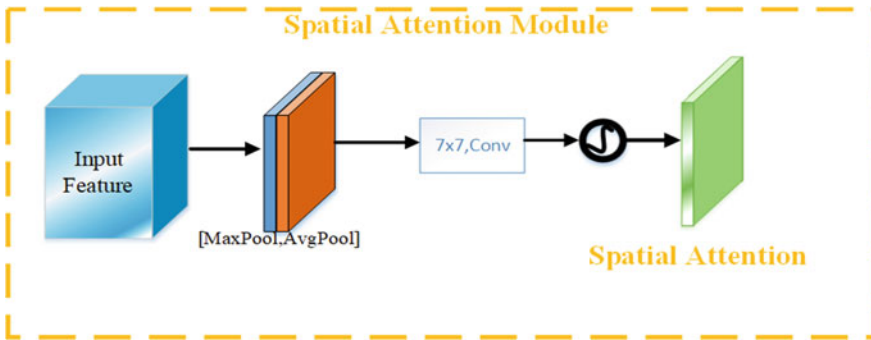
In addition to the linear normalization formula of Formula 1, the 3×3 convolution neural network is used to extract the normalized feature information and input it to the subsequent twin network.

Spatial Attention and Channel Attention Mechanisms

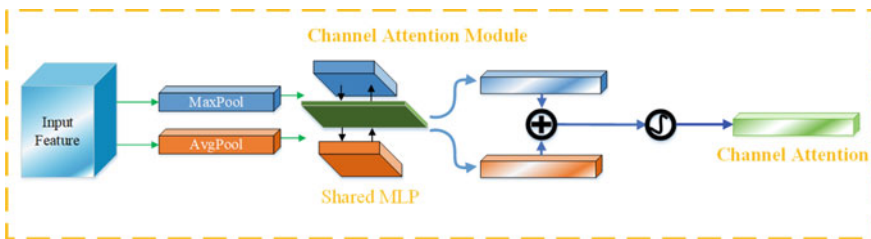
As shown in Fig. 4, it is the spatial attention and channel attention module. The main principle of this module is to evaluate the key information of the image in spatial domain and channel domain, and assign different weights.

The main uses of the above two attention mechanisms are divided into the following two aspects:

- (1) Spatial attention module: As shown in Fig. 4a, the main purpose is to ensure a higher correspondence to the rail area during convolution. That is to say, it keeps a high response level and a high weight for the rail spatial area, and ensures



(a) Spatial Attention Module



(b) Channel Attention Module

Fig. 4 Spatial attention and channel attention mechanism

that the twin network can extract better spatial position information and object structure information from the 2D information image and depth information image of the rail area.

- (2) In this module, the feature matrix input into the network is compressed at the channel level by using Average pooling and max pooling. Then, the average pooling matrix and the feature matrix output from the maximum pooling matrix are Concat operated, and then a convolution kernel with the size of 7×7 and Sigmoid activation layer are used to ensure that the final output feature matrix is consistent with the input feature matrix in dimension.
- (3) Channel attention module: As shown in Fig. 4b, the main purpose of this module is to better fuse the information of different channels of the feature matrix input into this module, and ensure the integration and extraction of depth information and 2D image information.

In this module, the maximum and average pooling operations are performed on the input feature matrix, and the one-dimensional maximum pooling matrix and average pooling matrix are obtained. The global average pooling matrix mainly reflects the information of each element in the original input matrix, while the maximum pooling matrix mainly responds to the information of elements with greater weight. After that, the elements in the corresponding positions in the two pooled matrices are activated by sharing multi-layer perceptrons, and a one-dimensional channel attention weight output is obtained.

The weight is output and multiplied with the original feature matrix. On the basis of not affecting the dimensions of the original feature matrix, the information weights in different dimensions are strengthened to improve the network training speed and the fusion degree of key depth information and 2D image information.

3.3 Decoding Information Module

As shown in Fig. 2, after the depth information and 2D image information input to the neural network are deeply fused and extracted by the encoded information module, it is necessary to further restore the information to the original image size, so as to obtain the size and position of rail surface defects.

In this module, the horizontal connection part in the original UN is improved. The channel attention mechanism is mainly added to each layer of network. The original horizontal single input mode is changed to the joint input of depth information feature matrix and 2D information feature matrix. In addition, the channel attention mechanism is used to further enhance the weight of different channels, so as to ensure that the network can achieve better information fusion effect between depth information and 2D information.

3.4 Loss Function

Because depth information is used to identify rail surface defects in network input and network flow, it is impossible to simply feed back the difference between network output and label data as loss to the network mentioned in the preceding paragraph. In the process of measuring the loss, it is necessary to further consider the influence of depth information on the network. Therefore, the following formula 2 pairs are mainly used as the loss function of this network.

$$f_{loss} = \frac{\sum_{i=0}^{n-1} (Y_i^D \cdot Y_i^{GT} - Y_i^O)^2}{n} \tag{2}$$

Y_i^D represents the normalized depth data value; Y_i^{GT} represents a valid label information value; Y_i^O represents the output probability diagram of neural network. Firstly, Y_i^D point multiplication is carried out on and Y_i^{GT} . Then, Y_i^O the mean square difference is obtained by combining the output of neural network as the loss function of neural network for back propagation.

4 Experiment and Analysis

On the basis of the above twin Unet-3D+ neural network, further verification and comparative experiments are carried out to prove the effectiveness of the neural network proposed in this paper.

4.1 Experimental Environment

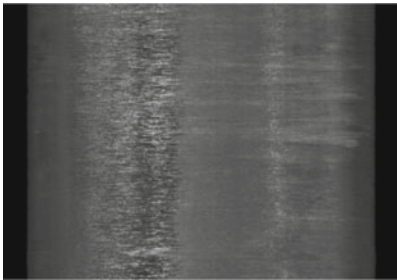
In order to ensure the repeatability of the experiment, the experimental environment is explained now. The experimental environment is: processor IntelE5-2670, memory 8G, graphics card GTX1080Ti, video memory 12G, operating system Windows10 Professional Edition, and deep learning framework PyTorch. At the same time, in order to improve the convergence speed of the model, some basic parameters of network training are shown in Table 1.

Table 1 Basic parameter setting of neural network

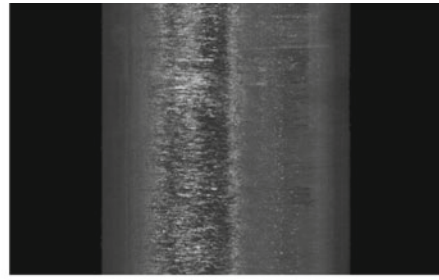
Parameter name	Parameter value	Parameter name	Parameter value
Learning rate	10e-5	Learning momentum	0.9
Iterative algebra	400	Batch size	20
Optimization mode	Adam	Learning strategy	Steplr

Table 2 Basic parameters of camera

Camera name	Accuracy of camera in X direction	Accuracy of camera in Z direction	Acquisition frequency
Kearns 3D line scanning camera	0.5 mm	0.1 mm	1600 Hz



(1) Normal Rail Surface



(2) Worn Rail Surface

Fig. 5 2D rail surface image

In this network, the depth image and 2D image data are used as the input of neural network to judge the rail surface defects. Therefore, the rail surface defect data set used for training and testing is mainly collected by Keens 3D line scanning camera. The main parameters of the camera are shown in Table 2.

4.2 Establishing a Dataset

The accuracy index of the collected data needs to ensure that the distance between the camera and the photographed object, that is, the rail surface, needs to be between 300 and 500 mm. Its 2D image data is shown in Fig. 2 (Fig. 5).

It can be seen from the figure relatively intuitively that the collected rail surface images can clearly see the rail surface texture, rust and stains, etc., which can fully meet the image quality requirements for rail surface defect recognition.

4.3 Comparative Experiment

Comparative experimental standard for defect detection

The objective, accurate and unified evaluation criteria of the algorithm can help people better compare the results of the algorithm and promote the improvement of the effect of the algorithm. For segmentation algorithms, MIoU (Mean Intersection

over Union) is mainly used for comparative evaluation. As shown in Formula 3.

$$MIoU = \frac{1}{k+1} \sum_{i=0}^k \frac{p_{ii}}{\sum_{j=0}^k p_{ij} + \sum_{j=0}^k p_{ji} - p_{ii}} \quad (3)$$

In Formula 3, p_{ij} represents the number of real values i and predicted j , and $k+1$ is the number of classes (including empty classes). p_{ii} is the true positive. p_{ij} is a false positive and p_{ji} is a false negative, respectively.

On the premise of clear comparison experimental standards, the neural network proposed in this paper is compared with several popular neural networks. The data set of other methods mainly uses 2D data collected by camera as training set for training.

Experiments show that compared with other methods, the neural network method proposed in this paper is not only better in detection effect, but also better than other neural networks. At the same time, compared with other networks, the time required for detection is less, which is more in line with the actual needs of engineering.

Comparative experiment of defect detection

As shown in Table 3, the comparison effect between this method and other methods on objective indicators of MIoU.

It can be seen that compared with other detection methods, the method proposed in this paper has better performance and actual detection effect on MIoU.

It can be seen intuitively from Table 3 that compared with other methods, the index of MIoU has been greatly improved.

At the same time, in order to further explain the influence of eliminating rail surface stains on network recognition effect, this paper further recalculates p_{ij} of the MIoU formula, and the recalculated formula is shown in formula (4).

$$MIoU_{(False\ Positive)} = \frac{1}{k+1} \sum_{i=0}^k \frac{\sum_{j=0}^k p_{ij}}{\sum_{j=0}^k p_{ij} + \sum_{j=0}^k p_{ji} - p_{ii}} \quad (4)$$

The results are shown in Table 4.

Table 3 MIoU contrast experiment (Unit:%)

Method	MIoU
FCN	55.2
Unet	58.3
Unet++	58.5
DeeplabV3	68.7
Deeplabv3+	70.9
DPLBD	33.5
Ours	80.3

Table 4 MIOU (False Positive) contrast experiment (Unit:%)

Method	MIOU
FCN	38.4
Unet	40.3
Unet++	44.6
DeeplabV3	25.8
Deeplabv3+	28.2
DPLBD	60.5
Ours	10.3

Table 5 Comparison of elapsed time (unit: ms)

Method	CostTime
FCN	65.9
Unet	35.5
Unet++	74.5
DeeplabV3	786.6
Deeplabv3+	503.4
DPLBD	87.6
Ours	40.3

It can be seen that compared with other neural networks which only use 2D image information as network input, the twin Unet & 3D+ neural network proposed in this paper has better performance in reducing the false positives due to non-defects such as rail surface stains, water stains and oil stains, and can effectively reduce the workload of manual review.

As shown in Fig. 6, the detection results of some rail surface defects are compared and displayed.

In addition to the comparison of rail surface defect detection results, this paper also compares the time required for each neural network to process single image data, as shown in Table 5.

4.4 Experimental Analysis

Through the above-mentioned comparative experiments, it is obvious that the network proposed in this paper has a better effect on rail surface defect detection than other algorithms that only use 2D images as input. Through the analysis of MIOU and MIOU (False Positive) data, the improvement of the detection effect of neural network proposed in this paper is mainly due to the effective reduction of the probability of false recognition by combining 2D image information with depth information. At the same time, for the real rail surface defects. By means of

"strengthening" depth image information, Compared with the previous network, it has better segmentation effect in edge details, By further judging these information, we can determine whether the defects are rail head fracture, large-scale block falling, etc., and then transform the surface defect information into rail defect hazard grade information, thus helping public works maintenance personnel to determine the emergency degree of maintenance and ensure the safety of train running (Fig. 6).

In addition to relatively good detection results, the neural network proposed in this paper has a good performance in detection time. This is mainly due to the selection of

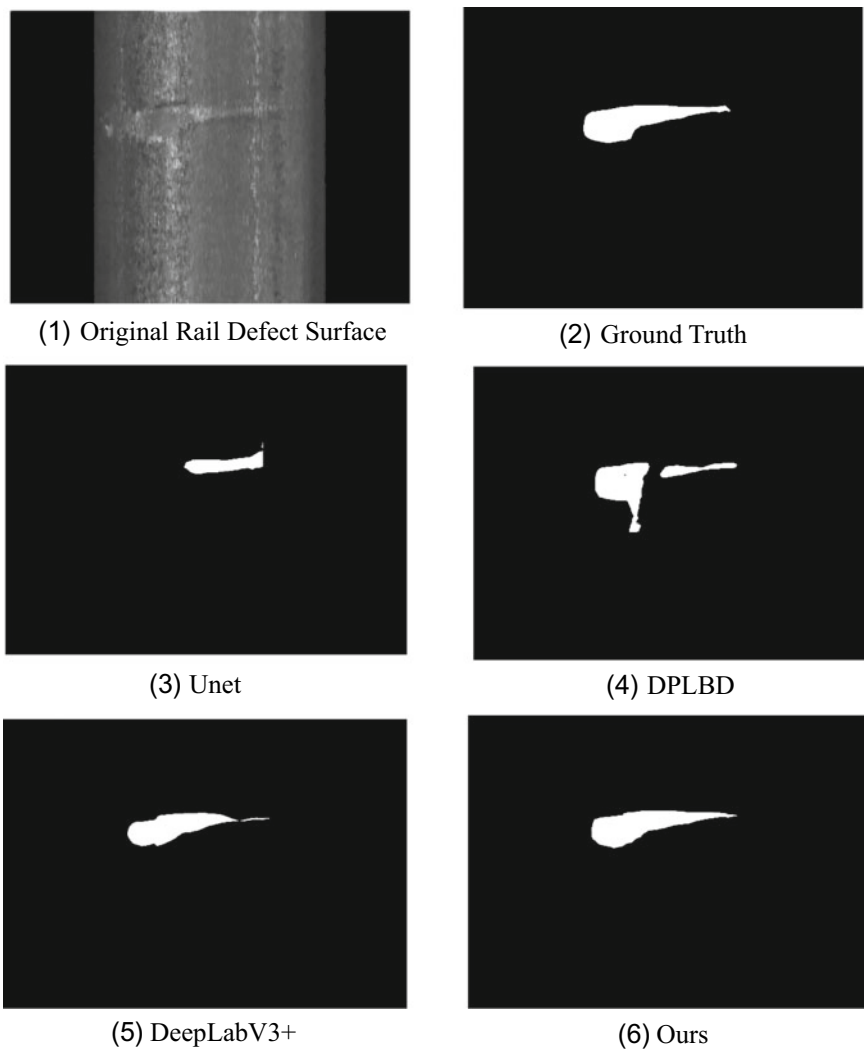


Fig. 6 Comparison of detection effects

the network, mainly using a simple Unet as the main structure of the neural network proposed in this paper. At the same time, the twin network structure further reduces the calculation parameters needed by the neural network. Therefore, even if the depth image information is added as the input of neural network, compared with the original Unet neural network structure, its reasoning speed is basically consistent, and there is no obvious time consumption.

5 Conclusions

Combining the actual engineering situation and the advantages of neural network detection method in defect detection, this paper proposes a way to detect rail surface defects by combining depth image information with 2D image information. Through the method proposed in this paper, compared with the previous methods of rail surface defect detection, the twin Unet-3D+ neural network proposed in this paper has better performance in detection effect. Compared with other methods, because of the combination of depth image information, a large number of stains, water stains, oil stains and light spots can be effectively eliminated, which greatly improves the accuracy of detection. At the same time, the time cost of the neural network proposed in this paper is also within the acceptable range, which ensures its engineering practicability and has great significance for improving the work efficiency of public works inspection. However, due to the limitation of data set, some rail surface defects that have not learned similar features are difficult to identify accurately. Therefore, in the follow-up work, in addition to further increase the rail surface defect data set, it is necessary to further improve the generalization of the neural network model and the recognition effect of rail surface defects with large gaps between classes.

Acknowledgements This paper is supported by the National Key R&D Program of China (2018YFB2100903) and Service capacity building of Hubei innovative method promotion and application base (2020IM020800).

References

1. Zhang S (201) Research on ultrasonic propagation simulation and defect detection method in rail. Central South University
2. Chen S, Chang H, Zhang R et al (2021) Rail surface defect detection based on projection histogram. *Mod Ind Econ Inf* 11(11):19–20, 76
3. Xiating J, Yaonan W, Hui Z et al (2019) Rail surface defect detection system based on Bayesian CNN and attention network. *Chin J Autom* 45(12):2312–2327
4. Deqiang H, Jian M, Jiajun Z et al (2020) Weld defect detection of subway vehicles based on improved Faster R-CNN. *Chin J Railway Sci Eng* 17(4):996–1003
5. Xiaobin T (2013) Research on pantograph wear detection system based on machine vision. Guangdong University of Technology, Guangdong

6. Brox T, Fischer P, Ronneberger O (2015) U-net: convolutional networks for biomedical image segmentation. International conference on medical image computing and computer-assisted intervention. Springer, Cham, pp 234–241
7. Chen LC, Kokkinos I, Papandreou G et al (2014) Semantic image segmentation with deep convolutional nets and fully connected crfs. arXiv preprint [arXiv:1412.7062](https://arxiv.org/abs/1412.7062)
8. Chen LC, Papandreou G, Kokkinos I et al (2017) Deeplab: Semantic image segmentation with deep convolutional nets, atrous convolution, and fully connected crfs. *IEEE Trans Pattern Anal Mach Intell* 40(4):834–848
9. Chen LC, Papandreou G, Zhu Y et al (2018) Encoder-decoder with atrous separable convolution for semantic image segmentation. In: Proceedings of the European conference on computer vision (ECCV), pp 801–818
10. Koch G, Salakhutdinov R, Zemel R (2015) Siamese neural networks for one-shot image recognition. In: ICML deep learning workshop, vol 2
11. Woo S, Park J, Lee J Y, et al (2018) Cbam: convolutional block attention module. In: Proceedings of the European conference on computer vision (ECCV), pp 3–19

Open Access This chapter is licensed under the terms of the Creative Commons Attribution 4.0 International License (<http://creativecommons.org/licenses/by/4.0/>), which permits use, sharing, adaptation, distribution and reproduction in any medium or format, as long as you give appropriate credit to the original author(s) and the source, provide a link to the Creative Commons license and indicate if changes were made.

The images or other third party material in this chapter are included in the chapter's Creative Commons license, unless indicated otherwise in a credit line to the material. If material is not included in the chapter's Creative Commons license and your intended use is not permitted by statutory regulation or exceeds the permitted use, you will need to obtain permission directly from the copyright holder.



Research on Damage Mechanism and Structural Optimization of Joints in Cavity Shear Wall Structure



Yong Tian, Guanghui Shi, Bo Zhang, Kun Guo, Fajiang Luo, Shengjie Chen, and Yibo Bai

Abstract After pouring concrete precast cavity shell structure has been developing rapidly in recent years, compared with cast-in-place structure, the new fabricated structure has low cost, high construction efficiency, and the advantages of green environmental protection, the shear wall structure is most widely used, which includes the prefabricated plate shell, annular tendon layout, cast-in-situ construction important process. But by several times with the stress of the casting of concrete and the overall disposable pouring forms have obvious differences, including the layered interface, the material interface, the cross section of damage caused by the stiffness degradation, and eventually results in the decrease of carrying capacity. In this paper, the damage mechanism of precast shear wall with cavity is analyzed, and the optimization method of connecting parts is studied and discussed.

Keywords Shear wall structure · Connection node · Damage mechanism · Structural optimization

1 Introduction

Prefabricated composite shear wall is a combination of double-sided composite shear wall, and then the reinforcement is inserted into the central cavity, and then the concrete is poured to complete. Due to the large size of the cavity, the construction of double-sided superimposed shear wall is convenient and fast in the process of component installation [1, 2].

Prefabricated superimposed shear wall is widely used because of its high applicable height, good applicability, good integrity and seismic performance. In order to meet the requirement of “equivalent cast-in-place”, the joint connection is the key, and the quality of joint connection directly affects the safety performance of assembled concrete structure [3]. As shown in Fig. 1.

Y. Tian · G. Shi · B. Zhang · K. Guo (✉) · F. Luo · S. Chen · Y. Bai
China Construction Third Engineering Bureau Group Co., Ltd., Xi'an 710065, China
e-mail: gk_changan@163.com

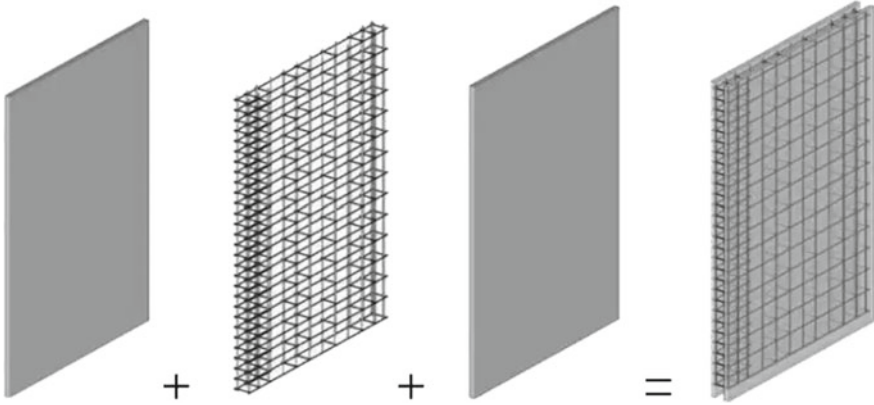


Fig. 1 Structure of cavity shear wall structure system

However, because the connecting steel bars in the shear wall are inserted artificially in the construction site, rather than buried in advance in the component factory, the following problems may occur:

- (1) The difficulty of vibration leads to the incompactness of cast-in-place concrete, which affects the grip of reinforcement in concrete [4].
- (2) The combination quality of old and new concrete is poor, and the bond is not strong enough to lead to the hollow of the laminated surface.
- (3) transportation, storage and other non-construction factors caused by the deformation of the panel, steel distortion.

At present, there are many researches on the mechanical and seismic performance of prefabricated composite shear wall at home and abroad [5, 6], but the damage mechanism derived from the above basic problems and optimization measures for construction need to be solved urgently. In this paper, based on refined finite element analysis software, a systematic analysis is made on the multiple factors affecting the composite shear wall.

2 Engineering Survey

The construction project includes 7 prefabricated residential buildings, office buildings, commercial and community facilities and supporting underground garages. The total land area is 50109 m², the construction area is about 248,000 m², the highest height is 94.45 m, the structure form is the frame shear wall structure, is a collection of residential, commercial, office and community supporting in one of the comprehensive building. To meet the needs of the building owners, the assembled shear wall adopts the cavity wall system, composed of two sides of the page with internal precast steel cage, the thickness of the two sides of the precast page is 50 mm, using

the sandwich area of concrete cast-in-place with forming the connection of the steel cage connection form. The cavity precast shear wall panel is shown in Figs. 2 and 3.

Fig. 2 Cavity shear wall

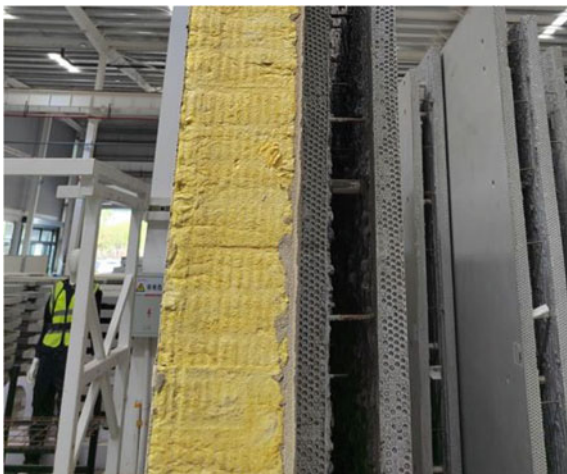
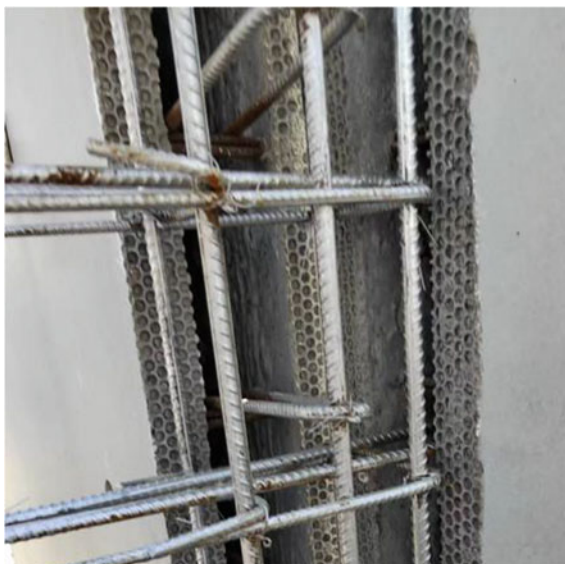


Fig. 3 Cavity shear wall joint



3 Structural Modeling and Analysis

3.1 Calculation Assumption

In numerical simulation analysis, the following assumptions are made [7, 8]:

- (1) It is assumed that concrete is an elastic body and is in the elastic deformation range in the whole process simulation.
- (2) The relative slippage of the contact part between reinforcement and concrete is not considered [9].
- (3) There is no difference in the uniform quality of concrete.

3.2 Finite Element Modeling

According to the actual construction situation, the proposed working condition is: there is an initial dislocation of 5 mm between the plates. Finite element program Midas was used to establish a shear wall panel with a size of 1 m \times 1 m, and the spacing between transverse connecting bars was 20 cm. The concrete shell is built by plate element, and the steel bar is built by beam element, which is divided into 200 units and 485 nodes. The basic model is shown in Fig. 4.

3.3 Finite Element Model Calculation

Stress calculation result

According to the present working condition, one side is consolidated and the other side is moved 5 mm down the vertical direction. The reinforcement stress calculation results are shown in Figs. 5 and 6.

Displacement calculation result

Taking the same working conditions for calculation, the displacement results of shear wall panels in different directions obtained are shown in Fig. 7–8. (The uncolored line segment is the position before deformation).

4 Data Analysis and Processing

Through the calculation of the overall model, the consolidation part is taken as the initial origin, and the vertical connection part of steel bar and wall plate is taken as the data extraction point. The internal force of steel bar and deformation displacement

Fig. 4 Finite element modeling of cavity shear wall structure

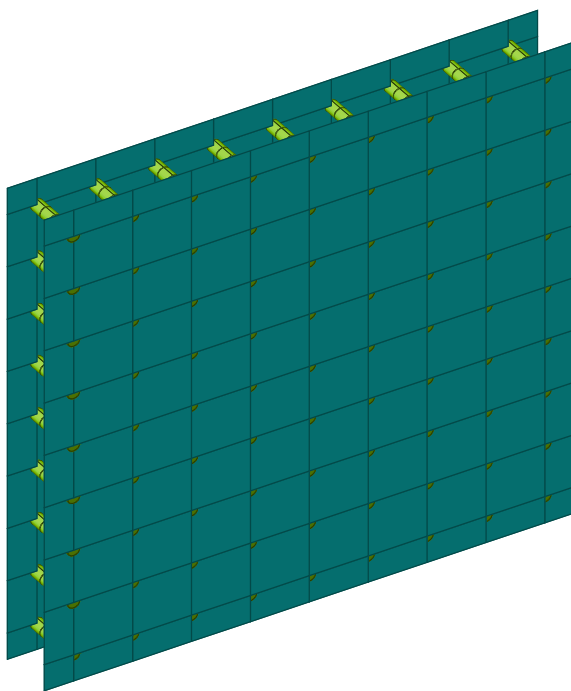


Fig. 5 Cloud diagram of maximum shear calculation results. (unit: kN)

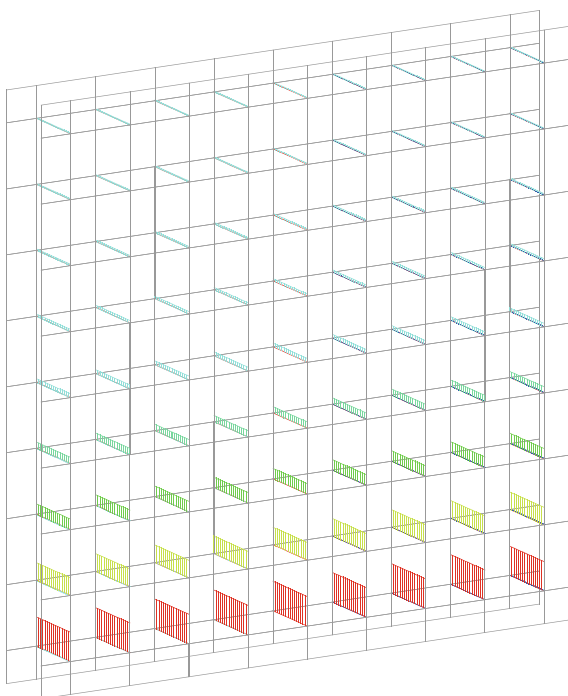


Fig. 6 Cloud image of calculation results of maximum bending moment. (unit: Mpa)

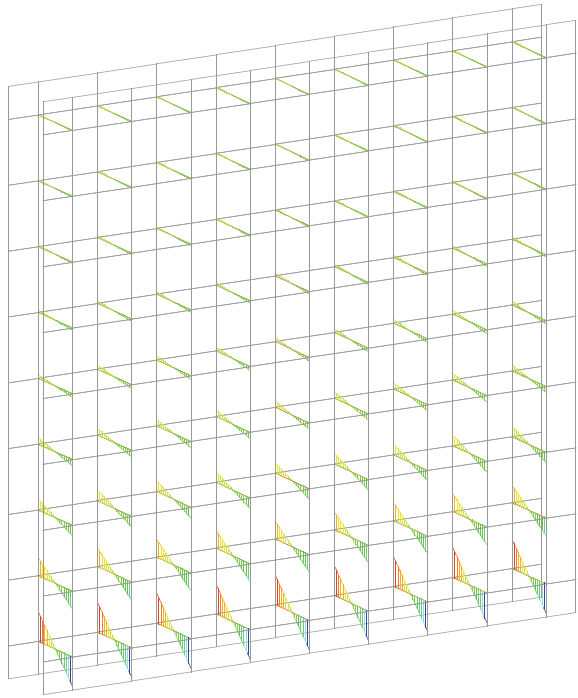


Fig. 7 Cloud image of lateral displacement calculation results. (unit: mm)

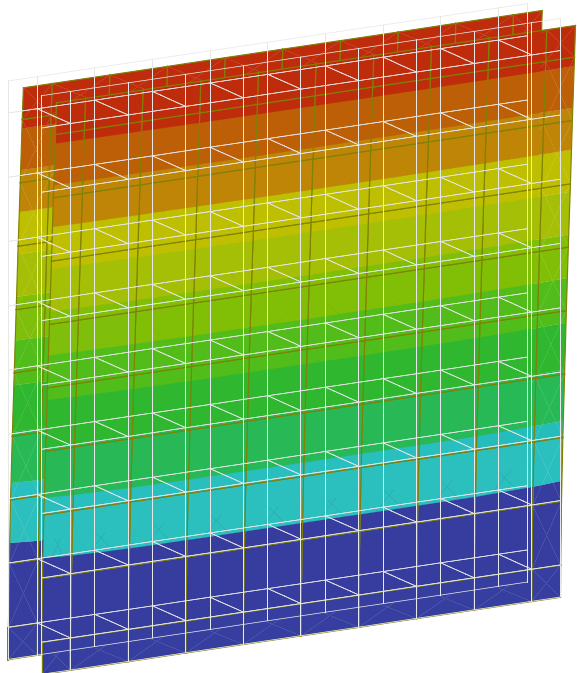
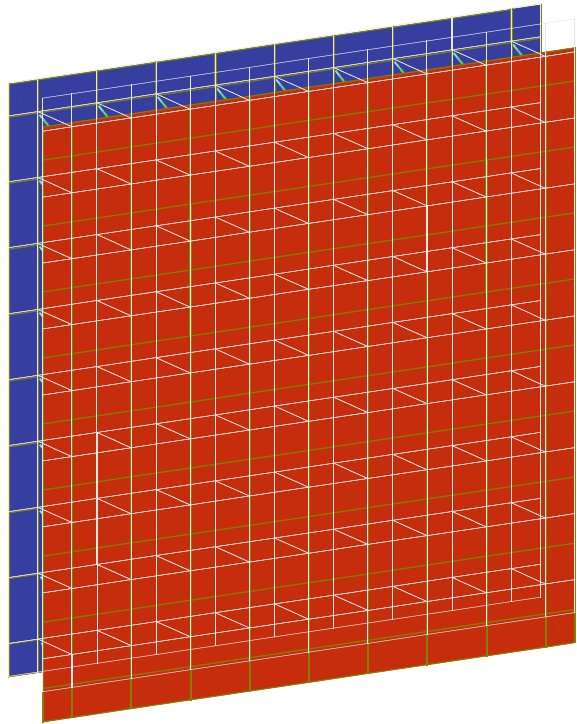


Fig. 8 Cloud image of vertical displacement calculation results. (unit: mm)



of shear wall plate are summarized, and the internal force and displacement change analysis chart is obtained in Table 1:

The abscissa is the fixed distance, and the ordinate is the corresponding data value of a specific position. They're all shown in Figs. 9 and 10.

Table 1 Summary of calculation results of internal force and displacement

Position (bottom as origin)	Maximum shear force (kN)	Maximum bending moment (Mpa)	Lateral displacement (mm)	Vertical displacement (mm)
1 (0.05 m)	65.71	3.29	0.29	5.00
2 (0.15 m)	39.34	1.97	2.11	4.95
3 (0.25 m)	23.28	1.16	5.06	4.89
4 (0.35 m)	13.73	0.69	8.69	4.86
5 (0.45 m)	8.10	0.41	12.73	4.84
6 (0.55 m)	4.83	0.24	17.01	4.83
7 (0.65 m)	2.98	0.15	21.42	4.82
8 (0.75 m)	2.00	0.10	25.90	4.81
9 (0.85 m)	1.58	0.08	30.43	4.81

Fig. 9 Trend of shear force and bending moment

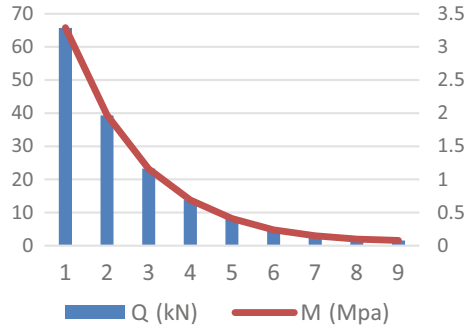
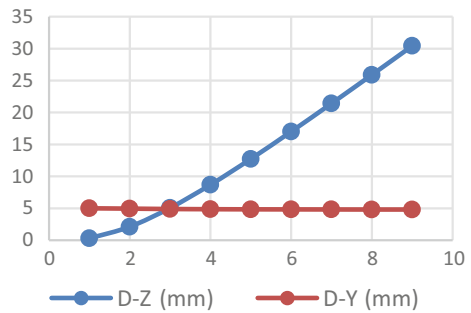


Fig. 10 Trend of transverse and vertical displacement



It can be clearly seen from the table and picture data that in the case of initial damage caused by relative dislocation of the wall panels on both sides, the overall change of displacement and internal force presents a nonlinear trend, mainly as follows:

- (1) When the prefabricated slabs of cavity shear wall are constrained at one end, the relative dislocation of 5 mm will cause the reinforcement at the connecting part to produce the shear force of 65.71 kN (The corresponding bending moment is 3.29 Mpa), and the shear stress can reach 328 Mpa according to the reinforcement diameter of 16 mm.
- (2) The rebar nearest to the constraint end bears 79.4% of the internal force, while the rebar at the free end only bears 4.06% of the internal force, and the actual bearing ratio at both ends is about 20:1.
- (3) There is little difference in vertical dislocation displacement between nodes, the maximum value is 5 mm, the minimum value is 4.81 mm, and the difference ratio between the maximum and minimum value is 3.8%, basically no difference.
- (4) The transverse dislocation displacement of each node varies greatly, the maximum displacement is 30.43 mm, the minimum displacement is 0.29 mm, and the warpage Angle is only 1° 43', which shows a linear change trend relative to the calculation plate.

5 Conclusion

According to the calculation and data analysis in the preceding chapters, the following conclusions can be drawn:

- (1) For the shear wall panel with cavity system, the relatively small dislocation between the two plates will cause the initial internal force, which is mainly concentrated at the near fixed end, because the shear transfer at the near fixed end lags behind the displacement transfer, and the larger the structure size, the more obvious this effect will be.
- (2) The horizontal and vertical deformation is not synchronous, on the one hand, because concrete is an elastic body that can resist partial deformation, and on the other hand, because the reinforcement as a stressed structure produces energy dissipation effect, which leads to the slope of deformation along the reinforcement direction and the slope of vertical reinforcement direction is not synchronous;
- (3) The transfer of internal force and deformation is not coordinated, which will cause the warping deformation of the structure in a specific direction. Considering that there is no difference between the inside and outside of this kind of wall panel, the warping deformation is completely random, and irregular distortion will occur in the plane under the stacking of multiple layers.

In order to meet the construction quality requirements, it is recommended to optimize as follows on the basis of meeting the requirements of the specifications:

- a. It is necessary to increase the number of steel bars connected near the constrained end, and the number of steel bars should be gradually increased from the free end to the fixed end.
- b. Attention should be paid to the connection between the steel bar and the wall panel to ensure that no concrete spalling or loosening occurs.
- c. In the construction of high-rise buildings, due to the randomness of warpage direction, it is necessary to measure single error and accumulate error in time to ensure accurate positioning.

References

1. Cheng B, Shi C, Xu J (2017) Research on connection technology of prefabricated reinforced concrete beam-column members. *Ind Constr* (7)
2. Jing Z, Liu B, Li X et al (2018) Review on reinforcement connection technology of assembled integral concrete structure. *Constr Technol* (10)
3. Pessiki S, Mlynarczyk A (2003) Experimental evaluation of the composite behavior of precast concretesandwich wall panels. *PCI J* 48(2):54–71
4. Oberlender GD (1973) Strength investigation of reinforced concrete load bearing wall panels. University of Texas, Arlington

5. Benayoune A, Samad AAA, Trikha DN (2013) Flexural behaviour of precast concrete composite panel-Experimental and theoretical investigations. *Constr Build Mater* 55(2):42–49
6. Zhang W, Yang L, Yu S (2018) Research on key problems of double-sided composite shear wall: seismic performance test of horizontal joints. *China Civ Eng J* 51(12):28–41
7. Hou H, Yan X, Cheng J (2019) *J Civ Environ Eng* 41(5):73–81
8. Yang L, Yu S, Zhang Q (2016) Numerical analysis of ultimate bearing capacity of composite shear wall with composite face. *J Tongji Univ* 44(12):1810–1818
9. Yang L, Yu S, Zhang Q, Cui J-C (2017) *J Tongji Univ* 45(5):664–672

Open Access This chapter is licensed under the terms of the Creative Commons Attribution 4.0 International License (<http://creativecommons.org/licenses/by/4.0/>), which permits use, sharing, adaptation, distribution and reproduction in any medium or format, as long as you give appropriate credit to the original author(s) and the source, provide a link to the Creative Commons license and indicate if changes were made.

The images or other third party material in this chapter are included in the chapter's Creative Commons license, unless indicated otherwise in a credit line to the material. If material is not included in the chapter's Creative Commons license and your intended use is not permitted by statutory regulation or exceeds the permitted use, you will need to obtain permission directly from the copyright holder.



Theoretical Study on Natural Vibration Frequency of Externally Prestressed Simply Supported Steel Beams



Zhengyu Wang, Hongming Li, and Huibin Chen

Abstract Prestress is an important index of the mechanical performance of prestressed structures, which will have a certain impact on the natural vibration frequency of the structure. In this paper, based on the action mechanism of the prestressing system, the externally prestressed simply supported steel beams are classified, and the energy method is used to establish the dynamic equations of the prestressed steel beams with three forms of cable distribution, with a view to exploring the relationship between the magnitude of prestressing force, cable distribution form, and cable section size and the natural vibration frequency of externally prestressed simply-supported steel beams. Through a numerical example, the theoretical calculation results are compared with the finite element simulation results to verify the theoretical calculation formula derived in this paper and reveal the action law of the prestressed system on the natural vibration frequency of the simply supported steel beam.

Keywords Natural vibration frequency · Dynamic performance · External prestress · Steel beam

1 Introduction

At this stage, the existing research at home and abroad involves the experimental research, theoretical analysis, and finite element simulation of the natural vibration frequency of externally prestressed components, with the experimental study being the majority and the basic theory being relatively scarce [1, 2]. The conclusions drawn by the researchers based on the experiments are basically the same [3–5], but it was found that the experimental results are quite different from the classical kinetic theory [6–9]. To this end, some scholars have done some research in theoretical analysis. The researchers mainly use the stiffness correction method [2, 10, 11], the nonlinear calculation method [12], the equivalent stiffness method [13], and other

Z. Wang (✉) · H. Li · H. Chen
Department of Civil Engineering and Architecture, Jiangsu University of Science and Technology,
Zhenjiang 212100, Jiangsu, China
e-mail: 1743121471@qq.com

© Crown 2023

Y. Yang (ed.), *Advances in Frontier Research on Engineering Structures*, Lecture Notes in Civil Engineering 286, https://doi.org/10.1007/978-981-19-8657-4_7

71

analysis methods to explore the influence of prestress parameters on the frequency. However, due to the lack of a unified mechanism, the theoretical calculation of the influence of prestress parameters on the dynamic performance of the structure has not been consistent, and there are differences in the viewpoints that have been put forward. Many laws are diametrically opposite and inconsistent with the experimental conclusions [14].

In addition, in the classical theory, the microelement method is used to establish the equilibrium equation under uniform load, but when the external load is changed to a concentrated force, the load function on the prestressed cable is a point function, and the vibration equation is only defined at several points. In fact, the body force does not meet the applicable conditions of the micro-element method [15], so it is impossible to intercept the single body for analysis. Therefore, this paper uses the energy method to analyze the structure as a whole [16]. From the perspective of the action mechanism of the prestressed system in the steel structure, a new analysis idea is proposed, that is, the structure is first classified according to the action mechanism of the prestressed system. Then, the natural vibration frequency of each type of externally prestressed simply supported steel beams is theoretically analyzed by the method of structural dynamics, and the frequency calculation formula is finally obtained..

2 Classical Theoretical Analysis and Its Errors and Corrections

The traditional vibration theory regards the prestressed tendons as applying a pair of constant axial forces F at both ends of an ordinary simply supported beam, as shown in Fig. 1.

According to D'Alembert's principle and the assumption of the plane section, the differential equation of beam free vibration under the action of axial force is established by neglecting the influence of shear deformation and moment of inertia:

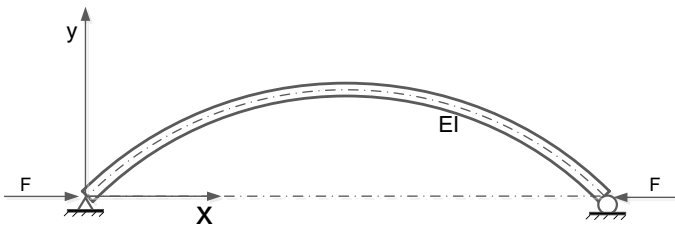


Fig. 1 Schematic diagram of bending vibration calculation of simply supported beam under the action of axial force

$$EI \frac{\partial^2 M(x, t)}{\partial x^2} + F \frac{\partial^2 y(x, t)}{\partial x^2} + \bar{m} \frac{\partial^2 y(x, t)}{\partial t^2} = 0 \quad (1)$$

where $y(x, t)$, EI , and \bar{m} have the same meaning as above; $M(x, t)$ —Bending moment of steel beam section.

From Formula (1), the expression for the natural vibration frequency of a simply supported beam is:

$$\omega_n = \left(\frac{n\pi}{l}\right)^2 \sqrt{\frac{EI}{\bar{m}}} \sqrt{1 - \frac{F}{n^2 \frac{EI\pi^2}{l^2}}} = \omega_n \sqrt{1 - \frac{F}{n^2 P_c}} \quad (2)$$

In the formula: $n = 1, 2, 3 \dots$; l is the beam length; $P_c = \frac{EI\pi^2}{l^2}$.

Formula 2 shows that the presence of the prestress reduces the natural bending frequency of simply supported beams, and the degree of reduction decreases with the increase of i . However, it cannot explain the experimental phenomenon that the natural frequency of precast beams increases with the increase of prestress. Some scholars use experimental data to correct the EI value in Eq. 1. Although the modified formulas are not exactly the same, they are all based on the test results to modify the stiffness, so they can be expressed as follows:

$$(EI)_e = (1 + \alpha)EI_0 \quad (3)$$

where: $(EI)_e$ —the stiffness of the modified prestressed simply supported beam;

α —stiffness correction factor; $(EI)_0$ —stiffness of the front beam body before correction.

The modified formula of stiffness is obtained by fitting the test data, and finally, the modified natural frequency calculation formula is obtained. Although a large number of researchers have revised Eq. 3, it is still empirical and not fully supported by theory, and thus not of general applicability.

3 Theoretical Analysis of the Natural Vibration Frequency of Steel Beams Based on the Action Mechanism of the Prestressed System

3.1 Prestressed Components

The mechanism of the externally prestressing system can be summarized as follows:

- (1) The prestress itself causes stress and deformation of structural members and affects the stiffness of the structure, such as the cable arch structure.
- (2) Under the action of the prestress, the prestressed carrier provides additional stiffness to the structure and adjusts its mechanical performance.

There are two manifestations of the stiffness provided by the prestressed carrier: (a) The prestressed carrier establishes the axial stiffness under the action of the prestress, and forms a new structural form with the original structure, which improves the stiffness and stability of the original structure and makes the prestressed structure more stable. As a two-force rod, the tightened cable can bear both tension and pressure, and within the elastic range, the axial stiffness of the cable has nothing to do with the cable force, such as cable-stayed structure, cable support structure, etc. (b) The second-order effect of axial force provides stiffness to the structure. The carrier does not directly provide stiffness and stability to the structure after prestressing, but when the cable is deformed perpendicular to the cable axis, stiffness is formed through the second-order effect of the central axial force (tension) of the cable. It often appears in point-supported curtain wall structures and string-supported structures.

3.2 Calculation of the Natural Vibration Frequency of the Externally Prestressed Steel Beams with Linear Coupling Cables

Based on three prefabricated members, the energy method is used to calculate the natural vibration frequency of the external prestressed members arranged with straight bars. The three assumptions presented here are consistent with the traditional Euler Bernoulli bending beam theory. In addition, the following three assumptions are added: (1) The i -th order vibration mode can be expressed as $y_i = A_i \sin(i \pi x / l) \sin(\omega_i t + \phi_i)$, $i = 1, 2, 3, \dots$, where A_i , ω_i , and ϕ_i are the vibration amplitude, circular frequency, and the i -th order vibration phase angle, respectively; (2) The axial force change of the steel bar is neglected; (3) The axial deformation of the beam caused by the axial force of the ribs is ignored.

3.3 Influencing Factors of Natural Vibration Frequency of Externally Prestressed Steel Beams with Linear Coupling Cables

In addition to being related to the inherent properties of steel beams such as E , I , m , and L , the natural vibration frequency f of the steel beam is also affected by three main parameters, namely, the cable force F , the eccentric distance e , and the cable cross-sectional area A in the prestressed cable. In order to directly reflect the influence of the relationship between the above-mentioned cable parameters and the natural vibration frequency, a binary surface graph of the first-order frequency variation of the linearly coupled cable-clipped steel beam with any two parameters is drawn. (Note: Because the first-order vibration is usually the most important in practical engineering, only the first-order natural frequency is considered here.)

The figure below directly reflects their effect on the first-order natural frequency of the externally prestressed steel beam.

According to Fig. 2a, the natural vibration frequency of the prestressed steel beam of the linearly coupled cable arrangement shows an increasing trend with the increase of the prestress and the eccentricity. According to the slope of the F-f and e-f curves, when other conditions are the same, the influence of the eccentricity on the natural vibration frequency of the steel beam is equivalent to the prestress. It can be seen from Fig. 2b that the natural vibration frequency of the prestressed steel beam increases with the increase of the cross-sectional area A of the cable, and the influence of the cross-sectional area on the natural vibration frequency is also equivalent to that of the prestressing force. The surface shapes of Fig. 2c are basically the same, and the natural vibration frequency of the prestressed steel beam increases gradually with the increase of the cross-sectional area and eccentricity of the cable.

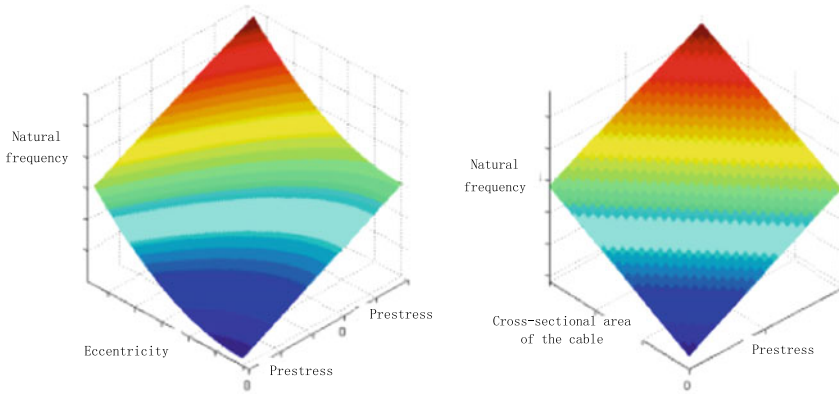
4 Analysis of Influencing Factors of Natural Vibration Frequency

Under the three cable routing methods, the effects of prestressing system parameters on the first-order frequency of prestressed simply supported steel beams were compared and analyzed. The theoretical value of the natural vibration frequency of the prestressed steel beam is calculated according to Sect. 2; according to the above finite element model, the finite element software ANSYS is used to analyze the influence of the prestress size, cable eccentricity, and the cross-sectional area of the cable on the natural vibration frequency of the prestressed steel beam, and the theoretical value and the simulated value are compared and analyzed. All analyses were performed within the linear elastic range.

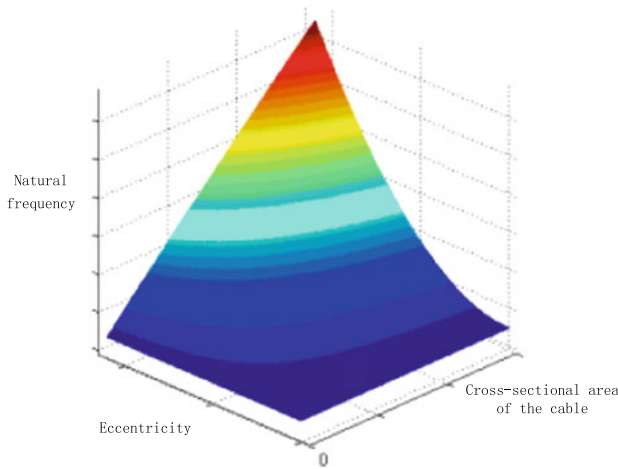
4.1 Influence of Prestress on Natural Vibration Frequency

For prestressed steel beams with straight and linear coupling cables, the prestressed cables are arranged along the axis; the mid-point of the cable is anchored on the mid-span stiffener of the steel beam, 110 mm away from the neutral axis of the beam. The cross-sectional area A of the cable is taken as 139 mm^2 . Under different prestresses, the theoretical and simulated values of the first-order frequency of the prestressed steel beam are shown in Table 1.

According to the analysis of the chart, under different prestresses, the theoretical and simulated values of the frequency of the steel beam are basically consistent: when the linear cable routing method is adopted, the first-order frequency of the steel beam gradually increases with the increase of the prestress; when the linear coupling cable routing method is used, the first-order frequency of the steel beam gradually decreases



(a) The first-order frequency variation of the steel beam with the prestress and eccentricity (b) The first-order frequency variation of steel the beam with the prestress and cable cross-sectional area relationship curve relationship curve



(c) The relationship curve of the first-order frequency of the steel beam with the eccentric distance and the cross-sectional area of the cable

Fig. 2 First-order frequency binary surface diagram of steel beam

with the increase of the prestress; when the single-broken-line cable routing method is employed, the first-order frequency of the steel beam gradually decreases with the increase of the prestress. The error of the theoretical calculation results is smaller than that of the finite element simulation results, and the error rate of the first-order frequency of the steel beam under the three cable routing methods is less than 5%.

According to the above analysis, the effect of prestress on the natural vibration frequency of steel beams is related to the way of prestressing cables. The

Table 1 Theoretical and simulated values of the first-order frequency of prestressed steel beams under different prestresses

Prestress value (kN)	Theoretical value (Hz)	Rate of change (%)	Simulated value (Hz)	Rate of change (%)	Relative error (%)
0	50.26	–	49.75	–	1.03
200	50.82	– 1.02	50.71	– 1.89	0.21
400	51.37	– 2.16	51.67	– 3.72	– 0.59
600	51.91	– 3.18	52.61	– 5.44	– 1.33
800	52.45	– 4.18	53.53	– 7.06	– 2.01
1000	52.99	– 5.15	54.43	– 8.60	– 2.65

above conclusions are explained in combination with the action mechanism of the prestressing system.

As shown in Fig. 2, when the steel beam adopts the linear coupling type cable, with the increase of the prestress, the first-order frequency of the steel beam gradually increases. In this case, due to the mid-span coupling between the cable and the steel beam, the cable is deformed perpendicular to the cable axis during the vibration process. Both the axial expansion of the cables and the second-order effect of the axial force increase the stiffness of the beam, and the contribution of increased stiffness to frequency is greater than the attenuation of the axial force F to frequency. Therefore, both the prestress and the frequency of the prestressed steel beams with linear coupling cables increase. And as the prestress increases gradually, the second-order effect of the axial force of the cable becomes more and more obvious, the stiffness provided to the beam body also increases continuously, and finally, the frequency of the prestressed steel beam is greater than that of the single-broken prestressed steel beam.

4.2 Effect of Eccentricity on Natural Vibration Frequency

The prestress F in the prestressed cable is 800 kN, and the cross-sectional area A of the cable is 139 mm². Under different eccentric distances, the theoretical and simulated values of the first-order frequency of the prestressed steel beam are shown in Table 2, and the trend curve of the frequency variation of the steel beam with the eccentric distance is drawn, as shown in Table 2.

According to the above chart, under different eccentric distances, the theoretical value of the first-order frequency of the steel beam and the calculation result of the simulated value are basically consistent. The error of the theoretical calculation results is smaller than that of the finite element simulation results, and the error rate of the natural vibration frequency of the steel beam under the three cable routing methods is less than 5%.

Table 2 Theoretical and simulated values of natural vibration frequencies of prestressed steel beams

Eccentricity (mm)	Theoretical value (Hz)	Rate of change (%)	Simulated value (Hz)	Rate of change (%)	Error (%)
0	52.45	–	53.53	–	– 2.01
30	52.67	0.42	53.74	0.39	– 2.00
50	53.05	1.13	54.39	1.58	– 2.47
70	53.61	2.16	55.37	3.32	– 2.84
90	54.35	3.50	55.77	4.02	– 2.55
110	55.26	5.10	56.79	5.74	– 2.70

It can be found from Fig. 2 that the first-order frequency of the prestressed steel beam increases gradually with the increase of the eccentricity under the three cable routing methods. Combining with Table 2, it can be seen that when the steel beam adopts the linear cable arrangement, as the eccentric distance of the cable increases, the simulated value of the first-order frequency of the steel beam increases from 1.87 to 6.15%, and the rate of change of the theoretical value increases from 0.80 to 4.95%. The rate of change increases continuously, and the relationship between the first-order frequency and the eccentricity is close to a quadratic function; when the steel beam adopts the linear coupling type cable, the rate of change of the simulated value of the first-order frequency of the steel beam increases from 0.70 to 5.10%, while the theoretical value increases from 0.73 to 4.55%. The rate of change increases continuously, and the relationship between the first-order frequency and the eccentricity is close to a quadratic function; when the single-broken line cable is used, the rate of change of the simulated value of the first-order frequency of the steel beam changes from 1.93 to 2.50%, while the theoretical value changes from 1.57 to 2.55%, and the rate of change is almost unchanged. The linear correlation coefficient R^2 between the first-order frequency and the eccentricity is the highest among the three distribution methods, reaching 0.99, so the difference between the first-order frequency and the eccentricity is 0.99, which is closer to a linear relationship.

4.3 Influence of the Cross-Sectional Area of the Cable on Natural Vibration Frequency

The prestress F in the prestressed cable is taken as 800 kN, and the eccentricity e of the three cable routing methods is taken as 70 mm. Using steel strands with different cross-sectional areas as prestressed cables for analysis, the theoretical and simulated values of the first-order frequency of the prestressed steel beams are shown in Table 3, and the trend curve of the frequency variation of the steel beams with the cross-sectional area of the cables is drawn, as shown in Table 3.

Table 3 Theoretical and simulated values of the first-order frequency of prestressed steel beams

Sectional area (mm ²)	Theoretical value (Hz)	Rate of change (%)	Simulated value (Hz)	Rate of change (%)	Relative error (%)
54.8	52.91	–	55.05	–	– 3.89
98.7	53.28	0.64	55.23	0.33	– 3.54
139	53.61	1.31	55.37	0.58	– 3.19
191	54.03	2.07	55.54	0.88	– 2.71
285	54.79	3.43	55.79	1.33	– 1.78

Under different cross-sectional areas of the cables, the theoretical and simulated values of the natural vibration frequency of the steel beam are basically consistent. The error of the theoretical calculation results is smaller than that of the finite element simulation results, and the error rate of the natural vibration frequency of the steel beam under the three cable routing methods is less than 5%.

According to Table 3, when the cross-sectional area of the cable gradually increases from 54.8 mm² to 285 mm², the change rate of the simulated value of the first-order frequency of the linear cable prestressed steel beam decreases from 1.00 to 0.71%, and that of the theoretical value decreases from 0.91 to 0.88%; the rate of change of the simulated value of the first-order frequency of the linear coupling type cable prestressed steel beam is reduced from 0.41 to 0.27%, and that of the theoretical value is reduced from 0.84 to 0.80%; the rate of change of the simulated value of the first-order frequency of the linear cable prestressed steel beam is reduced from 1.05 to 0.69%, and that of the theoretical value is reduced from 1.94 to 1.83%. Therefore, the first-order frequencies of the prestressed steel beams in the three cable routing methods all increase with the increase of the cross-sectional area of the cables, and the rate of change gradually decreases.

5 Conclusion

- (1) The size of the prestress, the eccentric distance, and the cross-sectional area of the cable will have a certain influence on the natural vibration frequency of the prestressed simply supported steel beam;
- (2) The calculation formula of the natural vibration frequency of the externally prestressed simply supported steel beam deduced in this paper can accurately obtain the natural vibration frequency of the structure. The variation law of the first-order frequency of the steel beam reflected by the formula with the prestress is basically consistent with the finite element simulation results, and has good calculation accuracy, which can provide a certain reference for engineering applications;
- (3) The effect of prestress on the natural vibration frequency of steel beams is related to the way of prestressing cables. When the prestressed steel girder adopts linear

cable distribution, the frequency of the steel girder decreases gradually with the increase of the prestress; when the prestressed steel girder adopts linear coupling cable distribution, with the increase of the prestress, the frequency of the steel beam increases gradually; when the prestressed steel beam adopts the single broken line cable, with the increase of the prestress, the frequency of the steel beam gradually decreases;

- (4) The natural vibration frequency of the externally prestressed simply supported steel beam increases with the increase of the eccentric distance;
- (5) The natural vibration frequency of the externally prestressed simply supported steel beam increases with the increase of the cross-sectional area of the cable.

References

1. Wang LL (2013) Analysis of prestress effect on natural frequency of simply supported beams. Jilin University, Jilin
2. Miyamoto A, Tei K, Nakamura H, Bull JW (2009) Behavior of prestressed beam strengthened with external tendons. *J Struct Eng* 1033–1044
3. Xiao JT, Wu HL (2010) Influence of prestress on natural frequency of prestressed simply supported beam. *Sci Technol Eng* 10(4):2909–2912
4. Zhang YT, Wang XL, Li RG (2007) Theoretical analysis and experimental study on vibration frequency of fully prestressed beams. *Eng Mech* 24(8):116–120
5. Ding HY, Meng LY, Liu P, Guo YH (2016) Experimental study on the effect of prestress on the natural frequency of simply supported beams. *J Hebei Univ Technol* 45(5):100–105
6. Saiidi M, Douglas B, Feng S (1994) Prestress force effect vibration frequency of concrete bridges. *J Struct Eng* 120(7):2233–2241
7. Xue G, Hu XF (2012) Research on the natural frequencies of externally prestressed concrete simply supported beams. *J Guangxi Univ (Nat Sci Ed)* 37(4):671–675
8. Zhang J, Zhou ZW, Ni XL, Chen H, Zhu PC (2012) Modal test on an external prestressed steel beam. *Adv Mater Res* 446–449:3123–3127
9. Li FG, Li R (2012) Theoretical analysis of natural vibration frequency for unbonded prestressed concrete beams. *Adv Mater Res* 594–597:882–885
10. Kim J-T, Ryu Y-S, Cho H-M, Stubbs N (2003) Damage identification in beam-type structures: frequency-based method vs mode-shape-based method. *Eng Struct* 25(1):57–67
11. Zheng SM, Ma L, Wan S (2014) Analysis of influence of external prestress on natural vibration frequency of corrugated steel web box girder. *J Southeast Univ (Nat Sci Ed)* 44(1):140–144
12. Tan GJ, Liu ZY, Wei HB, Wang LL (2016) Calculation method of natural vibration frequency of simply supported beam with eccentric linear prestressed tendons. *J Jilin Univ (Eng Ed)* 03:798–803
13. Yang ZJ, Bai YD, Chen X, Wang M, Jiang ZW (2015) Approximate analytical solution of equivalent stiffness and natural frequency of prestressed beams. *Sci China Phys Mech Astron* 07:98–104
14. Hamed E, Frostig Y (2006) Natural frequencies of bonded and unbonded prestressed beams—prestressing force effects. *J Sound Vib* 295:28–39
15. Gao DY (1997) Micro-element method in mechanics. *J Yuxi Teachers Coll* 06:24–27
16. Ma JM (2012) Advanced structural dynamics. Xi'an: Xi'an Jiaotong University Press

Open Access This chapter is licensed under the terms of the Creative Commons Attribution 4.0 International License (<http://creativecommons.org/licenses/by/4.0/>), which permits use, sharing, adaptation, distribution and reproduction in any medium or format, as long as you give appropriate credit to the original author(s) and the source, provide a link to the Creative Commons license and indicate if changes were made.

The images or other third party material in this chapter are included in the chapter's Creative Commons license, unless indicated otherwise in a credit line to the material. If material is not included in the chapter's Creative Commons license and your intended use is not permitted by statutory regulation or exceeds the permitted use, you will need to obtain permission directly from the copyright holder.



Finite Element Analysis of Punching Shear of Reinforced Concrete Mushroom Slab-Column Connections Using ABAQUS



Yueqiao Jia and Jeffrey Choong Luin Chiang

Abstract Capital is one of the common measures to strengthen the slab-column connections. It can make the joint's load capacity increase. However, when the connection is subjected to the unbalanced bending moment, the reduction effect of the capital on the bending moment is to be studied. Nonlinear finite element analysis is performed on reinforced concrete slabs with column capital for various moment-to-shear (M/V) ratios. The effect of capital radius on the punching shear resistance of slab-column connections is investigated. The 3D finite element modeling is performed using the concrete damage plasticity model and concrete constitutive equations. The concrete damage plasticity model parameters are calibrated by the experiment results of specimens. Increasing the radius of capital can improve the bearing capacity of nodes and reduce the moment transfer effect obviously.

Keywords Finite element method · Mushroom slab · Column capital · Moment transfer · Punching shear

1 Introduction

Many experiments have been done by researchers to study slab-column connections. The disadvantage of slab-column connections is the possibility of punching shear damage in the vicinity of the column. One of the measures to enhance the joints is to provide drop panels at the head of the column. There are many different forms of drop panels, as shown in Fig. 1. However, there are few experiments on drop panels for slab-column connections in the database and almost none for different moment-to-shear ratios. Finite element analysis can be used to supplement the existing experiments after parameter calibration. The use of finite element methods allows the

Y. Jia (✉) · J. C. L. Chiang
Infrastructure Geo-Hazards & Sustainable Materials Research Centre, Faculty of Engineering,
Built Environment and Information Technology, SEGi University, Kota Damansara, Kuala
Lumpur, PJ, Selangor, Malaysia
e-mail: Yueqiao1993@gmail.com

J. C. L. Chiang
e-mail: jeffreychiang@segi.edu.my

This is a U.S. government work and not under copyright protection in the U.S.; foreign copyright protection may apply 2023

Y. Yang (ed.), *Advances in Frontier Research on Engineering Structures*, Lecture Notes in Civil Engineering 286, https://doi.org/10.1007/978-981-19-8657-4_8

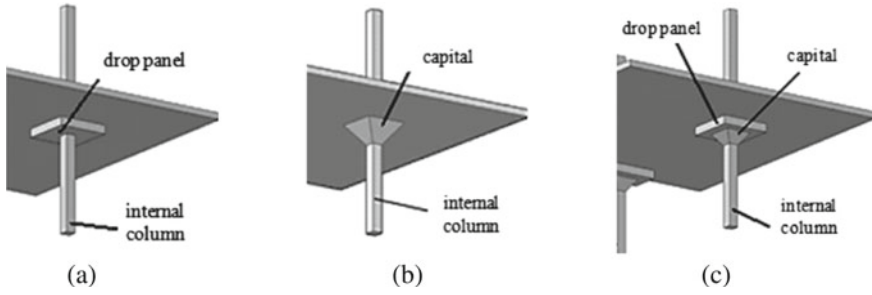


Fig. 1 Drop panel types **a** flat drop panel **b** capital **c** drop and capitals

investigation of aspects not measured in the experiments. In this paper, the mushroom slab experiment of Lima Neto et al. [1] was selected for numerical simulation and analysis using the finite element software ABAQUS.

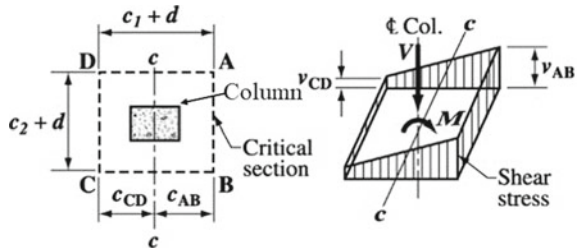
In practice, due to eccentric loading, the slab-column connections are subjected to both vertical loads and bending moments, as in Fig. 2, and the transmission of unbalanced bending moments reduces the punching shear resistance. The ACI-318 [2] for the moment transfer coefficient is calculated by Eq. (1).

$$\gamma_v = 1 - \frac{1}{1 + \frac{2}{3} \sqrt{\frac{c_1+d}{c_2+d}}} \tag{1}$$

where, c_1 and c_2 are the side length of the column d is the effective thickness of the slab.

Because of the great harm of unbalanced bending moment to the slab-column connections and the risk of continuous collapse of the structure, it is particularly important to strengthen the joints. The purpose of this paper is to investigate the effect of the size of the capitals of the mushroom slab on the moment transfer coefficient for different moment-to-shear ratios. Based on the results of numerical simulation, some suggestions are put forward for practical design.

Fig. 2 Assumed distribution of shear stress from ACI



2 Test Specimens

Interior slab-circular column connections with circular capitals of different radii were tested by Lima Neto et al. [1]. The slab is square, with a side length of 2600 mm and a thickness of 140 mm, and is supported on a circular central stub with a diameter of 250 mm. The flexural reinforcement with 12.5 mm diameter bars spaced 105 mm in the x-direction and 115 mm in the y-direction. Concrete covered the top surface of the slab by 15 mm and the bottom surface by 10 mm. The reinforcement arrangement is the same for each specimen. The four sides of the slab are fixed, and jacks apply loads from the bottom up. Figure 3 shows the dimensions of the slab and loading device. Specific information is presented in Table 1.

3 Finite Element Method

3.1 Methodology

ABAQUS is a commercial finite element software that requires many steps to complete a numerical simulation, as shown in the flow chart in Fig. 4. The concrete is simulated using C3D8R units and the reinforcement is simulated using T3D2 units. The combination of the two is embedded. To avoid hourglassing problems, it is necessary to ensure that at least 4 meshes are divided in the direction of the slab thickness [3]. Therefore, the mesh size of this test model is 35 mm. Figure 5 shows the boundary conditions and load position of the model in ABAQUS. The purpose of setting the columns longer than the test specimens was to subsequently apply lateral forces to the columns to simulate the bending moments applied to the slab.

3.2 Concrete Damage Plasticity Model

The Concrete Damage Plasticity Model (CDP) [4, 5] is a model built into ABAQUS to simulate the behavior of concrete under tensile cracking and compression crushing. The application of this model requires the input of the stresses and inelastic strains of concrete in tension and compression, calculated from the concrete constitutive equations. And the damage factor also needs input. In this paper, the concrete constitutive equations are taken from the Chinese Code for the Design of Concrete Structures GB50010-2010 [6] and the damage factor is calculated using Sidoroff's formula [7].

For model accuracy, two parameters in the CDP model, the dilation angle and the viscosity coefficient need to be calibrated by trial calculations. The dilation angle φ is set to simulate the volume expansion of concrete as a brittle material due to inelastic strain when subjected to tension. A larger dilation angle indicates more brittle concrete. The viscosity parameter μ is a time-dependent parameter that

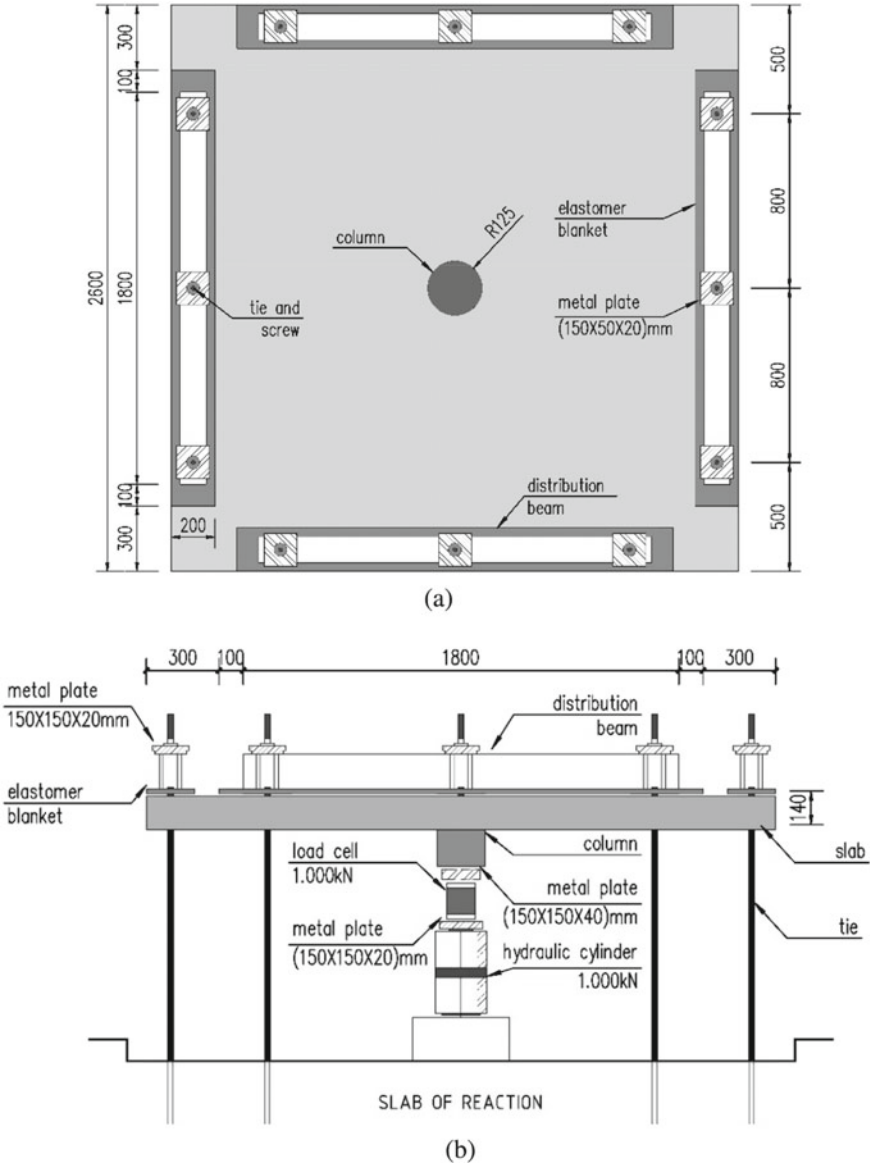


Fig. 3 Schematic drawings of the specimens of Lima Neto et al. **a** Test system in top view. **b** Test system in section **c** Dimensions of the capitals

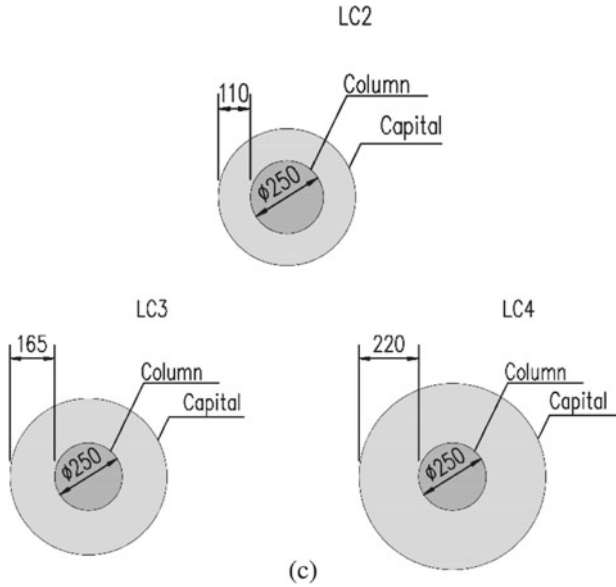


Fig. 3 (continued)

Table 1 Characteristics of the Lima Neto et al. test slabs

Specimen	Concrete	Reinforcement	Dimensions		
	f_{cu} (MPa)	ρ (Tension surface) (%)	Efficient thickness of slab (mm)	Thickness of capital (mm)	l_H^a (mm)
LC2	31	1.04	111	55	110
LC3	33	1.03			165
LC4		1.05			220

^a l_H is the difference between the radius of the capital and the radius of the column

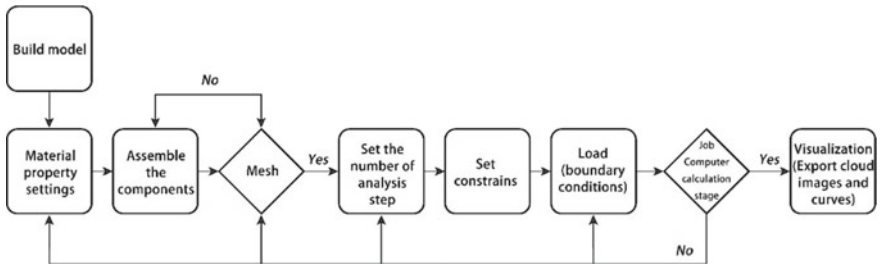


Fig. 4 Simulation flow chart

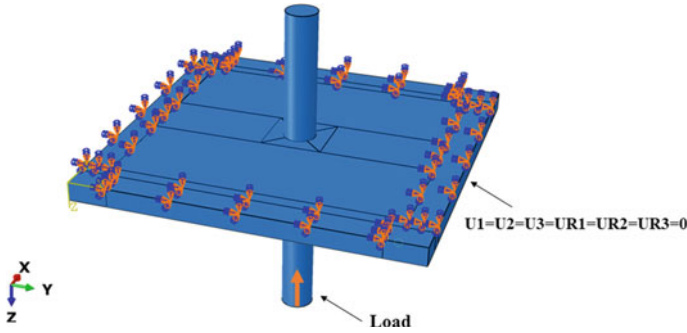


Fig. 5 Boundary conditions and loading of the specimens of Lima Neto et al. in ABAQUS

controls the convergence of the model and the accuracy of the calculation. When μ is equal to 0, the material is purely plastic, when μ is equal to 1, the material is purely elastic. The smaller the value of μ , the more precise the accuracy, and consequently the speed of the calculation decreases.

After trial calculations, it was concluded that the dilation angle φ of 40° was appropriate to simulate this experiment. The viscosity coefficient of LC2 is 0.0005, and the μ of LC3 and LC4 is 0.001.

4 Finite Element Analyses Results

4.1 Load–deflection Response

Figure 6 shows a comparison of experiment and numerical load–displacement responses. The experiment's ultimate loads of LC2, LC3, and LC4 are 427 kN, 518 kN, and 513 kN, respectively. The numerical simulation results were 431 kN, 526 kN, and 511 kN, respectively. The ratios of test to simulated values were 0.99, 0.98 and 1.0, respectively. It can be seen that the simulation results are in good agreement with the experiment. Therefore, this set of CDP parameters can be used to simulate the bending moment of the three slabs.

4.2 Crack Pattern

The experiment cracking photos are not shown in the experiment, so there is no comparison of crack patterns here. However, the test results showed that LC2 damage occurred outside the capital, while LC3 and LC4 damage occurred inside the capital

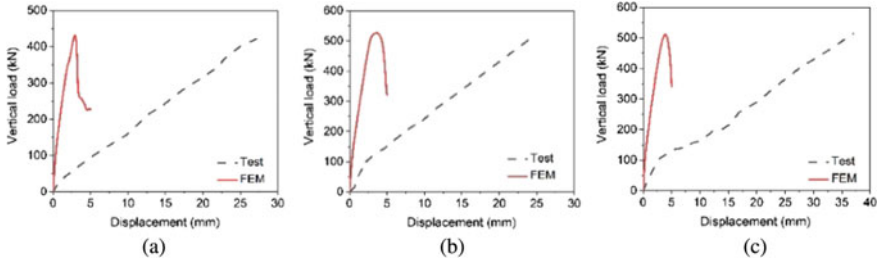


Fig. 6 Load-displacement response for experiment versus FEM of Lima Neto et al. slabs **a** LC2, **b** LC3, **c** LC4

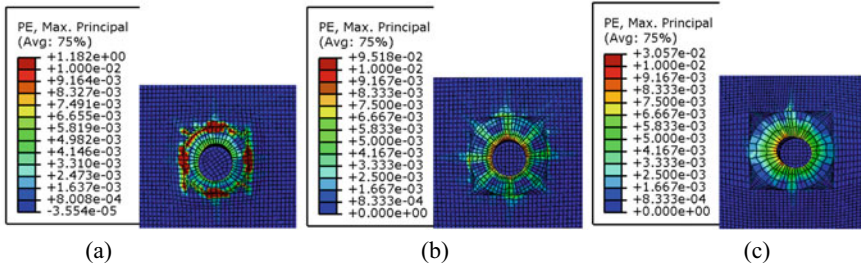


Fig. 7 Crack patterns of Lima Neto et al. slabs in ABAQUS **a** LC2 **b** LC3 **c** LC4

area. Simulation results are consistent with this description, as shown in Fig. 7. Further demonstrating the accuracy of the simulation.

4.3 Coefficient of Bending Moment Transferred by Eccentric Shear Force

Different transverse and vertical forces were applied to each of the three slabs at the ends of the column. The stresses at a distance $d/2$ from the surface of the column, i.e., the location of the critical section as specified in the ACI-318, were obtained for different values of M/V . Substitute the stress into Eq. (2) to obtain the value of the moment transfer coefficient.

$$\gamma_v = \frac{(v_u b_0 d - V) J_c}{M x b_0 d} \tag{2}$$

where, v_u is the shear stress on the perimeter of the critical section of the eccentric force side, b_0 is the critical section perimeter, d is the effective slab thickness, V is the vertical load, J_c is the property of assumed critical section analogous to the polar

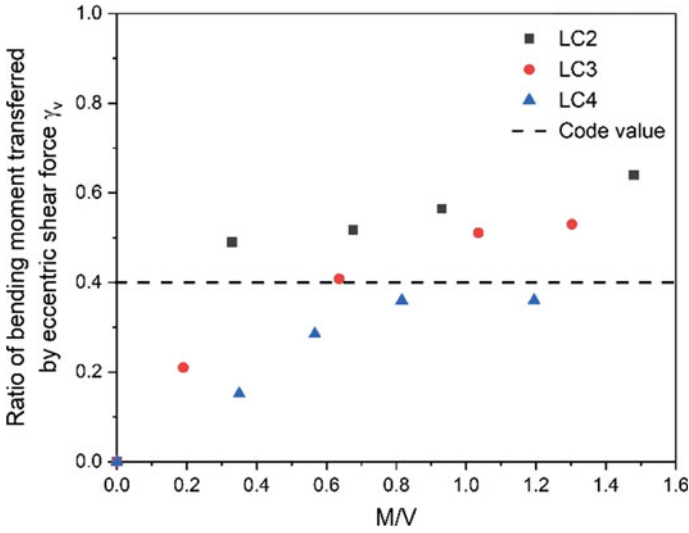


Fig. 8 M/V versus moment transfer coefficient for different widths of drop panel

moment of inertia, M is the bending moment generated by the lateral force, x is the centroid of the shear perimeter.

From this, the trend of the moment transfer coefficient with M/V was obtained, as shown in Fig. 8. The three slabs have similar trends and M/V is positively correlated with the γ_v . As the radius of the capital increases, the γ_v decreases for the same value of M/V . As can be seen from Fig. 8, only the LC4 has all values below the code value. Therefore, increasing the width of the drop panel can increase the load-carrying capacity and at the same time reduce the moment transferred coefficient.

5 Conclusions

A finite element model is developed to simulate the existing experiment and complement the test results. The concrete damage plasticity model was used to describe the cracking behavior of concrete. The CDP parameters were calibrated and accurate simulation results were obtained by comparing the experiment load–displacement response and crack location. The capital has an enhanced effect on the load-bearing capacity of the slab-column connections. The larger the radius of the capital, the more obvious the reduction in the transmission of bending moments. From LC2 to LC4, the radius of the capital is increased by 55 mm each. The LC3 has a 13.3% reduction in the moment transfer coefficient compared to LC2 and LC4 has a 30.7% reduction compared to LC3. This indicates that the larger the capital the higher the safety when the joint is subjected to bending moments.

In this paper, the optimum result is obtained when the ratio of the difference between the radius of the capital and the column to the thickness of the capital is 4. Therefore, in practical design, a larger radius of the capital would be more secure for the safety of the structure. However, more experiments are needed to investigate exactly what ratio of the radius of the capital to its thickness is the optimal solution.

References

1. Lima Neto A, Ferreira M, Oliveira D, Melo G (2013) Experimental and numerical analysis of reinforced concrete mushroom slabs. *Revista IBR-ACON de Estruturas e Materiais*. 6:270–306. <https://doi.org/10.1590/S1983-41952013000200007>
2. ACI Committee 318 (2019) Building code requirements for structural concrete and commentary. American Concrete Institute, Farmington Hills, MI
3. ABAQUS Analysis user's manual 6.12-3, Dassault Systems Simulia Corp., Providence, RI, USA
4. Lubliner J, Oliver J, Oller S, Onate E (1988) A plastic-damage model for concrete. *Int J Solid Struct* 25(3):299–326
5. Lee J, Fenves GL (1998) Plastic-Damage model for cyclic loading of concrete structures. *J Eng Mech* 124(8):892–900
6. GB50010-2010 (2011) Code for design of concrete structures (in Chinese)
7. Sidoroff F (1981) Description of anisotropic damage application to elasticity. In: *Physical non-linearities in structural analysis*. Springer, Berlin Heidelberg

Open Access This chapter is licensed under the terms of the Creative Commons Attribution 4.0 International License (<http://creativecommons.org/licenses/by/4.0/>), which permits use, sharing, adaptation, distribution and reproduction in any medium or format, as long as you give appropriate credit to the original author(s) and the source, provide a link to the Creative Commons license and indicate if changes were made.

The images or other third party material in this chapter are included in the chapter's Creative Commons license, unless indicated otherwise in a credit line to the material. If material is not included in the chapter's Creative Commons license and your intended use is not permitted by statutory regulation or exceeds the permitted use, you will need to obtain permission directly from the copyright holder.



Research on Restoring Force Model of Built-in Steel Tube Reinforced STRC Column Joints



Jiahao Zhang and Qiuwei Wang

Abstract In the circular steel tube confined reinforced concrete (STRC) column frame structure, because there is no effective restraint of steel tube in the joints area, it becomes a relatively weak part. Therefore, this paper proposes a STRC column joints with a section of steel tube built in the joints area, and expounds the structural form of the new joints. ABAQUS finite element analysis software is used to simulate the quasi-static test of joints. On the basis of verifying the rationality and reliability of the finite element analysis method, six joints models of build-in steel tube reinforced STRC columns with different lengths are established. Based on the model skeleton curve obtained by simulation analysis, the eigenvalues of each loading stage are fitted to obtain the skeleton curve model regression equation and stiffness degradation law. The three fold restoring force model of steel tube STRC column joints with different lengths is established. The skeleton curves of restoring force model and finite element calculation results are compared and analyzed to verify the correctness of restoring force model. The results show that the restoring force model is in good agreement with the finite element analysis results. The established restoring force model can provide a reference for the elastic-plastic change and seismic analysis of build-in steel tube reinforced STRC column joints.

Keywords STRC column · Build-in steel tube · FEA · Skeleton curve · Restoring force mode

J. Zhang (✉) · Q. Wang

College of Civil Engineering, Xi'an University of Architecture and Technology, Xi'an 710055, China

e-mail: ZJH1001L@163.com

Q. Wang

State Key Laboratory of Green Building in Western China, Xi'an University of Architecture and Technology, Xi'an 710055, China

This is a U.S. government work and not under copyright protection in the U.S.; foreign copyright protection may apply 2023

Y. Yang (ed.), *Advances in Frontier Research on Engineering Structures*, Lecture Notes in Civil Engineering 286, https://doi.org/10.1007/978-981-19-8657-4_9

1 Introduction

Steel tube confined concrete column is a new type of composite member in which the steel tube does not directly bear the longitudinal load [1]. In practical engineering, frame columns are usually subjected to the combined action of axial force, shear force and bending moment. Therefore, it is necessary to configure reinforcement in steel tube confined concrete columns to form steel tube confined reinforced concrete (STRC) [2]. In STRC column frame structure, because the outer steel pipe of the column is disconnected in the joints area, without the effective restraint of the steel pipe, the joints will become a relatively weak part. Therefore, strengthening measures should be taken for the joints area of STRC column frame to meet the seismic design requirements of “strong joints and weak members”.

In recent years, domestic and foreign scholars [3–11] have conducted a lot of research on the structure of steel tube confined concrete column and various joints strengthening measures. In terms of joints, Jianguo Nie proposed the form of steel tube non penetrating ring beam joints, and multiple reinforcement rings are arranged horizontally in the joints area, so that the concrete in the joints area is subject to multiple constraints [7]. The results show that under the action of transverse multiple constraints, the axial compressive strength of the core concrete in the joints area can make up for the strength weakening caused by the disconnection of the steel tube in the joints area. Liangcai Xiao conducted axial compression test research and nonlinear finite element analysis on 18 steel tube confined concrete joints with high longitudinal reinforcement ratio. The test results show that reducing the height of the joints area and increasing the number of beams can improve the axial compression bearing capacity [8]. Xuhong Zhou strengthened the circular steel tube confined concrete beam column joints through the structural measures of horizontal haunching and stirrup densification in the joints area. The test results show that this structural measure improves the axial compression performance of the steel tube confined concrete beam column joints, and the damage degree in the core area of the joints is relatively light [9]. Qingjun Chen and others have conducted a series of studies on the column steel pipe incomplete through joints in the joints area. These joints form mainly increases the area of the joints area by adding the ring beam or horizontal reinforcement cage in the joints area, so as to increase the bearing capacity of the joints. The results show that, under the constraints of ring beam and circumferential reinforcement, the steel tube incomplete through joint has high bearing capacity and good ductility, but the volume of outer ring beam is large, so it has some limitations when applied to corner joints [10, 11].

To sum up, the main problems of the joints strengthening measures proposed for STRC column joints are as follows: (1) the structure is complex; (2) The increase of node section size affects the appearance of the building and the construction is complex; (3) The strengthening measures have poor reinforcement effect on edge joints and corner joints. Therefore, the author of this paper proposes to build a section of build-in steel tube reinforced STRC column joints. Through finite element analysis, the restoring force characteristics of build-in steel tube reinforced STRC

column joints with different lengths are analyzed and studied. In this paper, the author proposes a section of build-in steel tube reinforced STRC column joints. Through finite element analysis, the restoring force characteristics of build-in steel tube reinforced STRC column joints with different lengths are analyzed and studied. According to the characteristics of skeleton curve, a three fold restoring force model is proposed by using regression analysis method, and the stiffness degradation law and hysteretic rule of hysteretic curve are analyzed and compared with the simulation results, it provides a reference for the seismic performance prediction and structural design of the proposed new joints.

2 Establishment of Finite Element Model

2.1 Material Constitutive Relation

The steel used in the finite element analysis is mainly divided into reinforcement and steel tube. Assuming that they are ideal elastic-plastic materials, they are divided into elastic section and yield section according to the binary constitutive relationship. The slope of the elastic section is the elastic modulus of the corresponding reinforcement or steel, the slope of the yield section is 0, the poisson's ratio is 0.3, the elastic modulus is 2.06×10 MPa, and the yield strength of the material is 235 MPa.

There are mainly two kinds of concrete constitutive models. The concrete outside the steel tube restraint area adopts the uniaxial tension and compression constitutive relationship of ordinary concrete recommended in GB50010-2010 code for design of concrete structures. The tensile constitutive of concrete in the confined area of steel tube is consistent with that of ordinary concrete. The compressive constitutive model adopts the equivalent stress-strain relationship of concrete considering different restraint levels proposed in document 12, and the specific expression is as follows:

$$y = \begin{cases} 2x - x^2 & (x \leq 1) \\ \frac{x}{\beta_o \cdot (x-1)^2 + x} & (x > 1) \end{cases} \quad (1)$$

where: $x = \frac{\varepsilon}{\varepsilon_{co}}$; $\varepsilon_{co} = \varepsilon_c + 800 \cdot \xi^{0.2} \cdot 10^{-6}$; $\xi = \frac{f_y A_s}{f_{ck} A_c}$; $y = \frac{\sigma}{\sigma_{co}}$; $\varepsilon_c = (1300 + 12.5 f_{co}) \cdot 10^{-6}$; $\sigma_{co} = f_{co}$; f_{co} is the axial compressive strength of concrete; σ_{co} and ε_{co} are the corresponding peak stress and peak strain in the equivalent stress-strain relationship, respectively; f_y and f_{ck} are the standard values of yield strength of steel and compressive strength of concrete respectively; A_s and A_c are the cross-sectional areas of steel tube and concrete in the core area respectively [12].

2.2 Model Establishment

C3D8R eight node linear reduced integral hexahedron element is selected to simulate concrete; the S4R four node curved thin shell reduced integral element is used to simulate the steel tube; the reinforcement is simulated by two node linear three-dimensional truss element (T3D2). The elements size is taken as 1/50 of the height of the node model.

The interaction between beam and column reinforcement and concrete and the interaction between steel core embedded in concrete and concrete are simulated by embedded region, which has simple operation and high calculation efficiency. For the interaction between the steel tube wrapped around the column and the concrete surface, it is transmitted through the contact surface, which can be simulated by considering the normal and tangential interface properties of the contact surface. Normal upward, it is generally considered that the pressure at the interface can be completely transmitted, and the “hard contact” simulation is adopted; In the tangential direction, it can be considered that the interaction between concrete and steel tube conforms to the Coulomb friction model, and the shear stress transfer between interfaces can be described by the following formula:

$$\tau = \mu \cdot p \geq \tau_{bond} \quad (2)$$

where μ is the friction coefficient between interfaces; p is the normal pressure of the interface; τ_{bond} is the average bond force between steel tube and concrete interface. Cai Shaohuai et al. made a detailed analysis on the bonding mechanism and pointed out that the surface condition of steel tube, concrete strength and concrete curing conditions have a significant impact on the bonding strength of the interface. When the steel tube is mechanically derusted before pouring concrete, the average bonding force of the interface can be calculated according to formula (3) [13, 14]. Considering the test and engineering practice, the steel tube will be derusted before pouring concrete, which meets the application conditions of Eq. (3), so the parameter value will be taken as the basis.

$$\tau_{bond} = 0.1 \cdot (f_{cu})^{0.4} \quad (3)$$

Referring to the boundary conditions and loading methods of the previous quasi-static test [15], the column end loading is adopted, and the boundary condition setting is divided into two steps: (1) apply axial force: the column bottom is set as hinged, the beam end is free end, and the axial force is perpendicular to the column top plane. (2) Apply horizontal displacement: the beam end is set as sliding hinge support, the column bottom remains hinged, and displacement loading is adopted.

2.3 Verified by Experiments

In order to verify the reliability of the finite element analysis method, the test piece in literature 15 is selected as the research object for finite element analysis of the test piece. The comparison between the test results and the results obtained by the finite element analysis method in this paper is shown in Fig. 1. It can be seen that the finite element analysis results are in good agreement with the test results.

On the basis of verifying the reliability of the finite element analysis method, six finite element analysis models of build-in steel tube reinforced STRC column joints with different lengths are established. All the test pieces have the same parameters except the length of the build-in steel tube. The height of the test piece is 2360 mm. The outer steel pipes of the upper and lower columns are made of Q235 steel, with a diameter of 273 mm and a thickness of 3 mm. In order to make the column steel pipe not bear the longitudinal load, the outer steel pipes of the column are disconnected from the column top and the node area respectively, and the joint width is 10 mm, 8C10 is configured in the column. Stirrup selection A8@100, 4 stirrups are set in the core area of the joint, with a spacing of 60 mm; The distance between the loading points of the left and right beams of the test piece is 3000 mm, and the section size of the beam is 200 mm × 350 mm, the longitudinal reinforcement of the beam is equipped with 16C16, and the stirrup is made of A8@100. The concrete strength is C60. The relevant parameters of the test piece are shown in Table 1.

Fig. 1 Force-displacement curves comparison between test and FEA results referred to specimen

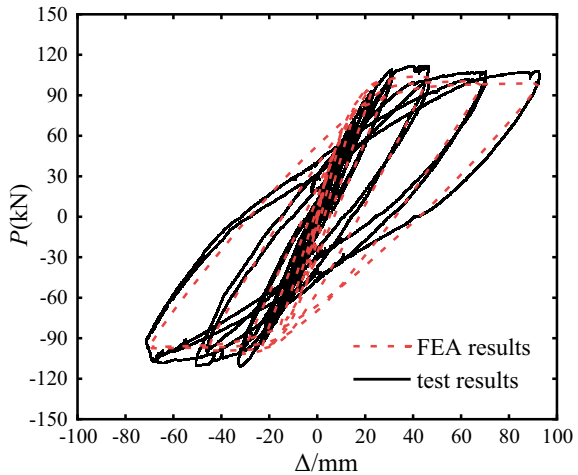


Table 1 Summary of test specimens

Node number	Specification of built-in steel tube ($D \times \delta$)	Section steel content (β) (%)	Length of built-in steel tube (h_e /mm)	Axial compression ratio (λ)
JD-1	149 × 6	4.61	400	0.5
JD-2	149 × 6	4.61	500	0.5
JD-3	149 × 6	4.61	600	0.5
JD-4	149 × 6	4.61	700	0.5
JD-5	149 × 6	4.61	800	0.5
JD-6	149 × 6	4.61	900	0.5

Note build-in steel tube specification D and δ represents the outer diameter and thickness of the build-in steel tube respectively. Section steel content $\beta = A_s/A_c$, where A_s is the net cross-sectional area of build-in steel tube and A_c is the cross-sectional area of steel tube confined concrete column. Axial compression ratio λ . The calculation formula of axial bearing capacity of steel tube confined concrete members given in the technical specification for steel tube confined concrete structures is adopted $\lambda = N/N_0$

2.4 Finite Element Analysis Results

The skeleton curve is the envelope of peak points at all levels in the hysteretic curve obtained by repeated cyclic loading. The node hysteretic curve is obtained through finite element simulation, and the skeleton curves of 6 specimens are extracted, as shown in Fig. 2.

Stiffness degradation refers to the phenomenon that the peak displacement increases with the increase of the number of cycles when the same peak load is maintained under the action of cyclic repeated load. In order to quantitatively describe

Fig. 2 FEA results of skeleton curve

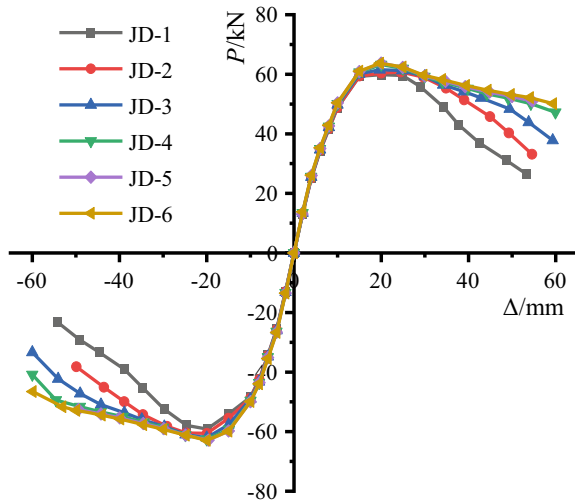
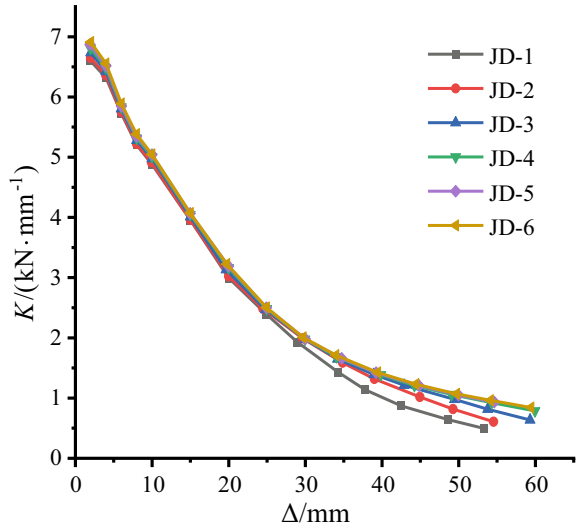


Fig. 3 Stiffness degradation curve



the stiffness degradation, the ratio of the sum of the maximum horizontal load of N cycles to the sum of displacement amplitude is defined as the equivalent stiffness K , and the calculation formula is as follows:

$$K_i = \frac{\sum_{i=1}^n P_i}{\sum_{i=1}^n \Delta_i} \tag{4}$$

where: K is the equivalent stiffness; P_i is the horizontal load corresponding to the i -th displacement angle; Δ_i is the amplitude of stage i .

The stiffness degradation curve can be obtained after data processing, as shown in Fig. 3. By analyzing the skeleton curve and stiffness degradation curve of 6 specimens, it can be seen that: (1) The initial stiffness of each specimen before yield is roughly the same. (2) In the elastic-plastic stage, the stiffness of each specimen increases with the increase of the length of the built-in steel tube, and the ultimate bearing capacity increases slightly. The built-in steel tube of specimen JD-6 is the longest, so its ultimate bearing capacity is the highest. (3) The stiffness degradation rate decreases with the increase of loading displacement. In the failure stage, the stiffness degradation rate decreases with the increase of the length of the built-in steel tube.

3 Establishment of Resilience Model

Structural members will produce a series of nonlinear performance strains under seismic conditions. In order to analyze the mechanical performance of members in the

whole process of earthquake, the elastic–plastic time history analysis of the structure must be carried out. The relationship between the elastic and plastic restoring force of the structure is obtained from the simplified mathematical model, and the appropriate restoring force of the structure is obtained from the mathematical model of the seismic response, it can reflect the mechanical properties of joints in strength, stiffness, energy consumption and ductility.

3.1 Four Basic Assumptions

In order to establish the restoring force model of build-in steel tube reinforced STRC column joints with different lengths, the following four assumptions are adopted: (1) the maximum elastic load point is taken as the yield load point; (2) In the elastic stage, the unloading stiffness is the initial stiffness, and after the elastic stage, the stiffness begins to deteriorate; (3) The skeleton curve adopts the three line model considering stiffness degradation; (4) Repeated cyclic loading conforms to the fixed-point pointing law [16].

3.2 Establishment of Skeleton Curve

With the increase of the length of the build-in steel tube, the ultimate bearing capacity of the joint specimen increases slightly. At the same time, the bearing capacity of the specimen decreases slowly in the failure stage, the deformation capacity increases gradually in the later stage, and the ductility is improved. The restoring force model is simplified according to the dimensionless skeleton curve of build-in steel tube reinforced STRC column joints with different lengths and the data results obtained from numerical simulation analysis. The specific description is divided into the following three stages:

- (1) Elastic stage: Through the analysis of the skeleton curves of six specimens with different lengths of build-in steel tube reinforced STRC column joints, it is found that there are no obvious cracking points. The main reason is that the build-in steel tube in the joint area can well restrict the transverse deformation of the concrete in the joint core area, and resist shear together with the concrete, so the stiffness attenuation of the joint area is small in the elastic stage. Connecting the coordinate origin O and yield point a, the OA section is regarded as the elastic section of the build-in steel tube reinforced STRC column joint specimen. This stage refers to the process from the loading of the specimen to the yield of the specimen. The load displacement curve is basically linear. The slope of this stage is the initial stiffness of the member, and the calculation formula of its equivalent stiffness is:

$$K_e = P_y / \Delta_y \tag{5}$$

- (2) Elastoplastic stage: This stage refers to the process from the yield of the specimen to the peak point of the specimen. With the increase of displacement, the growth of load becomes slower than that in the previous stage, and the stiffness degradation is significant. The elastic-plastic stage of the skeleton curve is regarded as AB, and its equivalent stiffness is described as follows:

$$K_s = \frac{P_{max} - P_y}{\Delta_{max} - \Delta_y} \tag{6}$$

- (3) Plastic stage: This stage refers to the process from the maximum bearing capacity of the specimen to the failure of the specimen. At this stage, the load of the specimen begins to decrease with the increase of displacement, which is simplified as section BC in Fig. 4. The equivalent stiffness K_p of the specimen in the plastic stage is:

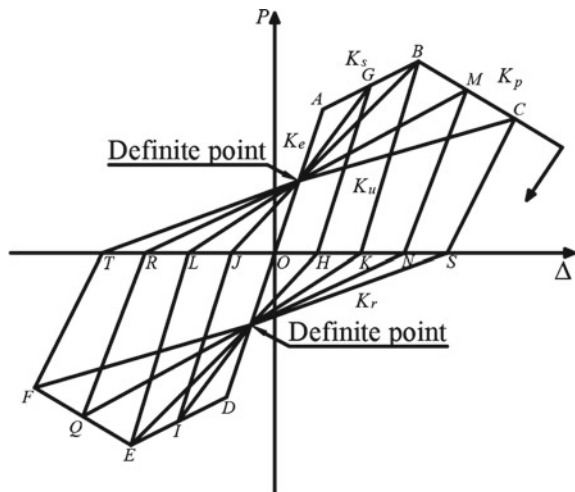
$$K_p = \gamma_d K_e \tag{7}$$

The regression analysis of the data points of the finite element analysis results shows that the relationship between the length of the build-in steel tube and the stiffness degradation rate in the plastic stage of the specimen is:

$$\gamma_d = -0.05153 - 1.45512 \cdot e^{-0.00548h_e} \tag{8}$$

where γ_d is stiffness degradation rate; h_e is the length of build-in steel tube, unit: mm.

Fig. 4 Degenerative three-line resilience model



3.3 Determination of Unloading Stiffness and Reloading Stiffness

With the increase of loading displacement, the strength and stiffness of the specimen degenerate. Therefore, the slope changes of loading section and unloading section in hysteresis loop can be used for quantitative calculation. Based on the analysis of the simulation data of six specimens with different lengths of build-in steel tube reinforced STRC column joints, the positive and negative loading and unloading stiffness are dimensionless, and the following formula can be obtained by fitting:

$$K_u/K_e = (\Delta_y/\Delta_l)^U \quad (9)$$

$$K_r/K_e = (\Delta_y/\Delta_l)^R \quad (10)$$

where $U = -0.58541 + 5.51436 \cdot 10^{-4} \cdot h_e - 3.04018 \cdot 10^{-7} \cdot h_e^2$; $R = -2.22731 + 0.00485 \cdot h_e - 3.7909 \cdot 10^{-6} \cdot h_e^2$.

3.4 Hysteresis Loop Rule

By analyzing the characteristics of build-in steel tube reinforced STRC column joints with different lengths, the three fold linear restoring force model is shown in Fig. 4.

The hysteresis loop rules can be summarized as follows:

- (1) From the initial loading to the yield value of the specimen, the loading and unloading are carried out according to the elastic section of the skeleton curve (OA/OD section in Fig. 4), and the loading and unloading stiffness is the initial elastic stiffness K_e .
- (2) After the specimen reaches the peak load, it enters the strengthening stage along the AG load path. When unloading in the forward direction, the unloading direction changes from G to H, and the unloading stiffness begins to deteriorate, which can be determined by formula (9); When reverse loading, take the intersection of the curve with zero unloading and the coordinate axis as the starting point and carry out along the skeleton curve. The reverse loading path is HI, and the reverse loading stiffness is calculated by formula (10); The corresponding path during reverse unloading is the IJ segment in Fig. 4.
- (3) When the extreme load point is reached, if the load is unloaded at the peak point B, the corresponding unloading path is section BK in Fig. 4. When the load is unloaded to 0, the load is loaded reversely, and the loading path points to the reverse peak load point E. If it is unloaded at point M, the unloading path is MN section. During reverse loading, it is carried out along the path NQ, and during unloading, it is from point Q to point R.

4 Conclusion

- (1) The build-in steel tube has an obvious enhancement effect on the seismic performance of STRC column joints. When the length of the core steel tube increases, the stiffness of the joint specimen increases, the ultimate bearing capacity increases, the stiffness degradation rate slows down with the increase of loading displacement, and the stiffness degradation rate of the specimen in the plastic stage slows down with the increase of the length of the build-in steel tube.
- (2) On the basis of verifying the rationality and reliability of the finite element analysis method, through the analysis and fitting regression of the simulation results, the calculation formula of the skeleton curve characteristic parameters of steel tube STRC column joints with different lengths is obtained, and the three broken line skeleton curve model is proposed. The comparison between the calculation results and the simulation results shows that there is little difference between them.
- (3) Based on the skeleton curve model obtained by regression analysis, the calculation method of loading and unloading stiffness in hysteretic curve is determined. At the same time, the length of build-in steel tube is introduced as a parameter, and the calculation formula of loading and unloading stiffness is obtained. According to the finite element simulation results and the three fold skeleton curve, the stiffness degradation law and hysteretic rule of the model are analyzed. The established degraded three fold restoring force model can effectively reflect the hysteretic characteristics of steel tube STRC column joints with different lengths, which can provide a reference for the elastic-plastic analysis and engineering application of the structure.
- (4) This paper only studies the seismic performance of in-plane joints of steel tube reinforced STRC columns under low cyclic loading. The seismic performance of edge joints, corner joints, spatial joints and frame structures and the similarities and differences between them need to be further studied.
- (5) The restoring force model proposed in this paper is only based on the length of build-in steel tube. For the case of multi parameters in practical engineering, it needs more comprehensive and in-depth research.

References

1. Jianyang XUE (2007) Steel and concrete composite structure. Science Press, Beijing, p 221
2. Xuhong ZHOU, Jiepeng LIU (2010) Performance and design of steel tube confined concrete column. Science Press, Beijing, p 268
3. Choi S-M, Park S-H, Yun Y-S, Kim J-H (2010) A study on the seismic performance of concrete-filled square steel tube column-to-beam connections reinforced with asymmetric lower diaphragms. *J Constr Steel Res* 66(7):962–970

4. Qudah S, Maalej M (2014) Application of engineered cementitious composites (ECC) in interior beam-column connections for enhanced seismic resistance. *Eng Struct* 69(9):235–245
5. Kiamanesh R (2010) The effect of stiffeners on the strain patterns of the welded connection zone. *Steel Constr* 66(1):19–27
6. Huang Y, Helen G, Emad G (2008) Experimental and numerical investigation of the tensile behavior of blind-bolted t-stub connections to concrete-filled circular columns. *J Struct Eng* 134(2):198–208
7. Jianguo NIE, Yu BAI, Fujun LIU, Jingming FU (2004) Experimental study on axial compression behavior of layered concrete filled steel tubular joints. *Building Structures* 34(12):57–59
8. Xiao L (2011) Static axial compression behavior of tubed RC beam-column joint with high longitudinal reinforcement ratio. Harbin: Harbin Institute of Technology, 2011:10–38
9. Xuhong ZHOU, Biao YAN, Dan GAN et al (2013) Experimental research on circular tubed RC beam-column joints with horizontal haunches under axial compression. *J Build Struct* 34(S1):59–65
10. Qingjun CHEN, Jian CAI, Gang XU et al (2008) Experimental investigation into a new type of concrete filled steel tubular column-beam joint with the discontinuous column tube in joint zone under compression. *J South China Univ Technol (Nat Sci Ed)* 36(6):10–16
11. Qingjun CHEN, Jian CAI, Ping YANG et al (2009) Seismic behavior of concrete filled steel tubular column-beam joints with discontinuous column tubes. *Chin Civil Eng J* 42(12):33–42
12. Linhai HAN (2000) Concrete filled steel tube structure. Science Press, Beijing, pp 101–118
13. Lihong XUE, Shaohuai CAI (1996) Bond strength at the interface of concrete-filled steel tube columns. *Build Sci* 3:22–28
14. Lihong XUE, Shaohuai CAI (1996) Bond strength at the interface of concrete-filled steel tube columns. *Build Sci* 4:19–23
15. Biao YAN (2008) Research on the static and seismic behavior of circular tubed RC column to RC beam joints. Lanzhou University, Lanzhou
16. Jinjie MEN, Peng LI, Zhifeng GUO (2015) Research on restoring force model of RC column-steel beam composite joints. *Ind Constr* 45(5):132–137

Open Access This chapter is licensed under the terms of the Creative Commons Attribution 4.0 International License (<http://creativecommons.org/licenses/by/4.0/>), which permits use, sharing, adaptation, distribution and reproduction in any medium or format, as long as you give appropriate credit to the original author(s) and the source, provide a link to the Creative Commons license and indicate if changes were made.

The images or other third party material in this chapter are included in the chapter's Creative Commons license, unless indicated otherwise in a credit line to the material. If material is not included in the chapter's Creative Commons license and your intended use is not permitted by statutory regulation or exceeds the permitted use, you will need to obtain permission directly from the copyright holder.



Study on Frost Resistance of Steel-PVA Hybrid Fiber Concrete



Ditao Niu, Siyu Gong, Bingbing Guo, Zhiyuan Cao, and Yan Wang

Abstract Freeze–thaw damage in cold areas is an important reason for the deterioration of durability of concrete structures, and the addition of fiber can effectively improve the frost resistance of concrete. To study the effect of steel fiber and polyvinyl alcohol (PVA) fiber on the frost resistance of concrete, an orthogonal experimental method was applied to analyze the frost resistance of steel-PVA hybrid fiber concrete. The effect of the steel fiber content, PVA fiber content, and steel fiber types were investigated on the mass-loss rate and relative dynamic elastic modulus of fiber concrete, to explore the mechanism of high frost resistance of it. The results show that steel fiber content has a significant effect on the mass-loss rate and relative dynamic elastic modulus of fiber concrete. The influence of PVA fiber content on the relative dynamic elastic modulus is relatively great, and the influence of steel fiber types of the mass-loss rate is the same. The frost resistance of concrete can be improved by adding hybrid fiber in concrete. When 1.0% End-hook steel fibers and 0.3% PVA fibers are added, the concrete specimen has the best frost resistance.

Keywords Freeze–thaw cycle · Steel fiber · PVA fiber · Frost resistance · Orthogonal experiment

1 Introduction

Professor Mehta [1] has pointed out that the freeze–thaw cycle is one of the main reasons for the reduction of concrete durability. In northeast and northwest of China, a large number of concrete structures are damaged due to long-term freeze–thaw cycles of varying degrees, seriously affecting the service life and safety performance of concrete structures, and causing certain economic losses [2, 3]. Therefore, improving

D. Niu · S. Gong · B. Guo (✉) · Z. Cao
College of Civil Engineering, Xi'an University of Architecture and Technology, Xi'an 710055,
China
e-mail: 18392775037@163.com

Y. Wang
College of Materials Science and Engineering, Xi'an University of Architecture and Technology,
Xi'an 710055, China

This is a U.S. government work and not under copyright protection in the U.S.; foreign copyright protection may apply 2023

Y. Yang (ed.), *Advances in Frontier Research on Engineering Structures*, Lecture Notes in Civil Engineering 286, https://doi.org/10.1007/978-981-19-8657-4_10

the frost resistance of concrete material is helpful to improve the durability of concrete structures.

Under the action of freeze–thaw cycle, the micro-cracks and pores in concrete gradually expand under the influence of hydrostatic pressure and osmotic pressure, and finally cause the freeze–thaw damage to concrete. To study the influence of fiber on the frost resistance of concrete, scholars at home and abroad has done a lot of research and found that the addition of fiber can effectively slow down the cracking of concrete and improve its frost resistance [4–7]. With the deepening of research, the fibers mixed in concrete have gradually developed from single fibers to incorporate fibers of different types and sizes. When two or more fibers were incorporated, they were able to achieve different effects on the concrete [8, 9].

In this paper, the freeze–thaw cycle experiment of steel -PVA hybrid fiber concrete was carried out by orthogonal experiment to study the effects of different steel fiber content, PVA fiber content and steel fiber type on the mass-loss rate and relative dynamic elastic modulus of the specimen, and the mechanism of high frost resistance of steel -PVA fiber concrete was expounded.

2 Experiment

2.1 Raw Materials of Experiment

The strength of concrete used in the experiment is C35. The cement is P·O42.5 ordinary Portland cement; the coarse aggregate is crushed stone with 5 ~ 10 mm continuous gradation, and the fine aggregate is natural medium sand with fineness modulus of 2.54. The water reducing agent is polycarboxylate superplasticizer with a water-reducing rate of $\geq 10\%$; Three types of steel fibers are selected: end hook type with a length of 30 mm, a diameter of 0.6 mm, an aspect ratio of 50, indentation type with a length of 32 mm, a diameter of 0.7–1.2 mm, an aspect ratio of 45.7–26.2, and high-strength ultra-fine steel fiber with a length of 13 mm, a diameter of 0.18–0.25 mm and an aspect ratio of 72.2–52. The PVA fiber is 12 mm in length, 14 μm in diameter and 845 in length-diameter ratio.

2.2 Design of Mix Proportion

To study the influence of steel fiber content, PVA fiber content and steel fiber types on the frost resistance of concrete, the experiment was designed by orthogonal test method, each influencing factor was selected at three levels, and the L9(3³) orthogonal table was used to design the orthogonal test with three factors and three levels, as shown in Table 1.

Table 1 Orthogonal factor table

Factor	Steel fiber content (%)	PVA fiber content (%)	Steel fiber type
Level 1	0.1	0.05	End hook steel fiber
Level 2	0.5	0.1	Indented steel fiber
Level 3	1.0	0.3	Superfine steel fiber

According to the orthogonal factor table, 9 groups of mix proportion are designed, as shown in Table 2.

Table 2 Mix proportions of hybrid fiber concrete

Group	Cement (kg)	Sand (kg)	Pebble (kg)	Water (kg)	Water reducers (kg)	PVA fiber content (%)	Steel fiber content (%)	Steel fiber type
G1	480	730	1062	240	0.5	—	—	—
G2	480	730	1062	240	1.5	0.05	0.1	End hook steel fiber
G3	480	730	1062	240	4.5	0.05	0.5	Indented steel fiber
G4	480	730	1062	240	4.5	0.05	1.0	Superfine steel fiber
G5	480	730	1062	240	5.5	0.1	0.1	Indented steel fiber
G6	480	730	1062	240	5.5	0.1	0.5	Superfine steel fiber
G7	480	730	1062	240	5.5	0.1	1.0	End hook steel fiber
G8	480	730	1062	240	6.5	0.3	0.1	Superfine steel fiber
G9	480	730	1062	240	7.5	0.3	0.5	End hook steel fiber
G10	480	730	1062	240	7.5	0.3	1.0	Indented steel fiber

Table 3 Orthogonal test results

Group	Mass-loss rate (%)				Relative dynamic elastic modulus (%)			
	n ^a = 25	n = 50	n = 75	n = 100	n = 25	n = 50	n = 75	n = 100
G1	- 0.19	- 0.31	0.21	1.13	82.52	58.52	34.86	16.24
G2	- 0.18	- 0.22	- 0.41	- 0.48	81.51	76.69	54.05	41.04
G3	- 0.1	- 0.24	- 0.36	- 0.42	91.85	76.75	59.71	36.83
G4	- 0.04	- 0.07	- 0.08	- 0.07	98.41	97.16	96.24	91.84
G5	- 0.14	- 0.15	- 0.19	- 0.09	89.07	70.81	50.95	34.87
G6	- 0.06	- 0.25	- 0.38	- 0.53	93.55	65.99	47.32	28.53
G7	- 0.02	- 0.05	0.00	0.01	99.37	100	99.68	101.61
G8	- 0.19	- 0.33	- 0.42	- 0.63	90.46	80.56	64.42	43.24
G9	0.00	0.02	0.02	- 0.01	100.33	98.44	97.51	91.69
G10	- 0.07	- 0.1	- 0.12	0.07	100.95	100.31	99.68	99.37

^a Number of freeze–thaw cycles

3 Experimental Results and Analysis

3.1 Experimental Results

The mass-loss rate and relative dynamic elastic modulus of steel -PVA fiber concrete during freeze–thaw cycles are tested, and the specific test results are shown in Table 3.

3.2 Range Analysis

To investigate the influence of three factors on the mass-loss rate and relative dynamic elastic modulus of steel -PVA fiber concrete, the range analysis of each test result is carried out, and the analysis results are shown in Fig. 1.

It can be seen from Fig. 1a that with the increase of freeze–thaw cycles, the influences of three factors on the mass-loss rate of concrete gradually increase. When the number of freeze–thaw cycles is the same, the steel fiber content has the greatest influence on the mass-loss rate of concrete, followed by the type of steel fiber, and the PVA fiber content has the smallest influence on it.

It can be seen from Fig. 1b that with the increase of freeze–thaw cycles, the influence of three factors on the relative dynamic elastic modulus of concrete gradually increases. When the number of freeze–thaw cycles is the same, the steel fiber content has the greatest influence on the relative dynamic elastic modulus of concrete, and the PVA fiber content and the type of steel fiber have similar influences on it.

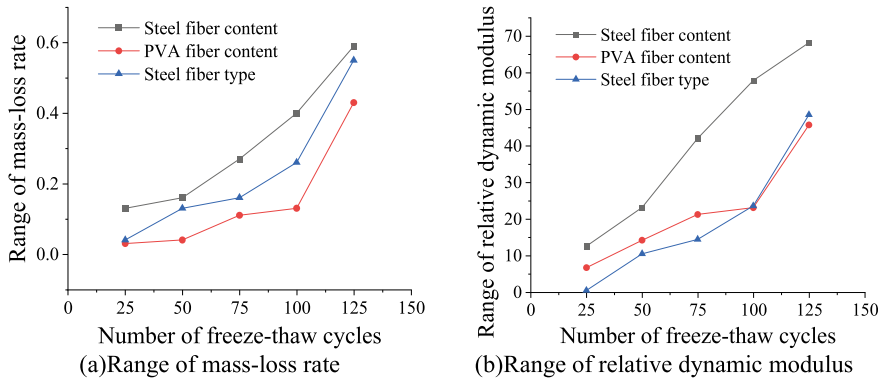


Fig. 1 Range analysis result

3.3 Factor-Index Analysis

According to the orthogonal experimental method, the mass-loss rate and relative dynamic elastic modulus are called indexes. Combined with Tables 2 and 3, the average values of the three factors at each level can be obtained, as shown in Figs. 2 and 3.

It can be seen from Fig. 2 that the greater the steel fiber content, the greater the mass-loss rate of concrete; With the increase of freeze–thaw cycles, the mass-loss rate of concrete gradually decreases, but the PVA fiber content has no obvious relationship with the mass-loss rate. With the increase of freeze–thaw cycles, different types of steel fibers have different effects on the mass-loss rate of concrete; generally speaking, the end hook steel fiber has the largest mass-loss rate, followed by indentation steel fiber and superfine steel fiber.

It can be seen from Fig. 3 that the greater the steel fiber content, the greater the relative dynamic elastic modulus of concrete; The greater the PVA fiber content, the greater the relative dynamic elastic modulus of concrete. The relative dynamic

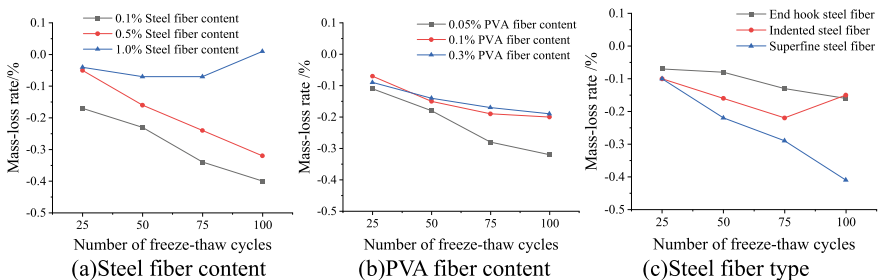


Fig. 2 Relationship between three factors and mass-loss rate

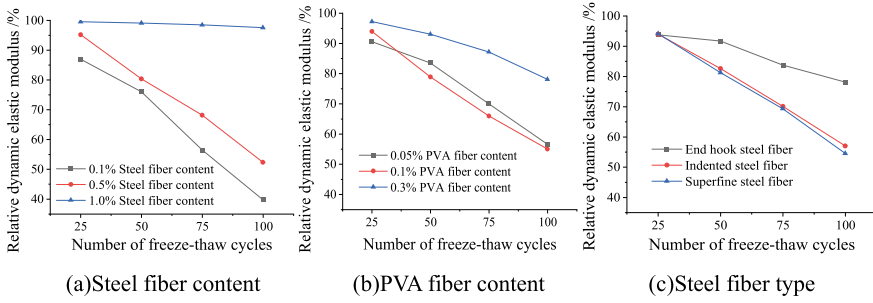


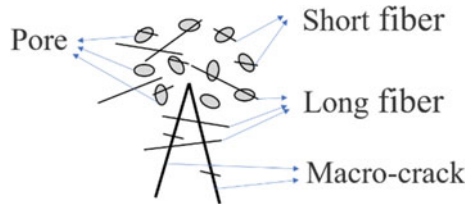
Fig. 3 Relationship between three factors and relative dynamic elastic modulus

elastic modulus of hook-shaped steel fiber is the largest, and the relative dynamic elastic modulus of indentation steel fiber is close to that of superfine steel fiber.

3.4 Mechanism of High Frost Resistance of Steel—PVA Fiber Concrete

It can be seen from the above analysis that adding PVA fiber based on steel fiber can refine the pore structure, reduce the appearance of initial cracks and inhibit the development of freeze–thaw cracks. This is because the mixture of steel fiber and PVA fiber can play a role in different stages and scales of crack development. The effect model of high frost resistance of steel -PVA fiber concrete is shown in Fig. 4. PVA fibers are evenly dispersed in the concrete to bridge the micro-cracks in the concrete. Hook-shaped steel fiber can bridge the macro-cracks, transfer the stress on both sides of the cracks, reduce the stress at the crack tip, and effectively prevent the macro-cracks from further expanding. Moreover, the interface transition zone between the smooth fiber surface and cement paste has good hydration and compact structure. For indented steel fiber, the hydration effect of cement around it is worse than that around the end hook steel fiber, because of uneven surface curvature and uneven water distribution. The shape of superfine steel fiber is similar to PVA, so it is difficult for them to give full play to the complementary advantages of fiber length in concrete.

Fig. 4 Hybrid fiber distribution in concrete



To sum up, the frost resistance of end-hooked steel—PVA hybrid fiber concrete is better, mainly because dense hydration products can be formed around the smooth surface of end hook fiber, which reduces the permeability of concrete. PVA fiber has small volume and many elements per unit volume, which can refine pores, reduce connected pores, make the air in the concrete evenly distributed and bridge micro-cracks. Therefore, the end hook steel fiber -PVA fiber hybrid can realize the complementary functions of the two fibers, resist the freeze–thaw damage more effectively, and show the "positive" hybrid effect of fibers.

4 Conclusion

Through the freeze–thaw cycle experiment of steel -PVA hybrid fiber concrete, the mass-loss rate and relative dynamic elastic modulus of the specimen are analyzed, and the frost resistance mechanism is explored, so as to obtain the optimal mix ratio of high frost resistance concrete, which provides a certain reference value for practical projects. The main conclusions are as follows:

- (1) Different factors have different effects on the mass-loss rate and relative dynamic elastic modulus of concrete. The steel fiber content has the greatest influence on them, the PVA fiber content has a great influence on the relative dynamic elastic modulus, and the content of steel fiber has a great influence on the mass-loss rate. With the increase of freeze–thaw cycles, the influence of three factors on the frost resistance of concrete gradually increases.
- (2) The more steel fiber content, the better frost resistance of concrete. The more PVA fiber content, the better frost resistance of concrete. Steel fiber concrete with end hook has the best frost resistance. When the fiber content is 1.0% end hook steel fiber + 0.3%PVA fiber, the frost resistance of concrete is the best.
- (3) The end hook steel fiber and PVA fiber are overlapped and complementary to each other in the concrete to improve the initial strength and permeability resistance of concrete, effectively prevent the development of micro-cracks in concrete, and thus improve the frost resistance of concrete.

At present, there are many studies on the frost resistance of concrete, but the problem of freeze–thaw damage of concrete has not been solved from the root. It is necessary to further study the mechanism and measures of frost resistance of fiber reinforced concrete and do more in-depth research on the frost resistance of concrete.

References

1. Mehta PK (1991) Concrete durability-fifty year's progress. In: Proceeding 2nd international conference on concrete durability, American, p 31
2. Yu X, Zang Y, Yuan S, Dong J, Wang Q (2017) Research progress of frost resistance and durability of concrete. *Concrete* 4:15–20

3. Jin S, Li Z, Zhang J, Wang Y (2015) Experimental study on frost resistance of basalt fiber reinforced concrete under corrosive conditions. *Eng Mech* 5:178–183
4. Dong Z, Zhao K, Wang Y (2017) Experimental study on frost resistance of high-strength steel fiber reinforced concrete. *Concrete* 2:63–65
5. Wang L (2014) Experimental study on frost resistance of basalt fiber reinforced concrete. Inner Mongolia University of Technology, Hohhot
6. Haiyan M, Hongfa Y, Wei S (2013) Freezing–thawing durability and its improvement of high strength shrinkage compensation concrete with high volume mineral admixtures. *Constr Build Mater* 39(2):124–128
7. Richardson AE, Coventry KA, Wilkinson S (2012) Freeze/thaw durability of concrete with synthetic fiber additions. *Cold Reg Sci Technol* 83–84
8. Zhang X, Chai Y, Liu J (2014) Experimental study on the proportion optimization of fiber concrete based on freeze-thaw cycle. *Bulletin of Silicate* 33(8):2021–2026
9. Niu D, Jiang L, Bai M (2012) Experimental study on frost resistance of steel fiber reinforced concrete. *Civ Eng Environ Eng* 34(04):80–84+98

Open Access This chapter is licensed under the terms of the Creative Commons Attribution 4.0 International License (<http://creativecommons.org/licenses/by/4.0/>), which permits use, sharing, adaptation, distribution and reproduction in any medium or format, as long as you give appropriate credit to the original author(s) and the source, provide a link to the Creative Commons license and indicate if changes were made.

The images or other third party material in this chapter are included in the chapter's Creative Commons license, unless indicated otherwise in a credit line to the material. If material is not included in the chapter's Creative Commons license and your intended use is not permitted by statutory regulation or exceeds the permitted use, you will need to obtain permission directly from the copyright holder.



Experimental and Numerical Investigation of Weak-Axis Connected Steel Plate Shear Wall with Non-slotted and Partially Slotted Infill Plates



Jiping Hao, Xinghuang Wu, Weifeng Tian, Shenghui Li, and Rong Wang

Abstract All Components with H-shaped section are widely used in steel structures, in which the connection of beam section to column flange (i.e. weak-axis connection) is inevitable. In order to study the mechanical properties of weak-axis connected steel plate shear walls, a 1/3 scaled steel plate wall specimen was designed and subjected to a cyclic test to investigate the properties of stiffness, strength, ductility and energy dissipation. On the basis of this, the partially slotted steel plate shear wall was proposed. The FE model of the test specimen was developed and verified with the test results by FE software Abaqus. Subsequently, the FE model of the partially slotted steel plate wall was developed to study mechanical properties by comparing it with the test specimen. The analysis results show that the partially slotted infill plate can fully play the tension field and avoid the beam's in-span bending, which effectively improves the structural ductility and energy consumption. Although the partially slotted infill plate will weaken the lateral resistance, the partially slotted SPSW still accounts for 75% of that one without slots in lateral bearing capacity. Additionally, the ductility of this partially slotted one is up to 5.79, and its equivalent viscous damping ratio reaches 30%.

Keywords Steel plate shear wall · Weak-axis connection · Partially slotted panel · Cyclic test · Numerical investigation

1 Introduction

Steel plate shear wall (SPSW) is composed of boundary elements and infill steel plates (panels). Compared with the traditional concrete shear wall, the SPSW has excellent performance with the lightweight, high strength, high ductility, good energy dissipation, and flexible installation. In recent years, the SPSWs have been widely used to resist lateral force in high-rise buildings.

J. Hao · X. Wu (✉) · W. Tian · S. Li · R. Wang
School of Civil Engineering, Xi'an University of Architecture and Technology, Xi'an 710055, China
e-mail: flammy0812@163.com

The SPSWs emerged in developed countries such as the United States [1], Japan [2], etc., and have been rapidly developing in China [3–7] since the twenty-first century. In the early stage, the elastic buckling of the infill panel was typically taken as the limit state [8]. This led to the necessity of designing the SPSW as a thick steel plate shear wall to resist seismic forces by increasing the infill plate thickness or using stiffeners [9]. Since the 1980s, Thorburn et al. [10] had noted the post-buckling strength of SPSWs and firstly proposed the tensile strip model for the thin infill plate. Afterwards, using the post-buckling strength rather than the critical buckling strength of the thin infill plate to resist lateral force had already formed a broad consensus. To investigate the mechanical performance of SPSWs, a lot of related research has been done. Literatures [11, 12] firstly summarized the past typical experiments and detailed them numerically. Berman and Bruneau [13–15] put forward the plastic uniform yielding mechanism and developed the plastic design of SPSWs. In the past decade, Tsai et al. [16–18] conducted experimentally and numerically investigations of two-story SPSWs with reduced-beam-section (RBS) connections. Besides, Hao, et al. [3–7, 19] have done a lot of research about SPSWs with various panel treatments, beam-to-column connections, etc. Previous research and engineering practices have shown the good prospect of SPSW in lateral-force resistance.

It is noted that the SPSW subjected to cyclic or seismic load has excellent behavior showing a promising application in high-rise buildings but it is also easily affected by the configuration of panels and beam-to-column joints. In view of this, exploring suitable beam-column connections and infill plate configurations is becoming increasingly necessary. Weak-axis connections, as an inevitable type of beam-to-column connections in steel structures, have been reported in some literatures [20–22]. But there are limited reports about the application of beam-to-column weak-axis connections in SPSWs. In this paper, a 4-story 1/3 scaled weak-axis connected steel plate shear wall is designed and tested under cyclic loading for examining its cyclic behavior. Based on the cyclic test, an improved infill plate configuration that partially slotted on the infill plate is proposed. To further investigate the mechanical performance of weak-axis connected SPSWs, the FE models of the test specimen and the partially slotted SPSW are developed and conducted numerical analysis through the FE software Abaqus.

2 Experimental Work

2.1 Test Specimen and Test Setup

The 4-story scaled specimen denoted as S4RN was designed per related provisions [12], as shown in Fig. 1. It is made of Chinese Q235B steel with a nominal yield stress of 235 MPa mainly consisting of the infill plates (QB), horizontal beams (HL1, HL2) and vertical columns (WZ, NZ). The QB configuration is composed of the flat panels (QB), the angle steels (JG), cover plates (GB), and fishplates (YWB). The

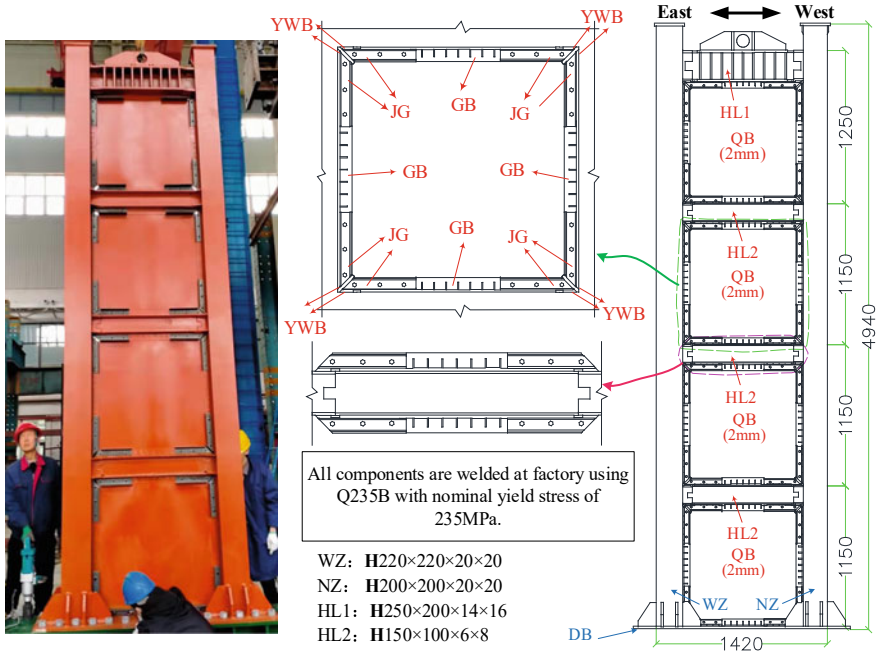


Fig. 1 Geometry and details of test specimen (units: mm)

test setup for S4RN is shown in Fig. 2, in which the test specimen S4RN is pinched by bracing system and mounted on the floor beam through M30 bolts; the S4RN is loaded by the horizontal actuator and vertical Jack through the transfer beam and distribution beam, respectively.

2.2 Loading Protocol and Measurement

The pseudo-static loading of the specimen is mainly divided into vertical loading and horizontal loading. First, the vertical load is applied to the specimen by the hydraulic Jack until the axial compression ratio is about 0.2 on each column. After checking the test setup is working well, the actuator supplies the horizontal load to the specimen by displacement control (Fig. 3) until the specimen happens failure or the lateral fore has dropped to 85% of the max peak lateral force. The horizontal cyclic loading history has thirteen drift levels, each with two cycles, including the drift levels of 0.1, 0.25, 0.5, 0.75, 1.0, 1.5, 2.0, 2.5, 3.0, 3.5, 4.0, 4.5, and 5.0%.

To monitor the concerned deformation of the specimen in real time, displacement meters and strain gauges are selected to place at the corresponding measuring points, as shown in Fig. 4. The displacement meters set on each floor are aimed to gain the specimen’s lateral displacement state. The strain rosettes and strain gauges glued on

Fig. 2 Test setup for S4RN

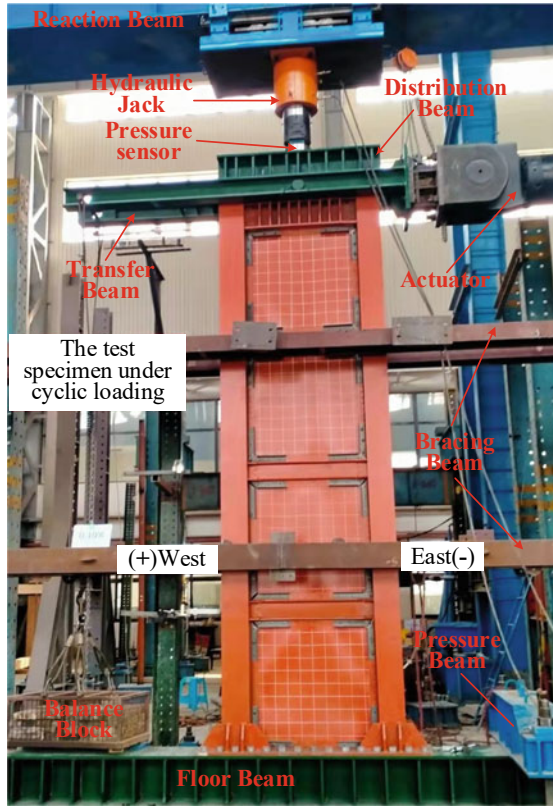


Fig. 3 Cyclic loading history

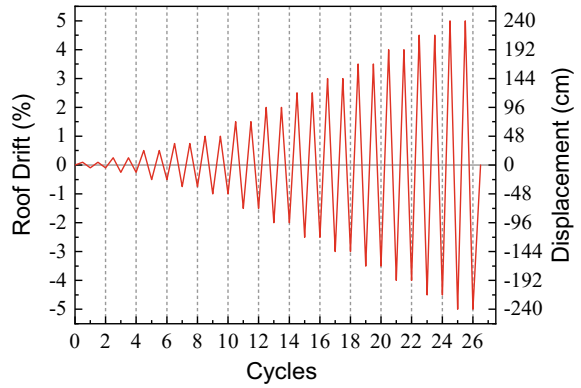
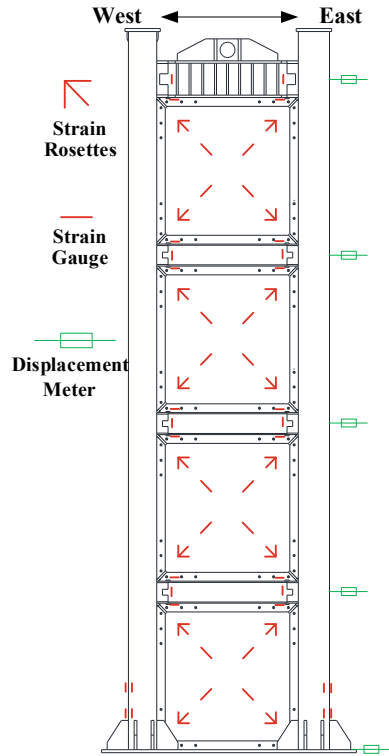


Fig. 4 Layout of measuring points



the infill plates, including the strain gauges attached to the ends of horizontal beams, are aimed to monitor the strain state. Besides, the columns’ flanges are also glued with vertical strain gauges to determine the yielding of the column’s edge.

2.3 Cyclic Behavior of Test Specimen

During the horizontal loading of 0.1~0.25% drift levels, slight local buckling (Fig. 5a) and crisp sound occurred in the 2nd and 3rd story infill plates due to the initial defects and compression. In the 0.5% drift level, infill plates of the 2nd and 3rd stories appeared outside protrusions then the tension bands with the inclined angle of about 36° were observed. Afterward, similar out-of-plane deformation and buckling were observed in the 0.75% drift level.

Until the 1.0% drift, creases and yielding first appeared at the corners of the 2nd story infill plate then developed in the 3rd story. During the 1.5% lateral-drift cycles, multiple local yielding and main tension bands were obvious, the cracks occurred continuously in the corners of the 2nd ~ 4th story infill plates. During the 2.0% drift cycles, secondary tension bands on both sides of the main tension bands along the

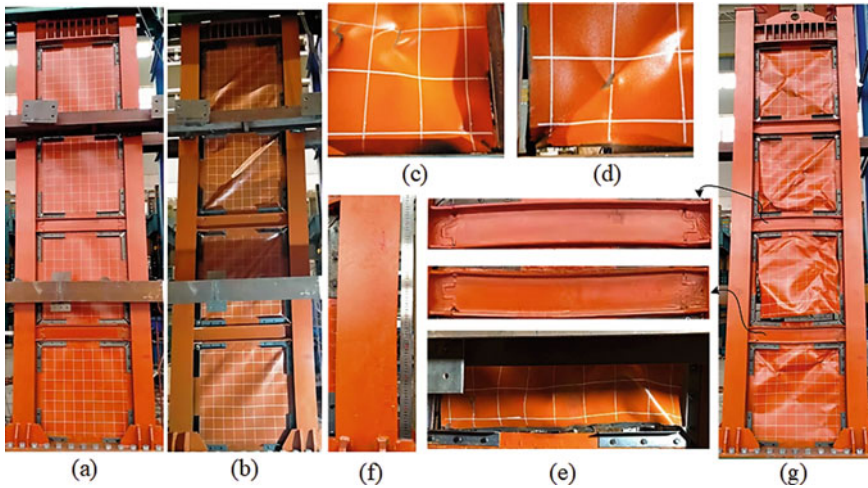


Fig. 5 Details of the S4RN during test: **a** the 1st 0.25% drift cycle; **b** the 1st 3.0% drift cycle; **c** corner tearing of the 3rd story infill plate (2.0% drift); **d** corner fracture and folds of the 2nd story infill plate (3.0% drift); **e** lower edge fracture of the 2nd story infill plate (3.5% drift); **f** flexural hinge of the 1st story west column after the end of test; **g** final failure state of the S4RN

diagonal direction (about 45°) increased, and X-shaped creases near the corners of the 2nd and 3rd story infill plates cracked slightly. At the end of 2.0% drift level, except for the corners in the 1st story infill plate, the others were found horizontal and longitudinal cracks torn, especially the 3rd story infill plate (Fig. 5c). The corner cracks of infill plates developed and extended constantly during the drift level of 2.5 ~ 3.0%, after the first cycle of 3.0% drift (Fig. 5b), serious fracture (the horizontal crack length was about 95 mm) and obvious folds (Fig. 5d) were observed in the lower-left corner of the 2nd story infill plate while the folds on the diagonal of the 3rd story appeared multiple cracks. At this 3.0% drift, the specimen hit the peak shear capacity of 643.57 kN.

During the 3.5% drift cycles, the shear capacity of the specimen began to decrease gradually. The horizontal and longitudinal cracks in the lower corners of the 2nd story infill plate rippled outward in the 1st cycle of 3.5% drift, furthermore, the horizontal cracks in the lower edge extended along the whole edge, and suddenly the whole fractured and lifted outward (Fig. 5e) in the 2nd cycle. In this cycle, bending over the 1st- and 2nd-floor beams was observed. In the 4.0% drift level, the specimen's shear capacity dropped rapidly to less than 85% of the peak shear capacity. At the end of test, a pronounced curvature (Fig. 5f) of the 1st story west column was observed while no buckling or cracks were detected after the end of test (Fig. 5g).

2.4 Cyclic Behavior of Test Specimen

In the whole horizontal loading, the load-displacement state is analyzed based on the cyclic behavior in Sect. 2.3. The hysteretic and envelope curves are shown in Fig. 6. Considering the first cycle of each drift level largely reflects the maximum capacity of the specimen, therefore, the first cycle is used for the subsequent examination.

As Fig. 6 depicted, the envelope curve looks like an S-shape, the hysteresis loops are stable before 3.5% drift and start to open in the 1.0% drift level due to the QB yielding. The specimen has happened QB buckling during the 0.5% drift cycles, then found QB yielding during the 1.0% drift cycles. The lateral force hits the peak at 3.0% drift then begins to decline since the HL end yielding and QB edge fracture. Finally, the lateral force has dropped to less than 85% of the max peak lateral force at 4.0% drift. Moreover, the hysteretic curve shows a little pinch near the zero drift. Figure 7 presents the secant stiffness state of the test specimen. It is noted that the initial stiffness of the specimen is 15.55 kN/mm; the stiffness decline gradually in the whole loading, it is almost 50% of the initial stiffness at 1.5% drift and increasingly declines to 3.73 kN/mm at 3.5% drift.

Based on Fig. 6, the characteristic points and ductility for the test specimen are summarized in Table 1. The equivalent viscous damping ratio (η) is presented in Fig. 8, but the η before 0.5% drift is neglected since the specimen is almost elastic. The yield point is obtained by the geometric method [23]. The limit displacement is determined by the limit state (i.e. lateral force drops to 85% of the peak load). Table 1 indicates that the specimen yields roughly at 1.2% drift with the lateral force of 534.92 kN, then hits the peak at 3.0% drift with the lateral force of 643.57 kN, finally reaches the limit state at approximately 3.8% drift. Moreover, the ductility of test specimen is about 3.05. As illustrated in Fig. 8, the 1.0% drift is clearly the line that divided the whole loading into elastic and plastic stages, respectively. In addition, the η is increasing and climbs to 23.94% at 3.5% drift.

Fig. 6 Hysteretic and envelope curves

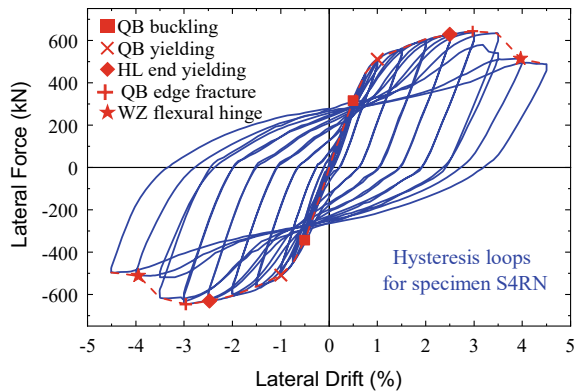


Fig. 7 Peak secant stiffness state

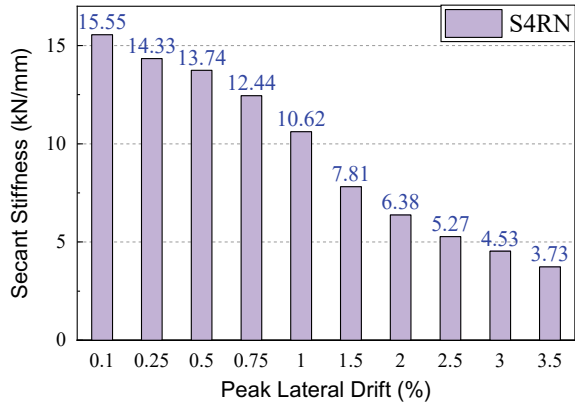
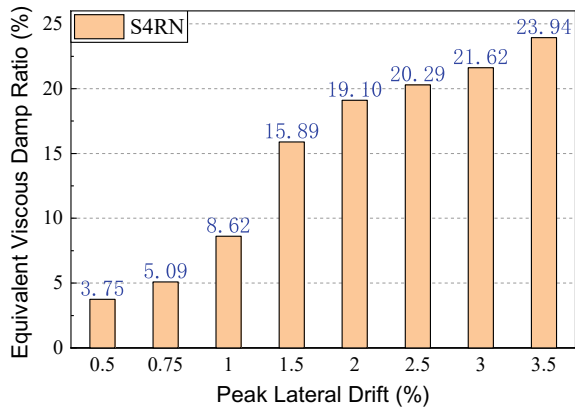


Table 1 Characteristic points and ductility

Test specimen		S4RN
Yield point	Δy (mm)	59.49 (1.2%)
	F_y (kN)	534.92
Peak point	Δm (mm)	142.80 (3.0%)
	F_m (kN)	643.57 (1.20)
Limit disp.	Δu (mm)	181.24 (3.8%)
Ductility	μ_d	3.05

Note Δy , F_y , Δm , F_m and Δu is yield displacement, yield load, peak displacement, peak load and ultimate displacement, respectively; $\mu_d = \Delta u/\Delta y$, represents the displacement ductility, the bracketed value is the roof drift, the value in square bracket is the overstrength factor (i.e. F_m/F_y)

Fig. 8 Equivalent viscous damping ratio (η)



3 Numerical Analysis

3.1 Validation of FE Model

To further investigate the mechanical properties of the weak-axis connected SPSW, the finite element (FE) model of the test specimen has been developed and simulated by the FE software Abaqus, as shown in Fig. 9. The FE model was meshed by shell element (S4R) with a grid size of 50 mm, while the regions of beam-to-column connections and the perimeter of infill plates were refined with a grid size of approximately 25 mm. The steel materials used in the FE model are the same as the test specimen, and these steel properties are obtained from the tensile test. For simplicity, the stress–strain behavior of materials is considered as multi-linearity, provided that the materials are isotropic in the elastic stage while following the Von-Mises yield criterion and associated plastic flow law after yielding. Thus, a trilinear stress–strain curve with combined isotropic and kinematic hardening was used to simulate the FE model. This trilinear curve reflects an elastic modulus and 1% strain hardening up to the ultimate stress. The nominal yield and ultimate strength of the infill plate, beam and column are reported in Table 2. In addition, the mental ductile damage based on stress triaxiality [24] was considered in the infill plates to reflect the cyclic cumulative damage.

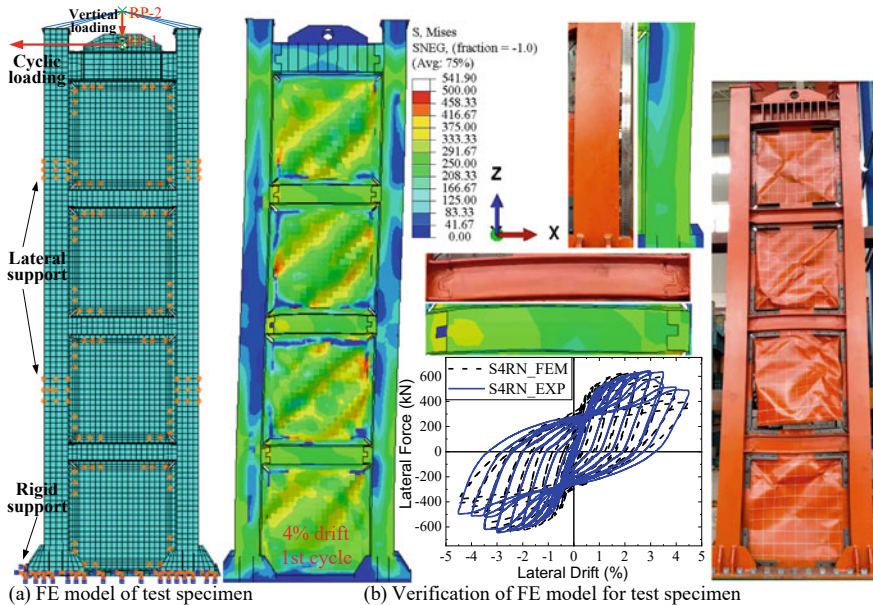


Fig. 9 Development and validation of FE model

Table 2 Material property of tensile coupon test

Thickness	2 mm	6 mm	8 mm	14 mm	16 mm	20 mm
Yield stress (MPa)	314.43	287.35	300.64	291.53	307.41	306.09
Ultimate stress (MPa)	441.38	446.20	449.95	450.00	444.86	455.64
Elastic modulus (GPa)	212	213	198	208	208	208

To make the loading and boundary conditions of the FE model consistent with the experiment, the lateral support that restrains out-of-plane deformation and the rigid support with encastre constraints were adopted, as shown in Fig. 9a. Also, the cyclic loading and vertical loading were applied on reference points RP-1 and RP-2, respectively. The RP-1 and RP-2 were coupling constrained with the center hole of the top beam and the top surface of the columns, respectively. To verify the validity of the FE model, an implicit method (quasi-static) is used for the nonlinear analysis of the FE model. The hysteretic curve and cyclic behavior compared with that of the test specimen are present in Fig. 9b. It can be seen that the hysteretic curves of the test specimen and FE model are in good agreement. Also, the FE model has well predicted the failure mode of the test specimen, which indicates that the FE model developed and the numerical analysis method are applicable and valid.

3.2 Partially Slotted Steel Plate Shear Wall

The experiment has shown that the designed test specimen (i.e. the SPSW with no slotted infill plates) can well develop the tension field of infill plates, but the infill plates in the middle story level may eventually tear severely along the whole edge, which leads to a rapid loss of lateral force while the beam would happen overall bending (Fig. 9b) due to the incomplete synchronization of the tearing at adjacent story infill plates. In terms of the above issues, a partially slotted infill plate was proposed. The original infill plates in the test specimen were only slotted in the middle region of each side, i.e. each infill plate was divided into four corner regions and one central region. As shown in Fig. 10a, the total width of inter-slot steel strips in each side is about 1/3 length of the edge, each steel strip was designed as a flexural member with the height-width ratio of six per Chinese code [25], which can fully perform its deformation and obstacle the tearing along the whole edge.

To verify the effectiveness of the partially slotted SPSW, a FE model for the partially slotted SPSW, denoted as S4RNf, was established and performed cyclic loading according to the numerical method discussed in Sect. 3.1. The FE model for the test specimen, denoted as S4RNm, was selected for comparison. The only difference between S4RNf to S4Rm is the infill plate with slots. Comparing Fig. 9b with Fig. 10, it is noted that the partially slotted SPSW exhibits a plump hysteretic curve, and the infill plate at each story level has fully played the primary and secondary tension band. Besides, neither tearing along the whole edge nor beam overall bending

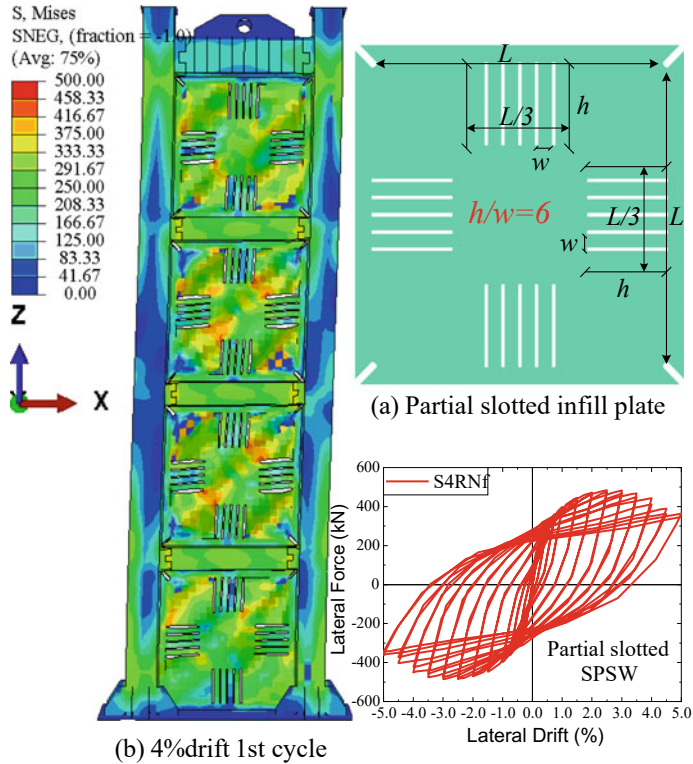


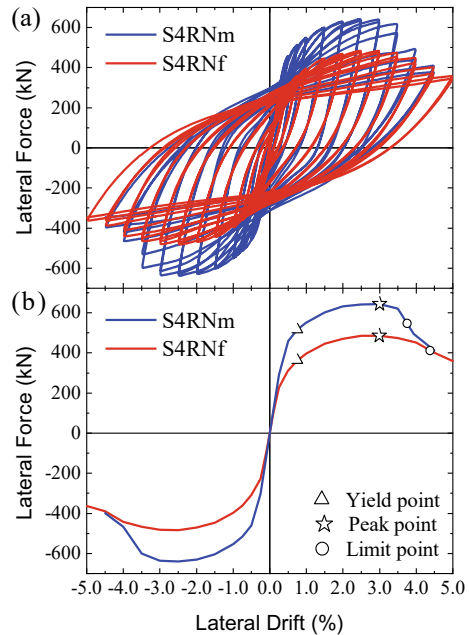
Fig. 10 Modeling for partially slotted SPSW

happened in S4RNf until 4% roof drift, meanwhile, the stress of the bottom columns is smaller than that of S4RNm.

3.3 Comparison of Mechanical Performance

To further assess the characteristics of the weak-axis connected SPSWs with no slotted and partially slotted infill plates, the mechanical properties including strength, stiffness, energy dissipation, ductility, etc. were analyzed. In addition, the comparison of mechanical performance between the S4RNm and S4RNf was made as follows. The Figs. 11, 12 and 13 illustrated the variation of hysteresis, strength and energy, respectively. As shown in Fig. 11, the partially slotted SPSW (S4RNf) exhibits a plumper hysteretic curve than that one without slots (S4RNm), and both of them almost yield and hit the peak at the same lateral drift but the S4RNm is damaged too early to get a larger limit displacement. Also, the S4RNf shows more stable strength variation with a strength ratio of greater than 0.95, while, the S4RNm exhibits a severe

Fig. 11 Hysteresis and skeleton



strength degradation after 3.0% drift and shows a faster stiffness degradation than the S4RNf after yielding, as shown in Fig. 12. In addition, the energy dissipated and equivalent viscous damping ratio have been assessed, as shown in Fig. 13. It can be seen that the energy dissipated and damping ratio of S4RNf is climbing increasingly and hitting the maximum damping ratio of approximately 30%, which indicates that the partially slotted SPSW has a better performance in energy dissipation than that non-slotted SPSW.

Based on Fig. 11, the characteristic points of S4RNm and S4RNf were summarized in Table 3. Besides, the lateral displacement and inter-story drift were illustrated in Fig. 14. As shown in Table 3, the S4Rm and S4Rf both yield at 0.76% drift and hit the peak at 3.0% drift. However, the partially slotted SPSW (S4RNf) has a greater overstrength factor of 1.34. Also its peak lateral force still accounts for 75.37% of the S4RNm, although the S4RNf has been weakened by the slots in the infill plates. Moreover, the S4RNf hits the limit state at 4.4% drift while the S4RNm at 3.8% drift. The ductility of the S4RNf is up to 5.79 but 4.95 the S4RNm, which obviously indicates that the partially slotted SPSW has excellent properties in deformation and ductility. Furthermore, the S4RNf and S4RNm both exhibit a similar lateral deformation pattern (i.e. the deformation transitioned from flexural mode to shear mode). But the S4RNf has a smaller lateral deformation than the S4RNm after 3.0% drift, as shown in Fig. 14a. The S4RNf demonstrates almost the same inter-story drift mode before the 4.0% drift, while the S4RNm obviously has a larger inter-story drift at the 2nd floor due to the severe tearing along the whole edge, as shown in Fig. 14b.

Fig. 12 Strength and stiffness state

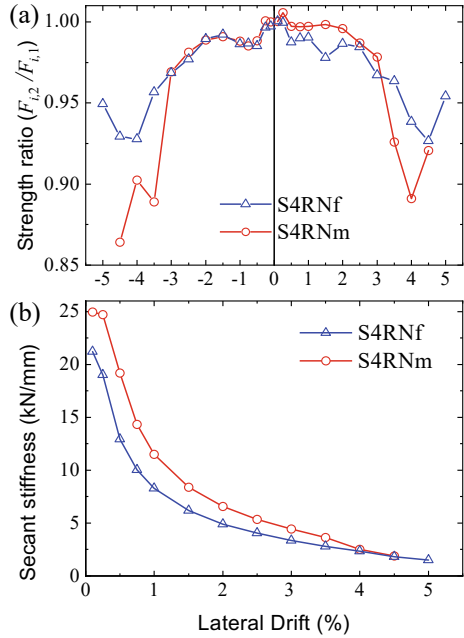


Fig. 13 Energy dissipation

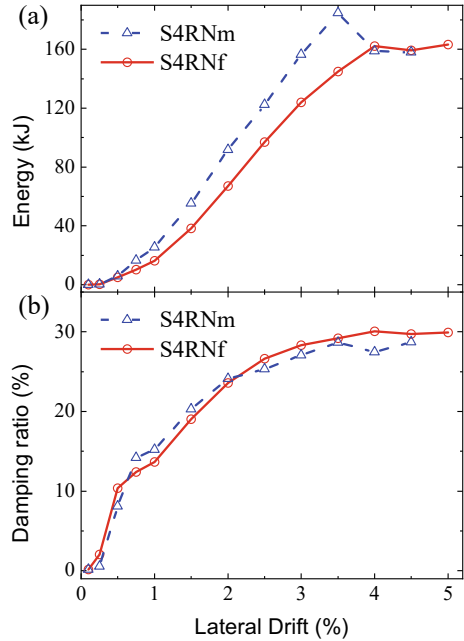


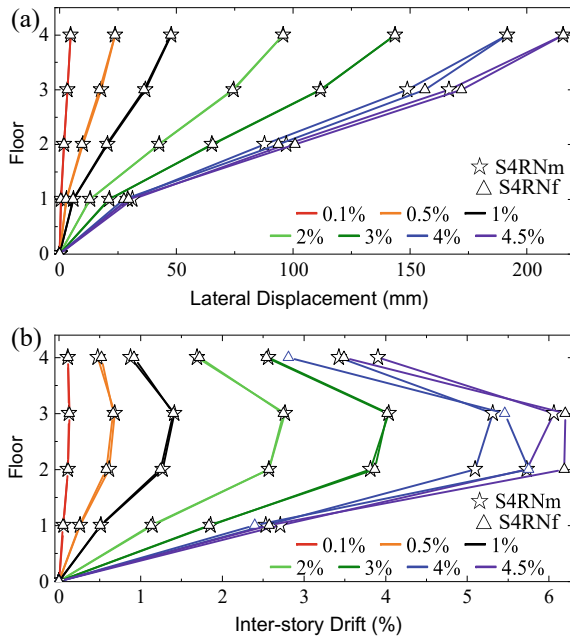
Table 3 Characteristic points and ductility for the S4RNm and S4RNf

Specimens		S4RNm	S4RNf
Yield Point	Δy (mm)	36.38 (0.76%)	36.29 (0.76%)
	F_y (kN)	516.01	362.39
Peak Point	Δm (mm)	144 (3.0%)	143.92 (3.0%)
	F_m (kN)	643.51 [1.25]	485.03 [1.34]
Limit Disp.	Δu (mm)	180.23 (3.8%)	210.12 (4.4%)
Ductility	μ_d	4.95	5.79

Note Δy , F_y , Δm , F_m and Δu is yield displacement, yield load, peak displacement, peak load and ultimate displacement, respectively; $\mu_d = \Delta u/\Delta y$, represents the displacement ductility, the bracketed value is the roof drift, and the value in the square bracket is the overstrength factor (i.e. F_m/F_y)

Taking the limit displacement as criteria, the limit inter-story drift of S4RNf at the 3rd floor is up to 6.1% but 5.5% the S4RNm.

Fig. 14 Lateral deformation state



4 Conclusions

The ordinary SPSWs have been studied comprehensively. But limited studies on weak-axis connected SPSWs and partially slotted infill plates have been reported, which restrict the improvement and extension of SPSWs. Thus, a 1/3 scaled weak-axis connected SPSW was designed and constructed. After it was tested under cyclic loading, the corresponding nonlinear FE model was developed and validated by test results. Based on the test results and FE model, the partially slotted SPSW was proposed and established the FE model. Finally, the nonlinear FE analysis was performed to further investigate the mechanical performance of these SPSWs with non-slotted and partially slotted infill plates. It is can be drawn from the experimental work and numerical analysis that:

1. The weak-axis connected SPSWs with non-slotted and partially slotted infill plates have good properties in strength, ductility and energy dissipation. Both of them hit the peak lateral force at 3.0% drift and the ratio of peak load to yield load is roughly more than 1.2. Also, the ductility for them is greater than 3.0.
2. Comparing the weak-axis connected SPSW with non-slotted infill plates, the proposed partially slotted SPSW exhibits a plumper hysteretic curve without visible pinch phenomenon. Moreover, it has a more gentle stiffness degradation and stable strength variation with a strength ratio of more than 0.93.
3. Replacing traditional flat steel plates by introducing partially slotted infill plates in SPSWs, which can effectively improve the structural deformation, ductility and strength redundancy, i.e. the limit inter-story drift can be enhanced from 5.5 to 6.1% and the overstrength factor enhanced from approximately 1.2–1.34.
4. Although the partially slotted infill plate will weaken the lateral resistance, the partially slotted SPSW still accounts for 75% of that one without slots in lateral bearing capacity. Furthermore, the proposed partially slotted infill plate can fully play the tension field and effectively obstacle severe tearing along the whole edge then avoid beam's in-span bending. In addition, the ductility of the partially slotted SPSW is up to 5.79, and its equivalent viscous damping ratio is up to 30%.

Although this work is focused on weak-axis connected SPSWs, it can be extended to coupled steel plate shear walls due to their similar characteristics. Besides, the partially slotted infill plates can be extended to other structures with infill panels to serve as energy-consuming elements, provided that a proper plastic mechanism and design method was proposed. This will be examined in our future work.

Acknowledgements The authors gratefully acknowledge the funding provided by the National Natural Science Foundation of China (Grant No. 51878541). Gratitude is also extended to all members of the Key Lab. of Structure Engineering and earthquake Resistance, Ministry of Education (XAUAT).

References

1. Celebi M (1997) Response of olive view hospital to Northridge and Whittier earthquake. *J Struct Eng* 123(4):389–396
2. Nakashima M, Fujiwara T, Suzuki Y (1995) Damage to engineered buildings from the 1995 great Hanshin earthquake. *J Nat Disaster Sci* 16(20):71–78
3. Hao J, Cao C, Wang Y (2009) Test on thin steel plate shear wall with opening under cyclic loading. *China Earthq Eng Eng Vibr* 29(2):79–85
4. Nie J-G, Zhu L, Fan J-S, Mo Y-L (2013) Lateral resistance capacity of stiffened steel plate shear walls. *Thin-Walled Struct* 67:155–167
5. Guo H-C, Hao J-P, Liu Y-H (2015) Behavior of stiffened and unstiffened steel plate shear walls considering joint properties. *Thin-Walled Struct* 97:53–62
6. Ge M, Hao J, Yu J, Yan P, Xu S (2017) Shaking table test of buckling-restrained steel plate shear walls. *J Constr Steel Res* 137(1):254–261
7. Du Y, Hao J, Yu J, Yu H, Deng B, Lv D, Liang Z (2018) Seismic performance of a repaired thin steel plate shear wall structure. *J Constr Steel Res* 151:194–203
8. Takahashi Y, Takemoto Y, Takeda T (1973) Experimental study on thin steel shear walls and particular bracings under alternative horizontal load. In: IABSE symposium on resistance and ultimate deformability of structures acted on by well-defined repeated loads, Lisbon, Portugal, pp 185–191
9. Bruneau M, Berman JW, Garcia D, Vian D (2005) Steel plate shear wall buildings: design requirements and research. North American steel construction conference, Montreal, Canada (2005)
10. Thorburn LJ, Kulak GL, Montgomery CJ (1983) Analysis of steel plate shear walls. Structural Engineering Report, University of Alberta, Canada
11. Behbahanifard MR, Grondin GY, Elwi AE (2003) Experimental and numerical investigation of steel plate shear wall. Structural Engineering Report, University of Alberta, Edmonton, Canada
12. AISC (2007) Steel design guide 20, Steel Plate Shear Walls, American Institute of steel construction, Chicago
13. Berman J, Bruneau M (2003) Plastic analysis and design of steel plate shear walls. *J Struct Eng* 129(11):1448–1456
14. Berman JW, Bruneau M (2008) Capacity design of vertical boundary elements in steel plate shear walls. *Eng J Am Inst Steel Constr Inc* 45(1):57–71
15. Berman JW (2011) Seismic behavior of code designed steel plate shear walls. *Eng Struct* 33(1):230–244
16. Tsai K-C, Li C-H, Lin C-H, Tsai C-Y, Yu Y-J (2010) Cyclic tests of four two-story narrow steel plate shear walls—Part 1: analytical studies and specimen design. *Earthq Eng Struct Dynam* 39(7):775–799
17. Li C-H, Tsai K-C, Lin C-H, Chen P-C (2010), Cyclic tests of four two-story narrow steel plate shear walls. Part 2: experimental results and design implications. *Earthq Eng Struct Dyn* 39(7):801–826
18. Vian D, Bruneau M, Tsai KC, Lin Y-C (2009) Special perforated steel plate shear walls with reduced beam section anchor beams. I: experimental investigation. *J Struct Eng* 135(3):211–220
19. Meng B, Hao J, Zhong W (2021) Numerical study on the anti-progressive collapse performance of steel frame-steel plate shear wall structures, *J Build Eng* 35
20. Wenling LI, Jiping HAO, Liankun W, Hongying C, Junfeng Z (2008) Experimental and analytical study on stiffness of beam-to-column minor axis top-and-seat angle connection in steel frames. *Chin J Build Struct* 29(2):125–131
21. Shim HJ, Lee ET, Kim SB, Kim SS (2014) Development and performance evaluation of weak-axis column bending connections for advanced constructability. *Int J Steel Struct* 14(2):369–380
22. Ying-lu X, Yao-xuan S, Yong-fang S (2021) Finite element analysis of rib reinforced weak-axis connection in steel frame. *Chin Eng Mech* 38(Suppl):31–38
23. Feng P, Qiang H, Ye L (2017) Discussion and definition on yield points of materials. *Members Struct Chin Eng Mech* 34(3):36–46

24. Bao Y, Wierzbicki T (2004) On fracture locus in the equivalent strain and stress triaxiality space. *Int J Mech Sci* 46(1):81–98
25. JGJ/T 380-2015 (2015) Technical specification for steel plate shear walls. China Architecture Building Press, Beijing

Open Access This chapter is licensed under the terms of the Creative Commons Attribution 4.0 International License (<http://creativecommons.org/licenses/by/4.0/>), which permits use, sharing, adaptation, distribution and reproduction in any medium or format, as long as you give appropriate credit to the original author(s) and the source, provide a link to the Creative Commons license and indicate if changes were made.

The images or other third party material in this chapter are included in the chapter's Creative Commons license, unless indicated otherwise in a credit line to the material. If material is not included in the chapter's Creative Commons license and your intended use is not permitted by statutory regulation or exceeds the permitted use, you will need to obtain permission directly from the copyright holder.



Full-Permeability Analysis of Normal Amplitude and Variable Amplitude Fracture of M24 High Strength Bolts



Rong Xing, Junjie Zhang, and Honggang Lei

Abstract Fatigue problem on high strength bolts have already become more and more important in modern times and it is essential that we do research on bolt fatigue mechanism by the fatigue fracture analysis of the failed bolt because of fatigue. Through detailed analysis of constant amplitude stress and variable amplitude stress on M24 high strength large hexagonal head bolts, it is concluded that there are three common failure mode among all bolts' fatigue failure. Fatigue failure characteristics and fracture developing status of source region, transient broken zone and extension zone were obtained, and it provides a important basis for the study on fatigue performance and life estimation of high strength bolt connection, and meanwhile it also expands the application range of bolt joint of prefabricated steel structure.

Keyword Prefabricated steel structure · High strength bolt · Fatigue failure · Fatigue fracture · Constant amplitude · Variable amplitude

1 Introduction

Steel structure is a kind of popular structure type in modern times, which is applicable in various types of buildings. It has light weight, and it also has high bearing capacity, as makes many designers achieve a variety of spectacular steel structure buildings. Different buildings can make use of different linking ways to make their components form an integral whole, so the connection mode is relatively crucial, and it is especially obvious that the security of our residential buildings which are lived daily is deeply rooted in the heart of the people. With the frequent occurrence of natural disasters, the citizens are concerned about safety question mostly. The

R. Xing · H. Lei (✉)

Civil Engineering College of Taiyuan University of Technology, Taiyuan, China

e-mail: lfgang168@126.com

R. Xing

Shanxi Vocational University of Engineering Science and Technology, Taiyuan, China

J. Zhang

Architectural Design and Research Institute of Taiyuan University of Technology, Taiyuan, China

© Crown 2023

Y. Yang (ed.), *Advances in Frontier Research on Engineering Structures*, Lecture Notes in Civil Engineering 286, https://doi.org/10.1007/978-981-19-8657-4_12

131

problem of high-strength bolts used in steel structure dwellings is becoming more and more prominent, and among all questions especially vital one is the fatigue problem of high-strength bolts under the cyclic action of long-term load. The urgent solution of fatigue problem caters to the aspirations of lots of people.

Fatigue problem was put forward on the basis of repeated loading test of the chain by the German engineer W A J Albert in 1829 early [1]. The essence of fatigue problem is fatigue failure, which occurs under the local place of high stress and high strain, and then it causes fatigue crack or complete fracture due to fatigue. Because of high strength bolt fatigue many engineering accidents occurred, it is well known that on June 4th, 1979 the hung bolt broke in Kemper Stadium, which led to the part collapse of the center of the roof [2]. Therefore, the fatigue of high-strength bolt is always a important and difficult point in the engineering and academic circles.

High-strength bolt fatigue is a fatigue problem of metal structure. Fatigue problem has its complexity, and it need to be solved by the way of fatigue test study [3, 4]. Fatigue failure occurs accompanying with cracking formation, and then cracking expands at the concentration of stress, eventually leading to fracture. Domestic and foreign scholars have paid a lot of attention to stress concentration [5–9]. Insides these, scholars from various countries have also done a lot of research on the fatigue damage mechanism [10–12] and fatigue life estimation. So it is essential that we do research on bolt fatigue mechanism by the fatigue fracture analysis of the bolt that failed because of fatigue [13–17]. It is an important method to describe fatigue crack's extension process and to reveal the mechanism of fatigue failure.

Many domestic and foreign scholars have made experimental study and theoretical analysis on the fatigue performance and fatigue life of high strength bolt connection, thus drawing important conclusions. Lei [13, 18–20] from Taiyuan University of Technology had had metallographic analysis on the fatigue fracture of the M20 high strength bolt used in the bolt-ball-mesh frame, revealing the mechanism of fatigue failure; the main application is that on the basis of the analysis of fatigue damage mechanism and cumulative damage process; he had the experimental study on the fatigue performance of fifteen Grade 8.8 M24 high strength bolts. Bolt's fatigue failure originated at the root of the thread, which is gradually formed from multiple point sources to line sources firstly, and then gradually expanding along annular and radial respect, and the annular expanding rate is higher than the radial expanding rate. These results are all closely related to the fatigue fracture of high strength bolts.

2 Experiment Analysis

2.1 Experiment Purpose

Based on the experiment study of the tension fatigue performance about M24 high strength hexagonal headed bolt, this paper analyzes the fatigue fracture of shear bolt

and establishes the fatigue design method in detail, which lays a solid theoretical foundation for the extended application of the prefabricated steel structure buildings.

2.2 *Materials and Method*

The fatigue failure of the high strength bolt in this experiment was mainly caused by the fatigue break which occurred at the thread root between the bolt rod and the nut, which is the same as this damage mode of most high strength bolts in the experiment; secondly, the fatigue fracture occurs at the thread root that doesn't occlude with the nut, which is the same as only one among high strength bolts, therefore this damage mode is more special; finally, the high strength bolt is not completely broken, you can see the fatigue cracking that makes the bolt connection fail, which is the same as only three bolts' damage mode in the experiment, and especially occurs at the multi-bolt connection nodes. This paper mainly analyzes the fatigue fracture of the first two high-strength bolts with fatigue break. The number of bolts that are studied under constant amplitude stress is ten, which are named M24-1, M24-2, M24-3, M24-4, M24-5, M24-6, M24-7, M24-8, M24-9 and M24-10. Among them analyzed object is the typical samples such as M24-1 and M24-5; the special samples includes M24-5 and M24-10. The number of bolts that are studied under variable amplitude stress is four, which are named M24-B1, M24-B2, M24-B3 and M24-B4 successively. Among them M24-B2 and M24-B3 are selected for analyzed object.

This content is completed by the combination way of micro and macro analysis, and macroscopic fracture analysis mainly makes use of naked eye, magnifier and camera etc., while microscopic fracture needs use the scanning electron microscope. The experiment used Phenom XL desktop scanning electron microscope. Each equipment and research object are shown in Figs. 1 and 2. The macro and micro analysis methods of the fracture have advantages because of the observable range and observation level, which cannot be replaced each other in practical use. The combination of macro and micro analysis, mutual evidence and common application effect is better.

The ten constant fatigue fractures were classified, and by the way of the macro and micro analysis this experiment have studied not only the typical and special morphology fatigue features of constant amplitude, but also fatigue source's failure of variable amplitude, and it can reveal the fatigue cracks' extending process and fatigue failure mechanism commonly applied in the fatigue failure.

Fig. 1 Experiment equipment



(a) Ultrasonic cleaner

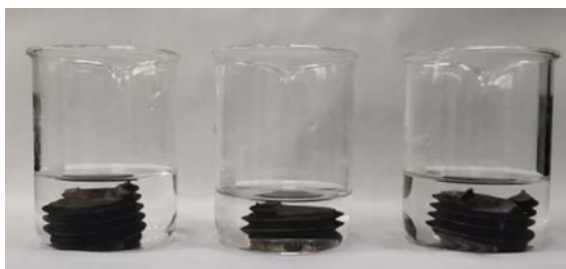


(b) anhydrous ethanol

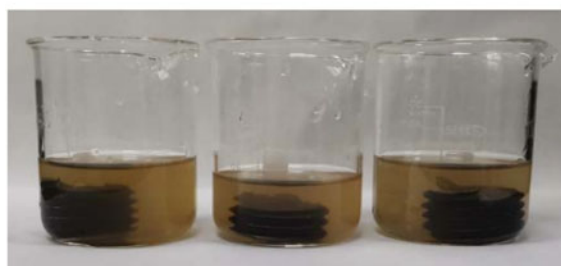


(c) SEM

Fig. 2 Research objects



(a) Bolts section before cleaning



(b) Bolts section after cleaning

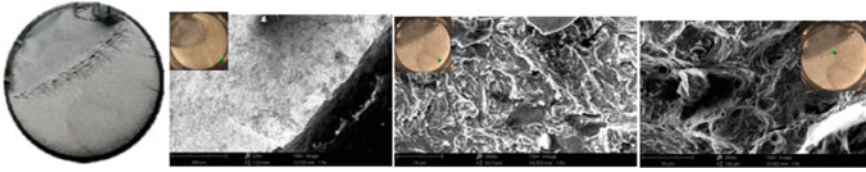


Fig. 3 M24-2 macro and micro fractures ($\Delta\sigma = 190$ MPa, $N = 230.234 \times 10^4$)

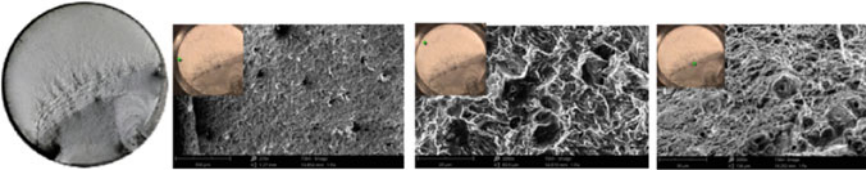


Fig. 4 M24-5 macro and micro fractures ($\Delta\sigma = 206$ MPa, $N = 48.9235 \times 10^4$)

2.3 Discussion

Typical Fatigue Fractures of Constant Amplitude

Firstly, the typical fatigue macro breaks and micro breaks of M24-2, M24-5 under different stress amplitude and cycles shown in Figs. 3 and 4, emphasizing the fatigue failure characteristics of their fatigue source zone, fatigue extension zone and transient zone.

In Figs. 3 and 4 above there are macroscopic fracture, 200 \times source, 3000 \times extension and 2000 \times instantaneous zone from left to right respectively. It can be seen that they have some common characteristics:

- (1) Macroscopic fracture: The three fractures all have the smooth fatigue source area which is flatter, fatigue extension zone accounting for about two-thirds of the fracture area, and the instantaneous area which shows plastic deformation and tension breaking, which is a typical fatigue fracture.
- (2) Microscopic fracture: Similarities are that fatigue source originates from the side of the fracture; initial defects are the main cause of early caused fatigue crackings. The characteristics of 3000 \times extension zone mainly shows the fatigue striation morphology; the distribution of the fatigue striation is not regular, and the spacing of the adjacent fatigue strips is quite different, which fully indicates that the bolt's force is complex. The characteristics of 2000 \times instantaneous area is observed that there is a large number of toughness nests, and there are obvious signs before fracture, it belongs to the failure type of plastic deformation.

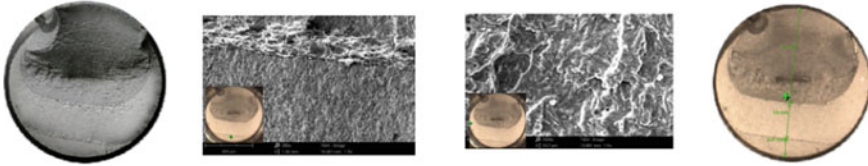


Fig. 5 M24-1 macro and micro fractures ($\Delta\sigma = 210$ MPa, $N = 55.8769 \times 10^4$)

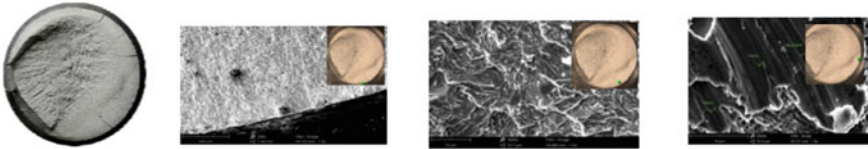


Fig. 6 M24-10 macro and micro fractures ($\Delta\sigma = 195$ MPa, $N = 76.8906 \times 10^4$)

Special Fatigue Fractures of Constant Amplitude

Among them, the fracture morphology of M24-1 and M24-10 under different stress amplitude and cycles are more special fatigue fractures, analyzing the macro and micro fractures combining with loading process.

Figure 5 is the macroscopic break, the junction of the $200\times$ expansion area, $5000\times$ the expansion area and the three-section length (Fig. 6).

The above figures are macroscopic fracture, $200\times$ source area, $3000\times$ extension area $5000\times$ extension area. Their similarities and differences is shown in the following:

- (1) Macroscopic fracture of M24-1: The above fatigue fracture is divided into three areas, among which the expansion is divided into two parts;
- (2) Microscopic fracture of M24-1: In fatigue source, there are the visible junctions of extension zone. In extension zone there is the obvious fatigue strips, and at the junction of the two extension areas, there are toughness nests.
- (3) Macroscopic fracture of M24-10: The fatigue source occurs on the lower right side of the fracture, and the transient zone is located on the upper left side of the fracture.
- (4) Microscopic fracture of M24-10: In fatigue source, the spacing of adjacent striation extends from one direction, such as 856 nm, 916 nm, and 1220 nm respectively.

Fatigue Fractures of Various Amplitude

The constant amplitude fatigue fracture analysis cannot fully reflect the fatigue failure characteristics of the M24 high strength large hexagonal head bolt, then making the detailed analysis of the macro and micro parts of M24-B2, and M24-B3 under various amplitude stress, which is shown in Figs. 7 and 8; Tables 1 and 2.

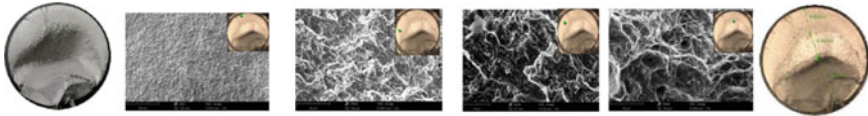


Fig. 7 M24-B2 macro and micro fracture

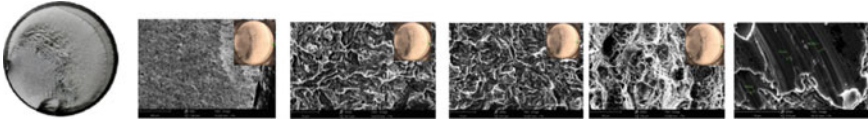


Fig. 8 M24-B3 macro and micro fracture

Table 1 Fracture analysis of M24-B2

Loading process		(1) $\Delta\sigma = 200 \text{ MPa}$, $N = 49.0045 \times 10^4$; (2) $\Delta\sigma = 220 \text{ MPa}$, $N = 40.0765 \times 10^4$
Macroscopic		It is divided three failure zone
Microscopic	200× source	The fatigue source originates from the upper part of the fracture, and the length along the diameter is 4.86 mm;
	2000× extension zone	Through the regional boundary, the angle between the fatigue cracking extension direction and the cross section can change. The failure characteristics of the boundary zone is plastic tearing The length along the diameter is 4.56 mm;
	5000× extension zone	Significant fatigue striation appears, it is more easier to observe the direction of cracking extension The length along the diameter is 9.6 mm

3 Conclusion

With the help of magnifying glass, camera and advanced SEM, this paper makes macro and micro analysis of ten constant amplitude fatigue fractures and four variable amplitude fatigue fractures, so as to obtain the fatigue failure characteristics of torsion-shear high strength bolts, and it further studies the fatigue failure mechanism combining with loading process.

Firstly, analyzing the macro and micro fracture of constant fatigue. It is known that fatigue source usually occurs at the part with the initial defects; the spacing between the fatigue strips of the cracking extension area can roughly reflect the loading level of the stress amplitude. There are a lot of toughness nests that can reflect plastic fracture characteristics.

In the case of the single fatigue source, the fatigue source area and the transient break area are always in the opposite part of the fracture diameter direction, and the instantaneous break area is in proportional to the loading stress. In the case of

Table 2 Fracture analysis of M24-B3

Loading process		(1) $\Delta\sigma = 220$ MPa, $N = 36.8906 \times 10^4$; (2) $\Delta\sigma = 210$ MPa, $N = 3.1516 \times 10^4$
Macroscopic		The right area of the fracture has the obvious boundary, and the fracture is obviously divided into three regions
Microscopic	200 \times source	The fatigue source originates from the upper right of fracture
	5000 \times extension zone	Showing the characteristics of plastic fracture, the boundary of the fracture should be the trace loaded twice by variable amplitude fatigue, and the toughness nests and morphology are diverse and irregular In addition, showing the irregular distribution of the fatigue striation;
	2000 \times instantaneous break zone	The transient fracture zone is located on the lower left side of the fracture, and the fatigue cracking extends from the upper right side to the lower left side

multiple fatigue source, the fatigue step generally forms on the fracture, judging the order that the fatigue source comes to being according to the distance of the fatigue source from the fatigue step.

Secondly, the variable fatigue fracture is analyzed and it is discovered that the fracture morphology is more complicated. After the loading-stopping-reloading process, the bolts will generally leave a significant boundary in the fracture expansion area, and the boundary area presents the plastic fracture characteristics. Through the dividing line, the fatigue cracking extends again.

These conclusion can provide more information for the study on fatigue performance and life estimation of high strength bolt connections, avoiding or debasing the probability of fatigue failure on high strength bolt connections. And meanwhile it also expands the application range of bolt joint of prefabricated steel structure.

Acknowledgements We are grateful for the support from the National Science Foundation (51578387).

References

1. Wang GZ (1991) Basic mechanism of metal fatigue. Graduate topic handout in the Institute of Metal Research of Chine Academy of Sciences, China
2. Lei HG (2003) Analysis and treatment of steel structure accident. China Building Materials Industry Press, China

3. Chen CY (2002) Fatigue and fracture. Huazhong University of Science and Technology Press, China
4. Feng XJ, Lin XS, Pan W, Huang BS (1995) Fatigue performance of the bolt ball node mesh frame under the action of the suspension crane. *Archit Struct J* 04:3–12
5. Lei HG, P Y, Yin DY (2002) Stress concentration of high strength bolts on bolt-ball-nodes mesh. In: *The Proceedings of academic conference 10th on space structure*. The Chinese civil engineering society, pp 138–145
6. Liu LJ (2005) Analysis of gap effect of high strength bolts for the bolt ball nodes of steel mesh. *J Xiamen Univ (Nat Sci En)* 44(6):783–786
7. Zhang CL (2006) Analysis and suggestion of stress concentration of high strength bolts on end-plate connection. *China Sci Technol Pap Online* 02:150–152
8. Yang G, Lei H G, Jiao JF (2019) Analysis of stress concentration coefficient of friction type high strength bolts for steel structure. *Sci Technol Eng* 19(15):233–237
9. Peng J (2019) Study on fatigue and high temperature mechanical properties of bolt-ball-node. Lanzhou University of Technology, China
10. Shyam A, Allison JE, Szczepanski CJ et al (2007) Small fatigue crack growth in metallic materials: a model and its application to engineering alloys. *Acta Materialia* 55(19):6606–6616
11. Zhang J, He XD, Du SY (2005) Analyses of the fatigue crack propagation process and stress ratio effects using the two parameter method. *Int J Fatigue* 27(10–12):1314–1318
12. Leguillon D, Quesada D, Putot C, Martin E (2004) Prediction of crack initiation at blunt notches and cavities—size effects. *Eng Fract Mech* 74(15):2420–2436
13. Lei HG, Li Y, Jiao JF (2004) Analysis of fatigue fracture of M20 high strength bolt in bolt-ball-node mesh China Steel Structure Stability and Fatigue Branch. In: 2004 Proceedings of academic conference. Taiyuan University of Technology, China, pp 363–370
14. Dong RH (2010) Study on the fatigue failure mechanism and influencing factors of the welded hollow ball node connection. Taiyuan University of Technology, China
15. Li N (2003) Fatigue failure mechanism and life estimation of 40 Cr high strength bolt for bolt-ball-node mesh. Taiyuan University of Technology, China
16. Zhao SL (1995) Analysis of the fatigue failure mechanism. *J Ningxia Inst Technol* 03:33–40, 62
17. Yang X, Wang YB, Lei HG (2016) Study on the fatigue failure characteristics of high strength bolts under different stress amplitude. *J Taiyuan Univ Technol* 47(02):239–243
18. Lei HG (2008) Theoretical and experimental study on the fatigue performance of high strength bolt connection. Taiyuan University of Technology, China
19. Zhang Y (2015) Fatigue analysis and experimental study on high strength bolt M39 for bolt mesh structure in service. Taiyuan University of Technology, China
20. Jiao JF, Jia PP, Liu Y, Liu JQ, Lei HG (2019) Study on constant amplitude fatigue performance of high strength bolt M24 under critical stress ratio. *J Taiyuan Univ Technol* 50(6):749–755

Open Access This chapter is licensed under the terms of the Creative Commons Attribution 4.0 International License (<http://creativecommons.org/licenses/by/4.0/>), which permits use, sharing, adaptation, distribution and reproduction in any medium or format, as long as you give appropriate credit to the original author(s) and the source, provide a link to the Creative Commons license and indicate if changes were made.

The images or other third party material in this chapter are included in the chapter's Creative Commons license, unless indicated otherwise in a credit line to the material. If material is not included in the chapter's Creative Commons license and your intended use is not permitted by statutory regulation or exceeds the permitted use, you will need to obtain permission directly from the copyright holder.



Research on Health Assessment Model and Data Analysis Method of Steel-Concrete Composite Girder Bridge



Jizhuang Hui, Haobo Zhang, Nima Zhaxi, Duojie Cidan, Yongjian Liu, Gao Cheng, and He Shi

Abstract In order to evaluate the health status of Steel-concrete composite girder bridges, a health status assessment model based on the bridge monitoring scheme is proposed, and a matching data analysis method is established on this basis. Firstly, the data are divided into two index layers: monitoring projects and monitoring points, and a health status assessment model is established based on this. Secondly, the fuzzy comprehensive evaluation of the state of Steel-concrete composite girder bridges is realized by the membership vectorization processing of the monitoring data. Finally, the method is applied to an actual bridge to evaluate the health status. The results show that the established model and method can evaluate the state of the Steel-concrete composite girder bridge, and the state of the bridge evaluated by this method is level 1 and the health is better. The health status assessment model and data analysis method of Steel-concrete composite girder bridges establishes a direct connection between objective data and subjective assessment, provides an effective way for the real-time evaluation of bridge health status.

Keywords Steel-concrete composite girder bridge · Health monitoring · State model · Data analysis · Status evaluation

1 Introduction

The safety of bridges is the core issue of bridges in service [1]. With the deep integration of artificial intelligence and engineering, the intelligent operation and maintenance of bridges has received extensive attention [2]. At present, the health

J. Hui (✉) · H. Zhang · Y. Liu · G. Cheng · H. Shi
National Engineering Research Center of Highway Maintenance Equipment, Chang'an University, Xi'an 710064, Shaanxi, China
e-mail: huijz@chd.edu.cn

H. Zhang
e-mail: haoboz@126.com

N. Zhaxi · D. Cidan
Research Center, Tibet Tianlu Co. Ltd., Lhasa 850000, Tibet, China

status assessment of bridges is generally carried out by deploying sensors in key structural parts of the bridges, using sensors to collect data such as service environment and structural response, and then intelligently analyzing and processing the data to achieve monitoring and assessment of bridge status. However, due to the process of data collection and health status assessment containing a large number of uncertain factors, the real-time assessment of the comprehensive status of bridge structures has not been fully realized at this stage [3].

In terms of health status assessment models and methods, Liu et al. [4] refer to the component classification method recommended in the American maintenance management system, and use the method of hierarchical evidence reasoning to establish a bridge condition assessment framework. Liang et al. [5] started from environmental erosion, material aging and external load, and used variable weight and D-S evidence theory to propose a multi-factor bridge condition assessment method based on information fusion. Liu et al. [6] constructed a bridge index system from four dimensions of geometric characteristics, material properties, environmental conditions and action types, and used the dynamic hierarchical clustering method and the entropy weight comprehensive ranking method to propose an evaluation model for the service status of bridges. Qiao et al. [7] constructed a safety evaluation model of simply supported girder bridges based on the extenics theory based on the safety evaluation index system of simply supported girder bridges. The above research uses various index systems as grading standards to establish a state evaluation model, which provides ideas for the model creation in this paper.

In terms of data analysis methods for the health status of steel-concrete composite girder bridges: Wang et al. [8] established a bridge safety assessment system using adaptive fuzzy reasoning and radial basis function neural network. Jia et al. [9] established a discrete dynamic Bayesian network model based on time series to evaluate the bridge state; Qin et al. [10] proposed 3A indicators and comprehensive safety evaluation indicators to evaluate the overall safety state of the superstructure of a bridge. Xu et al. [11] analyzed the change law of the weights of replaceable and non-replaceable components with time, and proposed a state evaluation method based on a time-varying weight model Liu et al. [12] based on improved Bayesian. The theory proposes a method for evaluating the overall state of the bridge. The above research uses various algorithms for data processing, which provides a reference for the data analysis of this paper.

In this paper, a state assessment model based on monitoring scheme is proposed. On this basis, a data analysis method matching the model is established to realize the assessment of bridge health status.

2 Assessment Model

2.1 Evaluation Model Based on Bridge Monitoring Scheme

Relying on the monitoring scheme of Steel-concrete composite girder bridges, the monitoring data can be divided into: monitoring project layer and monitoring point layer from high to low.

The monitoring project layer is expressed as:

$$U = \{ U_i \} \quad i = 1, 2, 3, \dots, m \tag{1}$$

In the formula: U_i is the i -th physical quantity that affects the state of the bridge. Monitoring point layer: The monitoring point layer is expressed as:

$$U_i = \{ U_{ij} \} \quad j = 1, 2, 3, \dots, n \tag{2}$$

In the formula: U_{ij} is the j -th monitoring point deployed by the i th-influencing state physical quantity.

According to the bridge monitoring scheme shown in Table 1, a matching model for evaluating the health status of Steel-concrete composite girder bridges is established as shown in Fig. 1.

Table 1 Bridge monitoring scheme

	Monitoring point 1	Monitoring point 2	...	Monitoring point 4
Monitoring project 1	U_{11}	U_{12}	...	U_{1n}
Monitoring project 2	U_{21}	U_{22}	...	U_{2n}
...
Monitoring project m	U_{m1}	U_{m2}	...	U_{mn}

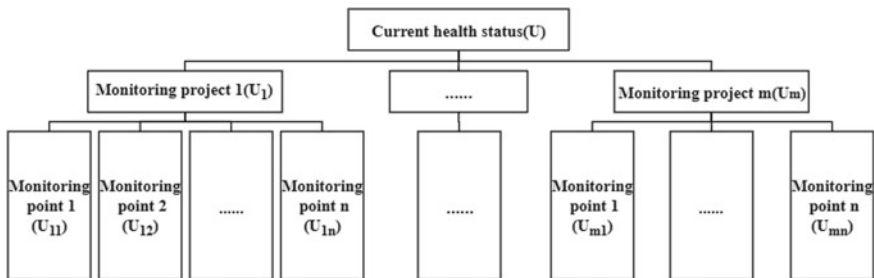


Fig. 1 Health status assessment model of steel-concrete composite girder bridge

2.2 Model Weights

Experts make decisions on the weights of each factor in the model, and construct a judgment matrix A:

$$A = \begin{pmatrix} r_{11} & r_{12} & \cdots & r_{1j} \\ r_{21} & r_{22} & \cdots & r_{2j} \\ \vdots & \vdots & \ddots & \vdots \\ r_{i1} & r_{i2} & \cdots & r_{ij} \end{pmatrix} \quad (3)$$

In the formula: r_{ij} represents the importance of the i -th factor relative to the j -th factor, and the relative importance is measured on a scale of 1–9:

The consistency test is used for the n -order judgment matrix, and the calculation formula of the index CI is:

$$CI = \frac{\lambda_{\max} - n}{n - 1} \quad (4)$$

The formula for calculating the consistency ratio CR is:

$$CR = \frac{CI}{RI} \quad (5)$$

In the formula: λ_{\max} is the largest eigenvalue of the judgment matrix. RI is the random consistency index, which is only related to the order of the matrix. When $CR < 0.1$, the judgment matrix is said to be consistent. Find the eigenvector corresponding to the largest eigenvalue, and after normalization, it is the weight vector A of the factor.

3 Data Analysis Methods

3.1 Data Membership Vectorization

The text of your paper should be formatted as follows:

Establish the evaluation level set V of the data on this basis, which is expressed as:

$$V = \{evaluation\ 1, evaluation\ 2 \dots evaluation\ i\} \quad (6)$$

The corresponding state space S is established to quantify the evaluation level set, which is expressed as:

Table 2 Membership vector table of monitoring projects

State interval $\left(\frac{\omega_{real}}{\omega_{thr}}\right)$	Membership vector (X)	Evaluation level (V)			
		Evaluation 1	Evaluation 2	...	Evaluation i
$(0, C_1]$	X_1	$X_1^{(1)}$	$X_1^{(2)}$...	$X_1^{(i)}$
$(C_1, C_2]$	X_2	$X_2^{(1)}$	$X_2^{(2)}$...	$X_2^{(i)}$
...
$(1, \infty)$	X_j	$X_j^{(1)}$	$X_j^{(2)}$...	$X_j^{(i)}$

$$S = \{M_1, M_2, \dots, M_i\} \tag{7}$$

Based on the ratio of the real-time data value ω_{real} of the monitoring project to the response threshold ω_{thr} , the data range of the monitoring project is divided into k state intervals, Establish the membership degree $X_j^{(i)}$ of the i-th evaluation in the j-th state interval. The real-time data ω_{real} in the jth state interval is represented by the membership vector X_j ($j = 1, 2, \dots, k$):

$$X_j = \left(X_j^{(1)}, X_j^{(2)}, X_j^{(3)}, \dots, X_j^{(i)}\right) \tag{8}$$

Establish a membership vector table for all monitoring projects, as shown in Table 2.

Further, set a data evaluation period. For the N pieces of data collected in the evaluation period, the data quantity n_j ($j = 1, 2, \dots, k$) in each state interval is counted as the weight of the state interval. All data in the evaluation period are represented by a membership vector r_i :

$$r_i = \frac{\sum_{j=1}^k n_j X_j}{N} \tag{9}$$

3.2 Comprehensive Assessment

Based on the model shown in Fig. 1, and after performing membership vectorization processing on the data, the steps to realize the fuzzy comprehensive assessment of highway health status are as follows:

Comprehensive evaluation of the monitoring point layer: Construct the fuzzy matrix R_i of the monitoring point layer by the membership vector r_i determined by Eq. (9):

$$R_i == (r_1 \ r_2 \ r_3 \ \dots \ r_m)^T \tag{10}$$

Combined with the model monitoring point layer weight \tilde{A}_i to evaluate each monitoring project U_i . Obtain the comprehensive evaluation result B_i of each project monitoring point layer:

$$\mathbf{B}_i = \tilde{\mathbf{A}}_i \cdot \mathbf{R}_i \quad (11)$$

Comprehensive evaluation at the monitoring project layer: After normalizing the comprehensive evaluation results at the monitoring point layer, a fuzzy matrix \mathbf{R} at the monitoring project layer is established:

$$\mathbf{R} = (B_1 \ B_2 \ B_3 \ \dots \ B_n)^T \quad (12)$$

In the formula: n is the number of monitoring projects.

Combined with the monitoring project layer weight $\tilde{\mathbf{A}}$ of the model, the comprehensive evaluation \mathbf{B} of the current state \mathbf{U} of the bridge is realized:

$$\mathbf{B} = \tilde{\mathbf{A}} \cdot \mathbf{R} \quad (13)$$

After normalization, the state space \mathbf{S} is used to determine the total score of the state as:

$$\mathbf{F} = \mathbf{B} \cdot \mathbf{S}^T \quad (14)$$

Finally, the real-time health status of the bridge is determined by the corresponding relationship between the score and the evaluation level set.

4 Case Studies

In order to evaluate the health status of a small-span Steel-concrete composite girder bridge in real time. The known monitoring scheme established for this bridge is shown in Table 3. In this scheme, the fatigue cracking, deflection response, stress state, and ambient temperature of the bridge are monitored in real time. The layout of the monitoring points is shown in Fig. 2.

4.1 Establish a Health Status Assessment Model

Establish a health status assessment model based on monitoring scheme (Fig. 3):

Set model weights:

Take the weight setting of the monitoring project layer as an example, the constructed judgment matrix \mathbf{A} is shown in Table 4.

Table 3 Monitoring scheme of a small-span steel-concrete composite girder bridge

	Monitoring point 1	Monitoring point 2	Monitoring point 3	Monitoring point 4	Monitoring point 5
Fatigue cracking	✓	✓	✓	✓	✓
Deflection response	✓	✓	✓	✓	✓
Stress state	✓	✓	✓	✓	✓
Ambient temperature		✓	✓	✓	

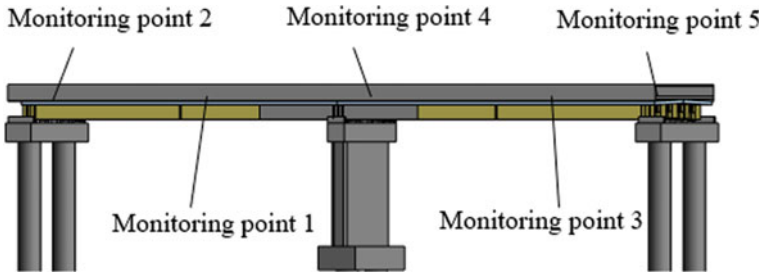


Fig. 2 Deployment diagram of monitoring points of the steel-concrete composite girder bridge

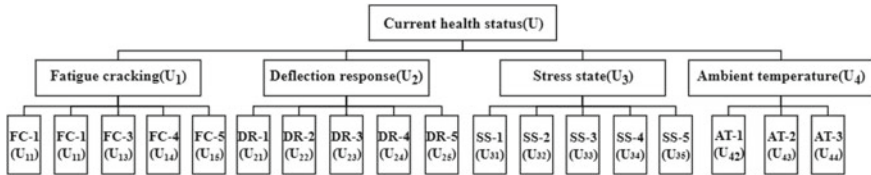


Fig. 3 Health status assessment model of a small-span steel-concrete composite girder bridge

Table 4 Judgment matrix A at the monitoring project layer

A	U_1	U_2	U_3	U_4
U_1	1	2	4	5
U_2	1/2	1	3	4
U_3	1/4	1/3	1	2
U_4	1/5	1/4	1/2	1

Check the judgment matrix: $CR = 0.0190 < 0.1$, therefore, CR satisfies the judgment matrix consistency requirement. The weight vector of the monitoring item layer after normalization is obtained from the matrix A as:

$$\tilde{A} = (0.49 \ 0.31 \ 0.12 \ 0.18)$$

The establishment of each judgment matrix of the monitoring point layer adopts the same method, and its weight vectors are: Fatigue cracking: $\tilde{A}_1=(0.08 \ 0.33 \ 0.08 \ 0.18 \ 0.33)$; Deflection response: $\tilde{A}_2=(0.36 \ 0.07 \ 0.36 \ 0.14 \ 0.07)$; Stress state: $\tilde{A}_3=(0.06 \ 0.34 \ 0.06 \ 0.20 \ 0.34)$; Ambient temperature: $\tilde{A}_4=(0.34 \ 0.36 \ 0.30)$.

4.2 Data Processing and Comprehensive Evaluation

Data membership vectorization processing.

With reference to the “Maintenance Specification for Highway Bridges and Culverts”, establish the evaluation level set V:

$$V = \{Better, Good, Bad, Worse, Worst\}$$

The corresponding state space S is determined as:

$$S = (100, 95, 80, 60, 40)$$

Taking the deflection response as an example, the membership vector table of the deflection response is established as shown in Table 5:

Similarly, the membership vector table of fatigue cracking, stress state and ambient temperature is established.

The data collection period of deflection response is 1.2 min. The evaluation period is set to 1 h. During the evaluation period, the 50 real-time data ω_{real} collected by deflection monitoring point 1 (DR-1) were compared with the deflection response threshold ω_{thr} respectively to determine the state interval of the real-time data. The statistics of the results are shown in Table 6.

Taking the deflection response as an example, use Eq. (9) to process Table 6. During this evaluation period, the deflection response data collected at monitoring point 1 (DR-1) are represented by membership vectors as:

Table 5 Membership vector table of deflection response

State interval $\left(\frac{\omega_{real}}{\omega_{thr}}\right)$	Membership vector	Evaluation level				
		Better	Good	Bad	Worse	Worst
(0,0.1]	X_1	1	0	0	0	0
(0.1,0.3]	X_2	0.3	0.7	0	0	0
(0.3,0.6]	X_3	0	0.25	0.75	0	0
(0.6,1]	X_4	0	0	0.1	0.9	0
(1,∞)	X_5	0	0	0	0	1

Table 6 Statistical table of 50 monitoring data within 1 h of deflection monitoring point 1 (DR-1)

Status level	State interval/ $\left(\frac{\omega_{real}}{\omega_{hr}}\right)$	The amount of data/ (n_j)	Membership vector/ (X_j)
Level 1	(0,0.1]	4	[1,0,0,0,0]
Level 2	(0.1,0.3]	15	[0.3,0.7,0,0,0]
Level 3	(0.3,0.6]	30	[0,0.25,0.75,0,0]
Level 4	(0.6,1]	1	[0,0,0.1,0.9,0]
Level 5	(1, ∞)	0	[0,0,0,0,1]

$$r_1 = (0.17 \ 0.36 \ 0.45 \ 0.02 \ 0)$$

Similarly, the membership vector of the data at the deflection monitoring points 2 ~ 5 (DR-2 ~ 5) in this evaluation period can be calculated as $r_2 \sim r_5$.

Comprehensive assessment of health status:

The fuzzy relationship matrix of the monitoring point layer of the deflection response is established:

$$R_2 = (r_1 \ r_2 \ r_3 \ r_4 \ r_5)^T$$

Combined with the deflection response monitoring point layer weight \tilde{A}_2 , a comprehensive evaluation is carried out:

$$B_2 = \tilde{A}_2 \cdot R_2 = (0.27 \ 0.34 \ 0.37 \ 0.02 \ 0)$$

In the same way, the fuzzy relationship matrices R_1, R_3 and R_4 of monitoring point layers for fatigue cracking, stress state and ambient temperature, and evaluation results B_1, B_3 and B_4 are established. From this, the fuzzy matrix of the monitoring project layer is constructed:

$$R = \begin{pmatrix} B_1 \\ B_2 \\ B_3 \\ B_4 \end{pmatrix} = \begin{pmatrix} 0.87 & 0.13 & 0 & 0 & 0 \\ 0.27 & 0.34 & 0.37 & 0.02 & 0 \\ 0.51 & 0.32 & 0.13 & 0.04 & 0 \\ 1 & 0 & 0 & 0 & 0 \end{pmatrix}$$

Combined with the monitoring project layer weight \tilde{A} , a comprehensive evaluation of the current health status of the bridge is carried out:

$$B = \tilde{A} \cdot R = (0.65 \ 0.21 \ 0.13 \ 0.01 \ 0)$$

Calculate the total status score for this evaluation period:

$$F = B \cdot S^T = 95.95$$

The value of F is at $(95,100]$, the current status of the bridge is level 1, and the health is better.

5 Conclusion

This paper constructs a multi-attribute comprehensive evaluation model of Steel-concrete composite girder bridges with monitoring projects and monitoring points as the index layers, and proposes a data processing method for the health status evaluation of Steel-concrete composite girder bridges:

Based on the monitoring scheme of the bridge, a model matching the characteristics of the bridge is constructed to realize the evaluation of the bridge state. The method has better adaptability to different bridges;

The monitoring data is processed by membership vectorization using fuzzy mathematics theory. A fuzzy evaluation of the bridge state was carried out. The direct connection between real-time data and fuzzy state is established, which provides a guarantee for the real-time evaluation of the health state of bridges.

The proposed model and data analysis method are used to evaluate the health status of an actual steel-concrete composite girder bridge. The results show that in the set evaluation period, according to the analysis and calculation results of the monitoring data of the bridge, the current state score of the bridge is 95.95, which is in the 1st-level state range, and the health is better.

Acknowledgements This work was partly funded by the Tibet Autonomous Region Science and Technology Project (XZ2019TL-G-03), and partly by the Shaanxi Provincial Department of Transportation (17-21K).

References

1. Liang ZB, Chai J, Na SY et al (2021) Validity analysis of bridge health monitoring data based on deep learning. *J Chongqing Jiaotong Univ (Nat Sci Ed)* 40(03):78–83
2. Ma J, Sun S, Yang Q (2021) Review of academic research on bridge engineering in China. *Chin J Highways* 34(02):1–97
3. Shan DS, Luo LF, Li Q (2020) Research progress of bridge health monitoring in 2019. *Chin J Civ Environ Eng* 42(05):115–125
4. Liu XL, Wang B, Huang Q et al (2020) Condition assessment model of cable-stayed bridge based on evidence reasoning framework. *J S China Univ Technol (Nat Sci Ed)* 48(06):69–76
5. Liang L, Sun S, Li M et al (2019) Bridge safety assessment based on variable weight and D-S evidence theory. *J Northeast Univ (Nat Sci Ed)* 40(01):99–103
6. Liu CF, Cao CB, Liu CW et al (2018) Dynamic hierarchical clustering model of bridge structure service status. *Chin J Saf Sci* 28(09):98–102
7. Qiao JG, Cheng C (2018) Research on safety evaluation model of simply supported girder bridges based on extensibility theory. *J Saf Environ* 18(06):2096–2102
8. Wang B, Xu XL, Li XH et al (2017) Bridge safety assessment based on adaptive fuzzy reasoning and RBF network. *Chin J Saf Sci* 27(05):164–168

9. Jia BY, Yu XL, Yan QS (2016) Bridge condition assessment method based on discrete dynamic Bayesian network. *Bridge Constr* 46(03):74–79
10. Qin JD, Fang SG, Zhang W et al (2022) Condition assessment of cable-stayed bridge superstructure based on 3A index. *Chin J Civ Environ Eng (Chin Engl)* 44(03):71–78
11. Xu X, Ren Y, Huang Q et al (2018) State assessment method of suspension bridge based on time-variable weight model. *J S China Univ Technol (Nat Sci Ed)* 46(06):48–53
12. Liu LJ, Wu D, Zhang X et al (2017) Application of improved bayesian method in bridge condition assessment. *J Chang'an Univ (Nat Sci Ed)* 37(06):47–53

Open Access This chapter is licensed under the terms of the Creative Commons Attribution 4.0 International License (<http://creativecommons.org/licenses/by/4.0/>), which permits use, sharing, adaptation, distribution and reproduction in any medium or format, as long as you give appropriate credit to the original author(s) and the source, provide a link to the Creative Commons license and indicate if changes were made.

The images or other third party material in this chapter are included in the chapter's Creative Commons license, unless indicated otherwise in a credit line to the material. If material is not included in the chapter's Creative Commons license and your intended use is not permitted by statutory regulation or exceeds the permitted use, you will need to obtain permission directly from the copyright holder.



Finite Element Analysis of Anchor Length Detection Method Based on Parallel Seismic Methods



Yi Hu, Hong Lin Cao, Qiang Liu, and Xian Li

Abstract As an important component of the tunnel support structure, the effective length and compactness of the anchors have a direct impact on the load-bearing capacity and safety. Anchor reinforcement is characterised by rapid construction and concealment. Traditional tension tests are difficult to meet the current requirements for quality control in engineering construction. In recent years, elastic wave anchor non-destructive technology has gradually emerged and achieved certain results, but still cannot solve the identification of anchor lengths in long anchor rods and complex surrounding rock conditions. In this study, the theory of parallel seismic methods is applied to the verification of anchor length by drawing on the technical means of pile foundation detection. The feasibility of the implementation of the method is verified by simulating the anchor-anchor solid-surrounding rock elastic wave conduction system using ABAQUS to analyse the anchor length detection process.

Keywords Anchor · Nondestructive testing · ABAQUS · Anchorage length

1 Introduction

The side-hole projection theory was used in the early 1990s in Europe and the USA for practical engineering purposes. Liao et al. [1] proposed to identify the intersection point as the pile length by fitting the initial wave of the depth-time curve to two line segments via Snell's law. With the continuous development of the parallel seismic methods of pile foundation inspection technology in recent years, domestic

Y. Hu

Qingdao Metro Group Co., Ltd Third Construction Branch, Qingdao, China

H. L. Cao (✉) · Q. Liu · X. Li

Shandong Transportation Institute, Qingdao, China

e-mail: caohonglin@sdjtky.cn

Q. Liu

e-mail: liuqiang@sdjtky.cn

X. Li

e-mail: lixian@sdjtky.cn

© Crown 2023

Y. Yang (ed.), *Advances in Frontier Research on Engineering Structures*, Lecture Notes in Civil Engineering 286, https://doi.org/10.1007/978-981-19-8657-4_14

153

scholars have scrambled to study and establish simplified calculation models and correction methods [2–5], there are now relevant specification documents applied to pile foundation inspection [6].

Traditional anchor testing methods rely on equipment such as displacement convergence meters, roof separation indicators and drawing meters, but these destructive testing methods cannot be promoted due to the irreversible damage they cause to the support structure [7]. With the development of non-destructive testing technology, the corresponding techniques are gradually being applied to anchor detection. Common detection methods include the stress wave method, ultrasonic method, etc. [8, 9]. However, as the working conditions of anchor anchoring system are more complex compared with foundation piles, the identification of elastic wave reflection signal is difficult, and the accuracy of identifying the length of long anchor bar in complex surrounding rock conditions is extremely limited, so the quality control of anchor bar construction is still restricted by the detection means. In this study, ABAQUS was used to simulate the application of the parallel seismic methods in tunnel anchor length detection and to verify its feasibility.

2 Principle of Parallel Seismic Methods

2.1 Basic Principle

Parallel seismic methods were first used as a method to determine the length of foundation piles for foundation integrity testing [10]. According to Fermat's principle, waves always propagate along the path with the shortest duration, and this principle provides the mathematical basis for the path and duration of initial wave propagation. According to Snell's law, stress wave propagation along a pile foundation produces a refracted longitudinal wave and a refracted transverse wave after shock-excitation. The elastic waves conducted within the pile can be approximated as plane waves due to the large difference in wave impedance at the pile boundaries, which is in line with the theory of one-dimensional wave conduction. The geophone in the side bore will be the first to receive the elastic wave conducted from the pile [11, 12].

The tunnel anchorage body consists of metal anchors, and grip-coated mortar together and can be seen as an ideal one-dimensional anchor bar. The exposed end of the anchor rod is excited to produce a compressional (P-wave) or shear (S-wave) wave, which is transmitted down the anchor solid and produces a refracted longitudinal (PP) and transverse (PS) refraction wave inside the anchor bar in the bottom, with sine value of refraction angle equal to the ratio of the stress wave velocity of the surrounding rock to that of the anchor solid. First, stress wave signals can be collected at different depths by drilling a bypass hole near the anchor bar or by using a geophone placed in an adjacent ungrouted borehole. The equation for the first PS wave duration at any depth z above the point Q (depth is $L + D \tan \beta$, L is the pile length and D is the side hole distance) in the side borehole, without considering the

effect of 3D effects on the pile, is shown in Eqs. (1–3).

$$m = \frac{V_{pp}}{V_{ss}} = \frac{1}{\sin\beta} \quad (1)$$

$$Z_s = D \tan \beta = \frac{D}{\sqrt{m^2 - 1}} \quad (2)$$

$$t_s = \frac{z - z_s}{V_{pp}} + \frac{D}{V_{ss} \cos\beta} = \frac{z}{V_{pp}} + \frac{D\sqrt{m^2 - 1}}{V_{pp}} \quad (3)$$

where D is the net horizontal spacing between the side of the anchor solid and the side hole, hereinafter referred to as the borehole distance; V_{pp} is the one-dimensional P-wave velocity of the anchor solid; V_{ss} is the S-wave velocity of the surrounding rock where the anchor solid is located; β is the angle of projection of the stress wave from the anchor solid to the surrounding rock; Z is the depth of burial of the geophone; Z_s is the propagation depth of the S-wave in the surrounding rock.

The equation for the first PS wave duration at any depth z in the borehole below point Q is shown in (4), where L is the anchor length.

$$t_s = \frac{L}{V_{pp}} + \frac{\sqrt{D^2 + (z - L)^2}}{V_{ss}} = \frac{L}{V_{pp}} + \frac{z - L}{V_{ss}} \sqrt{1 + \left(\frac{D}{z - L}\right)^2} \quad (4)$$

It can be seen from Eq. (4) that the maximum error of $\sqrt{1 + \left(\frac{D}{z-L}\right)^2} \approx 1$ is no greater than 2% for $z-L \geq 5D$, which can be approximated by writing it in a form independent of D as shown in Eq. (5).

$$t_s = \frac{z}{V_{ss}} - \frac{m - 1}{m} \cdot \frac{L}{V_{ss}} \quad (5)$$

When $z-L \geq 5D$, the effect of the side hole distance D on the first PS wave time-depth relationship is small, and the wave time-depth relationship corresponding to different side hole distances can be approximated as a straight line (Fig. 1).

2.2 Calculation of Anchor Length

As can be seen from Sect. 2.1, when $z-L \leq 5D$, the $t \sim z$ relationship of the first PS wave is a straight line with a slope of $1/V_{pp}$, i.e. the time-depth line inside the anchor; when $z-L \geq 5D$, the $t \sim z$ relationship is a straight line with a slope $1/V_{ss}$, i.e. the time-depth line of the surrounding rock at the bottom of the anchor. The formula for calculating the depth of the anchor is Eq. (7).

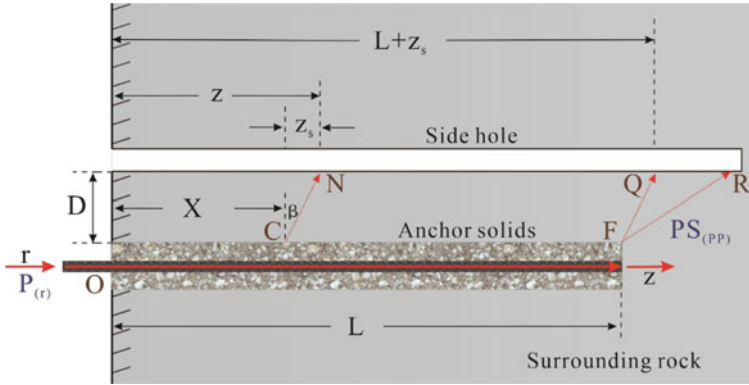


Fig. 1 A simplified computational model for the parallel seismic methods

$$L_c = D\sqrt{(m + 1)/(m - 1)} \tag{6}$$

$$L = z_i - L_c \tag{7}$$

where, z_i is the depth of the intersection of the time-depth line within the anchor bar and the time-depth line of the surrounding rock at the bottom of the bar; When $D = 0$, $L = z_i$ means that the excitation point is at the exposed end of the anchor bar and the side hole is immediately adjacent to the anchor solid. If the time-depth line in the anchor bar is translated past the origin, the depth of its intersection with the time-depth line at the bottom of the bar can be regarded as the length of the anchor bar. The above method is called the translation line intersection method, also called the intersection correction method, and is illustrated in Fig. 2.

3 Non-destructive Testing Method for Tunnel Anchor Lengths

Based on the above theory and the more refined theory of non-destructive testing of anchor bar anchorage quality (one-dimensional bar) [13], a non-destructive testing method for tunnel anchor length is proposed, as shown in Fig. 3.

The detection device consists of an excitation hammer, an excitation wave receiver, a transmissive wave receiver and a mainframe. To detect, a PVC pipe of suitable size is embedded in the borehole, the transmittance receiver is fed into the bottom of the hole, then the exposed end of the anchor is tapped and the signal is collected, followed by lifting the receiver at equal intervals and repeating the tap to collect the signal. The detection host analyses the anchor length by recording the time difference between the signals received by the excitation and transmission wave receivers to create a time-depth curve.

Fig. 2 Schematic diagram of the translating line plus dot method

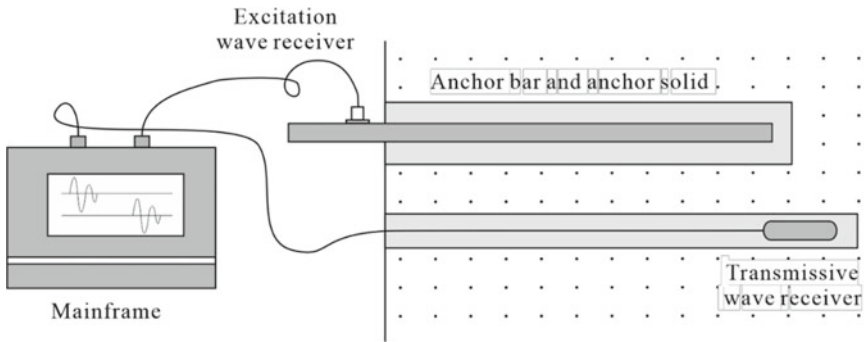
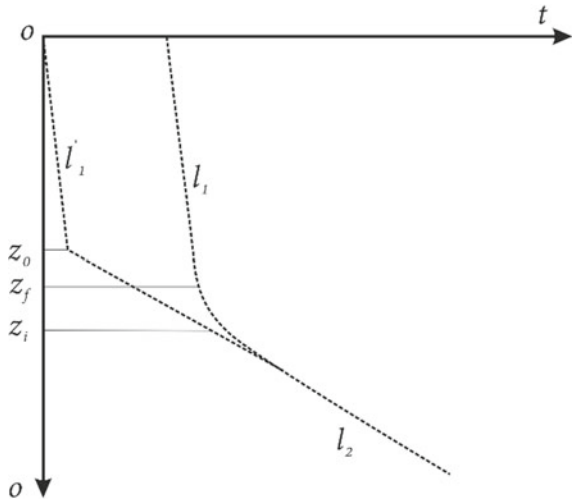


Fig. 3 Tunnel anchor length detection device

4 Simulation Analysis of Abaqus-Based Tunnel Anchor Length Detection

4.1 Finite Element Modelling

ABAQUS software was used to build the anchor-anchor solid-surrounding rock model. The total length of the model is preset to was 6 m, the length of the anchor solids was 4 m, the diameter was 0.4 m and the diameter of the anchors was 4 cm. According to the one-dimensional elastic wave theory, the wave velocity in the anchor and the surrounding rock is calculated by Eq. (8).

Table 1 Formatting sections, subsections and subsubsections

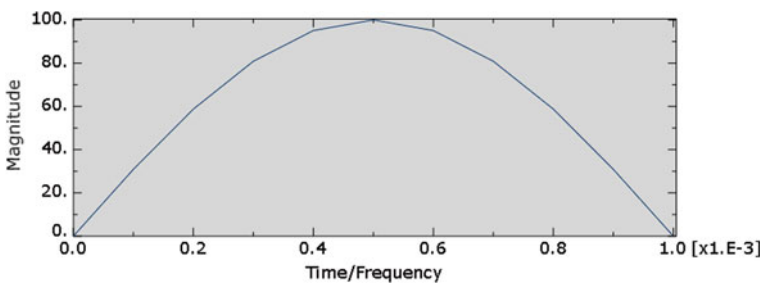
Materials	Density (kg/m ³)	Poisson ratio	Elastic modulus (GPa)	Wave velocity (m/s)
Anchor bar	7800	0.3	207	5151.55
Surrounding rock	2700	0.2	33	3496.03

$$V = \sqrt{\frac{E}{\rho}} \quad (8)$$

The material parameters for the anchors and the surrounding rock are defined with reference to «Design specification of highway tunnel», as shown in Table 1.

The Moore-Coulomb model was chosen for the surrounding rock materials model, with an internal friction angle of 55° and cohesion of 2.0 MPa. The anchor bar selects dynamic surface contact, and the contact algorithm is a symmetric function method [14], that is, at each node, first check whether the node penetrates the main interface, if it does not, no processing is done; If there is penetration, a larger contact force (the magnitude of the force is determined by the stiffness of the main surface and the depth of penetration) is applied between the main interface and the node, which can be seen as adding a spring with greater stiffness between the main and secondary interfaces to reduce the penetration degree of the primary surface of the secondary node. The boundary conditions are set both at the bottom of the anchor and around the anchor solid. The bottom end of the anchor is set to “fully fixed” as it will not be displaced; around the anchor, the displacement in the X and Y directions is constrained and set to 0. The solids are meshed and divided into hexahedral meshes in a swept form.

The excitation method uses uniform excitation force, using the excitation hammer to produce uniform transient excitation, the excitation force pulse is a half-sine pulse [15], the size of $P = P_0 \sin \omega t$, $0 < t < t_c$, P_0 is the peak excitation force, take 10 N, t is the excitation force action time, take $1 \times e^{-3}$ s, the form of pulse force is uniform force, as shown in Fig. 4. The vertical excitation point is located at the exposed end of the anchor bar and the measurement holes are placed 0.5 m from the edge of the anchor bar.

**Fig. 4** Loading frequency

4.2 Point Wave Speed Processing

The results of the wave speed distribution at the point after submission of the above model are shown in Fig. 5. The results show that the stress propagates in the form of fluctuations towards the bottom of the anchor and bends back after reflection from the surrounding rock at the bottom of the anchor. The generation of fluctuations indicates that the finite element model developed is reasonable. The variation of velocity with time on a straight line at 20 cm from the edge of the anchor bar was extracted and the velocity-time curve at 0.5 m from the top of the anchor bar is shown in Fig. 6.

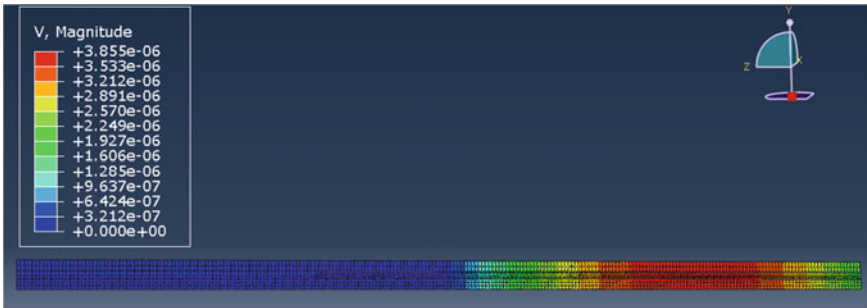


Fig. 5 Point wave speed distribution

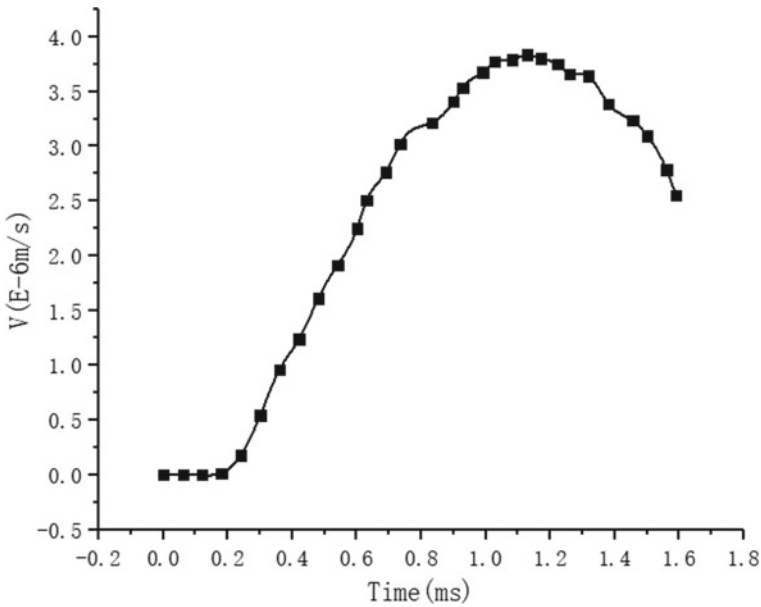


Fig. 6 Point wave speed plotted against time

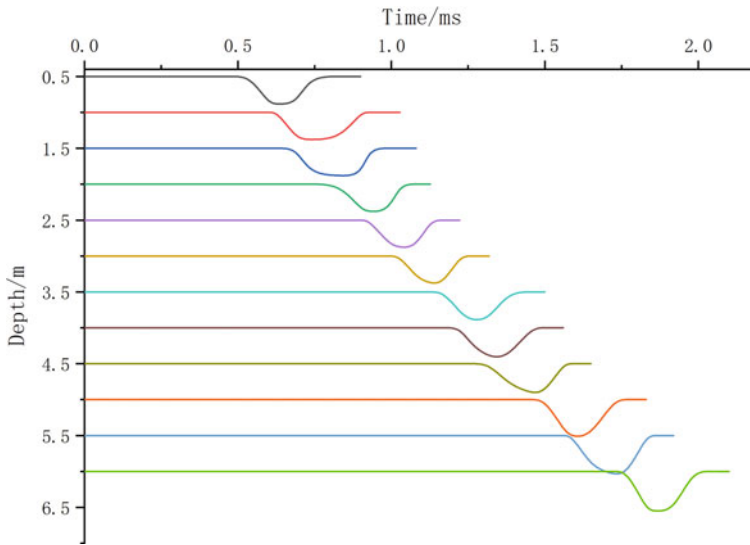


Fig. 7 Waveform plots at different depths

4.3 Linear Fit Analysis

A measurement point was placed at 0.5 m intervals and time-velocity data was extracted from each measurement point and the waveforms at each depth were plotted as shown in Fig. 7. The peak points were automatically identified and extracted using Matlab software and a linear fit was performed, the results of which are shown in Fig. 8. The slopes of the straight lines above 4 m and below 4 m were 5090.18 and 3576.4 respectively, with errors of 1.19 and 2.3% compared to the calculated wave speeds. The two straight lines in the graph are compared at a depth of 4.06 m with an error of 1.5%.

The analysis of the causes of errors consists of two main aspects. For one, the condition for viewing the time-depth curve as a straight line in the envelope is $Z-L \geq 5D$, but when $0 < Z-L < 5D$, the time-depth curve is a hyperbola and approximates this part as a straight line yields a large wave speed in the envelope. Secondly, the overall translation of the time-depth curve above 4 m to the right is due to the presence of the side hole distance, so the translation line intersection method has been proposed to correct this error [16]. The errors arising from the above-mentioned causes have little effect on the measurement of anchor lengths and it is therefore theoretically feasible to use the parallel seismic methods to detect the length of tunnel anchors.

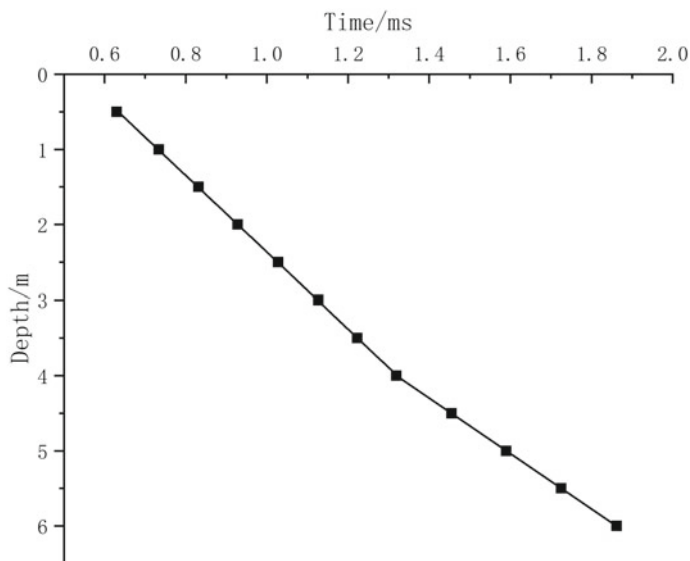


Fig. 8 Peak point fitted straight line

5 Conclusion

A comprehensive analysis of the above computational derivations and simulation results resulted in the conclusion that the parallel seismic methods are theoretically feasible for the verification of anchor lengths. During the construction of the support structure, the existing boreholes can be used to test the surrounding anchor structure. At the end of construction, the method can still be used as an effective evaluation tool for post-facto quality surveys, breaking the deadlock of difficult to detect anchor lengths and difficult to identify at the end of construction, and providing strong technical support for anchor anchoring quality control.

References

1. Liao ST, Tong JH, Chen CH et al (2006) Numerical simulation and experimental study of parallel seismic test for piles. *Int J Solids Struct* 43(7/8):2279–2298
2. Du Y (2017) Study on the analysis method of transmission wave detection of pile foundation boreholes. Shanghai Jiao Tong University
3. Zheng WZ, Zhao DY (2020) ABAQUS-based numerical analysis of the parallel seismic methods. *Guangdong Civ Eng Constr* 27(1):17–19
4. Wei DM, Wang P, Xu MJ (2019) The parallel seismic methods for existing pile foundations based on first wave amplitude. *J Undergr Space Eng* 15(S1):243–248
5. Liang YZ, Wang JB, Wang XY et al. (2020) Study on the factors influencing the length of existing pile foundations tested by parallel seismic methods, *36(S1):253-260*

6. JGJ 106-2014 (2014) Technical specifications for the inspection of building foundation piles. China Construction Industry Press
7. Li QF, Liao XX (2015) NDT mechanism and application practice of anchor support based on stress wave theory
8. Yang F (2018) Research on the application of non-destructive testing of tunnel anchors based on acoustic stress wave method, 40(08):94–98
9. Liu LL, Zhu J, Zhang ZH et al. (2022) ICEEMDAN-based ultrasonic guided wave non-destructive detection of anchor defects in anchor rods, 05:1–17
10. US Department of Transportation-Federal Highway Administration. Borehole nondestructive test (NDT) methods/Parallel seismic (PS) [EB/OL]
11. Guo X (2021) Pile foundation testing the by parallel seismic methods for existing
12. Chen LZ, Zhao RX (2010) Evaluation of the calculation method for determining the depth of the pile bottom by the parallel seismic methods, 6(1):157–161
13. Li Y, Zhang CS, Wang C (2008) Study of several key issues in the non-destructive testing of anchor rod anchorage quality. *J Rock Mech Eng* 27(01):108–116
14. Zhuang Z, You XC, Liao JH (2009) ABAQUS-based finite element analysis and applications. Tsinghua University Press
15. Tang H, Liu DJ (2010) Numerical simulation of excitation forces by reflected wave method for foundation pile inspection. *J Geotech Eng* 32 (S2):224–227
16. Ginger CEBTP. Controlling foundation length by the parallel seismic method (CS97: Mesure de longueur de fondation par la méthode de sismique parallèle) [EB/OL]. <http://www.groupe-cebtp.com/produit/equipement-cs97/>

Open Access This chapter is licensed under the terms of the Creative Commons Attribution 4.0 International License (<http://creativecommons.org/licenses/by/4.0/>), which permits use, sharing, adaptation, distribution and reproduction in any medium or format, as long as you give appropriate credit to the original author(s) and the source, provide a link to the Creative Commons license and indicate if changes were made.

The images or other third party material in this chapter are included in the chapter's Creative Commons license, unless indicated otherwise in a credit line to the material. If material is not included in the chapter's Creative Commons license and your intended use is not permitted by statutory regulation or exceeds the permitted use, you will need to obtain permission directly from the copyright holder.



Numerical Simulation of Rockburst Characteristics of Tunnel Surrounding Rock Under Dilatancy Effect



Jian-qiang Yu, Qi Li, Yong-lu Wang, and Shuai Tao

Abstract Rockburst is one of the most intense reactions in various instability phenomena of underground cavern surrounding rock, which seriously threatens the safety of underground engineering construction personnel and equipment. Based on Mohr–Coulomb strain softening model, the non-associated flow rule is adopted for plastic flow after material yield. By implanting Gu Ming-cheng and Tao Zhen-yu rockburst criterion in the software, the effects of different dilatancy angles on rockburst grade and circumferential stress distribution of surrounding rock of circular tunnel are simulated. The calculation results show that the larger the dilatancy angle is, the more difficult the rock burst pit is to form. The elements of serious rockburst are mainly concentrated in the wall of the tunnel, and the shear bands formed in the high value area of shear strain increment are short. When the dilatancy angle is small, the circumferential stress reaches the maximum at the interface of elastic-plastic zone. With the increase of dilatancy angle, the number of elements entering the plastic state and occurring medium and severe rockburst increases first and then decreases, while the number of elements occurring slight rockburst decreases monotonously. Different dilatancy angles have significant effects on the number of elements occurring rockburst at all levels.

Keywords Dilatancy effect · Rockburst · Strain softening · Circumferential stress

J. Yu · S. Tao (✉)

POWERCHINA Huadong Engineering Corporation Limited, Hangzhou 311122, Zhejiang, China
e-mail: tao_s@hdec.com

Zhejiang Huadong Engineering Consulting Corporation Limited, Hangzhou 311122, Zhejiang, China

Q. Li

Powerchina Road Bridge Group Corporation Limited, Beijing 100048, China

Y. Wang

Sinohydro Bureau 14th Corporation, Kunming 650051, China

© Crown 2023

Y. Yang (ed.), *Advances in Frontier Research on Engineering Structures*, Lecture Notes in Civil Engineering 286, https://doi.org/10.1007/978-981-19-8657-4_15

163

1 Introduction

Rockburst is one of the most intense reactions in various instability phenomena of underground cavern surrounding rock, which seriously threatens the safety of underground engineering construction personnel and equipment. At present, scholars in various countries have conducted in-depth research on the mechanism and influencing factors of rockburst in hard brittle surrounding rock with high geostress, especially the research on the early prediction of rockburst concerned by the engineering community is very active [1–3]. The research methods of rockburst prediction mainly include acoustic emission method, seismic monitoring method and the combination of the two methods. In addition, numerical methods are also widely used for rockburst prediction. With the help of appropriate rockburst criteria, numerical methods can be used to directly analyze the possibility of rockburst and the location and intensity classification of possible rock bursts, and be corrected in time with field construction [4–6]. Geotechnical materials often show volume expansion in the process of loading deformation, which will produce expansion behavior after the peak. The volume change of rock and soil mass in the shear yield process is significantly affected by the dilatancy angle.

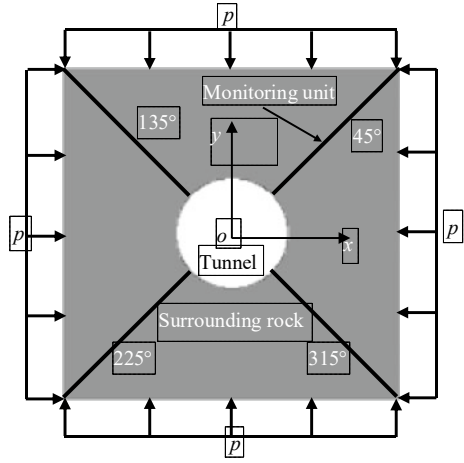
The dilatancy angle is usually used to describe the mechanical behavior of rock and soil material after peak expansion in continuum mechanics [5–7]. Therefore, it is an important parameter to measure the volume change of rock and soil material and the expansion phenomenon, and it is one of the hot issues in geotechnical engineering. However, in theory and numerical analysis of rock mechanics, the dilatancy angle is often simplified to 0° or equal to the internal friction angle, sometimes completely ignored [6–8]. At present, in the constitutive relationship of geotechnical materials using the non-associated flow rule, the value of dilatancy angle ψ is generally smaller than that of internal friction angle φ , but the specific value is still uncertain, which is usually approximated as 0 [7–10]. On the basis of previous studies, this paper adopts Gu Ming-cheng and Tao Zhen-yu rockburst criterion [11, 12] to discuss the influence of different dilatancy angles on rockburst grade and circumferential stress distribution of surrounding rock of circular tunnel by changing the value of dilatancy angle.

2 Calculation Model, Scheme and Rock Burst Criterion

2.1 Calculation Model, Scheme and Constitutive Parameters

The length (x direction) and height (y direction) of the model are both 10 m, which are divided into 40,000 rectangular elements with the same area. Before the tunnel excavation, in order to make the calculation model reach the static equilibrium state as soon as possible, the stress of each small unit is set to be equal to the confining pressure. When the calculation reaches the equilibrium, the tunnel with a radius of

Fig. 1 Model geometry and boundary conditions



1.66 m is excavated in the model. The model after excavation is shown in Fig. 1. After tunnel excavation, the stress of surrounding rock is redistributed. When the calculation reaches 50,000 time steps, the model reaches the static equilibrium state again.

In order to study the distribution of circumferential stress of surrounding rock of tunnel, four rows of elements whose center is located on the four vertices connecting the center of tunnel to the model are selected as the monitored elements, namely, the elements in the directions of 45, 135, 225 and 315°, as shown in Fig. 1. This paper only gives the calculation results when the model reaches the static equilibrium state in each scheme.

In this paper, four calculation schemes are completed to study the influence of dilatancy angles on the rockburst and circumferential stress distribution of surrounding rock. The dilatancy angles of schemes 1–4 are 0°, 15°, 25° and 35°, respectively, and other parameters are the same, as shown in Table 1.

2.2 Rockburst Criterion

In this paper, the Gu-Tao rockburst criterion [11, 12] is used as the main stress rockburst criterion. The rockburst is divided into three levels (slight rockburst, moderate rockburst and severe rockburst), and the ratio of the maximum principal stress σ_1 to the uniaxial compressive strength of the rock σ_c is used to judge:

$$\sigma_c/\sigma_1 = 5.0 \sim 6.67 \quad (\text{slight rockburst}) \tag{1}$$

$$\sigma_c/\sigma_1 = 2.5 \sim 5.0 \quad (\text{moderate rockburst}) \tag{2}$$

Table 1 Mechanical parameters of surrounding rock

Scheme	P/MPa	K/GPa	G/GPa	c/MPa	c_v/MPa	σ_t/MPa	σ_c/MPa	R/m	$\varphi_0/^\circ$	$\varphi_r/^\circ$	$\psi/^\circ$	ν
Scheme 1	50	28.1	26.2	23.4	7.8	11.7	175	1.66	60	40	0.0	0.25
Scheme 2	50	28.1	26.2	23.4	7.8	11.7	175	1.66	60	40	15	0.25
Scheme 3	50	28.1	26.2	23.4	7.8	11.7	175	1.66	60	40	25	0.25
Scheme 4	50	28.1	26.2	23.4	7.8	11.7	175	1.66	60	40	35	0.25

$$\sigma_c/\sigma_1 < 2.5 \quad (\text{severe rockburst}) \tag{3}$$

3 Result Analysis and Discussion

3.1 Influence of Dilatancy Angle on Rockburst Grade of Tunnel Surrounding Rock

Figures 2–5 show the calculation results of schemes 1–4 at 50,000 time steps, respectively. The dark area in the figure is the high value area of rockburst at all levels and shear strain increment. In Scheme 1 ($\psi = 0^\circ$), the rockburst notches are formed in all four quadrants by the units with rockburst at all levels. The rockburst notch formed by the units with moderate and severe rockburst are obvious. The units with moderate rockburst are distributed uniformly along the surface of the tunnel in addition to the rockburst notch. The units with severe rockburst are mainly concentrated in the position of the rockburst notch, and other positions on the surface of the tunnel are only sporadically distributed by some units, as shown in Fig. 2a–c. It can be found from Fig. 2d that the high value area of the shear strain increment of the surrounding rock of the tunnel develops into multiple shear bands, and the two shear bands converge to form a shape similar to the rockburst notch, and the position is basically consistent with the rockburst notch.

From Fig. 3a–c, it can be found that in scheme 2 ($\psi = 15^\circ$), moderate and severe rockburst occurred only in quadrants 1, 2 and 4, where obvious rockburst notch were formed and the depth of the notches was greater than that in scheme 1. The unit where moderate rockburst occurs is not only concentrated at the location of rockburst notch, but also evenly distributed on the surface of tunnel. The unit where serious rockburst occurs is mainly concentrated at the location of rockburst notch. The units with slight rockburst did not form rockburst notch, but some units near the top of rockburst notch occurred slight rockburst. Figure 3d shows that the high value area of the shear strain increment of the surrounding rock of the tunnel develops into several narrow and

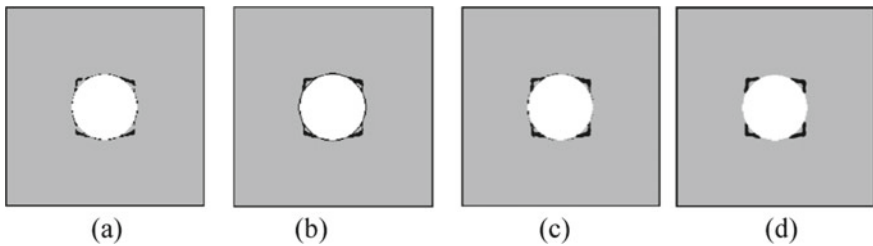


Fig. 2 Numerical results in scheme 1: **a** slight rockburst; **b** moderate rockburst; **c** serious rockburst; **d** elements having higher shear strain increments

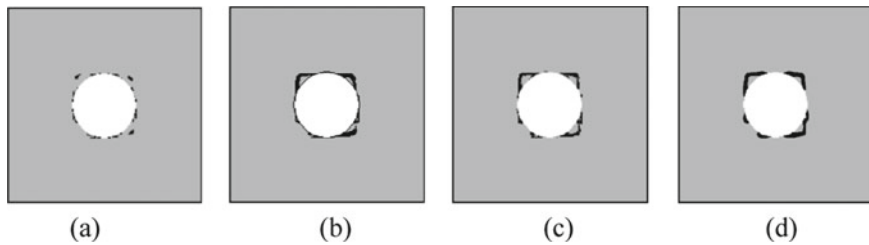


Fig. 3 Numerical results in scheme 2: **a** slight rockburst; **b** moderate rockburst; **c** serious rockburst; **d** elements having higher shear strain increments

long shear zones in the 1st, 2nd and 4th quadrants, and the two confluence forms a shape similar to the rockburst notch. However, in the 3rd quadrant, the surface distribution of the rock tunnel in the high value area of the shear strain increment does not develop into the shear zone inside the surrounding rock.

From Fig. 4a–c, it can be found that in scheme 3 ($\psi = 25^\circ$), the moderate and severe rockburst units formed rockburst notch only in quadrants 3 and 4, and the moderate rockburst units accumulated in the surrounding rock, forming shallow rockburst notch, and the serious rockburst units formed obvious rockburst notch. In quadrants 1 and 2, the units where serious rockburst occurred did not form rockburst notch, but mainly concentrated near the top and both sides of the tunnel.

From Fig. 4d, it can be found that although the high value area of the shear strain increment of the surrounding rock of the tunnel develops into several shear zones, the shear zones distribute along the surface of the tunnel in the first and second quadrants, and do not extend to the interior of the surrounding rock to form a shape similar to that of the rockburst notch.

In the third and fourth quadrants, the shear zones are longer and slightly extend to the interior of the surrounding rock, and the two shear zones converge to form a shape similar to that of the rockburst notch formed by the unit with moderate rockburst. Compared with the results of Schemes 1 and 2, the shear bands formed by Scheme 3 are relatively smooth, and there are no obvious sharp points and corners when the two shear bands converge.

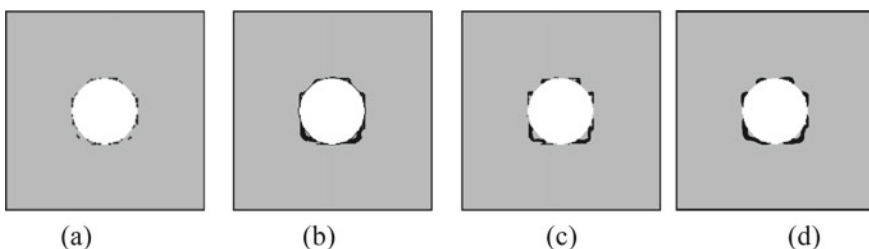


Fig. 4 Numerical results in scheme 3: **a** slight rockburst; **b** moderate rockburst; **c** serious rockburst; **d** elements having higher shear strain increments

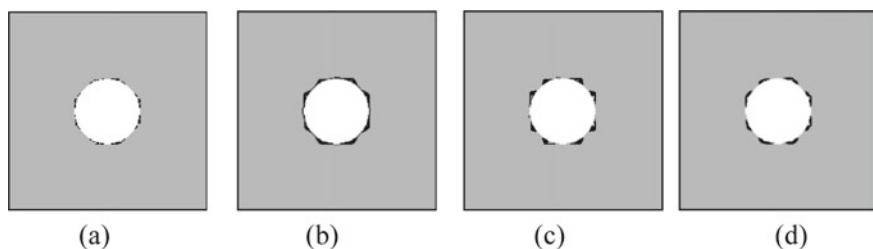


Fig. 5 Numerical results in scheme 4: **a** slight rockburst; **b** moderate rockburst; **c** serious rockburst; **d** elements having higher shear strain increments

From Fig. 5a–c, it can be found that in scheme 4 ($\psi = 35^\circ$), there is no rockburst notch in all levels of rockburst units. The units with slight rockburst are scattered on the surface of the tunnel, and the units with moderate rockburst are evenly distributed on the surface of the tunnel, and accumulate slightly to the interior of the surrounding rock. The units with serious rockburst are massively accumulated in the interior of the surrounding rock. It can be found from Fig. 5d that although the high value area of the shear strain increment of the surrounding rock of the tunnel develops into several short shear bands along the surface of the tunnel, its position is near the position where the unit with serious rockburst accumulates inside the surrounding rock.

3.2 Influence of Dilation on Circumferential Stress Distribution of Tunnel Surrounding Rock

Figure 6a–d show the circumferential stress distribution of the monitored units in four directions from scheme 1–scheme 4, where the ordinate is the circumferential stress value (σ_θ) of the monitored units, and the abscissa is the distance (R) from the center of the monitored units to the center of the tunnel.

From Fig. 6a, it can be found that in scheme 1 ($\psi = 0^\circ$), the circumferential stress distribution curves of the monitored units in four directions have large fluctuations. Before reaching the maximum value, the absolute value of the circumferential stress decreases to 0 MPa, then increases to the peak value, and finally decreases and gradually tends to a certain value.

It can be found from Fig. 2a–c that all the monitored units pass through the area where the rock burst notch is located, and the units in the elastic state inside the notch are unloaded due to rockburst. Therefore, the distribution law of the annular stress of the monitored unit is shown in Fig. 6.

It can be found from Fig. 6b that in scheme 2 ($\psi = 15^\circ$), the circumferential stress distribution curves of the monitored units in the directions of 45, 135 and 315° show obvious fluctuations. Similar to the results in scheme 1, the absolute value of circumferential stress first decreases, then increases to the peak, and finally decreases and gradually tends to a certain value.

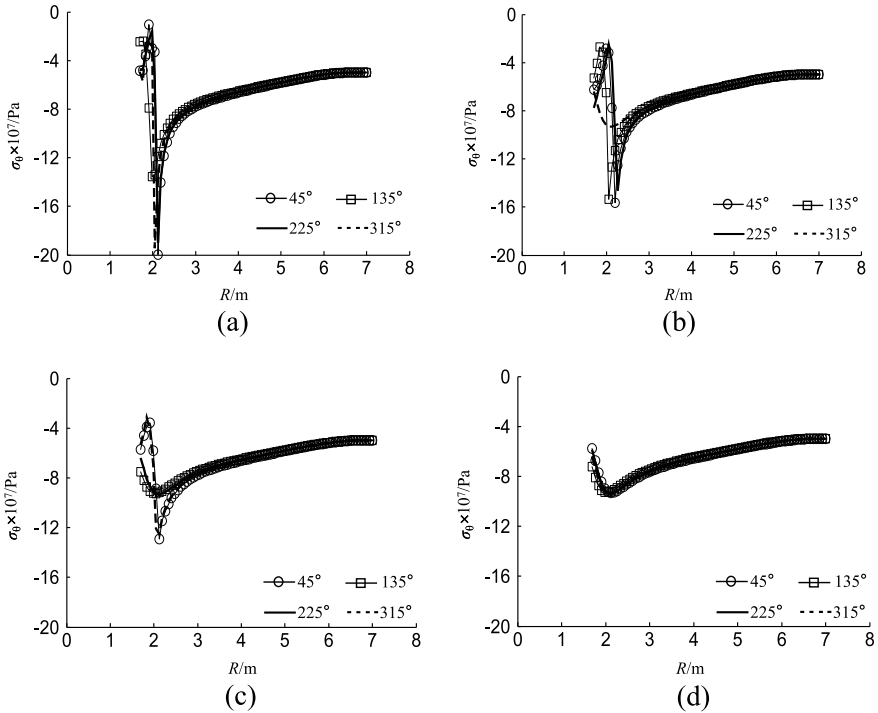
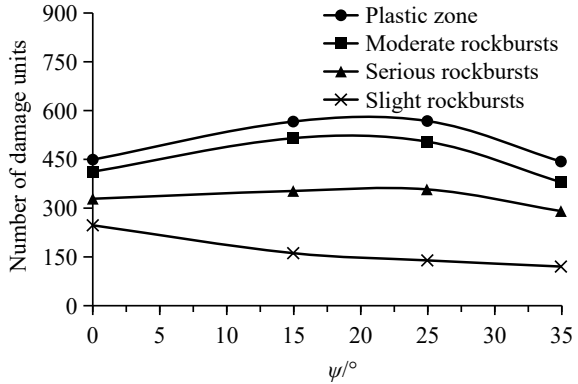


Fig. 6 Tangential stress distribution of monitored elements under different schemes: **a** scheme 1; **b** scheme 2; **c** scheme 3; **d** scheme 4

The fluctuation of circumferential stress distribution curve in scheme 2 is smaller than that in scheme 1, and the minimum value and maximum value of absolute value are between the minimum and maximum values in scheme 1. When the monitored unit in the direction of 225° is near the surface of the tunnel, the absolute value of the circumferential stress increases monotonically. With the increase of the distance from the center of the monitored units to the center of the cavern, the circumferential stress gradually tends to a certain value. From Fig. 3a–c, it can be found that the rockburst units are mainly concentrated in the first, second and fourth quadrants of the model, where the monitored unit passes through the area where the rockburst notch is located. The monitored unit located in the notch is similar to that in scheme 1, and is also unloaded due to rockburst. Therefore, the circumferential stress distribution curve will have the results shown in Fig. 6b.

From Fig. 6c, it can be found that in scheme 3 ($\psi = 25^\circ$), only the circumferential stress distribution curves of the monitored units in 225 and 315° directions appear fluctuations similar to those in scheme 1 and 2. The absolute value of the circumferential stress of the unit near the surface of the tunnel first decreases to the minimum, then increases to the maximum, and finally decreases and gradually tends to a certain value. Compared with the first two schemes, the number of elements with reduced

Fig. 7 The number of damage units distribution in all schemes



circumferential stress absolute value is reduced. From Fig. 4a–c, it can be found that the rockburst notch is formed only in the third and fourth quadrants, but the rockburst notch is shallow, and there are few monitored units in the elastic state in the notch. However, in the first and second quadrants, no rockburst notch is formed, and only the units on the surface of the tunnel have rockburst, so the distribution curve of the circumferential stress of the monitored unit will appear the result shown in Fig. 6c.

It can be found from Fig. 6d that in Scheme 4 ($\psi = 35^\circ$), the overall trend of the circumferential stress distribution curve of the monitored unit in four directions is basically the same, which is relatively smooth and has no obvious fluctuation. It can be found from Fig. 6a–c that no rockburst notch is formed in the four quadrants of the model for the units with rockburst at all levels. Most of the monitored units in the four directions do not enter the plastic state, and rockburst occurs only in the units near the surface of the cavern. Therefore, the distribution curve of the circumferential stress of the monitored units will appear as shown in Fig. 6d.

Figure 7 gives the distribution curves of the number of elements entering the plastic state and causing minor, moderate and severe rockburst in the surrounding rock of tunnels in schemes 1 to 4. It can be found that with the increase of the dilatancy rock angle, the number of elements entering the plastic state and causing moderate and severe rockburst increases first and then decreases. When $\psi = 25^\circ$, the number of elements entering plastic state and serious rockburst is the largest. When $\psi = 15^\circ$, the largest number of units were moderate rockburst. When $\psi = 35^\circ$, the minimum number of elements entering the plastic state, moderate and severe rockburst occurred. With the increase of dilatancy angle, the number of units with slight rockburst decreases monotonously, and when $\psi = 35^\circ$, reaches the minimum.

4 Conclusions

Gu Ming-cheng and Tao Zhen-yu (Gu-Tao) rockburst criterion is introduced into numerical calculation to simulate the rock burst process of circular tunnel

surrounding rock with different dilatancy angles. The influence of dilation on the rockburst grade of surrounding rock and the circumferential stress distribution of surrounding rock is analyzed and discussed. The calculation results show that the larger of the dilatancy angle, the more difficult to form rockburst notch, and the more difficult of the high value region of shear strain increment to extend into surrounding rock. With the increase of dilatancy angle, the elements that cause serious rockburst will accumulate near the surface of the tunnel, and the shear band formed by the high value area of shear strain increment is shorter. When the dilatancy angle is small, because the monitored unit passes through the area where the rockburst notch is located, the hoop stress value of the unit near the surface of the tunnel decreases due to unloading, and the hoop stress value of the monitored unit at the junction of the elastic-plastic zone reaches the maximum.

With the increase of dilatancy angle, the number of failure units decreases, and the stress distribution curve of the monitored unit fluctuates less and smoother. The number of elements entering the plastic state and occurring medium and severe rockburst increases first and then decreases with the increase of dilatancy angle, while the number of elements occurring slight rockburst decreases monotonously. Different dilatancy angles have significant indigenous effects on the number of elements occurring rockburst at all levels. In this paper, the principal stress rockburst criterion is introduced into the calculation process, and the circumferential stress and energy criterion can be integrated in the next step. Considering the rockburst process of surrounding rock under the influence of multiple factors, the comprehensive evaluation calculation method of rockburst is finally given.

References

1. Patel S, Martin CD (2020) Impact of the initial crack volume on the intact behavior of a bonded particle model. *Comput Geotech* 127:1–10
2. Cabezas R, Vallejos J (2022) Nonlinear criterion for strength mobilization in brittle failure of rock and its extension to the tunnel scale. *Int J Min Sci Technol*. <https://doi.org/10.1016/j.ijmst.2022.04.002>
3. Nicksiar M, Martin CD (2012) Evaluation of methods for determining crack initiation in compression tests on low porosity rocks. *Rock Mech Rock Eng* 45(4):607–617
4. Perras MA, Diederichs MS (2014) A review of the tensile strength of rock: concepts and testing. *Geotech Geol Eng* 32(2):525–546
5. Alejano LR, Alonso E (2005) Considerations of the dilatancy angle in rocks and rock masses. *Int J Rock Mech Min Sci* 42(4):481–507
6. Lee YK, Pietruszczak S (2008) A new numerical procedure for elasto-plastic analysis of a circular opening excavated in a strain-softening rock mass. *Tunn Undergr Space Technol* 23(5):588–599
7. Zhao XG, Cai M, Cai MF (2010) A rock dilation angle model and its verification. *Chin J Rock Mech Eng* 29(5):970–981
8. Chandler NA (2013) Quantifying long-term strength and rock damage properties from plots of shear strain versus volume strain. *Int J Rock Mech Min Sci* 59:105–110
9. Walton G, Hedayat A, Kim E, Labrie D (2017) Post-yield strength and dilatancy evolution across the brittle-ductile transition in Indiana limestone. *Rock Mech Rock Eng* 50(7):1691–1710

10. Walton G (2018) Scale effects observed in compression testing of Stanstead granite including post-peak strength and dilatancy. *Geotech Geol Eng* 36(2):1091–1111
11. Gu MC (2001) Research on rockburst in Qinling railway tunnel. *Res Water Resour Hydropower* 3(4):19–26
12. Zhang JJ, Fu BJ (2008) Rockburst and its criteria and control. *Chin J Rock Mech Eng* 27(10):2034–2042

Open Access This chapter is licensed under the terms of the Creative Commons Attribution 4.0 International License (<http://creativecommons.org/licenses/by/4.0/>), which permits use, sharing, adaptation, distribution and reproduction in any medium or format, as long as you give appropriate credit to the original author(s) and the source, provide a link to the Creative Commons license and indicate if changes were made.

The images or other third party material in this chapter are included in the chapter's Creative Commons license, unless indicated otherwise in a credit line to the material. If material is not included in the chapter's Creative Commons license and your intended use is not permitted by statutory regulation or exceeds the permitted use, you will need to obtain permission directly from the copyright holder.



Credibility of Estimating the Hysteretic Energy Demands of Concentrically Braced Steel Frames



Cuiling Ma

Abstract Earthquake happens frequently in China, and seismic design is of high importance for buildings. The energy-based seismic design method with clear conception has attracted attention of more and more researchers. One of the initial questions is how to determine the energy requirement. In this paper, the finite element software is used to analyze the time history of the concentrically braced steel frames designed according to the current codes and standards. The analysis shows that the cumulative demand obtained by time history analysis is similar to the estimated value. The hysteretic energy dissipation of the concentrically braced steel frames is of small top and big bottom along the height of the structure, and the energy dissipation of the floors below the height of $H/3$ (H is the height of the structure) is larger. Under rare earthquakes, the yield mode of structures designed according to the elastic design method of small earthquakes is uncontrollable, so it is necessary to study the design method based on energy behavior.

Keywords Concentrically braced steel frame · Hysteretic energy demands · Energy-based seismic design method

1 Introduction

Earthquake happens frequently in China. Several strong earthquakes, such as Wenchuan earthquake and Taiwan Chi-chi earthquake, have caused large casualties and property losses. Seismic design of buildings can effectively withstand the damage caused by earthquakes.

The performance-based seismic design is committed to clearly controlling the state of the structure under different earthquake intensity, so that the damage of the structure does not exceed the specific behavior of the expected strength earthquake, and has the expected level of reliability. Since this method was proposed, it has attracted wide attention [1–6, 8–12].

C. Ma (✉)

College of Urban Construction and Transportation, Hefei University, Hefei, China

e-mail: 415997243@qq.com

© The Author(s) 2023

Y. Yang (ed.), *Advances in Frontier Research on Engineering Structures*, Lecture Notes in Civil Engineering 286, https://doi.org/10.1007/978-981-19-8657-4_16

175

The estimation of energy demands of multi-degree-of-freedom architectures is a key step in the research of energy-based seismic design methods. In this paper, examples of the concentrically braced steel frames designed in accordance with Chinese current norms and standards was used to evaluate the rationality of the equivalent velocity spectra of cumulative hysteretic energy established in Literature [7] in accordance with Chinese site classification for hysteretic energy demand estimation.

2 Design Overview

The elevation and plan layout of chevron concentrically braced steel frames (“CBSF” for short) are shown in Fig. 1. The seismic design parameters are as follows. Seismic fortification intensity is 8° (0.3 g), soil type II, site group 2, category C, 50 years for the design working life. The bidirectional span is 7.8 m, and the storey height is 3.3 m, with 10 and 15 floors. In Fig. 1, dotted lines denote secondary beams, a span of 2.6 m, which are hinged to the primary beams. The measurements of the parapet are 1.1 m for height by 0.2 m for thickness. The thickness of outer wall is 0.2 m.

The dead and live loads of floor are 4.5kN/m² and 2.0kN/m² respectively, while the dead and live loads of roof are 5.0kN/m² and 2.0kN/m² respectively. Q235B. Steel supports and beams adopt welded I-shaped section members with flange as shear edge, steel columns adopt box section members, and rigid joints.

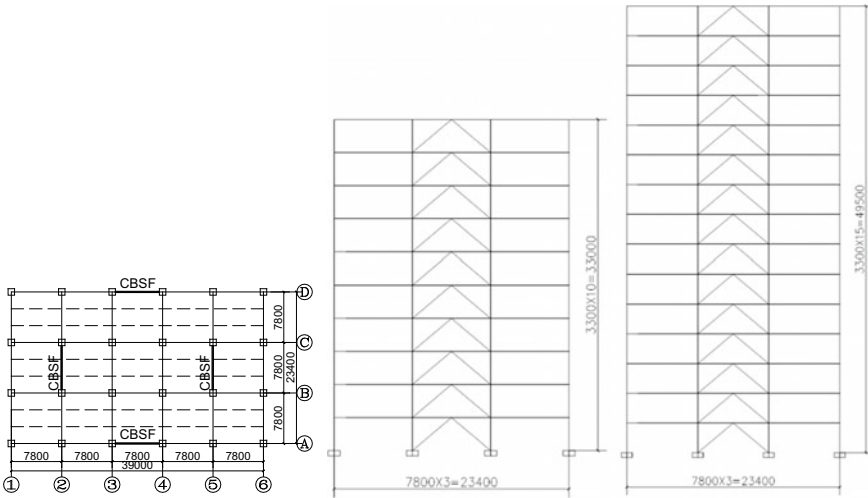


Fig. 1 CBSF plane view and elevation (unit: mm)

Table 1 Member sections of 10-story CBSF

Number of stories	Column sections		Beam sections		Brace section
	Interior column	Exterior column	Middle beam	Side beam	
1–3	□600*24	□600*20	H600*250*14*20	H600*250*14*20	H300*300*16*18
4–6	□500*22	□500*20	H600*250*14*18	H600*250*14*18	H250*250*10*12
7–9	□400*20	□400*18	H600*250*14*18	H600*250*14*18	H250*250*10*12
10	□400*20	□400*18	H600*250*14*18	H600*250*14*18	H250*250*10*12

Table 2 Member sections of 15-story CBSF

Number of stories	Column sections		Beam sections		Brace section
	Interior column	Exterior column	Middle beam	Side beam	
1–3	□700*24	□700*22	H600*250*16*20	H600*250*14*20	H300*300*18*20
4–6	□600*24	□600*22	H600*250*14*20	H600*250*14*20	H300*300*16*18
7–10	□500*24	□500*20	H600*250*14*18	H600*250*14*18	H250*250*10*12
11–14	□400*22	□400*18	H600*250*14*18	H600*250*14*18	H250*250*10*12
15	□400*22	□400*18	H600*250*14*18	H600*250*14*18	H250*250*10*12

3 Design Standards

Relevant provisions in current codes and standards, including “Standard for design of steel structures” GB 50017-2017, “Code for seismic design of buildings” GB 50011-2010, “Technical specification for steel structure of tall buildings” GJG 99-2015, “Load Code for design of building structures” GB50009-2012, can provide guidance for design.

The seismic grade is three for 10-story building, and two for 15-story building, respectively. The damping ratio of CBSFs for elastic design under frequent earthquakes is set according to Code for seismic design of buildings, and the damping ratio is set as 0.05 for the energy analysis of structures under rare earthquake. The characteristic period value T_g is 0.40 s. The STS module in PKPM software and the finite element software SAP2000 were used to determine the beam, column and support sections of CBSFs as shown in Tables 1 and 2

4 Estimation of Structural Hysteretic Energy Demand

The cumulative hysteretic energy demand of multi-degree-of-freedom (MDOF) system, as shown in Table 3, can be obtained according to the existing formulas in

Table 3 Accumulated hysteretic energy demand

Example	Accumulated hysteretic energy demand of an equivalent SDOF system corresponding to the j th mode $E_h(\text{ESDOF})$, j/kNm			Accumulated hysteretic energy demand of an MDOF $E_h(\text{MDOF})/\text{kNm}$
	$E_h(\text{ESDOF}), 1$	$E_h(\text{ESDOF}), 2$	$E_h(\text{ESDOF}), 3$	
10-story CBSF	740.422	1172.438	708.081	1939.806
15-story CBSF	674.509	1557.067	1807.700	2356.936

Literatures [7, 11]. In order to obtain a better cumulative hysteretic energy demand of the structure, the sum of modal participating mass ratio should exceed 90%.

5 Time-History Analysis

Compared with static elasto-plastic analysis, time history analysis can reflect the structural response under earthquake. In this paper, the finite element software ABAQUS is used to analyze the elastic-plastic time history of frame structures. The beam elements (B31) are utilized to simulate the braces, columns, and beams. Considering the nonlinearity of the material, a bilinear follow-up strengthening model and Rayleigh damping model were used. The size of beam element grid is 0.2 m.

Earthquakes are sudden and random, and the corresponding structural ground motion response is also a random process, so it is necessary to select earthquake wave reasonably. In addition to the three elements of ground motion such as peak value, spectrum and duration, the energy factor should also be considered during wave selection. Earthquake waves were screened according to the principle of wave selection, and only one earthquake wave measured by the same seismic station in the same earthquake is selected. The earthquake waves used in the 10-story CBSF are P216, P322, P544, P735, P947, P951, P961, P1149, P1766, RSN2602E, respectively; The earthquake waves used in the 15-story CBSF are P735, P154, P836, P947, P951, P961, P850, P2714, RSN2361E, RSN2602N, respectively.

5.1 Comparison of Hysteretic Energy Analysis Value with Estimated Value

By using finite element software ABAQUS for time history analysis, the hysteretic energy demand of the structure under different far-field vibrations is extracted and the average value is taken as the analysis value. Finally, it is compared with the estimated value obtained by equations in Literatures [7, 11], as shown in Figs. 2–3.

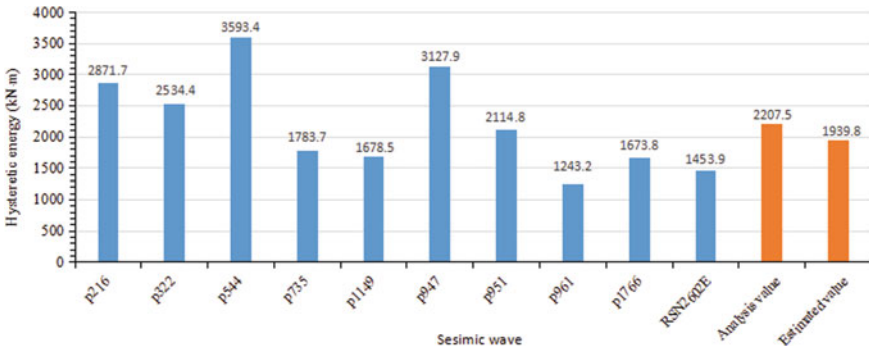


Fig. 2 Comparison of hysteretic energy analysis value with estimated value for 10-story CBSF

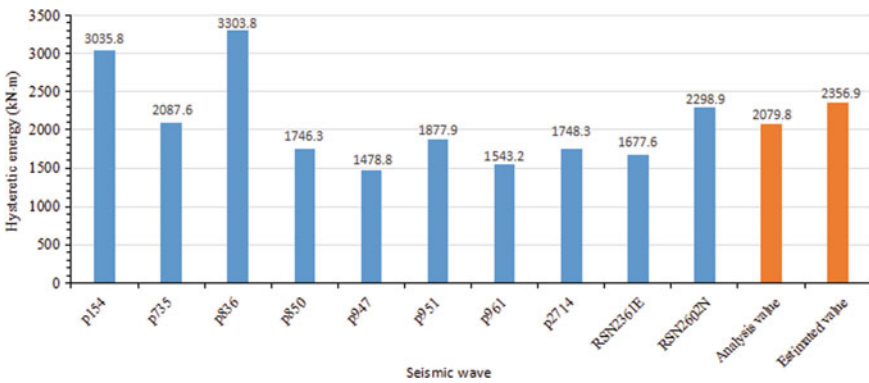


Fig. 3 Comparison of hysteretic energy analysis value with estimated value for 15-story CBSF

It can be seen from Figs. 2 and 3 that the hysteretic energy obtained by the same example under different earthquake waves is different, and there is a certain dispersion. The average value of hysteretic energy under the action of multiple seismic waves on the same example is basically consistent with the estimated value. The time-history analysis values of the 10-story and 15-story CBSF are 2207.5kN·m and 2079.8kN·m, and the corresponding estimated values are 1939.8kN·m and 2356.9kN·m, with errors of 13.8% and 11.7%, respectively. The analysis value of the 10-story CBSF is larger than the estimated value, which may be because the target ductility factor selected in the estimated calculation of hysteresis energy demand of the example is slightly smaller than the real target ductility, or the characteristic period of a seismic wave used in the analysis is close to the natural vibration period of the example structure, and resonance occurs.

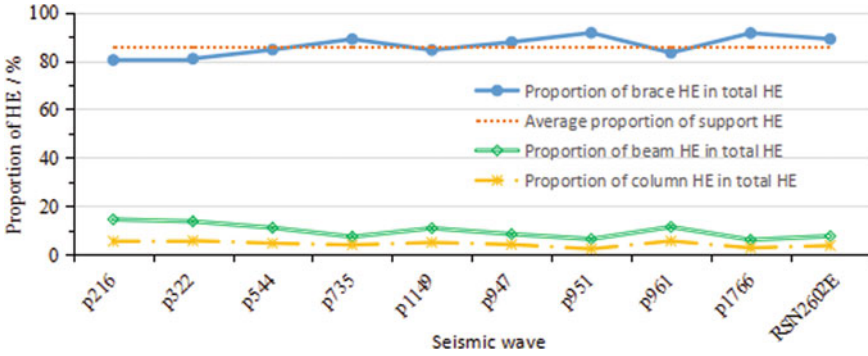


Fig. 4 Hysteretic energy distribution in 10-story CBSF components under different seismic waves

5.2 Distribution of Hysteretic Energy Dissipation in Different Members

Overall, the content in Sect. 5.1 of this paper can only judge the reliability of the relevant formulae in the Literatures [7, 11] to estimate the hysteretic energy demand value of the structure. The proportion of hysteretic energy of various components in different structures is different, resulting in different damage degrees of each component. Then, the distribution law of hysteretic energy among different components of each structure needs to be analyzed.

From Fig. 4, it can be seen that the distribution law of hysteretic energy among the components of the CBSFs is similar under different seismic waves, and the proportion for the 10-story CBSF is between 80.3 and 91.6%, with an average value of 85.8%. And the proportion for the 15-story CBSF is between 34.7 and 64.0%, with an average value of 47.2%. The ratio tends to decrease with the increase of structure layers. All components appear plastic deformation, resulting in different degrees of damage. Compared with the 10-story and 15-story CBSFs designed based on the energy design method in the Literature [13], the CBSFs designed in this paper according to the current codes are severely damaged under rare earthquakes, which is inconvenient to control. Therefore, it is necessary to seek more reasonable design method.

5.3 Interlayer Distribution Model of Hysteretic Energy

The distribution of hysteretic energy along the height of the structures can reveal whether there is obvious energy concentration, which provides a reference for the comprehensive evaluation of the seismic performance of the structure (Fig. 5).

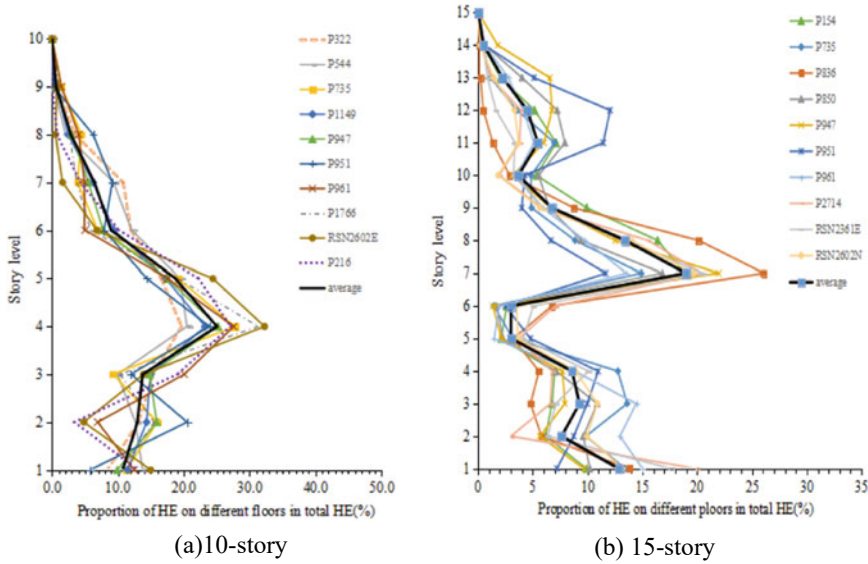


Fig. 5 Proportion of interlayer HE of CBSFs in total HE under different seismic waves

The hysteretic energy dissipation values of the same example under different seismic waves are different, and the maximum relationship is three times. The distribution patterns of hysteretic energy among the same support structure with different layers are similar but not identical. As the number of structural layers increases from 10 to 15, the proportion of hysteretic energy consumption in the upper floors increases, which is mainly due to the influence of high-order mode. It also indicates that the equivalent velocity spectrum of hysteretic energy and the mode superposition method of multi-degree of freedom structure can consider the energy carried by high-order mode. The hysteretic energy dissipation of the concentrically braced steel frames is of small top and big bottom along the height of the structure, and the energy dissipation of the floors below the height of $H/3$ (H is the height of the structure) is larger. The hysteretic energy dissipation of different examples is not a single linear distribution along the height direction of the structure, and the hysteretic energy dissipation at the variable section is accompanied by a sudden change.

6 Conclusion

The reliability of the hysteretic energy spectrum and mode shape superposition methods in the existing literatures to estimate the energy demand of braced steel frames is evaluated in this paper. Firstly, the member sections of the CBSFs are determined for elastic design method according to the current codes, and the hysteretic energy demand value of examples is obtained by using the relevant formula. Then, 10

seismic waves are selected based on certain principles, and the cumulative hysteretic energy dissipation under different seismic waves through time history analysis. At the same time, the distribution of hysteretic energy along the height of the structure and the distribution law of each member are studied. The results show that the cumulative hysteretic energy demand obtained by time history analysis is basically consistent with the estimated value. The hysteretic energy dissipation of the concentrically braced steel frames is of small top and big bottom along the height of the structure, and the energy dissipation of the floors below the height of $H/3$ is larger.

Acknowledgements This research is funded by the 2020 Excellent and Top-notch University Talent Cultivation Program (No. gxyq2020068) and the 2021 Scientific Research Program for Talents in Hefei University (No. 21-22RC39)

References

1. Berg GV, Thomaidis SS (1960) Energy consumption by structures in strong-motion earthquakes. In: Proceedings of the second world conference on earthquake engineering, vol 2, pp 681–697
2. Chopra AK, Goel RK (2002) A modal pushover analysis procedure for estimating seismic demands for buildings. *Earthquake Eng Struct Dyn* 31(3):561–582
3. Chopra AK, Goel RK (2004) A modal pushover analysis procedure to estimate seismic demands for unsymmetric-plan buildings. *Earthquake Eng Struct Dyn* 33(8):903–927
4. Ghosh S, Collins KR (2006) Merging energy-based design criteria and reliability-based methods: exploring a new concept. *Earthquake Eng Struct Dyn* 35(13):1677–1698
5. Housner GW (1956) Limit design of structures to resist earthquakes. In: Proceedings of the 1st world conference earthquake engineering, Berkeley
6. Liu ZF, Zhao P, Chen K (2017) Cyclic pushover analysis method based on the seismic energy dissipation course characteristics. *World Earthquake Eng* 33(2):39–45
7. Ma CL, Gu Q, Sun GH (2019) Mathematical expression of design hysteretic energy spectra based on Chinese soil type. *Math Probl Eng* 11:1–10. <https://doi.org/10.1155/2019/3483516>
8. Ma HW, Yang JY, Pan CQ (2022) Energy-based seismic design method for energy-dissipation steel frame. *Build Struct* 52(5):55–62
9. McKeivitt WE, Anderson DL, Cherry S (1980) Hysteretic energy spectra in seismic design. In: Proceedings of the 2nd world conference on earthquake engineering, vol 7, pp 487–494
10. Prasanth T, Ghosh S, Collins KR (2008) Estimation of hysteretic energy demand using concepts of modal pushover analysis. *Earthquake Eng Struct Dyn* 37:975–990
11. Sun GH, Gu Q, He RQ, Fang YZ (2012) Evaluation of seismic energy of steel frames based on energy spectrums. *China Civ Eng J* 45(5):41–48
12. Uang CM, Bertero VV (1990) Evaluation of seismic energy in structures. *Earthquake Eng Struct Dyn* 19(1):77–90
13. Zhang HD (2016) Energy-based seismic design method of chevron concentrically braced steel frame under far-field earthquake. Master Degree Thesis of Suzhou University of Science and Technology

Open Access This chapter is licensed under the terms of the Creative Commons Attribution 4.0 International License (<http://creativecommons.org/licenses/by/4.0/>), which permits use, sharing, adaptation, distribution and reproduction in any medium or format, as long as you give appropriate credit to the original author(s) and the source, provide a link to the Creative Commons license and indicate if changes were made.

The images or other third party material in this chapter are included in the chapter's Creative Commons license, unless indicated otherwise in a credit line to the material. If material is not included in the chapter's Creative Commons license and your intended use is not permitted by statutory regulation or exceeds the permitted use, you will need to obtain permission directly from the copyright holder.



Analysis of Key Points of Steel Structure Construction Technology in Film Engineering Projects



M. Alashoub Turki Sulaiman and Chunyu Liang

Abstract According to the soil conditions of high-rise buildings and foundation pits of steel structure projects, the technical analysis of steel structure projects is carried out. Because the project is located at an earthquake-resistant fortification intensity of 8 degrees, and the design basic seismic acceleration value is 0.30 g, the high-rise building adopts steel structure structure to ensure the performance of seismic performance, safety level, bearing capacity and other aspects. This paper introduces the steel structure construction technology in detail from the five links of steel structure deepening, construction sequence, component manufacturing process, fire prevention and anti-corrosion, and component hoisting, and analyzes the construction process and the key points of quality control in construction. Practice shows that the application effect of this technology is good and the economy is reasonable.

Keyword Steel structure; High-rise building; Quality control

1 Project Overview

This project has three workshop buildings (1#, 2#, 3#) and one supporting comprehensive service building (4#). Among them, Buildings 1# and 2# are Class E high-rise workshops with 12 floors above ground and 2 floors underground, their building height is 95.60 m; Building 3# is a Class E high-rise factory building, with 8 floors above ground and 2 floors underground, whose height is 65.60 m. The standard floor height of the building is 7.8 m, the land area is 30997.27m², the total construction area is 149041.11m² (see Fig. 1), and the building's fire rating is Class 1.

M. Alashoub Turki Sulaiman (✉) · C. Liang
Jilin University, ChangChun, China
e-mail: 2363760116@qq.com

© The Author(s) 2023
Y. Yang (ed.), *Advances in Frontier Research on Engineering Structures*, Lecture Notes in Civil Engineering 286, https://doi.org/10.1007/978-981-19-8657-4_17

185



Fig. 1 Caption of a typical figure

1.1 Geological Conditions of Foundation Pit

The survey report found that, within the drilling depth range, based on the field characteristics of the stratum and the results of the indoor geotechnical test, the strata of the proposed site from top to bottom are plain fill, Quaternary Holocene flushing, The alluvial layer, Quaternary residual layer and Yan shanian granite.

1.2 Ground Motion Parameters of the Project

According to the relevant provisions of Appendix A.0.19 of “Code for Seismic Design of Buildings” (GB50011-2010) (2016 Edition) and “China Earthquake Parameter Zoning Map” (GB18306-2015), the seismic fortification intensity of this site is 8 degrees, and The acceleration value of the basic seismic design is 0.30 g, and the design earthquake is grouped into the first group.

1.3 Site Soil Type

According to the name and properties of the rock and soil in the site, combined with local experience, the estimated shear wave velocity experience value of each layer is shown in Table 1:

Table 1 Estimated value of shear wave velocity for each soil layer

Strata	Shear wave velocity empirical value/m.s ⁻¹	Type of soil
Plain fill	135	Soft soil
Silty clay	210	Medium soft soil
Sandy clay soil	260	Medium hard soil
Strongly weathered granite	550	Soft rock
Medium weathered granite	850	Hard rock

According to the empirical values in the table, three borehole numbers are selected for shear wave velocity estimation, and the equivalent shear wave velocity estimation results are 179.4, 210.7 and 218.4 m/s, ranging from 150 to 250 m/s. According to the nearby data and the survey results, the thickness of the covering layer is between 3 and 50 m in this site, and the construction site category is Class II.

2 Technical Analysis of Steel Structure

2.1 Basic Idea

Compared with traditional buildings, steel structure houses can better meet the requirements of flexible separation of large bays in buildings, and can improve the area utilization rate by reducing the cross-sectional area of columns and using lightweight wall panels, the use of steel structure systems in residential buildings can fully has good ductility, strong plastic deformation ability, and excellent seismic and wind resistance, especially in the event of earthquakes and typhoons, which can avoid the collapse of buildings.

In view of the characteristics of high seismic performance and flexible space of this project, the use of steel structure frame is particularly prominent. According to the actual construction conditions on site, the steel structure construction technology is planned to be selected.

2.2 Basic Principles

- (1) Reasonable selection of materials, structural plans and structural measures to meet the strength, stability and stiffness requirements of the structure during transportation, installation and use.

- (2) Corresponding fire protection measures should be taken according to the fire resistance level. The heat resistance of the steel structure is good, but the fire resistance performance is poor. Steel is heat-resistant but not high-temperature resistant. As the temperature increases, the strength decreases, and structural safety problems are prone to occur.
- (3) Before hoisting, the strength and stability of the steel structure should be checked, and the hoisting point should be defined to prevent the deformation of the component due to uneven stress.
- (4) Welding is the most important step in construction, which is very important for every construction worker. If the welding is not in place, it is difficult to ensure the safety of the project, so the welding quality is particularly critical.

3 Analysis of Key Points of Installation and Construction Technology

3.1 The Deepening of the Steel Component Assembly Plan and the Key Points of Assembly Construction

The deepening assembly scheme of steel columns and steel beams

The floor height of this project is high, and the total amount of steel structure is 20,000 tons. The key work of the steel structure deepening joint design is to solve the relationship between the steel structure and the concrete structure, and the operability of complex joints in the process of factory processing and on-site welding. The depth of the detailed design node diagram can not only meet the requirements of steel procurement, but also meet the requirements of processing drawing design, and do a good job in the preliminary design work such as holes for civil reinforcement, holes for mechanical and electrical equipment, and curtain wall connectors [1, 2].

The deepening assembly scheme of steel columns and steel beams

- (1) The structural engineering is absolutely safe and reliable;
- (2) Grasp the intention and structural characteristics of the original structural design;
- (3) Coordinate with other professional designs (outdoor curtain wall engineering, interior decoration engineering, mechanical and electrical engineering, etc.);
- (4) The steel structure design should be deepened and optimized scientifically and rationally to fully reflect its economic rationality;
- (5) The design drawings must meet the requirements of factory processing and on-site installation;
- (6) Strictly follow the design procedures and cooperate closely with the owner and the design institute to ensure the smooth progress of the design work.

Key points of steel structure deepening

- (1) Improve the structure of the components and determine the size of the gusset plate;
- (2) Calculation of welded joints or bolted joints to determine the length of the welds of certain components and the dimensions of the connecting plates;
- (3) Determine the form of connecting nodes in the component;
- (4) Considering the transportation and installation capabilities of the transportation department and the installation department, determine the segments of the components.

3.2 Optimizing the Construction Sequence

The steel structure construction mostly adopts the construction technology of segmented ground assembly and segmented hoisting inside and outside the site. In view of the characteristics of this project, such as a high degree of multi-professional interleaving and collaboration, and a small site, based on comprehensive consideration of the site conditions, The general construction sequence is the first underground and then the above ground; structure first, then enclosure; first steel structure and then civil construction.

3.3 Main Components Manufacturing Process and Quality Control Points

The sequence of steel structure welding is pre-welding inspection → preheating and rust removal → installation of welding pad and arc strike plate → welding → inspection. The steel structure welding quality of this project is high, and all of them are required to be full penetration welds. The main welding types are on-site butt welding, assembly welding and high-altitude welding. According to the characteristics of long structural welds and thick plate thickness, CO₂ gas protection semi-automatic welding is adopted on site. Welding process combined with solid wire weld fill. In order to ensure the welding quality of the project, in strict accordance with the relevant provisions of GB 50661-2011 “Steel Structure Welding Specification” and GB 50205-2020 “Steel Structure Engineering Construction Quality Acceptance Specification” [3], the welding process plan and the inspection and evaluation are formulated.

Welding process flow

For projects with large steel structures and complex joints, strict welding procedures should be formulated to ensure the quality of on-site welding. Combined with the welding process on the construction site, the welding process formulated in this project is shown in Fig. 2.

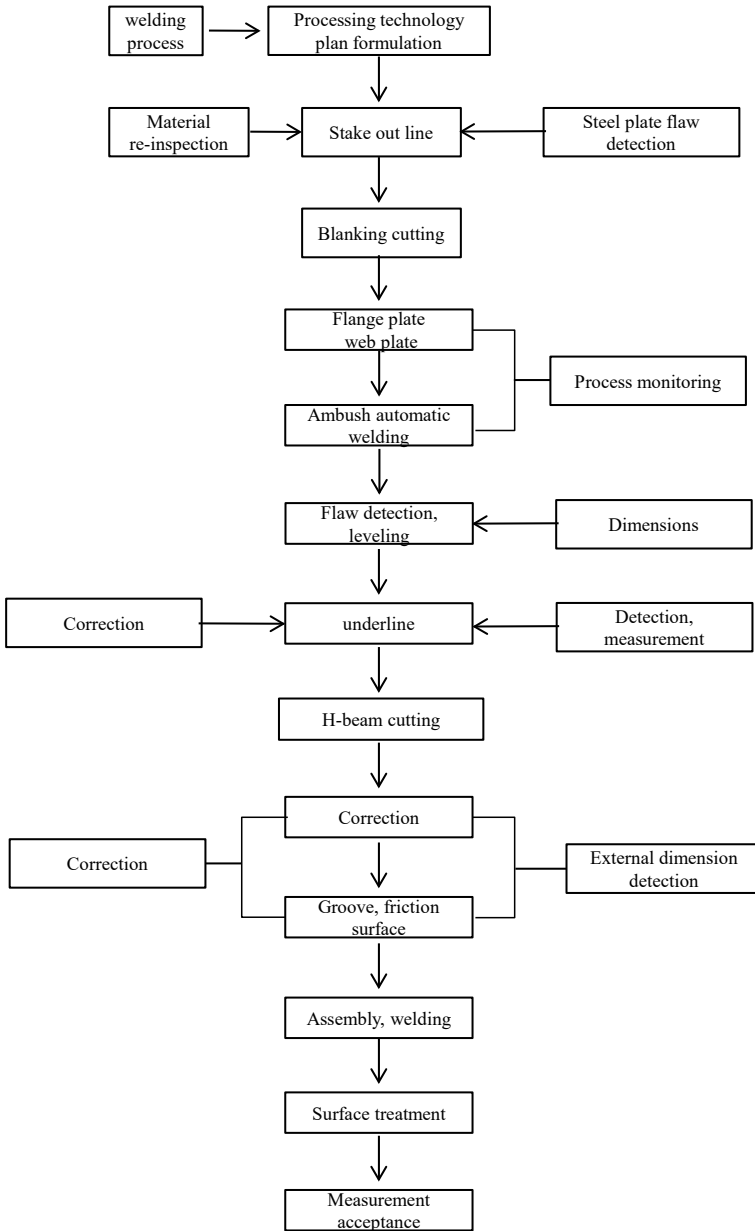


Fig. 2 The welding process formulated

Preparation before welding

Before welding, the welding process document should be prepared according to the welding process evaluation results. The assembly of the welding parts, the surface cleaning quality and the position deviation of the components should be checked. The welding procedure document mainly includes the following contents [4]:

- (1) Determine the welding method of different components;
- (2) Clarify the information such as the grade and specification of the welding base metal used in the project;
- (3) Determine the form of welded joints and grooves;
- (4) Give the welding tolerance requirements;
- (5) Clarify the relevant technical requirements of each process (fixtures, backing plates, current, voltage, etc.) and process parameters;
- (6) Determine the quality inspection standards.

Key points of welding quality inspection

All outer frame beam and column connections and component splicing welds of this project are fully penetrated welds, which is primary welds. The main inspection points are as follows:

- (1) Check the weld surface for defects such as cracks, slag inclusions, weld penetrations, arc craters and pores.
- (2) According to the relevant national standards, check whether there are defects in welds, joints, etc. that do not meet the requirements of defect classification.
- (3) After completing the visual inspection of the weld, the flaw detection should be carried out. For different weld types and thicknesses, different methods such as ultrasonic flaw detection, magnetic particle flaw detection or color flaw detection are used.
- (4) When local flaw detection finds that there are permissible defects in the weld, the flaw detection length shall be increased by not less than 10% of the length of the weld at its extension. If there are still permissible flaws, 100% flaw detection shall be carried out.

Measurement control points

- (1) The positioning measurement of steel structure construction should first establish a reliable plane control network and elevation control network.
- (2) For the positioning of inclined steel columns, a precise three-dimensional control network must be established, and the preset accuracy is calculated according to the requirements of the steel structure measurement progress.
- (3) When measuring the ground assembly process, control points should be set up in each assembly site first, and a local plane and elevation control network should be established to provide a benchmark for accurate positioning of the tire frame and subsequent position re-measurement.
- (4) When performing error detection and correction on the relative position of each component in the structure [5].

3.4 Anti-corrosion and Fire-Proof Coating Control

Main points of anti-corrosion coating technology

- (1) All steel components shall be subjected to surface sandblasting (shot) derusting treatment before painting, and the derusting grade shall be Sa2.5.
- (2) Airless spraying is required for the surface anticorrosion of all components.
- (3) The construction environment temperature is 5 ~ 38°C, and the relative humidity is 30 ~ 85%.
- (4) There are generally oxide scale and rust on the surface of ferrous metals, which must be removed before painting, otherwise economic losses will be caused.
- (5) When the shot blasting and rust removal is completed, remove the dust and other debris on the surface of the metal coating.
- (6) Spray primer. After shot blasting and rust removal, the primer must be sprayed within 6 h.
- (7) Paste or oil-based pen to mark the component number on the painted surface or bare metal surface, and mark the installation direction of the component, which is convenient for on-site identification and installation.

Technical points of fire protection coating

- (1) Steel columns, steel beams, steel supports, steel stairs, etc. should be protected by fire-resistant paint, and the type of fire-resistant paint should meet the requirements of architectural drawings.
- (2) Fire retardant paint and steel structure anti-rust paint must be compatible and adaptable.
- (3) After the construction of the fire-resistant and anti-corrosion coating is completed, the data such as the thickness and adhesion of the paint film should be tested.
- (4) The fire retardant coating is applied by spraying to ensure that it does not fall off and is not hollow during normal use.
- (5) The fire retardant coating should be able to maintain good durability under the action of wind speed and wind pressure generated by elevator operation in the elevator shaft.

3.5 Steel Structure Hoisting Scheme

Technical points of fire protection coating

The hoisting of components adopts the comprehensive construction technology of high-altitude hoisting of steel structure. The frame column adopts the vertical section hoisting technology; the truss adopts the factory section processing and aerial docking installation technology. When the floor structure is installed, the frame bay is used as a unit, and the installation is started in the order of the steel column first, then

Table 2 The statistics of the steel components of each building in this project

Standard floor components		Building 1#	Building 2#	Building 3#
Outer framesteel column	Qty/piece	35	43	32
	Weight/ton	400	330	200
Core tube steel column	Qty/piece	30	25	24
	Weight/ton	20	20	18
Steel beams	Qty/piece	187	261	258

the main beam and the secondary beam. After forming a stable frame, it gradually spreads to all sides. After the hoisting, the measurement and correction, the initial and final tightening of the high-strength bolts, and the welding should be carried out in time.

Technical points of fire protection coating

The film factory project is a pure steel structure. The statistics of the steel components of each building in this project are as follows (Table 2):

According to the component characteristics of the project’s steel components, the largest component section, and the largest single-section weight of the steel column, the TC8039 tower crane (55-m arm length) is used, and the hoisting performance is as follows (Table 3):

Selection of sling wire rope and snap ring

In this project, the high-strength carbon steel wire rope commonly used in the hoisting project is selected, and the 6 × 37 wire rope is selected. If the force of the steel wire is uneven, the breaking force of the whole steel wire rope should be calculated as follows:

$$SP = \lambda \times \sum S_i \tag{1}$$

Table 3 The hoisting performance

Amplitude /m		3.5–18.85	20	23	25	28	30	33	
Lifting capacity/t	Double rate	12.5							
	Quadruple	25	23.32	19.80	17.94	15.67	14.42	12.83	
Amplitude/m		35	38	40	43	45	48	50	53
Lifting capacity/t	Double rate	12.5	11.87	11.19	10.29	9.76	9.05	8.63	8.05
	Quadruple	11.93	10.76	10.08	9.18	8.65	7.94	7.52	6.94
Amplitude /m		55							
Lifting capacity/t	Double rate	7.70							
	Quadruple	6.59							

In the formula: SP —the breaking force of the wire rope, kN;

$\sum Si$ —the sum of the breaking force of the steel wire provided in the specification table of the steel wire rope, kN;

λ —Uneven reduction coefficient of steel wire twisting, for 6×37 rope, $\Psi = 0.82$.

The heaviest steel column in this project is about 12t, and four steel wire ropes are used for hoisting. Considering the most unfavorable situation, 2 steel wire ropes will bear the full weight. Considering the minimum tension calculation: $SP = \Psi \sum Si = 156 \times 0.82 \times 0.102 = 13.05 > 12$, which meets the requirements.

According to the relevant regulations of “Forged Shackles for General Lifting-D Shackles and Bow Shackles”, 2 T, 3.25 T, 6.5 T, 8.5 T, 12 T and other shackles are mainly selected for this project, among which shackles below 3.25 T are used for hoisting lighter components such as steel beams, and shackles of 6.5 T above are used for hoisting heavier components such as outer frame columns, which meet the requirements.

4 Conclusion

Combining with the characteristics of the project, this paper makes a comprehensive study on the construction sequence, component assembly, hoisting, welding, welding inspection and control of anti-corrosion and fire-proof coating in the steel structure construction process for the project using reinforced concrete + steel structure frame structure system. The actual construction period of the project is 45d ahead of the planned construction period, and the economic benefits are obvious, which provides a reference for similar projects of high-rise buildings.

References

1. Yanlin G, Xiaoqiang C (2004) Several technical problems and discussions in the construction of large-span complex steel structures. *J Ind Archit* 12:1–5, 22
2. Xiaoyue L, Shuangquan X, Zhengli C et al. (2016) Key construction technology of Hangzhou Olympic sports center main stadium project. *J Constr Technol* 9:41–45
3. Ministry of Housing and Urban-Rural Development of the People’s Republic of China (2020) GB 50205-2020 Code for acceptance of construction quality of steel structure engineering. China Construction Industry Press, Beijing
4. Yanhui H, Chengfu T, Lili Z (2016) Welding process and properties of building steel structures. *J Foundry Technol* 2:339–342
5. Jianlong S, Tao J, Dezhi Z et al (2017) Three-dimensional space measurement and positioning monitoring technology of special-shaped steel structure of Shanghai Shimao Shengkeng Hotel. *J Build Struct* S1:1170–1175

Open Access This chapter is licensed under the terms of the Creative Commons Attribution 4.0 International License (<http://creativecommons.org/licenses/by/4.0/>), which permits use, sharing, adaptation, distribution and reproduction in any medium or format, as long as you give appropriate credit to the original author(s) and the source, provide a link to the Creative Commons license and indicate if changes were made.

The images or other third party material in this chapter are included in the chapter's Creative Commons license, unless indicated otherwise in a credit line to the material. If material is not included in the chapter's Creative Commons license and your intended use is not permitted by statutory regulation or exceeds the permitted use, you will need to obtain permission directly from the copyright holder.



Analysis of the Influence of Foundation Pit Excavation on the Surrounding Surface Settlement and Retaining Structure



LingChao Shou, HeQuan Zhao, XiaoBo Sun, Jin Pang, Ting Bao,
and LiFeng Wang

Abstract This paper analyzes the foundation pit of Gen Shan East Road through tunnels under the river. The results show: When digging to the bottom, the maximum horizontal displacement of the wall is located at 2 ~ 4 m above the bottom of the pit, and the maximum value is 0.57‰ ~ 0.64‰H. The surface subsidence is mainly of groove type. The maximum surface settlement is 0.107%H. The mean value of the maximum surface settlement is about 0.91 times the maximum horizontal displacement of the wall, and the maximum surface settlement is between 0.58 and 1.91 times the maximum horizontal displacement of the wall.

Keywords Foundation pit · Ground surface settlement · Horizontal displacement

1 Introduction

The soil unloading of foundation pit causes deformation of surrounding strata, which causes formation loss behind the retaining wall in a certain range and causes ground settlement. Large ground settlement will have a great impact on the surrounding structures and underground pipelines of the foundation pit, and even cause damage [4, 5]. Due to the great difference of stratum conditions in different regions, foundation pit engineering has strong regional characteristics [2]. Zhu et al. [6] collected the measured data of the surface subsidence outside the pit of 38 subway stations and studied the surface subsidence deformation law outside the pit of Changzhou subway

L. Shou (✉) · J. Pang · T. Bao · L. Wang
Chinese Zhejiang Mingsui Technology Co. Ltd., Hangzhou, Zhejiang Province, China
e-mail: slczust@163.com

J. Pang
e-mail: pangj00@163.com

L. Wang
e-mail: wanglfzust@163.com

H. Zhao · X. Sun
Publishers Chinese China Railway 14th Bureau Group Mege Shield Construction Engineering Co.
Ltd., Jinan, China

stations from the perspective of statistical analysis. Guo [3] studied the influence of foundation pit excavation process on the deep horizontal displacement of retaining structure and the settlement of soil outside the pit. Cheng et al. [1] took a 30.2 m deep foundation pit project in Hangzhou as the research object, and analyzed the development and evolution rules of ground wall heave and flexural deformation, ground wall wall stress, column heave, supporting axial force, earth pressure, and surface settlement in the whole process of excavation of a 30.2 m deep foundation pit.

2 Project Summary

Take Gen Shan East Road crossing tunnel project as an example, The project located in Hangzhou city, includes a cross-river tunnel, a working well, and an open pit. This paper analyzes the influence of the excavation on the surrounding environment and the enclosure structure itself. The depth of the foundation pit is 15 ~ 21 m. Figure 1 shows the monitoring plan of the foundation pit, Fig. 2 shows the profile of the enclosure structure, and Table 1 shows the soil layer distribution.

3 Analysis of Deformation Law of Underground Disphragm Wall

The deformation shape of the retaining structure of foundation pit is closely related to the form, stiffness and construction method of the retaining structure. In general, the lateral displacement of the enclosure structure is obtained by burying the inclined pipe in the reinforcement cage and collecting the data along with the foundation pit excavation. The deformation value at the end of excavation is counted to reflect the maximum horizontal displacement distribution of the foundation pit enclosure structure.

Figure 3a–f show the variation of wall horizontal displacement with the excavation condition. The figure shows: With the increase of excavation depth, the lateral deformation of wall gradually increases, and the depth of maximum deformation gradually moves down. The deformation shape of the wall changes from the initial top to the offset in the foundation pit into a “bulging” distribution with large middle and small ends. In the early stage of excavation, the maximum deformation value of the wall mainly occurs in the shallow position of the excavation depth, and the deformation amount is small, which is mainly because the excavation depth of the foundation pit is shallow, and the difference between the earth pressure inside and outside the pit is small. During the excavation to 5.8 m, the deformation of the foundation pit wall is large. The main reason is that the soil in the pit decreases and the difference between the earth pressure inside and outside the pit is formed. However,

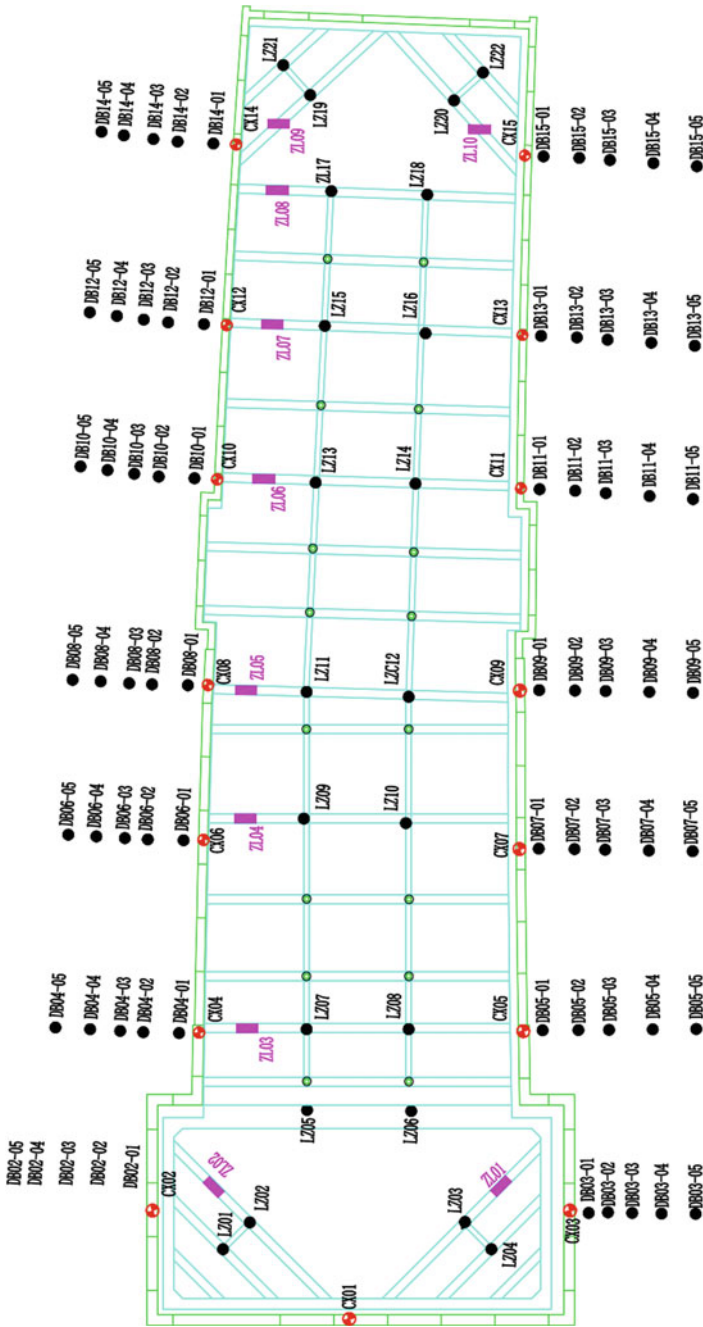


Fig. 1 The monitoring plan of the foundation pit

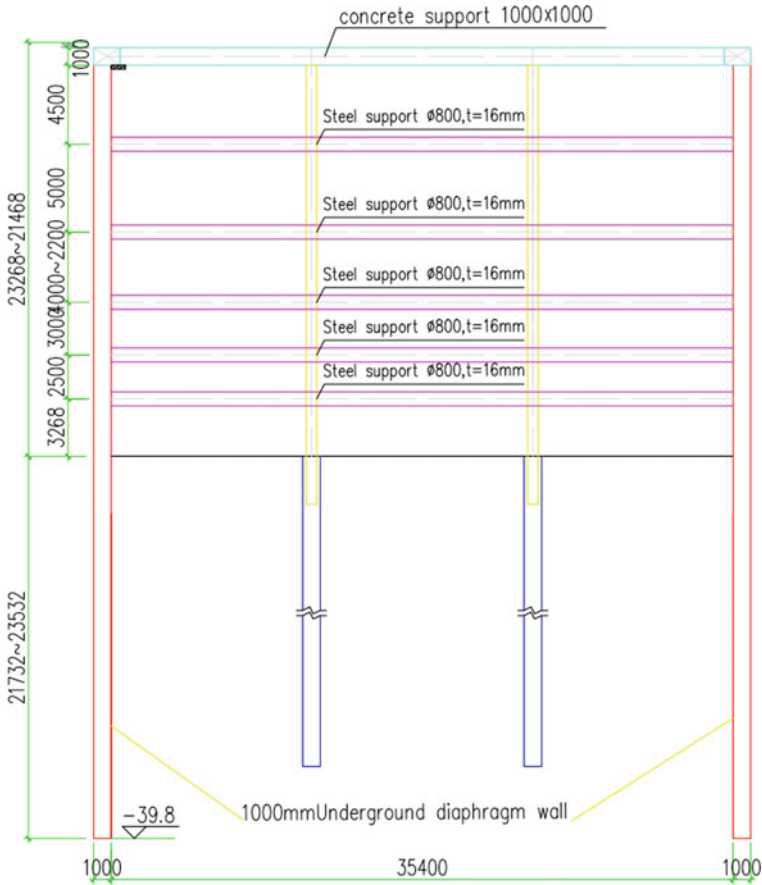


Fig. 2 Section view of the envelope

the wall deformation mainly occurred during the excavation period from 5.8 to 12 m, mainly because of the large difference of earth pressure between inside and outside the pit. The monitoring data of the six typical monitoring sites are summarized as shown in Table 2. The maximum value of horizontal displacement at the end of excavation is 2 ~ 4 m above the bottom of the pit, and the maximum value is 9 ~ 11.2 mm (0.57% ~ 0.64%*H*).

Figure 4 shows the relationship between the maximum horizontal displacement of the wall and the excavation depth obtained from the measurement points of the wall of Gendong Road working well. It can be seen from the figure that the horizontal displacement of the wall increases with the increase of the excavation depth, with a roughly linear distribution. The upper limit of the maximum horizontal displacement is 0.101%*H*, the lower limit is 0.042%*H*, and the average value is 0.069%*H*.

Figure 5 shows the relationship between the relative maximum horizontal displacement and the relative excavation depth. The relative maximum horizontal

Table 1 Soil layer distribution table

Serial number	Geotechnical name	Natural gravity	Characteristic value of foundation bearing capacity/kPa	Thickness/m	Cohesive/kPa	Internal friction angle/°
1	Miscellaneous fill	18	80	0.2 ~ 4.1	10	12
2	Sandy silt	19.7	110	2.9 ~ 18.9	6	26
3	Silty clay	17.6	90	22.9 ~ 41.8	12	15
4	clay	19.7	220	31.3 ~ 40.2	40	16
5	Conglomeratic clay	20.6	240	37.4 ~ 73.8	30	22
6	Fully weathered argillaceous siltstone	20.4	200	39.0 ~ 74.6	30	16

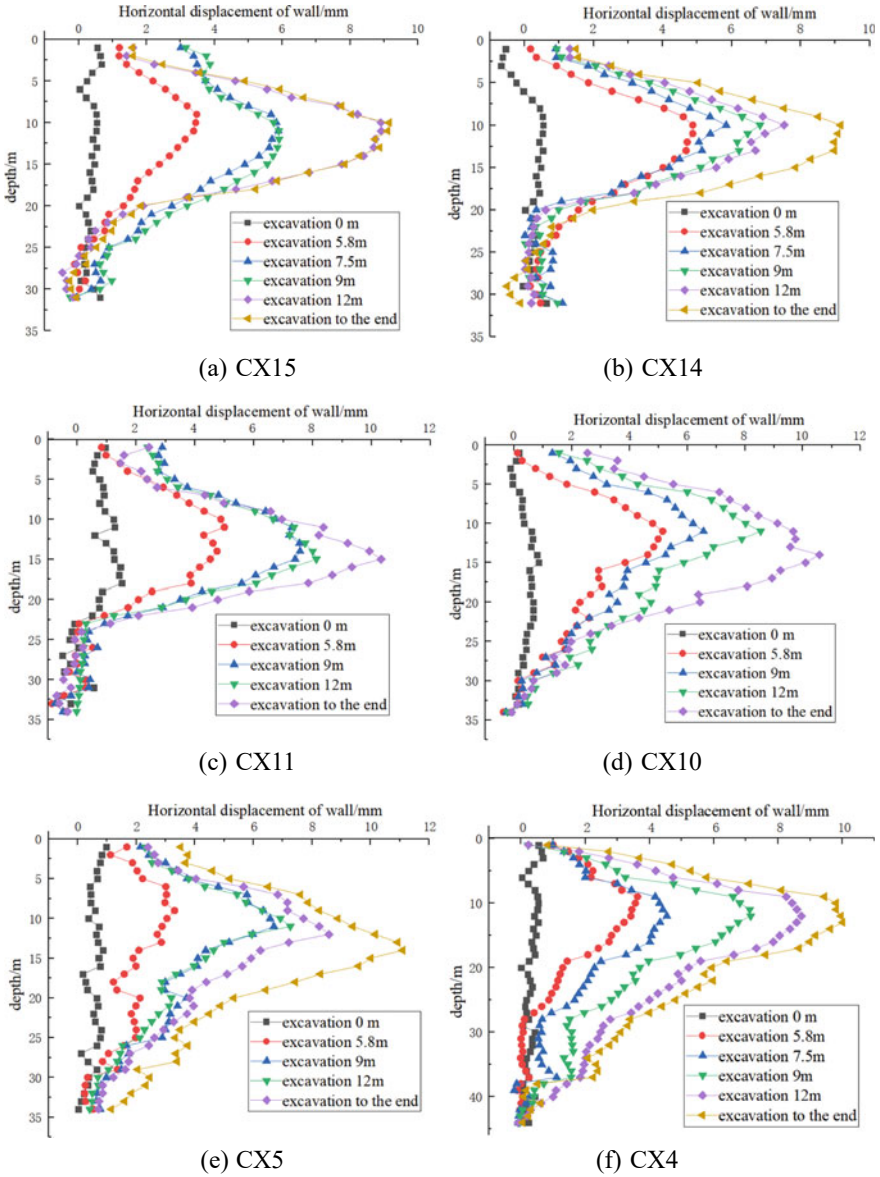


Fig. 3 Variation of wall horizontal displacement with excavation conditions

Table 2 Summary of monitoring sites

Serial number	Monitoring stations	Location	Max/mm	Relationship with excavation depth (% α H)
1	CX4	15 m above the surface (3 m above the bottom of the pit)	11	0.61
2	CX5	14.5 m above the surface (3.5 m above the bottom of the pit)	11.2	0.62
3	CX10	15.5 m above the surface (1.5 m above the bottom of the pit)	10.8	0.64
4	CX11	15 m above the surface (2 m above the bottom of the pit)	10.3	0.61
5	CX14	12 m above the surface (4 m above the bottom of the pit)	9.12	0.57
6	CX15	12 m above the surface (4 m above the bottom of the pit)	9.2	0.57

displacement has a linear relationship with the excavation depth, mainly because the excavation soil layer is soft soil layer such as silt and clay layer, and the distribution of the soil layer is relatively uniform.

Figure 6 shows the relationship between the maximum horizontal displacement depth and the excavation depth of the foundation pit. The figure shows: most scatter points are within a certain range, with the upper limit of 1.6 and lower limit of 0.67, and the average value is about 0.87H. This is close to Xu Zhonghua's conclusion that the maximum horizontal displacement depth of foundation pit retaining structure in Shanghai soft soil area is about 0.89H. However, there is a little error with the maximum horizontal displacement depth rule proposed by Ou. Among them, the rise of the maximum horizontal displacement depth is due to the better soil quality of the lower strata, which makes the overall stiffness of the enclosure structure increase. The overall stiffness of the project is larger than that of the soft soil area, and the excavation depth of the foundation pit with the maximum horizontal displacement depth of about 0.69 times is reasonable.

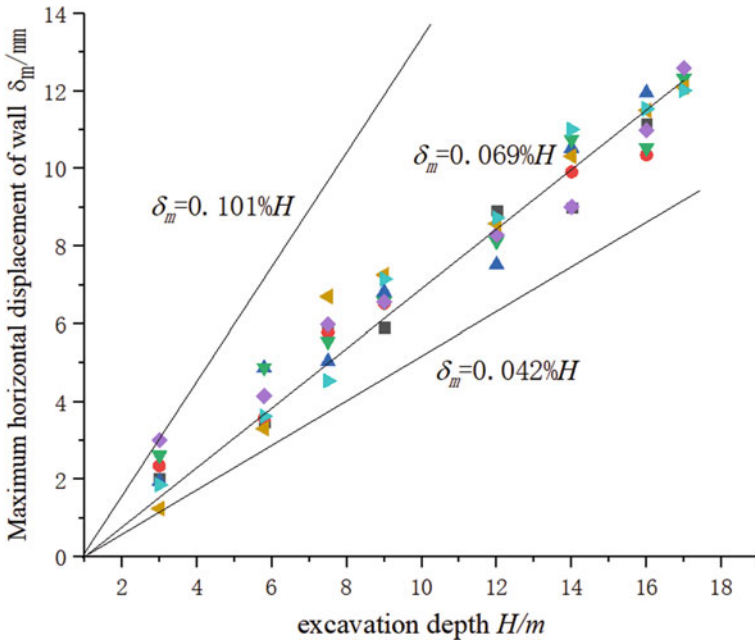


Fig. 4 Relationship between maximum horizontal displacement of wall and excavation depth

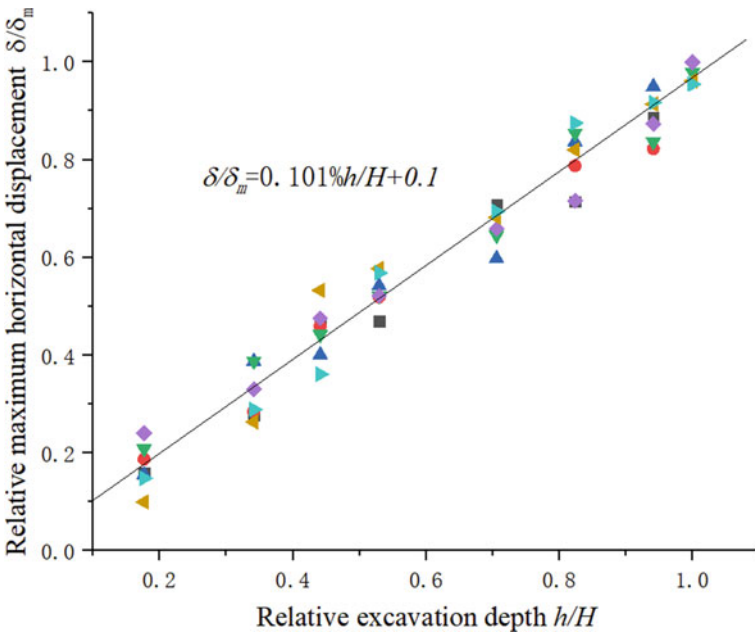


Fig. 5 Relationship between relative maximum horizontal displacement and relative excavation depth

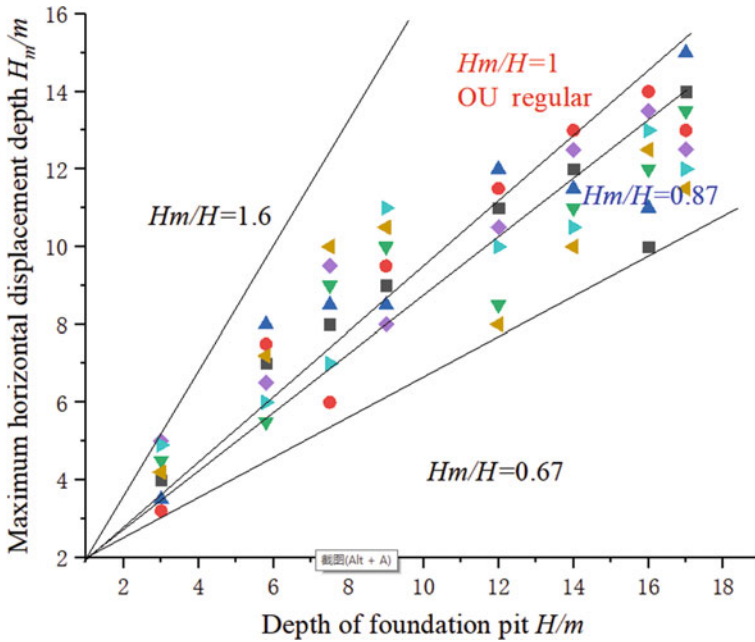


Fig. 6 Relationship between maximum horizontal displacement depth and excavation depth of foundation pit

4 Surface Settlement Analysis

The excavation depth of the foundation pit is from 16 to 21.5 m, showing a downward slope. Fifteen surface settlement monitoring profiles are laid on both sides of the foundation pit, and the monitoring points vary from 5 to 7 according to the actual situation. Starting from the edge of the foundation pit, the spacing is 2 m, 4 m, 6 m, 8 m, 8 m, 10 m respectively. The spacing can be adjusted appropriately according to the actual situation on site.

Figure 7 shows the map of surface subsidence with working conditions for typical profiles of monitoring sites. The figure shows: at the beginning of excavation, the surface settlement is small. With the progress of excavation, the surface settlement is constantly increasing, and the surface settlement is stable and does not change after the demolition and support is completed. The maximum settlement value is basically located at 12.5 m outside the pit, and the maximum value at the section is 17 mm, 0.08%H (H is the excavation depth of 21.5 m). The surface settlement value of 50 m outside the foundation pit is within 2 mm. It shows that the influence of foundation pit excavation on this site is small and can be ignored. The surface subsidence is mainly of groove type.

Figure 8 shows the distribution of ground settlement behind the wall. The settlement range of area I, II, III of surface subsidence behind the wall proposed by Peck

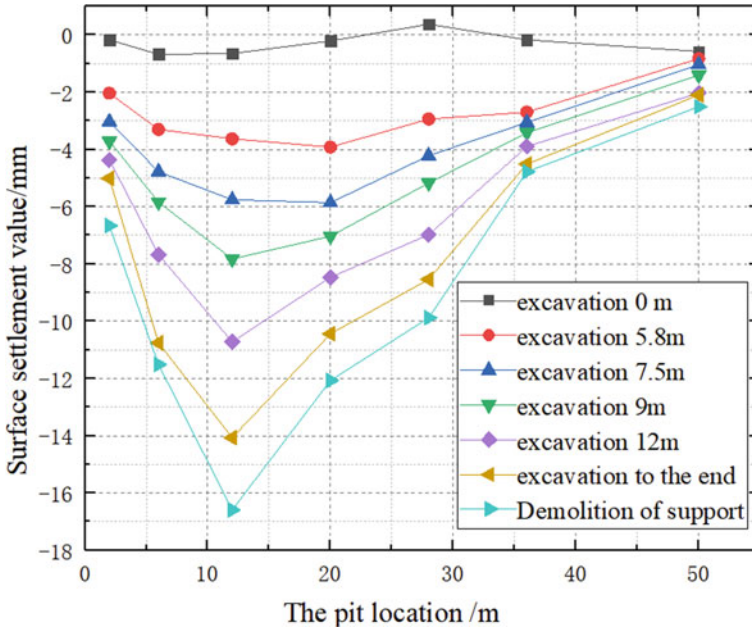


Fig. 7 Surface subsidence curve of typical section

is shown in the dashed area. According to the results obtained in this example, the settlement influence range in this area is $2H$, and the monitoring underestimated the settlement influence range in this area. The settlement range of known settlement points is all distributed in area I, which is in good agreement with the soil conditions in this area. Figure 9 shows the envelope diagram of surface settlement. Most of the measurement points are distributed within the predicted range, but a small number of measurement points are outside it, which may be caused by external overload and nearby construction.

Figure 10 shows the relationship between the maximum surface settlement behind the wall and the excavation depth. With the increase of excavation depth, the maximum surface settlement also increases gradually. The surface settlement distribution outside the foundation pit can be basically divided into two parts. The first part is before the excavation of the foundation pit 12 m, when the mean value of the maximum surface settlement is about $0.075\%h$. The second part is between 12 m of excavation and the end of excavation, when the mean value of the maximum surface settlement is about $0.112\%h$. However, the upper limit of the maximum surface subsidence is $0.107\%H$.

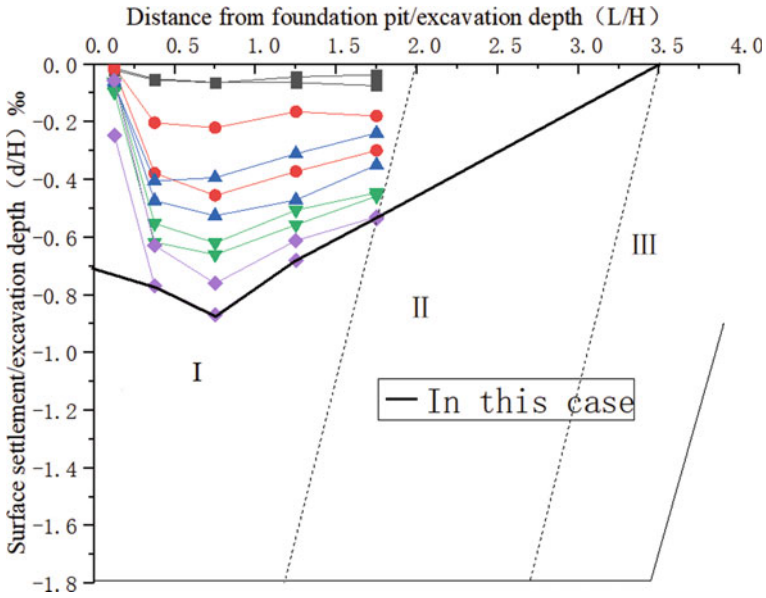


Fig. 8 Dimensionless diagram of surface settlement curve behind foundation pit wall

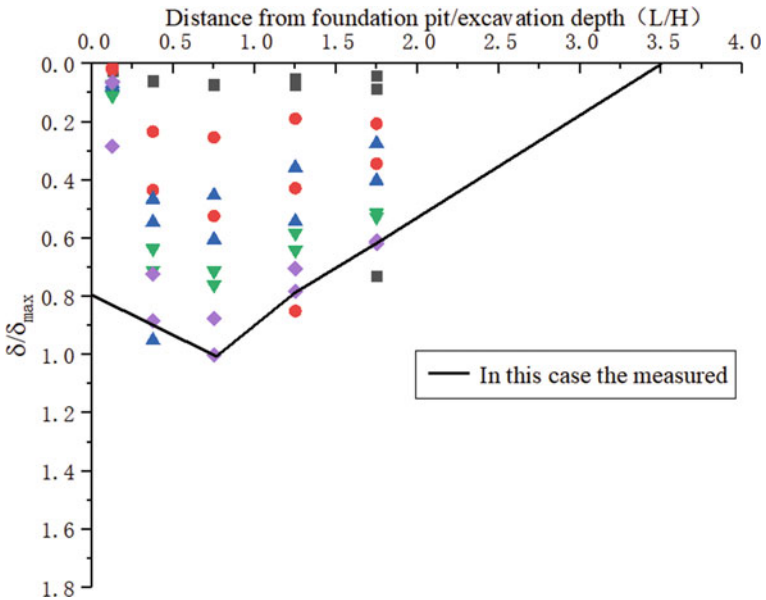


Fig. 9 Surface settlement envelope diagram behind foundation pit wall

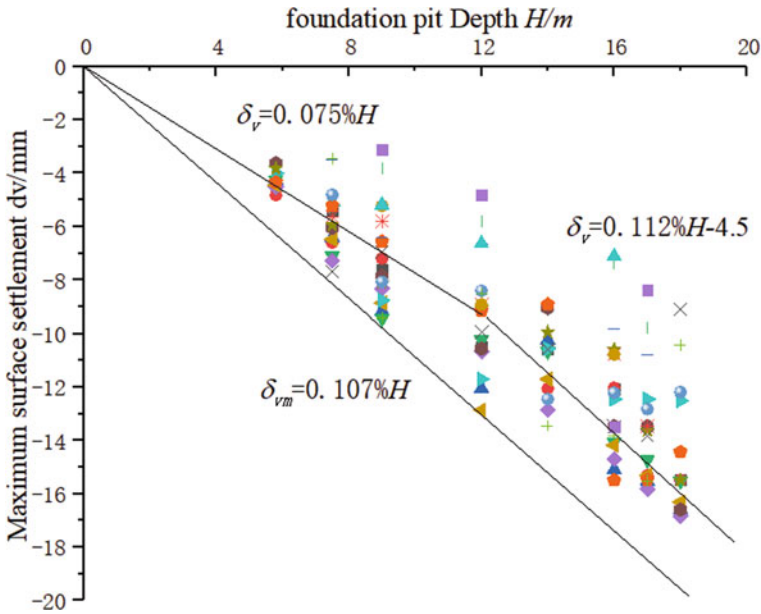


Fig. 10 Relationship between maximum surface settlement behind the wall and excavation depth

5 Relationship Between Surface Settlement Behind the Wall and Lateral Deformation of the Wall

Figure 11 shows the relationship between the maximum surface settlement and the maximum horizontal displacement of the wall in the process of foundation pit excavation. The figure shows: The mean value of the maximum surface settlement is about 0.91 times the maximum horizontal displacement of the wall. The maximum surface settlement is between 0.58 and 1.91 times the maximum horizontal displacement of the wall.

6 Conclusion

- (1) At the end of excavation, the maximum horizontal displacement of the wall is located at 2 ~ 4 m above the bottom of the pit, and the maximum value is 0.57‰ ~ 0.64‰H. The horizontal displacement of the wall increased with the increase of the excavation depth, and the distribution was roughly linear. The upper limit of the maximum horizontal displacement was 0.101%H, the lower limit was 0.042%H, and the average value was 0.069%H. The maximum horizontal displacement depth of the wall is about 0.87H.

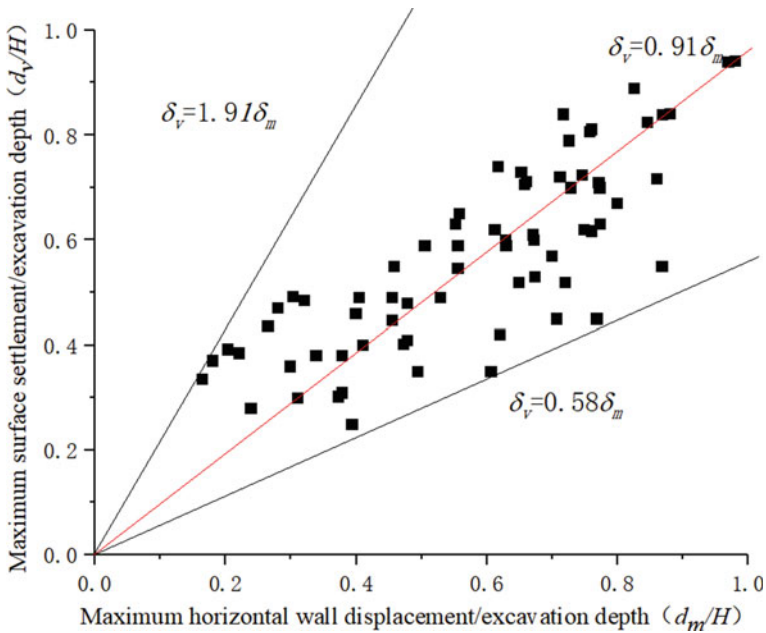


Fig. 11 Relationship between maximum surface settlement and maximum horizontal displacement of wall

- (2) When the foundation pit is excavated to the end, the surface settlement is mainly in the form of groove. The influence range of settlement in this area is $2H$, and the upper limit of the maximum surface settlement is $0.107\%H$.
- (3) The mean value of the maximum surface settlement is about 0.91 times the maximum horizontal displacement of the wall, and the maximum surface settlement is between 0.58 and 1.91 times the maximum horizontal displacement of the wall.

References

1. Cheng K, Xu RQ, Ying HW et al. (2021) Measurement analysis of excavation behavior of a 30.2m deep foundation pit in soft clay area of Hangzhou. *J Rock Mech Eng* 40(04):851–863
2. Gong XN (2005) Some thoughts on foundation pit engineering. *J Civ Eng* 38(9):99–102, 108
3. Guo BH (2021) Study on influence of foundation pit excavation on deformation of retaining structure and settlement of soil outside the pit. *J Shaanxi Water* 06:183–185
4. Liu GB, Wang WD (2009) Foundation pit engineering manual. China Architecture and Building Press, Beijing

5. Xu ZH (2007) Study on deformation behavior of deep foundation pit combined with supporting structure and main underground structure in Shanghai area. Shanghai Jiao Tong University, Shanghai
6. Zhu WJ, Zhang SY, Tong LY (2022) Study on the law of ground subsidence deformation outside pit of Changzhou Metro station based on measured data. J Constr Technol (06):51(7):15–18

Open Access This chapter is licensed under the terms of the Creative Commons Attribution 4.0 International License (<http://creativecommons.org/licenses/by/4.0/>), which permits use, sharing, adaptation, distribution and reproduction in any medium or format, as long as you give appropriate credit to the original author(s) and the source, provide a link to the Creative Commons license and indicate if changes were made.

The images or other third party material in this chapter are included in the chapter's Creative Commons license, unless indicated otherwise in a credit line to the material. If material is not included in the chapter's Creative Commons license and your intended use is not permitted by statutory regulation or exceeds the permitted use, you will need to obtain permission directly from the copyright holder.



Numerical Simulation with FLAC^{3D} on Excavation Process of Underground Powerhouse of Kaluma Hydropower Station



An Liu, Hua Li, Fei Lu, and Meifeng Niu

Abstract The dam site of Kaluma Hydropower Station is located on the Nile River in northern Uganda. It is a diversion power station with a total installed capacity of 600 MW. The gneissic fissures and medium dip fissures in the plant area not only reduce the strength of the rock mass, but also easy to form adverse combinations and cuts, which adversely affecting the stability of the cavern. Therefore, surrounding rock deformation and block instability are the key factors affecting the stability of underground caverns. Based on the field investigation data, according to the research of geological prototypes such as rock mass structural plane investigation and quality classification, this paper uses the finite element numerical analysis software FLAC^{3D} to establish and calculate the numerical model, adjusts the boundary conditions of the model through parameter inversion, and then calculates the stress and strain of each part of the rock mass, so as to evaluate the excavation stability of underground powerhouse construction. The actual situation of construction and excavation verifies the accuracy of numerical analysis and calculation.

Keywords Underground powerhouse · Stability of surrounding rock mass · FLAC 3D

A. Liu (✉) · H. Li · F. Lu · M. Niu
PowerChina Huadong Engineering Corporation Limited, Hangzhou, China
e-mail: liu_a2@hdec.com

H. Li
e-mail: li_h5@hdec.com

F. Lu
e-mail: lu_f9@hdec.com

M. Niu
e-mail: niu_mf@hdec.com

1 Introduction

The dam site of Kaluma Hydropower Station is located on the Nile River in northern Uganda. It is a diversion power station with a total installed capacity of 600 MW, mainly composed of water retaining sluice dam, diversion system, underground powerhouse, tailrace tunnel and other buildings. The head sluice dam, with the maximum dam height of about 14 m and the normal pool level of 1030 m; The size of the plant is 200 m \times 19.6/21.3 m \times 53 m (length \times wide \times height).

Underground powerhouse cavern group mainly includes main (auxiliary) powerhouse, main transformer tunnel, tailrace surge chamber, tailrace adit, bus tunnel, outgoing shaft, construction adit and other caverns. Among them, the buried depth of the powerhouse, main transformer tunnel and tailrace surge chamber is about 69 ~ 140 m, and the axis orientation of the cavern is N39° W. The ground elevation of this area is about 1057 ~ 1062 m. Among them, the size of underground powerhouse is 200 m \times 19.6/21.3 m \times 53 m (length \times wide \times height), the top arch elevation is 971 m, and the floor elevation is 916 ~ 947.55 m.

The rock mass mechanical environment where the cavern is located is the basis for stability evaluation and support design, including geological environment (rock mass structural characteristics), mechanical environment (including rock mass stress field conditions and rock mass strength conditions), dynamic environment (including seismic geological environment and groundwater dynamic conditions). The stability analysis methods of surrounding rock of underground caverns can be roughly summarized as engineering geological analogy method, rock mass structure analysis method, rock mass stability mechanical analysis method and simulation test method [1]. The simulation test method includes physical simulation and numerical simulation. With the development of calculation technology and the wide use of computers, the numerical simulation method has obvious advantages in studying the development of stress, deformation and failure of surrounding rock of underground caverns, and then quantitatively evaluating the stability of surrounding rock. It has increasingly become the most powerful tool to solve the problems of underground engineering design and construction.

Therefore, based on solid and detailed field investigation data, this paper will analyze the mechanical environmental conditions of rock mass and their relationship, establish the constitutive model of rock mass, and adopt appropriate data processing technology and calculation methods to accurately evaluate the stability of underground powerhouse caverns.

2 Rock Mass Quality Classification

The stability of underground caverns is closely related to rock strength and discontinuous structural plane, of which the latter has a greater impact, that is, the rock mass shows strong anisotropy [2]. Due to the size effect, poor representativeness and many

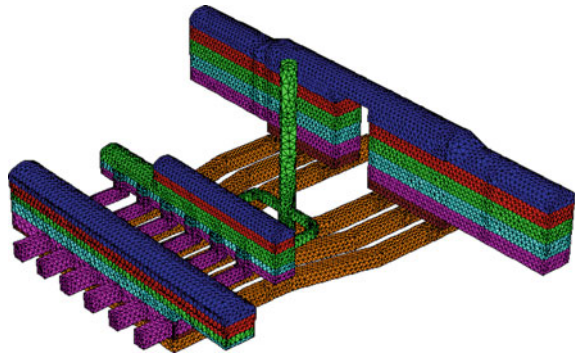
other adverse effects of indoor rock tests, rock mass classification systems have gradually developed [3]. Among them, RMR and Q systems are the most popular in the world, and suggestions for supporting support systems have been put forward respectively [4]. Generally, they are mainly considered: rock strength, rock mass structure, roughness of discontinuous structural planes, extensibility alteration degree, fillings, groundwater, in-situ stress conditions, excavation methods and other factors [5].

The surrounding rock classification of underground powerhouse area adopts Q system and RMR classification method for comprehensive evaluation. As the surrounding rock in the underground powerhouse area is mainly slightly weathered ~ fresh granite gneiss, the rock mass is hard and relatively complete, the structural plane is slightly ~ moderately developed, most of the caverns are dry, and there is only a small amount of seepage and dripping water locally, so it is mainly class II surrounding rock (RMR = 64 ~ 77, Q = 16 ~ 32), but the local tunnel section passing through the alteration zone is class III surrounding rock (RMR = 43 ~ 47, Q = 0.92).

3 Model of Underground Cavern Rock Mass

The boundary of the calculation area shall meet the requirements that the thickness of surrounding rock around the cavern is not less than 3 ~ 5 times the excavation diameter. The calculation area of Kaluma underground cavern group model includes the horizontal section of headrace tunnel, main power house, main transformer chamber, bus tunnel, ventilation shaft, tailrace tunnel, etc. The calculation range is 332 m × 440 m × 199 m, the coordinate origin is located at the bottom of the model. In the calculation model, the grid model of the underground cavern is shown in Fig. 1. The total number of discrete nodes is 119867, and the total number of elements is 709255.

Fig. 1 Grid diagram of underground cavern

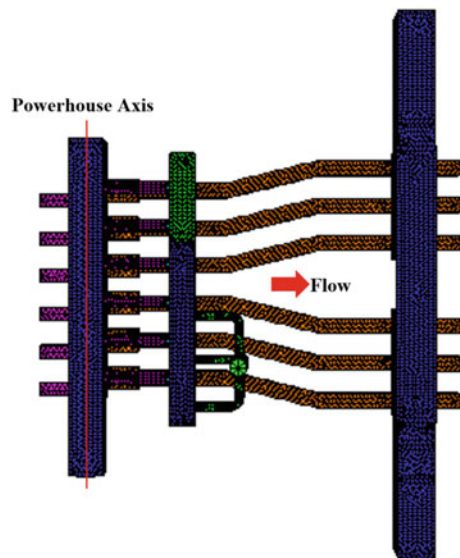


4 Results and Analysis

Through three-dimensional numerical simulation analysis, the construction process of the excavation of the cavern group is simulated, and the surrounding rock deformation field, stress field, plastic zone, etc. in order to reasonably evaluate the stability of the surrounding rock of the cavern group, combined with the engineering geological conditions and the structural form of the underground cavern group, the vertical section of the powerhouse axis is selected to analyze the calculation results after the excavation of the underground cavern. The specific location of the vertical section of the powerhouse axis is shown in Fig. 2.

After the excavation of the powerhouse, the maximum deformation of the surrounding rock of the section is mainly the rock wall between the end wall, the bottom plate boss and the machine nest, with the maximum deformation of 10 ~ 16 mm, the deformation of the end walls on both sides of 9 ~ 10 mm, and the deformation of the vault within the range of 4 ~ 5 mm (Fig. 3a). According to the stress analysis of the section, the maximum principal stress around the Powerhouse Tunnel is about $-10 \sim -13$ MPa, and the stress concentration of surrounding rock is not obvious (Fig. 3b); However, there is a certain stress relaxation. The minimum principal stress of surrounding rock at the vault and floor is about -0.5 MPa, and there is no tensile stress in the rock around the tunnel (Fig. 3c); Compared with the displacement nephogram, the stress relaxation part is basically the same as the part with large deformation of surrounding rock, indicating that the deformation of surrounding rock in the section is mainly caused by the stress relaxation of surrounding rock after excavation. According to the plastic zone analysis of the section (Fig. 3d), the maximum plastic zone of the section is located in the rock wall between the bottom plate boss

Fig. 2 Schematic diagram of plant axis position



and the machine socket, and the maximum depth is 8 m; The depth of the plastic zone of the arch crown is about 2 ~ 3 m; The maximum depth of the plastic zone of the end walls on both sides is about 5 ~ 6 m.

It can be seen from the above that the deformation of the surrounding rock after the excavation of the power house is large, mainly the rebound deformation of the bottom plate boss and the rock wall between the machine sockets. There is a certain

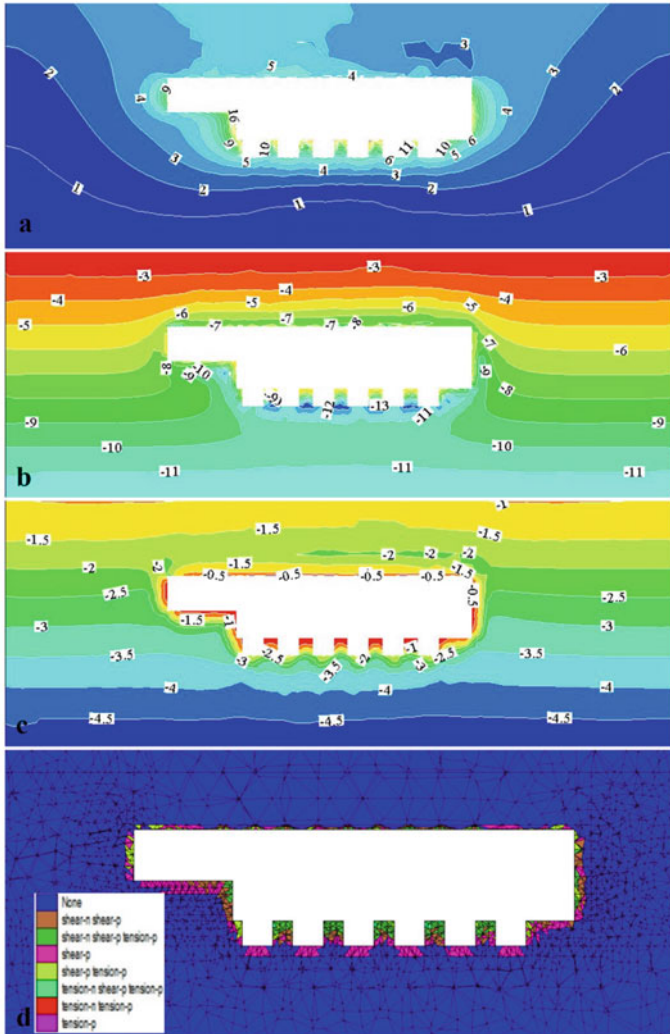


Fig. 3 Numerical simulation calculation results of surrounding rock of vertical section of plant axis after plant excavation: **a**-displacement (mm); **b**-maximum principal stress (MPa); **c**-minimum principal stress (MPa); **d**-plastic zone distribution

depth of plastic damage area on the vault of the power house. During the construction, attention should be paid to the removal of dangerous rocks, but the deformation and plastic area of the surrounding rock of the end walls on both sides of the power house, the bottom plate boss and the rock wall between the machine sockets are not small, so reinforcement and support should be considered.

After the excavation of the main power house is completed, the stress level of the crown is 7 ~ 8 MPa, the cumulative deformation of the crown is about 5 mm, the cumulative deformation of the upstream side wall of the main power house is about 15.6 mm, and the cumulative deformation of the downstream side wall is about 14.0 mm; The depth of the plastic zone of the crown is about 2 m, and the depth of the plastic zone of the side wall is generally 2 ~ 3 m; It can be seen that the stress value, deformation and plastic zone depth are very small, so the cavern is generally stable.

From the characteristics of surrounding rock deformation, plastic zone and secondary stress distribution, the powerhouse cavern group has good overall stability after excavation. It should be pointed out that the occurrence of plastic zone does not mean that the surrounding rock has obvious loosening. The in-situ stress characteristics and rock mass strength determine that the powerhouse tunnel group is mainly dominated by unloading relaxation and rebound deformation in the excavation process, and the stress adjustment generally will not lead to obvious loosening of the surrounding rock.

5 Conclusion

In this paper, the excavation process of underground powerhouse caverns is analyzed by using the finite element numerical analysis software FLAC^{3D}. The main conclusions are as follows:

In the buried area of underground powerhouse, the initial horizontal stress is greater than the vertical stress, so the stress concentration phenomenon appears in the top arch and bottom plate of Powerhouse after excavation. However, due to the small initial stress, the maximum value of secondary stress is generally about 10 MPa, which is far lower than the strength of rock mass, which is not enough to cause stress-induced failure of surrounding rock. During the excavation of underground caverns in the plant area of Kaluma Power Station, no obvious deformation damage and unstable block damage have occurred. Therefore, the actual situation of construction and excavation verifies the accuracy of numerical analysis and calculation.

References

1. Li B, Xu M, Liu Y (2015) Improvement of Hoek Brown strength criterion for intact rocks under triaxial conditions. *J Min Saf Eng* 32(06):1010–1016
2. Zhu H, Zhang Q, Zhang L (2013) Review on research progress and application of Hoek Brown strength criterion. *J Rock Mech Eng* 32(10):1945–1963
3. Zhang C, Zhou H, Feng X (2007) Evaluation of geotechnical engineering stability based on failure proximity. *J Rock Mech Eng* 28(5):888–894
4. Jiang Q, Feng X, Xiang T (2011) Numerical simulation study on stability analysis and intelligent dynamic optimization design of large caverns. *J Rock Mech Eng* 30(3):524–539
5. Zeng J, Sheng Q, Liao H (2006) FLAC 3D numerical simulation of excavation process of underground powerhouse of foziling pumped storage hydropower station. *Geotech Mech* 27(4):637–642

Open Access This chapter is licensed under the terms of the Creative Commons Attribution 4.0 International License (<http://creativecommons.org/licenses/by/4.0/>), which permits use, sharing, adaptation, distribution and reproduction in any medium or format, as long as you give appropriate credit to the original author(s) and the source, provide a link to the Creative Commons license and indicate if changes were made.

The images or other third party material in this chapter are included in the chapter's Creative Commons license, unless indicated otherwise in a credit line to the material. If material is not included in the chapter's Creative Commons license and your intended use is not permitted by statutory regulation or exceeds the permitted use, you will need to obtain permission directly from the copyright holder.



Study on Sound Insulation of Integrated Composite Wallboard Made of ALC and Rock Wool Panel



Renjie Shang, Zhaoxin Hou, Zhenlong Mao, and Yundong Liang

Abstract The integrated composite wallboard is a new type of prefabricated building enclosure wallboard made of autoclaved aerated concrete (ALC) and rock wool panel, which can meet the thermal requirements of cold areas in China without additional insulation. The ALC of the integrated composite wallboard is divided into local four-sided supported plates by vertical and horizontal ribs, which makes the wallboard have a different sound insulation performance from the wallboard of single uniform material and the composite wallboard of double-layer lightweight plates. The authors investigate the sound insulation performance of the integrated composite wallboard and compare it with other lightweight wallboards. They have found an apparent coincidence frequency region of air-borne sound insulation, which coincides with the natural vibration frequency of the local four-sided supported panel of ALC. Such an anastomosis effect seriously affects the weighted sound reduction index R_w , which reduces the weighted sound reduction index by 6 ~ 8 dB. The sound insulation experiment of integrated composite wallboard of ALC and rock wool panel objectively reflects the adverse effects of the sandwiched wallboard structure and provides a reference for improving the sound insulation performance by structurally upgrading the integrated composite wallboard.

Keywords Autoclaved aerated concrete · Integrated composite wallboard · Sound insulation in buildings · Sound insulation experiment

R. Shang (✉) · Z. Hou
Central Research Institute of Building and Construction Co., Ltd, MCC Group, Beijing 100088, China
e-mail: shangrenjie@aliyun.com

Z. Mao · Y. Liang
China Aluminum International (Tianjin) Construction Co., Ltd., Tianjin 300308, China
e-mail: maobianlong510@126.com

1 Introduction

1.1 The Template Files

Prefabricated buildings have been developing in China in recent years, and the prefabricated envelope structure is an important part of prefabricated buildings. According to the Standard for Evaluation of Prefabricated Building GB/T51129-2017, the external envelope and internal partition wall account for 20 out of 100 points in the prefabricated building. Lightweight concrete insulation integrated composite wallboard is an important form of prefabricated building envelope structure, which has been developed with many types of composite wallboard products in China.

Autoclaved aerated concrete (ALC) is a porous concrete product made of fly ash (or silica sand), lime, cement, aerating agent, and other raw materials cured by high-pressure steam, which features lightweight, high strength, heat preservation, and insulation, fire resistance, and sound insulation, easy processing, etc. Autoclaved aerated concrete slabs have been widely used in building envelope structures, and their applications have been studied extensively. However, in the cold areas of northern China, the autoclaved aerated concrete slabs cannot meet the thermal insulation requirement, and buildings still need to add insulation layers. In the research and experimental building project of China Metallurgical Construction Research Institute Co., Ltd., combined with the subject “Technology and Products of Lightweight and Environment-friendly Envelope System for Steel Structure Building” under the National Key Research and Development Program “Key Technology and Demonstration for Industrialization of Steel Structure Building,” we have developed an integrated composite insulation exterior wallboard of ALC and rock wool, using autoclaved aerated concrete as the load-bearing material and rock wool as the sandwich insulation material. The composite exterior wallboard can meet the insulation requirements in cold areas without additional insulation [1, 2]. In this paper, its sound insulation performance will be studied.

For ordinary reinforced concrete, the exterior wall with a thickness of 180 ~ 200 mm can achieve good sound insulation performance. While lightweight concrete has low density, the exterior wall of the same thickness will have much lower sound insulation performance, so it needs to add sound insulation panels to meet sound insulation requirements [3]. The sound insulation of single-layer uniform lightweight concrete wallboard basically meets the mass law of sound insulation [4]. The composite wallboard consists of two layers of thin plates, an air layer, and a layer of sound-absorbing material, and there have been numerous studies on the sound insulation of double-layer composite wallboard [5, 6]. Similar to the integrated wallboard structure presented in the paper, there have been studies on two-layer LSP panels composite exterior walls [7] and the prefabricated composite wall with a layer of rock wool sandwiched between the two-layer ALC panels [8]. Among them, the composite wallboard of ALC with rock wool panels is widely used, and the sound insulation has an obvious coincidence frequency region.

The ALC + rock wool integrated composite wallboard we have developed has a standard width of 600 mm, longitudinal ribs of 75 mm width on both sides of the wallboard, and transverse ribs at both ends and in the middle span of the wallboard. In the middle of the composite panel lies the rock wool sandwich panel, which not only plays the role of heat preservation but also improves sound insulation performance. The structural form of ALC + rock wool integrated composite wallboard will affect its sound insulation performance. Its structure does not conform to the characteristics of a two-layer thin panel structure [5, 6] or two-layer thick plates + interlayer [7, 8]. This paper will study the sound insulation performance of ALC + rock wool integrated composite wallboard.

2 Sound Insulation Requirements and Measurement of Enclosure Walls

With the development of the economy and science and technology, more vehicles and outdoor recreational activities increase noise sources continuously. At the same time, many new lightweight building materials weaken the ability of sound insulation and noise reduction of civil buildings. Improving the sound insulation index of the building envelope is an important measure to solve the noise interference problem in civil buildings. The standards of foreign developed countries have high requirements for building sound insulation. For example, the British standard is $D_{nt,w} + C_{tr} = 43\text{dB} \sim 45\text{dB}$, the Australian standard is $D_{nt,w} + C_{tr} = 45\text{dB}$, and the American standard is STC 45, equivalent to $D_{nt,w} + C_{tr} = 45\text{dB}$. *Code for Design of Sound Insulation of Civil Buildings* (GB50118-2010) of China stipulates the air sound insulation index of the exterior wall: the air sound insulation single value evaluation + traffic noise correction should be more than 45 dB.

The measurement of sound insulation of the outer envelope consists of field measurement and laboratory measurement. The field measured data results can be evaluated by the single value of standardized sound pressure level difference D_{nT} :

$$D_{nT} = L_1 - L_2 + 10\lg \frac{T}{T_0} \quad (1)$$

The data results measured in the laboratory can be evaluated by the single value of weighted sound insulation R_w :

$$R_w = L_1 - L_2 + 10\lg \frac{ST}{0.161V} \quad (2)$$

where, L_1 is the average sound pressure level in the sound chamber(dB); L_2 is the average sound pressure level in the sound receiving chamber(dB); T is the reverberation time of the sound receiving chamber (s); T_0 is the reference reverberation time (s), which is generally 0.5 s for residential buildings; S is the area of the specimen

(m²), which is equivalent to the area of the test hole; V is the volume of the sound receiving chamber (m³). According to Eqs. (1) and (2), the air sound insulation of the 1/3 frequency band can be calculated. With the sound insulation characteristic curve drawn on the sound insulation value-frequency coordinate system, the weight of a single value of sound insulation evaluation can be calculated according to the code *Rating Standard of Sound Insulation in Buildings* GB 50121.

3 Comparison of Sound Insulation Performance of Lightweight Concrete Walls

3.1 Foamed Cement Composite Wallboard

The research group has conducted sound insulation research on foamed cement composite wall panels. The bulk density of foamed cement is 680 kg/m³, the wall thickness is 250 mm, and the surface density is 170 kg/m². The size of a piece of wallboard is 1965 × 2500 mm, two pieces are put together for the test, and the gap is filled with cement mortar. The size of the wall for the sound insulation test is 4000 × 2500 mm, and the total area is 10m². The experimental data are shown in Fig. 1. The single value evaluation of air sound insulation obtained is $R_w(C; C_{tr})=47(0; -2)$ dB, and the curve has no obvious coincidence frequency valley.

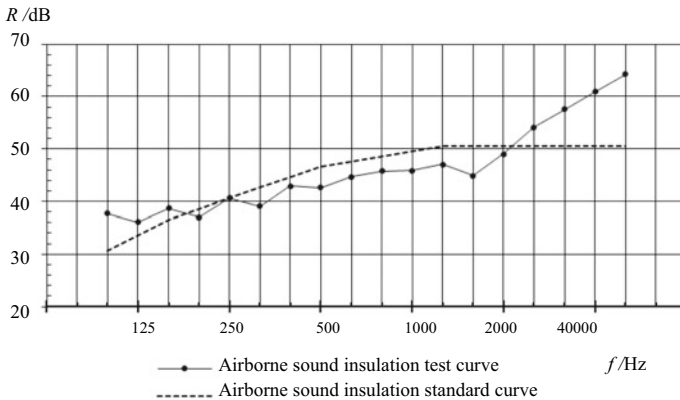


Fig. 1 Sound insulation frequency characteristic curve of foamed cement composite wallboard

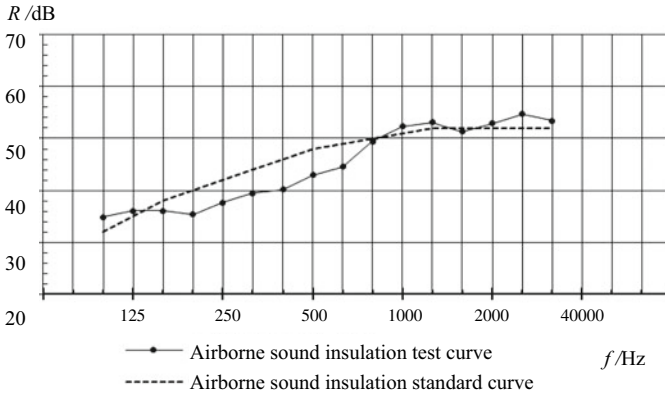


Fig. 2 Sound insulation frequency characteristic curve of ALC block wall

3.2 ALC Block Wall

The autoclaved aerated concrete block size is $600 \times 180 \times 240$ mm, and the density grade is 750 kg/m^3 . The weight of the single block is 19.8 kg. After the putty is put on the wall for 10 mm, the thickness of the wall is 200 mm, and the surface density is 170 kg/m^2 . The sound insulation test hole size is 3585×2800 mm, and the total area is 10.04 m^2 .

The experimental data [3] are shown in Fig. 2. The single value evaluation of air sound insulation is $R_w(C; C_{tr}) = 48(-1; -4)\text{dB}$, and the curve has no obvious coincidence frequency valley. The surface densities of the ALC block wall and foamed cement wall are 170 kg/m^2 , and since they are made of uniform material, their sound insulation values are the same, with only a 1 dB difference.

3.3 Composite Wall with Rock Wool Panel Sandwiched Between Two-Layer ALC Panels

Reference [6] presents an experimental study of sound insulation for the composite wall of 75 mm thick ALC panel + 50 mm rock wool panel + 75 mm thick ALC panel. The wall structure is shown in Fig. 3, and the ALC density is 650 kg/m^3 , the rock wool panel density is 100 kg/m^3 , and the wall surface density is 102.5 kg/m^2 . The experimental curve is shown in Fig. 3. As seen from the curve, there is an obvious sound insulation anastomosis valley near 630 Hz, which ranges from 500 to 800 Hz. When the frequency passes the anastomosis zone, the sound insulation increases with the increase of the sound frequency.

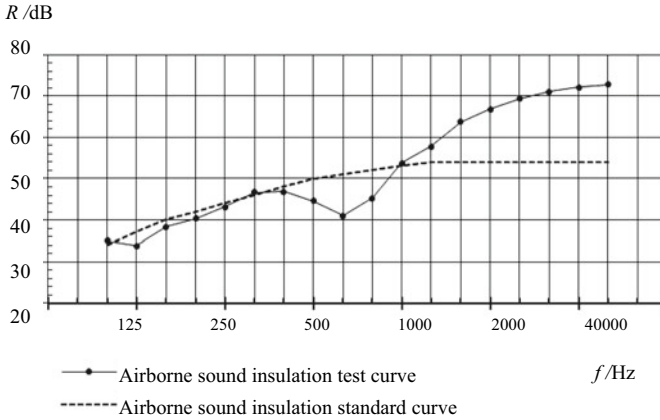


Fig. 3 Sound insulation characteristic curve of two-layer ALC panel with rock wool

4 Integrated Composite Wallboard ALC + Rock Wool Sound Insulation

4.1 ALC + Rock Wool Integrated Composite Wallboard Structure

ALC (Autoclaved Aerated Concrete) + rock wool integrated composite wallboard is incorporated by autoclaved aerated concrete and rock wool and placing reinforcement to improve the bearing capacity and crack resistance, as shown in Fig. 4. The density of ALC is controlled from 500 to 800 kg/m³, and the strength is not less than 3.5 MPa, which can meet the strength requirements of the wallboard. The density of rock wool is not less than 120 kg/m³. The composite density of ALC and rock wool panel is generally 400 ~ 600 kg/m³, equivalent to the weight of wallboard is 100 ~ 150 kg/m², which can effectively reduce the weight of the wall and the seismic response of the structure. The thermal conductivity of ALC is no more than 0.15 W/(m·K), the thermal conductivity of rock wool is no more than 0.04 W/(m·K), and the heat transfer coefficient of composite wallboard can reach 0.31 W/(m²·K) [9]. Rock wool is water-repellent and has the highest fire rating, with a combustion performance rating of A1.

4.2 Sound Insulation Experimental Scheme

The sound insulation experiment is carried out on ALC + rock wool composite wallboards according to the standard method. The measured wall is installed with

Fig. 4 Structure of ALC + rock wool integrated composite wallboard

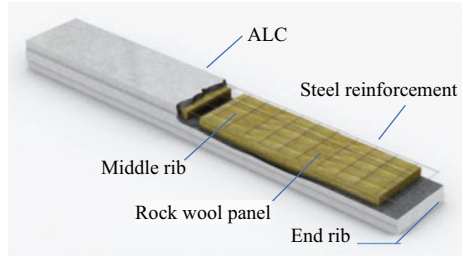
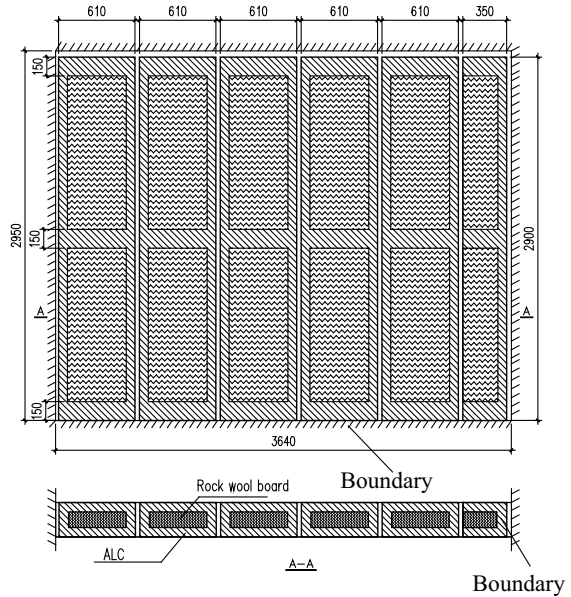


Fig. 5 Layout of wallboard for sound insulation experiment



five standard panels and one non-standard panel, as shown in Fig. 5. The gaps are sealed by cement mortar, as shown in Fig. 6.

The weight of each piece of each wallboard is 278 kg on average, and the surface density of the wallboard is 157 kg/m². The volume density of rock wool panels is 140 kg/m³, the volume density of ALC is 750 kg/m³, and the density of cement mortar is 1800 ~ 1900 kg/m³. The average surface density of the whole wall is 182 kg/m².

4.3 Prediction of Sound Insulation Experimental Results

When the sound waves incident at an irregular angle, the mass law of sound insulation of a single-layer homogeneous solid wall can be expressed as:

Fig. 6 Installation of wallboard for sound insulation experiment



$$R = 20 \lg f + 20 \lg m - 48 \quad (3)$$

where f — the frequency of the incident wave; m —the mass of the unit area of the wall. When the surface densities and the material properties are relatively similar, the sound insulation values of two wallboards have the following relationship:

$$R_2 = R_1 + 20 \lg \frac{m_2}{m_1} \quad (4)$$

Firstly, the integrated wallboard is considered single material wallboard. According to the experimental data of Sect. 3.1 of cement foamed concrete wallboard and Sect. 3.2 of ALC block wall, the surface densities are 170 kg/m^2 , and the sound insulation is 47 dB and 48 dB, respectively. According to Eq. (4), it can be approximately obtained that when the surface density is 182 kg/m^2 , the sound insulation is:

$$R_A = 47 + 20 \lg \frac{182}{170} = 47.6(\text{dB}) \quad (5)$$

The sound insulation will be increased if the sandwiched rock wool panel is considered.

4.4 Experimental Results of Sound Insulation

The sound insulation experiment is carried out four days after the installation of the experimental wallboard, and the experimental results are shown in Table 1 and Fig. 7. $R_w=43.8\text{dB}$ is obtained, and the integer number is $R_w(C, C_{tr})=43(0, -2)\text{dB}$. Compared with $R_w=47.6\text{dB}$ predicted by the previous theoretical analysis, it is 4 dB

Table 1 Experimental data of ALC + rock wool composite wallboard sound insulation

<i>f</i> /Hz	R/dB	<i>f</i> /Hz	R/dB	<i>f</i> /Hz	R/dB
100	34.0	400	35.0	1600	50.6
125	38.6	500	37.2	2000	53.9
160	39.8	630	40.2	2500	55.4
200	36.9	800	41.6	3150	57.5
250	35.7	1000	44.6	4000	60.0
315	35.0	1250	47.5	5000	61.5

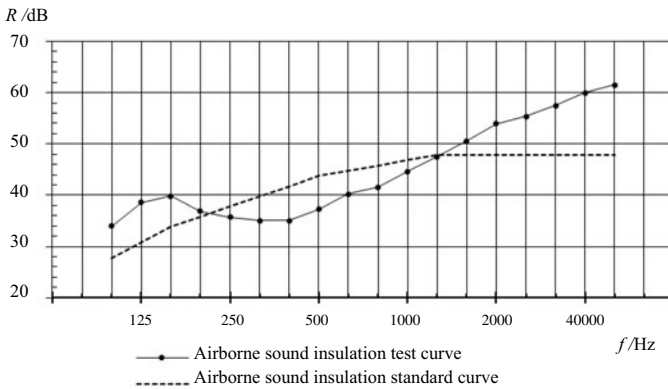


Fig. 7 Sound insulation frequency characteristic curve of ALC + rock wool integrated wallboard

smaller, and the sound insulation is significantly reduced. The abnormal reduction of sound insulation of ALC + rock wool integrated composite wallboard must be related to the structure of the composite wallboard, which needs further analysis and research.

As can be seen from Fig. 7, an anastomosis valley appears between 315 and 400 Hz. Compared with Fig. 4, the range of the anastomosis valley is larger. After the coincidence frequency, the sound insulation is proportional to the logarithm of the frequency, and the fitting relationship is shown in Eq. (6):

$$R_2 = R_1 + 25.1 \times \lg \frac{f_2}{f_1} \tag{6}$$

According to Eq. (3), the logarithmic relationship between sound insulation value and frequency is shown as Eq. (7):

$$R_2 = R_1 + 20 \times \lg \frac{f_2}{f_1} \tag{7}$$

By comparing Eqs. (6) and (7), it can be found that the sound insulation value of the integrated composite wallboard is proportional to the logarithm of the frequency after the coincidence frequency of 400–5000 Hz, but the proportional coefficient changes from 20 to 25 in the mass law, reflecting the influence of the sandwich rock wool panel on the sound insulation.

4.5 Analysis of Sound Insulation and Coincidence Frequency of Integrated Composite Wallboard

According to the thin panel sound insulation and anastomosis frequency theory [9], the incident frequency is:

$$f_c = \frac{c_0^2}{2\pi \sin^2 \vartheta} \cdot \sqrt{\frac{\rho}{D}} \quad (8)$$

Where $D = \frac{h^3 E}{12(1-\nu^2)}$ is the bending stiffness of the single-layer plate, $h = 0.075$ m is the thickness of the plate, ν is the Poisson's ratio, E is the elastic modulus, ρ is the surface density, c_0 is the sound speed in the air, and ϑ is the incident Angle. According to Eq. (8), the coincidence frequency is $f_c = \frac{504}{\sin^2 \vartheta}$, f_c is minimum when $\vartheta = \pi/2$, which is 504 Hz. Obviously, the coincidence frequency of composite wallboard cannot be reflected by the thin panel theory.

ANSYS carried out the finite element modeling analysis of single ALC + rock wool composite wallboard. Since there are two hollow-filled rock wool panels in the 610 mm wide and 2900 mm high single-span wall panels, the rock wool panel has almost no stiffness compared with ALC, so the rock wool stiffness can be ignored for analysis. A single hollow surface is the vibration of half a wave with the lowest frequency of 355 Hz. At the fundamental frequency of local vibration of the ALC panel, around 355 Hz, acoustic resonance occurs in the front and rear panels. The sound insulation value shows a coincidence valley, which is completely consistent with the test results.

The experimental results show an obvious sound insulation trough in the frequency 315 ~ 400 Hz, which is located in the coincidence effect area. Compared with Fig. 4, the coincidence effect area has a larger range. The local bending deformation vibration frequency of the composite wallboard is consistent with the acoustic frequency, and the sound insulation ability is significantly reduced, with the reduction amount reaching 6 ~ 8 dB. As the frequency continues to increase, when the sound source frequency passes the anastomosed effect area, the bending vibration frequency of the panel increases and becomes the main contributor to the acoustic impedance rate. The sound insulation quantity continues to increase with the increase of frequency.

5 Conclusions

The sound insulation of the integrated composite wallboard of the ALC + rock wool panel is different from that of a single material wall as well as that of the on-site composite wall with two-layer of ALC panels and one layer of rock wool panel. Both experimental research and theoretical analysis show new sound insulation characteristics, and the following conclusions can be drawn through the experimental research and theoretical analysis:

- (1) The integrated composite wallboard of the ALC + rock wool panel belongs to non-uniform material wallboard due to structural reasons. Therefore, the relationship between the sound insulation volume and the mass surface density of the wallboard does not conform to the law of mass, which should be measured by experiment.
- (2) There are two local four-sided supporting ALC panels on each side of the integrated composite wallboard of the ALC + rock wool panel, and there is local vibration. The vibration frequency of the local four-sided supporting panel calculated by the finite element method is 355 Hz. In this experiment, the thickness of the local ALC panel is 75 mm, and the density is 750 kg/m^3 . Since there is no experimental measuring point at 355 Hz, the coincidence frequency obtained in the experiment is between 315 and 400 Hz, which is completely consistent with the finite element calculation results.
- (3) The sound insulation single evaluation value of 75 mm ALC + 125 mm rock wool panel + 75 mm ALC integrated composite wall panel is 43.8 dB. Compared with the wallboard with the same mass density and considering rock wool inter-layer, the sound insulation single evaluation value is reduced by about 6 ~ 8 dB, which is unfavorable to the wall's sound insulation.
- (4) It is necessary to improve the structural form of the integrated composite wallboard or add sound insulation measures to meet the standard of sound insulation required by the specification, such as adding a 10 mm thick sound insulation panel, adjusting the thickness of the ALC panel on both sides of composite wallboard rock wool to avoid local resonance before and after.

Acknowledgements This work is financially supported by the National Key Research and Development Program (2017YFC0703807) Fund.

References

1. Renjie S, Xiao Y, Zhaoxin H (2020) Study and application of heat transfer coefficient of lightweight concrete sandwich composite wallboard. *J China Concr Cem Prod* 9:57–61
2. Guowei Z, Lei G, Qisong M (2018) Flexural behavior study of composite B03-grade autoclaved aerated concrete slabs. *J Build Struct* 48(22):61–71,77

3. Dongbin L, Jianjun W, Yong C (2018) Study on light gauge steel skeleton and lightweight concrete partition wall. *J Build Sci* 34(3):145–150
4. Cheng Q, Shengquan Z, Dingdang L (2020) Experimental study on sound insulation performance of autoclaved aerated concrete block walls. *J Qingdao Univ Technol* 41(4):49–54
5. Chengxun C (2011) Experimental study on sound reduction index of double lightweight panel. *J Build Sci* 27(10):63–69
6. Zuomin W, Zaixiu J (2011) Impedance analysis method for sound insulation of double panels. *J Tongji Univ (Nat Sci)* 39(9):1383–1386, 1412
7. Fei W, Shengyun H (2020) Study on sound insulation performance of prefabricated LSP exterior wall in Ningxia composite structure building. *J Build Sci* 36(4):178–183
8. Jie D, Yang H, Bin W (2016) Experiment on sound insulation performance of fabricated ALC composite wall. *J Changzhou Inst Technol* 29(6):18–20
9. Jianchun C (2019) *Principle acoustics*, vol 1. Science Press, Beijing

Open Access This chapter is licensed under the terms of the Creative Commons Attribution 4.0 International License (<http://creativecommons.org/licenses/by/4.0/>), which permits use, sharing, adaptation, distribution and reproduction in any medium or format, as long as you give appropriate credit to the original author(s) and the source, provide a link to the Creative Commons license and indicate if changes were made.

The images or other third party material in this chapter are included in the chapter's Creative Commons license, unless indicated otherwise in a credit line to the material. If material is not included in the chapter's Creative Commons license and your intended use is not permitted by statutory regulation or exceeds the permitted use, you will need to obtain permission directly from the copyright holder.



Study on the Properties of Concrete with Different Admixtures in Acid Corrosive Environment



Lei Yu, Tianyuan Zhao, and Zhi Wang

Abstract To study the deteriorating law and find a proper admixture to enhance the durability of the concrete in the acid corrosion environment, the corrosion and deterioration of concrete with different types and proportions of admixtures were studied. The appearance morphology, strength, chloride penetration depth, and porosity of ordinary concrete and concrete with different types of admixtures under water curing and corrosion solution erosion were compared. The results show that in terms of improving the corrosion resistance of concrete, the single-mixed mineral powder shows excellent performance. The addition of fly ash significantly increases the content of 10–100 nm pores, and the strength is low at an early age, but the strong growth is limited at the later stage.

Keywords Concrete · Corrosive environment · Deterioration law · Admixture

1 Introduction

During construction of the highway, the route may pass through some areas where the soil or the water contain some H^+ and some Cl^- or SO_4^{2-} [2]. The bridge is the main style to pass through the river or the valley. These ions will lead to corrosion during service item of the pile foundation of the bridge [3]. Harmful particles enter concrete from initial micro-cracks or internal pores of the concrete, corrode the internal structure of concrete through physical penetration and chemical action [5], and finally cause damage to the structure of concrete materials, especially in the chemical neutralization, which is more serious under acidic conditions.

Many scholars have systematically studied the durability of concrete and obtained lots of great progress and rich engineering experience and which put forward a feasible method to improve the durability of concrete [1]. Coating is a main method to

L. Yu (✉) · Z. Wang

Beijing Xinqiao Technology Development Co., Ltd., Beijing, China

e-mail: yuleimabel@163.com

T. Zhao

Guangdong Nanyue Transportation Investment and Construction Co., Ltd., Guangdong, China

Table 1 List of cement properties

Fineness (80 μm square hole sieve) / (%)	Water requirement of normal consistency / %	Setting time (h: min)		Compressive strength (MPa)		Splitting strength (MPa)		Stability (boiling method)
		Initial set	Final set	3d	28d	3d	28d	
3.1	27.6	2:59	3:59	29.8	49.9	6.7	9.3	Conformity

enhance the durability of the concrete [4]. While, brush with anticorrosive paint is not a practical method because the pile foundation is under ground. From the perspective of the concrete material itself, adding admixtures or improving the variety of binders and other methods could increase the density and reduce the probability of initial cracks [6], and it also can promote their acid corrosion resistance.

Based on the investigation, analysis, and evaluation of the corrosive environment, the laboratory conditions are used to simulate the typical corrosive environment of acid chloride ions in the engineering site. This paper mainly investigates the deterioration rules of adding some admixtures into the concrete. The more dense of the concrete is, the better its anti-corrosion ability.

2 Material and Experiments

2.1 Materials

The cement is P.O 42.5 ordinary Portland cement and the properties are shown in Table 1. The fine aggregate is river sand with a fineness modulus of 2.8. The coarse aggregate is 5–31.5 mm continuous graded crushed stone, the mixing water is drinking water, and the water reducing agent is polycarboxylic acid. Water reducing rate of the water reducing agent is 20%.

2.2 Mix Proportion

The mix ratios of 4 groups of ordinary concrete are designed, as shown in Table 2. The C group is the control group, the CH-1–CH-3 groups used to study the effect of admixtures on the corrosion and deterioration law of concrete. When mixing with concrete, the concrete slump is 200 ± 20 mm.

Table 2 The proportion of ordinary concrete (kg/m³)

Number	Cement	HVFA	Fine ore	Water	Sand	Stone
C	360	0	0	170	817	1083
CH-1	252	108	0	170	817	1083
CH-2	252	0	108	170	817	1083
CH-3	252	54	54	170	817	1083

3 Experimental Section

3.1 Design of Simulated Test

The test solution was a NaCl solution with $\text{pH} = 2$ and a concentration of 6%. The cube blocks of $100 \times 100 \times 100$ mm were made and cured to 28d age under standard curing conditions, then put into the corrosion solution, and the compressive strength was tested at 28, 56, and 90 d age.

3.2 Test Method

According to ISO 4012-1978 to test the compressive strength, the chloride penetration resistance was tested by the RCM method, and the pore structure parameters of concrete were tested by mercury injection test.

4 Analysis of Test Results

The appearance morphology, quality, strength, chloride penetration depth, and porosity of ordinary concrete and concrete with different proportions and types of admixtures under water curing and corrosion solution erosion were compared.

4.1 Morphology Changes

The morphology changes of concrete with different proportions and types of admixtures in a corrosive environment are shown in Fig. 1.

It can be seen from Fig. 1 that the appearance morphologies of concrete with different proportions and types of admixtures are significantly different from those of ordinary concrete. In particular, the concrete mixed with ore powder is brown and



Fig. 1 Influence of admixtures on appearance morphology of concrete

has many black spots on the surface, which is the typical appearance characteristic of H^+ and chloride ion erosion.

4.2 Variation of Intensity

Strength Variation

Test the compressive strength of concrete blocks in different ages of corrosion environment, and compare the strength changes. The compressive strength loss rate is used to represent the strength change of concrete after sulfate erosion, and the calculation method is as follows:

$$\Delta CS = \frac{CS - CS_0}{CS_0} \times 100\% \quad (1)$$

ΔCS —Loss rate of compressive strength;

CS —Compressive strength after immersion in a corrosive solution;

CS_0 —Compressive strength from water curing to age.

The strength changes of concrete with different proportions and types of admixtures in the corrosive environment are shown from Figs. 2, 3, and 4.

As can be seen in Fig. 2, the strength of fly ash concrete specimens decreases obviously at an early age. However, the fly ash began to play the pozzolanic reaction and the strength increased in the later period, but the strength was lower than that of the ordinary concrete specimen group.

The strength of the sample group mixed with ore powder and concrete is improved at an early age, and which is mainly because the fineness of ore powder is finer than that of cement, and the gradation of concrete is improved, the pore structure of concrete is reduced, and the compactness is improved. At the later stage of hydration, the strongest growth effect brought by the improvement of compactness decreases, the mineral powder begins to play the pozzolanic reaction, and the

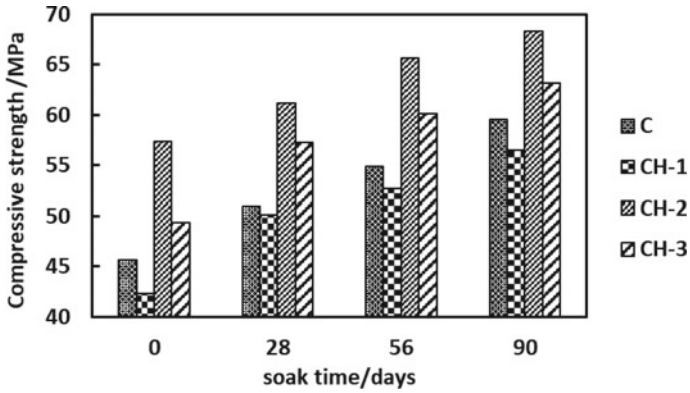


Fig. 2 Strength development law (water curing)

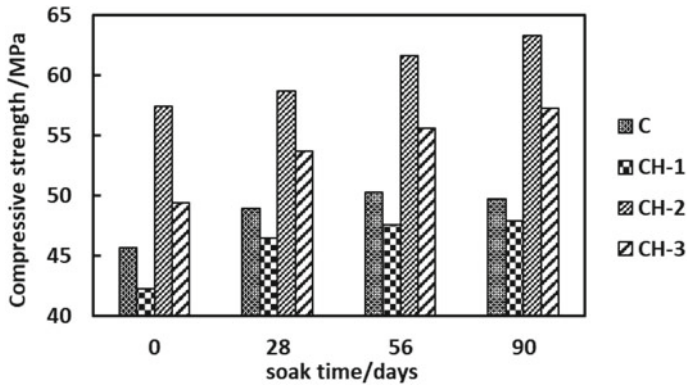


Fig. 3 Strength development law (acid solution)

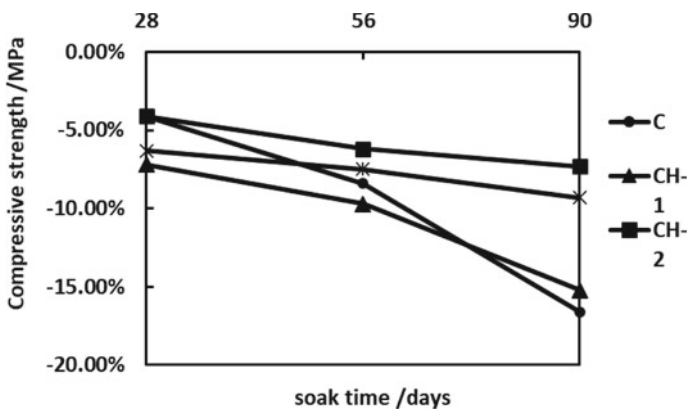


Fig. 4 Strength variation of admixture concrete in the corrosive environment

Table 3 Change of chloride penetration depth of admixture concrete in the corrosive environment

Concrete type	Without admixture	Single fly ash	Single mixed ores	Mixed fly ash, mineral powder
Depth of chloride penetration /mm	16.6	14.8	12.1	14.3

strength of concrete continues to grow, showing a much higher strength than that of ordinary concrete.

In the early age of the fly ash concrete specimen group, the strength of the concrete improved by the ore powder on the compactness increased significantly, and the strength was slightly higher than that of ordinary concrete. In the late hydration period, the ore powder and fly ash gradually played the pozzolanic effect, and the strength increased significantly.

As can be seen from Fig. 4, the strength of the fly ash concrete specimen group is lower than that of ordinary concrete at an early age, and which is also slightly higher than that of ordinary concrete in a later stage because fly ash begins to play volcanic ash effect in the later stage.

Due to the improvement of the density and pore structure of concrete by ore powder at an early age and the excellent pozzolanic effect at the later stage, the strength of the sample group of ore powder mixed with concrete is higher than that of ordinary concrete at each age, especially the improvement of the corrosion resistance of concrete at the later stage is particularly obvious.

The strength loss rate of fly ash mineral powder concrete specimen group at an early age is higher than that of ordinary concrete, and it shows better corrosion resistance in the later stage.

Change of Chloride Penetration Depth

The change of chloride penetration depth of admixture concrete in a corrosive environment is shown in Table 3.

As can be seen from Table 3, the incorporation of fly ash has a certain inhibitory effect on the infiltration of chloride ions, the incorporation of ore powder has a significant inhibitory effect on the infiltration of chloride ions, and the incorporation of fly ash and ore powder has the same inhibitory effect on the infiltration of chloride ions as that of the single incorporation of fly ash.

Because the fineness of fly ash is finer than cement, the gradation of concrete is improved by adding fly ash, the pore structure of concrete is reduced, the compactness of concrete is improved, and the infiltration of chloride ions is inhibited. However, the improvement of pore structure and compactness of concrete is limited.

Mineral powder is a finer powder material than fly ash, which has a better effect on improving the pore structure and compactness of concrete and which has the strongest inhibition on chloride penetration.

Although both fly ash and ore powder can improve the pore structure and compactness of concrete, the micropores of concrete are limited, the improvement of pore

Table 4 Variation of porosity of admixture concrete in the corrosive environment

Number	Erosion conditions	Porosity/%	Average pore diameter/nm
C	pH = 2, Cl% = 6%	13.82	23.7
CH-1		16.27	19.5
CH-2		9.26	21.5
CH-3		12.31	19.7

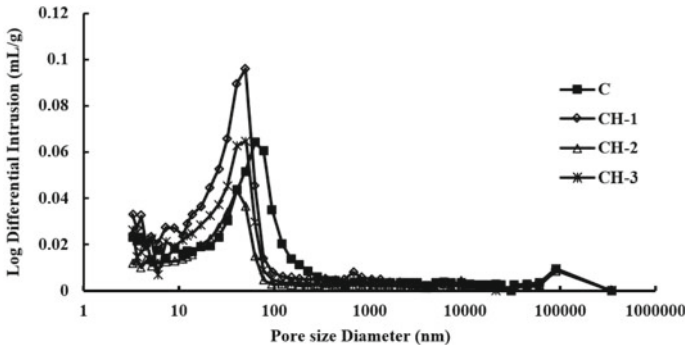


Fig. 5 Variation of concrete porosity of admixtures

structure and compactness after double mixing cannot be superimposed, and the infiltration effect of chloride ion is slightly better than that of single mixing fly ash.

Porosity Change

The porosity changes of admixture concrete in a corrosive environment are shown in Table 4 and Fig. 5.

As can be seen from Fig. 5, the pore size of the fly ash concrete specimen group is optimized to a certain extent. The pore content of 100–1000 nm decreases, while the pore content of 10–100 nm increases, mainly because fly ash has more particles with smaller particle sizes than cement. These particles fill the pore structure of concrete and also improve its compactedness.

The pore structure of the sample group of powdered ore concrete is significantly improved. Large pores not only transform into small holes, but the content of small holes is reduced, the result indicates that the particle size of powdered ore is much smaller than that of cement, and the pore structure of concrete is well filled after incorporation.

The fly ash and ore powder concrete specimen group combine the improvement effect of fly ash and ore powder on concrete pore structure in gradation. The content of small holes in concrete is the same as that of ordinary concrete, and the overall pore structure is fully optimized in the test.

5 Conclusions

This paper mainly investigated the influence of corrosion conditions, cementing material composition, cement type, and other factors on the law of corrosion and deterioration of concrete, and the main conclusions are as follows:

- (1) After the addition of admixtures, the content of 100–1000 nm holes in concrete can be significantly reduced. The improvement of corrosion resistance of concrete by single ore powder is the most significant.
- (2) The addition of fly ash significantly increases the content of 10–100 nm pores, and the strength is low at an early age, but the strong growth is limited at the later stage, which has a certain inhibition effect on the penetration of chloride ions.
- (3) After the addition of ore powder, the content of the 10–100 nm hole is significantly reduced, the strength of concrete is significantly improved, and the inhibition of chloride ion penetration is the most significant.
- (4) With the addition of fly ash and ore powder, the improvement of concrete pore structure in gradation is well combined. The content of pore in concrete is the same as that of ordinary concrete, but the overall pore structure is fully optimized, and concrete strength is improved, but the infiltration effect of chloride ion is slightly better than that of single fly ash.

References

1. Li B, Fang Q, Fang P (2020) Durability of high-volume mineral admixture concrete half immersed in sodium sulfate solution. *J Harbin Eng Univ* 41(6):892–898
2. Chen M (2021) Effect and mechanism analysis of modified admixtures on properties of mortar under partial sulfate immersion. Zhengzhou University for the degree of Master
3. Wang C, Liu ZL, Yu L (2018) Relationship between anti-frozen durability and pore structure on concrete in freeze and thaw cycle environment. *Matec Web Conf* 238:64–68
4. Yu L, Lv S, Zhao Z, Liu Z (2022) Effect of slurry coating modified methods on water absorption of recycled coarse aggregate. *Coatings* 12:363
5. Yu L, Zhang SX, Chen L (2018) Anti-acid corrosion property of concrete improved by microstructure optimizing. In: *International conference on novel functional materials, ICNFM 2018*, vol 238. EDP Sciences, pp 56–59
6. Yu L (2018) Durability of concrete material and its optimization method. China Building Industry press

Open Access This chapter is licensed under the terms of the Creative Commons Attribution 4.0 International License (<http://creativecommons.org/licenses/by/4.0/>), which permits use, sharing, adaptation, distribution and reproduction in any medium or format, as long as you give appropriate credit to the original author(s) and the source, provide a link to the Creative Commons license and indicate if changes were made.

The images or other third party material in this chapter are included in the chapter's Creative Commons license, unless indicated otherwise in a credit line to the material. If material is not included in the chapter's Creative Commons license and your intended use is not permitted by statutory regulation or exceeds the permitted use, you will need to obtain permission directly from the copyright holder.



Monitoring and Analysis of Dam Deformation in Yuankou Reservoir



Ming Xu

Abstract Dam plays an important role in regulating the flow of water. It is the key to ensure the safe and stable operation of reservoir. Taking Yuankou Reservoir Dam as the research object, this paper monitored the horizontal displacement, settlement displacement and the internal deformation of upstream dam slope from December 15, 2006 to November 27, 2017. The results show that the horizontal deformation, settlement deformation and internal deformation of upstream dam slope are within a reasonable range. The deformation distribution and variation trend conform to the general law, and the deformation of the dam is in the normal range.

Keywords Dam · Source-mouth reservoir · Deformation monitoring · Horizontal displacement · Vertical displacement

1 Introduction

The deformation is accompanied by the whole life cycle of the dam. The earth-rock dam will be settled and displaced due to its weight, initial impoundment and other reasons. During stable operation, the settlement caused by the dead weight will gradually decrease, and the change of external load caused by the change of water level is the main reason for the deformation of the dam [4]. Deformation is a macroscopic effect size that can directly reflect the safe operation performance of dam [2]. Long-term deformation monitoring is an important task to the safe operation of a reservoir [1]. Therefore, reliable and efficient safety monitoring of dam becomes more and more important, and accurate prediction of dam deformation development is an important part of the whole monitoring process [3, 5]. This paper takes Yuankou Reservoir dam as the research object to monitor the horizontal displacement, settlement displacement and internal deformation of the upstream dam slope. The temporal and spatial development law of dam deformation is emphatically analyzed, and the

M. Xu (✉)
Jinyun County Water Conservancy Bureau, LiShui, ZhangJiang, China
e-mail: 187369867@qq.com

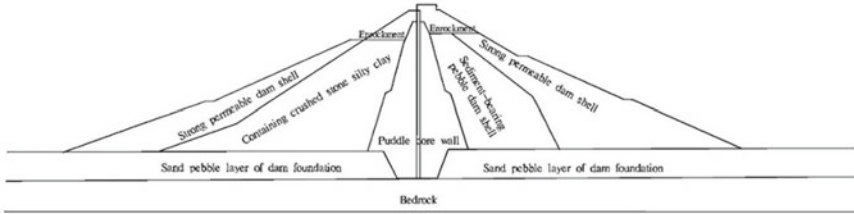


Fig. 1 Internal structure and material of the dam3 monitoring point arrangement

overall deformation safety state of the dam is evaluated. The purpose is to provide reference for the safe operation of the reservoir dam. 2 Project summary.

Yuankou Reservoir is located in Wuyi County, Jinhua City, Zhejiang Province, China. It is a medium-sized reservoir mainly for flood control and irrigation. The dam is 509 m long, 6 m wide at the crest, and 43.30 m high at the maximum. The designed normal water level of the reservoir is 208.20 m, the corresponding storage capacity is 22.2 million m³, the designed flood water level is 212.12 m, and the checked flood water level is 212.50 m. The dam is a clay core wall dam with sand and gravel shell. The height of the clay core wall is 210.00 m, and the cross-section is approximately isosceles trapezoid. In order to increase the drainage capacity of the non-impermeable area of the dam, the part above 203.0 m elevation of the upstream slope of the original dam and the part above 205 m elevation of the downstream dam slope were excavated and backfilled with rockfill. The dam section is shown in Fig. 1.

1.1 Layout of Dam Surface Deformation Monitoring Points

Three surface deformation observation sections were arranged parallel to the dam axis. The first deformation observation section (0 + 1) was located on the upstream side of the dam, 1.31 m away from the dam axis. The numbers of each measurement point are LD13, LD18, LD23, LD28, LD33, LD38 and LD43. The second deformation observation section (0 + 30) is located at the downstream side of the dam, 30.11 m away from the dam axis. The numbers of each measurement point are LD4, LD8, LD12, LD17, LD22, LD27, LD32, LD37 and LD42. The third deformation observation section (0 + 62) is located at the upstream side of the dam, 62.01 m away from the dam axis, and the numbers of each measurement point are LD2, LD6, LD10, LD15, LD20, LD25, LD30, LD35 and LD40.

A total of 25 surface deformation observation points. One working basis point and one checking basis point are arranged on the rocks at both ends of the above three sections. A total of six working basis points and six checking basis points. Two leveling basis points are arranged at the same time.

1.2 Layout of Deformation Monitoring Points in Upstream Dam Slope

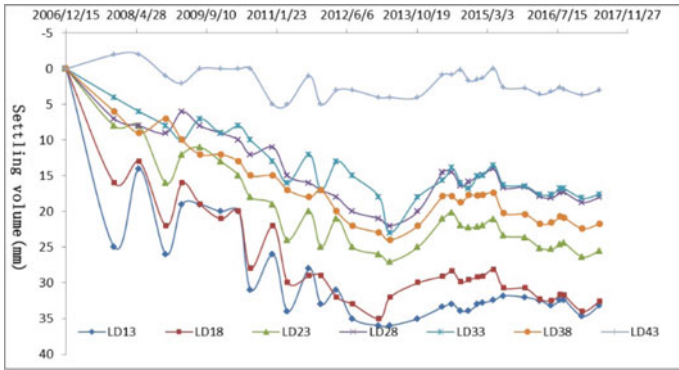
Two monitoring sections (0 + 245 and 0 + 380 m) are set up 245 and 380 m away from the right bank of the dam to monitor the downstream dam slope deformation. Two survey pipes were arranged for each section, and a total of four survey pipes were arranged.

2 Analysis of Monitoring Results

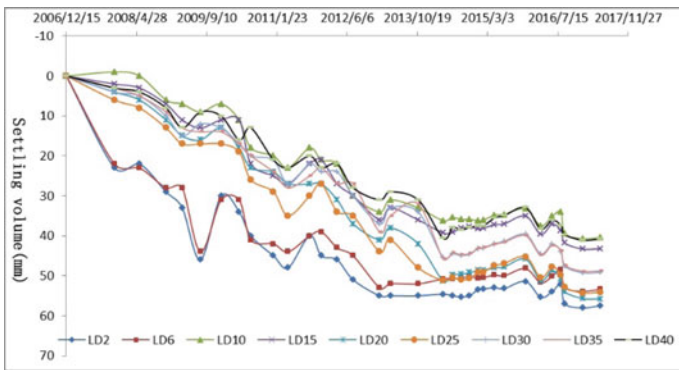
2.1 Observation of Dam Surface Deformation

The vertical deformation of the dam is basically proportional to the height of the dam. The settlement is large where the dam is high and small where the dam is low. It accords with the general deformation law of earth-rock dam. The changes of dam settlement over the years are shown in Fig. 2. The downstream dam has less low settlement, and the settlement is between 3 and 33 mm. The downstream side of the dam crest has the largest settlement, and the settlement is between 65 and 96 mm. The subsidence displacement is fast in the early stage and slow in the late stage. Most of the points showed a subsidence trend before 2013, after which the settlement tended to be stable. The settlement rate of the last year is 0 ~ 7 mm/ year, and the settlement rate of the measuring point upstream of the dam crest is 3 ~ 7 mm/ year. The overall sedimentation rate is small.

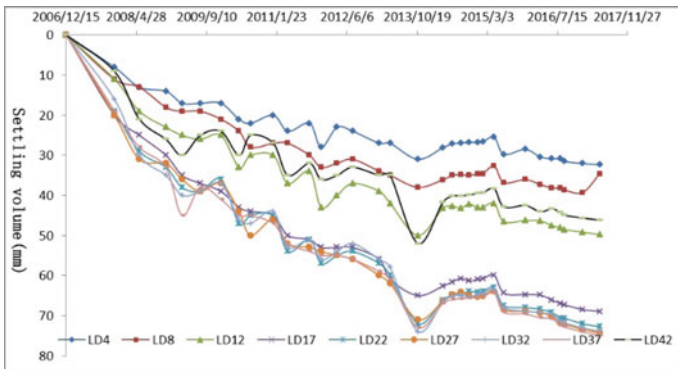
The horizontal displacement of dam surface deformation measurement points over the years is shown in Fig. 3. After the reservoir impoundment, the horizontal displacement of the dam surface is the largest at the 0 + 350 m section (1.0 m upstream of the dam axis), which is 57.0 mm, pointing to the downstream of the dam. The cumulative minimum displacement is - 13 mm, pointing upstream of the dam. Most of the horizontal displacement deformation was completed before 2013, and the basic process was stable in the later period. During the past year, the maximum horizontal displacement was located on the upstream side of the crest, at a distance of 7 mm, pointing upstream. Overall, the displacement is relatively small. The horizontal displacement on both sides of the dam in the cross section is relatively small. The horizontal displacement in the middle of the dam is large. The displacement of the left and right parts of the longitudinal section is relatively small, and the displacement of the middle dam section is large. It conforms to the general deformation law of dam. The maximum horizontal displacement of the dam is 57 mm, pointing downstream. The overall displacement is small. The annual maximum horizontal displacement is 7 mm, and the dam is in a safe and stable state.



(a) Curve of surface deformation, settlement and displacement of 0+62.0 section with time

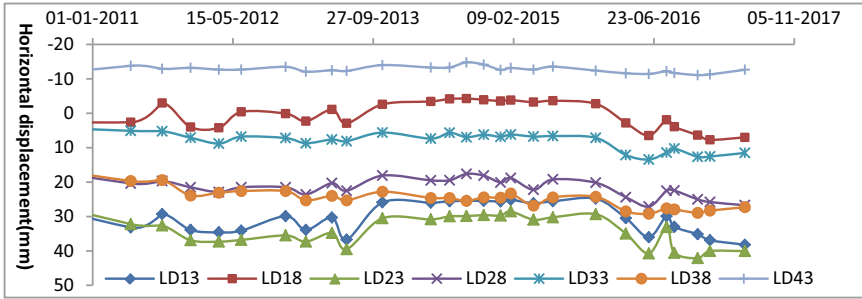


(b) Curve of surface deformation, settlement and displacement of 0+1.0 section with time

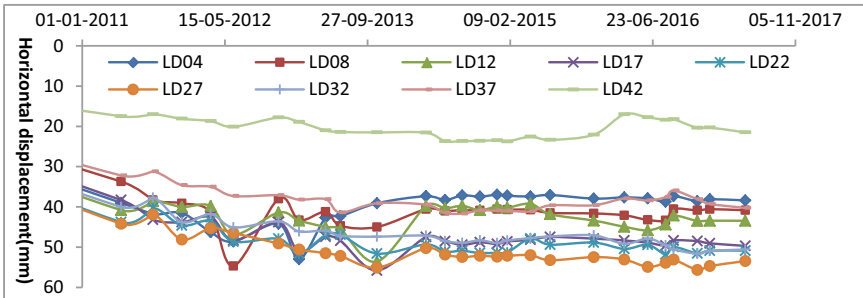


(c) Curve of surface deformation, settlement and displacement of 0+30.0 section with time

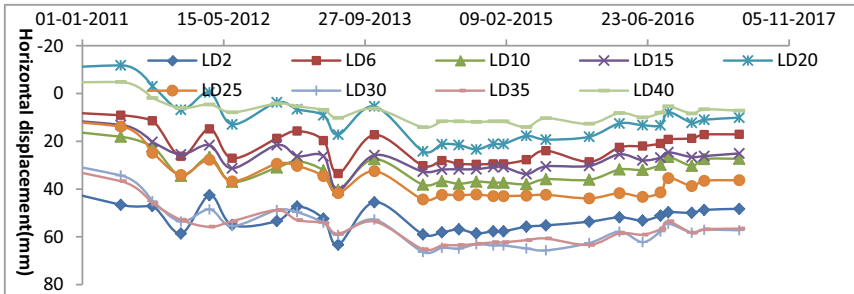
Fig. 2 Three curves of surface deformation, settlement and displacement with time



(a) Curve of horizontal displacement with time for surface deformation of 0+62.0 section



(b) Curve of horizontal displacement with time for surface deformation of 0+30.0 section



(c) Curve of horizontal displacement with time for surface deformation of 0+1.0 section

Fig. 3 Curve of horizontal displacement of section surface deformation with time

2.2 Internal Deformation of Upstream Dam Slope

Dam internal deformation is mainly related to dead weight, pore pressure, filling height, construction scheme and construction water content. The sedimentation is mainly affected by humidification and rheology, and is also related to the upstream real-time water level, rate of change, precipitation and temperature. The data measured at section 0 + 245 and section 0 + 380 were sorted out and calculated to obtain the distribution map of upstream and downstream horizontal displacements

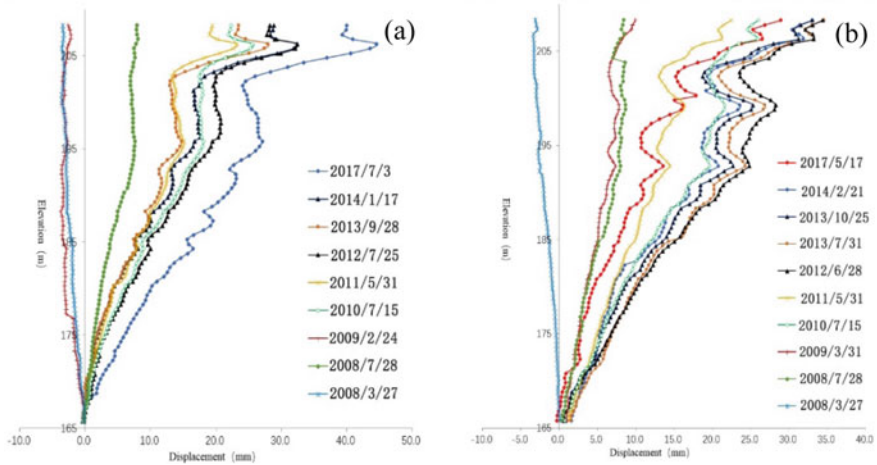


Fig. 4 Deformation curves of upstream dam slope of two sections with elevation variation (a represents the 0 + 245.0 section, b represents the 0 + 380.0 section)

along the elevation of each measuring point (Fig. 4). The horizontal displacement is positive to the downstream and negative to the upstream. It can be seen from the figure that before 2013, the horizontal displacements of sections 0 + 245 and 0 + 380 basically showed a downstream displacement trend, and then showed a stable trend. During normal operation, the deep horizontal displacement of the dam is basically related to the reservoir water level. At high water, the dam moves downstream; At low water levels, the dam moves upstream. The maximum downstream displacement of section 0 + 245 m is 44.6 mm, and the elevation is near 206.0 m. The maximum displacement in the downstream direction of section 0 + 380 m is 39.5 mm, and the elevation is 208 m. The horizontal displacements of the two sections conform to the general law of deformation during normal storage period, and the horizontal displacements are small. This indicates that the upstream dam slope is in a stable state.

3 Conclusion

- (1) The dam settlement varies from 3 to 96 mm over the years, and the overall settlement is small. The subsidence displacement is fast in the early stage and slow in the late stage. The sedimentation rate in the last year is 0 ~ 7 mm/year. The annual settlement rate of the observation point on the upstream side of the dam crest is 3 ~ 7 mm/year. The overall sedimentation rate is small. Dam deformation is basically proportional to height. The settlement of high dam position is large, the settlement of low dam position is small. It accords with the general deformation law of earth-rock dam.

- (2) In the cross section, the horizontal displacement on both sides of the dam is relatively small, while the horizontal displacement in the middle of the dam is large. The maximum horizontal displacement is 57 mm, pointing downstream, and the overall displacement is small. The maximum horizontal displacement rate is 7 mm/ year, and the dam is safe and stable state.
- (3) Before 2013, the horizontal displacements of the two sections showed a downstream trend. Then its displacement shows a stable trend. At the section 0 + 245 m, the maximum downstream displacement is 44.6 mm and the elevation is near 206.0 m. At the section 0 + 380 m, the maximum displacement in the downstream direction was observed to be 39.5 mm, which was located at the elevation of 208 m. During normal operation, the deep horizontal displacement of the dam is related to the reservoir water level. The horizontal displacements of the two sections conform to the general law of dam construction period and normal storage period, and the horizontal displacements are small. This indicates that the upstream dam slope is a stable state.

References

1. He X, Yang G, Ding X et al (2004) Application and evaluation of a GPS multi-antenna system for dam deformation monitoring. *Earth Planets Space* 56(11):1035–1039
2. Lin C, Li T, Chen S et al (2019) Gaussian process regression-based forecasting model of dam deformation. *Neural Comput Appl* 31(12):8503–8518
3. Li M, Shen Y, Ren Q et al (2019) A new distributed time series evolution prediction model for dam deformation based on constituent elements. *Adv Eng Inf* 39:41–52
4. Scaioni M, Marsella M, Crosetto M et al (2018) Geodetic and remote-sensing sensors for dam deformation monitoring. *Sensors* 18(11):3682
5. Xu C, Yue D, Deng C (2012) Hybrid GA/SIMPLS as alternative regression model in dam deformation analysis. *Eng Appl Artif Intell* 25(3):468–475

Open Access This chapter is licensed under the terms of the Creative Commons Attribution 4.0 International License (<http://creativecommons.org/licenses/by/4.0/>), which permits use, sharing, adaptation, distribution and reproduction in any medium or format, as long as you give appropriate credit to the original author(s) and the source, provide a link to the Creative Commons license and indicate if changes were made.

The images or other third party material in this chapter are included in the chapter's Creative Commons license, unless indicated otherwise in a credit line to the material. If material is not included in the chapter's Creative Commons license and your intended use is not permitted by statutory regulation or exceeds the permitted use, you will need to obtain permission directly from the copyright holder.



Experimental Study on Mix Ratio Design of High Coal Gangue Content Concrete



Yingran Liu, Yu Sun, Jian Gong, Yafeng Zhang, and Zhewei Sun

Abstract In order to improve the utilization rate of coal gangue as aggregate in concrete, based on the orthogonal experimental design method, the L16 (4^5) orthogonal table was used to initially prepare the mix ratio, and the concrete compressive specimens were poured, and their compressive strength was tested after standard curing for 7 days. The significance of the three factors of coal gangue ratio, coal gangue-sand ratio and water-binder ratio on strength was preliminarily understood. Then adjust the factor levels, use the L9 (3^4) orthogonal table to arrange the factor levels, formulate the mix ratio, test its strength after curing under the same conditions, and finally analyze that the optimal mix ratio of high-volume coal gangue concrete is 90% of coal gangue. Coal gangue sand accounts for 60% of the total sand, the water-binder ratio is 0.4, the sand rate is 35%, and the amount of cement per cubic meter is 350 kg. This mix ratio can use a large amount of coal gangue as a concrete cushion or sub-base in road engineering.

Keywords Coal gangue concrete · Orthogonal test design · Mix ratio · Compressive strength

Y. Liu (✉) · J. Gong · Y. Zhang · Z. Sun
Zhengzhou University of Technology, Zhengzhou, China
e-mail: liuyingran@zzut.edu.cn

J. Gong
e-mail: 20171034@zzut.edu.cn

Y. Zhang
e-mail: 20201031@zzut.edu.cn

Y. Sun
The Forth Geological Exploration Institute of Henan Geology and Mineral Bureau, Zhengzhou, China

1 Introduction

Concrete is the most widely used material in civil engineering construction. According to the data released by the National Development and Reform Commission, the output of commercial concrete in 2021 will be 3293.3 million cubic meters, an increase of 6.9%, and the growth rate will increase by 4 percentage points year-on-year. The output and increment of the above concrete show that my country still has a large demand for concrete in infrastructure construction, and it will not decrease in a short time. In the face of such a huge amount of concrete, coupled with the carbon neutrality goal proposed by the central government, all industries are required to steadily promote the “dual carbon” work. In the “14th Five-Year” development guideline for the concrete and cement products industry, it is proposed to develop low-carbon carbon-fixing concrete materials and use suitable industrial solid waste to manufacture concrete. Coal gangue is a solid waste generated in the process of coal mining. The existing coal gangue stockpile in my country is about 7 billion tons, and the annual output is increasing by more than 3 tons [1]. The existing coal gangue in northern Shaanxi alone accounts for one-seventh of the country’s total, more than 1 billion tons [2]. The storage of coal gangue not only takes up a lot of cultivated land, but also causes serious pollution to the environment. Due to its strong water absorption, it will bring serious haze under the catalysis of wind after drying and weathering, resulting in environmental pollution. The annual sales of sand and gravel in my country can reach 20 billion tons, and the production of machine-made sand has exceeded 18 billion tons [3]. Due to the limitation of natural sand and gravel mining, it is necessary to find as many sources of machine-made sand and gravel as possible. By comparing the composition of coal gangue sand with natural sand, researchers believe that coal gangue sand can be used as a raw material for preparing concrete [4]. However, due to the different sources of coal gangue and different dosages, it will affect the strength of concrete. Some scholars believe that the content of coal gangue instead of coarse aggregate below 30% has the least effect on the compressive strength of concrete [5], which seriously restricts the utilization rate of coal gangue in concrete. In response to the above situation, the team of this research group, based on the concept of green development, carried out experimental research on high-volume coal gangue concrete, improved the utilization rate of coal gangue in concrete, and provided solutions for consuming a large amount of coal gangue.

2 Materials and Methods

2.1 Experimental Materials

The materials tested in this paper are coal gangue, coal gangue sand, natural crushed stone, water-washed machine-made sand, cement, water reducing agent and tap water.

1. Coal gangue

The coal gangue selected in this experiment is all from northern Shaanxi. According to the literature research, the chemical composition of coal gangue in this area is mainly SiO₂ and Al₂O₃, the mineral composition is mainly quartz and clay minerals, and the aluminum-silicon ratio is between 0.31 and 0.39. Intermediate aluminum-silicon ratio coal gangue. The calcium and magnesium content is between 2.11 and 5.03%, which belongs to the silicon-alumina gangue, and the water absorption rate is 5-8% [6]; it can be used as concrete aggregate.

The coal gangue particles sampled on site are large, and they need to be crushed first, and the experimental jaw crusher is used for crushing. The crushing value of the crushed coal gangue was tested, and the crushing value was higher than 19%.

The coal gangue used in this experiment was screened with a square-hole sieve, and its gradation curve was obtained (Fig. 1). According to the gradation curve, it can be seen that the coal gangue particle size is relatively continuous between 0 and 10 mm.

2. Coal gangue sand

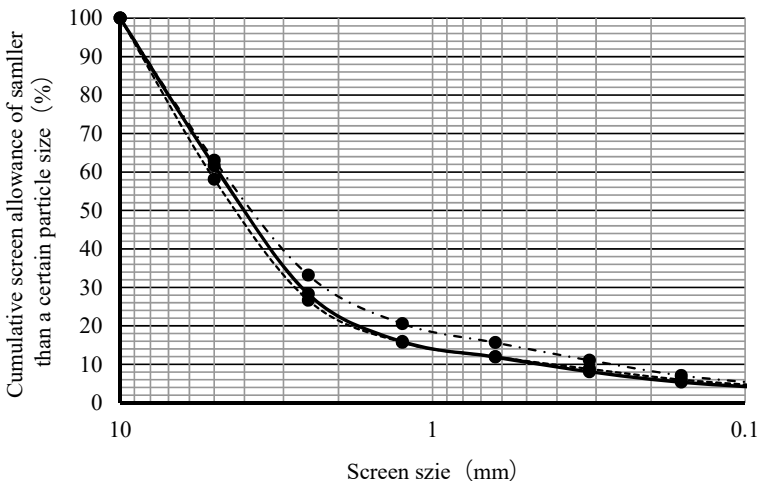


Fig. 1 Gradation curve of gangue after crushing

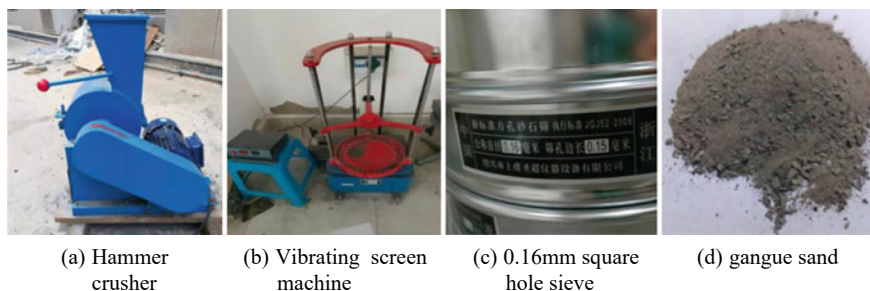


Fig. 2 Preparation process of coal gangue sand

The coal gangue sand in this paper is the sand obtained after crushing the above coal gangue with a hammer crusher, and then passing through a 0.16 mm sieve (Fig. 2).

3. The natural crushed stone

The natural crushed stone (Fig. 3) comes from around Zhengzhou City, with a particle size of 10–20 mm and a crushing value of 2–10%.

4. Machine-made sand

Machine-made sand choose water-washed machine-made sand (Fig. 4), the fineness modulus is about 3.2, and the average particle size is above 0.5 mm.

5. Cement

P-O42.5 bagged ordinary Portland cement is used for cement, and its main component content is shown in Table 1.

6. Water reducer

Fig. 3 Natural gravel



Fig. 4 Machine-made sand**Table 1** Contents of main components of ordinary Portland cement in bags

Component	SiO ₂	Fe ₂ O ₃	Al ₂ O ₃	CaO	MgO	SO ₂	Loss
Content	29.80	2.69	12.80	40.19	4.26	0.30	5.26

The water-reducing agent is a high-efficiency polycarboxylate water-reducing agent (Fig. 5). The water-reducing rate is about 20%. This time, the powder is directly added, and the dosage is 1.5% of the amount of the cementitious material.

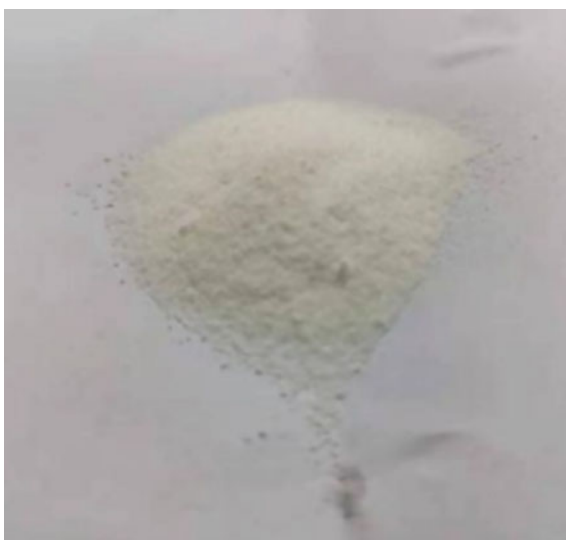
Fig. 5 Polycarboxylate water reducer

Table 2 Level table of preliminary factors for coal gangue concrete

Level of factor	Ratio of coal gangue	Ratio of coal gangue sand	Water-binder ratio
1	70	70	0.35
2	80	80	0.40
3	90	90	0.45
4	100	100	0.50

2.2 Experimental Method

This experiment needs to study the influence of coal gangue content, coal gangue sand content and water-binder ratio on the strength of coal gangue concrete. Four levels are initially proposed for each factor. If a comprehensive test is to be done, $4^3 = 64$ groups of tests need to be completed. Each group of three specimens needs to be prepared and maintained for 192 specimens. The workload is very large and it is difficult to complete in a short time; Arrangement of factor water using orthogonal experimental design method flat. Orthogonal experimental design is to select some representative points from the comprehensive test according to the orthogonality. These representative points have the characteristics of “evenly dispersed, neat and comparable” orthogonal table, only 16 groups of experiments can be arranged to complete the preliminary experimental plan.

In order to use coal gangue in a large amount in concrete, the ratio of coal gangue and coal gangue sand is initially planned to be four levels of 70 ~ 100%, and the water-binder ratio is four levels of 0.35 ~ 0.50. The factor level table is shown in Table 3. The parameter combination of the test plan was designed according to the orthogonal experimental design method, and the amount of materials in each group was calculated according to the compressive test block of $150 \times 150 \times 150$ mm, and each group of 3 test blocks. When calculating the amount of material, the sand rate of 35% is selected with reference to the relevant specifications [7], and the concrete density is designed according to 2300 kg/m^3 (Table 2).

According to the material dosage in Table 4, mix it in a 30L horizontal concrete mixer for 3 min, pour the concrete into a $150 \times 150 \times 150$ mm compressive test mold, put it into a concrete curing box for standard curing for 7d, and test its compressive strength [8]. Because the water absorption of coal gangue was not considered in the preliminary test mix ratio, the fluidity of individual groups of concrete was poor, and the strength was not formed after curing for 7 days. Therefore, the test plan was designed again according to the preliminary test results. The orthogonal table design of L9 (3^4) was used to design the experimental mix ratio. The proportion of coal gangue was 80 ~ 100%, the proportion of coal gangue sand was 60 ~ 80%, and the water-binder ratio was 0.40 ~ 0.60.

Table 3 The parameter combination of the test scheme and the amount of materials in each group

No.	Ratio of coal gangue %	Ratio of coal gangue sand %	Water-binder ratio	Amount of material per group (kg)					
				Cement	Water	Coal gangue	Gravel	Coal gangue sand	Sand
1	70	70	0.35	3.54	1.24	8.42	3.61	4.53	1.94
2	70	80	0.40	3.54	1.42	8.34	3.57	5.13	1.28
3	70	90	0.45	3.54	1.59	8.26	3.54	5.72	0.64
4	70	100	0.50	3.54	1.77	8.18	3.50	6.29	0
5	80	70	0.40	3.54	1.42	9.53	2.38	4.49	1.92
6	80	80	0.35	3.54	1.24	9.62	2.41	5.18	1.30
7	80	90	0.50	3.54	1.77	9.35	2.34	5.66	0.63
8	80	100	0.45	3.54	1.59	9.44	2.36	6.35	0
9	90	70	0.45	3.54	1.59	10.62	1.18	4.45	1.91
10	90	80	0.50	3.54	1.77	10.51	1.17	5.03	1.26
11	90	90	0.35	3.54	1.24	10.82	1.20	5.83	0.65
12	90	100	0.40	3.54	1.42	10.72	1.19	6.41	0
13	100	70	0.50	3.54	1.77	11.68	0	4.40	1.89
14	100	80	0.45	3.54	1.59	11.80	0	5.08	1.27
15	100	90	0.40	3.54	1.42	11.91	0	5.77	0.64
16	100	100	0.35	3.54	1.24	12.03	0	6.48	0

Table 4 L9 (3⁴) orthogonal experiment design factor levels

Level of factor	Ratio of coal gangue	Ratio of coal gangue sand	Water-binder ratio
1	80	60	0.40
2	90	70	0.50
3	100	80	0.60

3 Results and Discussion

The compressive strength of coal gangue concrete (7d) under the mix ratio of two orthogonal tests was tested respectively.

According to Table 7, the range analysis of the compressive strength of coal gangue concrete with the mix ratio of the first orthogonal test shows that the coal gangue ratio has little effect on the strength, and the water-binder ratio has the greatest influence, followed by the coal gangue sand ratio. The compressive strength increases with the increase of the water-binder ratio and decreases with the increase of the proportion of coal gangue and coal gangue sand (Tables 5 and 6).

Because the strength of the 11th and 16th groups of the first mix ratio test was not formed, some errors were caused to the results of this test; for this reason, the research group summed up the experience, adjusted the factor level and carried out

Table 5 L16 (4⁵) orthogonal test mix ratio compressive strength test results

Test No.	1	2	3	4	5	6	7	8
Compressive strength (MPa)	3.17	3.20	9.70	8.75	7.14	2.80	7.97	7.34
Test No.	9	10	11	12	13	14	15	16
Compressive strength (MPa)	9.85	12.46	0.00	2.17	14.19	7.55	2.54	0.00

Table 6 L9 (3⁴) orthogonal test mix ratio compressive strength test results

Test No.	1	2	3	4	5	6	7	8	9
Compressive strength (MPa)	12.05	9.63	9.06	10.92	10.92	12.69	10.16	2.56	2.65

Table 7 L16 (4⁵) orthogonal test range analysis results

Evaluation index	Factor	Ratio of coal gangue	Ratio of coal gangue sand	Water-binder ratio
Compressive strength (MPa)	T1	24.82	34.35	5.97
	T2	25.25	26.01	15.05
	T3	24.48	20.21	34.44
	R	0.77	14.14	28.47

Table 8 L9 (3⁴) orthogonal test range analysis results

Evaluation index	Factor	Ratio of coal gangue	Ratio of coal gangue sand	Water-binder ratio
Compressive strength (MPa)	T1	30.74	33.13	27.30
	T2	34.53	23.11	23.20
	T3	15.37	24.40	30.14
	R	19.16	10.02	6.94

the L9 (3⁴) orthogonal test. The experimental design, the test results are shown in Table 7, and the range analysis is as follows (Table 8):

Table 7 shows that under the design level of this orthogonal test, the most significant effect on the compressive strength (7d) of coal gangue concrete is the ratio of coal gangue, followed by the ratio of coal gangue and sand, and the third is the water-binder ratio. In order to see the results of the range analysis more intuitively, draw the curve with the factor level as the abscissa and the average value of the compressive strength under each factor level as the ordinate (Fig. 6).

According to the L9 (3⁴) orthogonal test design range analysis results, the compressive strength (7d) of coal gangue concrete increases first and then decreases with the increase of the proportion of coal gangue, first decreases and then increases with the increase of the proportion of coal gangue sand, and increases with the increase of the proportion of water glue. The increase of the ratio also decreases first and then increases. Combined with the mix ratio results of the two orthogonal test designs, it is necessary to maximize the amount of coal gangue and not to reduce the strength. Comprehensive analysis shows that the optimal mix ratio is that 90% of the coarse aggregate uses coal gangue, and the coal gangue mechanism. The amount of sand can reach 60% of the proportion of sand, and the water-to-binder ratio is 0.4.

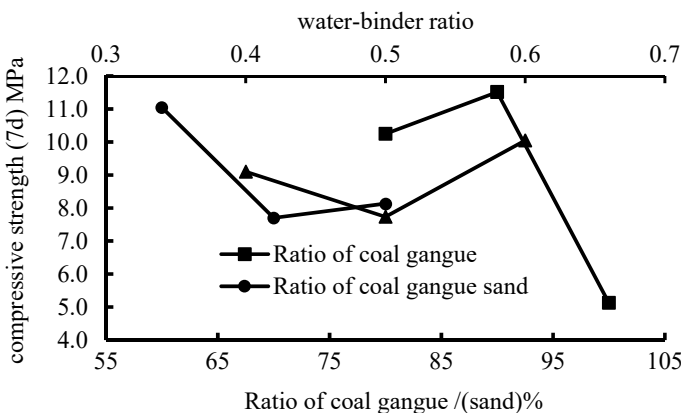


Fig. 6 Analysis of compressive strength (7d) of coal gangue concrete with the factors level

4 Conclusion

Under the dominance of the high content of coal gangue, the proportion of coal gangue, the proportion of coal gangue and sand and the water-binder ratio were preliminarily calculated, and the L16 (4^5) orthogonal experimental design table was used to arrange the test mix ratio; compressive strength factor. Based on the test results of the first orthogonal test, considering the strong water absorption of coal gangue, adjust the level of the above three factors to carry out the second orthogonal test design mix ratio arranged by the L9 (3^4) orthogonal table, after 7 days of standard curing, The compressive strength (7d) of coal gangue concrete was tested. The significance of the factor level was obtained by range analysis.

Combined with the results of two orthogonal test designs, it is concluded that the optimal mix ratio of high-volume coal gangue concrete is 90% coal gangue, 60% coal gangue sand, and 0.40 water-binder ratio. Large, natural crushed stone should not use crushed stone with a larger average particle size than coal gangue, and should use “rice stone” (0 ~ 5 mm crushed stone) that can hold the coarse aggregate of coal gangue. The sand rate is 35%, and the amount of cement per square is 350 kg. The compressive strength (7d) of gangue concrete under this mix ratio can reach more than 10 MPa. Innovation points and application prospects.

Acknowledgements Authors wishing to acknowledge assistance or encouragement from colleagues, special work by technical staff or financial support from Scientific Research Foundation of Zhengzhou University of Technology (20190243). Supported by Key Scientific Research Projects of Henan Colleges and Universities (Grant No. 20A440012).

References

1. Liu H, Chen F (2020) Feasibility analysis of coal gangue used as concrete aggregate. *J Shaanxi Coal* 39(2):60–63, 91
2. Bai G, Liu H, Zhu K et al. (2022) Experimental study on compressive strength of coal gangue concrete from different ore sources in Northern Shaanxi mining area. *China Civ Eng J* 1–11
3. Chen W, Huiqi L, Quanquan B (2021) Research progress of manufactured sand from coal gangue. *J China Coal* 47(7):68–76
4. Su Y (2021) Experimental study on basic mechanical properties of gangue concrete. Xi'an University of Architecture and Technology
5. Chenchen W, Wangxuezhi HJ (2022) Review on the effect of industrial solid waste reuse on compressive strength of concrete. *Jilin Water Resour* 1:10–16
6. Bai G, Liu H, Liu H (2022) Physicochemical properties of coal gangue and its influence on concrete strength. *J Build Struct* 1–12
7. Ministry of Construction of the People's Republic of China, Specification for Mix Proportion Design of Ordinary Concrete (JGJ 55-2011) [S] (2011). China Building Industry Press
8. Ministry of Housing and Urban Rural Development of the People's Republic of China. Standard for Test Methods of Concrete Physical and Mechanical Properties (GB/T 50081-2019) [S] (2020). China Building Industry Press

Open Access This chapter is licensed under the terms of the Creative Commons Attribution 4.0 International License (<http://creativecommons.org/licenses/by/4.0/>), which permits use, sharing, adaptation, distribution and reproduction in any medium or format, as long as you give appropriate credit to the original author(s) and the source, provide a link to the Creative Commons license and indicate if changes were made.

The images or other third party material in this chapter are included in the chapter's Creative Commons license, unless indicated otherwise in a credit line to the material. If material is not included in the chapter's Creative Commons license and your intended use is not permitted by statutory regulation or exceeds the permitted use, you will need to obtain permission directly from the copyright holder.



Analysis on Reinforcement of Statically Indeterminate Truss



Ziyi Liang, Mingjun Wei, and Long Yu

Abstract With the slowdown of the urbanization rate and new buildings in China, the old houses have different degrees of safety problems. Therefore, the importance of reinforcement and reconstruction of old houses has become increasingly apparent. This paper intends to study statically indeterminate trusses in buildings. Based on the finite element analysis, the paper compares the influence of the method of increasing section area on the original truss structure by establishing the reconstruction scheme of the same statically indeterminate truss. The numerical simulation results show that the ultimate bearing capacity of the structure is increased to achieve the purpose of strengthening.

Keywords Indeterminate truss · Reinforcement · Strengthening

1 Introduction

During the actual use of the building structure, it will be affected by the external environment. Therefore, the stability and firmness of the building itself will be affected to a certain extent, especially the reliability of the building structure. The research on the development process of foreign structural engineering shows that when the engineering construction reaches a certain degree, the reinforcement of engineering structure will become one of the main construction methods. It can be seen from relevant studies that civil engineering directly affects the process of urbanization.

Ziyi Liang, Mingjun Wei and Long Yu contributed equally.

Z. Liang (✉)

College of Harbor and Coastal Engineering, Jimei University, Xiamen, Fujian, China
e-mail: 201921181014@jmu.edu.cn

M. Wei

School of Architecture and Civil Engineering, Heilongjiang University of Science and Technology, Harbin, Heilongjiang, China

L. Yu

CSUST International College of Engineering, Changsha University of Science and Technology, Changsha, Hunan, China

© Crown 2023

Y. Yang (ed.), *Advances in Frontier Research on Engineering Structures*, Lecture Notes in Civil Engineering 286, https://doi.org/10.1007/978-981-19-8657-4_24

261

Drawing on the development history of developed countries, the initial stage of urbanization is the establishment of large-scale new buildings. Since then, the city has gradually matured in the process of urbanization, the scale of new buildings has continued to decline, and then the proportion of old houses has gradually increased, which are the three stages of urban development. Taking civil engineering in developed countries such as the United Kingdom and the United States as an example, the cost of building renovation in the United Kingdom in 1978 was more than three times nearly four times that in 1965. The industry of old house renovation is rising. According to a survey report of the United States, the heat of old house renovation was going to rise in the future gradually [1]. The development of civil engineering in China is relatively backward and started relatively late. After the Tangshan earthquake, the national group gradually paid more attention to the safety of buildings, especially old buildings. The group has formulated a series of standards led by the standard for seismic appraisal of industrial structures for seismic safety. To meet the gradually improved building standards, the industry of strengthening old buildings is also gradually emerging in China [2]. At present, most experts and scholars have done a lot of research on truss structure reinforcement based on actual cases. Bai [3] increased the section of a truss soffit member and achieved the goal of strengthening the connection between the upper and lower chords of the truss arch, which plays an important role in improving the overall dynamic performance of the structure after reconstruction. Yang et al. [4] adopted the expanded section method to strengthen the original lower chord members in the transformation of the truss structure of the corridor of a belt yard so that the out of the plane whole of the upper chord of the second span of the original corridor can meet the requirements. Liao et al. [5] adopted the external prestressing reinforcement method to fundamentally improve the bearing capacity of the grandstand components and narrow or close the original gap when transforming the arc grandstand structure of the Wuhan Xinhua Road stadium; it reduces the deflection of the components and is convenient for maintenance while effectively improving the rigidity of the building. Hayashi et al. [6] proposed a method combining reinforcement learning and graph embedding to optimize the binary topology of truss structures, achieving the goal of minimizing the total structure volume under stress and displacement constraints. When discussing the quality defects and reinforcement methods of an existing steel structure workshop, Guo [7] pointed out that when the steel material strength is insufficient, the reinforcement methods such as increasing the section reinforcement method and pasting steel plate reinforcement method should be adopted to make the material strength meet the requirements of the bearing capacity and stability of the truss structure. However, there is relatively few research on the reinforced truss structure in buildings worldwide. This paper discusses the application of the reinforcement method which changes the cross-sectional area of the truss in the truss structure, and the Abaqus finite element analysis and calculation software is used to establish the statically indeterminate truss simulation model to simulate the reinforcement effect. The main research contents are as follows: (1) This paper expounds on the stress characteristics of statically indeterminate truss. Then it establishes the finite element model of statically indeterminate truss by using the Abaqus. After that, the paper

calculates the stress condition of the truss before reinforcement, which finds out the most unfavorable load combination, and selects the reinforcement analysis object; (2) Based on the finite element simulation model, the paper emphatically analyses the stress state of trusses strengthened by increasing section method, and the stress variation trend and reinforcement effect of each control section.

2 Finite Element Modeling

To analyze more visually the similarities and differences between the two reinforcement methods, a typical super-stationary truss model was selected for this numerical simulation. The truss model was designed to meet the requirements of the GB50017-2017 Steel Structure Design Standard [8]. The truss consists of three vertically placed square column modules (Fig. 1), which are supported by two fixed hinge supports A and B and to which three horizontal set forces F are applied at their left nodes. Specific values required are in Table 1.

The truss was modeled using Abaqus finite element software and the forces on each Rod of the truss were derived from the simulation experiments as shown in Table 2. The results obtained were also compared with two sets of accurately calculated force data for each Rod from a similar model in Rebielak [9]. Most of the experimental data differed from the literature data by less than 10%. The simulated experimental values fall within the two accurately calculated model values when the difference between the calculated results of the two sets of accurately calculated models in the paper is greater than 10%. The model is thus correctly modeled and the experimental data modeled by the Abaqus finite element software is reliable.

3 Finite Element Model Analysis and Discussion

3.1 Finite Element Model Analysis

The methods of applying prestressing reinforcement generally fall into two categories, the first being the installation of prestressing tendons within the girders and the other being the external application of prestressing. The principle is that the middle of a truss bridge is subjected to the greatest bending moment and the external application of prestressing creates an upward support force that reduces the stress of the load on the bridge mechanism [10].

The trusses mentioned in this paper cannot be reinforced using prestressing methods as they do not have anchorage points on both sides for fixing the prestressing strands, so the reinforcement method of increasing the cross-sectional area was chosen for reinforcement [11].

Fig. 1 Model of truss [9]

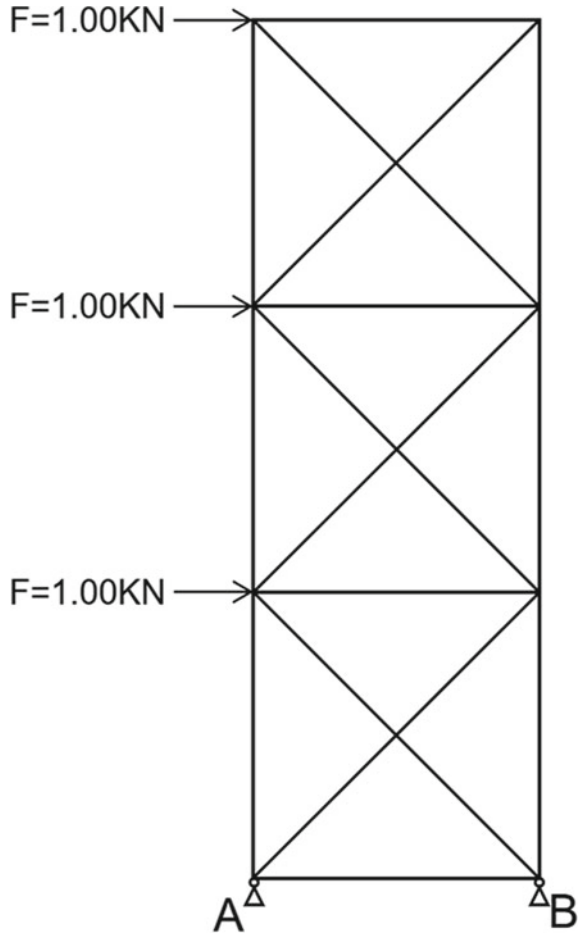


Table 1 Specification of super-static truss members before reinforcement [9]

Side length (mm)	Young's modulus (GPa)	Poisson's ratio	Cross-sectional area (mm ²)	Concentration F(N)
1000	210	0.3	706.86	1000

Analysis of the force cloud of the joist (Fig. 2) shows that the reinforcement is located at the most stressed positions, which are Rod 9 and Rod 10. When the load is too high, the modified rod will be damaged first compared to the other rods, so Rods 9 and 10 determine the ultimate load capacity of the joist structure.

Table 2 Forces on each abaqus rod before reinforcement and comparison with literature (in KN)

Rods	Abaqus simulation values	In the two-stage method	By the means of computer software
1	- 2.19	- 2.12	- 2.19
2	- 2.19	- 2.12	- 2.19
3	1.41E - 32	0	0
4	2.05	2.12	2.05
5	2.05	2.12	2.05
6	- 1.91	- 2	- 1.92
7	1.29	1.41	1.3
8	1.29	1.41	1.3
9	4.55	4.5	4.55
10	- 4.45	- 4.5	- 4.55
11	- 1.54	- 1.41	- 1.53
12	- 1.54	- 1.41	- 1.53
13	0.57	0.71	0.43
14	0.57	0.71	0.43
15	- 0.41	- 0.5	- 0.31
16	- 0.84	- 0.71	- 0.98
17	- 0.32	- 0.5	- 0.23
18	0.59	0.5	0.69
19	- 0.45	- 0.5	- 0.31
20	- 0.36	- 0.5	- 0.37
21	2.09	2	2.08
22	- 0.84	- 0.71	- 0.98

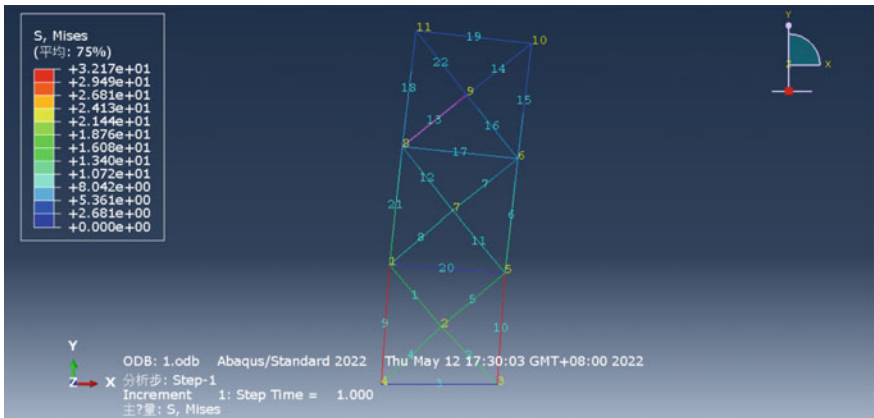


Fig. 2 Force cloud diagram of the truss

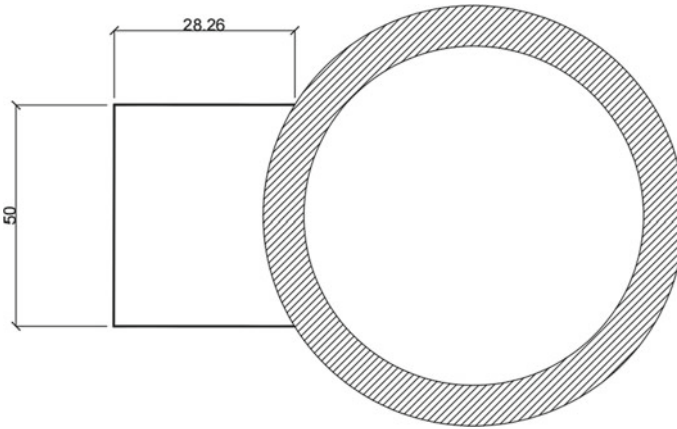


Fig. 3 The shape of truss section reinforcement (in mm) [12]

3.2 Increased Cross-Section Method

Based on the structural form and force characteristics of the joist, the Abaqus was used again to model the joist and to compare the joist before strengthening with the joist after strengthening by the increased section method. Considering the horizontal load and the steel joist forces, the calculation results were analyzed and the final retrofit reinforcement scheme adopted was determined as follows:

Welded channels were added to the left end of Rod9 and the outer end of Rod 10 [12]. The cross-sectional area after strengthening is 1413 mm^2 . The shape of the cross-section is shown in Fig. 3, resulting in model No. 2.

3.3 Specific Research

By Abaqus simulation increasing section method, the performance of the after-reinforced joist has been analyzed. The analysis bases on the original joist shows that the force on the joist Rod 9 and Rod 10 is the largest among all the joists, as shown in Fig. 2, and in case of damage to the joist, Rod 9 and Rod 10 will be damaged before the other rods, so a sub-model is established for the ultimate bearing capacity analysis of these two rods.

Rod 9 sub-model

(1) Original cross-sectional area model

To simulate the unilateral axial tension of the truss in the laboratory, one end of the rod is constrained and the other end is subjected to a boundary displacement of 100 mm at the reference point. The reference point is connected to the upper annular

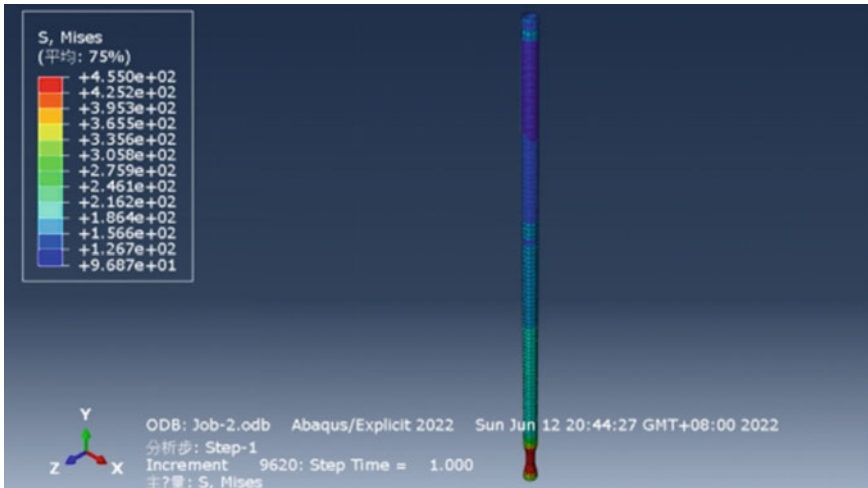


Fig. 4 Stress nephogram of rod 9

surface of the steel pipe by a “coupled” relationship, and to ensure synchronization between the reference point and the upper section when moving, the mesh is finally divided and solved to obtain a stress cloud as shown in Fig. 4.

The force and displacement relationship curve are the output for this stressed rod in the post-processing stage (Fig. 5). The support reaction force RF2 at the unique node reference point is output in the ODB field variable output. In contrast, its displacement U2 is output, and the relationship curve between U2 and RF2 is obtained with the combined command. Its highest point is the limit value of the tensile strength, as shown in Fig. 5. Its highest point value of 128.591 can be obtained by clicking on the vertical coordinate KN. After the highest point, the curve drops because the rod cross-section becomes thinner in tension, and the tensile strength slips.

(2) Double cross-sectional area model

The same method was used to measure the ultimate load-carrying capacity after increasing the section to twice the original section and outputting a displacement versus force graph (Fig. 6). The highest value of 256.149KN was obtained.

Only the cross-sectional dimensions of the member changed between the two modeling processes. The materials, analysis methods, and boundary displacements were the same. It can be seen that the maximum tensile force applied to the Rod increased after the model cross-section was increased to twice its original size, and it can be concluded that the increased cross-section method effectively raised the tensile limit.

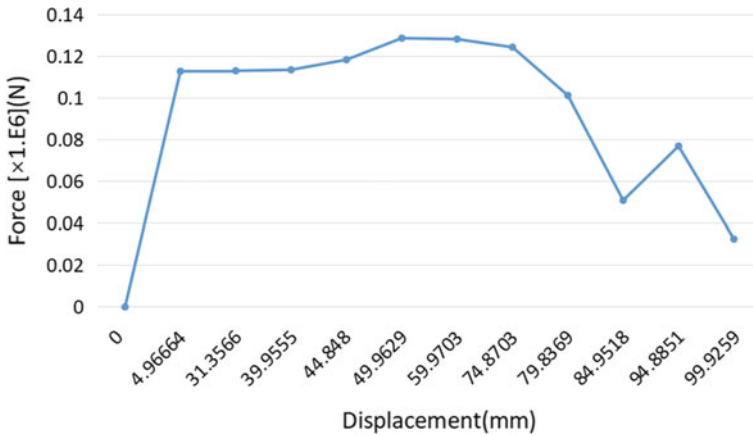


Fig. 5 Relation curve between output force and displacement of stressed rod 9

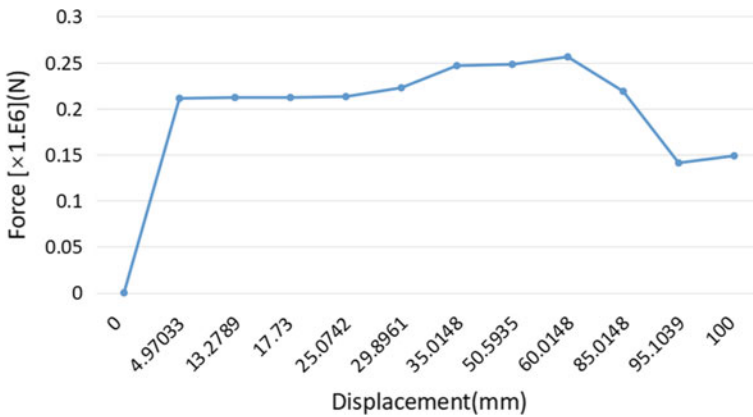


Fig. 6 Relation curve between output force and displacement of stressed rod 9 increased by twice its sectional area

Rod 10 flexure simulation

Rod 10 is in the compression zone, and its damage is characterized by rod instability. The characteristic value of first-order buckling is its ultimate load in buckling through buckling simulation.

(1) Original cross-sectional area model

The rod is modeled with the same material and the same structure as rod 9, with the linear set dynamic buckling set in the analysis step, one end of the rod is fixed, and a unit load-1 is applied to its upper end at the reference point, again the reference point is linked to the upper surface using a “coupled” relationship, the mesh is divided,

and a working analysis is created to obtain its cloud (Fig. 7), with an eigenvalue of 11.812KN.

(2) Double cross-sectional area model

The same double cross-sectional area model was constructed with the same material properties, applied loads, and other conditions, and the cross-section of the member was increased to twice its original size, and the stress cloud shown in Fig. 8 was obtained, with an increase in its characteristic value of 30.398KN.

It is concluded from the two modeling runs that increasing the cross-sectional area, as with the tie, results in a significant rise in the limit of force. Increasing the

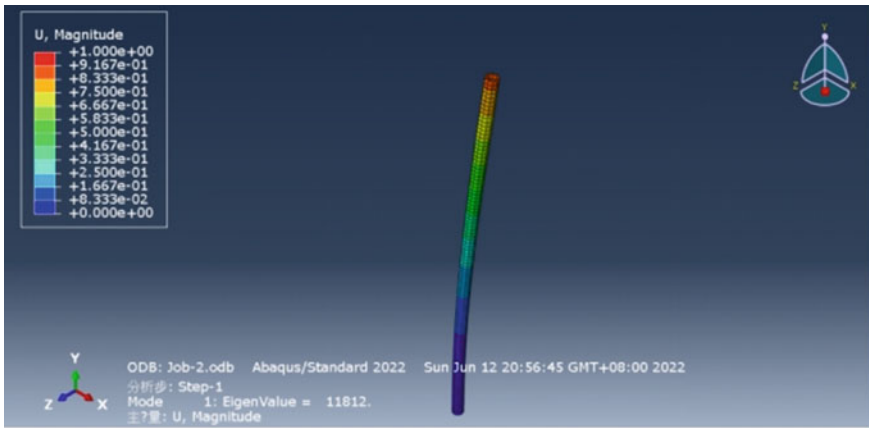


Fig. 7 Stress nephogram of rod 10

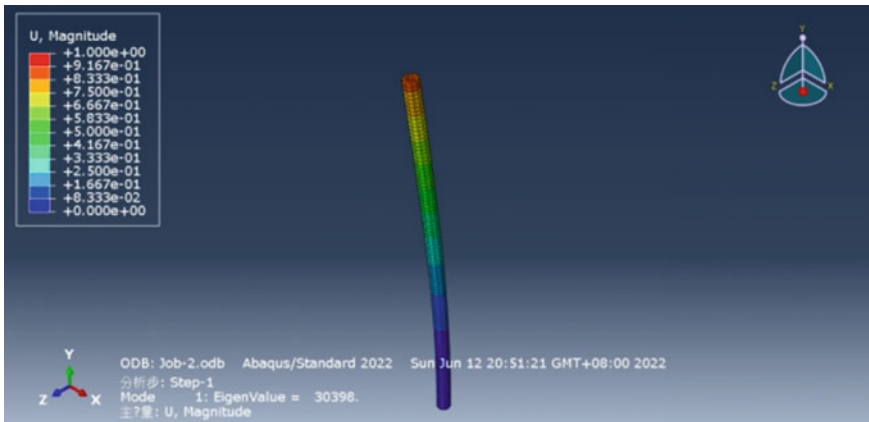


Fig. 8 The stress nephogram of rod 10 increased by twice its sectional area

cross-section, whether it is a tie or a compression Rod, increases the load-carrying capacity.

3.4 Discussion

(1) Comparison of the overall load capacity of the trusses

The test of the ultimate load-carrying capacity of the truss is carried out utilizing a trial method, which is based on the principle of continuously applying loads, the magnitude of the corresponding axial forces is close to the ultimate value measured by the sub-model.

(2) Carrying capacity trial calculation

The modeling adopts 2D modeling, the direction of applied load and the point of action are the same as the original model, and the field outputs the S11 stress value, multiplying the stress value of the most and least stressed rod by its corresponding cross-sectional area of 706.86 mm² to get its axial force, compared with the ultimate load of the sub-model, it can be obtained that its lateral load can be increased between 2.65 ~ 2.66 KN closest to its compressive ultimate load-bearing capacity. Meanwhile, the ultimate load-bearing capacity of the tensile rod is much greater than the ultimate load-bearing capacity of the compressive zone, so the overall force limit of the joist is determined by the rod with the greatest axial compression. The trial calculation results are shown in the Table 3.

(3) Double section truss model trial calculation

The modeling process properties, analysis steps, etc., remain the same, change its cross-sectional area to 1033.77 mm², and carry out trial calculations to find the ultimate load of the truss. Its ultimate load is between 6.8 ~ 6.84 KN. The trial calculation results are shown as Table 4.

According to the experimental results, the compressed rods are damaged first. Then the limit values range from 2.65 to 2.66KN before the lateral resultant load reinforcement in the joist, From the results of compression, their limit values range from 6.8 to 6.84KN after the increase of cross-sectional area, and it can be concluded that the bearing capacity of the joist structure is very obviously improved by the method of increasing the cross-section.

4 Conclusion

In this paper, a model of a super-stationary truss is developed by using numerical simulation. The analysis of strengthening by the increased section method using the Abaqus model increases the ultimate load capacity of the truss and the ultimate

Table 3 Trial calculation results of overall stress limit of the truss

Trial number	Lateral load magnitude (KN)	Force direction	Stress S11 Max/Min (MPa)	The maximum value of axial force (take absolute value) (KN)
①	5	Tension	32.1669	22.7375
		Compression	- 31.4950	22.2626
②	3	Tension	19.3001	13.6425
		Compression	- 18.8970	13.3575
③	2.8	Tension	18.0134	12.7330
		Compression	- 17.6372	12.4670
④	2.7	Tension	17.3701	12.2782
		Compression	- 17.0073	12.0218
⑤	2.6	Tension	16.7268	11.8235
		Compression	- 16.3774	11.5765
⑥	2.65	Tension	17.0484	12.0508
		Compression	- 16.6923	17.7991
⑦	2.66	Tension	17.1128	12.0964
		Compression	- 16.7553	1184.37

load capacity of the corresponding rod has been increased. The strengthening and modification work reduces the maximum axial force of the super-static truss, reduces the maximum deformation, and improves the structural stiffness significantly, thus achieving the purpose of strengthening.

As numerical simulations are used in this paper and no experiments are carried out, a practical comparative study of the model should be carried out in the future to compensate for the limitations of this study.

Table 4 Trial calculation results of overall stress limit of truss by twice its sectional area

Trial number	Lateral load magnitude (KN)	Force direction	Stress S11 Max/Min (MPa)	The maximum value of axial force (take absolute value) (KN)
①	5	Tension	21.9947	22.7374
		Compression	- 21.5353	22.2625
②	6	Tension	26.3936	27.2849
		Compression	- 25.8424	26.7155
③	9	Tension	39.5905	40.9274
		Compression	- 38.7635	40.0725
④	7.5	Tension	32.9921	34.1062
		Compression	- 32.3029	33.3937
⑤	7	Tension	30.7926	31.8320
		Compression	- 30.1484	31.1675
⑥	6.9	Tension	30.3527	31.3800
		Compression	- 29.7187	30.7220
⑦	6.85	Tension	30.1327	31.1500
		Tension	- 29.5033	30.4990
⑧	6.84	Compression	30.0.0888	31.1049
		Tension	- 29.4603	30.4552
⑨	6.8	Compression	29.9128	30.9230
		Tension	- 29.2880	30.2771

References

- Zhang X, Li A, Zhao K (2011) Advances in assessment and retrofitting of building structures. *J Eng Mech* 28(01):1–11+25
- Liu J (2020) Technical progress of building structure appraisal and reinforcement. *J Jiangxi Build Mater* 08:40–42
- Bai P (2021) Structure dynamic performance and reinforcement design of Truss Arch. *J Build Technol Dev* 48:22
- Yang J, Zheng Q, Han M (2013) The inspection and reinforcement of the steel truss of a belt transport corridor. *J. Ind Constr* 43:03
- Liao M, Gao J, Li G et al (2019) Reinforcement of curved stand structure of Wuhan Xinhua Road stadium by the external prestressing method. *Ind Constr* 49:07
- Hayashi K, Ohsaki M (2020) Reinforcement learning and graph embedding for binary truss topology optimization under stress and displacement constraints. *J Front Built Environ* 6:1–15
- Guo X (2021) Exploring the quality defects and reinforcement methods of an existing steel structure plant. *J Popular Stand* 23:14–17+20
- GB 50017-2003 (2003) Code for design of steel structures. China Planning Press, Beijing
- Rebielak J (2021) Two-Stage method applied for approximate calculations of selected types of statically indeterminate trusses. *J Comput Methods* 18(03)
- Zhang G, Zhang N, Ren H (2016) Study of the bonded reinforced concrete column based on ABAQUS. *J Gansu Sci* 28(2):5

11. Cheng J, Cheng B, Qiu H et al (2012) Research development of steel structure reinforcement. *J Steel Constr* 27(11):7
12. Liu Z, Zhang L, Wang T et al. (2014) Research on reinforcement and reconstruction technology of a steel truss bridge. In: Proceedings of the 15th academic conference on space structure

Open Access This chapter is licensed under the terms of the Creative Commons Attribution 4.0 International License (<http://creativecommons.org/licenses/by/4.0/>), which permits use, sharing, adaptation, distribution and reproduction in any medium or format, as long as you give appropriate credit to the original author(s) and the source, provide a link to the Creative Commons license and indicate if changes were made.

The images or other third party material in this chapter are included in the chapter's Creative Commons license, unless indicated otherwise in a credit line to the material. If material is not included in the chapter's Creative Commons license and your intended use is not permitted by statutory regulation or exceeds the permitted use, you will need to obtain permission directly from the copyright holder.



Measurement of Velocity and Particle Size in Shock Wave Area Generated by Experimental Granular Flow Impacting on a Cylinder Based on Image Processing Methods



Jing Xu, Jian Wang, Dongpo Wang, and Zheng Chen

Abstract The measurement of flow velocity and particle size remains an important issue in granular flow dynamics and can provide important basis to better understand the physics in granular material, particularly when it impacts on a structure. In this study, laboratory chute experiments were performed with quartz-glass particle materials to investigate the characteristics of granular shock developed upstream of a cylinder generated by granular flow impacts. A time series of flow images recorded by a camera has been analyzed and processed using the digital image processing methods such as the gray processing, the image binarization, the image corrosion and expansion, and the generative adversarial networks, with a goal of obtaining flow velocity and particle size in the granular shock area. The experimental results reveal that the granular-flow velocity grows with increasing slope angle. The granular shock thickness shows a general increase with the growing number of particles in the shock area, and the number of particles demonstrates an inversely proportional to increasing Froude number, providing a potential method for determining the particle size of dense granular flow. The findings of this study could help to better understand the shock dynamics of granular flow impacting on an obstacle.

Keywords Granular flow · Image processing · Velocity · Particle size

J. Xu · J. Wang · D. Wang · Z. Chen (✉)
State Key Laboratory of Geohazard Prevention and Geoenvironment Protection, Chengdu
University of Technology, Chengdu, China
e-mail: zheng.chen@cdut.edu.cn

J. Xu
e-mail: 1819207598@qq.com

J. Wang
e-mail: jianwang@stu.cdut.edu.cn

D. Wang
e-mail: wangdongpo@cdut.edu.cn

This is a U.S. government work and not under copyright protection in the U.S.; foreign copyright protection may apply 2023

Y. Yang (ed.), *Advances in Frontier Research on Engineering Structures*, Lecture Notes in Civil Engineering 286, https://doi.org/10.1007/978-981-19-8657-4_25

1 Introduction

Geophysical hazardous granular flows such as landslides, debris flows, and rock avalanches commonly occur in mountainous areas, causing massive lives and economic losses each year [7, 6]. Accurate measurement of such granular flows, focusing on some key parameters like flow velocity and particle size, can greatly help disaster prevention and mitigation. It is also an important basis for studying the dynamics between a granular flow and a structure, especially for the design of hazard defense structures [4]. Some measuring methods to extract granular-flow velocity consisted of placing tracer particles in the flows and using image processing methods, including the particle image velocimetry (PIV), the particle tracking velocimetry (PTV), the laser speckle velocimetry (LSV), etc. The traditional PIV technology [1] belongs to the Euler method, which employs laser irradiation to view tracer particles dispersed in the flows, and performs correlation calculation on two adjacent image frames. This method has high calculation accuracy, but its operation is complicated [11, 15]. In contrast, the PTV method belongs to the Lagrangian method [10], calculating the velocity by measuring the length of the particle optical trajectory under an exposure time interval. This method has strong real-time performance and the operation is simple [2], but the accuracy is relatively lower compared to the PIV algorithm. The LSV method is generally applied to dense granular flow. The original pixels of particle are replaced by speckles, and the flow velocity is then determined by using the two adjacent speckle images. Therefore, this method is only suitable for measuring an averaged flow velocity of the directional flow field [12].

With the development of technology, the digital image processing method shows great potential for measuring the granular flows in the laboratory and the field [5, 13]. Image processing technologies are commonly utilized with modern computers to analyze and process flow images, and quickly generate the required images through the use of digital combinations. Digital image processing, in particular, can filter out two-dimensional array pixels, generating the final image that is required by using image compression, image restoration, image transformation, chromaticity reconciliation and some other methods [3].

The aim of this study is to investigate the flow velocity and particle size of dry dense granular flow impacting on an obstacle. First, a small-scale laboratory chute experiments were performed with quartz-glass material. The cameras were used to record images of granular flow moving and impacting on a cylindrical structure. Second, on the basis of the video material recorded during experiments, the grayscale processing, the binarization and other digital image processing technologies were utilized to identify granular-flow velocity. In addition, the generative adversarial network (GAN) for image processing was also used to identify particle size in granular shock area upstream of the obstacle generated when granular flow impacts on the obstacle surface.

2 Methods

2.1 Experimental Set-Up

Laboratory chute experiments were performed with quartz-glass particles impacting on a cylindrical obstacle varying in radius R_c [5], using an experimental chute facility at the Institute of Mountain Hazards and Environment, Chinese Academy of Sciences, Chengdu, China. The experimental chute system consists of three functional parts, including the top start-up area, the flowing reach in the middle, and the bottom collection box. The top of the chute is a hopper that is made of plexiglass, which is 0.6 m in length, 0.8 m in width and 0.4 m in height (a total volume of 0.192 m³). The total length of the flowing area of the chute system with a rectangular cross-section is 2.5 m, the channel width is 0.8 m, and the transparent side walls are 0.35 m in height, all of which are made of plexiglass material. A hollow cylindrical barrier that is made of aluminum (Fig. 1a), 280 mm high and 10 mm thick, with a radius R_c ranging from 60 to 140 mm, was installed in the middle of the flow reach and 780 mm away from the chute outlet.

During the experiment, the first step is to store the granular materials in the top hopper, and a gate system controls the flow rate of the particles into the chute channel

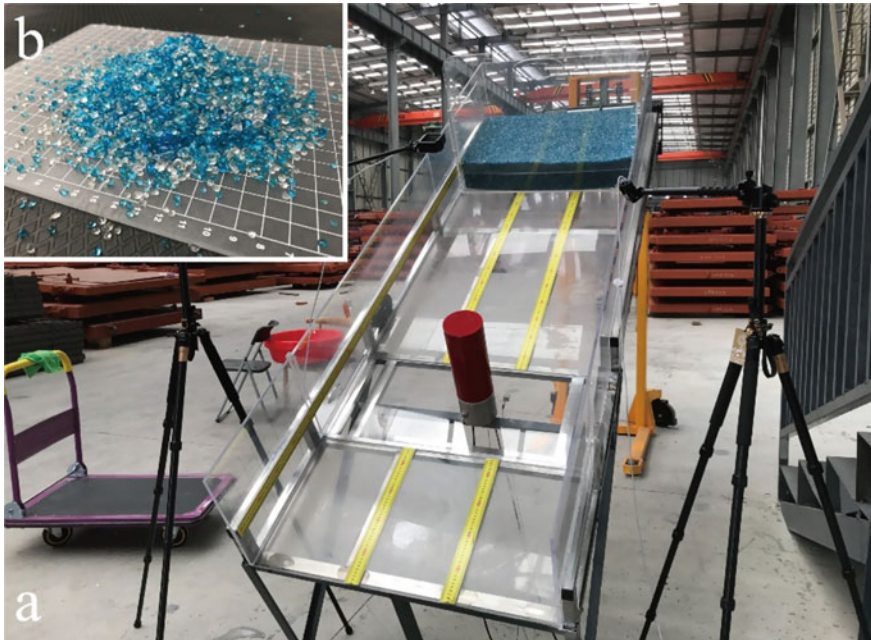


Fig. 1 a Experimental set-up of the chute facility using for granular flow test. b Quartz-glass grains used in the experiments

with an inclination angle θ , and the granular flow continues to flow down and impact on the cylinder. The cameras (GOPRO) are installed just above and on the side of the chute to obtain experimental videos for further analysis, with a maximum resolution of 4 k and a frame rate of 240 fps.

2.2 Granular Material

The granular material used in this study was quartz-glass particles as mentioned above, with particle shape approximately ellipsoid, an average diameter ranging from 1.7 mm to 4.0 mm, and the colored in blue and transparent (see Fig. 1b). During the test, the initial granular mass was 100 kg and the density was tested as 1646 kg/m^3 . Find more information about the granular material (e.g. internal friction angle, cohesion and friction between the particles and the chute bed) used for impact experiments in Chen et al. [5]. For different experimental runs, they were controlled by the parameters θ and R_c .

2.3 Image Processing Methods

In this study, the image processing methods used for the analysis of granular-flow velocity and particle size include the grayscale processing, the image binarization, and the image erosion and dilation. The flow chart of the image processing is presented in Fig. 2.

The grayscale processing of the experimental images refers to the process of converting a color image into a so-called grayscale image. The color of each pixel of a color image is determined by three monochromatic components, namely, red (R), green (G), and blue (B). Thus, such a pixel has a color variation range of more than 16 million (255^3). The grayscale image is a special color image with the same three components R, G, and B, and the variation range of each pixel is 255. Grayscale images, like the color images, reflect the overall and local characteristics and distribution of luminance and chromaticity, but they can speed up calculations.

A threshold value Q (gray value) is used here for the image binarization. Comparing the gray value Q_1 with Q at the target, if $Q_1 < Q$, the value of Q_1 becomes zero; otherwise, if $Q_1 > Q$, then the value of Q equals to 255. By selecting an appropriate threshold to reflect the contour of the desired image, the gray value of the image after binarization is only zero or 255, making the contour features of the image more obvious and simplifying the image.

Image erosion and dilation are the most basic morphological operators in mathematical morphology. The following Eqs. (1) and (2) are used to represent the image erosion and dilation techniques, respectively:

$$A \ominus B = \{z | (B)_z \cap A^c = \emptyset\} \quad (1)$$

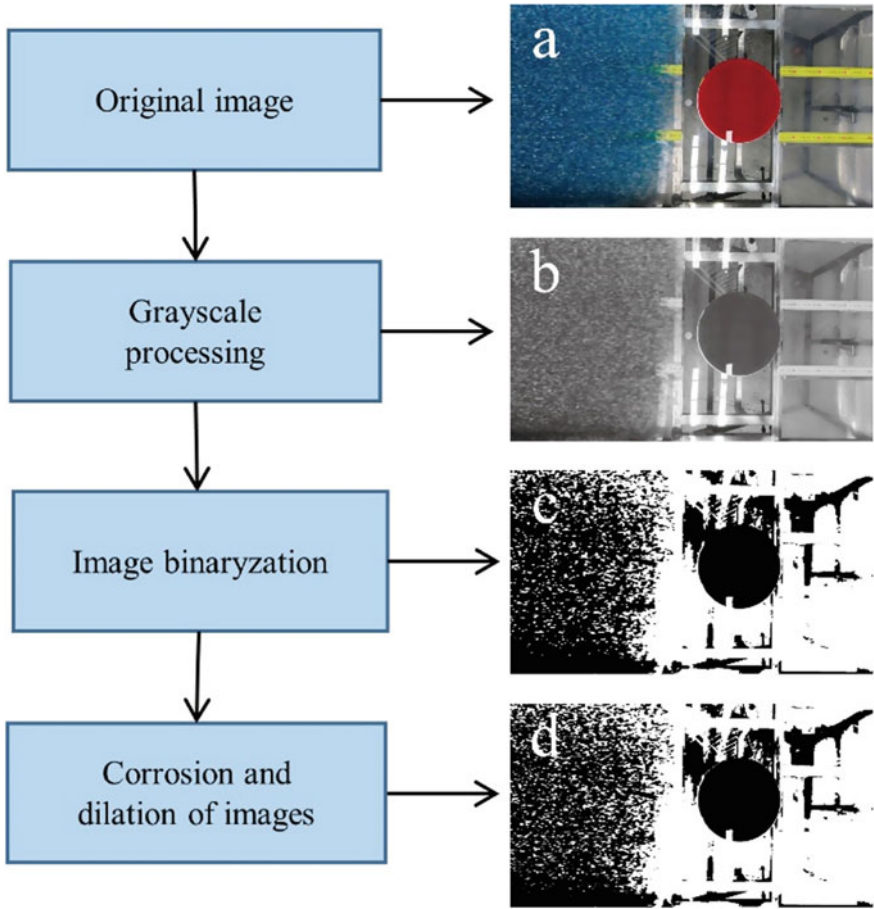


Fig. 2 The image processing of granular flow using the grayscale processing, the image binarization, and the image erosion and dilation

where $A \ominus B$ indicates the corrosion of B on A ; z is the set of all points; A^c is the complement of set A ; \emptyset represents the empty set.

$$A \oplus B = \left\{ z \mid \left[\left(\hat{B} \right)_z \cap A \right] \subseteq A \right\} \tag{2}$$

where $A \oplus B$ is the inflation of B to A ; \hat{B} is the image of B about the origin.

Image erosion and expansion technologies can quickly extract the outline of granular flow for each image frame. The specific operation processes are (1) select a convolution kernel of an appropriate size, and (2) perform image erosion and expansion processing on the binarized image. These processes ... can remove some noises,

however, considering that the image is generally compressed, which results in a restored original shape.

2.4 Velocity Measurement Based on Moving Images

Based on the scale mark (with an accuracy of 1 mm) on the chute bed, the movement velocity of granular flow can be calculated, using the image frames captured by the camera that is set in the overhead view. In this paper, the digital image processing method is utilized to obtain an envelope of the granular-flow head, as presented by the red line in Fig. 3. It has been observed that the front part of granular flow generally shows the lighter color than that of the middle part, indicating some saltation particles in the front of granular flow [5]. Therefore, these saltation particles are not considered for the determination of the flow head envelope. Consequently, the determined envelope can be integrated to obtain a coverage area of granular-flow head, and the mean line of the flow head (see the blue dotted line in Fig. 3) is calculated according to the principle of area equivalence, as shown in Eq. (3).

$$\bar{X}_h = \frac{1}{W} \int_L^R E_h dy \quad (3)$$

where \bar{X}_h is the coordinate of the mean line of the granular flow head; L and R are the upper and lower limits of the integral determined by the true left and true right boundaries of the chute, respectively; E_h represents the envelope of the flow head; W is the width of the chute.

The transport velocity u_1 can be then determined as a ratio of the changes of \bar{X}_h between image frames (three frames were selected in this study) to the corresponding time interval, as seen in Eq. (4).

$$u_1 = \frac{1}{m\Delta t} \sum_m^k \left\| \bar{X}_{h,k}^t - \bar{X}_{h,k}^{t-\Delta t} \right\| \quad (4)$$

where $\bar{X}_{h,k}^t$ is the coordinate value at time t ; $k = 1, 2$; We only considered to use the last three frames of images before impacting, so $m = 2$; $\Delta t = 1/60$ s.

2.5 Particle Identification Using the Image Deblurring Method

Granular shock wave is formed (with a thickness of standoff distance $D_{standoff}$ [6]) due to the disturbance of the cylindrical obstacle to the granular-flow field. In this

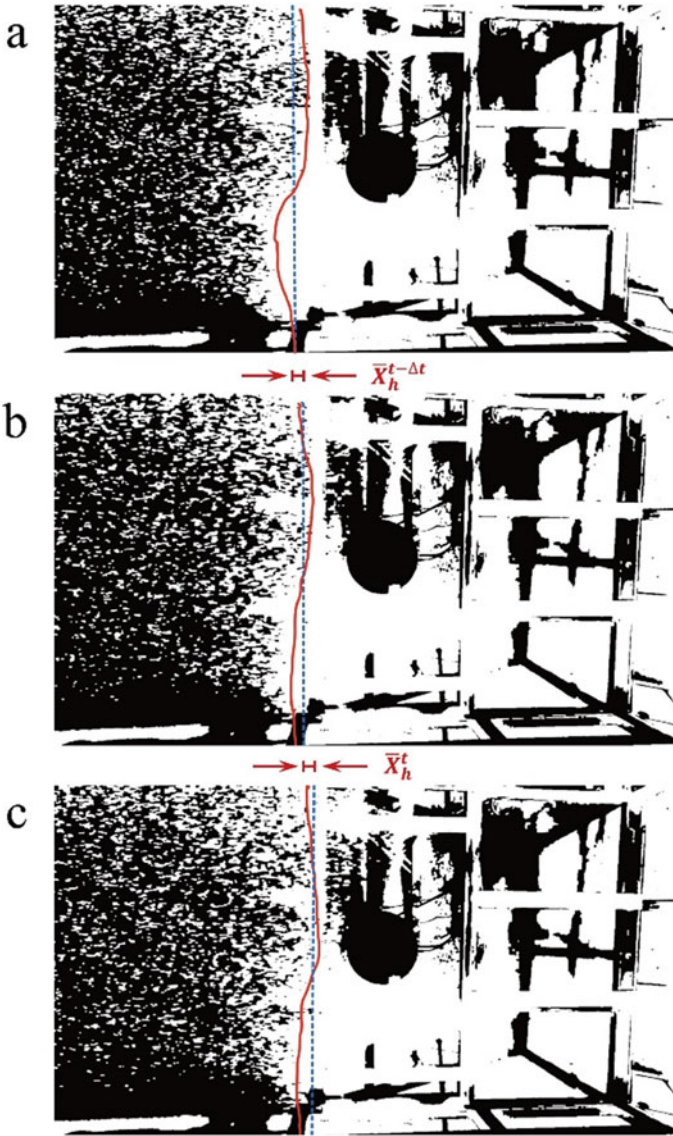


Fig. 3 Measurement of the velocity using a time series of experimental images from an overhead view of the granular flow before impacting on the cylinder

study, the changes of the shock thickness at the steady state with changing obstacle size are also determined by analyzing the video frames, and the numbers particles within the shock influencing area in the flow direction is counted using the image processing method.

The granular flow has some saltation particles in the front during the movement and impact with the obstacle, leading to a blurring of images. Hence, we consider to use the generative adversarial networks (GAN) to make the moving images clearer, so as to better identify the particles. The GAN method can be expressed as [8]:

$$\min_G \max_D V(D, G) = E_{x \sim P_{data}(x)} [\log(D(x))] + E_{z \sim P_Z(z)} [\log(1 - D(G(z)))] \quad (5)$$

where D is the discriminator, G is the generator, e is the expectation, X is the real data, P_{data} is the data distribution of the generator, z is the random noise, P_Z is the a priori probability of the input noise, and the logarithmic function “log” has no specific base.

When using the real data as input, the closer the value of $D(x)$ is to one, the better the discriminator. While if the input is the generated data, it is expected that the closer the $D(G(z))$ value is to zero, the discriminator should be better. The two terms are combined to optimize the objective function of the discriminator. The larger the value of $D(G(z))$ when the generated data $G(z)$ is input to the discriminator, the better the generator, indicating that the generated data is closer to the real data and minimizing the generator objective function [9]. Figure 4 shows the processed images of granular shock generated by the cylinder. In this study, particle number N_p refers to only the number of surface particles arranged in the shock influencing area along the flow direction, as seen in Fig. 4c.

3 Results

According to the above-mentioned methods, the image processing programs used for our granular flow experiments were conducted with PYTHON [14], and in the following the summary statistics of calculated flow velocity u_1 and counting of particles are presented under different experimental conditions.

3.1 Granular Flow Velocity

The granular flow velocity u_1 increases strongly with increasing slope angle θ ranging from 30° to 38° (see Fig. 5). In addition, the variability of the measured velocity also grows with increasing θ .

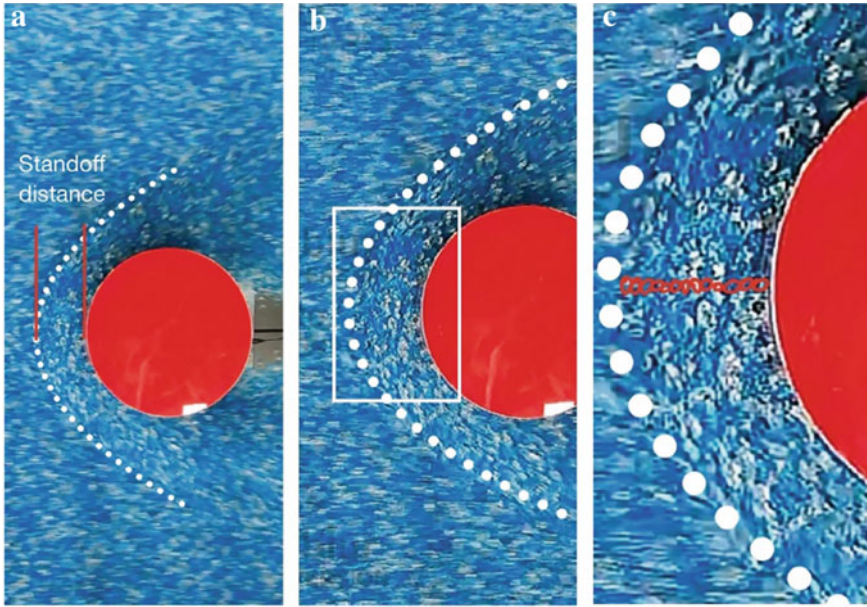
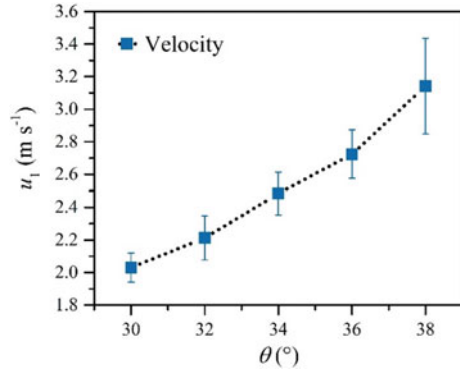


Fig. 4 a Original image of a granular shock. b Image after the GAN processing. c Counting of particles in granular shock area

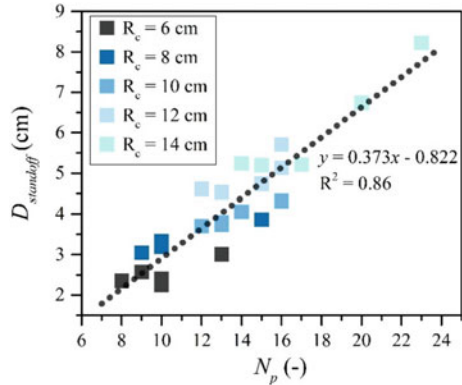
Fig. 5 Granular flow velocity u_1 measured by image processing method as a function of slope angle θ



3.2 Particle Size Identification

According to the results of linear regression analysis, the R^2 value of the linear model between the standoff distance $D_{standoff}$ and particle number N_p is 0.86, which means that the thickness of a granular shock wave increases nearly linearly with increasing number of particles N_p in the shock area for all obstacle sizes R_c (Fig. 6). The obstacle with the larger diameter tends to generate the greater value of $D_{standoff}$.

Fig. 6 Relationship between $D_{standoff}$ and particle number N_p



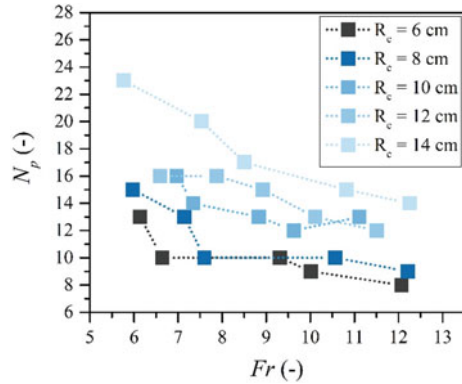
4 Discussions

The measured granular-flow velocity u_1 using the image processing method is growing linearly with increasing slope angle θ (see Fig. 5), which is reasonable. This is due to the fact that the increased Y-component (flow direction) gravity acceleration generated by the greater slope angle accelerates granular flows, hence increasing the particle velocity. The variation of flow velocity for each slope angle θ is mainly considered to be caused by saltation particles in the front of granular flows on the chute bed. Relatively high agreement is observed between the calculated front envelope for the early flow stage and the mean line of the granular-flow head. However, the difference between the two increases with the development of granular flow. This is likely due to that the more saltating particles are produced during the acceleration process of the granular flow. Nevertheless, the image processing method still shows potential good applications for measuring granular-flow velocity. It is also worth noting that this method is possibly only suitable for measuring the surface velocity of granular flow. The velocity and displacement distance of the surface particles are considerably larger than those of the middle and bottom particles due to friction, also contributing to a variability in recognizing an envelope of the flow head.

The thickness of granular shock wave generated upstream of the cylinder is characterized as the value of the standoff distance $D_{standoff}$, demonstrating a positive relationship with the number of particles N_p in the shock area, as seen in Fig. 6. It can be calculated that the averaged particle size is about 3 mm, while the particle size range used in our experiments ranges from 1.7 mm to 4.0 mm, showing a good agreement. Note that both the standoff distance and the particle number were measured at the steady state of granular flow for each experimental run.

The granular shock thickness or the standoff distance can be used to characterize the shock intensity [5], demonstrating an inversely proportional to increasing Fr . Here we investigated the relationship between the number of particles N_p in the shock area and Fr , as shown in Fig. 7. The value of N_p decreases with increasing Froude number Fr ranging from about 6–12.5, trending to change less and approaching to

Fig. 7 Counting of particle number N_p as a function of Froude number Fr



a limit varying with obstacle size. This shows the effect of particle size on granular shock thickness possibly due to that a force chain is formed at the steady state, also providing a potential way to measure particle size of dense granular flow.

5 Conclusions

In this paper, controlled laboratory experiments were performed to study characteristics of granular flow moving and impacting on a cylinder varying in size. The experimental images were obtained with cameras and were analyzed through some image processing methods such as the grayscale processing, the image binarization, and the image erosion and expansion. Key parameters including the granular-flow velocity and particle number in the granular shock area were obtained.

The measured granular-flow velocity and its variability obtained using the image processing method increases with increasing slope angle. The calculated envelope shows a good agreement with the mean front line of granular flow head at the early stage. The thickness of granular shock wave formed upstream of the obstacle demonstrates a positive relationship with the number of particles in the granular shock area. Furthermore, this particle number decreases nonlinearly with increasing Froude number, approaching to a limit value. This finding could be helpful for the analysis and particle size identification of dense granular flow when impacting on an obstacle.

References

1. Adrian RJ (2005) Twenty years of particle image velocimetry. *Exp Fluids* 39(2):159–169
2. Baldassarre A, Delucia M, Nesi P, Rossi F (2001) A vision-based particle tracking velocimetry. *Real-Time Imaging* 7(2):145–158

3. Chen Y (2021) Innovation and practice of dark field image processing algorithm based on MATLAB—comment on digital image processing technology and application. *Sci Technol Manage Res* 41(21):231 (in Chinese)
4. Chen Z, He S, Shen W, Wang D (2022) Effects of defense-structure system for bridge piers on two-phase debris flow wakes. *Acta Geotech* 17(5):1645–1665
5. Chen Z, Rickenmann D, Zhang Y, He S (2021) Effects of obstacle's curvature on shock dynamics of gravity-driven granular flows impacting a circular cylinder. *Eng Geol* 293:106343
6. Cui X, Gray JMNT (2013) Gravity-driven granular free-surface flow around a circular cylinder. *J Fluid Mech* 720:314–337
7. Froude MJ, Petley DN (2018) Global fatal landslide occurrence from 2004 to 2016. *Nat Hazards Earth Syst Sci* 18(8):2161–2181
8. Jia F, Zhang Y, Xie B (2021) Real-time video image deblurring model based on lightweight GAN. *Comput Syst Appl* 30(10):31–39 (in Chinese)
9. Li Y, Xu Q, Li K (2020) New method of residual dense generative adversarial networks for image restoration. *J Chin Comput Syst* 41(04):830–836 (in Chinese)
10. Liu M, Yang Z, Ji B, Huai W, Tang H (2022) Flow dynamics in lateral vegetation cavities constructed by an array of emergent vegetation patches along the open-channel bank. *Phys Fluids* 34(3):035122
11. Lueptow RM, Akonur A, Shinbrot T (2000) PIV for granular flows. *Exp Fluids* 28(2):183–186
12. Ma S, Yang H, Li R, Sheng X, Zheng G, Wang S, Yao X (2016) Study on the mechanism of the pattern transition of granular flow based on the technique dynamic speckle. *Opt Instrum* 38(2):8 (in Chinese)
13. Peng S, Ke L, Zheng T, Xu J (2021) Particle distribution characteristics of rock avalanche and the interaction between rock avalanche and houses based on image recognition. *Bull Geol Sci Technol* 40(06):226–235 (in Chinese)
14. Van Rossum G (1995) Python tutorial. In: Technical Report CS-R9526, Centrum voor Wiskunde en Informatica (CWI), Amsterdam
15. Westerweel J (1997) Fundamentals of digital particle image velocimetry. *Measur Sci Technol* 8(12):1379–1392

Open Access This chapter is licensed under the terms of the Creative Commons Attribution 4.0 International License (<http://creativecommons.org/licenses/by/4.0/>), which permits use, sharing, adaptation, distribution and reproduction in any medium or format, as long as you give appropriate credit to the original author(s) and the source, provide a link to the Creative Commons license and indicate if changes were made.

The images or other third party material in this chapter are included in the chapter's Creative Commons license, unless indicated otherwise in a credit line to the material. If material is not included in the chapter's Creative Commons license and your intended use is not permitted by statutory regulation or exceeds the permitted use, you will need to obtain permission directly from the copyright holder.



Analysis on Fatigue Crack of Orthotropic Steel Bridge Decks



Rui Ma, Peng Dong, and Zigang Xv

Abstract Through the detection of the steel structure bridge for 7 years, the main distribution of cracks in steel box girder of steel structure bridge was presented. Through the numerical analysis of the steel box girder of steel structure bridge, the stress distribution of the diaphragms was obtained. The result of detection and the numerical analysis was compared, and showed that the cracks mainly appeared in the welding parts and the arc notch of the diaphragms. The cracks at the welding part mainly came from the welding defects. And the cracks at the arc notch of the diaphragms were due to the stress concentration.

Keywords Steel structure bridge · Diaphragm · Fatigue crack

1 Introduction

Steel box girders are made of top plate, bottom plate, web plate, diaphragm, longitudinal spacer and stiffening ribs connected by full welding. The structure welded by top plate, longitudinal ribs and diaphragm is called orthotropic steel bridge panel. The longitudinal ribs are divided into two structural forms, including mouth ribs and closed ribs. According to statistics, the longitudinal ribs of orthotropic steel bridge panels used in steel box girders in recent years are mostly in the form of closed ribs, especially U-shaped ribs [1].

At the intersection of the U-shaped rib and the diaphragm, the diaphragm is perforated, and the U-shaped rib continuously passes through the diaphragm. All the joints are welded, including the joints between the diaphragm and the top plate, the U-shaped rib and the diaphragm, the U-shaped rib and the top plate. In order to release the vertical deformation of the U-shaped rib, a certain gap is left between the bottom surface of the U-shaped rib and the diaphragm. The complex stress at the

R. Ma · P. Dong (✉)

Research Institute of Highway Ministry of Transport, Beijing 100088, China

e-mail: 1219567292@qq.com

Z. Xv

National Engineering Laboratory of Bridge Safety and Technology, Beijing 100088, China

© Crown 2023

Y. Yang (ed.), *Advances in Frontier Research on Engineering Structures*, Lecture Notes in Civil Engineering 286, https://doi.org/10.1007/978-981-19-8657-4_26

287

bottom of the U-shaped rib is avoided, the out plane deformation of the diaphragm is reduced. And the stress distribution of the entire orthotropic steel deck is more clear. [2, 3].

The damages of steel bridges due to insufficient strength rarely occur, but the fatigue damages are common appeared to cause failures of structures. Fatigue cracking is an important and direct manifestation of fatigue damage. Crack inspection is also an important indicator to measure the technical condition of a bridge when following up on steel bridges during operation.

2 Crack Disease Inspection

After a steel bridge is put into operation, the overall performance of the bridge will gradually deteriorate as the service time grows, so regular inspection of the bridge is required. The appearance of bridge defects will directly affect the safety and durability of steel bridges, of which cracking is one of the main forms of steel bridge defects.

From 2012 to 2018, a seven-year follow-up inspection was conducted on a large-span suspension bridge in China. The bridge had a stiffened steel box girder with a welded connection for the main girder. Cracking, as one of the important indicators of the operational condition of steel bridges, was statistically collated for each inspection. According to the occurrence of cracks, all cracks of the steel box girders were classified into 5 categories: (I) cracks at the joint between U-shaped ribs and top plates; (II) cracks at the intersection between the diaphragm and U-shaped ribs (lower root welding areas); (III) cracks at the curved notch of the diaphragm; (IV) cracks at the butt joint of U-shaped ribs; (V) cracks at the joints between the diaphragm, U-shaped ribs and the top plate (upper welding area of the diaphragm).

The addition of the five types of cracks is shown in Table 1, and the development of the original cracks is shown in Table 2 and Fig. 1.

Based on the results of the bridge's 7-years follow-up inspection, the following conclusions can be drawn:

- (1) The number of IV cracks was the lowest and the extension was not obvious. The number of II cracks was the largest. The number of cracks in the steel box

Table 1 2012–2018 table of new cracks

	Before 2012	2013	2014	2015	2016	2017	2018	Total
I cracks	58	18	19	5	35	8	6	149
II cracks	125	61	75	62	11	26	17	377
III cracks	106	61	52	15	3	0	3	240
IV cracks	13	0	0	2	0	0	0	15
V cracks	50	24	25	12	2	11	16	140

Table 2 The development of the original cracks

	2013	2014	2015	2016	2017	2018
I cracks	0	6	0	18	5	11
II cracks	32	26	14	33	2	53
III cracks	26	35	112	56	31	47
IV cracks	0	0	0	0	0	0
V cracks	0	0	0	2	2	17

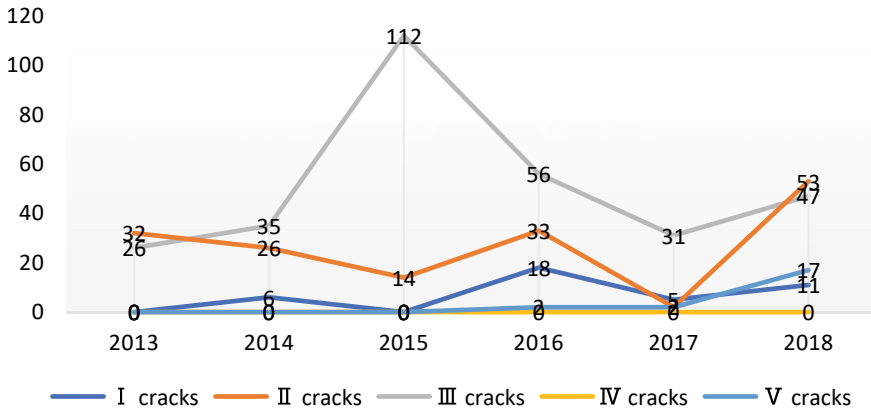


Fig. 1 The development of the original cracks (from 2013–2018)

girder was increased with the growth of service time, and the cracks had been extended.

- (2) According to the crack disease inspection results, the crack occurrence sites can be summarized into two categories, one is the welding site, and the other is the curved cutout of the cross-sectional plate (non-welding site). Due to the limitation of structural deformation by the welding connection method and the residual stresses and welding defects that easily appear during the welding process, the welded parts of the steel box girder are prone to fatigue cracking.
- (3) In order to determine the reason for the ease of fatigue cracking at the curved cutout (non-welded part) of the diaphragm, further research and analysis using numerical analysis methods is required.

3 Numerical Analysis of the Diaphragm

3.1 Finite Element Model

The numerical analysis model was established using finite elements to analyze the forces on orthotropic anisotropic steel bridge panels.

According to the literature [2, 4], the structural systems of orthotropic steel bridge panels can be divided into three types, and the stresses in the second and third systems are usually the main factors causing fatigue problems in orthotropic steel bridge panels.

In order to obtain the stress state of the diaphragm of the steel box girder, a finite element numerical model was established using the second system consisting of U-shaped ribs, diaphragm and top plate, and the relevant parameters of the numerical model were as follows [5–8].

Bridge deck (top plate): the top plate was 15.6 m (i.e. the spacing between 6 diaphragms). 3 U-shaped ribs were a calculation unit (150 mm + 300 × 5 mm + 150 mm). 5 calculation units were the width of the top plate, i.e. 9 m, and the thickness of the bridge deck plate was 16 mm.

U-shaped ribs: the upper part was 300 mm wide, the lower part was 180 mm wide, the rib thickness was 8 mm, the U-shaped rib spacing was 300 mm, the length was 15.6 m, the same as the length of the top plate.

The diaphragm: the width of the diaphragm was 9 m, the same width of the top plate. The height was 1000 mm, the thickness was 12 mm, the spacing of the diaphragm was 3120 mm, the diaphragm in the corresponding part with the bottom of the U-shaped ribs into an arc cut, the bottom of the U-shaped ribs and the diaphragm to leave a gap of 25 mm.

The diaphragm acted as a vertical support for the top plate and U-shaped ribs. The diaphragm connected the top plate, U-shaped ribs and the bottom plate. The 4-node shell unit with 6° of freedom at each node was used in the calculation, the effect of large deformation effect was considered.

The boundary: all degrees of the diaphragm were fixed. The both sides of the diaphragm limited the displacement in the X and Y directions only.

The fatigue load model of *Technical Specification for Design and Construction of Orthotropic Steel Bridge Deck of Highway Steel Bridge* was used. The transverse distance of the two wheel loads was 2 m. A wheel load was 120 KN, and the load area was 0.6 × 0.2 m. In order to reflect the stress state of the boundary, the loads were applied on the top plate directly to the position of the diaphragm, symmetrically distributed in the centerline of the top panel (Fig. 2).

In the paper, the force characteristic of the diaphragm was focused on. In order to improve the computational efficiency, different meshing accuracy was used for the top plate, the U-shaped ribs and the diaphragms when dividing the cells. The top plate had a rectangular shape, so the coarsest cell mesh was used. The U-shaped ribs are curved, so a slightly more precise cell mesh was used than that of the top

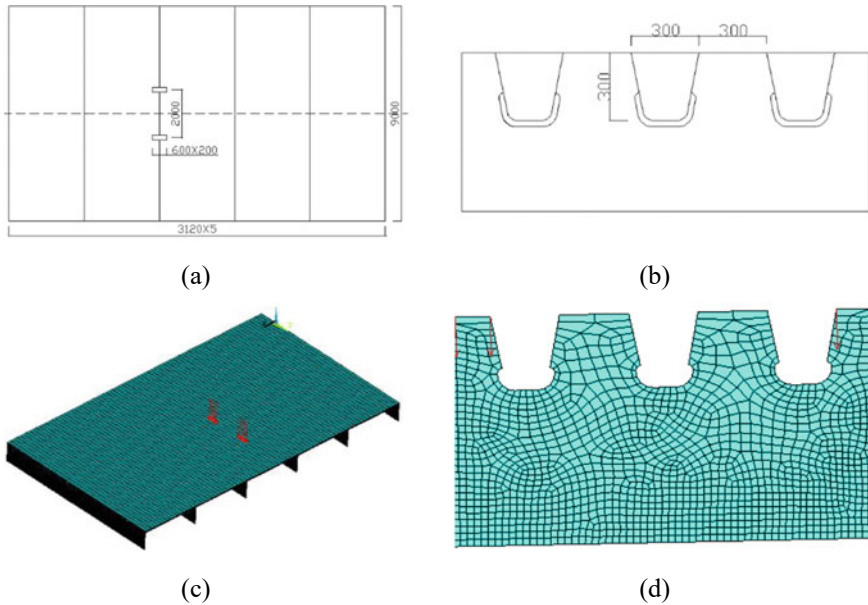


Fig. 2 Schematic diagram of the calculation model (mm)

plate. The arc cut resulted in an irregular shape of the diaphragms, so the diaphragms required a finer grid of cells.

3.2 Finite Element Analysis Results

From the numerical analysis results, the stress state of diaphragms is extracted (Fig. 3). The top part of the diaphragms connected to the top plate is directly transferred the load to the diaphragms. The stress is higher at both ends than at the middle part. The left and the right sides of the cutout are subjected to the load transferred from the U-shaped ribs, and the stress is higher due to the influence of the welded connection, which restricts the out-of-plane displacement of the diaphragms, and the curved cutout is the largest part of the diaphragms, where there is an obvious stress concentration.

The above numerical analysis results are consistent with the fatigue cracks of the diaphragms in the second part of the bridge tracking inspection results. Therefore, in addition to fatigue cracking in the welding area, the curved cutout area of the spacer is also susceptible to fatigue cracking due to the existence of the stress concentration phenomenon.

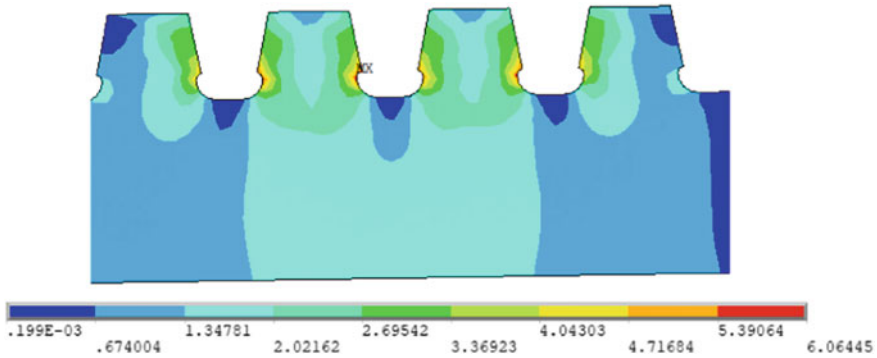


Fig. 3 Stress distribution diagram of diaphragms

4 Conclusions

In this paper, the main distribution parts and distribution rules of steel box girder cracks in steel bridges were obtained through a continuous 7-year follow-up inspection of large span steel bridges during the operation period, and according to the results of the follow-up inspection, the crack-prone parts of steel box girder were the welding parts of steel box girder and the diaphragms cutout.

The numerical analysis of the steel diaphragms was obtained, and the results showed that the diaphragms had obvious stress concentration phenomenon, which was the main cause of fatigue cracks at the diaphragms cutout, and the numerical analysis results were consistent with the bridge inspection results.

Acknowledgements This work was financially supported by Central Public-Interest Scientific Institution Basic Research Fund (2021–9049a and 2021–9049b) and Open Project of National Engineering Laboratory of Bridge Safety and Technology (Beijing).

References

1. Zhu J (2020) Fatigue performance analysis of orthotropic steel bridge deck weld of rail-highway bridge. Nanjing Forestry University 06
2. Tong L, Shen Z, Chen Z (1998) Structural analysis of orthotropic steel bridge deck during fatigue checking. Shanghai Mech 19(3):204–212
3. Ke L, Lin J, Li C (2017) Fatigue performance and structural optimization of steel box girder diaphragm with arc notch. Bridge Constr 47(5):18–23
4. Liu X, Tao X, Zhang Y (2010) Theoretical analysis and research on orthotropic steel bridge deck system and structure. In: Bridge steel structure branch of china steel structure association 274–278
5. Yu H, Zhang N (2021) Finite element analysis of structural stress of orthotropic steel bridge deck system. Sichuan Archit 12:187–193

6. Tao X, Liu X, Zhang Y (2020) Research on stress characteristics of orthotropic steel bridge deck. *Steel Struct.* 7:12–14
7. Du B, Xu Z, Zhou W, Zhong Z (2022) *Journal of Chongqing Jiaotong University (Natural Science edition)* 1:59–66
8. Lv Z, Xu J, Qiang X, Wang X (2021) *Structural Engineering* 12:163–171 (in Chinese)

Open Access This chapter is licensed under the terms of the Creative Commons Attribution 4.0 International License (<http://creativecommons.org/licenses/by/4.0/>), which permits use, sharing, adaptation, distribution and reproduction in any medium or format, as long as you give appropriate credit to the original author(s) and the source, provide a link to the Creative Commons license and indicate if changes were made.

The images or other third party material in this chapter are included in the chapter's Creative Commons license, unless indicated otherwise in a credit line to the material. If material is not included in the chapter's Creative Commons license and your intended use is not permitted by statutory regulation or exceeds the permitted use, you will need to obtain permission directly from the copyright holder.



Research on Mechanical Properties of Steel Shell Concrete Immersed Tube Shear Connectors



Guoping Xu, Qingfei Huang, Shenyou Song, Hai Ji, Bin Deng, and Tian Song

Abstract Structural designs of shear connector in immersed tunnel is one of the most significant key technical problems in tunnel designing. According to investigations conducted in Shenzhong Link project, this paper combined numerical simulation methods and experimental verifications and to research effects of shear connector void, stress state, and opening holes on performances of steel–concrete connectors, and also discussed differences of shear slip curves under the influence of factors above, as well as impacts on bearing capacities and stiffnesses of connectors. Through numerical simulations of void and non-void connectors by finite element method, patterns of concrete stress, connector behaviors under tension and compression and shear stresses were analyzed respectively. Additionally, reductions of bearing capacity and stiffness caused by voids and openings which were controlled as variables were discussed. Furthermore, a calculation formula of shear connector bearing capacity is proposed which is in consistent with experimental verifications with considerations of void, stress state and opening. Researches in this paper could provide knowledge for reasonable structural designs of structural connectors in future immersed tunnel engineering construction.

G. Xu · Q. Huang · H. Ji · B. Deng · T. Song
CCCC Highway Consultants Co. Ltd, Beijing, China
e-mail: xuguoping@hpdi.com.cn

Q. Huang
e-mail: huangqingfei@hpdi.com.cn

H. Ji
e-mail: jihai@hpdi.com.cn

B. Deng
e-mail: dengbin@hpdi.com.cn

T. Song
e-mail: tian.song12@foxmail.com

S. Song (✉)
Shenzhong Link Management Center, Zhongshan, China
e-mail: 919962750@qq.com

Keywords Shear connection · Connection type · Finite element analysis · Failure modes · Shear capacity

1 Introduction

With the increasing demand of submarine tunnels in transportation, the role of immersed tunnels has gradually become significantly important. Engineering challenges of immersed tunnels include large back-silting, high water pressure, complex geological conditions, super-long longitudinal span and super-wide cross-section. Long length of variable-section curved pipe sections, and types of immersed tunnel and the longitudinal structural system have become the key technical issues in tunnel construction [9, 10, 16]. The optimized structural design of connectors can significantly improve bonding between ribs and surrounding concrete to improve bearing conditions.

In recent years, many scholars have researched mechanical properties of steel–concrete composite connectors, and proposed many types of shear connectors [1, 2, 6, 11]. A flexural test [14] used a steel–concrete composite beam, and its result showed that the composite structure had better elasticity, and also performed better under the condition of large deformation. Structural failure was usually caused by yielding and tearing of flange plate and web. A paper researching shear connectors [5] indicated that performances of shear connectors by evaluating the influences of thickness, size, number and loading conditions of connectors would lead to changing patterns of bearing capacities of different structural designs. According to a flexural loading tests report [7] on thin-walled steel–concrete composite structure with bend-up bars and steel studs, bending capacity of steel–concrete composite structure was significantly higher than the reinforced concrete beams. The shear resistances of the different designs differs significantly. According to paper researching U-shaped steel–concrete composite members [17], bearing mechanisms would be impacted by different shear-span ratios, height-to-thickness ratios, connector spacings, and wing plate thicknesses. Accordingly, the bearing capacity, ductility of each specimen and their shear force transfer model were investigated and established. Another research [3] compared and contrasted the failure modes of connectors with different thicknesses, studs and spacings, and obtained respective effects on the shear performance of composite structures. Additionally, they also proposed a new shear strength calculation method of connectors with more approachable calculation theory for the shear bearing capacity. One published paper [13] indicated the shear mechanical properties of short steel bar connectors based on static push-out loading tests. Results show that failure modes of composite members could be generally divided into two categories. The bearing capacity of the connector is affected by welding length. Research results solved the problem that thin UHPC layer generally needs conventional shear connectors.

Based on backgrounds above, plenty of researches for reinforced concrete composite members, and investigations of influencing factors of steel ribs and studs

were conducted. However, the calculation methods and theoretical models for shear resistances, designing guidance and bearing capacities were rarely researched. Nowadays, applications of steel connectors, which work as reinforced ribs on steel plates, have been widely used by immersed tunnel projects [12, 15]. In this paper, structural tests were carried out for steel connectors to research bonding forces between concrete and steel plates, and the influence of each designs on the performance of connectors. The combination of loading test and numerical calculations is used to research the overall tension and compression stressing state, voids and connector openings.

2 Loading Tests

2.1 Testing Apparatus

All specimen tested were full-scale models including 11 groups of test pieces in total, and 3 identical specimen are casted and tested in each group, with a total of 78 specimen. The controlled variables of specimen include: void size, tension/compression state of the connector and opening holes. The detailed controlled parameters of the shear connector are listed in Table 1. Size of the concrete specimen is $300 \times 450 \times 600$ mm, and cement used in specimen is C60. The void shape is a triangular prism (as shown in Fig. 1), the void heights are 10 and 20 mm, dimensions in Table 1 are length \times width \times height, and the void length to height ratio is 10.

For the specimen of which concrete is under compression, the traditional push-out test were conducted. For the specimen of which concrete is under tension, the inner

Table 1 Detailed parameters of shear connectors

No	Variables	Steel connector	Stress state	Openings	Void	Loading
T1	Basic	L150 \times 90 \times 10	Compression	NO	/	Positive
T3	Com/Ten	L150 \times 90 \times 10	Tension	NO	/	Positive
T4	Com/Ten	L150 \times 90 \times 10	Tension	NO	/	Positive
T5	Opening	L150 \times 90 \times 10	Compression	YES	/	Positive
T6	Opening	L150 \times 90 \times 10	Tension	YES	/	Positive
T8	Void	L150 \times 90 \times 10	Compression	NO	300 \times 100 \times 10	Positive
T11	Void	L150 \times 90 \times 10	Compression	NO	300 \times 200 \times 20	Positive
T19	Void	L180 \times 110 \times 10	Compression	NO	300 \times 100 \times 10	Positive
T20	Void	L180 \times 110 \times 10	Compression	NO	300 \times 100 \times 20	Positive
T23	Void	L200 \times 125 \times 12	Compression	NO	300 \times 100 \times 10	Positive
T24	Void	L200 \times 125 \times 12	Compression	NO	300 \times 100 \times 20	Positive

Fig. 1 Schematic diagram of specimen void testing

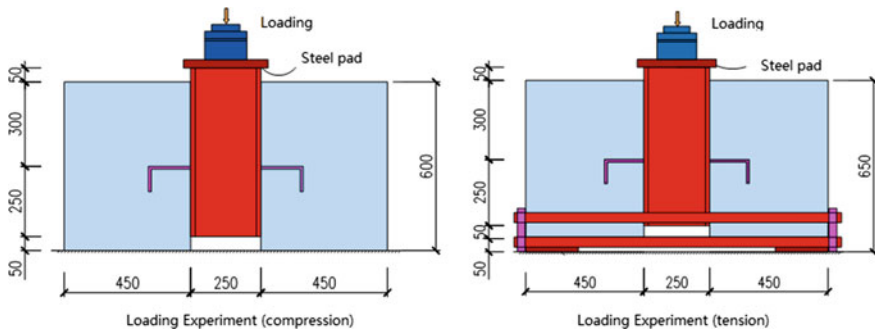
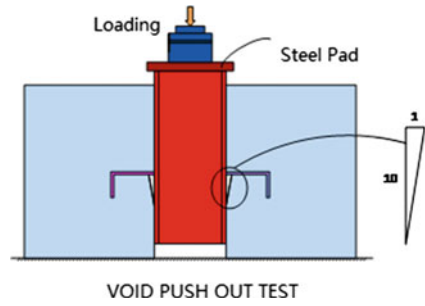


Fig. 2 Stress form of connector

side of the concrete slab that pushes out the specimen is padded, and the outer side is restrained by steel bars, as shown in Fig. 2.

2.2 Experiment Designs

In the loading test, connectors are in the form of L shape steel ribs. Double fillet welding were used for H-beam flange plate, connector web, and flange plate design. Experimental specimen including concrete casting were shown in Figs. 3 and 4.

The tested specimen were casting in four batches. A 150 mm standard cube concrete reference block is reserved for each pouring, and is maintained under the same conditions to obtain concrete strengths. The concrete strength adopts the compressive strength of the 150 mm cube test. Steel used for tested connectors and I beam were Q345 steel. There are four types of connectors with different thicknesses used, including 6 mm, 8 mm, 10 mm, and 12 mm. Standard tests results are carried out respectively [4]. Table 2 shows the results of each batch of concrete test and steel mechanical property test.

Fig. 3 Steel structure diagram under test

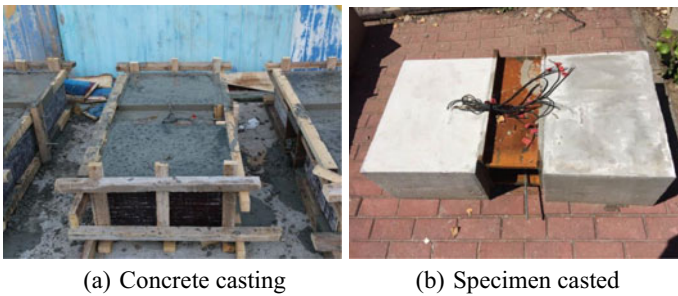
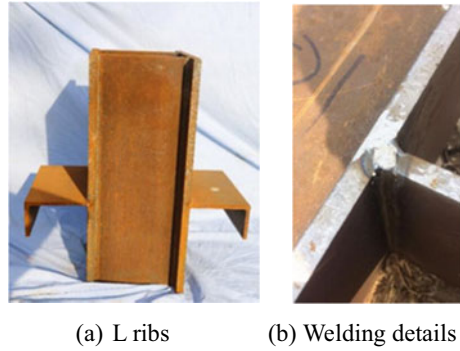


Fig. 4 Pouring process and formed connections

Table 2 Test results of mechanical properties of concrete and steel

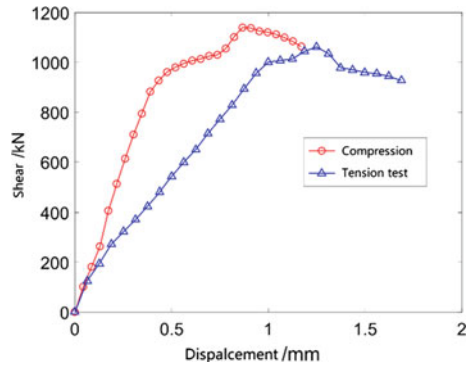
Concrete properties			Steel properties				
No	Connector	Strength /MPa	Thickness (mm)	Yeilding strength /MPa	Yeilding strain /10-6	Ultimate strength /MPa	Elongation (%)
1	T1/T5/T9/T10/T11/T16	51.5	6	363	1640	501	24
2	T12/T14/T15/T17/T25	55.8	8	383	1850	515	34
3	T3/T4/T6/T8/T13/T21/T26	48.4	10	341	2109	502	28
4	T7/T19/T20/T23/T24	49.2	12	392	1872	543	26

2.3 Test Data Analysis

Effects of stress conditions of connectors

The differences of shear-slip curves between connectors under tension and compression are significant. The results of the shear-slip curves of the specimens T1 and T3 were used as examples to discuss loading patterns and mechanisms due to similar trends of all other comparisons. The general trends of the tensile and compressive

Fig. 5 Comparison of shear slip curves of tension compression connectors (T1, T3)



shear-slip curves are similar. Before the maximum shear limit is reached, there were two loading stages: a quasi-elastic stage and a nonlinear stage as Fig. 5 shows.

The figure above shows relationship between the strain changes of upper/lower surfaces of connectors and the stress state. A great difference between tensile and compressive ones also exist. Test results of T1-3 and T6-3 could be shown as examples, Fig. 6 shows the strain comparison of stress and compression connectors. The strain of upper and lower surfaces of compressive connector are basically identical at initial stage. With increasing shear loading, strains of upper and lower surface begins to differ.

The strain variation pattern of upper and lower surfaces of the tension connector is basically identical. Before the maximum shear force is reached, the strain increases slowly and increase rate is relatively small. After the maximum shear force is reached, the strain increases rapidly and the increase rate would remain unchanged.

The curvature pattern of web for tension and compression connectors is significantly impacted by stress state. And trend would be different with the increase of the height. The specimen tests of T1-1 and T3-1 were used to discuss changing pattern

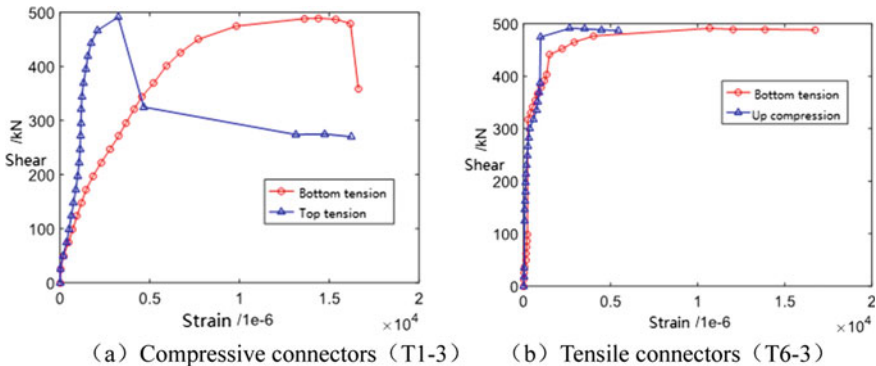


Fig. 6 Strain comparison between stressed and compressed connectors

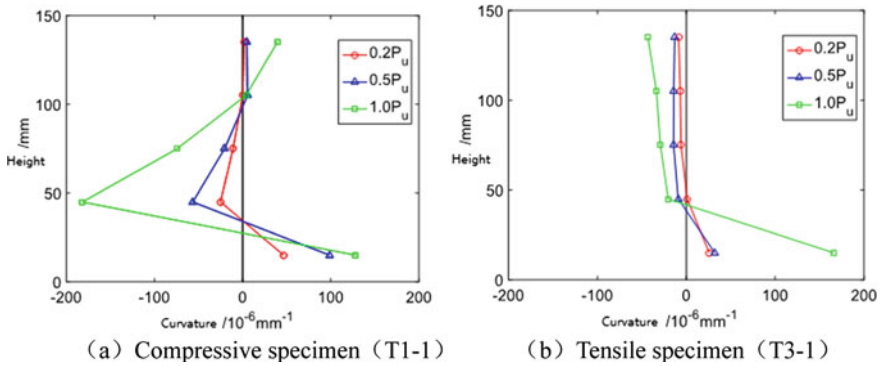


Fig. 7 Comparison of web curvature changes between tension and compression connectors

of the web curvature. Figure 7 is the comparison of the variation of the web curvature for tensile and compressive connectors.

Research on mechanism by voids

Experiments tested three different connectors with voids: L150 × 90 × 10 (L150 for short, same below), L180 × 110 × 10 (L180, same below) and L200 × 125 × 12 (L200, same below). The void between steel and concrete is simulated by using the EVA material with low elastic modulus. The failure mode is discussed by taking L50 as an example and loading tests of crack start, development and failure were shown in the Fig. 8.

Failure modes of specimen with void and without void are similar. First, inclined cracks are formed at tips of steel ribs, then vertical cracks are developed at bottom of steel ribs, horizontal cracks are developed inside specimen, and finally concrete at bottom zone of steel ribs is crushed.

The results of shear resistance capacity of each group of connectors are shown in Table 3. According to Table 3, it is certain that bearing capacity of specimens with void is significantly lower than specimens without void. In addition, for different types of large-size connectors, effects of different void height on shear resistance are similar. The larger void height generally lead to significant reduction of its bearing capacity. When void height reaches 10 mm, the bearing capacity is reduced by a maximum of 16% and a minimum of 9%. When the void height reaches 20 mm, the bearing capacity is reduced by a maximum of 36% and a minimum of 28%. The influences of the void depth by loading tests were similar to conducted results of literature investigating mechanical properties of connectors [8].

Besides impacts on ultimate bearing capacity of connectors, the void height also affects the shear-slip curves. Figure 9 shows the comparison between the shear-slip curve and stiffness of the void and non-void connectors. From the comparison of the shear-slip curves, it could be certain that voids has crucial effects on bearing capacity of three groups of connectors.

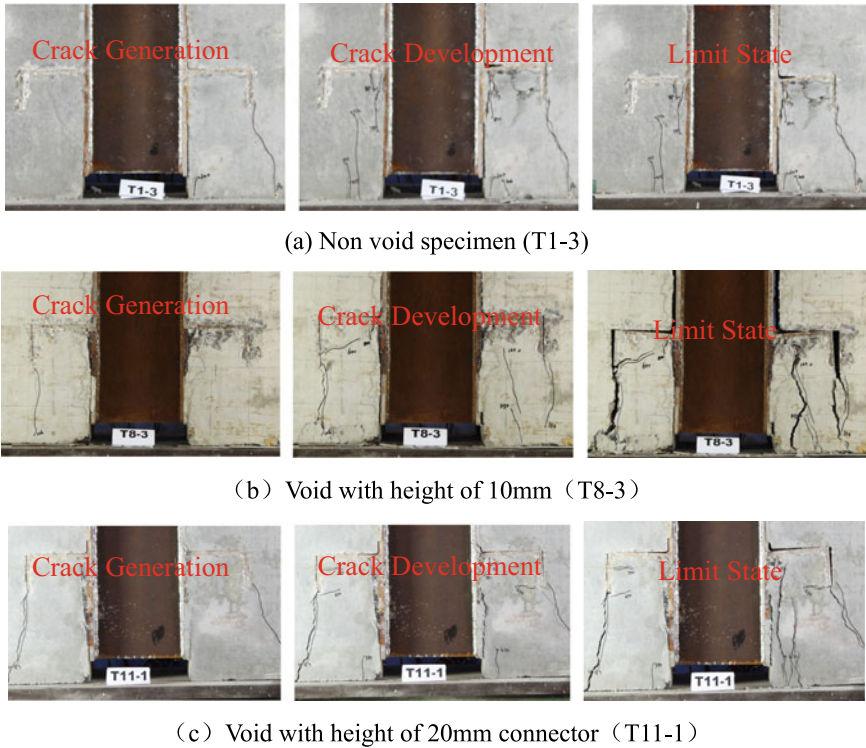


Fig. 8 Failure process of different void connectors

Table 3 Comparison of bearing capacity of hollow connectors

Size	Non-void (kN)	With void of 10 × 100		With void of 20 × 200	
		Bearing (kN)	Lower (%)	Bearing (kN)	Lower (%)
L150 × 90 × 10	1194	998	16	763	36
L180 × 110 × 10	1105	978	11	792	28
L200 × 125 × 12	1014	924	9	721	29

Figure 10 shows differences of the web curvature of with or without void connectors. The greater the curvature of the web, the greater the bending moment it bears. The change of the web curvature reflects the change of the bending moment. At the height of 50 mm, the non-empty connector has a large difference in curvature and bending moment, while the difference in curvature and bending moment of the hollow connector at different heights is large, and reaches the maximum at 50 mm. The curvature value between the two reverse bending points of the plate is significantly larger than that of the specimen without void.

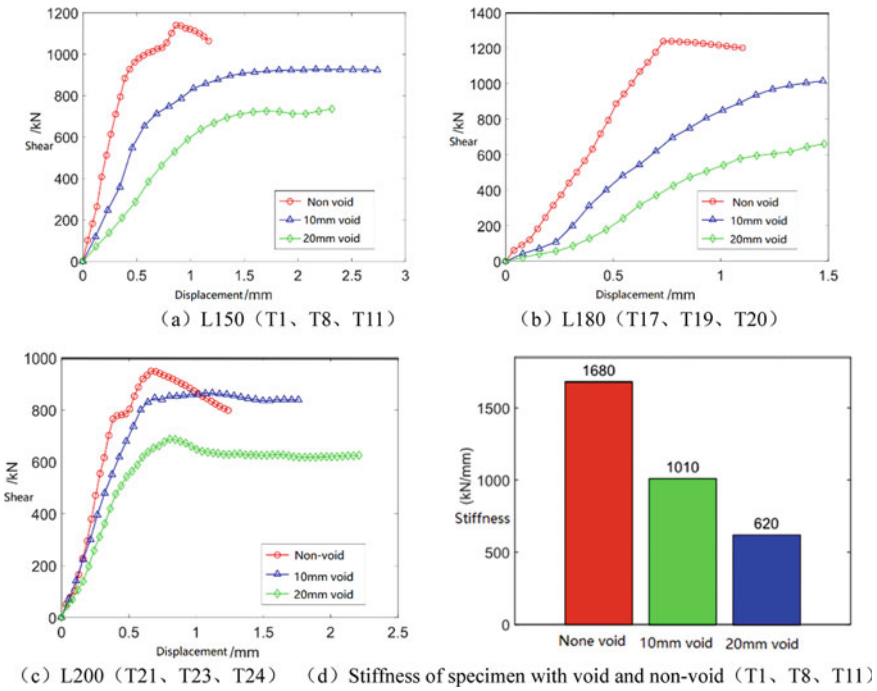


Fig. 9 Comparison of shear slip curve and stiffness between void and non-void connectors

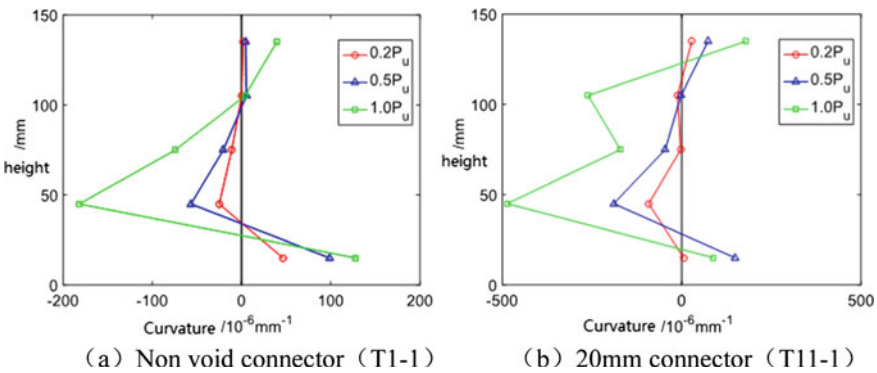


Fig. 10 Comparison of curvature pattern of non-void and with void connector webs

Research on mechanisms of opening holes

The mechanical properties of the connector with open-holes and connector without holes in the push-out test are different. Figure 11 shows the comparison of failure modes of two settings with similar failure mechanisms. First, inclined cracks occur at the tip of steel ribs, then vertical cracks and horizontal cracks occur in the concrete

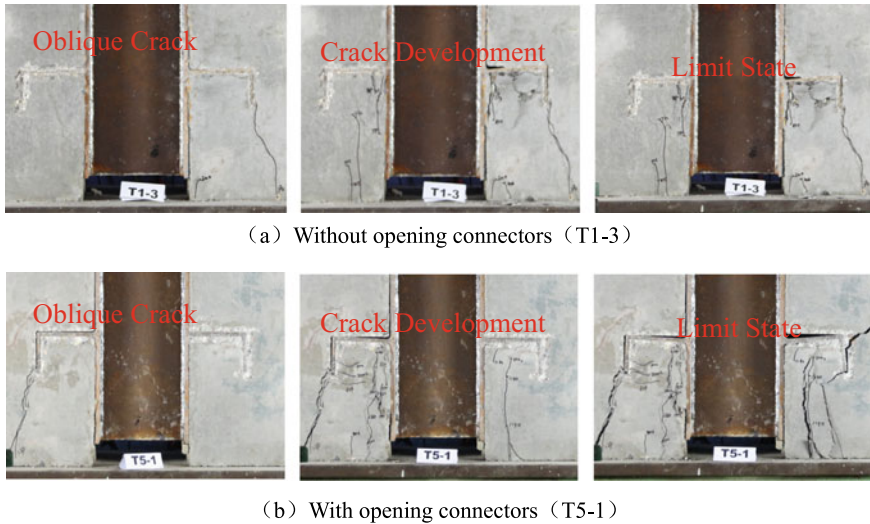
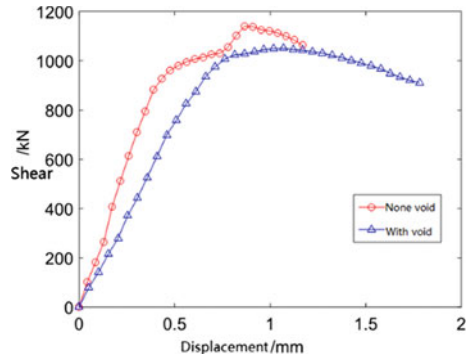


Fig. 11 Comparison of failure process between open and non-open connections

around steel ribs, and finally concrete at bottom of the angle steel is crushed to fail. The failure mode of connectors with open holes are relatively severe with more and larger cracks on both sides.

Figure 12 shows the comparison of the shear-slip curves of the open-hole and non-open-hole connectors. From the analysis of the figure, it could be certain that “shear force fluctuation phenomenon” occurs in the curve of the open-hole connector which was caused by easily damaged open-hole part. The damage of open-holes aggravates differential stress distribution. Compared with non-opening connectors, the bearing capacity of connectors with holes is reduced by about 10%. Taking the secant stiffness of 0.5 mm as the stiffness of the connector, it can be found that the opening can lead to a 20% reduction in stiffness. The main reason is that openings reduced effective contact area between the web of connector and concrete, so is the bonding area of surface of the connector and concrete. When area of opening hole at bottom of steel ribs reaches 20%, the bearing capacity is reduced by 10%, indicating that concrete at the opening is partially involved in compression but the compressive strength is not fully achieved. The main reason could be that concrete at the opening can also be constrained by the surrounding concrete to a certain extent to provide compressive strength.

Fig. 12 Comparison of shear slip curves of with open-holes and without open connectors (T1, T5)



3 Numerical Analysis of Connectors

3.1 Finite Element Modelling and Settings

Finite element analysis software MSC.MARC was used to simulate loading test. The concrete, steel ribs and connecting flange plate are simulated by the solid element SOLID75. According to the symmetry of structure, only one side structure is calculated for analysis. The FEM model is shown in Fig. 13, in which light red part is concrete, the dark red part is connecting steel ribs, the yellow part is the flange plate connected with the steel ribs, and the green part is the right side plate. Contact algorithm is used for interactions between concrete and the connector, and 0.1 friction coefficient was taken between the steel and the concrete according to reference specification.

To simulate actual contact interaction at the bottom of the connector, the right backing plate (green one) is used to simulate the actual supporting surface of actual pressure testing machine. Accordingly, the right side of the supporting surface is set as fixed constraints. With considerations of uniformities of the force along the length

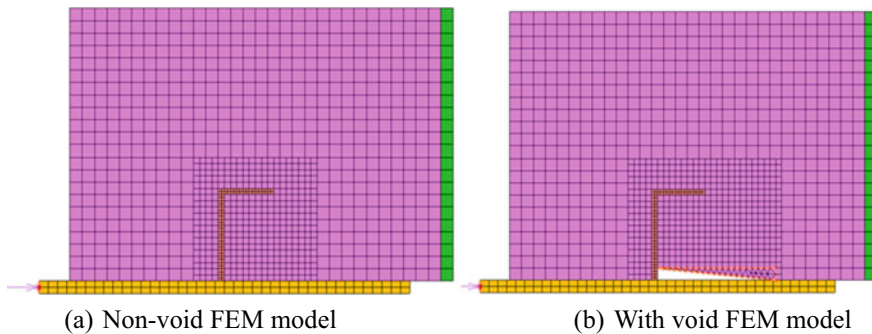


Fig. 13 Finite element model of connector

of the connector, the plane strain and plane stress models were established separately to conduct calculation and comparison.

The non-linear material of concrete element has compressive linear plasticity and tensile non-linear cracking behavior. The material of the steel rib elements is an ideal elastic-plastic material with tested yield strength. And the von Mises yield criterion is used.

3.2 Numerical Calculation Results Analysis

The non-void connector and void connector (void height of 20 mm) were calculated and simulated respectively. The stress calculation results of each model at the limit state are shown in Figs. 14 and 15.

The results of three finite element models show that compressive stress distributions of concrete in three FEM models are similar, non-void model concrete compressive stress is higher at a height of about 20 mm from the bottom where the maximum compressive stress has reached design strength. For FEM models with voids, concrete compressive stress is more concentrated and the high stress zone is smaller, which leads to reduction of bearing capacity. The tensile and compressive stress distributions of the connectors of the three models are similar in which tensile stress is greater than compressive stress, showing a mode of tensile-bending stress, and a part of the bottom of connector is yield. The bending stress at the bottom of connector with void is larger than that of the non-void connector, while the deformation and yield range are also larger. The bottom shear stress for solid model and plane strain model is more fully developed, and shear stress decreases rapidly with height. The plane stress model only has a large shear stress in a small zone near the bottom, and the shear stress above the bottom is relatively small. However, all shear stress in the three models are only half of the yielding stress, indicating that for structural design of connectors, bending capacity and deformation are governing.

The comparisons of bearing capacity and stiffness between FEM calculations and loading test results are shown in Tables 4 and 5. In terms of bearing capacity, the solid model and the plane strain model are basically identical, both of which are larger than the plane stress model. In terms of stiffness, the solid model is larger than the planar model. Both the finite element model and the experimental results show that voids have a significant effects on the bearing capacity and stiffness of connectors. For stiffness calculations, results of plane strain model can better simulate the experimental results, whereas the stiffness of the solid model is significantly greater than the tested results, which is mainly because the stiffness of the solid element is enlarged by using contact algorithm.

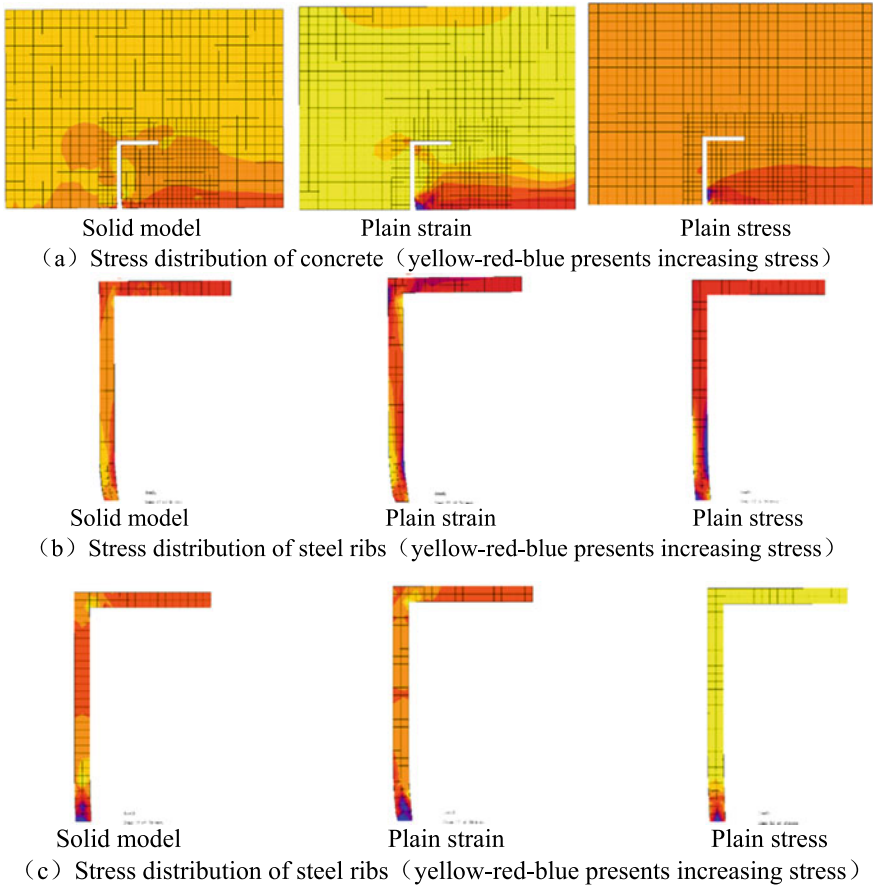


Fig. 14 Finite element simulation of non-void components

4 Theoretical Calculation Method Proposal

According to the analysis of FEM calculation results and experimental verifications, main factors impacting bearing capacity of connector include: (1) the tensile and compressive state of the concrete at the connector, that is, the connector under tension and compression; (2) the concrete void; (3) the opening hole. Compared with the compression state, the bearing capacity of the connector under tension state is reduced by less than 10%. The comparison of the push-out test results of connectors with different of void heights shows bearing capacity of the connector is reduced by 9–15% when the void height reaches 10 mm; the bearing capacity is reduced by 28–36%, when the void is 20 mm. The comparison of the push-out test results of connectors with different degrees of void shows that when void is 10 mm, the bearing capacity

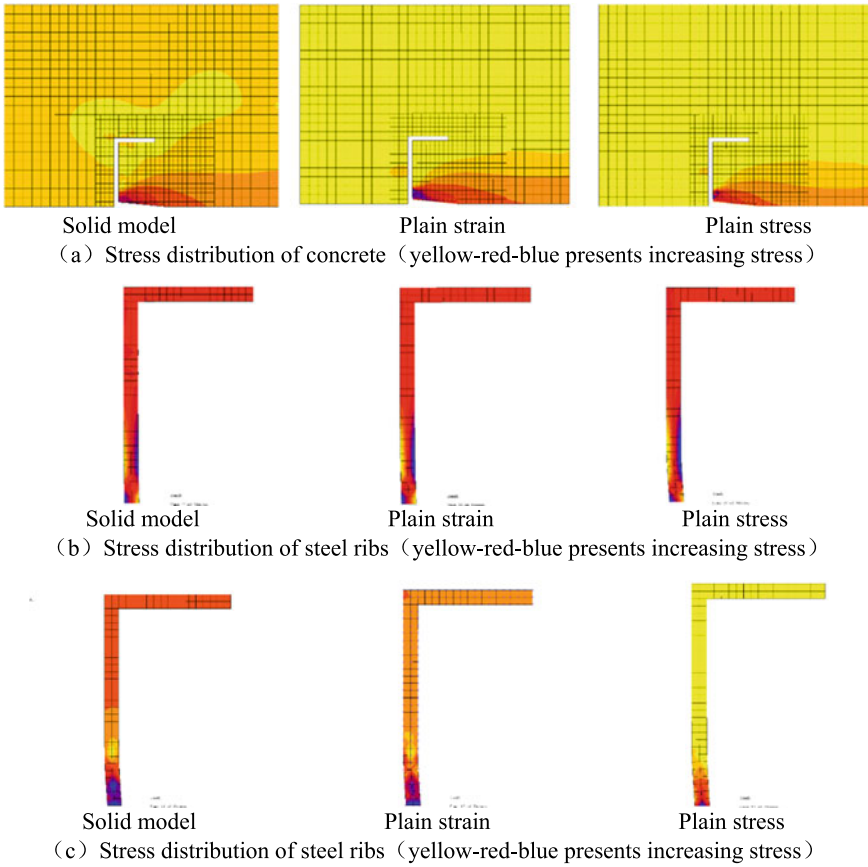


Fig. 15 Finite element simulation of with-void components

Table 4 Comparison results of bearing capacity (kN)

Connectors	Test results	Solid model	Strain model	Stress model
Non-void	1194	1205	1210	835
10 mm void	998	847	810	693
20 mm void	763	613	615	513

Table 5 Stiffness comparison results (kN/mm)

Connectors	Test results	Solid model	Strain model	Stress model
Non-void	1560	1995	1488	1400
10 mm void	1320	1700	1180	1056
20 mm void	620	1650	810	706

Table 6 Two parameter analysis of bearing capacity of connectors with holes and voids

Connectors	Without opening	20% opening rate
Non-void	1194 kN	1076 kN
Void height of 10 mm	998 kN	956 kN

of the connector is reduced by 9–15%; when the void is 20 mm, the bearing capacity is reduced by 28–36%.

Both opening holes of connector and voids of between concrete would reduce contact area between bottom of connector and surrounding concrete. Besides these holes also reduced effective area of steel ribs. By comparison, it can be concluded that when connectors designed with no holes and with 10 mm void, bearing capacity is reduced by 15%; when connectors designed with opening hole rate of 20% and without voids, the bearing capacity is reduced by 10%; when connectors designed with hole rate of 20% and with void height of 10 mm, the bearing capacity is reduced by 20% as Table 6 shows.

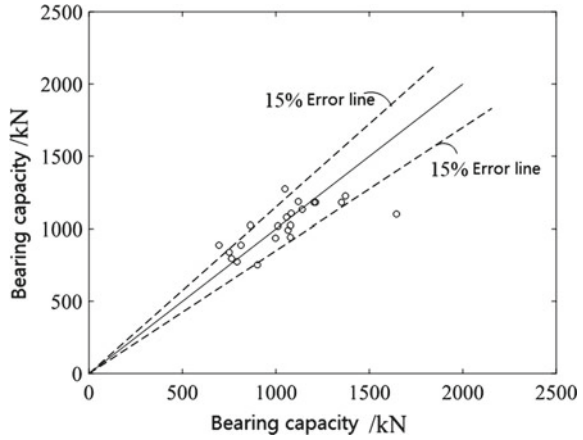
In project, opening hole rate is generally less than 20%, and the maximum void height is no more than 20 mm. Under such circumstance, calculation formula of bearing capacity considering multiple factors is determined through the above analysis as follows:

$$\begin{aligned}
 V &= 5.6l_c h_c \sqrt{f_c} k_1 k_2 k_3 \eta \times \left(1 - \frac{1.5h_e}{100} - \frac{0.5l_h}{l_c} + \frac{1.5h_e}{100} \times \frac{l_h}{l_c} \right) \\
 &\leq (l_c - l_h) t_c f_y / \sqrt{3}
 \end{aligned}
 \tag{1}$$

where: V = shear resistance with unit of kN; η = stress factor with 1 for compressive elements and 0.9 for tensile elements; k_1 is dimensional factor in which $k_1 = 2.2(t_c/h_c)^{2/3} \leq 1$; k_2 is bottom stress factor in which $k_2 = 0.4(t_f/t_c)^{0.5} + 0.43 \leq 1$; k_3 is spacing factor, in which $k_3 = (s_c/h_c/10)^{\frac{1}{2}} \leq 1$; l_c = length of connector with unit of mm; h_c = height of connector with unit of mm; s_c = spacing between connectors with unit of mm; t_c = the thickness of connector with unit of mm; t_f = thickness of flange of connector with unit of mm; l_h = length of part with opening holes with unit of mm; h_e = void height with unit of mm; f_c = strength of concrete with unit of MPa; f_y = strength of steel connector with unit of Mpa.

Figure 16 shows the comparison between results calculated by the proposed Formula (1) and the test results. It can be concluded that most of results calculated are within the 15% error rate, and differences between test results and theoretical results relatively insignificant. Considering the error of loading tests and dispersion of results, the proposed calculation formula could lead to accurate results.

Fig. 16 Comparison between new calculation method and test results



5 Conclusion

In this paper, the mechanical properties of shear connectors with different factors are analyzed by combination of experimental verifications, theoretical analysis and numerical calculations. Finally a calculation method for the bearing capacity of shear connectors with considerations of multiple factors is established. The following conclusions can be determined:

- (1) The overall trends of the shear-slip curve under tension and compression state are all similar, which indicates that stress state has minor effect on bearing capacity for connectors. The bearing capacity in the compression state is slightly higher, whereas stiffness in compression is significantly higher than the one in tension.
- (2) The failure modes of with-void and non-void connectors are also similar, whereas crushed damages of connectors with void are more severe. With increased height for void, the failure of connector are more apparent. Cracks development for non-void specimen are more regular, whereas cracks for with-void specimen were caused by multiple failure mechanisms. The curvature of steel ribs will increase significantly when void exists, which is mainly due to the lack of supportive bottom concrete.
- (3) The failure modes of connectors with and without opening holes are similar. The yielding damage of with-opening connector is relatively more obvious. Cracks of the non-opening connector develops regularly from the inward and extends outward gradually, while the development of cracks of with opening connector is complex which will develop back inward. For connectors with opening, the stress distribution is uneven, and shear force fluctuation phenomenon will appear in the shear-slip curve, which is caused by the decreased contact area of concrete and steel and reduced effective area of steel plate of connectors.

- (4) The numerical calculation results of the non-void and with-void connector show that the compressive stress of concrete for the with-void model is more concentrated, the crushing area is smaller, the bending stress at the bottom of steel connector is larger than that of the non-void. Additionally, the deformation and yield range is also large, and shear stress of with-void connector decreases rapidly with height. The stiffness and bearing capacity of with-void connector will decrease with the increase of height, and calculated stress on the model will also be unevenly distributed.
- (5) According to the test and numerical calculation results, with considerations of tensile and compressive states of concrete and connector with or without voids and openings, the influence of three factors above on the bearing capacity of the shear connector is discussed and determined. In addition, the shear capacity formula with considerations of three factors is established and proposed. Accordingly, the proposed formula is also verified by loadings tests above.

Acknowledgements The authors gratefully acknowledge the financial support by “Key-Area Research and Development Program of Guangdong Province, China (No.2019B111105002)”.

References

1. Ahmed SHS, Theodore LK (2020) Demountable steel-concrete composite beam with full-interaction and low degree of shear connection. *J Constr Steel Res* 171:106152
2. Chen J, Wang W, Ding F, Fu X, Long S, Yang C (2019) Shear performance of high-strength bolted shear connections of steel-concrete composite beams. *J Railway Sci Eng* 16(10):2553–2561
3. Chen L, Gao H, Liu Y, Yu C, Chen X, Zhang W (2021) Research on calculation method of shear capacity of cold-formed steel angle steel connection. *Buil. Struct* 51(23):76–81
4. GB/T 50107 (2010) Concrete strength determination and evaluation standard. Beijing: China Construction Industry Press
5. Fox SR (2005) Strength of CFS floor assemblies with clip angle bearing stiffeners. University of Waterloo, Waterloo
6. Hou H, Zengyun Z, Lu Y, Liu J, Ji K, Wang Y (2020) Experimental research on the launch of new fully assembled steel-concrete composite beam connectors. *Eng Mech* 37(02):201–210
7. Ipe VT, Bai SH, Vani MK et al (2013) Flexural behavior of cold-formed steel concrete composite beams. *Steel Compos Struct* 14(2):105–120
8. Kiyomiya O, Kimura H (1996) Mechanical properties of shear key by angle. *Proc Jpn Concr Inst* 18(2) (in Japanese)
9. Li B, Gao G, Zhang J (2021) Analysis of instantaneous settlement law of immersed tunnel of Hong Kong-Zhuhai-Macao Bridge. *Chin J Geotech Eng* 43(S2):263–266
10. Liu L, Wei L, Huang X, Yang C (2018) Analysis of floating flow and bollard reliability of variable cross-section sections of immersed tunnels. *Tunn Constr (Chi Engl)* 38(S1):45–50
11. Jie-peng L, Baoxu Z, Jie Y, Yuhang W (2017) Experimental study on mechanical properties of bolt-shear connectors of assembled integral steel-concrete composite beams. *J Build Struct* 38(S1):337–341
12. Piotr L, Jacek N, Anna D, Julita W (2018) Numerical and experimental tests of steel-concrete composite beam with the connector made of top-hat profile. *Compos Struct* 211(1):244–253

13. Shao X, Zhang H, Li J, Cao J, Gan Y (2020) Study on shear performance of steel-ultra-thin UHPC light composite deck short steel bar connectors. *Chin J Civil Eng* 53(01):39–51
14. Turetta M, Odenbreit C, Khelil A et al (2020) Investigation on the flexural behavior of an innovative U-shaped steelconcrete composite beam. *Steel Compos Struct* 34(3):441–452
15. Wang YH, Tilak PS, Lu JY, Zhai XM (2021) Behavior of steel-concrete-steel sandwich beams with blot connectors under off-center impact load. *J Constr Steel Res* 186:106889
16. Xie X, Yi C, Li W, Fang Y (2019) Security analysis of joint monitoring data during operation of Yongjiang immersed tunnel. *Chin J Geotech Eng* 41(12):2338–2344
17. Yuanlong Y, Tianpei S, Jinjun H (2022) Study on shear performance of U-shaped steel-concrete composite beams with embedded webs. *Eng Mech* 39(7):120–135

Open Access This chapter is licensed under the terms of the Creative Commons Attribution 4.0 International License (<http://creativecommons.org/licenses/by/4.0/>), which permits use, sharing, adaptation, distribution and reproduction in any medium or format, as long as you give appropriate credit to the original author(s) and the source, provide a link to the Creative Commons license and indicate if changes were made.

The images or other third party material in this chapter are included in the chapter's Creative Commons license, unless indicated otherwise in a credit line to the material. If material is not included in the chapter's Creative Commons license and your intended use is not permitted by statutory regulation or exceeds the permitted use, you will need to obtain permission directly from the copyright holder.



Research on Dam Deformation Monitoring Model Based on BP + SVM Optimal Weighted Combination



Shuangping Li, Yonghua Li, Min Zheng, Jun Geng, Zuqiang Liu, and Bo Shi

Abstract It is an important means to ensure the safe operation of dam to establish accurate and effective deformation monitoring data analysis and prediction model. In view of the complex conditions in dam safety monitoring, there are many unknown or uncertain factors, and they are difficult to have a single model to apply all problems. The optimal weighted combination method is constructed by combining neural network model and support vector machine model, which is used in the deformation monitoring analysis of concrete dam. The research shows that the prediction results of the optimal weighted combination model are highly consistent with the measured results, and have certain feasibility and practicability in the dam deformation monitoring work.

Keywords Dam safety monitoring · Neural network model · Support Vector Machine · Optimal weighted combination model

S. Li

School of Geodesy and Geomatics Wuhan University, Changjiang Technology Engineering Co., Ltd, Hubei Water Conservancy Information Perception and Big Data Engineering Technology Research Center, Wuhan, China
e-mail: lishuangping@cjwsjy.com.cn

Y. Li (✉) · M. Zheng · Z. Liu · B. Shi

Changjiang Spatial Information Technology Engineering Co., Ltd, Hubei Water Conservancy Information Perception and Big Data Engineering Technology Research Center, Wuhan, China
e-mail: 1051158892@qq.com

M. Zheng

e-mail: zhengmin@cjwsjy.com.cn

Z. Liu

e-mail: liuzuqiang@cjwsjy.com.cn

B. Shi

e-mail: shibo@cjwsjy.com.cn

J. Geng

China Three Gorges Corporation River Basin Complex Administration Center, Yichang, China
e-mail: geng_jun@ctg.com.cn

© Crown 2023

Y. Yang (ed.), *Advances in Frontier Research on Engineering Structures*, Lecture Notes in Civil Engineering 286, https://doi.org/10.1007/978-981-19-8657-4_28

313

1 Introduction

The analysis and prediction model of deformation monitoring data are significant to dam safety monitoring [1]. At present, statistical model [2], deterministic model [3] and mixed model are usually used to process and analyze dam monitoring data. Different processing methods have different advantages and certain applications in practical engineering, but these methods also have certain limitations. In the actual work of monitoring data analysis, insufficient data samples or complex environmental factors have a great impact on the establishment of the model, and the model may have more errors and poor fitting effect, so the model cannot be applied to the actual work [4].

The paper mainly researches the BP neural network model and support vector machine model (SVM) [5]. These two models are organically combined and applied to the dam deformation analysis example [6]. The results show that the optimal weighted combination model can maximize the information of each monitoring model, reduce the mean square error of the prediction model, and improve the accuracy of dam deformation monitoring [7]. This paper can provide new ideas and reference for dam safety monitoring data analysis and prediction model.

2 BP Neural Network Model

Artificial neural network (Ann) is a kind of distributed parallel information processing algorithm mathematical model which imitates the behavior characteristics of animal neural network [8]. The input signal x_i acts on the output node through the intermediate node (Hidden layer point), and the output signal Y_k is generated through nonlinear transformation [9]. Each sample of network training including the input vector x and the desired output t , network output value Y and t . By adjusting the w_{ij} which means connection strength between the input node and the hidden node, T_{jk} which means the connection strength between the hidden node and the output node, and the threshold, the error decreases along the gradient direction. After repeated learning and training, the training stops immediately when determining the network parameters (weights and thresholds) corresponding to the minimum error.

In the dam deformation monitoring system, we generally build the BP neural network of multi-layer perceptron composed of input layer, output layer and hidden layer, and determine the number of input layer node n , hidden layer node l , hidden layer excitation function f , and output layer node m . The connection weight w_{ij} and hidden layer threshold a_j between the input layer and hidden layer are initialized, so that we can determine parameters such as learning rate and activation function. After the sample data is sent to the input node and processed layer by layer through the hidden layer, the following formula is used to calculate the output H_j of the hidden layer.

$$H_j = f\left(\sum_{i=1}^n w_{ij}x_i - a_j\right) \quad j = 1, 2, \dots, l \quad (1)$$

We initialize w_{jk} which is the weight between the hidden layer and the output layer, and also the output layer threshold b_k . Then the BP neural network will predict the output O_k .

$$O_k = \sum_{j=1}^l H_j w_{jk} - b_k \quad k = 1, 2, \dots, m \quad (2)$$

According to the network prediction we can output O_k and Y_k , and can press the following formula to calculate the network prediction error. This neural network will calculate the error value of each input sample data. If the error is relatively large, the error starts to reverse transmission, and adjust the neural network parameters until the system converges.

$$e_k = Y_k - O_k \quad k = 1, 2, \dots, m \quad (3)$$

Through network training, weights w_{ij} and w_{jk} which are updated according to network prediction error.

$$w_{ij} = w_{ij} + \eta H_j (1 - H_j) x(i) \sum_{k=1}^m w_{jk} e_k \quad i = 1, 2, \dots, n; \quad j = 1, 2, \dots, l \quad (4)$$

$$w_{jk} = w_{jk} + \eta H_j e_k \quad j = 1, 2, \dots, l; \quad k = 1, 2, \dots, m \quad (5)$$

Next update the network node thresholds a_j and b_k .

$$a_j = a_j + \eta H_j (1 - H_j) x(x) \sum_{k=1}^m w_{jk} e_k \quad j = 1, 2, \dots, l \quad (6)$$

$$b_k = b_k + e_k \quad k = 1, 2, \dots, m \quad (7)$$

If we determine the weights, we input the data into the model to predict the results.

3 SVM Support Vector Machine Model

Support vector machines are mostly used for classification problems, but they can also be used for regression, which is often referred to as support vector regression models [10]. The final model function is expressed as follows:

$$f(x) = w^T x + b \tag{8}$$

W and b are the main coefficients required by the model.

For a given training sample $D = \{(x_1, y_1), (x_2, y_2), \dots, (x_m, y_m)\}$, traditional regression models usually calculate losses directly based on the difference between model output and true value, while SVR only calculates the loss when the difference between $f(x)$ and y is greater than ε , and the parameters ε is specified by the user. Therefore, according to other theories of support vector machine model, the optimization objective of SVR problem is written as follows.

$$\min_{w,b} \frac{1}{2} \|w\|^2 + C \sum_{i=1}^m l(f(x_i) - y_i) \tag{9}$$

The C is the loss coefficient, which can be specified by users or optimized by genetic algorithm. l is ε 's insensitive loss function, calculating the loss only if the difference between $f(x)$ and y is greater than ε .

$$l(z) = \begin{cases} 0, & |z| \leq \varepsilon \\ |z| - \varepsilon, & |z| > \varepsilon \end{cases} \tag{10}$$

Considering the relaxation variable ξ and $\hat{\xi}_i$, the above equation can be rewritten as follows:

$$\min_{w,b,\xi_i,\hat{\xi}_i} \frac{1}{2} \|w\|^2 + C \sum_{i=1}^m (\xi_i + \hat{\xi}_i) \tag{11}$$

$$\begin{cases} \xi_i = y_i - (f(\mathbf{x}_i) + \varepsilon), & y_i > f(x_i) + \varepsilon \\ \xi_i = 0, & y_i \leq f(x_i) - \varepsilon \\ \hat{\xi}_i = (f(\mathbf{x}_i) - \varepsilon) - y_i & y_i < f(x_i) - \varepsilon \\ \hat{\xi}_i = 0, & y_i \geq f(x_i) - \varepsilon \end{cases} \tag{12}$$

To solve the above problems, we first introduce the Lagrange multiplier: $u_i \geq 0, u_i^* \geq 0, \alpha_i \geq 0, \alpha_i^* \geq 0$

Construct the Lagrange function:

$$\begin{aligned} L(w, b, \xi, \hat{\xi}, \alpha, \alpha^*, u, u^*) &= \frac{1}{2} \|w\|^2 + C \sum_{i=1}^m (\xi_i + \hat{\xi}_i) \\ &+ \sum_{i=1}^m \alpha_i (f(x_i) - y_i - \varepsilon - \xi_i) \\ &+ \sum_{i=1}^m \alpha_i^* (y_i - f(x_i) - \varepsilon - \hat{\xi}_i) \end{aligned}$$

$$+ \sum_{i=1}^m u_i(0 - \xi_i) + \sum_{i=1}^m u_i^*(0 - \hat{\xi}_i) \tag{13}$$

In order to find the minimum value of this function for $w, b, \xi, \hat{\xi}$, the model take the partial derivative of $w, b, \xi, \hat{\xi}$ respectively, and let the partial derivative be 0.

So the dual problem corresponding to SVR is follows:

$$\max_{\alpha, \alpha^*, u, u^*} L(w, b, \xi, \hat{\xi}, \alpha, \alpha^*, u, u^*) \tag{14}$$

We can solve the dual problem if the *KKT* condition is satisfied, and the *KKT* condition is as follows:

$$\begin{aligned} w &= \sum_{i=1}^m (\alpha_i^* - \alpha_i)x_i \\ 0 &= \sum_{i=1}^m (\alpha_i^* - \alpha_i) \\ C &= \alpha_i + u_i \\ C &= \alpha_i^* + u_i^* \end{aligned} \tag{15}$$

After taking partial derivatives, we substitute the various obtained into the dual formula and simplify, then can obtain the simplified dual formula.

$$\max_{\alpha, \alpha^*} \sum_{i=1}^m y_i (\alpha_i^* - \alpha_i) - \varepsilon (\alpha_i^* + \alpha_i) - \frac{1}{2} \left(\sum_{i=1}^m \sum_{j=1}^m (\alpha_i^* - \alpha_i) (\alpha_i^* - \alpha_j) x_i^T x_j \right) \tag{16}$$

SMO (Sequential Minimal Optimization) algorithm can solve the problem. Before solving, a^* and a_i should be converted into a coefficient, because SMO algorithm aims at the case that sample x_i only has one parameter a_i . It can be inferred from the first two expressions of the *KKT* (Karush–Kuhn–Tucker) condition that at least one of a_i and a_i^* is 0. If we assume that $\lambda_i = \alpha_i - \alpha_i^*$, we can infer that $|\lambda_i| = \alpha_i + \alpha_i^*$. Since the formula continues to be reduced to a form with only one variable, we can calculate through the SMO algorithm. We also can conclude the value of $\alpha - \alpha^*$ to calculate the w .

We can figure up that if $0 < \alpha_i < C$ and $\alpha_i(f(x_i) - y_i - \varepsilon - \xi_i) = 0$, there will be $\xi_i = 0$, so the calculation formula is as follows:

$$b = y_i + \varepsilon - w^T x_i \tag{17}$$

In the concrete implementation, the algorithm calculates all samples that meet the condition $0 < \alpha_i < C$ and takes the average of results.

4 Construction of Optimal Weighted Combination Model

In practice, suppose we construct m single dam deformation model $k_i (i = 1, 2, \dots, m)$, and construct a composite model $K_q = \varphi(k_1, k_2, \dots, k_n), n \leq m$ and q is the number of model combination.

Let the weight vector of each single model in the combined model be $p = [p_1, p_2, \dots, p_n]$, $\sum_{j=1}^n p_j = 1$, then the combined prediction model is as follows:

$$K = p_1 \hat{K}_1 + p_2 \hat{K}_2 + \dots + p_n \hat{K}_n = \sum_{j=1}^n p_j \hat{K}_j \tag{18}$$

The fitting residual of a single model can be expressed as follows:

$$e_{ti} = k_{ti} - \hat{K}_{ij} \quad (j = 1, 2, \dots, m; \quad t = 1, 2, \dots, n) \tag{19}$$

Then each single forecast model can form a fitting residual matrix:

$$V = \left[\sum_{t=1}^n e_{ti} e_{tj} \right] \quad (i, j = 1, 2, \dots, m) \tag{20}$$

The objective function is solved according to the least square principle.

$$\begin{cases} Q = \sum_{i=1}^n e_i^2 = \min \\ s.t. \sum_{j=1}^n p_j = 1 \end{cases} \tag{21}$$

If $R = [1, 1, \dots, 1]^T$, the formula above becomes as follows:

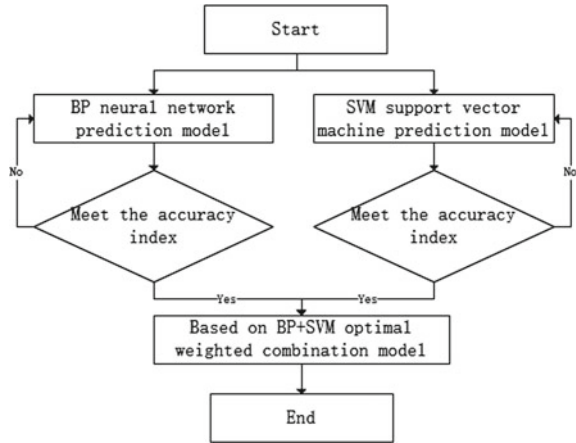
$$\begin{cases} Q = \sum_{i=1}^n e_i^2 = P^T V P = \min \\ s.t. \sum_{j=1}^n p_j = R^T P = 1 \end{cases} \tag{22}$$

The optimal weight vector is obtained:

$$P_0 = \frac{V^{-1} R}{R^T V^{-1} R} \tag{23}$$

By using the optimal weight ratio obtained from the above equation, the combined model prediction can maximize the information of each deformation model and reduce the mean square error of the prediction model, thus improving the accuracy of dam deformation analysis (Fig. 1).

Fig. 1 Flow of BP-SVM combination model modeling



5 Analysis of Examples

The paper selects the monitoring data of PL02 measuring point from 2006/5/14 to 2019/12/20 and conducts modeling using the data from 2006 to 2018. Then, we use the 2019 causative data to predict the 2019 effect size data and compare with the measured data to verify the effectiveness of the model.

Factors such as water level, temperature and time mainly affect the displacement and deformation of concrete gravity dams, and Table 1 shows the setting of influencing selection factors.

In order to prove the effectiveness and superiority of the combined model proposed in this paper, the example trains data and predicts result through the combined model, BP model and SVM model. Each model uses the same training samples and test data as control variables. In data processing, the input factor of the model is water level, temperature and aging, and the output factor is the predicted dam displacement.

Table 1 List of factor settings

Component type	Point type	Expression of factor calculation	Remarks
Water level component	Upstream water level	$x - 138$	Upstream water level—reference value
Water level component	Water level downstream	$x - 66$	Water level downstream—reference value
Temperature component	Temperature	$Average(x, 15) - 18$	Average temperature over 15 days—reference value
Time dependent component	Time	$\ln(1 + x/30)$	$x/30$ unit: month

The correlation coefficient is the fitting accuracy evaluation index in the model analysis and comparison. Table 2 shows the calculation results of the overall modeling accuracy index for each model. It can be seen that the training and prediction correlation coefficients of the combined model are higher than those of other models, indicating its high accuracy and more suitable for dam deformation prediction.

According to the modeling result and process line in Figs. 2 and 3, we can conclude that the monitoring data of PL02 measurement point from 2006 to 2018 are better modeled by the combined model.

Table 2 Summary of overall modeling accuracy indicators

Process	Mode	Correlation coefficient	Determination coefficient	Standard error	Weight
Training	Combination model	0.991	0.953	1.215	–
	BP model	0.969	0.940	1.371	0.219
	SVM model	0.976	0.952	1.228	0.781
Prediction	Combination model	0.993	0.960	1.108	–
	BP model	0.973	0.936	1.402	0.219
	SVM model	0.981	0.959	1.117	0.781

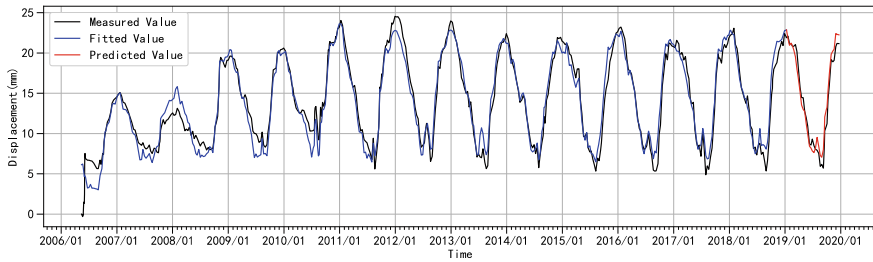


Fig. 2 Comparison between calculated value of model and measured value

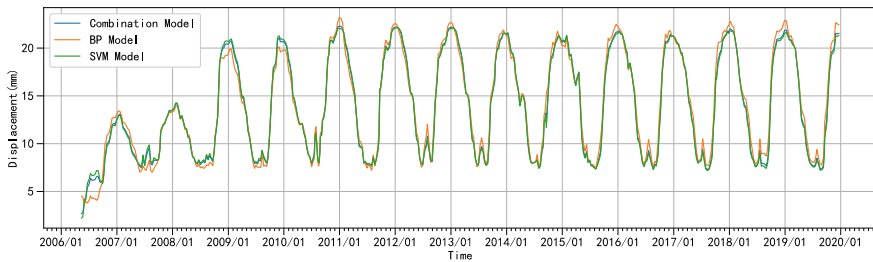


Fig. 3 The results of combination model and each sub-model are compared

Table 3 shows that the error of some calculated values in the optimal weighted combination model is larger than other models, the reason may be the influence of some abnormal points in the training process on the calculation results. In general, the calculation accuracy of the optimal weighted combination based on BP + SVM is higher than that of other models.

We can conclude from the above chart, that the fitting accuracy of BP model is lower than the SVM model. The combined model adopts the optimal weighted grouping method to reasonably determine the weight of the two models. Finally, the weight of the SVM model is higher, the BP is lower, and the relative relationship is reasonable. The fitting effect of the combined model is better than that of the sub-model, which indicates that the optimal weighted combination method is effective. It can be seen from Table 3 that the combined model is superior to the statistical model in all indicators of the training and prediction process, indicating that the optimization method adopted by the combined model is effective and further improves the calculation accuracy of the model.

6 Conclusion

Due to the complex dam working conditions and many influencing factors, a single analysis model is insufficient in stability. This paper adopts the optimal weighted combination method and organically combines the BP neural network model with support vector machine model (SVM), and the model can gain better and more stable modeling and prediction results. The model automatically determines the optimal weight, which improves the stability and prediction accuracy of the model and reduces the manual parameter adjustment.

The modeling and prediction results of the model are highly consistent with the measured results, and the overall accuracy of the model training results is good, indicating that the model is effective. From the results, the accuracy of the BP model is relatively low, while the accuracy of the SVM model is higher, and the combined model is better than other models. The optimal weighted combination method uses the best weight combination to ensure the reliability and stability of the final calculation results. When the model factors and options are not set properly, the optimal weighted combination model has stronger robustness and intelligence than the single model, which is helpful to obtain better calculation results.

Table 3 Comparison between measured and predicted values of dam deformation

Time	Measured value/mm	Combination model			BP model			SVM model		
		Calculated value/mm	Error	Relative error /%	Calculated value /mm	Error	Relative error /%	Calculated value /mm	Error	Relative error /%
2019-01-10	21.93	21.94	- 0.01	- 0.05	23.03	- 1.10	- 5.02	21.63	0.3	1.37
2019-02-10	21.15	20.90	0.25	1.18	21.44	- 0.29	- 1.37	20.75	0.4	1.89
2019-03-10	21.04	19.88	1.16	5.51	19.85	1.19	5.66	19.90	1.1	5.23
2019-04-10	15.73	14.70	1.03	6.55	15.24	0.49	3.12	14.55	1.2	7.63
2019-05-10	12.77	11.84	0.93	7.28	12.75	0.02	0.16	11.59	1.2	9.40
2019-06-10	8.70	8.21	0.49	5.63	8.73	- 0.03	- 0.34	8.07	0.6	6.90
2019-07-10	8.49	7.66	0.83	9.78	8.12	0.37	4.36	7.52	1.0	11.78
2019-08-10	7.54	7.97	- 0.43	- 5.70	8.54	- 1.00	- 13.26	7.81	- 0.3	- 3.98
2019-09-09	8.58	9.27	- 0.69	- 2.21	10.62	- 2.04	- 23.78	8.89	- 0.3	- 3.50
2019-10-10	14.23	15.08	- 0.85	- 3.16	15.99	- 1.76	- 12.37	14.83	- 0.6	- 4.22
2019-11-10	18.91	19.71	- 0.80	- 4.23	20.60	- 1.69	- 8.94	19.46	- 0.6	- 3.17
2019-12-08	21.18	21.54	- 0.36	- 1.70	22.60	- 1.42	- 6.70	21.24	- 0.1	- 0.47
Average value			0.20	1.57		- 0.61	- 4.87		0.33	2.40

References

1. Jiang Z, Xu Z, Wei B (2016) Monitoring model of dam displacement based on wavelet decomposition and support vector machine. *J Yangtze River Sci Res Inst* 33(1):43–47
2. Hongbo Y, Zhou B, Lu X et al. (2019) Prediction of dam deformation monitoring data based on EEMD-GA-BP model [J]. *J Yangtze River Sci Res Inst.* 36(9):6
3. Zhu M, Zhou X, Wang K (2016) Dam deformation monitoring model based on CS-SVM model [J]. *Cryog Constr Technol* 38(11):3
4. Wu Z (2003) Safety monitoring theory and application of hydraulic building [M]. Higher Education Press
5. Huang Z, Liao M, Zhang H, Zhang J, Ma S (2020) Prediction of surrounding rock deformation based on Incomplete data of SVM-BP Model [J]. *Mod Tunn Technol* 57(S1):141–150
6. Qin Z, Yang F, Huang S (2022) Prediction model of dam slope deformation based on GA-BP algorithm [J] (1)
7. Wang Y, Su H (2020) Prediction of dam deformation based on PCA-GMO-SVM [J]. *Yellow River* 42(423)(11):134–138
8. Haiyan X, Lihan Z (2010) Prediction model of dam settlement based on BP neural network [J]. *Water Sci Eng Technol* 1:3
9. Hongfei G, Ping J, Fei G et al (2019) Prediction analysis of slope stability based on BP neural network [J]. *Coal Geol China* 31(A01):3
10. Su H, Chen Z, Wen Z (2016) Performance improvement method of support vector machine-based model monitoring dam safety[J]. *Struct Control Health Monit* 23(2):252–266

Open Access This chapter is licensed under the terms of the Creative Commons Attribution 4.0 International License (<http://creativecommons.org/licenses/by/4.0/>), which permits use, sharing, adaptation, distribution and reproduction in any medium or format, as long as you give appropriate credit to the original author(s) and the source, provide a link to the Creative Commons license and indicate if changes were made.

The images or other third party material in this chapter are included in the chapter's Creative Commons license, unless indicated otherwise in a credit line to the material. If material is not included in the chapter's Creative Commons license and your intended use is not permitted by statutory regulation or exceeds the permitted use, you will need to obtain permission directly from the copyright holder.



Equivalent Standard Axle Load Analysis Considering Dynamic Load Based on Vehicle Axle-Tire Vertical Acceleration Field Testing



Wei Jiang, Wei Wang, Zhichao Song, Changqing Jiang, Chenglong Zhang, and Yijian Yuan

Abstract In order to examine equivalent axles load with dynamic load taken into account, pavement roughness test is carried out with a Vehicle Axle-tire Dynamic Load Tester, where axle-tire vertical acceleration of heavy trucks and light trucks are tested, respectively. Dynamic load is considered as a series of static loads following a normal distribution, and equivalent axles load is calculated according the Asphalt Pavement Design Specification. The results show that equivalent axles load time increase accordingly based on highway class. when tensile strain at bottom of surface is taken as design index, on high class highway equivalent standard load increases 8.3–14.9% for heavy truck, 3.6–5.4% for light truck; on low class highway, it increases 6.8–17.3% for heavy truck, 3.2–12.5% for light truck; when tensile stress at the bottom of semi-rigid base is taken as checking index. On a high class highway, it increases 34.2–64.9% for a heavy truck, 14.2–21.8% for a light truck; on a low class highway, it increases 27.5–77.1% for a heavy truck, 12.6–53.2% for a light truck. These research findings provide in-depth understanding regarding vehicle axle load conversion in dynamic load environment.

Keywords Highway engineering · Dynamic load · Pavement roughness · Vibration acceleration speed · Equivalent axle load

W. Jiang (✉)

Linyi Transportation Bureau, Linyi, Shandong Province, China

e-mail: 244835268@qq.com

W. Wang

Huawei Engineering Consulting Company, Weifang, Shandong Province, China

e-mail: 15621681372@163.com

Z. Song · C. Jiang · C. Zhang · Y. Yuan

East Highway and Bridge Construction Company, Linyi, Shandong Province, China

© Crown 2023

Y. Yang (ed.), *Advances in Frontier Research on Engineering Structures*, Lecture Notes in Civil Engineering 286, https://doi.org/10.1007/978-981-19-8657-4_29

325

1 Introduction

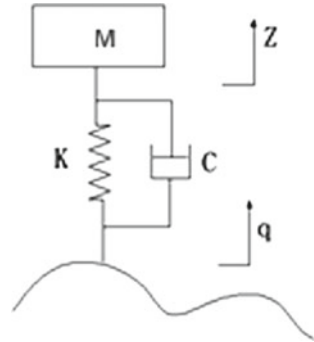
Current asphalt pavement design specifications in China fail to consider dynamic load in vehicle axle load analysis. Peer studies in China focused on dynamic theories as well as the magnitude of dynamic load, and significant research has been conducted. For instance, Zhong et al. [1] analysed the relationship between vehicle dynamic load and travel speed using two degree of freedom model. Huang [2], and Sun and Deng [3] investigated the relationship between pavement roughness and dynamic load. Assuming vehicle and ground structure as a synthetic system, Deng [4] developed a mathematical model to describe the contact roughness between vehicle and pavement surface. Additional studies focused on dynamic load characters and vehicle-pavement interaction force [5–8].

Numerous studies have been conducted worldwide as well regarding this topic. Dodds and Robson [9] took pavement roughness as a function of vehicle departing off flat pavement and utilized power spectral density (PSD) to calculate dynamic load [9]. Todd and Kulakowski [10] analysed dynamic load by quarter truck model and half truck model. Hunt [11] proposed a model for pavement vibrating PSD estimation. With the development of research, Watts and Krylov [12] examined vehicle vibrating characteristics when vehicles ran over pavement distress, such as pavement cracking, rutting, pot holes. By means of a three-dimensional truck model, Javier et al. [13] found that the vertical dynamic load applied by a tyre to the pavement depends not only on the profile under that wheel but also on the profile under the other wheels, mainly under the one on the same axle. Dae-Wook and Papagiannakis [14] formulated a continuous or distributed model using a two-dimensional (2D) half-truck finite element model. Using the 2D half-truck finite element model, numerical simulations were performed to obtain the dynamic loads using various parameters such as the road roughness, vehicle speed, suspension stiffness and damping in order to evaluate their individual effects on the dynamic axle load response. All these researches have supplied basic theories for dynamic load characters.

Obtaining acceleration speed of vehicle axles and tires is the basic method of obtaining dynamic load. Only a few studies obtained dynamic load by experiment tests. Chen et al. [15] invented a vehicle-pavement test rig including a vehicle model and a distributed stiffness pavement-roadbed model, and the vehicle model was simplified as a quarter of resonance source vehicle model. The dynamic response of distributed of stiffness pavement under moving resonance load and shock excitement were analysed respectively.

In this research a new testing instrument, Vehicle Axle-tire Dynamic Load Tester is employed to test vertical acceleration speed of vehicle axles and tires in different conditions. Mean square value of acceleration speed is analysed and dynamic load is obtained. Dynamic load is taken as a series of static load following normal distribution, and equivalent axles load is calculated according the Asphalt Pavement Design Specification, and the increasing rate of equivalent axle load is analysed after dynamic load is taken into account.

Fig. 1 Vehicle model with single degree of freedom



2 Vehicle Vibration Model and Dynamic Load

Vehicle vibration models with varying degrees of freedom are generally built to examine the dynamic load theoretically. In this study, a single degree of freedom vehicle model on a roughness pavement is established, as is shown in Fig. 1.

In this model, M is the sprung mass of vehicle; K is suspension stiffness; C is dampness coefficient of tires; the pavement profile is modelled as a one-dimensional random field and is represented by the height of pavement surface irregularities q ; Z is absolute displacements of sprung mass.

The dynamic load F_d is calculated by inertia mass of M as follows

$$F_d = MZ' \tag{1}$$

where, Z' represents the first derivative processes of Z .

It can be known that dynamic load is linearly dependent with acceleration speed of axle-tires, as frequency of dynamic load is same with acceleration of tires. So characteristics of acceleration reflect characteristics of dynamic load.

3 Axle-Tire Acceleration Field Test Design

3.1 Testing Road and Roughness Testing

Changxiao Road was selected as a low class highway and Jinan belt expressway was select as a high class highway for the field tests. Continuous pavement roughness tester was implemented on the low class highway, and laser pavement roughness tester was utilized on the high class highway. The test results are as follows: roughness variance of Changxiao road is 1.8 m/km, International Roughness Index (IRI) of Jinan belt expressway is 1.40 m/km.

Previous studies have examined the relationship between IRI and roughness variance, that is σ , the conclusions are almost the same [16–18] In this article it is assumed as follows [17]:

$$\sigma = 0.6 IRI \quad (2)$$

According to the two formulas and testing results in fields, roughness variance of high class road equals to 0.84, low class road equals to 1.8.

3.2 Test Vehicles

A light truck and a heavy truck were selected as testing vehicles. Vehicle Axle-tire Dynamic Load Testers were installed on the axles of the two trucks, and tests were carried out when the trucks were empty and fully loaded travelling at different speeds.

3.3 Testing Method and Data Collection

Real time vehicle travel speed is obtained from GPS modules, and vertical acceleration is obtained by three-axis acceleration sensor. In field, axles of trucks are fixed with the Axle-tire Dynamic Load Tester, and then empty trucks and fully loaded trucks travel at the speed of 40, 50, 60, and 70 km/h on the low class highway, and at 60, 80, and 100 km/h on the high class highway, travel speed of trucks and vertical vibration acceleration of axles are obtained.

4 Result Analysis

4.1 Vertical Axle-Tire Vibration Acceleration Temporal Analysis

Field tests were conducted and time travel curve of vertical vibration acceleration are obtained. Figures 2 and 3 are a part of time travel curve when the light truck ran on the low class highway with the speed of 60 km/h, and on the high class highway with the speed of 80 km/h, respectively.

Besides, tests are carried out in all scenarios where the heavy truck is empty or full loaded with different travel speeds, time travel curves of vertical vibration acceleration are obtained. When the tests are conducted, the trucks ran at least 3 min on the testing road with sampling frequency more than 100 Hz to ensure the enough data for analysing. Figure 4 demonstrate a part of time travel curve when the heavy

Fig. 2 Vertical acceleration time travel curve of empty loaded light truck traveling on low class highway (60 km/h)

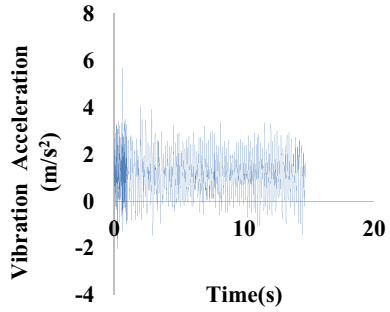
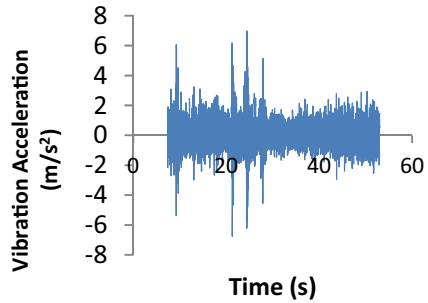


Fig. 3 Vertical acceleration time travel curve of fully loaded light truck traveling on high class highway (80 km/h)



truck is empty and travels at 40 km on the low class highway, and Fig. 5 illustrates a part of the travel time curve of the empty loaded heavy truck traveling at 80 km/h on the high class highway.

It is assumed that vehicle axle-tire vertical vibration acceleration follows a normal distribution with zero mean value, and therefore the standard variance is equal to mean square value. Since the mean square value reflects the size of vibration acceleration, standard variance also indicates vibration acceleration size patterns. Vertical vibration acceleration of different cases is listed in Table 1.

Fig. 4 Vertical acceleration time travel curve of empty loaded heavy truck traveling on low class highway (40 km/h)

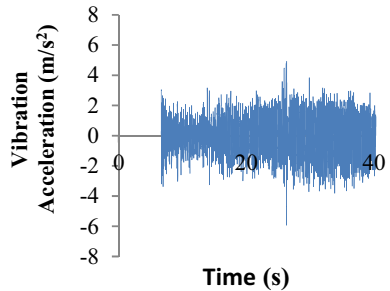


Fig. 5 Vertical acceleration time travel curve of empty loaded heavy truck traveling on high class highway (80 km/h)

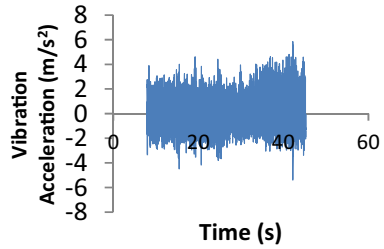


Table 1 Vehicle axle-tire vertical vibration acceleration mean square value (μ)

Highway class	Speed (km/h)	Empty heavy truck	Fully loaded heavy truck	Light truck	Light truck
Low class highway	70	1.65	1.53	1.77	1.3
	60	1.63	1.12	1.36	0.85
	50	1.24	1.03	1.32	0.79
	40	1.22	0.96	1.17	0.66
High class highway	100	1.89	/	1.9	0.86
	80	1.59	1.42	1.67	0.81
	60	1.51	1.06	1.26	0.7

Note travel speed of heavy truck can't reach at 100 km/h

As vehicle suspension, tires, loading mass, and pavement roughness vary greatly, the response of vehicles vary greatly while they are stimulated by pavement roughness. From the data, it shows that:

Mean square value of axle-tire vertical acceleration increases with the increase of vehicle travel speed for both light truck and heavy truck; the value is also the same when the trucks are empty, but vibration acceleration speed of light truck is much higher than heavy truck when they are fully loaded.

Loading mass has great influence on vehicle axle-tire acceleration, for a fully loaded truck it is obviously less than an empty truck.

The smoother the pavement is, the smaller the vibration acceleration is. Pavement roughness has a great influence on full loaded trucks while a lighter influence on empty trucks.

4.2 Axle Load Conversion Considering Dynamic Load

Vehicle vibration acceleration follows the normal distribution with zero mean value [4], and therefore vertical vibration acceleration probability distribution can be obtained following a normal distribution, shown in Table 2. (Spaces of acceleration is 0.2σ with 16 spaces, and the negative sign means upward acceleration).

Table 2 Vertical acceleration distributional probability Qi

Vertical acceleration distribution scope	> 3	2.8-3.0	2.6-2.8	2.4-2.6	2.2-2.4	2.0-2.2	1.8-2.0	1.6-1.8	$\times (\pm\sigma)$
Distribution probability %	0.135	0.1205	0.2106	0.3537	0.5705	0.8847	1.318	1.8869	
Vertical acceleration distribution scope	1.4-1.6	1.2-1.4	1.0-1.2	0.8-1.0	0.6-0.8	0.4-0.6	0.2-0.4	0-0.2	$\times (\pm\sigma)$
Distribution probability %	2.5958	3.4313	4.3585	5.32	6.2398	7.0325	7.6162	7.926	

According to asphalt pavement design code of China, equivalent standard axle load conversion can be inferred by the equation below when tensile strain at bottom of surface is checked as a design index:

$$N = \sum_{i=1}^k c_{1i}c_{2i}n_i \left(\frac{p_i}{P}\right)^4 \tag{3}$$

where N is accumulated equivalent standard axle load; c_{1i} is axle number coefficient, c_{2i} is tire number coefficient; n_i is traffic volume, veh/d; p_i is axle load, KN; P is standard axle load, 100 KN.

After dynamic load is taken into account, equivalent axle load conversion formula can be expressed as follows:

$$N' = \sum_{i=1}^k \sum_{j=1}^m c_{1i}c_{2i}n_i Q_j \left(\frac{p_i \pm F_D}{P}\right)^4 \tag{4}$$

where: m is numbers of separated acceleration distribution, $m = 1-16$; Q_j is the probability of acceleration distribution of each separated acceleration distribution.

After dynamic load is considered, equivalent standard axle load increasing rate is:

$$\gamma = \frac{N' - N}{N} \times 100\% \tag{5}$$

Using the values listed in Tables 1 and 2, vehicle axle-tire acceleration and distributional probability of different traveling speeds can be calculated. The dynamic load and distribution probability can be obtained from Eq. (1), and the equivalent standard axle load can be calculated using Eq. (3). The increasing rate of equivalent standard axles load can be calculated using Eq. (4), and the results are listed in Table 3.

It is shown in Table 3 equivalent standard axle load exhibits different increasing patterns for heavy truck and light truck after considering dynamic load. On high class highway it increases 8.3–14.9% for heavy truck, and 3.6–5.4% for light truck; on low class highway, it increases 6.8–17.3% for heavy truck, and 3.2–12.5% for light truck.

According to asphalt pavement design code of China, when tensile stress at the bottom of semi-rigid base is taken as a design index, equivalent standard axle load conversion can be obtained by the equation below:

$$N' = \sum_{i=1}^k c'_{1i}c'_{2i}n'_i \left(\frac{p_i}{P}\right)^8 \tag{6}$$

Table 3 Increasing rate of equivalent axles load times when tensile strain at bottom of surface is taken as design index

Highway class	Travel speed (km/h)	Equivalent standard axle load increasing rate/(%)	
		Heavy truck	Light truck
Low class highway	70	17.3	12.5
	60	9.2	5.3
	50	7.5	4.6
	40	6.8	3.2
High class highway	100	/	5.4
	80	14.9	4.8
	60	8.3	3.6

Note travel speed of heavy truck can't keep 100 km/h in the testing required time

where N' is accumulated equivalent standard axle load; c'_{1i} is axle number coefficient, c'_{2i} is tire number coefficient; n'_i is traffic volume, veh/d; p_i is axle load, KN; P is standard axle load, 100 KN.

Using the same method, equivalent standard axle loads and the corresponding increasing rates are obtained and listed in Table 4.

It shows in Table 4 that equivalent standard axle load increases differently for heavy truck and light truck after considering dynamic load when tensile stress at the bottom of semi-rigid base. On high class highway it increases 34.2–64.9% for heavy truck, 14.2–21.8% for light truck; on low class highway, it increases 27.5–77.1% for heavy truck, 12.6–53.2% for light truck.

Table 4 Increasing rate of equivalent axles load times when tensile stress at bottom of semi-rigid base is taken as design index

Highway class	Travel speed km/h	Equivalent standard axle load increasing rate/(%)	
		Heavy truck	Light truck
Low class highway	70	77.1	53.2
	60	38.3	21.2
	50	31.9	18.2
	40	27.5	12.6
High class highway	100	/	21.8
	80	64.9	19.2
	60	34.2	14.2

5 Conclusions

This study examines axle-tire vertical acceleration of heavy truck and light truck on low class highway and high class highway based on field tests and analyses. The main conclusions of this study include:

- (1) Travel speed, loading mass and pavement roughness have significant influence on axle-tire vertical acceleration. Mean square value of axle-tire vertical acceleration increases with the increase of vehicle travel speed; The mean square value of the vibration acceleration for a fully load truck is considerably less than that for an empty truck.
- (2) After considering dynamic load, equivalent standard load increase by vehicle traveling speed: when tensile strain at bottom of surface is taken as design index, on high class highway equivalent standard load increases 8.3–14.9% for heavy truck, 3.6–5.4% for light truck; on low class highway, it increases 6.8–17.3% for heavy truck, 3.2–12.5% for light truck; when tensile stress at the bottom of semi-rigid base is taken as checking index, On a high class highway it increases 34.2–64.9% for a heavy truck, 14.2–21.8% for a light truck; on a low class highway, it increases 27.5–77.1% for a heavy truck, 12.6–53.2% for a light truck.

References

1. Yang Z, Zhe-ren W, Xiao-ning Z (1992) Random dynamic load analysis for vehicle traveling on roughness pavement. *J China Highw* 5(2):41–43
2. Huang XM (1992) Relationship stochastic analysis between dynamic load and pavement roughnes. *J Southeast Univ* 23(1):56–61
3. Lu S, Xue-jun D (1996) Dynamic load caused by vehicle-pavement interactions. *J Southeast Univ* 26(5):142–145
4. Xue-jun D (2002) Study on dynamics of vehicle-ground pavement structure system . *J South-east Univ (Nat Sci Ed)* 32(3):474–479
5. Dong Z, Peng-min LV (2010) Dynamic load of vehicle on high-class pavement . *J Chang'an Univ (Nat Sci Ed)* 30(1):95–99
6. Yi-fan S, Rong-feng C (2002) Analysis method of vehicle vibration response caused by pavement roughness. *J Traffic Transp Eng* 7(4):39–43
7. Shi-Yin Y, Ren-yun S (2008) Simulation study on handling and stability performance of automobile dynamic model with 7 DOFs. *J Xihua Univ* 27(2):58–61
8. Hong-liang Z, Chang-shun H (2005) Study on the allowable differential slope of the approach slab with five degree freedom vehicle model. *Chin Civil Eng J* 38(6):125–130
9. Dodds CJ, Robson JD (1973) The description of road surface roughness [J]. *J Sound Vib* 31(2):175–183
10. Todd KB, Kulakowski BT (1989) Simple computer models for predicting ride quality and pavement loading for heavy trucks. *Transp Res Rec* 1215:137–150
11. Hunt HE (1991) Modeling of road vehicles for calculation of traffic-induced ground vibration as a random process. *J Sound Vib* 144(1):41–51
12. Watts GR, Krylov VV (2000) Ground-borne vibration generated by vehicles crossing road humps and speed control cushions. *Appl Acoust* 59(3):221–236

13. Javier O, Goicolea JM, Astiz ÁM, Antolín P (2013) Fully three-dimensional vehicle dynamics over rough pavement. *Proc Inst Civ Eng Transp* 116(3):144–157
14. Park D-W, Papagiannakis AT (2014) Analysis of dynamic vehicle loads using vehicle pavement interaction model. *KSCE J Civ Eng* 18(7):2085–2092
15. En-li C, Liu Y, Zhao JB (2014) Experiments on dynamic response of pavement under moving load. *Vib Shock* 33(16):62–67
16. Qing-xiong W, Bao-chun C, Ling-zhi X (2008) Comparison of PSD method and IRI method for road roughness evaluation. *J Traffic Transp Eng* 8(1):36–40
17. Xiao-qing Z, Li-jun S (2005) Relationship between international roughness index and speed of quarter car. *J Tongji Univ (Nat Sci)* 33(10):1323–1327
18. Xiang-dong Z, Wei-ming Y, Hui-juan G (2009) Study on simulation method of road roughness by international roughness index. *J Highw Transp Res Develop* 26(4):13–16

Open Access This chapter is licensed under the terms of the Creative Commons Attribution 4.0 International License (<http://creativecommons.org/licenses/by/4.0/>), which permits use, sharing, adaptation, distribution and reproduction in any medium or format, as long as you give appropriate credit to the original author(s) and the source, provide a link to the Creative Commons license and indicate if changes were made.

The images or other third party material in this chapter are included in the chapter's Creative Commons license, unless indicated otherwise in a credit line to the material. If material is not included in the chapter's Creative Commons license and your intended use is not permitted by statutory regulation or exceeds the permitted use, you will need to obtain permission directly from the copyright holder.



Slope Reliability Analysis Based on Nonlinear Stochastic Finite Element Method



Jing Cheng, Ziyao He, Zhong Liu, and Lei Zhang

Abstract In slope stability reliability analysis, the deterministic analysis method is usually used to calculate the safety factor to measure the stability of the slope, but the traditional deterministic analysis method cannot fully consider and describe the natural spatial variability of soil, which leads to the failure probability calculation of the slope is not accurate enough. Aiming at the problem of spatial variability of soil mechanical parameters in slope stability analysis, this paper proposes a stochastic finite element method for calculating the distribution of FS (factor of safety) of dam slopes, and MC (Monte Carlo) strength reduction combined method and MC direct method are proposed to calculate the reliability of slope. Taking isotropic two-dimensional slope as an example: firstly, the random field is sampled to get the corresponding random field of material properties, and then the slope displacement, stress and plasticity zone results are calculated; then on the basis of N_{MC} times sampling of random field, there are: (i) Combined method (M1): the strength reduction method is used to get the reduction coefficient of each sample, and then its distribution, slope failure probability and reliability index are calculated; (ii) MC direct method (M2): using the viscoplastic method to solve and judge the instability of slopes, and the instability cases under all sample conditions are counted to obtain the failure probability and reliability index of slopes. The results show that the slope stability analysis considering the random field of material properties can obtain the real and reliable slope stability analysis results by comprehensively evaluating the slope safety through the mean value, variance, distribution and reliability index of the slope safety factor.

J. Cheng (✉) · Z. Liu · L. Zhang
Yellow River Institute of Hydraulic Research, Zhengzhou, China
e-mail: cj042@126.com

Z. Liu
e-mail: liuzhong200707@163.com

L. Zhang
e-mail: hkyzhanglei@163.com

J. Cheng · Z. He
Hohai University, Nanjing, China

This is a U.S. government work and not under copyright protection in the U.S.; foreign copyright protection may apply 2023

Y. Yang (ed.), *Advances in Frontier Research on Engineering Structures*, Lecture Notes in Civil Engineering 286, https://doi.org/10.1007/978-981-19-8657-4_30

Keywords Slope stability · Nonlinear · SFEM · Distribution of safety factor · Reliability index

1 General Instructions

The safety of slope engineering (including dam slope and reservoir bank slope) is crucial to the safety of water conservancy projects. Slope stability analysis methods mainly include limit equilibrium method, limit analysis method and finite element method [1]. Generally speaking, the finite element method analysis methods are mainly divided into two categories, one method is to increase the gravity load, and the other method is to reduce the strength characteristics of the soil, i.e., the load increment method and the strength discount method. All the above-mentioned methods still use the traditional single factor of safety method, which is relatively easy to calculate, to assess the slope stability, but it is proved that this method does not effectively consider the uncertainty of the actual load and material parameters. Therefore, the introduction of the nonlinear stochastic finite element method, which takes into account the uncertainty, is more in line with the actual situation, and the improvement of computer performance and the continuous progress of numerical solution technology also makes the large-scale nonlinear and stochastic finite element analysis possible.

In the nonlinear stochastic finite element method, the selection of parameters related to soil spatial variability is extremely important, such as correlation distance, parameter mean value and variation coefficients. There are many ways to calculate the correlation distance, including Spatial average method, fitting sample autocorrelation function method, curve limit method, semi-variation function, mean average method and statistical simulation method, etc. [2]. However, in engineering practice, if it is not a particularly important slope project, the site survey data are always limited, and it is difficult to accurately estimate the relative distance of the soil parameters [3]. Song [4] summarized lots of soil parameters by the literatures and presented the corresponding value range. In the anisotropic soil, the vertical correlation distance ranges from 0.2 to 6 m, and the horizontal correlation distance ranges from 20 to 80 m. The specific correlation distance is related to the size of the model. Jiang [5] proposed that the value range of variation coefficients of internal friction angle and viscous force is [0.05, 0.2] and [0.2, 0.7].

To address the spatial variability of soil mechanical parameters in embankment dam projects, this paper combines the Monte-Carlo method with the nonlinear stochastic finite element method based on the viscoplastic method and the strength reduction method to propose a safety and stability analysis method in embankment dam projects, and develops a corresponding procedure to study the influence of the cohesion and internal friction angle variation coefficients on the distribution of FS, solves the reliability indexes using two different methods and comparative analysis is performed.

2 Slope Safety Analysis Method Based on Nonlinear Stochastic Finite Element Method

2.1 Local Average Method for Random Field Discretization

The common methods of random field discretization mainly include the center point method, the local average method, shape function interpolation method and so on. The center point method is simple and convenient and easy to program for uniform random field, whereas with low accuracy. Shape function interpolation method discretizes the original continuous random field into a still continuous function. It does not involve the calculation of the correlation between each unit caused by the random field. It only requires that the value of the random field at each node is known, so the calculation is relatively simple, more suitable for nonlinear and non-uniform random fields [6]. The local average method uses the local average value of each discrete unit to characterize the characteristics of each unit body, and the mutual covariance between discrete units can be used to characterize the correlation between them, which is more suitable for uniform random fields. Therefore, this paper adopts the local average method to discrete uniform random fields. For a two-dimensional continuous uniform random field $\alpha(x, y)$, the mean and variance are m and σ^2 , respectively, and the local average random field of element e is defined α_e as [7]:

$$\alpha_e(x_e, y_e) = \frac{1}{A_e} \int_{\Omega_e} \alpha(x, y) dx dy \tag{1}$$

where A_e = area of element e; Ω_e = domain of element e, the mean value of α_e is:

$$E(\alpha_e) = E\left(\frac{1}{A_e} \int_{\Omega_e} \alpha(x, y) dx dy\right) = m \tag{2}$$

The covariance of any two elements is:

$$Cov(\alpha_e, \alpha_{e'}) = \frac{\sigma^2}{A_e A_{e'}} \int_{\Omega_e} \int_{\Omega_{e'}} \rho(x - x', y - y') dx dy dx' dy' \tag{3}$$

where ρ = autocorrelation function; σ = standard deviation. Do coordinate isoparametric transformation for integral of Eq. (3):

$$x = \sum_{i=1}^n N_e^i x_e^i, \quad y = \sum_{i=1}^n N_e^i y_e^i \tag{4}$$

where n = number of nodes of element e ; N_e^i = shape function of displacement pattern of element e ; x_e^i and y_e^i = coordinate of nodes of element e . And do coordinate isoparametric transformation for integral of Eq. (3):

$$Cov(\alpha_e, \alpha'_e) = \frac{\sigma^2}{A_e A_{e'}} \int_{-1}^1 \int_{-1}^1 \int_{-1}^1 \int_{-1}^1 \rho(r, s) |J| |J'| d\xi d\xi' d\eta d\eta' \tag{5}$$

where J = Jacobian matrix; ξ and η = variates of x and y after doing coordinate isoparametric transformation.

The random field correlation structure often uses autocorrelation functions in the form of triangular, exponential, second-order AR, Gaussian, etc. In this paper, the following two-dimensional Gaussian-type correlation functions are selected for calculation.:

$$\rho(r, s) = \exp\left(-\pi\left(\frac{r^2}{\theta_h^2} + \frac{s^2}{\theta_v^2}\right)\right) \tag{6}$$

where θ_h = horizontal correlation distance; θ_v = vertical correlation distance; r and s = distance of two points in the horizontal direction and the distance of two points in the vertical direction.

2.2 Viscoplastic Method

There are two main methods for solving problems with material nonlinearity, which are “constant stiffness iterative method” and “variable stiffness method”. In this paper, the former method is adopted, which modifies the “load” vector on the right side of the stiffness equation during iteration to consider the nonlinearity of the problem. In each iteration of this method, the load vector is composed of external load and self-balancing “body load”. The viscoplastic method for generating body load is described below.

ZienKiewicz [8] proposed a variable load model that allowed the stress of the material to exceed the failure criterion within a limited “period”, which is the “time-step” derived by Corneau [9] for numerical calculation of absolute stability, which was related to the assumed failure criterion. The time-step of materials Mohr–Coulomb widely used in geotechnical engineering is:

$$\Delta t = \frac{4(1 + \nu)(1 - 2\nu)}{E(1 - 2\nu + \sin^2 \phi)} \tag{7}$$

If the viscoplastic strain rate is multiplied by a pseudo time step, the viscoplastic strain increment accumulated to the next time step can be obtained:

$$\dot{\varepsilon}^{\text{VP}} = F \frac{\partial Q}{\partial \sigma} \quad (8)$$

$$(\delta \varepsilon^{\text{VP}})^i = \Delta t (\varepsilon^{\text{VP}})^i \quad (9)$$

$$(\Delta \varepsilon^{\text{VP}})^i = (\Delta \varepsilon^{\text{VP}})^{i-1} + (\delta \varepsilon^{\text{VP}})^i \quad (10)$$

where $\dot{\varepsilon}^{\text{VP}}$ = viscoplastic strain rate; $(\delta \varepsilon^{\text{VP}})^i$ = viscoplastic strain increment of time-step i ; $(\Delta \varepsilon^{\text{VP}})^i$ = viscoplastic strain of time-step i ; F = failure criterion function; Q = plastic potential function.

The body load is the result of adding up at each “time-step” within a strength reduction and integrating and summing over all elements containing Gaussian yield points as follows:

$$P_b^i = P_b^{i-1} + \sum_{iel}^{nel} \int B^T D^e (\delta \varepsilon^{\text{VP}})^i d\Omega \quad (11)$$

where P_b^i = body load at the i -th time-step; iel = element i , nel = number of elements; B = strain matrix; D = elastic matrix.

2.3 Strength Reduction Finite Element Method

Under the condition of constant external load, divide the slope soil strength parameters by the same reduction coefficient to obtain the cohesion and internal friction angle under the current reduction coefficient, and use the reduced soil parameters as the new the calculation parameters are substituted into the calculation. After several times of reductions, the slope soil reached a critical failure state and became unstable. The reduction coefficient at this time is defined as the FS of the slope, and the corresponding failure surface is the slippery surface of the slope instability. The strength parameter reduction formula is:

$$c_1 = \frac{c_0}{K} \quad (12)$$

$$\varphi_1 = \arctan \frac{\tan \varphi_0}{K} \quad (13)$$

where K = reduction coefficient; c_0 and c_1 = before and after reduced cohesive force; φ_0 and φ_1 = before and after reduced internal friction angle.

2.4 Criterion for Judging Slope Instability

Three methods are generally used to judge slope instability in finite element strength reduction analysis: (i) the numerical iteration of finite element does not converge; (ii) the displacement of characteristic points changes abruptly; (iii) the generalized plastic strain or equivalent plastic strain penetrates from the foot to the top of the slope.

Among them, the sudden change of displacement of characteristic points and plastic zone penetration usually need to be judged artificially after the post-processing of calculation results, and there is no better automatic computer identification technology or method at present because the stochastic finite element requires a large number of sampling calculations. In this paper, in order to facilitate a large number of sampling calculations, the method of numerical iterative non-convergence is used to determine the slope instability.

3 Example Analysis

3.1 A Calculation Example of Homogeneous Slope

Using the homogeneous slope model in Dawson et al. [10] as the analysis object, the slope size is consistent with the literature, the slope height is 10 m, the slope angle is 45° , the horizontal constraint on both sides, the fixed constraint at the bottom, the weight is 20 kN/m^3 , the elastic modulus is 100 MPa, the Poisson's ratio is 0.3, the cohesion is taken as 17.77 kPa, and the internal friction angle is 20° . The FS of the above parameters obtained by the limit equilibrium method in the software GeoStudio is 1.2, as shown in Fig. 3, which is consistent with the value of FS of grade 3 slopes under normal operation conditions in the specification. The calculation model and constraints are shown in Fig. 1. The background grid as shown in Fig. 2 is used for slope finite element analysis and random field dispersion.

Fig. 1 Slope model and boundary conditions (M)

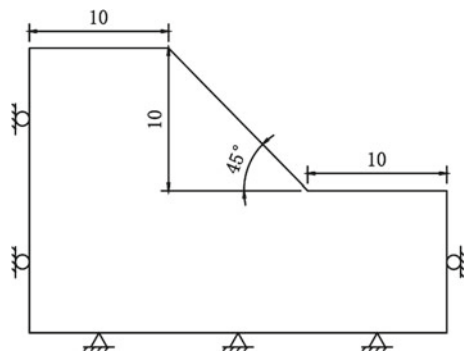


Fig. 2 Random field and slope grid division

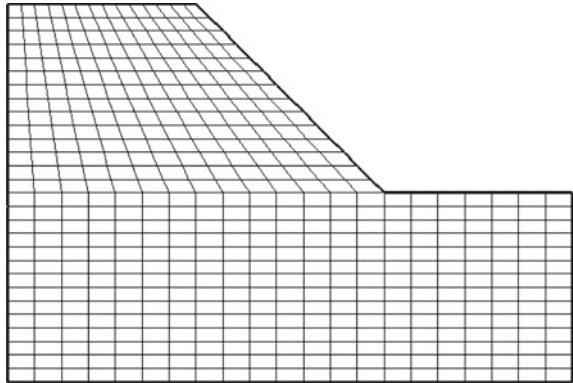
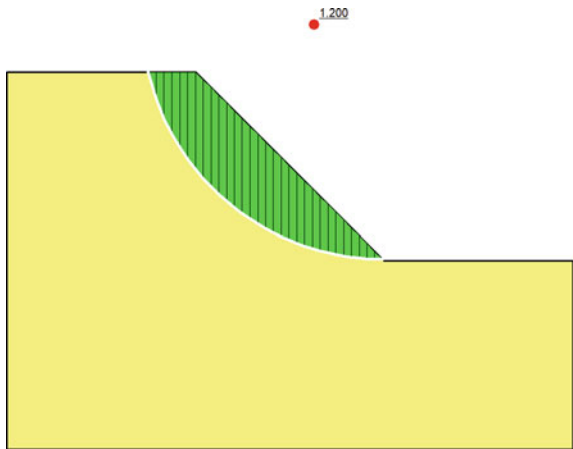


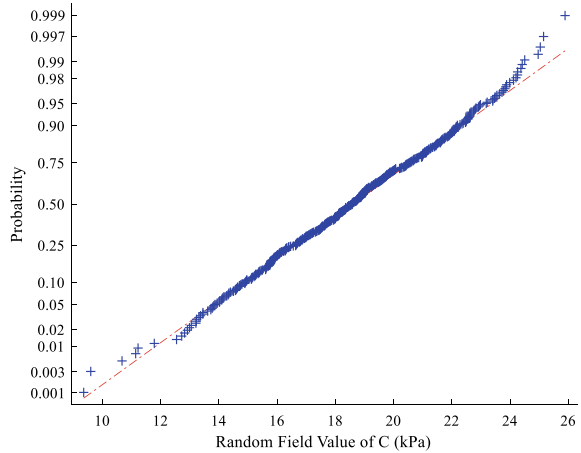
Fig. 3 Calculation results of the limit equilibrium method



3.2 A Calculation Example of Slope Considering Material Properties Random Field

In this section, on the basis of the homogeneous slope model and parameters in Sect. 3.1, the random field characteristics of cohesion and internal friction angle are considered, where the coefficient of variation of cohesion c and internal friction angle φ are taken as 0.2 and 0.05 respectively, and the horizontal and vertical correlation distances of both are taken as 5 m, and the correlation coefficients of both are taken as 0. The specific research ideas are as follows: (1) Firstly, the random field is sampled to get the corresponding random field of material properties, and then the slope displacement, stress and plastic zone results are calculated; (2) N_{MC} times sampling of the random field; (3) Combined method M1: On the basis of (2), the reduction coefficients under each sample condition are obtained by strength reduction method and their distribution is calculated, and then the corresponding slope failure

Fig. 4 Normality verification of the cohesion distribution



probability and reliability index are found; (4) MC direct method M2: On the basis of (2), the viscoplastic method is directly solved to determine the instability of the slope, and then the instability cases under all sample conditions are counted to obtain the failure probability and reliability index of the slope.

Calculation results of single sampling in random field

Based on the given random field parameters and the method in Sect. 2.1, the covariance matrix of the random field elements is obtained, and then the MC sampling of the random field is obtained using mathematical methods. By Fig. 4, normality of the once sampling results of the random field was examined, and the horizontal coordinate in the figure is the random field parameter values, and the vertical coordinates are the cumulative distribution probabilities of the parameter values in the horizontal coordinates. The distribution of points in the normal probability plots of the parameter random field is both approximated as a straight line, and their normal distribution properties can be verified accordingly.

For this sampling, when the reduction coefficient is 1.28, the displacement changes abruptly, indicating that the FS of slope in this sample is 1.28. The calculation results of slope material characteristics and displacement under this reduction coefficient are shown in Figs. 5, 6, 7, 8 and 9. In Fig. 5, the maximum value and minimum value of cohesion are 18 kPa and 8 kPa respectively, and the mean value of cohesion after reduction is 13.83 kPa. In Fig. 6, the maximum value and minimum value of the internal friction angle are 17° and 14.2° respectively, and the mean value of the internal friction angle after reduction is 15.6° .

As shown in the figure, the maximum value of X-direction displacement is near the foot of the slope, which is 19 mm, and the displacement near the slope surface in the plastic zone is relatively large, between 16 and 19 mm; the maximum value of Y-direction displacement is at the top of the slope, which is 42 mm, and the overall trend of Y-direction displacement is larger at the top and smaller at the bottom; the

Fig. 5 Slope cohesion distribution (Pa)

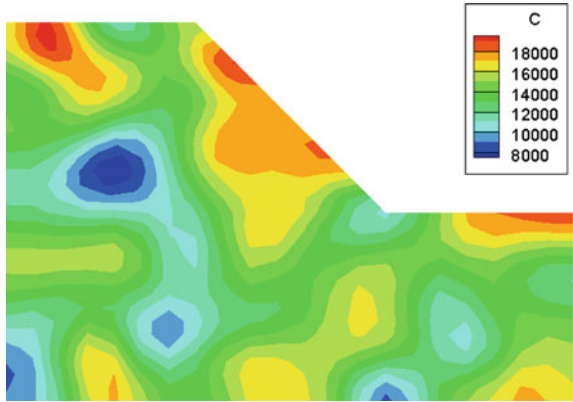


Fig. 6 Distribution of internal friction angle of the slope ($^{\circ}$)

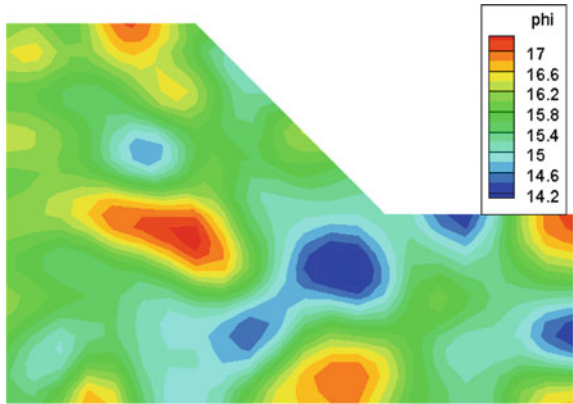


Fig. 7 Displacement U_x (m)

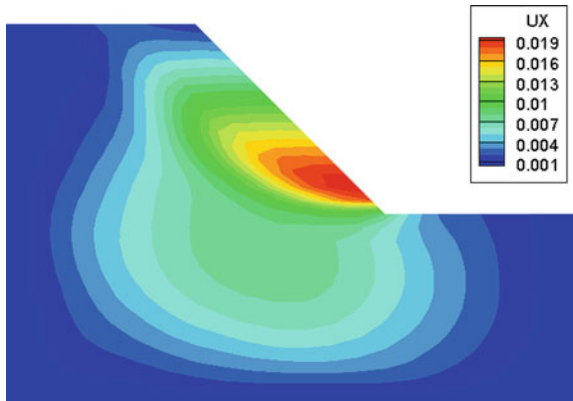


Fig. 8 Displacement U_y (m)

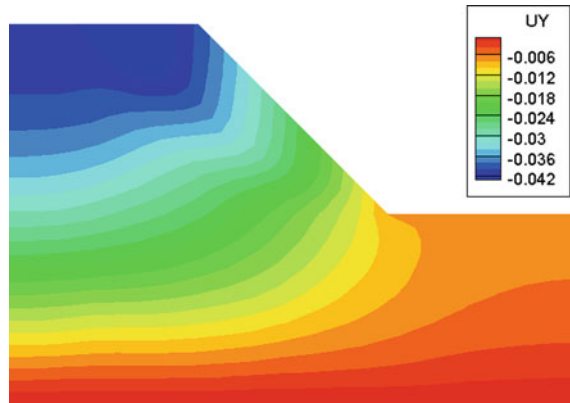
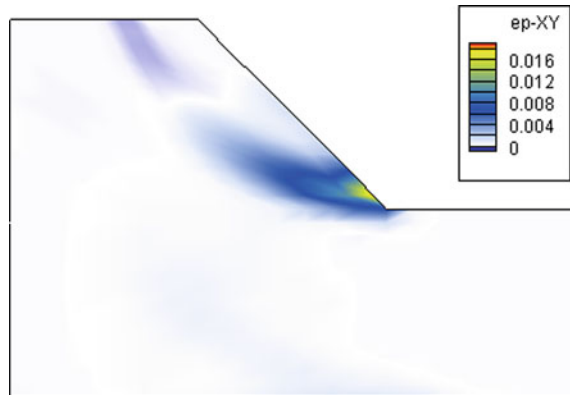


Fig. 9 Plastic zone of the slope



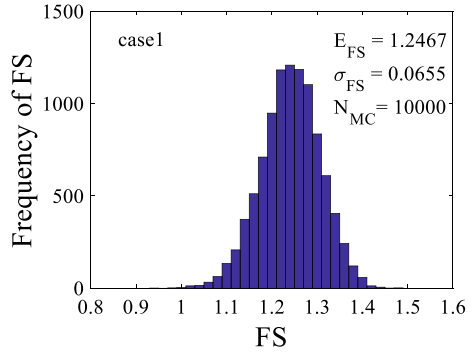
plastic zone is shown in Fig. 9, plastic yielding occurs from the foot of the slope to the slip arc-like area in the middle of the slope.

Calculation of slope reliability based on combined method (M1)

MC strength reduction combined method to solve the reliability: the number of samples with the FS less than 1 in the strength reduction calculation after the random field sampling is considered as the number of slope failures M_f . The number of values of FS less than 1 in the distribution of FS and divided by the number of random field sampling N_{MC} , the probability of failure can be obtained by $P_f = M_f/N_{MC}$. When the basic variables are normally distributed, the reliability index is $\beta = -\Phi^{-1}(P_f) = \Phi^{-1}(1 - P_f)$.

Figure 10 shows the statistical histogram distribution of the FS obtained by sampling random field for N_{MC} times ($N_{MC} = 10,000$). The corresponding probability cumulative distribution curve is shown in Fig. 11, and the specific description of each parameter in the figure is shown in Table 1. For this sampling, the mean value of the FS is 1.2467, slightly higher than 1.2 obtained by the limit equilibrium

Fig. 10 Frequency distribution of FS



method. The values of FS are concentrated in [1.2, 1.3], and the highest frequency is about 1250. The failure probability obtained by M1 method is 0.0003, and the corresponding reliability index is 3.4316.

Fig. 11 Cumulative distribution of FS

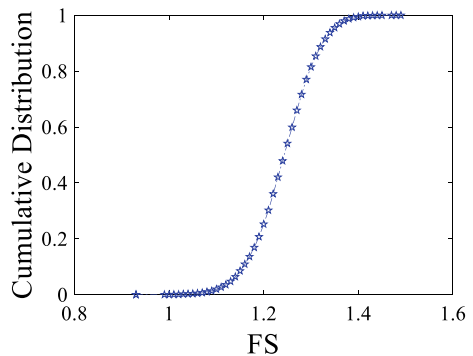


Table 1 Parameter values and calculation results

	Input parameters			Output parameters			
	N_{MC}	COV_c	COV_φ	E_{FOS}	δ_{FOS}	$P_{f0}(\%)$	β
Case1	10,000	0.2	0.05	1.2467	0.0655	0.03	3.4316
Case2	10,000	0.3	0.05	1.2278	0.1106	2.48	1.9634
Case3	10,000	0.2	0.1	1.2445	0.0720	0.09	3.1214
Case4	10,000	0.3	0.1	1.2246	0.1184	2.71	1.9252
Case5	10,000	0.2	0.2	1.2382	0.0930	0.56	2.5364
Case6	10,000	0.3	0.2	1.2169	0.1313	4.23	1.7246

Note N_{MC} = the number of MC samples; COV_c = variation coefficient of cohesion c ; COV_φ = variation coefficient of internal friction Angle φ ; E_{FOS} = mean value of FS; δ_{FOS} = variance of FS; P_{f0} = failure probability, obtained by M1 method; β = reliability index

Calculation of slope reliability based on MC direct sampling method (M2)

The calculation method of slope reliability based on MC direct sampling method: firstly, generate N groups of samples conforming to c and φ , and probability distribution and substitute into limit state function $Z = g(c, \varphi)$ (when $Z < 0$, it means the slope fails; $Z = 0$, it is the limit state equation of the slope, which means the slope is in the limit state; $Z > 0$, it means the slope is in the reliable state and can meet the functional requirements), and Z_1, Z_2, \dots, Z_N is a sample of the random variable Z with a capacity of N . If the number of samples in the failure zone is M , according to Bernoulli's large number theorem, the failure probability can be approximately expressed as $P_f = M/N$. The reliability index is solved in the same way as in previous section.

When MC direct sampling method is used for slope stability analysis and calculation, the strength reduction is no longer considered, and the reduction coefficient is set as 1. The random field is sampled N_{MC} times. The non-convergence of numerical iterations is taken as the criterion of slope instability, and the times of non-convergence are accumulated to obtain M , and the ratio of M to N_{MC} is the failure probability.

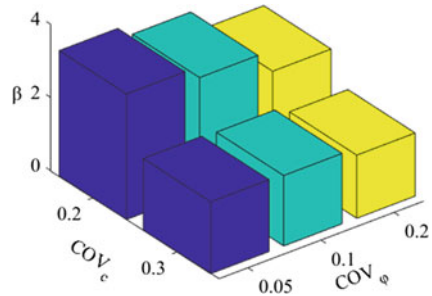
3.3 Comparison of FS Distribution and Reliability Index Solution of M1 Method

On the basis of the slope calculations based on the random field in Sect. 3.2, the variation coefficients of c and φ is changed to analyze its influence on the distribution of FS. Material variability and calculation results of each group are shown in Table 1.

Note: The slight mutations in the distribution of Case3 and Case4 are caused by insufficient sampling, and the mutations will become smooth if the sampling number is increased.

It can be seen from Fig. 12 that, with the increase of COV_c or COV_φ , the reliability index gradually decreases, but in the ascending direction of COV_c , the reliability index decreases at a faster speed and with a greater range. With different values of COV_c (or COV_φ), the distribution of the corresponding FS changes similarly when COV_φ (or COV_c) is changed, and the specific analysis is as follows: ① When COV_c is set to 0.2: compare Figs. 10, 14 and 16, the mean value of FS decreases gradually with the increase of COV_φ from 1.2467 to 1.2382, and the variance increases from 0.0655 to 0.093. The values of FS are concentrated in the area around 1.25, and the highest frequency is about 1250 times. ② When COV_φ is set to 0.2: compare with Fig. 16 and Fig. 17, the distribution of FS becomes more dispersed after the COV_c increase, and the smaller values of FS are more likely to appear. As shown in Fig. 16, values of FS are concentrated between [1.2, 1.25], with the highest frequency of about 1300 times. The values of FS of Fig. 17 are mainly distributed between [1.23, 1.25], and the highest frequency is only about 1000 times. ③ When the variability of φ is constant, the failure probability increases sharply with the increase of the

Fig. 12 Relationship between material variability and reliability index



variability of c , while the corresponding reliability index decreases rapidly. When the variability of c is kept constant, the failure probability increases relatively slowly with the increase of the variability of ϕ , and the reliability index decreases relatively slowly. Case1 has the lowest failure probability and the largest reliability index, which are 7×10^{-4} and 3.1947 respectively. ④ The variation trend of the mean value of FS is consistent with the reliability index, but opposite to the failure probability. While the mean value of FS decreases gradually, the reliability index also decreases gradually, and the failure probability increases gradually.

The probability density and cumulative distribution curves of FS of each scheme are shown in Figs. 18 and 19: (1) when COV_c is 0.2, the peak probability density of Case5 is the smallest ($PD_{min}^{0.2}$). When COV_c is 0.3, the peak probability density of Case2 is the highest ($PD_{max}^{0.3}$). Where $PD_{min}^{0.2} > PD_{max}^{0.3}$. (2) All schemes are sorted according to the descending order of the maximum probability density in the figure. The mean value of the probability density distribution graph decreases in this order, which shows that the normal distribution curve of each scheme moves to the left gradually. The variance of FS distribution increases in this order, which shows that the normal distribution curve and the cumulative distribution curve of each scheme gradually become more gentle.

3.4 Comparison Analysis of Reliability Indexes Obtained by M1 Method and M2 Method

In this section, MC direct sampling method (M2) is used to solve the slope failure probability and reliability indexes of the six groups of schemes in Sect. 3.3, and the results are compared with M1 method, as shown in Table 2:

According to the above table and the results in Figs. 12, 13, 14, 15, 16 and 17, it can be found that: the reliability index obtained by M2 method is slightly smaller than that obtained by M1 method. In fact, the results are very similar, so it can be considered that the failure probability and reliability indexes obtained by using M1 method are reliable.

Table 2 Comparison of the slope safety and reliability indexes obtained by different methods

	Input parameters			OP1		OP2	
	N_{MC}	COV_c	COV_φ	$P_{f0}(\%)$	β	$P_{f1}(\%)$	β
Case1	10,000	0.2	0.05	0.03	3.4316	0.070	3.1947
Case2	10,000	0.3	0.05	2.48	1.9634	2.890	1.8972
Case3	10,000	0.2	0.1	0.09	3.1214	0.012	3.0357
Case4	10,000	0.3	0.1	2.71	1.9252	3.110	1.8649
Case5	10,000	0.2	0.2	0.56	2.5364	0.079	2.4135
Case6	10,000	0.3	0.2	4.23	1.7246	4.780	1.6666

Note OP1 = output parameters (M1); OP2 = output parameters (M2)

Fig. 13 Frequency distribution of FS (Case2)

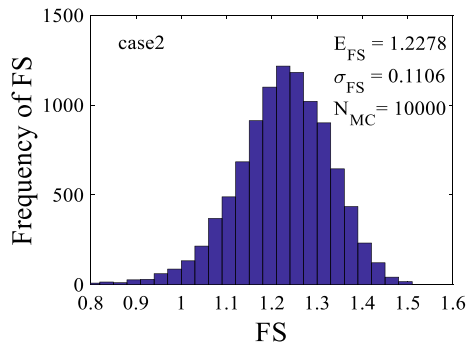
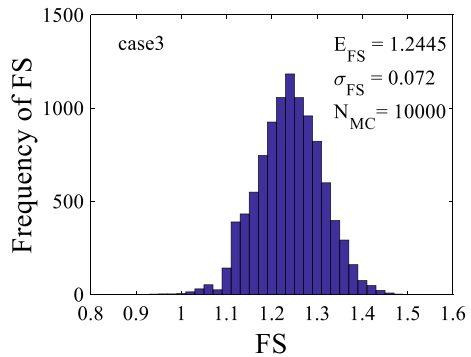


Fig. 14 Frequency distribution of FS (Case3)



4 Conclusion

This paper proposes a slope safety analysis method based on the nonlinear stochastic finite element method, investigates the influence of the variability of the mechanical parameters of the slope soil on the distribution of FS, and uses two methods to solve

Fig. 15 Frequency distribution of FS (Case4)

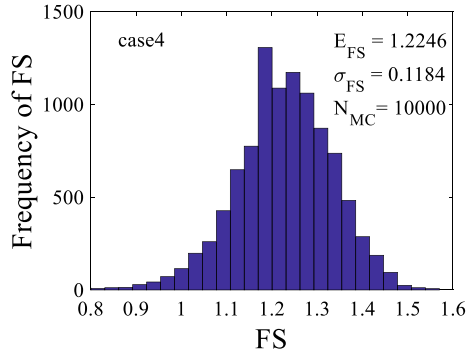


Fig. 16 Frequency distribution of FS (Case5)

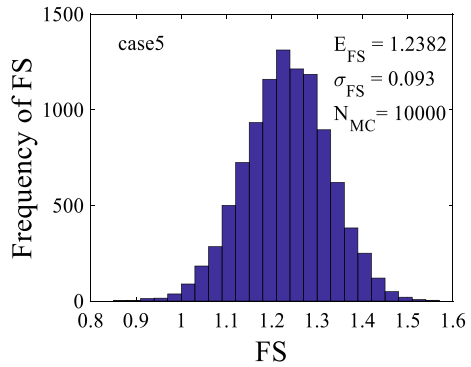
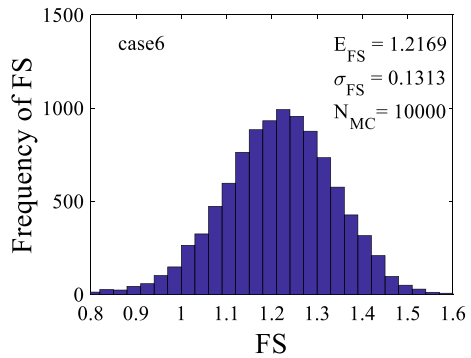


Fig. 17 Frequency distribution of FS (Case6)



and analyze the reliability index. The results shows that: the method can better simulate the spatial variability of materials; compared with the traditional single safety factor method, only a general empirical coefficient can be obtained, which cannot reflect the spatial variability of material parameters, the introduction of parameter random fields can reflect the spatial variability of material parameters in the mean,

Fig. 18 Probability density of FS

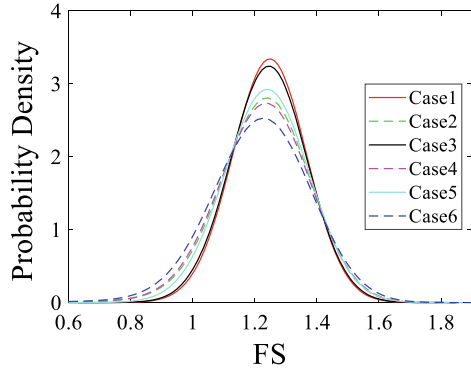
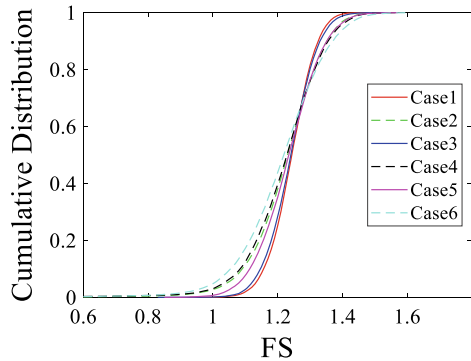


Fig. 19 Cumulative distribution of FS



variance and distribution of the slope safety factor, and then combined with the reliability index to conduct a more comprehensive evaluation of the slope safety; the variability of soil parameters has a greater influence on the distribution of FS and reliability index, and as the variability of different parameters increases, the mean value of FS and slope reliability gradually decrease as the variability of different parameters increases.

In order to further improve the application effect of this method in actual engineering, the following research work is needed: the slope is regarded as a uniform random field in this slope calculation example, but there are different material partitions in actual engineering, and there is a certain correlation between different partitions, and the requirements for random field are more strict; the coefficient of variation of soil parameters and the correlation distance have significant effects on the calculation results, but there is less engineering information and lack of unified and clear standards for their values, so a large number of parameter experiments need to be carried out in the later stage to obtain reliable parameters for the distribution of soil properties.

Acknowledgements The support of the Open Fund of Research Center on Levee Safety and Disaster Prevention, Ministry of Water Resources of PRC (DFZX202001), the Science and

Technology Funds by the Department of Water Resources of Guizhou Province (KT201812), and the Fundamental Research Funds for the Central Universities (2019B11414) is gratefully acknowledged.

References

1. Luan MT, Wu YJ, Nian TK (2003) A criterion for evaluating slope stability based on development of plastic zone by shear strength reduction FEM. *J Disaster Prev Mitig Eng* 23(3):1–8
2. Cheng Q, Luo SX, Peng XZ (2000) Correlation of scale of fluctuation with soil property parameters and its calculation method. *J Southwest Jiaotong Univ* 35(5):496–500
3. Wu ZJ (2009) Study on spatial variability simulation of soil properties and practical reliability analysis method of soil slope. Wuhan, China: Institute of Rock & Soil Mechanics, The Chinese Academy of Sciences
4. Song YD (2017) Study on slope reliability considering spatial variability of rock and soil strength parameters. University of Chinese Academy of Sciences, Beijing, China
5. Jiang SH (2014) A non-intrusive stochastic method for slope reliability in hydroelectricity engineering. School of Water Resources and Hydropower Engineering, Wuhan University, Wuhan
6. Zhen YN (2014) Study of reliability for loses slope based on random finite element. Xi'an: Ching'an University
7. Chen Q, Dai ZM (1991) The isoparametric local average random field and neumann stochastic finite element method. *Chin J Comput Mech* 8(4):397–402
8. Zienkiewicz OC, Corneau IC (1974) Visco-plasticity—plasticity and creep in elastic solids—a unified numerical solution approach. *Int J Numer Meth Eng* 8(4):821–845
9. Corneau I (1975) Numerical stability in quasi-static elasto/visco-plasticity. *Int J Numer Meth Eng* 9(1):109–127
10. Dawson EM, Roth WH, Drescher A (1999) Slope stability analysis by strength reduction. *Geotechnique* 49(6):835–840

Open Access This chapter is licensed under the terms of the Creative Commons Attribution 4.0 International License (<http://creativecommons.org/licenses/by/4.0/>), which permits use, sharing, adaptation, distribution and reproduction in any medium or format, as long as you give appropriate credit to the original author(s) and the source, provide a link to the Creative Commons license and indicate if changes were made.

The images or other third party material in this chapter are included in the chapter's Creative Commons license, unless indicated otherwise in a credit line to the material. If material is not included in the chapter's Creative Commons license and your intended use is not permitted by statutory regulation or exceeds the permitted use, you will need to obtain permission directly from the copyright holder.



Basic Research on Automatic Tying Equipment for Reinforced Steel Skeletons of Precast Shear Walls



Zhenlei Guo, Zhijie Gao, Zhongjian Duan, and Jiayang Zhang

Abstract In order to study the parameters of the automatic tying equipment for steel skeletons of precast shear walls, 19 precast-shear-wall projects and 16,036 precast-shear walls have been explored, with the thickness of the steel skeletons being studied according to the specifications and sleeve diameters, and the difference between production with and without edge forms being analyzed. The study displays that the automatic tying equipment for steel skeletons should be able to produce wall panels with a height of 2.5–2.95 m and a width of 0.8–5.9 m; the equipment should be able to produce 6–25 types of reinforcement bars with a diameter of 6–25 mm; the minimum spacing between the steel skeletons produced by the equipment should be 5 mm; the equipment should be able to produce shear-wall skeletons with a thickness of 150–170 mm; in case that the equipment producing the steel skeletons with side forms is more problematic, they should be produced without such edge forms.

Keywords Prefabricated buildings · Shear wall · Reinforced skeleton · Automatic tying · Equipment requirements

1 Introduction

The construction industry, as a pillar industry of the national economy, has provided strong support for the sustainable and healthy development of China's economy. Since the issuance and implementation of the Guiding Opinions of the General Office of the State Council on Vigorously Developing Prefabricated Building [3] No. 71, the new construction industrialization represented by prefabricated buildings has been rapidly promoted, and the construction level and building quality have been significantly improved.

Prefabricated buildings have come a long way in China, which, however, are limited by the unsatisfactory performance of intelligent equipment, leading to the fact that tying reinforcement in prefabricated component factories still depends on

Z. Guo (✉) · Z. Gao · Z. Duan · J. Zhang
Beijing General Research Institute of Building Materials Co., Ltd, Beijing, China
e-mail: 424285621@qq.com

manual work, far from industrialization. On 28 July 2020, the Ministry of Housing and Construction and thirteen other departments jointly issued the “Guidance on Promoting the Coordinated Issuance of Intelligent Construction and Building Industrialization” Jian Shi [8] No. 60. On 28 August 2020, the Ministry of Housing and Construction and nine other departments jointly issued “Several Opinions on Accelerating the Development of New Building Industrialization” Jianbiao Gui [9] No. 8.

Prefabricated component manufacturers need to produce a large number of steel skeletons for wall panels and staircases, but the steel skeletons in three-dimensional form cannot be intelligently tied and have to rely on manual work [1, 5, 7]. This accounts for low production efficiency and hence affects the transformation and upgrading of the construction industry [17].

At present, the main domestic prefabricated component factories, such as Beijing Building Industrialization Group Corp., Ltd., Beijing Yugou Group Co., Ltd., Changsha Broad Homes Industrial Group Co., Ltd., Sany Construction Technology Co., Ltd., China Construction Science & Technology Group Co., Ltd., Beijing Everest Green Building Technology Co., Ltd., My Home Real Estate Group and the like, still rely on manual tying for reinforcement skeletons of shear walls, which is not automated [2]. Among them, Beijing Yantong Architecture Component Co. Ltd. has demonstrated the process of tying steel skeletons with a mechanical arm, but the equipment lacks the functions like horizontal and vertical positioning of reinforcement, installment and welding of tension bars, with problems such as high equipment cost and low work efficiency, which can only be used for demonstration instead of actual production [19].

Domestic rebar line manufacturers including Sany Construction Technology Co., Ltd. and TJK Machinery (Tianjin) Co, Ltd can produce automatic equipment for straightening and bending reinforcement as well as positioning and tying of two-dimensional meshes [12]. However, there is a lack of positioning and tying equipment related to 3D rebar skeletons [13, 16].

There are already departments abroad doing related research and development, but no mature products have been developed [15]. Founded in 2016, US-based Toggle Construction is a manufacturer of industrial automation equipment that develops and introduces industrial robotics and automation into the construction sector to create prefabricated steel skeletons for columns, beams, walls and slabs. According to the information, Toggle’s R&D technology focuses on lifting, positioning, strapping and welding, without considering rebar feeding, arrangements of tension bars, and the relationship between the rebar skeletons and the molds [6, 11, 14].

2 Number and Volume Ratio of Three Types of Shear Walls

Precast shear walls can be divided into opening-less shear walls, single-opening shear walls and double-opening shear walls according to the situation of openings [10]. According to the study of 18 projects concerning prefab shear walls, a resettlement

housing project in Daxing, Beijing, has a total of 611 prefabricated shear walls with a volume of 923 m³, of which the number of shear walls without openings accounts for 53.19%, with its volume representing 50.26%; the number of single-opening shear walls accounts for 34.04%, with its volume representing 50.26%; the number of double-opening shear walls accounts for 12.77%, with its square volume representing 13.49%, as detailed in Fig. 1.

A residential project in Shunyi District, Beijing, has a total of 1164 precast shear walls and a volume of 821.0 m³, of which the number of shear walls without openings accounts for 52.75%, with its volume of 49.63%; the number of shear walls with single openings accounts for 47.25%, with its volume of 50.37%, and there are no shear walls with double openings; see Fig. 2 for details.

A residential project, 1#2#building, in Fengtai District, Beijing, has a total of 760 blocks of precast shear walls and a volume of 956.2 m³, of which the number of the shear wall without opening accounts for 100.0%, with its volume of 100.0%, and there are no single-opening shear wall and double-opening shear wall; see Fig. 3 for details.

A total of 19 precast shear wall projects have been counted, and the quantity percentages of shear walls without openings are distributed between 32–100%, depending on specific projects, and the percentages of volumes are between 23.69–100%, mainly concentrated in 50–70%. See Fig. 4.

Fig. 1 Resettlement housing project in Daxing district, Beijing

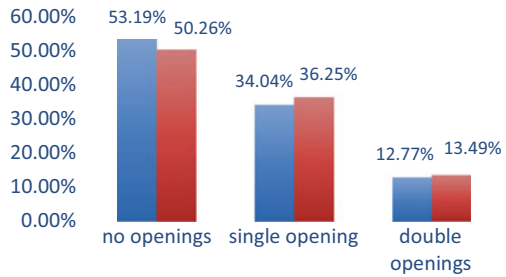


Fig. 2 Residential project in Shunyi district, Beijing

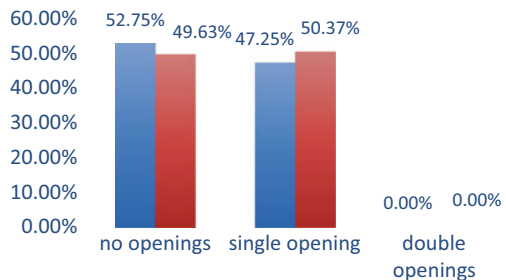


Fig. 3 Residential project (#1#2# Building) in Fengtai District, Beijing

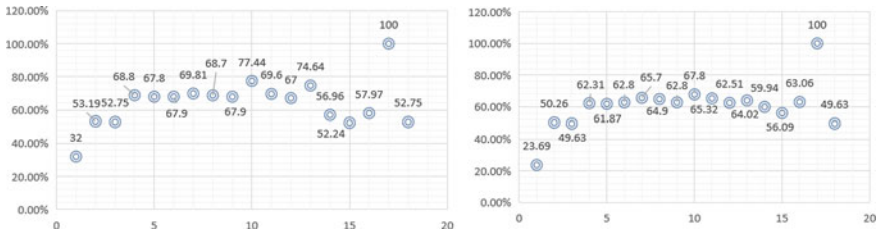
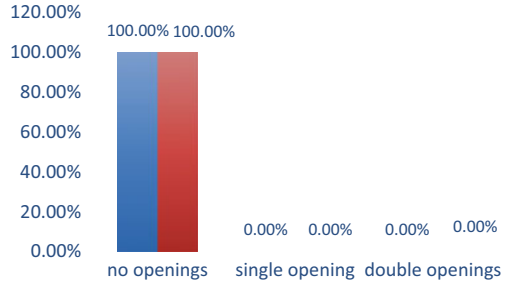


Fig. 4 Number of shear walls without openings and percentage of volume

3 External Profile Dimensions of Precast Shear Walls

A total of 19 precast shear wall projects and 9922 shear walls without openings have been studied, with a discovery of a height distribution between 2.5–2.95 m and a width distribution between 0.8–4.0 m, as shown in Fig. 5.

A total of 19 precast shear wall projects and 5050 single-opening shear walls have been studied, with a discovery of a height distribution between 2.58–2.95 m and a width distribution between 1.59–5.0 m, as shown in Fig. 6.

A total of 19 precast shear wall projects and 994 single-opening shear walls have been studied, with a discovery of a height distribution between 2.61–2.95 m and a width distribution between 3–5.9 m, as shown in Fig. 7.

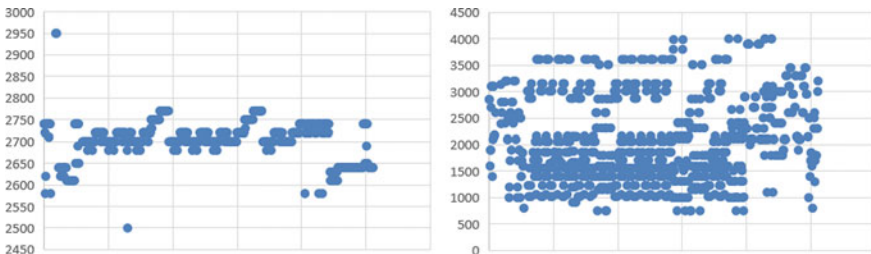


Fig. 5 Distribution of heights and widths of shear walls without openings

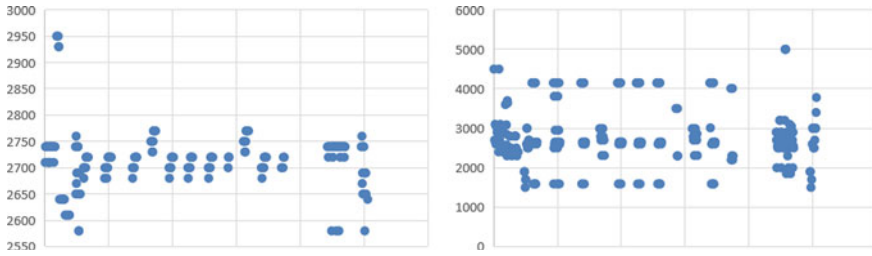


Fig. 6 Distribution of heights and widths of single-opening shear walls

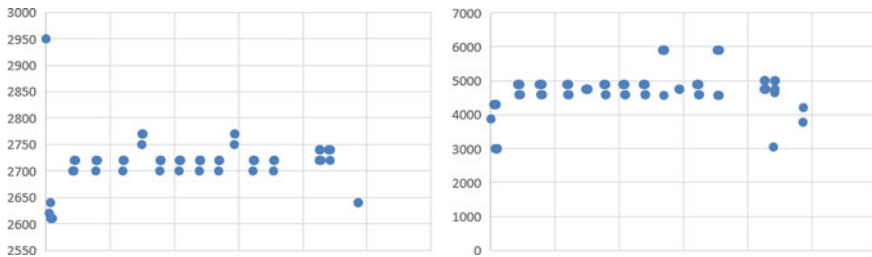


Fig. 7 Distribution of heights and widths of double-opening shear walls

Table 1 Summary table of shear wall heights and widths

Type	Height (m)	Width (m)
Shear walls without openings	2.5–2.95	0.8–4.0
Single-opening shear walls	2.58–2.95	1.59–5
Double-opening shear walls	2.61–2.95	3–5.9

A total of 19 projects and 16,036 walls have been studied, with the results shown in Table 1.

The equipment of steel skeletons for precast shear walls should be able to produce wall panels with a height of 2.5–2.95 m and a width of 0.8–5.9 m.

4 Types of Prefabricated Reinforcement

The connection method for common precast shear walls is sleeve joint, whose horizontal distribution reinforcement consists of 2 types: closed stirrups and open stirrups [4, 18]. The closed stirrups can guarantee the thickness of the reinforcement skeleton in the production process, but the vertical reinforcement needs to be put from the top to the bottom during construction, which is a large workload on site, so the open stirrups are in high demand; see Fig. 8.

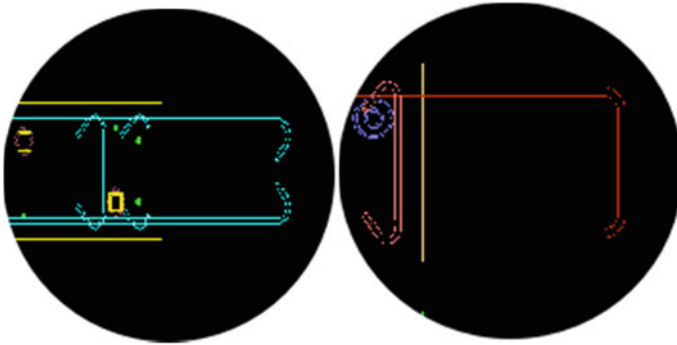


Fig. 8 Illustration of closed and open stirrups

There are 9 types of precast shear wall reinforcement for closed stirrups and 8 types of reinforcement for open stirrups; see Fig. 9.

According to the study, the following results could be obtained:

- (1) There are 6–9 reinforcement types for shear walls without openings and 25 reinforcement types for shear walls with openings.
- (2) Common reinforcement diameters are 6–25 mm.
- (3) Rebar spacing is diversified, including 50, 75, 117, 140, 150, 170, 200, and 300 mm.







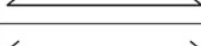
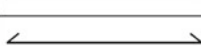

5 Thickness of Steel Skeletons

The thickness of a common load-bearing shear wall is 200 mm, with the minimum thickness of the concrete protection layer being 15–20 mm and the outer diameter of the grout sleeve being 32–50 mm, and hence the thickness of the steel skeleton is 150–170 mm; see Fig. 10.

6 Production Methods

A steel skeleton has to be threaded into an opening groove in the edge form, and the edge form of the shear wall weighs about 500–800 kg. If the steel skeleton is produced with the edge form, it is necessary to address the following problems:

- (1) Penetration of the reinforcement via visual identification. (b) The possibility of failing to identify exactly and the low efficiency of the work might occur due to the ease of rusting and bonding of the steel edge forms to the concrete and thus the small color difference with the mold table.

No.	Type	Diameter	Shape	Length	Spacing	Quantity
1.	Longitudinal bars1	16mm		2887mm	300mm	11
2.	Longitudinal bars2	6mm		2710mm	300mm	11
3.	Longitudinal bars3	12mm		2710mm		4
4.	stirrup1	8mm		6724mm	200mm	30
5.	stirrup2	8mm		6788mm	200mm	2
6.	stirrup3	8mm		5824mm		1
7.	Tension bars1	6mm		290mm	600mm	30
8.	Tension bars2	6mm		284mm	100mm	28
9.	Tension bars3	6mm		314mm	600mm	8




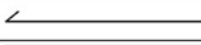


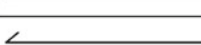
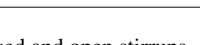
No.	Type	Diameter	Shape	Length	Spacing	Quantity
1.	Longitudinal bars1	12mm		2880	200	11
2.	Longitudinal bars2	8mm		2710	170/200	11
3.	Longitudinal bars3	12mm		2710		4
4.	stirrup1	8mm		2920	75/150/200	32
5.	stirrup2	8mm		5824	200	1
6.	Tension bars1	6mm		190	600	30
7.	Tension bars2	6mm		182	100	28
8.	Tension bars3	6mm		214	600	8

Fig. 9 Reinforcement types of closed and open stirrups

- (2) The deformation of bars is large. According to the study, if the bar is 8 mm in diameter and 3000 mm long, when only 2 ends are clamped, the middle of the bar will sag 150 mm.
- (3) The length and straightness adjustment of the reinforcement deviated from theories. If the theoretical length of the bar is 3000 mm, whose actual length is 2990–3010 mm after being cut, with an error of 10 mm.
- (4) Due to the large total weight, the finished steel skeletons are inconvenient to be transported between different production lines, different workshops and even different sites.

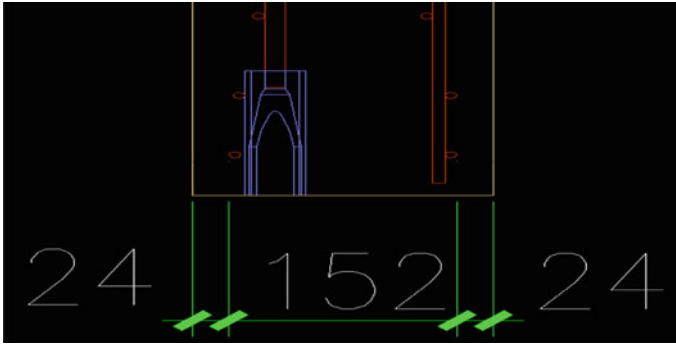


Fig. 10 Layout and thickness of reinforcement frame

7 Conclusions

It has been investigated that if automatic tying equipment for steel skeletons of precast shear walls is to be developed, the following requirements should be satisfied:

- (1) The focus needs to be on non-opening and single-opening shear walls, while double-opening shear walls can be ignored.
- (2) The equipment should be capable of producing wall panels with a height of 2.5–2.95 m and a width of 0.8–5.9 m.
- (3) The equipment shall be capable of producing 6–25 reinforcement types, whose diameters shall be ranging from 6 to 25 mm.
- (4) The equipment shall be capable of producing steel skeletons with a minimum spacing of 5 mm.
- (5) The equipment shall be capable of producing shear wall skeletons with a thickness of 150–170 mm.
- (6) When the equipment produces steel skeletons, if producing those with edge forms is facing more problems, they should be produced without edge forms.

References

1. Cai AJ, Ye K, Shu Z et al (2021) Effect of steel skeletons on vibratory compactness in precast concrete concrete components. *Concrete* 4:113–115
2. Chen SZ, Bai YF, Liu ZJ et al (2021) Effect of welding parameters on the mechanical properties of main bars of steel skeletons. *J Shenyang Jianzhu Univ (Nat Sci Ed)* 37(5):935–941
3. General Office of the State Council (2016) Guideline of the general office of the state council on vigorously developing prefabricated buildings. *Guo Changfa* 71
4. Gu WH, Wen XF, Zhao RQ et al (2018) New positioning technology for bored infill pile hole positions and steel skeletons. *China Concr Cem Prod* 3:93–95
5. Hou AS, Zhao HX, Yuan LY et al. (2022) Mechanical properties of steel skeletons and metallographic organization of welded joints. *Constr Mach* (5):123–126, 130

6. Li ZB, Zhao J, Cong ML et al. (2019) Application of grout sleeve joint in prefabricated steel skeletons for the artificial Island of Hong Kong-Zhuhai-Macao Bridge. *Constr Technol* 48(9):26–28, 70
7. Liu SL, Ma ZL (2021) BIM-based automatic generation algorithm of point cloud for semantic design of steel skeletons. *J Grap* 42(5):816–822
8. Ministry of Housing and Urban-Rural Development (2020) Guideline of ministry of housing and urban-rural development on promoting the coordinated development of intelligent construction and construction industrialization. *Jianguishi* 60
9. Ministry of Housing and Urban-Rural Development (2020) Several opinions on accelerating the development of new building industrialization. *Construction standard gauge* No. 8
10. Qi JY, Meng Y, Wei S et al (2016) Design of the control system of automatic complex shape tube steel-skeleton seam welder. *J Jiangsu Univ Sci Technol (Nat Sci Ed)* 30(5):450–456
11. Wang YH, Wang F, Tang MD et al (2020) Research on the thickness of first layer filling in artificial false ceilings based on bamboo reinforcement-steel skeleton and its application in the field. *Min Metall Eng* 40(6):17–21
12. Wang ZM, Wu HY, Qian J (2017) Alignment control method in the process of outsourcing concrete for stiff-skeleton reinforced concrete arch bridges with variable sections. *Technol Highw Transp* 34(6):106–113
13. Wang P, Zhu JL, Liu J et al (2021) Key design parameters of the main arches of reinforced concrete arch bridges with combined suspension casting-skeleton method. *Technol Highw Transp* 37(6):78–86
14. Yan YX, Qian YJ, Xie XR (2018) Rationality of beam-slab unit model in the simulation analysis of stiff-skeleton reinforced concrete arch bridges. *Railw Eng* 58(2):23–27
15. Yao YK, Xie XQ, Sun JS et al. (2017) Load-bearing characteristics of reinforced concrete columns after blasting of steel skeletons. *Blasting* 34(4):1–6, 16
16. Zhai SD, Jia CG, Wen H (2020) Research on automatic forming process of steel skeletons based on modularity. *Constr Technol* 49(5):72–75. <https://doi.org/10.7672/sgjs2020050072>
17. Zhang DC, Yin GH, Yue ZH (2018) Construction technology based on the specialized production of steel skeletons. *Constr Technol* 47(10):11–15
18. Zhao RJ, Wang CR (2018) Discussion on some problems and solutions in the production of steel skeletons for concrete drainage pipes. *China Concr Cem Prod* 4:33–37
19. Zhu YY (2017) Key technologies for accurate positioning of integrally-lifted box-girder steel skeletons in mobile moulding frames. *Railw Eng* 57(9):68–70

Open Access This chapter is licensed under the terms of the Creative Commons Attribution 4.0 International License (<http://creativecommons.org/licenses/by/4.0/>), which permits use, sharing, adaptation, distribution and reproduction in any medium or format, as long as you give appropriate credit to the original author(s) and the source, provide a link to the Creative Commons license and indicate if changes were made.

The images or other third party material in this chapter are included in the chapter's Creative Commons license, unless indicated otherwise in a credit line to the material. If material is not included in the chapter's Creative Commons license and your intended use is not permitted by statutory regulation or exceeds the permitted use, you will need to obtain permission directly from the copyright holder.



Bridge Comparison of Erection Solutions for Steel Box Girders Spanning from Anchorage in the Sea on Shenzhen-Zhongshan Bridge



Zhi-Wu Xue and Qiang Guo

Abstract The non-navigable hole bridge in the east and west flooding area of the Shenzhen-Zhongshan Bridge 110 m continuous steel box girder system, each with 2 holes of steel box girders spanning the Lingdingyang Bridge sea anchor, which is affected by the anchor and the subsidiary structure, and its installation is difficult. In view of the characteristics of the project, three installation solutions were proposed: large section lifting, small section incremental launching and large section incremental launching. Combined with the comparative analysis of construction efficiency, temporary structure usage, equipment input and construction risk, the large section incremental launching solution not only has less temporary structure input and controllable construction period, but also avoids the input of new equipment and has the best comprehensive economy, which is recommended as the preferred solution for this project. The finite element analysis of the incremental launching process shows that the structural forces meet the requirements after local reinforcement, and the scheme is safe and feasible.

Keywords Upper span anchor · Steel box girder · Comparison of erection · Comparison and selection · Finite element analysis

1 Introduction

The Shenzhen-Zhongshan Bridge is about 30 km from Humen Bridge in the north and 38 km from Hong Kong-Zhuhai-Macao Bridge in the south. The project connects the Airport-Load Highway in the east, crosses the Pearl River Estuary, and reaches Ma'an Island in Zhongshan in the west. It connects with the planned Zhongkai and

Z.-W. Xue (✉) · Q. Guo

Cccc WuHan Harbour Engineering Design And Research Co.Ltd, Wuhan 430040, Hubei, China
e-mail: 289574742@qq.com

Hubei Key Laboratory of Advanced Materials and Reinforcement Technology Research for Marine Environment Structures, Wuhan, China

Research and Development Center of Transport Industry of Intelligent Manufacturing Technologies of Transport Infrastructure, Wuhan, China

© Crown 2023

Y. Yang (ed.), *Advances in Frontier Research on Engineering Structures*, Lecture Notes in Civil Engineering 286, https://doi.org/10.1007/978-981-19-8657-4_32

365

eastern outer ring highway to land in Shenzhen, Zhongshan and Nansha District of Guangzhou City. The total length of the project is about 24.03 km, of which the cross-sea section is 22.39 km. The design speed of 100 km/h and the technical standard of two-way eight-lane highway are adopted. It is a system cluster project integrating bridge, island, tunnel and underground interchange.

The Lingdingyang Bridge in the middle of the Shenzhen-Zhongshan Bridge is a twin pylons three-span full suspended suspension bridge with the spans arranged as $(500 + 1666 + 500)$ m. The two ends of the bridge are connected to the non-navigable span bridge in the east and west flood discharge areas. The non-navigable span bridge in flood discharge area adopts continuous steel box girder system, 24×110 m girder in east area and 22×110 m girder in west area. The area above the anchorage of Lingdingyang Bridge is a six-span continuous beam bridge with a span arrangement of 6×110 m = 660 m. The main girder is a framing equal section and ship-shaped steel box girder with a single width of 20 m and a height of 4 m. The ratio of beam height to span is $1/27.5$. Segmented length is 133.5 m + 4×110 m + 86.5 m, weight is 1513 t + 1258.1 t + 2×1252.6 t + 1295.3 t + 1025 t. Steel box girder members are high strength low alloy structural steel Q345qD or Q420qD [1] (Fig. 1).

The east anchorage of Lingdingyang Bridge is a gravity anchorage structure in the sea. The foundation adopts an 8-shaped diaphragm wall foundation. The diaphragm wall is 2×65 m in diameter and 1.5 m in thickness. It is embedded in a moderately weathered granite layer of 5 m and the lining thickness is $1.5/2.5/3$ m. Anchorage foundation top elevation is + 3.0 m, bottom elevation is -39.0 m. The bottom elevation of the diaphragm wall is -44.6 to -63.0 m. The east anchorage adopts the combination scheme of locking steel pipe pile and I-shaped sheet pile to construct the cofferdam, and the diameter of the cofferdam is 150 m round. Construction area (diameter 200 m) after inserting plastic drainage board construction lock steel pipe pile cofferdam, cofferdam internal backfill sand. Outside the cofferdam throws sandbag for slope protection and use block stone for erosion protection. The upstream and downstream sides of the cofferdam are equipped with the steel platform of the mixing station and the steel platform of the living area [2] (Fig. 2).

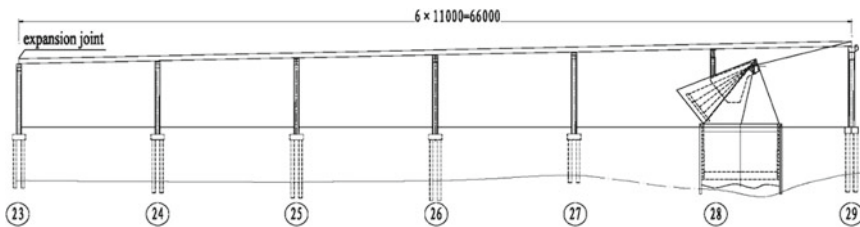


Fig. 1 Layout of steel box girder in east anchorage area



Fig. 2 Photo of structure layout in east anchorage area

2 Engineering Situations

The 110 m-span steel box girders in the east and west flood discharge areas of this project are all constructed by the floating crane large section installation technology. However, there are island cofferdams in the east and west anchorage areas, which have large influence areas and high requirements for the lifting amplitude of the crane ship. At the same time, due to close to the Lingdingyang Bridge, the maximum pier height is more than 63 m, which has exceeded the maximum lifting height of the ‘Tianyi’ special lifting ship for 110 m steel box girder installation. According to the structure and environmental characteristics of this project, three construction schemes of steel box girder above anchorage are proposed, including consolidation of long segment girder, small segment jack-in method and large segment jack-in method.

2.1 Consolidation of Long Segment Girder

Consolidation of long segment girder with precise positioning after hoisting the whole steel box girder to the bridge position by large floating crane is the main method for installation of prefabricated steel box girder of cross-sea bridge at present. Due to its high construction efficiency, small amount of temporary measures and mature technology, it has become the preferred installation technology for large section steel box girder of sea-crossing bridges [3].

This project hoisting affected area is 27#–29# pier interval two holes steel beam, weight is 1295.3t + 1025t. When the large floating crane is installed, the mixing station platform outside the cofferdam needs to be removed, and the temporary

wharf and the steel platform in the aquatic living area have the lifting conditions. Two hoisting schemes are considered: The first scheme is to remove only the outer steel platform of the cofferdam without removing the outer protective structure for hoisting the 27#–28# section steel box girder. At this time, the maximum lifting amplitude is not less than 91 m, the maximum lifting height is not less than 77 m, and the maximum lifting weight is 1470t. The maximum arm length is determined according to the inclination angle of the floating crane. In the second scheme, in addition to the removal of the outer steel platform, the outer protective structure and some locking steel pipe piles are also removed to excavate the island building area of the cofferdam to meet the requirements of floating crane entry. At this time, the maximum lifting amplitude is not less than 61 m, the maximum lifting height is not less than 77 m, and the maximum lifting weight is 1470t. According to the parameter selection floating crane, using scheme 1, floating cranes rated lifting capacity is not less than 4500t, jib length is not less than 120 m. Scheme 2, floating crane rated lifting capacity is not less than 3500t, jib length is not less than 90 m. The plan layout is shown in Fig. 3.

Consolidation of long segment girder has mature technology and high construction efficiency. But for this project, there are the following problems: (1) The affected steel beam above a single anchorage has only two holes and four a single anchorage, which need to be installed by large floating crane alone, and the cost is high [4]. (2) When the scheme 1 is adopted, 4500t large floating crane is needed, and the market resources are scarce, and the equipment schedule is difficult to meet the requirements of the project duration. In the scheme 2, the cofferdam protection structure and part of the locking steel pipe pile need to be demolished, the demolition and subsequent recovery work is heavy, the cost is high, and the safety risk is high. (3) Both schemes

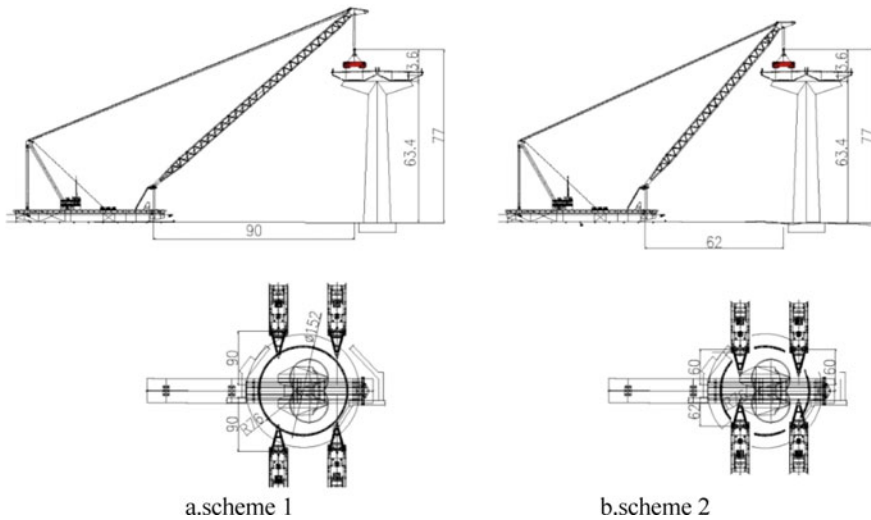


Fig. 3 Layout of large section hoisting scheme

need to dismantle the steel platform of the water mixing station and the platform of the living area, and recover after hoisting, which has a great influence on the subsequent construction of the project. In summary, for this project, the cost of consolidation of long segment girder is high. Although the hoisting workload is small, there are a large number of temporary structure demolition and restoration work, which has a great impact on the subsequent construction.

2.2 Small Segment Jack-In Method

Jack-in method is a method to design a bridge into several segments, which is completed in the factory, and use vehicles or ships to arrive on-site assembly. Then, the multi-point jacking equipment is used to assemble the assembled beam structure step by step forward or dragged bridge. At present, it is widely used in bridge construction under the conditions of water depth, pier height and span, namely cable.

The installation process of steel box girder above anchorage by small segment jack-in method is as follows: first it uses consolidation of long segment girder to install 23#–27# pier section steel box girder. Portal beam lifting station, assembled bracket and 1# temporary pier are set up in pier 27#–28#, and 2# temporary pier is set up in pier 28#–29#. One leg of the lifting station supports the steel box girder bridge deck at the top of 27# pier, The other end of the leg landing support. It is equipped with four 200t lifting jacks and longitudinal jacks, which can be suspended and lifted vertically along the bridge. The top of the assembly bracket and temporary pier is equipped with 1200t walking push equipment. The span of the assembly bracket and temporary pier is 51 + 80 m, and the assembly area is 24 m. Rails are laid on the surface of the steel box girder of pier 26#–27#, and the beam trolley moves along the track of the steel beam carried on the bridge deck.

It makes steel box girder growth about 20 m beam segment. The 600t floating crane is used to lift the beam section to the trolley of the bridge deck of 26#–27# pier and transport it to the beam pick-up position at the beam lifting station, and the beam section is lifted to the assembly platform at the beam lifting station. It lifts the guide beam to temporary pier and assembly platform, and complete the assembly of guide beam and steel box beam segment. The assembled beams were pushed forward section by section by using multi-point walking pushing equipment, each assembly section is pushed up once, so as to circulate until the whole two-hole steel beam is pushed up to the design mileage, the construction of the whole bridge is completed by adjusting the falling beam accurately, removing the guide beam and temporary pier. The scheme is shown in Fig. 4.

Two-hole beam needs 20 times pushing in place (double), pushing weight is 4641t, temporary measures input about 2600t. Small segment jack-in method uses the erected steel beam as the hoisting and transportation site to avoid the influence of anchorage cofferdam area. After dividing into small sections, no large floating crane is needed, and the beam can be directly dropped after pushing in place. It is lower risk. But there are also the following problems: (1) Due to the high height of

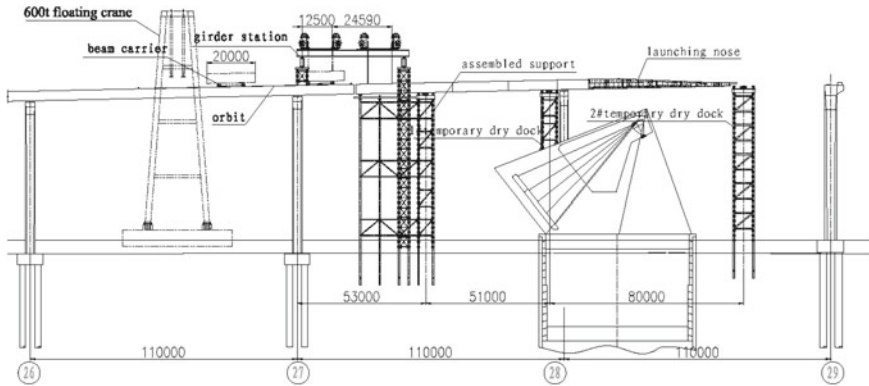


Fig. 4 Layout of jacking scheme for small sections

the bridge, it is necessary to enter a single 600t floating crane, and the lifting station is far away from the beam position to the assembled bracket. The maximum lifting weight reaches 280 t, and the overall temporary measure reaches 2600t. (2) The beam section is pushed several times on the assembly platform, with many components and large lifting weight. Under the action of self-weight, the pushing steel beam will have an impact on the docking posture of the assembled steel beam, and the overall assembly line control is difficult [5]. (3) There are many pushing times in small sections, and a single cycle includes multiple processes such as floating crane hoisting, transportation, beam lifting station lowering and pushing. The process is complex and the work efficiency is low. Overall, the cost is high, the construction period pressure.

2.3 Large Segment Jack-In Method

Different from the small segment jack-in method, the large segment jack-in method requires the jacking construction of the steel box girder across the anchorage before the installation of the steel box girder in the 25#–26# pier section. The process is as follows: In order to meet the requirements of the maximum lifting height of the ‘Tianyi’ crane ship at 61 m, the hanging beam area is set up in the 25#–26# pier section. The jacking area is equipped with 1#–4# temporary pier, of which 1#, 2# pier is water pier, 3#, 4# pier with cofferdam lock steel pipe pile as the foundation, for temporary pier on land. It installs 1200t jacking equipment at the top of temporary pier and 26#–28# permanent pier as jacking fulcrum, span arrangement is 45 + 45 + 65 + 50.5 + 59.5 + 79 m. The steel box girder is equipped with front guide beam and rear guide beam, and the length is 53 m and 43 m respectively.

The large section steel box girder is manufactured in the factory. The front guide beam is welded and hoisted to the top of 25# pier and 1# temporary pier in the beam

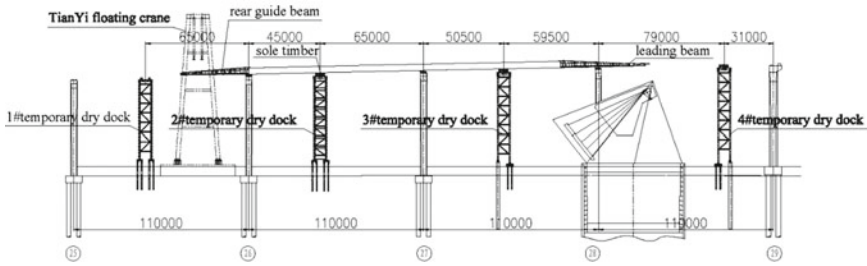


Fig. 5 Layout of large section jacking scheme

feeding area of 25#–26# pier by ‘Tianyi’ crane ship after being transported to the site [6]. The top of the steel box girder is pushed forward to the end of the beam body to the top of 25# pier by using the jacking equipment of the pier top. After installation, the guide beam continues to push. When the support of pier 26# and temporary pier 2# is reached, the rear guide beam is removed, and the next steel box beam is installed. The steel box beam is docked with the jacking steel beam, and the jacking moves forward. In this cycle, the steel box beam of pier 26#–29# three holes is pushed to the design mileage, and the jacking equipment is removed after the bridge axis is accurately adjusted. The steel beam is dropped to the permanent pier by using the falling beam jack, and the steel box beam is docked with the rear installed steel box beam to complete the whole bridge construction. The scheme is shown in Fig. 5.

The large section jacking scheme is divided into 6 times of jacking construction of 3 hole steel beam (double), the weight of jacking is 7146t, and the amount of temporary measures is about 2200t. The process uses the existing floating crane for steel beam hoisting, and uses the combination of permanent pier and temporary pier as the jacking fulcrum, which greatly reduces the amount of temporary measures and has better economy. The hoisting and docking times of large section jacking construction are less, the construction efficiency is higher, the linear control is simple, and the bridge quality is easy to guarantee. However, due to the use of permanent piers as push fulcrum, steel beam push in place after the need to be converted into beam jack for beam falling. The falling beam height is about 1.5 m, the process is mature but there is a certain risk.

According to the description of the above three erection schemes, the comparison of the advantages and disadvantages of each scheme is shown in Table 1.

Considering the work efficiency, construction quality, equipment investment and construction risk, the large segment thrusting method is recommended as the optimal scheme for the installation of the steel box girder across the anchorage in this project. Detailed design and calculation analysis are carried out to determine the structural safety.

Table 1 Comparative analysis of steel box girder erection schemes above anchorage

No	Project	Large section lifting	Section top push	Large section lifting
1	Work efficiency	High	Low	Medium
2	Investment of equipment	3500 T floating crane (new approach)	600 T (new entry)	Tianyi (existing equipment)
3	Construction quality	High	Medium	High
4	Measures input	Remove + restore about 3200 T	2600t	2200t
5	Construction risk	Low	Low	Medium
6	Impact on subsequent construction	Large	Small	Small
7	Recommended level	Not recommend	Not recommend	Recommend

3 Process and Simulation Analysis of Incremental Launching Construction

3.1 Construction Process

Large segment jacking construction structure mainly includes temporary pier, front and rear guide beam, equipment frame, falling beam cushion beam and 16 1200t jacking equipment. The general construction steps of large segment pushing steel box girder are as follows:

- (1) The first section 86.5 m steel box girder is hoisted to the top of 25 # pier and 1 # temporary pier by floating crane (see Fig. 6a).
- (2) The steel box girder is pushed to 17.5 m, and the guide beam is installed at the top of 25# pier (see Fig. 6b).
- (3) The steel box girder is pushed forward 95 m, the rear guide beam is removed, and the second section 110 m steel box girder is hoisted to the graphic position by floating crane (see Fig. 6c).
- (4) The steel box girder of the second section is welded into a whole by pushing forward about 8.6 m and accurately docking with the steel box girder of the first section. The pushing forward is continued for 15 m and the guide beam is installed (see Fig. 6d).
- (5) It installs the third section steel box girder according to the steps 2–4, push the steel box girder over 2 m to the graphic position, and remove the guide beam at 29# pier (see Fig. 6e).
- (6) It removes 25# pier jacking equipment and 1# temporary pier, hoist 25–26 # pier interval large section steel box girder, the steel box girder back to the design mileage, accurate adjustment axis deviation. The jack and cushion beam of the falling beam are installed, and the jacking equipment on the 26#–28# permanent pier is removed, and the bridge support is installed. The jacking equipment on

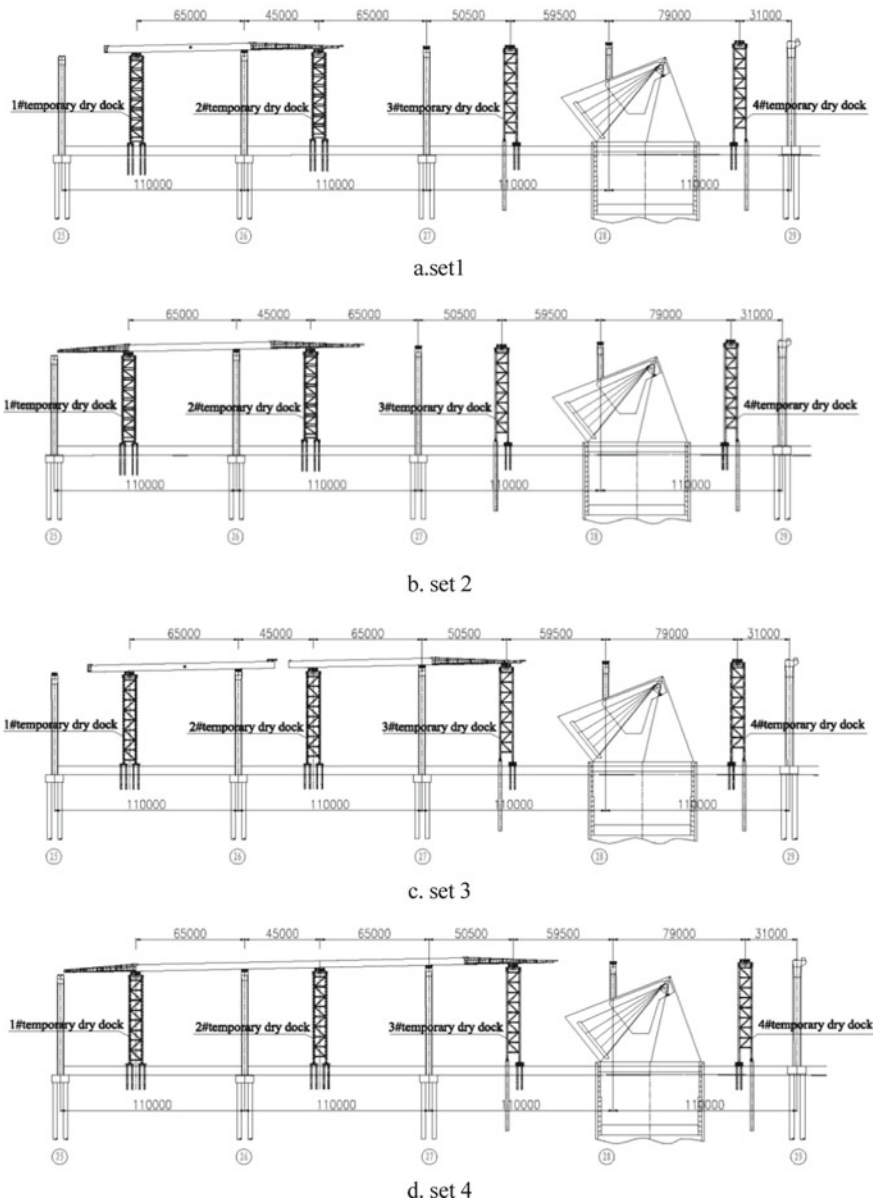


Fig. 6 Installation steps of large section jacking of steel box girder

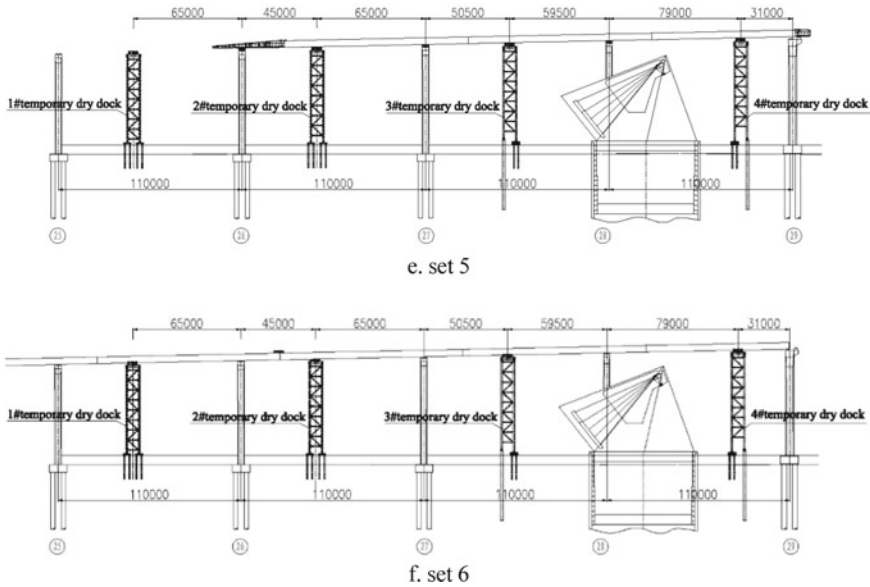


Fig. 6 (continued)

the jack and the temporary pier is gradually dropped to the support. The jacking beam is accurately docked with the steel box girder of the 25–26# pier and welded into a whole to complete the jacking construction (see Fig. 6f).

3.2 Load Combination

The fulcrum position of steel box girder is changing in the construction process and the stress state is also changing during jacking construction. The loads at different jacking stages vary greatly, so it is necessary to check and analyze the strength of steel beam, the force of temporary structure and the local stability of steel beam. The most unfavorable loading conditions at each stage of construction are as follows:

Maximum tail section cantilever state. Condition 1: The three-hole main beam is pushed to large cantilever state of tail. In 1# temporary pier backward cantilever 65 m, 28# pier forward cantilever 72.1 m.

Front end maximum cantilever state. Condition 2: The three-hole girder is pushed to the tail of the large cantilever state, in the 1# temporary pier backward cantilever 58.1 m, 28# pier forward cantilever 79 m.

Beam lowering state. Condition 3: The main beam is pushed in place, the beam is dropped, and the synchronization error of the fall beam fulcrum reaches 20 mm.

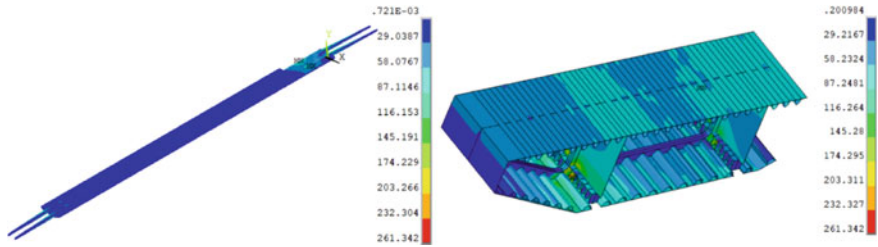


Fig. 7 Comprehensive stress nephogram of structure under the most unfavourable stress condition

3.3 The Computation

ANSYS finite element software was used to simulate the pushing process of steel box girder. Shell181 element was used to establish the shell element model. Material properties are ideal elastic–plastic constitutive model. In the modeling process, the structure is simplified accordingly. The attached structures such as guardrail are loaded on each node and unit with distributed mass, and the connection and jacking support of each component are simplified as common nodes and contact simulation. The load is mainly loaded by node force and acceleration.

The finite element analysis shows that in the process of steel box girder jacking, the maximum stress extremum appears in the front 79 m cantilever state, and the maximum single point fulcrum reaction force is 6657 kN. The local buckling of the web was rechecked. Compression zone $\sigma/\sigma_{cr1} + (\sigma_c/\sigma_{c,cr1})^2 + (\tau/\tau_{cr1})^2 = 1.48 > 1$ [7], local stability does not meet the requirements. Local reinforcement is needed. The reinforcement method is to increase 16 mm thick transverse stiffeners along the bottom of the middle web according to 400 mm spacing, increase the effective distribution length of the pushing fulcrum and reduce local compressive stress. Compression zone after reinforcement $\sigma/\sigma_{cr1} + (\sigma_c/\sigma_{c,cr1})^2 + (\tau/\tau_{cr1})^2 = 0.47 < 1$, local stability meets the requirements. The reinforced model is analyzed and the results are shown in Fig. 7.

In the process of pushing, due to the possible uneven settlement of support, steel plate over-cushion height difference and pushing system error and other factors. There is a relative height difference between the two sides of the steel beam. The sensitivity analysis of the jacking process is carried out. Considering the influence of 30 mm height difference at the maximum reaction fulcrum under working condition 2, the maximum stress of the steel box beam during the jacking process $f_{max} = 261.3 \text{ MPa} < f = 295 \text{ MPa}$, for local stress concentration, pushing the maximum stress of temporary pier $f_{max} = 193.2 \text{ MPa} < f = 295 \text{ MPa}$, The strength and stiffness of permanent structure and temporary structure meet the requirements, and the structure is safe and reliable.

Considering the convenience of subsequent demolition of the pile foundation, the temporary pier adopts the form of pile lifting. The maximum vertical load of a single



Fig. 8 Large section jacking of steel box girder

steel pipe pile is 1140 kN, the soil depth is 20.7 m, and the maximum bearing capacity of the pile foundation is 1222 kN. The bearing capacity meets the requirements.

4 Conclusions

The 110 m continuous steel box girder system is adopted for the non-navigable bridge in the east and west flood discharge areas of Shenzhen-Zhongshan Bridge, which both cross the sea anchorage of Lingdingyang Bridge. Affected by the anchorage itself and cofferdam, the installation of steel box girder is difficult. Through the scheme research, the large section jacking scheme saves the construction period and reduces the temporary structure investment, avoids the new hoisting equipment investment, and has better comprehensive cost and quality control. Through further detailed design and finite element analysis, the structural stress meets the requirements after local reinforcement of steel beams, and the scheme is safe and feasible, which can provide reference for similar projects (Fig. 8).

References

1. CCCC highway planning and Design Institute Co., Ltd. (2019). Construction drawing design of non navigable span bridge in flood discharge area of Shenzhen Zhongshan river crossing channel
2. CCCC Second harbor engineering company ltd. (2018). Special construction scheme for island cofferdam of East anchorage in S04 contract section of Shenzhong channel project
3. Lin G-W, Shi H (2021) Key lifting construction technique for existing simply supported steel Truss Girder bridge. *World Bridges* 49(03):108–112

4. Miao J-B, Luo Z-L (2019) Analysis and optimization of large segment hoist of steel box girder for the Hong Kong-Zhuhai-Macao bridge. Highway 64(03):89–94
5. Weng F-W, Tian Q, Tian F (2018) Research on controlling technology of incremental launching construction for large-span continues steel box Girders bridge. Highway 63(03):89–92
6. Zhang Y-T, Zhou R-Z, Gao J-B (2011) Research on hoisting techniques of huge segments of Chongqi bridge. Highway 10:82–89
7. Ministry of housing and urban rural development of the people’s Republic of China (2017). GB 50017–2017 Standard for design of steel structures

Open Access This chapter is licensed under the terms of the Creative Commons Attribution 4.0 International License (<http://creativecommons.org/licenses/by/4.0/>), which permits use, sharing, adaptation, distribution and reproduction in any medium or format, as long as you give appropriate credit to the original author(s) and the source, provide a link to the Creative Commons license and indicate if changes were made.

The images or other third party material in this chapter are included in the chapter’s Creative Commons license, unless indicated otherwise in a credit line to the material. If material is not included in the chapter’s Creative Commons license and your intended use is not permitted by statutory regulation or exceeds the permitted use, you will need to obtain permission directly from the copyright holder.



Analysis on Migration Mechanism of Chloride Ions in Concrete Close-End Pipe Piles



Bo. Yang

Abstract Different migration mechanisms of chloride in concrete are introduced and various kinds of influences on diffusion coefficient, including temperature, relative humidity and age are also elaborated. Based on Fick second law and the boundary condition of close-end pipe pile, the analytical solution to chloride migration equation due to the process of both diffusion and convection is deduced. Applying this result to a typical jacked *PHC* pile, the chloride concentration is analyzed and the effect, which the seepage velocity, thickness of pipe pile and the diffusion coefficient have on distribution of chloride concentration, is also discussed. This example provides a computational basis for the corrosion of steel bar and some reference values for durability design of pipe pile.

Keyword Pipe pile · Concrete · Diffusion · Convection · Durability

Bo. Yang (✉)

Shanghai Tongji Testing Technology Co., Ltd, Shanghai 200137, China

e-mail: yangbotongji@yeah.net

College of Civil Engineering, Tongji University, Shanghai 200092, China

© Crown 2023

Y. Yang (ed.), *Advances in Frontier Research on Engineering Structures*, Lecture Notes in Civil Engineering 286, https://doi.org/10.1007/978-981-19-8657-4_33

379

1 General Introductions

Chloride ions are transmitted from the surrounding environment to the interior of the concrete through the pores and micro-cracks in the concrete, so that the chloride ion concentration on the surface of the steel bar gradually increases. After reaching the critical concentration, the steel bar will corrode. Collepardi et al. [2] used the Laplace transform method to obtain a one-dimensional closed solution under strictly restricted conditions, assuming that the concrete specimen was a semi-infinite space body, and the analytical solution was described by a transcendental function.

The two major transport mechanisms of chloride ion, diffusion and convection, are first expounded in this paper, pointing out various factors that affect the chloride ion diffusion coefficient, including temperature, relative humidity and age. Then, according to the boundary conditions of the pipe pile, the transport equations under the action of diffusion and convection are solved, analyzing the influence of various parameters. Moreover, the obtained results are verified with the measured data.

2 Transport Mechanism of Chloride Ion in Concrete

2.1 Diffusion

Diffusion refers to the phenomenon of directional migration of ions in solution under the action of a chemical potential gradient.

According to Fick's first law, $\vec{J} = -D \cdot \nabla C$; Based on the conservation equation $\frac{\partial C}{\partial t} + \nabla \cdot \vec{J} = 0$ of ions in solution, Fick's second law is obtained,

$$\frac{\partial C}{\partial t} = \nabla^2 C$$

In the formula, \vec{J} is the chloride ion diffusion flux, C refers to the free chloride ion concentration (mol/L), and D is the diffusion coefficient (m^2/s).

2.2 Convection

Convection refers to the phenomenon in which ions migrate as a whole with a solution.

The convective flux of chloride ions can be expressed as $\vec{J} = -C \cdot \vec{v}$, where \vec{v} is the seepage velocity of the pore liquid in the concrete pores.

Pressure

The directional flow of pore fluid in porous media under external pressure difference obeys Darcy's law.

$$\vec{Q} = -\frac{k}{\eta} \nabla p$$

In the formula, \vec{Q} is the volume flow rate of pore fluid (m^3/s), and k is the permeability coefficient (m/s). η refers to the liquid viscosity coefficient (Pa s), and p is the pressure head (m).

Capillarity

The Capillarity can be equivalent to the pressure seepage in the calculation, which also conforms to Darcy's law.

Electromigration

Electromigration refers to the process that ions in pore fluid perform directional migration under the action of an applied potential.

After the movement speed of chloride ion tends to be stable, the stable speed is $\vec{v} = \frac{ze\vec{E}}{K}$, and the ion flux is $\vec{J} = -C \cdot \frac{zFD\vec{E}}{RT}$. In the formula, K is the viscosity coefficient of the ion ($\text{N}\cdot\text{s}/\text{m}$), F is the Faraday constant ($96,485.3 \text{ mol/L}$), and e is the electron charge (C). z is the ion charge, R is the universal gas constant ($8.31 \text{ J}/(\text{mol}\cdot\text{K})$), and T is the absolute temperature (K).

The chloride ion transport equation considering the processes of diffusion, convection and electromigration can be expressed as:

$$\frac{\partial C}{\partial t} = \nabla \cdot \left(D \cdot \nabla C + C \cdot (\vec{v}_p + \vec{v}_c) + C \cdot \frac{zFD\vec{E}}{RT} \right) \quad (1)$$

\vec{v}_p is the pore fluid velocity (m/s) caused by pressure seepage and \vec{v}_c refers to the pore fluid velocity (m/s) caused by capillary action.

3 Influencing Factors of Chloride Ion Diffusion Coefficient

The chloride ion transport process in actual concrete is very difficult to describe with an idealized model due to its complexity.

After comprehensively considering the effects of temperature, humidity and age, the effective chloride ion diffusion coefficient is:

$$D = D_0 \cdot f_1(T) f_2(h) f_3(t)$$

$f_1(T)$ is the temperature influence factor, and North American Life-365 (2018) suggested that $f_1(T) = \exp\left[\frac{U}{R}\left(\frac{1}{T_0} - \frac{1}{T}\right)\right]$. Stephen et al. (1998) suggested that $f_1(T) = \frac{T}{T_0} \exp\left[q\left(\frac{1}{T_0} - \frac{1}{T}\right)\right]$.

$f_2(h)$ is the relative humidity influencing factor, Bitaraf and Mohammadi [1] suggested that $f_2(h) = \left[1 + \frac{(1-h)^4}{(1-h_0)^4}\right]^{-1}$.

$f_3(t)$ is the age-related factor, and Thomas and Bamforth [6] suggested that $f_3(t) = \left(\frac{t_0}{t}\right)^m$.

Among them, D_0 refers to the diffusion coefficient of the reference chloride ion, which is measured by the test when the temperature is T_0 , the relative humidity is h_0 , and the age is t_0 . m is the attenuation coefficient. Usually, T_0 is room temperature, which is 293 K; h_0 is the critical relative humidity, which is 75%; t_0 is 28 days. For ordinary concrete, m is taken as 0.25; for fly ash and slag concrete, m is taken as 0.6 [4].

In addition, water-cement ratio, stress state of concrete members [9], cracks [3], aggregate shape [5] and gradation, environmental changes and chloride binding properties [8] all have a certain impact on the transport process of chloride ions, which includes complex mechanisms.

4 Transport Law of Chloride Ion in Concrete Pipe Pile

For long pipe piles, it can be assumed that the chloride ion diffusion in each cross-section is the same, thus transforming the three-dimensional problem into a two-dimensional problem. Considering the axial symmetry of the pipe pile, the chloride ion diffuses only in the radial direction (Fig. 1).

It is supposed that the wall thickness of the pipe pile is l , the outer wall is exposed to the chloride salt environment, and the environmental chloride ion concentration is u_0 . The inner wall is the closed surface, and the chloride ion concentration is 0. The initial chloride ion concentration inside the pipe pile is 0. No electric field acceleration exists in the natural environment. The pore fluid velocity caused by pressure seepage and capillary action is along the radial direction. From Formula (1), it can be obtained as follows.

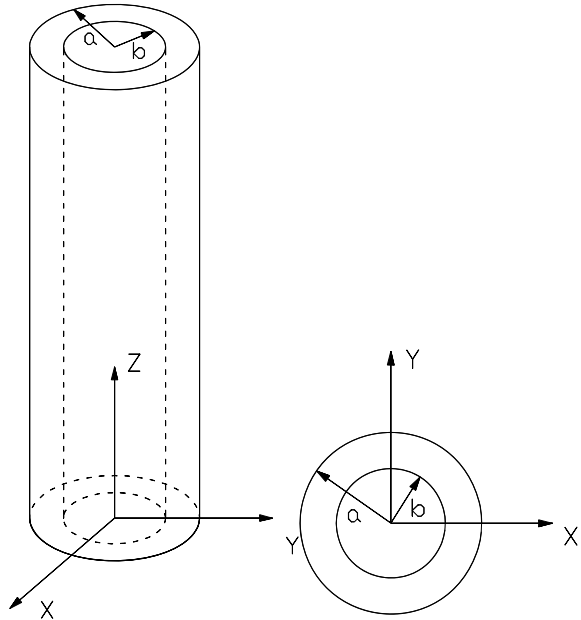
$$\frac{\partial C}{\partial t} = D \frac{\partial^2 C}{\partial x^2} + (v_p + v_c) \frac{\partial C}{\partial x} \quad (2)$$

Boundary conditions: $C|_{x=0} = u_s$, $C|_{x=l} = 0$;

Initial conditions: $C|_{t=0} = 0$, ($0 < x < l$).

Setting $v_p + v_c = v$ as the percolation velocity due to pressure and capillary action, and $C(x, t) = u(x, t) + w(x)$. $u(x, t)$ satisfies the secondary boundary condition, while $w(x)$ satisfies the non-secondary boundary condition. Considering that the

Fig. 1 Chloride diffusion model in pipe pile



seepage velocity is positively opposed to the coordinate, a minus sign should be added before v when it is brought into Eq. (2), and there will be:

$$w(x) = \frac{u_s}{1 - e^{\frac{v}{D}}} (e^{\frac{v}{D}x} - e^{\frac{v}{D}l}) \tag{3}$$

Then $u(x, t)$ needs to satisfy:

$$\frac{\partial u}{\partial t} = D \frac{\partial^2 u}{\partial x^2} - v \frac{\partial u}{\partial x}$$

Boundary conditions: $u|_{x=0} = 0, u|_{x=l} = 0$;

Initial conditions: $u|_{t=0} = -w(x), (0 < x < l)$.

Setting $u(x, t) = X(x)T(t)$, the separation variable method is used to solve the problem, which is transformed into the eigenvalue problem. Then, there will be

$$u(x, t) = \sum_{n=1}^{\infty} \varphi_n e^{-\left(\frac{n^2\pi^2 D}{l^2} + \frac{v^2}{4D}\right)t} \cdot e^{\frac{v}{2D}x} \sin \frac{n\pi}{l}x \tag{4}$$

Among them.

$$\varphi_n = -\frac{2}{l} \int_0^l w(x) \cdot e^{-\frac{v}{2D}x} \sin \frac{n\pi}{l}x \cdot dx, \tag{5}$$

Substitute (3) into (6) to get

$$\varphi_n = -\frac{4D^2n\pi}{(v^2l^2 + 4D^2n^2\pi^2)}u_s \tag{6}$$

Substitute (6) into (4) and add (3) to get

$$C(x, t) = \frac{u_s}{1 - e^{\frac{vl}{D}}} (e^{\frac{v}{D}x} - e^{\frac{v}{D}l}) - \sum_{n=1}^{\infty} \frac{4D^2n\pi u_s}{v^2l^2 + 4D^2n^2\pi^2} e^{-\left(\frac{n^2\pi^2D}{l^2} + \frac{v^2}{4D}\right)t} \cdot e^{\frac{v}{2D}x} \sin \frac{n\pi}{l}x \tag{7}$$

5 Analysis of Examples and Parameter Influence

The wall thickness of the PHC concrete pipe pile in marine engineering is $l = 60$ mm, the initial chloride ion concentration u_0 is 0, and the boundary chloride ion concentration u_s is 1.0%. The diffusion coefficient D is $20 \text{ mm}^2/\text{a}$, and the penetration rate is 2 mm/a . The calculation results that chloride ion concentration changes with time in the pipe pile are as follows (Fig. 2).

It can be seen from the calculation results that the overall trend of the chloride ion concentration in the pipe pile is increasing over time. Still, it is not higher than the ambient chloride ion concentration.

Fig. 2 Distribution of chloride concentration over time

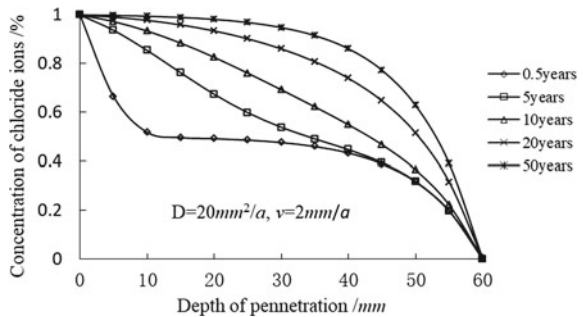
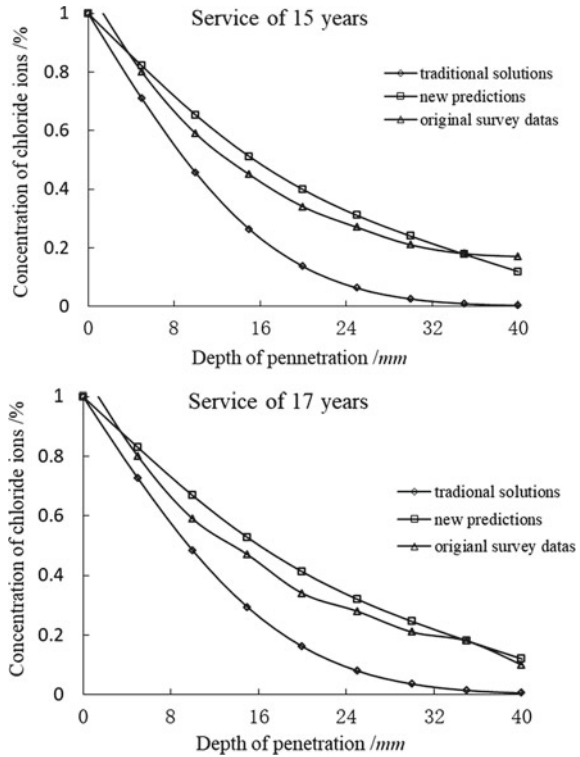


Fig. 3 Relationship between traditional solutions, original survey datas and new predictions



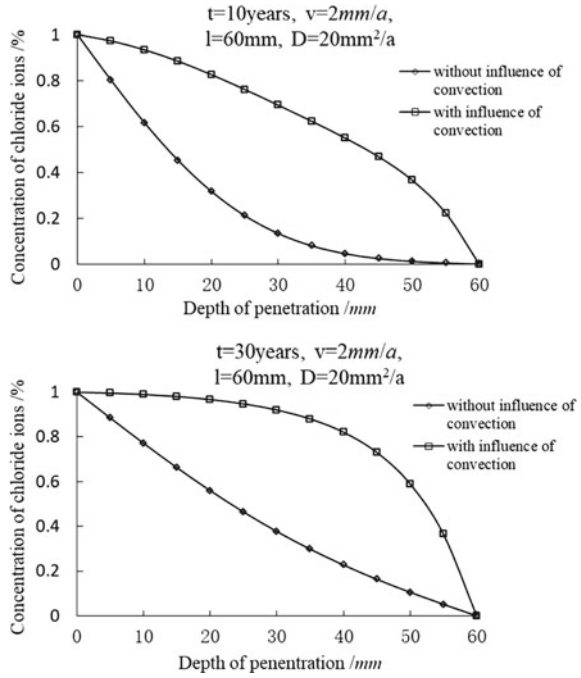
5.1 Comparison with Original Survey Data

The comparison results between the predicted values in this paper and the original survey data [7] are shown in Fig. 3. The comparison results show that the predicted values in this paper are better conformed with the measured data.

5.2 The Influence of Seepage

With or without influence of seepage, different results show that convection has a great impact on the diffusion of chloride ions in a design life of 10 and 30 years (Fig. 4).

Fig. 4 Influence of convection on distribution of chloride concentration



5.3 The Influence of Seepage Velocity

The greater the seepage velocity is, the stronger the chloride ion erosion will be, and the influence on the distribution of chloride ion concentration in deep concrete is more prominent (Fig. 5).

Fig. 5 Influence of different values of flow velocity on distribution of chloride concentration

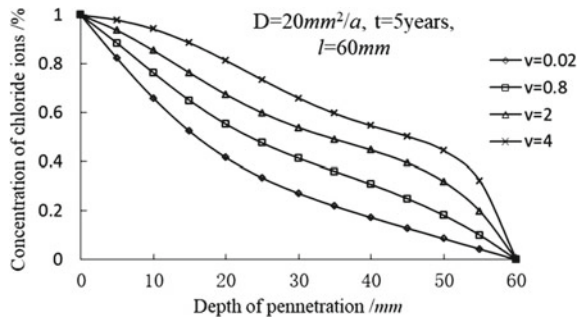
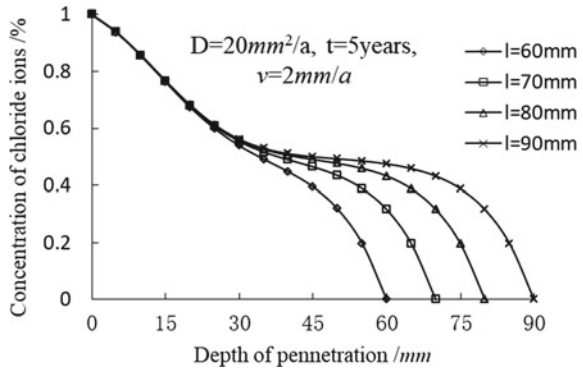


Fig. 6 Influence of different thickness of pipe piles on distribution of chloride concentration



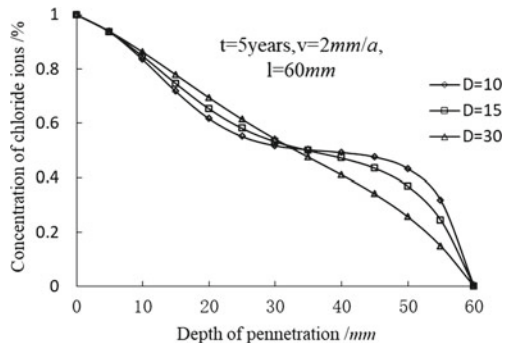
5.4 The Influence of Pipe Pile Thickness

For pipe piles with different thicknesses, the distribution of chloride ion concentration in shallow concrete is basically the same. Affected by the chloride ion concentration in the inner wall of the pipe pile, the distribution of chloride ion concentration in the deep concrete is quite different (Fig. 6).

5.5 The Influence of Diffusion Coefficient

The diffusion of chloride ions significantly influences the distribution of chloride ion concentration in shallow concrete. The greater the diffusion coefficient is, the faster the chloride ion erosion will be. However, the influence of chloride ion concentration in deep concrete is just the opposite. The larger the diffusion coefficient is, the slower the chloride ion erosion will be (Fig. 7).

Fig. 7 Influence of different diffusion coefficient on distribution of chloride concentration



6 Conclusion

- (1) For concrete pipe piles, considering the diffusion effect, the chloride ion transport law under the influence of convection can better reflect the objective reality, which can guide the design more economically and reasonably.
- (2) The greater the seepage velocity, the faster the chloride ion will be transported into the concrete. The seepage velocity significantly influences the chloride ion concentration distribution in the deep concrete. The diffusion influence of chloride ions obviously influences the distribution of chloride ion concentration in shallow concrete. The greater the diffusion coefficient is, the faster the chloride ion will be transported. The influence on chloride ion concentration in deep concrete is just the opposite.
- (3) For pipe piles with the same diffusion coefficient but different thicknesses, the distribution of chloride ion concentration in shallow concrete is basically the same, and the chloride ion concentration in deep concrete is significantly affected by the chloride ion concentration in the inner wall of pipe piles.

References

1. Bitaraf M, Mohammadi S (2008) Analysis of chloride diffusion in concrete structures for prediction of initiation time of corrosion using a new meshless approach. *Constr Build Mater* 22(4):546–556
2. Collepardi M, Marcialis A, Turrizzani R (1970) The kinetics of penetration of chloride ions into the concrete. *Il Cem* 4:157–164
3. Jin ZQ, Zhao TJ, Zhuang QC. et al. (2012) Chloride transport in splitting cracked concrete at marine tidal zone. *J Civil Archit Environ Eng* 34(2):52–57
4. Life-365 Service Life Prediction Model [CP/OP]. <http://www.life-365.org/download.html>
5. Peng GJ, Zheng JJ, Zhou YQ (2009) A numerical method for predicting the chloride diffusion coefficient of concrete with aggregate shape. *Adv Sci Technol Water Resour* 29(6):13–16
6. Thomas MDA, Bamforth PB (1999) Modeling chloride diffusion in concrete—effect of fly ash slag. *Cem Concr Res* 29(4):487–495
7. Wang DD, Wang CQ, Shi BL et al (2008) Field sampling, analysis and research on durability of large diameter cylindrical piles. *China Harbour Eng* 1:39–43
8. Yu HF, Sun W (2006) Model research on chloride ion diffusion on concretes. *J Southeast Univ (Nat Sci Ed)* 36(Sup(II)) 68–76
9. Yuan CB, Zhang DF, Liu RG et al (2003) Diffusivity of chloride in concrete in different stress states. *J Hohai Univ (Nat Sci)* 31(1):51–54

Open Access This chapter is licensed under the terms of the Creative Commons Attribution 4.0 International License (<http://creativecommons.org/licenses/by/4.0/>), which permits use, sharing, adaptation, distribution and reproduction in any medium or format, as long as you give appropriate credit to the original author(s) and the source, provide a link to the Creative Commons license and indicate if changes were made.

The images or other third party material in this chapter are included in the chapter's Creative Commons license, unless indicated otherwise in a credit line to the material. If material is not included in the chapter's Creative Commons license and your intended use is not permitted by statutory regulation or exceeds the permitted use, you will need to obtain permission directly from the copyright holder.



Numerical Simulation Research for Rock Stability of Ventilation and Safety Tunnel of Karuma Hydropower Plant



Hua Li, An Liu, Ting Shi, and Meifeng Niu

Abstract According to the latest physical mechanical parameter of rock, crustal stress, section style and support parameter, rock stability of intersection of EVT-Ventilation Tunnel 2-1 and Ventilation Shaft 2 is analyzed and verified through FLAC3D on the base of actual geology parameter and test value of crustal stress.

Keyword Hydropower plant · Rock stability

1 General Introduction

Karuma Hydropower Station is located at the Kyoga Nile River in Kiryandongo District in Uganda. It consists of such buildings as the gate dam, water conveyance system, underground powerhouse and tailrace tunnel [5]. The maximum height of planning head hub dam gate is about 20 m and the normal storage level is 1030 m. The powerhouse dimension is $226.5 \times 21 \times 56.5$ m (length \times width \times height) and the length of main tailrace tunnel is about 8.2 km. The preliminary planning installed capacity is 600 MW [2, 3].

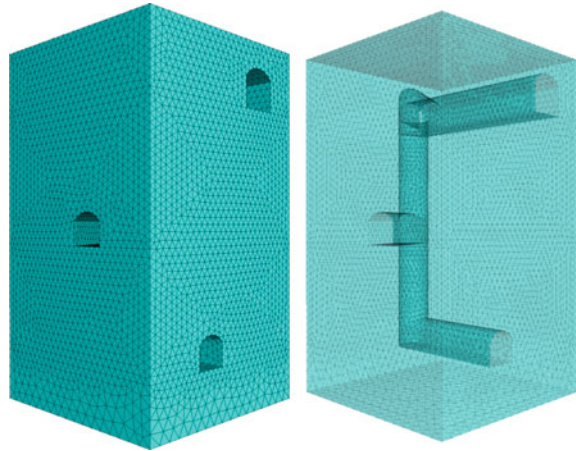
Ventilation shaft 2# of Karuma Hydropower Station is located at the ventilation and safety tunnel (EVT), MAT, adit-1, adit-2, ventilation tunnel 2-1, ventilation 2-2 and ventilation 2-3. The excavation diameter of shaft 2# is successively 6.1 m, tunnel section 6.2×6.1 m [4].

H. Li · A. Liu (✉) · T. Shi · M. Niu
PowerChina Huadong Engineering Corporation Limited, Hangzhou, China
e-mail: liu_a2@hdec.com

H. Li
e-mail: li_h5@hdec.com

T. Shi
e-mail: shi_t@hdec.com

M. Niu
e-mail: niu_mf@hdec.com

Fig. 1 Calculation model

Speculating according to the latest geology data, the ventilation shaft 2# is in the environment of Class II rock and the surrounding rock of ventilation tunnel 2-1 is in the environmental of Class III [1].

2 Calculation Illustration

2.1 Calculation Software

During calculation, the body of EVT, ventilation shaft and ventilation tunnel, and the bottom intersection are computed by three-dimension finite difference method.

2.2 Calculation Model

The bottom intersection of shaft adopts three-dimension calculation model, as is shown in Fig. 1. The ventilation bottom center is set as the model base point. The longitudinal and horizontal length of model are 70 m and 40 m, respectively. The grid element of calculation model is shown in Fig. 2.

2.3 Material Property

Model geology data: the basic geology data and detailed rock parameter is listed in the Table 1.

Fig. 2 The grid element of calculation model



Table 1 Physical mechanics parameter values of rock

Class	Unit weight (KN/m ³)	Modulus of deformation (GPa)	Poisson's ratio	Cohesive force (MPa)	Internal friction angle (deg)
II	27	14	0.18	1.6	49
III	26	6	0.23	1.0	42

3 Calculation Results and Analysis

Intersection of EVT- ventilation tunnel 2-1 and ventilation shaft 2 is located at the stratum with class III rock. After excavation of the intersection of EVT- ventilation tunnel 2-1 and ventilation shaft 2, maximum displacement of 7.39 mm occurs at the intersection of ventilation shaft 2 and ventilation tunnel 2-2. Along the ventilation tunnel 2-1, it can be seen that after excavation, the maximum displacement occurs at the junction of ventilation shaft and ventilation tunnel 2-1, up to 4.53 mm (Fig. 3).

After excavation, the range of plastic zone is large, and mainly concentrated in the left side and upper right side of EVT. The necessary supporting measures is applied through small advance pre-grouting duct, grouted anchor bar and so on. Meanwhile, the plastic zone of both side of shaft 2 is visible, as shown in Fig. 4.

4 Conclusion

Rock stability of intersection of EVT- ventilation tunnel 2-1 and ventilation shaft 2# is analyzed through FLAC^{3D} on the base of actual geology parameter and test value of crustal stress. The following conclusion is drawn:

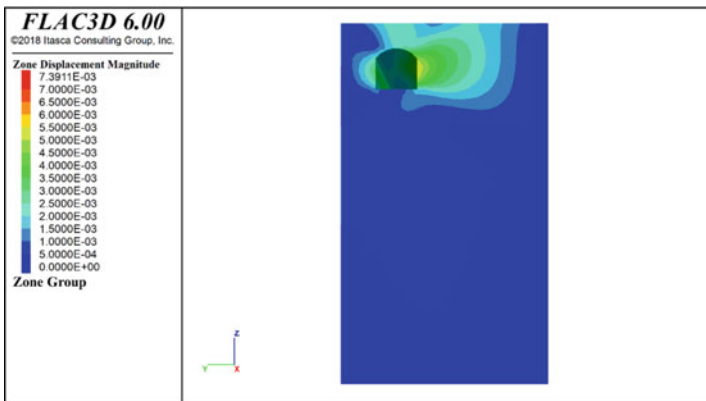
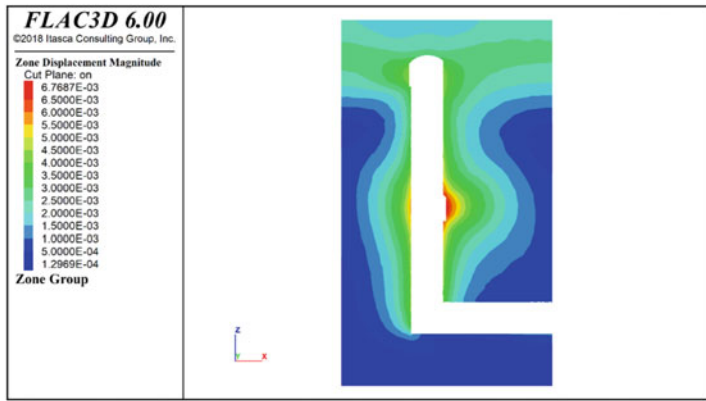
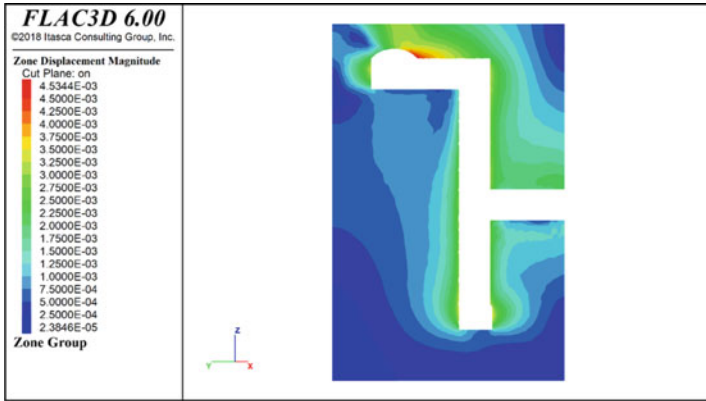
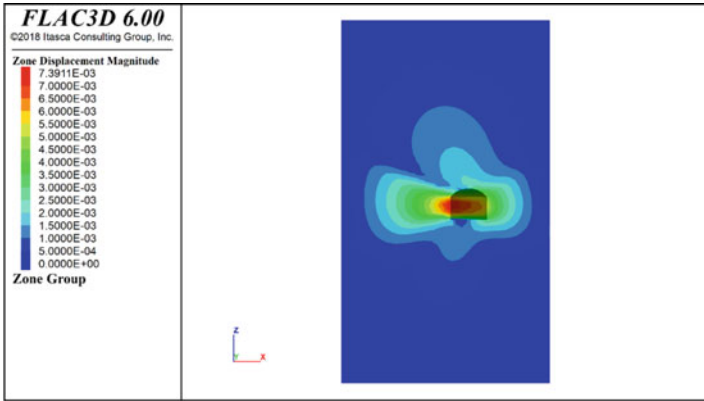
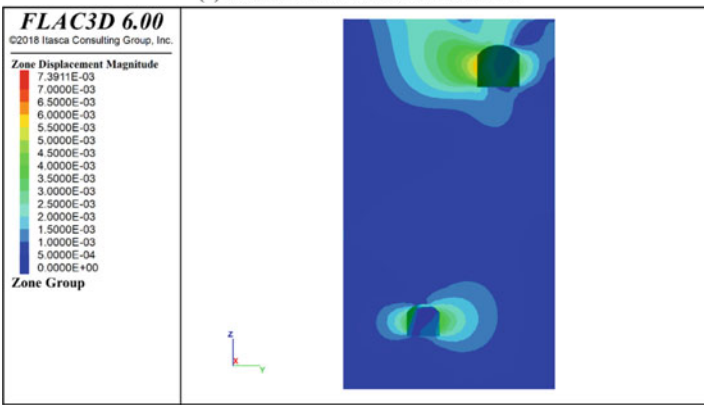


Fig. 3 Displacement cloud picture of the bottom intersection of ventilation shaft



(d) Outer surface of ventilation tunnel 2-2



(e) Outer surface of ventilation tunnel 2-3

Fig. 3 (continued)

- (1) After excavation, the maximum displacement 4.53 mm occurs at the upper-right junction of ventilation shaft and ventilation tunnel 2-1, from along the ventilation tunnel 2-1 perspective. The displacement value is related to crustal stress, physical mechanical parameters.
- (2) The plastic zone mainly concentrated in the left side and upper-right side of EVT.
- (3) Based on calculation results, without system support and local shotcrete with locking bolt at the intersection of EVT- Ventilation Tunnel 2-1 and Ventilation Shaft can satisfy the requirement of design.

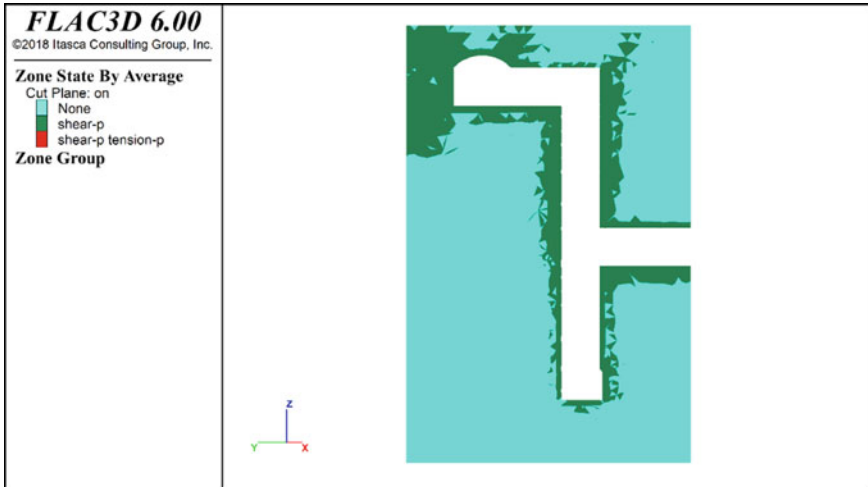


Fig. 4 Plastic zone cloud picture along the ventilation tunnel 2-1

References

1. Li B, Xu M, Liu Y (2015) Improvement of Hoek Brown strength criterion of intact rock under triaxial condition. *J Min saf Eng* 32(6):1010–1016
2. Lu B, Wang J, Ding X (2010) Study on the cracking and deformation mechanism of surrounding rock of underground powerhouse of Jinping I Hydropower Station. *J Rock Mech Eng* 29(12):2429–2441
3. Qin W, Li Q, Ren W (2010) Monitoring and analysis of surrounding rock displacement of tunnels with complex structures. Wuhan: *J Rock Mech Eng* 29(3):549–557
4. Su Y, Feng L, Li Z (2009) Quantification of geological strength index factors in Hoek Brown criterion. *J Rock Mech Eng* 28(4):679–686
5. Xiang T, Feng X, Jiang Q (2011) Dynamic identification and control of surrounding rock failure modes of large caverns. *J Rock Mech Eng* 30(5):871–883

Open Access This chapter is licensed under the terms of the Creative Commons Attribution 4.0 International License (<http://creativecommons.org/licenses/by/4.0/>), which permits use, sharing, adaptation, distribution and reproduction in any medium or format, as long as you give appropriate credit to the original author(s) and the source, provide a link to the Creative Commons license and indicate if changes were made.

The images or other third party material in this chapter are included in the chapter's Creative Commons license, unless indicated otherwise in a credit line to the material. If material is not included in the chapter's Creative Commons license and your intended use is not permitted by statutory regulation or exceeds the permitted use, you will need to obtain permission directly from the copyright holder.



Experimental Study on Mechanical Properties of the Damaged Hoop Head Mortise-Tenon Joint



Chengwei Peng and Wenlong Lv

Abstract Damage is a common condition in ancient timber structures, whose influence on the mechanical properties of structures cannot be ignored. To study the mechanical properties of damaged hoop head mortise-tenon joint, four specimens with shrinkage gauge, including one intact joint specimen and three artificial simulated damaged joint specimens, are designed, and fabricated in this paper by regarding the global damage degree and column axial force as the variation of parameters. The failure mode, hysteresis curve, skeleton curve, ductility, and energy dissipation capacity of the specimens are studied by low-cyclic reversed loading tests. The results show that the failure pattern is randomly manifested as parallel-to-grain tensile cracking failure or vertical splitting failure of the beam tenon. When the global damage degree increases, the two types of damage are more likely to appear simultaneously. The global damage degree has a significant influence on the ultimate bending moment and energy dissipation capacity of hoop head mortise-tenon joints, and 2.4% of the global damage degree can lead to a significant decrease in both. The column axial force can affect the ultimate bending moment, ductility, and energy dissipation capacity of hoop head mortise-tenon joints. When the column axial force increases, the ultimate bending moment and energy dissipation capacity will increase, while the ductility will decrease.

Keywords Damage · Hoop head mortise-tenon joint · Low-cyclic reversed loading test · Mechanical property

C. Peng (✉) · W. Lv

Guangdong Province, Guangdong Provincial Academy of Building Research Group Co., Ltd.,
Guangzhou 510500, China

e-mail: 874541364@qq.com

C. Peng

State Key Laboratory of Subtropical Building Science, Guangdong Province, South China
University of Technology, Guangzhou 510640, China

This is a U.S. government work and not under copyright protection in the U.S.; foreign
copyright protection may apply 2023

Y. Yang (ed.), *Advances in Frontier Research on Engineering Structures*, Lecture Notes
in Civil Engineering 286, https://doi.org/10.1007/978-981-19-8657-4_35

1 General Instructions

The historical architecture in China is an important carrier of Chinese civilization, which is also a valuable heritage in the architectural art of the world. Additionally, the Guangfu clan in Guangdong Province have inherited many historical buildings built during the Tang and Song Dynasties. According to statistics, as of May 2022, 4084 historical buildings have been registered in Guangdong Province. Among them, the typical Guangfu historical buildings account for about 68% of the total, and the structural types are mostly brick-timber structures and timber structures, accounting for about 62% of the total. The Guangfu ancient timber structures are usually constructed of wood with good performance such as merbau, and the joint form is mainly the hoop head mortise-tenon [3].

On the one hand, the environment in the Cantonese area is hot and humid, and moths are easy to breed. In addition, the ancient timber structures have been used for a long time, and the mortise-tenon joints are prone to suffering different types and degrees of damage, affecting the mechanical properties of the structures. On the other hand, some Guangfu historical buildings have been activated and utilized to form new functions, which may change the original stress state of the structures and aggravate the damage of the joints. Although the quantitative changes in the state and performance of the mortise-tenon joints mentioned above usually develop slowly, they may cause qualitative changes. Therefore, for the safety of the Guangfu ancient timber structures, research on the mechanical properties of the damaged hoop head mortise-tenon joint is important.

Nowadays, lots of scholars have studied the mechanical properties of various types of mortise-tenon joints, such as straight mortise-tenon joint, dovetail joint, and the hoop head mortise-tenon joint [1, 2, 4, 6, 7, 11]. At the same time, there are also some reports on the seismic performance of the damaged mortise-tenon joints which are artificially simulated [9, 10]. On the one hand, the research on the mechanical properties of the damaged hoop head mortise-tenon joint is extremely scarce. On the other hand, the way of artificial damage simulation in the existing literature is to disperse drilling uniformly at the tenon [9, 10], which deviates from the local concentration mode of the damaged parts in the actual ancient timber structure. Therefore, in this paper, the low-cycle reversed loading test is carried out on four hoop head mortise-tenon joints, three of which are damaged joints simulated artificially. Based on the test results, the effects of global damage degree and column axial force on the mechanical properties of the joints are discussed.

2 Experiment Design

2.1 Specimen Design and Material Properties

In this paper, four hoop head mortise-tenon joints are fabricated, as shown in Fig. 1. The specimens are designed and fabricated in a scale ratio of 1:2.7 [3], and the apparent sizes are consistent. The parameters of the specimens are listed in Table 1, among which J1 is the intact joint, and J2, J3, and J4 are damaged joints, which are artificially simulated. The artificial damage simulation is carried out in the form of drilling [9, 10]. The damaged area of drilling is a cylinder with diameter D and depth h , and is located at the center of the tenon (Fig. 1). The boreholes are evenly distributed in the damaged area, and their diameters are all 5 mm. The number of boreholes for different specimens is shown in Table 1.

References [9, 10] define the damage degree as the ratio of the drilling volume to the tenon volume. Different from References [9, 10], drilling is not performed evenly throughout the tenon, but only in the damaged areas mentioned above. Therefore,

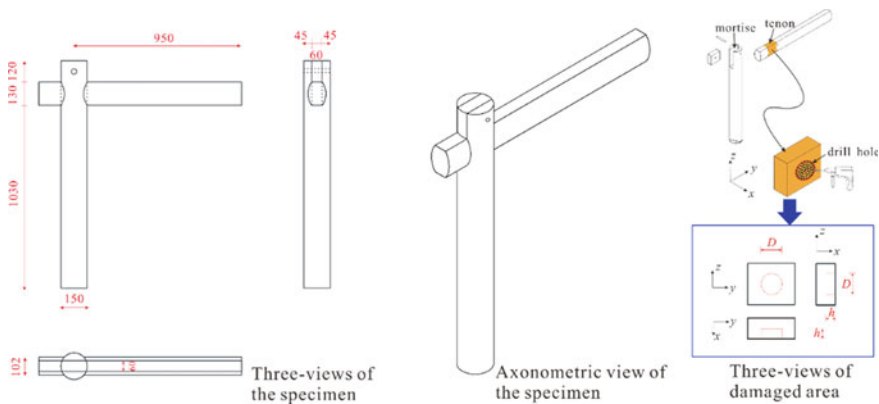


Fig. 1 Specimen design (unit: mm)

Table 1 Details of the specimens

Number of specimens	Diameter of the damaged area D (mm)	Diameter of drilling hole d (mm)	Number of drilling holes	Depth of the drilling hole h (mm)	Local damage degree η_{local} (%)	Global damage degree η_{global} (%)	Column axial force N (kN)
J1	—	—	—	—	0	0	20
J2	30	5	12	30	33.3	0.6	20
J3	60	5	48	30	33.3	2.4	20
J4	60	5	48	30	33.3	2.4	60

Table 2 Physical and Mechanical parameters of the timber

Parameter	Number of specimens	Average value	Standard deviation	Coefficient of variation (%)
f_{Lt}	10	106.73 MPa	14.76 MPa	13.83
f_{Lc}	12	76.35 MPa	4.33 MPa	5.67
f_{Rc}	12	17.13 MPa	1.10 MPa	6.39
f_{Tc}	12	17.54 MPa	1.06 MPa	6.04
ρ	20	0.982 g/cm ³	0.012 g/cm ³	1.24
ω	20	16.3%	0.6%	3.48

* f_{Lt} refers to tensile strength parallel to the grain. f_{Lc} is compressive strength parallel to the grain. f_{Rc} is radial compressive strength. f_{Tc} is chordal compressive strength. ρ is density. ω is moisture content

two different damage degrees are involved in the specimen design in this paper. One is the local damage degree η_{local} , which is the ratio of the drilling volume to the volume of the damaged area, and the other is the global damage degree η_{global} , which is the ratio of the drilling volume to the tenon volume.

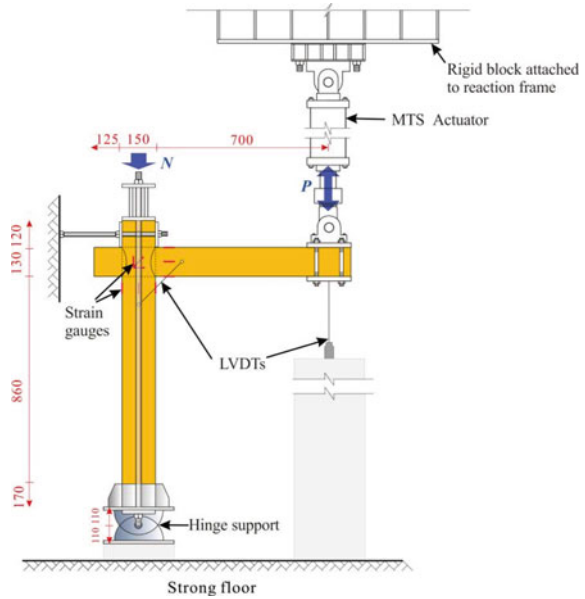
Two variable parameters are considered in the specimen design. One is the global damage degree η_{global} , which is 0%, 0.6%, and 2.4% for J1, J2, and J3, respectively. The local damage degree η_{local} of J2 is consistent with that of J3, which is 33.3%. The other is the column axial force N , which is 20 kN and 60 kN for the comparison specimens J3 and J4, respectively. The specimens are all made of merbau wood, and the physical and mechanical properties of the wood are measured in accordance with the Chinese national standard (GB/T 1927–1943–2009), as shown in Table 2.

2.2 Loading Device and Measuring Solution

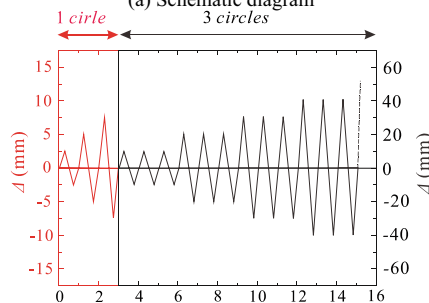
Figure 2 a shows the loading device and measurement scheme of the test. The bottom of the column relates to the hinge support, and the top of the column is provided with lateral supports to limit the lateral displacement. An axial force is applied to the column by tightening the bolts of the self-balancing device, and the axial force is read by the force sensor between the self-balancing device and the column. The cyclic loading at the beam end is applied by displacement control through the MTS actuator with a loading capacity of 500 kN. Two linear variable differential transducers (LVDTs) are arranged in the test. One is placed between the side of the beam and column to measure the rotation angle of the joint, and the other is placed between the MTS loading adaptor and the rigid ground as the basis for MTS displacement control. In addition, several strain gauges are pasted near the mortise-tenon joint to test the strain condition there.

The loading process of the test is divided into two steps. The first step is to impose axial force on the column and maintain constant throughout the test. The second step

Fig. 2 Experimental device and loading mode



(a) Schematic diagram



(b) Loading method

is to apply vertical low-cycle reversed load at the beam end by displacement control. The first three stages of the controlled displacement are 2.5, 5 and 7.5 mm, and each stage is circulated once. From the fourth stage (10 mm), the increment of the adjacent two stages of the controlled displacement is 10 mm, and each stage is circulated three times, as shown in Fig. 2b. The load is terminated when the structure is destroyed.

3 Experiment Results and Analysis

3.1 Failure Modes

During the loading process of the specimen, there is no obvious phenomenon of the mortise-tenon joint at the initial stage. As the displacement Δ of the beam end increases, the dislocation friction between the mortise and the tenon will occur and make a crisp sound. When the friction between the mortise and tenon reaches a certain level, cracks begin to appear in the beam tenon, which will continue to expand until the final failure.

Overall, the failure modes of the hoop head mortise-tenon joints tested in this paper can be divided into two types. One is the parallel-to-grain tensile cracking failure of the beam tenon, and the other is the vertical splitting failure of the beam tenon, as shown in Fig. 3. The two failure modes have been reported by previous scholars in the experimental study on the mechanical properties of the hoop head mortise-tenon joint, which shows certain randomness. In addition, the two failure modes can appear alone or simultaneously [3]. Parallel-to-grain tensile cracking failure and vertical splitting failure respectively appear in specimens J1 and J2, while the two failure modes mentioned above simultaneously appear in specimens J3 and J4, which shows that as the global damage degree increases, the hoop head mortise-tenon joint may be more likely to have multiple failure modes at the same time.

3.2 Hysteresis Curve

The hysteresis curves of all specimens are shown in Fig. 4. In the figure, the red mark “●” indicates the moment when the snap sound of wood dislocation friction begins to appear, and the mark “Δ” shows the moment when the test piece undergoes visible stress cracks. From Fig. 4, the following conclusions can be drawn:

- (1) The hysteresis curves of all the specimens are rod-shaped and have an obvious “pinching” phenomenon. In addition, there are significant twists at the ascending section in the middle and late stages of loading, proving that all the specimens have friction slip.
- (2) Overall, the rotation angle of the damaged hoop head mortise-tenon joint is smaller than that of the intact one when the friction sound and the stress crack occur, showing that under the same deformation, the damaged hoop head mortise-tenon joint is more likely to show signs of failure. In addition, the fullness of the hysteresis curve decreases with the increase of the global damage degree.
- (3) With the same global damage degree, the increase of the column axial force can delay the time when friction sound and the stress crack occur, for which the greater the axial force is, the greater the maximum static friction between the

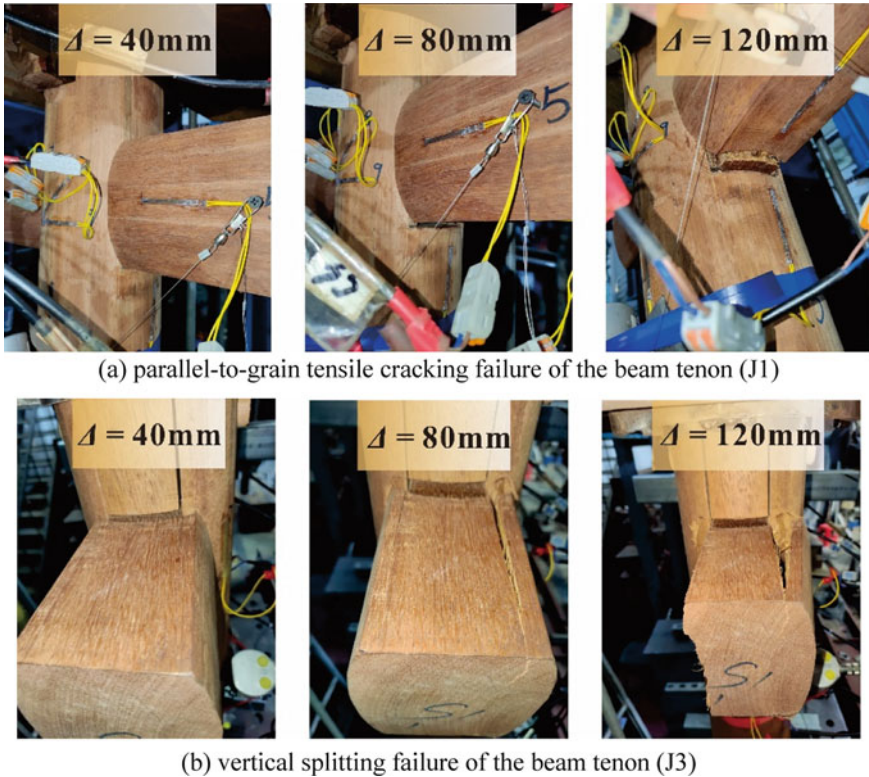


Fig. 3 Comparison of failure progresses

mortise and tenon will be, and the friction dislocation will be more difficult to occur.

3.3 Skeleton Curve and Ductility

Figure 5 shows the comparison of the skeleton curves of different specimens, and Table 3 lists the test and calculation results. M_{uc} refers to the peak bending moment. θ_{uc} is the peak rotation angle. θ_u is the ultimate rotation angle. μ represents the ductility factor. The ultimate rotation angle is defined as the rotation angle of the joint when the bending moment decreases to 85% of the peak bending moment. The ductility coefficient μ is determined as the method in reference [8]. The above physical quantities are obtained by averaging the results obtained in two loading directions. Based on Fig. 5 and Table 3, we can draw the following conclusions.

- (1) When the axial force of the column is small (20 kN), there is a lot of friction dislocation between the mortise and tenon, with many twists and turns in the

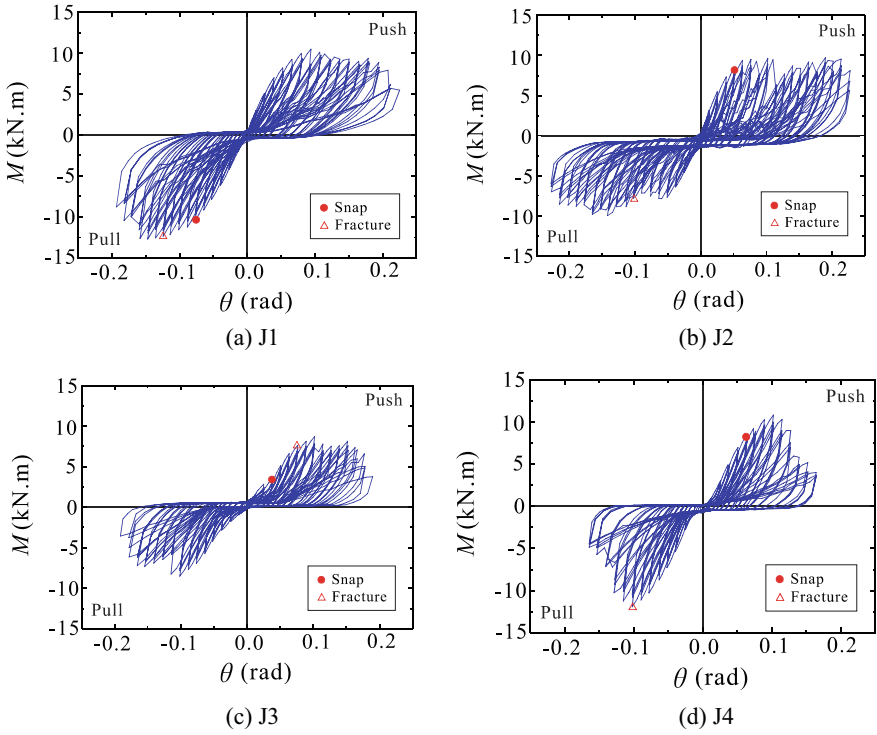


Fig. 4 Moment versus rotation hysteresis curves

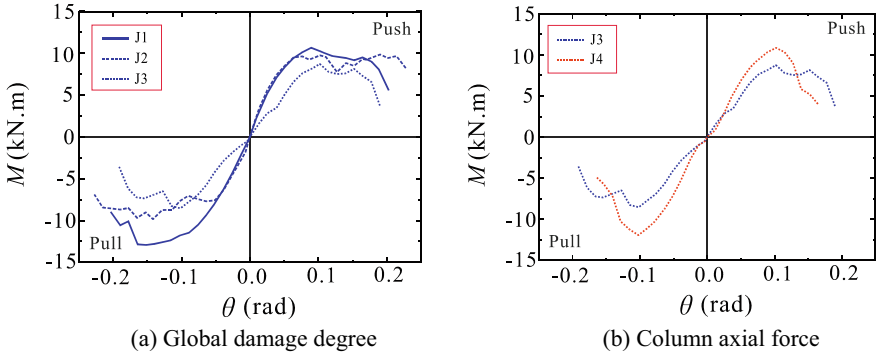


Fig. 5 Moment versus rotation backbone curves

Table 3 Experiment results

Number of specimens	Parallel-to-grain tensile cracking failure (Yes/No)	Vertical splitting failure (Yes/No)	M_{ue} (kN.m)	θ_{ue} (rad)	θ_u (rad)	μ	$E_{0.15}$ (J)
J1	Yes	No	11.62	0.121	0.176	2.375	823.5
J2	No	Yes	9.72	0.126	0.174	2.858	698.7
J3	Yes	Yes	8.63	0.102	0.163	1.818	500.9
J4	Yes	Yes	11.38	0.102	0.127	1.510	722.5

* M_{ue} refers to peak bending moment. θ_{ue} is peak rotation angle. θ_u is the ultimate rotation angle. μ is ductility factor. $E_{0.15}$ is the energy consumption of the first hysteresis loop on the loading stage when the rotation angle is about 0.15 rad

skeleton curve and good ductility. When the axial force of the column is large (60 kN), the friction dislocation between the mortise and the tenon is less, with a smooth skeleton curve and poor ductility. The ductility coefficient μ decreases by 16.9% when the column axial force increases from 20 to 60 kN.

- (2) Both the global damage degree and the column axial force have a significant effect on the peak bending moment M_{ue} of the joint. M_{ue} decreases with the increase of the global damage degree, while the increase of column axial force can increase M_{ue} . When the global damage degree increases from 0 to 2.4%, M_{ue} decreases by 25.7%. When the column axial force increases from 20 to 60 kN, M_{ue} increases by 31.9%.
- (3) When the global damage degree is small (0.6%), it has little effect on θ_{ue} and θ_u . However, when the global damage increases to 2.4%, θ_{ue} and θ_u decrease to a certain extent. The increase of column axial force makes θ_u decrease significantly but has little effect on θ_{ue} .

3.4 Energy Dissipation Capacity

The area enclosed by the hysteresis loop is the energy absorbed by the specimen. Table 3 lists $E_{0.15}$, the energy consumption of the first hysteresis loop on the loading stage when the rotation angle is about 0.15 rad, and we can obtain the following conclusions.

- (1) The global damage degree has a great influence on the energy consumption capacity of the joint. When the global damage degree increases from 0 to 2.4%, $E_{0.15}$ decreases by 39.2%.
- (2) The increase of the column axial force can significantly improve the energy dissipation capacity of the joint. When the column axial force increases from 20 to 60 kN, the $E_{0.15}$ increases by 44.2%, for which a larger axial force will lead to a larger friction force between the tenon and mortise, and the frictional energy consumption will be correspondingly larger.

4 Conclusions

The main conclusions of this paper are as follows.

- (1) The failure modes of the hoop head mortise-tenon joint mainly include the parallel-to-grain tensile cracking failure of the beam tenon and the vertical splitting failure of the beam tenon. When the global damage degree increases, the two failure modes are more likely to occur simultaneously.
- (2) The global damage degree has a significant impact on the ultimate bending moment and energy dissipation capacity of the hoop head mortise-tenon joint. In addition, 2.4% of the global damage degree can lead to a 25.7% and 39.2% decrease in M_{ue} and $E_{0.15}$, respectively.
- (3) The column axial force has a great influence on the ultimate bending moment, ductility, and energy dissipation capacity of the hoop head mortise-tenon joint. When the column axial force increases from 20 to 60 kN, M_{ue} and $E_{0.15}$ increase by 31.9% and 44.2%, respectively, and the ductility coefficient μ decreases by 16.9%.

References

1. Chen CC, Qiu HX, Xu MG (2014) Experimental study on flexural behavior of typical Mortise-Tenon joints. *Appl Mech Mater* 578–579:160–163
2. Chen LK, Li SC, Zhao KP et al (2020) Experimental and numerical investigation on seismic performance of one-way straight Mortise-Tenon joints based on a novel method to simulate damage of deteriorated ancient Chinese timber buildings. *Perform Constr Facil* 34(2):04019119
3. Chen QJ, Peng ZF, Cai J et al (2019) Seismic behavior of hoop head tenon-mortise joint in ancient wood structures in Guangfu. *J Build Struct* 40(10):168–179 (In Chinese)
4. Chun Q, Yue Z, Pan JW (2011) Experimental study on seismic characteristics of typical mortise-tenon joints of Chinese southern traditional timber frame buildings. *China Technol* 09:2404–2411
5. GB/T 1927–1943–2009. (2009). Beijing: Standards Press of China (In Chinese)
6. Li SC, Chen LK, Jiang LZ et al. (2019) Experimental investigation on the seismic behavior of the semi-rigid one-way straight Mortise-Tenon joint of a historical timber building. *Int J Archit Herit* 1–13
7. Shi YX (2017) FE Analyses of Dovetail joint and Shizigutou Mortise-tenon's seismic performance. D. Taiyuan University of Technology (In Chinese)
8. Wu B, Peng CW, Zhao XY (2020) Cyclic loading tests of semi-precast circular steel tubular columns incorporating precast segments containing demolished concrete lumps. *Eng Struct* 211:110438
9. Xie QF, Du B, Li S et al (2015) Tests for aseismic behaviors of damaged dovetail mortise-tenon joints of ancient timber buildings. *J Vibr Shock* 34(4):165–170 (In Chinese)
10. Xie QF, Zheng PJ, Xiang W et al (2014) Experimental study on seismic behavior of damaged straight mortise-tenon joints of ancient timber buildings. *J Build Struct* 35(011):143–150 (In Chinese)
11. Ying PJ (2016) Mechanical property analysis on Mortise-Tenon joints and its fine numerical simulation in ancient Chinese timber structures. D. Xi'an University of Architecture and Technology (In Chinese)

Open Access This chapter is licensed under the terms of the Creative Commons Attribution 4.0 International License (<http://creativecommons.org/licenses/by/4.0/>), which permits use, sharing, adaptation, distribution and reproduction in any medium or format, as long as you give appropriate credit to the original author(s) and the source, provide a link to the Creative Commons license and indicate if changes were made.

The images or other third party material in this chapter are included in the chapter's Creative Commons license, unless indicated otherwise in a credit line to the material. If material is not included in the chapter's Creative Commons license and your intended use is not permitted by statutory regulation or exceeds the permitted use, you will need to obtain permission directly from the copyright holder.



Experimental Study on the Self-Repair Properties of Shape Memory Alloy Concrete Beam



Yue Zhang and Xian Cui

Abstract The one-way memory composite super-elastic shape memory alloy wires were laid on the bottom of the reinforced concrete beam to make the intelligent concrete beam. The paper compares the self-repair properties of each test beam, and analyzes the influence of different memory filament ratio and different damage degree on the self-repair properties of SMA reinforced concrete beams. The test results suggest that the shape memory alloy can improve the self-repair ability of the concrete beam, the best when the damage degree is 70 and 50%.

Keywords Reinforced concrete beam · Shape memory alloy (SMA) · Self-repair

1 Introduction

Reinforced concrete structures are the most widely used and most abundant structural form in the world of construction today and will remain an essential structure in engineering for some time to come. However, during the long-term use of engineering structures, concrete in reinforced concrete structures often undergoes different degrees and types of cracks, which may lead to corrosion of reinforcement, thus causing permanent damage to the structure and seriously affecting the normal use and durability of the structure. Therefore, the study of the cracking and deformation resistance of structures is of great practical importance. At present, with the development and continuous progress of modern materials, concrete structure has achieved a new breakthrough in the process of moving towards intelligence and complexity, i.e., intelligent structures are used to solve the above problems.

At present, the main materials that can be used as driving materials in smart structures are current variant materials, magneto rheological materials, shape memory

The original version of this chapter was revised: The author Xian Cui now has been changed as corresponding author. The correction to this chapter is available at https://doi.org/10.1007/978-981-19-8657-4_48

Y. Zhang · X. Cui (✉)
Dept. of Structural Engineering, Yanbian University, Yanji, China
e-mail: 2013386407@qq.com

© Crown 2023, corrected publication 2023

Y. Yang (ed.), *Advances in Frontier Research on Engineering Structures*, Lecture Notes in Civil Engineering 286, https://doi.org/10.1007/978-981-19-8657-4_36

409

materials, etc. [4], among which shape memory alloys, as typical smart materials, are one of the best shape memory materials in terms of shape memory performance. Shape-memory alloy has two important properties: shape memory effect and super-elasticity, and can recover to the state before deformation after plastic deformation by heating them above a certain temperature [3]. At the same time, if the recovery process is limited, the material will produce a large recovery stress, that is, the SMA wire to produce a large recovery drive characteristics. Also, shape memory alloys are easy to combine with concrete and steel materials. In the repair and enhancement of concrete beam structure, the shape memory effect and super elasticity of shape memory alloy can effectively improve the mechanical properties of concrete structure, the shape memory effect has the advantage of easy application of prestress, and its super elasticity can control and recover the deformation and deflection of structural members, reduce the impact of typhoon and earthquake, and more effectively ensure the safety and reliability of the structure. It is because of these advantages that shape memory alloys have great application prospects and broad development space in various fields [1, 2, 5, 6].

In this paper, super-elastic SMA wires and unidirectional memory SMA memory wires were buried in the tensile zone of reinforced concrete beams to make smart concrete beams, and the self-healing ability of SMA concrete beams were studied by using the method of single-point loading test in the span. 15 SMA concrete beams were tested for their mechanical properties, and the effects of different unidirectional memory SMA wire and super-elastic SMA wire contents, degree of damage and other factors on their recovery.

2 Experimental Programme

2.1 Experimental Materials

Ni–Ti shape memory alloys were used for the test, and the diameter of both super-elastic SMA wire and unidirectional memory SMA wire was 1 mm. The parameters of the shape memory alloy used are shown in Table 1. The specimens were made of C20 concrete as the matrix material with the ratio of water:cement:sand:stone = 0.54:1:1.51:2.60, where the cement strength grade was 32.5 MPa. The average measured compressive strength of the concrete cubes measured by the test was 20.64 MPa.

Table 1 Chemical composition of SMA wire

Ni	Ti	C	Co	Cr	Nb	Fe	Cu	N	O	Unit
55.8	44.1	0.007	0.003	0.03	0.003	0.004	0.003	0.0015	0.043	%

2.2 Experimental Design

In order to investigate the mechanical properties of SMA smart concrete beams and to obtain a better design solution for the content of super-elastic SMA wires and unidirectional memory SMA wires, 15 reinforced concrete beam specimens with SMA wires were designed and fabricated for comparative analysis, numbered L1–L15, and the basic characteristics of the specimens are shown in Table 2. The geometry of the concrete base beam is 400 × 100 × 100 mm. Six SMA wires were preembedded in the tensile zone and the upper part was equipped with two 8 mm diameter reinforcement bars as erection bars. The longitudinal reinforcement of the beam was 2φ8 in the compression zone, 2φ8 in the tension zone, and the hoop reinforcement was taken as φ6@100, and the thickness of the concrete protective layer was 25 mm. The main variation parameters of the specimen were the content of super-elastic SMA wire and one-way memory SMA wire and the damage degree of the specimen. The specimens were formed in the mold by layered casting method, and after removing, they were maintained under standard maintenance conditions until the age of 28d, and single-point loading test was carried out in the span on the electronic material testing machine (Fig. 1).

Table 2 Experimental protocol

Specimen number	Super elastic ratio (%)	One-way memory ratio (%)	Degree of damage (%)
L1	100	0	30
L2	100	0	50
L3	100	0	70
L4	70	30	30
L5	70	30	50
L6	70	30	70
L7	50	50	30
L8	50	50	50
L9	50	50	70
L10	30	70	30
L11	30	70	50
L12	30	70	70
L13	0	100	30
L14	0	100	50
L15	0	100	70

Fig. 1 Reinforcement diagram of the test beam

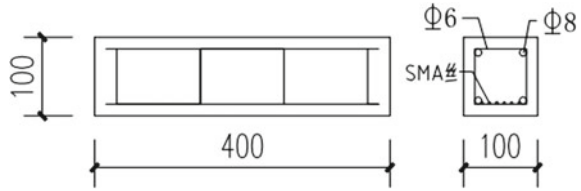


Fig. 2 Test equipment and instruments



2.3 Test Equipment, Instruments and Devices

Figure 2 shows the actual photo of the test beam when it was loaded. The test beam was loaded at a single point in the span and the test equipment used was PWS-500 hydraulic servo fatigue tester. The actuator of the tester has its own force sensor and displacement sensor. The strain gauges were pasted on both sides of the reinforcement in the tensile zone and on the top surface of the concrete compression zone at the mid-span position of the test beam to monitor the strain changes in the concrete beam.

2.4 Test Methods

(1) Test loading

Single point loading test at mid-span on beam specimens after maintenance. The displacement loading control mode was used with a loading rate of 0.1 kN/s. The loading method used for the test was single cycle loading, and the unloading was carried out on the basis of 30, 50 and 70% of the ultimate load.

(2) Self-repair test

The self-repair test mainly used a small sun heater to heat the deformed specimens after loading, and the temperature was observed by a thermometer placed on the

concrete beam specimens, and the specimens were heated until they reach about 20°. After stopping the heating, the self-repaired specimens were loaded again and loaded until the specimens were damaged or the maximum displacement of the loading was 20 mm.

3 Test Results and Observations

3.1 Test Results

During the loading process, the mid-span deflection of the specimen gradually increased with the increase of the load; tiny cracks appeared at the bottom of the specimen, after which the cracks widened and rapidly expanded along the height of the beam toward the top of the beam. When unloading, it can be seen that the cracks of the specimen have obvious recovery, which is due to the effect of SMA one-way memory and super-elastic.

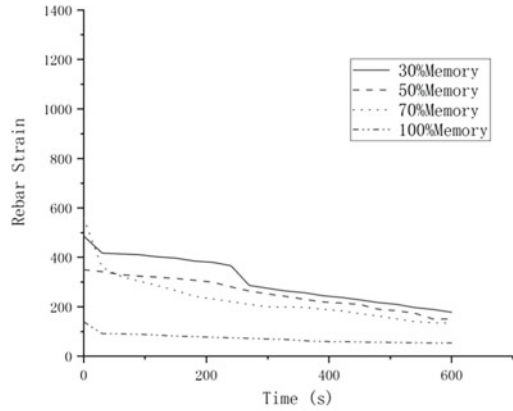
3.2 Recovery Effect Analysis

Figure 3 gives the strain of the reinforcement in each specimen during the heating process, from which the repair effect of SMA wire in each specimen can be analyzed. From Fig. 3, it can be seen that.

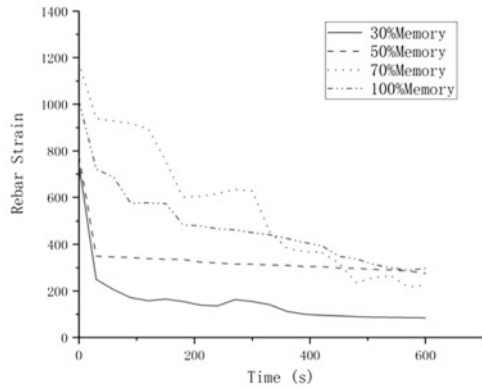
The strains of reinforcement at different levels of damage were reduced for different contents of super-elastic memory wire and unidirectional memory wire, indicating that SMA wire can improve the self-repair ability of reinforced concrete beams regardless of the material content percentage.

At 30% damage, the material percentage did not have a significant effect on the strain value of the reinforcement. At 50 and 70% damage, the difference in recovery strains was not significant. During unloading, the recovered strains were significantly higher in the 30 and 50% unidirectional memory wire specimens than in the 70 and 100% unidirectional memory wire specimens, but with increasing heating time, the recovered strains in the latter were significantly higher than those in the former. This is due to the fact that during unloading, the super-elastic memory wire can significantly improve the recovery of the beam, so the recovery of the specimen with higher content of super-elastic wire is more obvious; while with the increase of heating time, the unidirectional memory wire gradually plays the main role and makes the reinforcement of the specimen with higher content of unidirectional memory wire have higher recovery strain. The analysis of Fig. 3 shows that the recovery effect of the reinforced concrete beam with 70% unidirectional memory wire and 30% super-elastic wire is optimal.

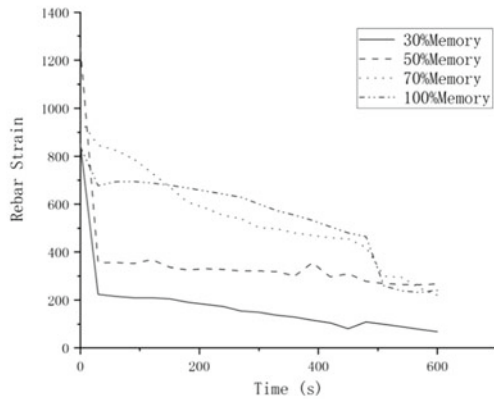
Fig. 3 Variation of recovery strain for **a** 30%, **b** 50% and **c** 70% of damaged level



(a)



(b)



(c)

3.3 Effect of Damage Level on Mechanical Properties of Test Beams

The load-displacement curves of reinforced concrete beams with 100% super-elastic memory wire (test beam L1–L3), 30% unidirectional memory wire (test beam L4–L6), 50% unidirectional memory wire (test beam L7–L9), 70% unidirectional memory wire (test beam L10–L12), and 100% unidirectional memory wire (test beam L13–L15) under different damage conditions are given in Fig. 4. Table 3 shows the test data of cracking load, ultimate load and displacement for specimens L1–L15.

As can be seen from Fig. 4, the specimens all have more obvious yield points and yield stages. When the content of super-elastic SMA wire and unidirectional memory SMA wire in the specimens is constant, in the elastic phase, with the increase of the damage degree, the bearing capacity of the specimens will subsequently increase in different degrees. As can be seen from Table 3: in the case of fully elastic memory wire reinforced concrete, the ultimate bearing capacity and ductility of the specimen with 70% damage are significantly higher than those of the other two damage levels; in the case of 30% unidirectional memory wire, the difference between the bearing capacity of 50% damage level and 70% damage level is less, but it is increased compared to the specimen with 30% damage level; in the case of unidirectional memory wire and super-elastic memory wire The ultimate bearing capacity and ductility of the 70% damage specimen are better than those of the 30 and 50% damage specimens when the content of the unidirectional memory wire is the same; while the ultimate bearing capacity of the 70% damage specimen is significantly higher than those of the 30 and 50% damage specimens in the case of 70% unidirectional memory wire, but its ductility is poor; in the case of all unidirectional memory wire reinforced concrete, the 50% damage specimen L14 The ultimate bearing capacity is higher than the other two beams, and the ductility is better than that of the specimen with 30% damage. It can be seen that the increase of damage degree can improve the mechanical properties of smart reinforced concrete beams to some extent, but the percentage of different unidirectional memory wires and super-elastic memory wires should be considered. The degree of damage required for the optimal unloading effect varies for different material occupancy ratios.

4 Conclusions

Smart concrete beams were made by using unidirectional memory composite super-elastic shape memory alloy wires laid on the bottom of reinforced concrete beams, and the mechanical properties of various test beams were investigated using mid-span single-point loading tests. The results show that the mechanical properties of concrete beams with different memory and super-elastic wire contents and different damage levels have differences, and SMA materials can significantly improve the

Fig. 4 Variation of load–displacement curve for **a** 30%, **b** 50% and **c** 70% of damaged level

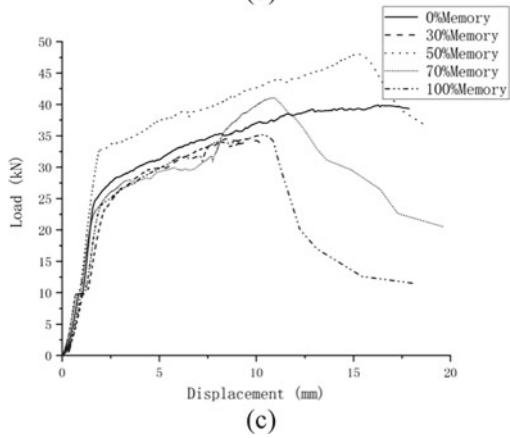
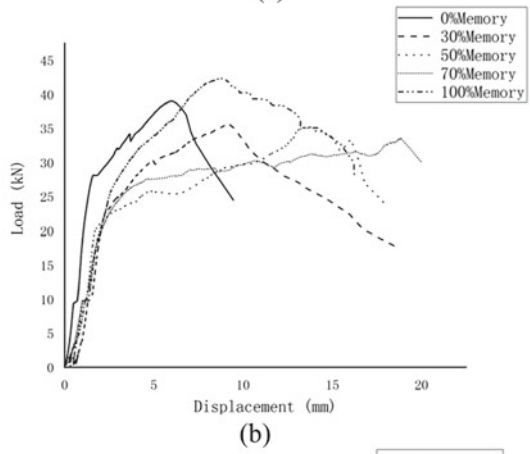
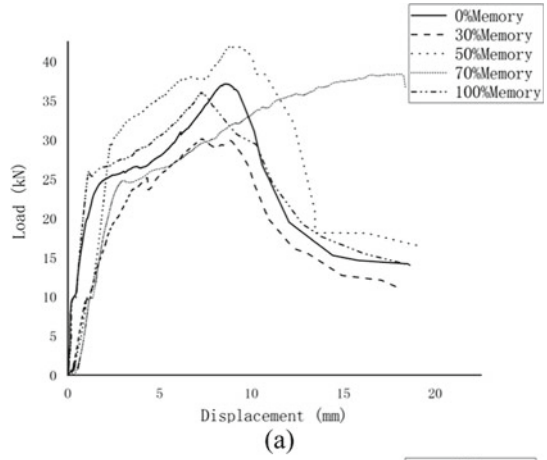


Table 3 Results of loading tests on SMA-confined concrete specimens

Specimen number	Cracking load (kN)	Ultimate load (kN)	Displacement (limit) (mm)	Displacement (steel yielding) (mm)
L1	6.1	33.6	8.7	1.6
L2	9.4	39.0	5.9	1.5
L3	9.7	39.5	17.8	1.6
L4	9.3	30.1	7.2	3.5
L5	9.7	35.4	8.9	2.3
L6	9.5	34.4	8.4	2.1
L7	9.9	41.8	9.0	2.3
L8	9.7	34.8	13.5	1.5
L9	9.8	48.1	15.4	1.9
L10	9.7	38.1	17.9	2.7
L11	9.7	33.5	18.9	3.3
L12	9.8	40.9	10.9	3.3
L13	6.1	32.3	7.3	1.2
L14	9.8	42.8	8.8	2.8
L15	9.8	34.8	10.4	2.2

mechanical properties of concrete beams and enhance their self-healing ability, with the following main conclusions:

- (1) With the same degree of concrete damage, the material percentage did not have a significant effect on the strain value of the reinforcement when the degree of damage was 30%; however, when the degree of damage reached 50 and 70%, the reinforced concrete beams with 70% unidirectional memory wire and 30% super-elastic wire had better recovery results than the other contents.
- (2) When the content of super-elastic SMA filaments and unidirectional memory SMA filaments in the specimen was constant, in the elastic phase, with the increase of the damage degree, the bearing capacity of the specimen would increase with it to different degrees. The mechanical properties of the smart reinforced concrete beams can be improved by appropriately increasing the degree of damage to a certain extent, but different percentages of unidirectional memory filaments and super-elastic memory filaments should be considered, which were particularly prominent at 50% of unidirectional memory filaments, where the specimen had the best self-repair effect.

References

1. Cui D (2010) Experimental study on the mechanical properties of concrete beams with shape memory alloy. *Eng Mech* 27(02):117–123
2. Li SB (2015) Study of shape memory alloy recovery performance and its application in concrete beam crack repair. *Concrete* 04:68–73
3. Sun L (2015) Experimental study on the repair performance of concrete beams configured with prestressed shape memory alloy wires. *J Build Struct* 36(S2):265–269
4. Xue WC (2009) Experimental study on the active control of intelligent prestressed beams based on SMA. *J Civil Eng* 42(06):22–27
5. Yang JN (2021) Review of mechanical behavior and applications of shape memory alloys. *J Solid Mech* 42(04):345–375
6. Zhou HK (2020) Study on the self-healing performance of UHTCC plates configured with shape memory alloy wires. *J Three Gorges Univ (Nat Sci Ed)* 42(04):66–70

Open Access This chapter is licensed under the terms of the Creative Commons Attribution 4.0 International License (<http://creativecommons.org/licenses/by/4.0/>), which permits use, sharing, adaptation, distribution and reproduction in any medium or format, as long as you give appropriate credit to the original author(s) and the source, provide a link to the Creative Commons license and indicate if changes were made.

The images or other third party material in this chapter are included in the chapter's Creative Commons license, unless indicated otherwise in a credit line to the material. If material is not included in the chapter's Creative Commons license and your intended use is not permitted by statutory regulation or exceeds the permitted use, you will need to obtain permission directly from the copyright holder.



Application of ABAQUS by Using Python in Concrete-Filled Steel Tube



Zhishuo Yang, Mingxia Chen, Feixin Chen, Zuorong Dong,
and Yiman Zhong

Abstract Concrete-filled steel tube (CFST) column have remarkable mechanical properties and are widely used in engineering. In order to avoid repeated work, this paper introduces a concrete model based on Python, which is used for automatic simulation of CFST columns under different loads. The pre-treatment and finite element analysis of CFST columns are carried out by using the model software. Finally, examples were cited to illustrate that the simulation results of the model are similar to the test results, and the purpose of engineering application is achieved.

Keywords The secondary development · Python · ABAQUS · Concrete-filled steel tube

1 Instructions

Concrete-filled steel tube (CFST) column is a hot topic in a structure design [1–3]. ABAQUS pre-processing and post-processing developed by Python language reduce the repeated work of modification and resubmission by modifying model parameters, submitting jobs and reanalyzing [3, 4].

In view of the wide application of CFST and the need for repeated modeling, calculation and post-processing in the calculation process, which increases a lot of unnecessary workload, we hope to reduce the amount of work and improve work efficiency through redevelopment.

Z. Yang · M. Chen (✉) · Z. Dong

College of Civil Engineering, Jiaying University, Meizhou, Guangdong, China
e-mail: yzs21@126.com

Z. Yang

School of Civil Engineering, Putian University, Putian, China

College of Civil Engineering and Architecture, Central South University, Changsha, Hunan, China

F. Chen

Guangdong Polytechnic Normal University, Guangzhou, China

Y. Zhong

University of Electronic Science and Technology of China Zhongshan Institute, Zhongshan, China

© Crown 2023

Y. Yang (ed.), *Advances in Frontier Research on Engineering Structures*, Lecture Notes in Civil Engineering 286, https://doi.org/10.1007/978-981-19-8657-4_37

419

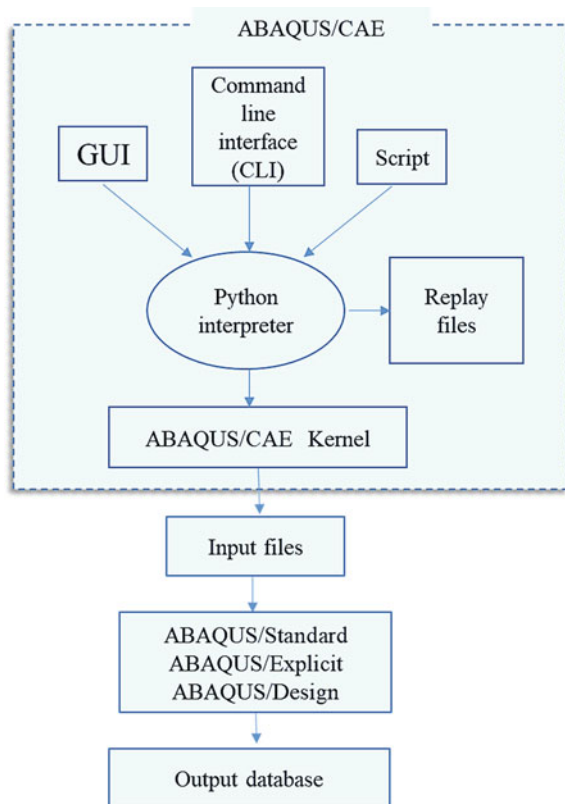
At present, few literatures introduce this content, so this paper introduces the application of Python for secondary development, which can realize the functions of parametric calculation and data analysis, and play a reference role for engineering applications.

2 Introduction of ABAQUS and Python

2.1 The Template File

ABAQUS can simulate the linear and nonlinear properties of materials, so it should be widely used in engineering design. ABAQUS/CAE module is a human–computer interface. ABAQUS provides many library functions for users in Python. You can call library functions through the calling interface. The Python language can be transmitted into kernel of Abaqus through forms shown in Fig. 1 [5].

Fig. 1 Abaqus scripting interface commands and Abaqus/CAE



The following functions can be achieved: (1) Create or modify model parameters (2) Create or modify ABAQUS analysis tasks (3) Operation field output and historical output data. (4) View the analysis results (5) Realize parametric analysis.

The script interface is an object-oriented library. ABAQUS provides an interface to implement the pre-processing and post-processing of the model. The relationship of the model is very complex, as shown in Fig. 2. It is divided into three forms: session object for defining views, model database and ODB object for analysis results [6–8]. ABAQUS secondary development can be realized by four methods: (1) User subroutines; (2) Abaqus environment files; (3) Abaqus scripting interface; and (4) Abaqus GUI Toolkit Fig. 3.

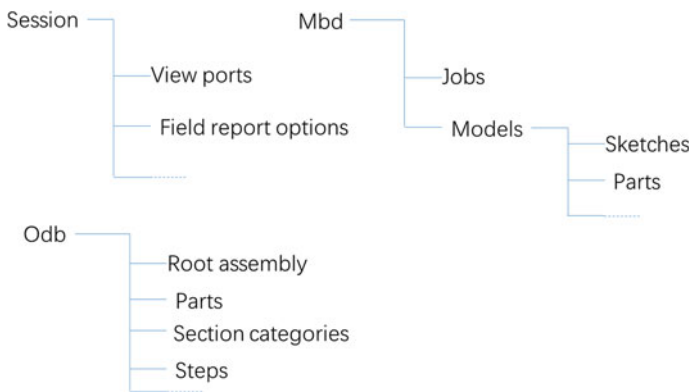


Fig. 2 Structure of the Abaqus object model

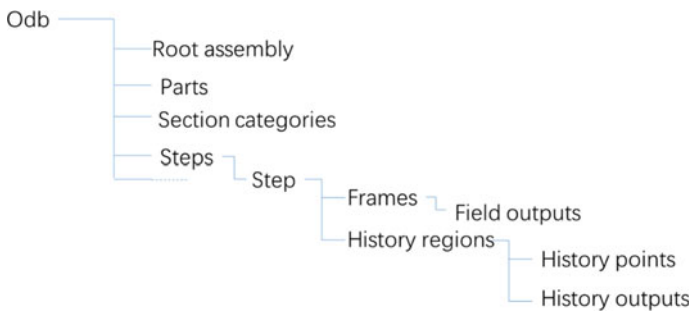


Fig. 3 Odb object model

3 Application

See Fig. 4.

This paper studies CFST column using Abaqus secondary development. By using secondary development, CFST column are modified individually. CFST column can be obtained at different concrete, plate and steel pipe. Modifying models, submitting tasks, restarting analysis, etc., can be implemented through software developed in python, thus improving the computing power of finite elements. For study of CFST column, first, some representative components are created, as shown in Fig. 3. Simultaneously, part of the codes of the function is given as follows:

```
GroupBox_1 = FXGroupBox(p = self, text = 'Create various components', opts = FRAME_GROOVE|LAYOUT_FILL_X)
```

```
HFrame_1 = FXHorizontalFrame(p = GroupBox_1, opts = 0, x = 0, y = 0, w = 0, h = 0, pl = 0, pr = 0, pt = 0, pb = 0)
```

```
GroupBox_2 = FXGroupBox(p = HFrame_1, text = 'Concrete', opts = FRAME_GROOVE)
```

```
AFXTextField(p = GroupBox_2, ncols = 6, labelText = 'Concrete diameter(mm):', tgt = self.form.diameterKw, sel = 0, opts = AFXTEXTFIELD_FLOAT)
```

```
AFXTextField(p = GroupBox_2, ncols = 6, labelText = 'Concrete length(mm):', tgt = self.form.lengthKw, sel = 0, opts = AFXTEXTFIELD_FLOAT)
```

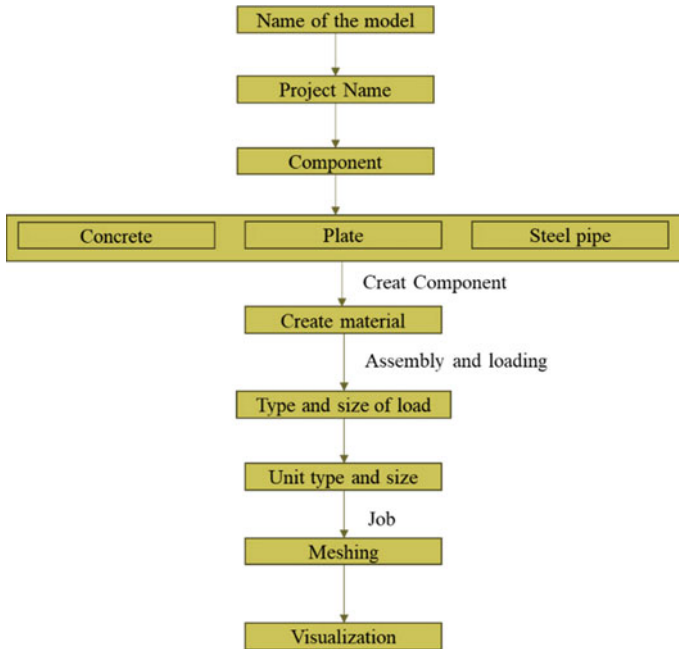


Fig. 4 Relationship of the main parts

```
GroupBox_3 = FXGroupBox(p = HFrame_1, text = 'Plate', opts =  
FRAME_GROOVE)  
self.ComboBox_1 = AFXComboBox(p = GroupBox_3, ncols = 10, nvis  
= 2, text = 'Type of Plate:', tgt = self, sel = self.ID_CBOX1)  
self.ComboBox_1.appendItem(text = 'Rigid surface')  
self.ComboBox_1.appendItem(text = 'Elastomer')  
self.ComboBox_1.setCurrentItem(1)  
self.form.RigidTypeKw.setValue(2)  
self.RigidDepthTF = AFXTextField(p = GroupBox_3, ncols = 6, labelText = 'Plate thickness(mm):', tgt = self.form.RigidDepthKw, sel = 0, opts = AFXTEXTFIELD_FLOAT)  
GroupBox_4 = FXGroupBox(p = HFrame_1, text = 'Steel Pipe', opts =  
FRAME_GROOVE)  
AFXTextField(p = GroupBox_4, ncols = 6, labelText = 'Pipe  
wall thickness(mm):', tgt = self.form.thicknessKw, sel = 0, opts =  
AFXTEXTFIELD_FLOAT)  
FXButton(p = GroupBox_4, text = 'Creating components', ic = None,  
tgt = self.form, sel = self.form.ID_DBBUTTON1, opts = BUTTON_NORMAL,  
x = 0, y = 0, w = 0, h = 0, pl = DEFAULT_PAD, pr = DEFAULT_PAD, pt =  
DEFAULT_PAD, pb = DEFAULT_PAD)
```

The results are as follows from Fig. 5

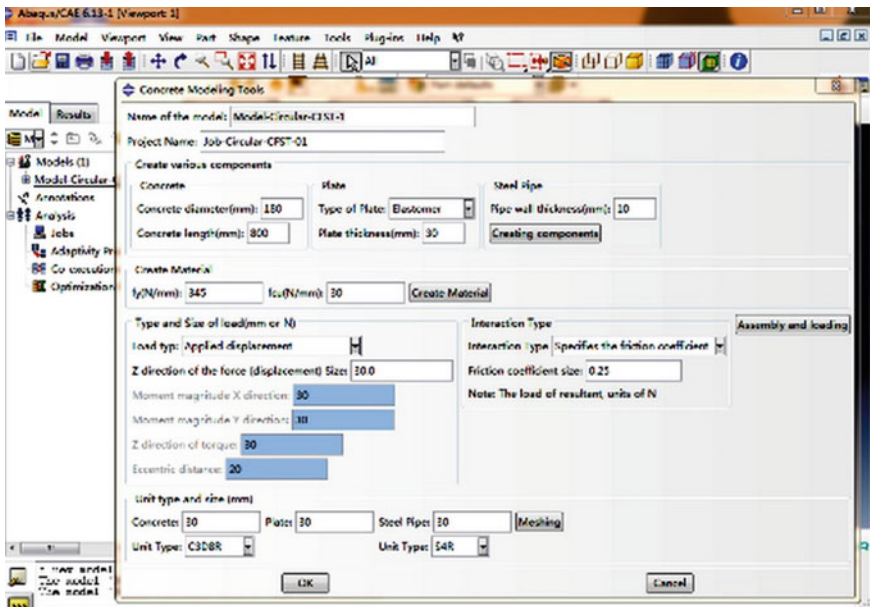


Fig. 5 Interface and models

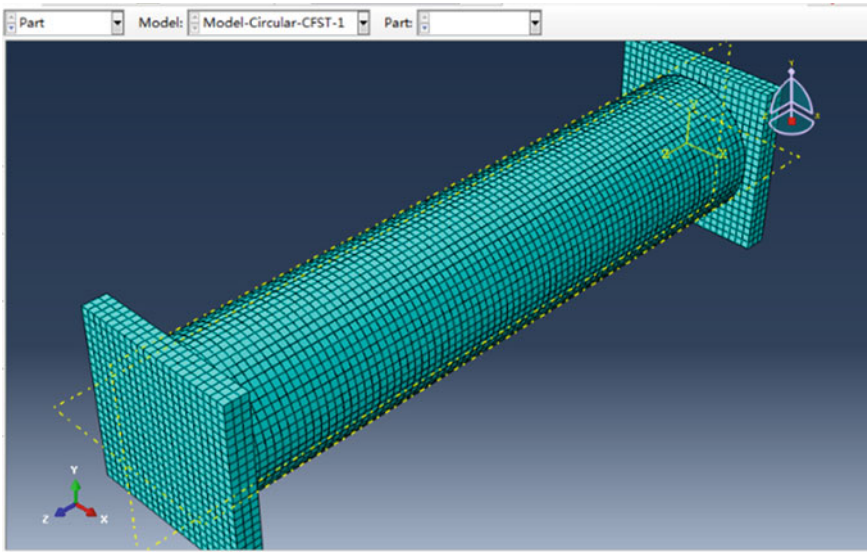


Fig. 6 Typical FE model adopted in numerical modeling

4 Verification

The numerical results compared with the testing which verifies the correctness of the programming. The experimental data are quoted in the published journals of the author. See Yang et al. [9], Yang et al. [10] and Yang et al. [11].

Figure 6 shows a typical FE model in which three-dimensional 8-node solid elements (C3D8) were adopted. Figure 7 shows the results of typical FE model. Figure 8 was the steel pipes after test.

By comparing the numerical results with the tests, the accuracy of the finite element model and the proposed stress–strain model of CFST column are verified. The relationship between the maximum compression load, and the deformation shape of the CFST column is studied. The maximum difference observed between the experimental and numerical results is not exceed 5%.

5 Conclusions

The following conclusions can be drawn.

Through Python script, the parametric model of a CFST column is established. Through customized parametric simulation modeling, the second development interface can be used to modify the parameters of concrete-filled steel tubular columns. The analysis and experimental results show that the obtained results are in good

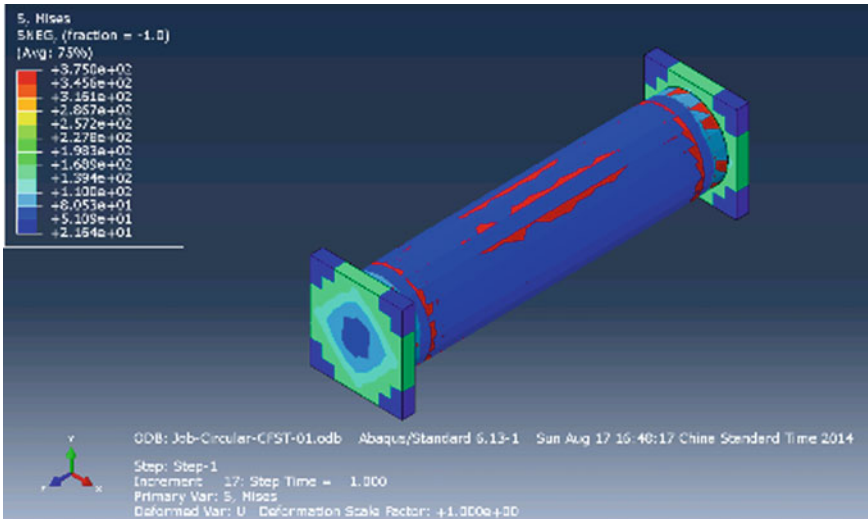


Fig. 7 Results of typical FE model



Fig. 8 The steel pipes after test

agreement with the experimental results, and the prediction accuracy is within an acceptable range.

Acknowledgements The authors gratefully acknowledge support from the Natural Science Foundation of Putian Municipal Fujian Province, China (2019SP002), the Fujian Housing and Construction Department of China (2020-K-19); Guangdong Province characteristic innovation project of universities (2019KTSCX086, 2021KTSCX123); 2021 Guangdong Province Undergraduate College Teaching Quality and Teaching Reform Project Construction Project; Guangdong Provincial Science and Technology Commissioner Project(GDKTP2021004800); The second batch of industry-university cooperative education projects in 2021(202102192010); 2021 Guangdong Province teaching quality and teaching reform project. 2019 Guangdong Province Undergraduate College Teaching Quality and Teaching Reform Project (420A020502). The authors gratefully acknowledge this support.

References

1. Bendsøe MP, Sigmund O (2003) Topology optimization: theory, methods and applications. Springer, Berlin
2. Andreassen E, Clausen A, Schevenels M, Lazarov BS, Sigmund O (2011) Efficient topology optimization in Matlab using 88 lines of code. *Struct Multidisc Optim* 43(1):1–16
3. Challis VJ (2010) A discrete level-set topology optimization code written in Matlab. *Struct Multidisc Optim* 41:453–464
4. Buhl T, Pedersen CBW, Sigmund O (2000) Stiffness design of geometrically nonlinear structures using topology optimization. *Struct Multidisc Optim* 19:93–104
5. Dassault Systems (2014). <<http://www.3ds.com/products-services/simulia/portfolio/abaqus/overview/>>
6. Guilian YI, Yunkang SUI, Jiazheng DU (2011) Application of python-based Abaqus preprocess and postprocess technique in analysis of gearbox vibration and noise reduction. *Front Mech Eng* 6(2):229–234
7. Osher SJ, Sethian JA (1988) Fronts propagating with curvature dependent speed: algorithms based on the Hamilton-Jacobi formulation. *J Comput Phys* 79:12–49
8. Radman A, Huang X, Xie YM (2014) Maximizing stiffness of functionally graded materials with prescribed variation of thermal conductivity. *Comput Mater Sci* 82:457–463
9. Yang z, Chen M, ye M (2021) Study on eccentric compression behavior of ultra-high strength basalt fiber reinforced concrete filled steel tubular columns. *Build Sci* 37(09):144–150
10. Yang z, Shen F, Chen M (2021) Push out test of steel tube ultra-high strength basalt fiber concrete column. *J Jiaying Univ* 39(03):45–49
11. Yang z, Chen M, Zou X (2020) Study on axial compression behavior of ultra-high strength basalt fiber reinforced concrete filled steel tubular columns. *J Jiaying Univ* 38(06):33–37

Open Access This chapter is licensed under the terms of the Creative Commons Attribution 4.0 International License (<http://creativecommons.org/licenses/by/4.0/>), which permits use, sharing, adaptation, distribution and reproduction in any medium or format, as long as you give appropriate credit to the original author(s) and the source, provide a link to the Creative Commons license and indicate if changes were made.

The images or other third party material in this chapter are included in the chapter's Creative Commons license, unless indicated otherwise in a credit line to the material. If material is not included in the chapter's Creative Commons license and your intended use is not permitted by statutory regulation or exceeds the permitted use, you will need to obtain permission directly from the copyright holder.



Establishment of Community Earthquake Vulnerability Assessment System



Xiao Wang, Qi Zhang, Guowei Zhang, Lihui Dong, and Qiuyu Zheng

Abstract Community, as the basic unit of the city, is not only the main body of earthquake response, but also the main body of urban emergency rescue response. The earthquake disaster emergency practices show that the losses of earthquake disaster are greatly affected by emergency preparedness. Therefore, it is urgent to conduct research on earthquake risk assessment and emergency preparedness capacity assessment for communities. HAZUS and Pushover method are used to establish an earthquake vulnerability assessment model based on community buildings. The vulnerability of personnel is calculated according to the probability value, which lays the foundation for emergency assessment. Finally, taking Xinchengzi community as an example, when the earthquake intensity is VII, the following conclusions are drawn: there are expected to be two deaths and seven serious injuries and 2855 displaced people in the community. The assessment system can provide reference for the government to improve the emergency response capacity.

Keywords Community earthquake · HAZUS · Pushover · Emergency preparedness

1 Introduction

At present, China is in a period of high incidence of earthquakes, and a series of social problems and urban development trends caused by earthquakes have also aroused widespread concern from government departments [1–3]. Communities are deductive of cities at a more accurate regional scale and therefore have common characteristics of exposure to different risks. The earthquake will lead to the destruction of community system. And then it can lead to the loss of life and property, the loss of community function, the imbalance of public order and a series of devastating consequences [4]. Experience shows that building collapse caused by earthquakes

X. Wang · Q. Zhang · L. Dong · Q. Zheng
School of Safety Engineering, Shenyang Aerospace University, Shenyang, China

G. Zhang (✉)
Mechanical School, Shenyang Institute of Engineering, Shenyang, China

is the most important factor of causing damage. Therefore, evaluating the building and judging the risk level of the building will directly affect the safety of the life and property of the community residents and the stability and development of the community. Emergency preparedness is the key to earthquake disaster reduction and management. Higher emergency preparedness can effectively reduce losses caused by earthquakes and ensure sustainable urban development [5]. On the contrary, it will enlarge the damage of earthquake and increase the loss of disaster. The emergency preparedness ability before earthquake is the main factor to judge the effectiveness of impending emergency and disaster emergency work. In addition, the earthquake emergency preparedness of a special region is closely related to the local earthquake risk, vulnerability of buildings and population distribution. The higher the level of earthquake emergency preparedness, the lower the loss of life caused by earthquakes. Therefore, scientific analysis of earthquake emergency preparedness and earthquake risk level is of practical significance to improve the efficiency of earthquake emergency work and reduce casualties and property losses.

2 Case Study

Xinchengzi Community is located in the center of Shenbei New District, Shenyang city, Liaoning Province. And it is located in the North China earthquake zone, with nearly 50 faults over 5 km in length and nearly 30 faults over 10 km in length. It is an area with high fracture activity in the approach zone, and there are geological tectonic conditions for the occurrence of magnitude 5–6 destructive earthquakes. The buildings in Xinchengzi community are divided into four categories: multi-storey masonry houses, reinforced concrete houses, single-storey factory buildings and old houses (brick and wood houses and simple houses). Most of the buildings in Xinchengzi community are built before 2010. Most of the buildings are 3–6-storey structures, and most of them are multi-storey masonry buildings. It is assumed that the seismic fortification intensity of Shenyang city is VII, and the basic acceleration value is 0.10 cm/s^2 .

2.1 Seismic Risk Analysis of Xinchengzi Community

Vulnerability analysis curve

The building information in this paper is mainly based on the field research. At the same time, we have referred to “Shenyang New Area Seismic Environment Assessment”, “General Code for Masonry Structure” (GB55007-2021), “Code for Concrete Design” (GB50010-2010(2015 edition)), “Industrial Building reliability Identification Standard” (GB50144-2019), “Wood Structure Engineering Construction Quality Acceptance Code” (GB50206-2012) and other standards. Details as below:

Construction of dormitory building of Xinchengzi 83 Middle School

The dormitory building of Xinchengzi 83 Middle School is a multi-storey (five floors) masonry building. The total height of the building is 16.5 m, and the site category is class I. The walls are MU10 page rock bricks, the first and second floors are M10 cement mortar, and the third and above floors are M7.5 cement mortar. The wall thickness is 240 mm. The ring beam is layered, the cross section is 240 mm * 220 mm, the concrete grade is C25, and the building steel bar is HPB235 [6]. Strip rubble concrete is used. And the concrete is marked with C15, and the deep is 2.5 m.

Construction of Huamei Shopping Mall in Xinchengzi

Xinchengzi Huamei shopping mall is a reinforced concrete frame structure. The mall is a total of four layers, longitudinal depth of 4 m, 3 cross transverse opening, the bottom layer of 3.9 m, the other layer of 3.6 m, site category iii. The concrete strength grade of the frame beam and column is C30, the longitudinal reinforcement is HRB400, the stirrup is HPB235, the cross-section size of the frame beam is 250 mm * 500 mm, and the cross-section size of the frame column is 500 mm * 500 mm [7].

The basic seismic intensity of Xinchengzi subdistrict is VII degree, and the designed basic seismic acceleration value is 0.10 cm/s². The buildings selected in this paper are modeled in 3D (see Fig. 1). The median value and standard deviation of buildings of the same type are found in HAZUS technical manual (see Table 1).

According to the vulnerability curve formula (1):

$$P[d_s | S_d] = \varphi \left[\frac{1}{\beta_{ds}} \right] \ln \left(\frac{S_d}{S_{d,ds}} \right) \tag{1}$$

where d_s denotes degree of damage; S_d (instead of peak ground acceleration S_a) is the peak ground displacement; $S_{d,ds}$ is the median value of peak ground acceleration borne by the disaster bearing body when it reaches the degree of failure d_s ; β_{ds} is the standard deviation of the natural logarithm of S_d ; φ is the standard normal distribution cumulative function.

Table 1 Frailty curve $S_{a,ds}$ and β_{ds}

Type	Destruction degree	Median	Standard deviation
Xinchengzi No.83 middle school dormitory building	Light	0.11	0.64
	Secondary	0.18	0.64
	Serious	0.24	0.64
	Whole	0.53	0.64
Xinchengzi Huamei shopping mall	Light	0.12	0.64
	Secondary	0.18	0.64
	Serious	0.29	0.64
	Whole	0.49	0.64

The vulnerability curves of the three types of buildings are obtained by using Matlab program (See Fig. 1) (Fig. 2).

Determination of capability curve

Using the relevant parameters of the target determined in Sect. 2.1 and the Pushover function of Huzus software, the capability-demand spectrum curve of Xinchengzi community is draw and the performance points are obtained. In the figure, the green curve starting from the origin is the capability curve, and the red curve is the demand spectrum, as shown in Fig. 3. In which the abscissa is S_d and the ordinate is S_a .

Determination of performance points and damage probability

Figure 3 illustrates the XinChengZi 83 dormitory building performance points corresponding to $S_a = 0.359 \text{ cm/s}^2$, $S_d = 0.339 \text{ m}$; the Huamei market performance points corresponding to $S_a = 0.144 \text{ cm/s}^2$, $S_d = 0.137 \text{ m}$. According to the S_a value determined by the above performance points and the vulnerability curve, the

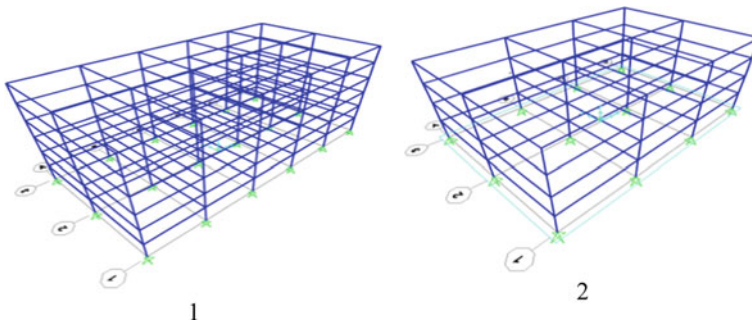


Fig. 1. 3D stereo view of the building. *Note* 1 3D stereo diagram of Xinchengzi 83 dormitory building. 2 Three-dimensional stereo map of Xinchengzi Huamei Shopping Mall

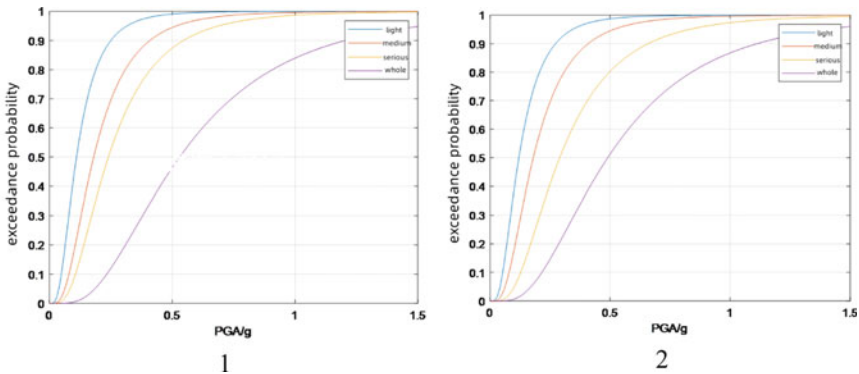
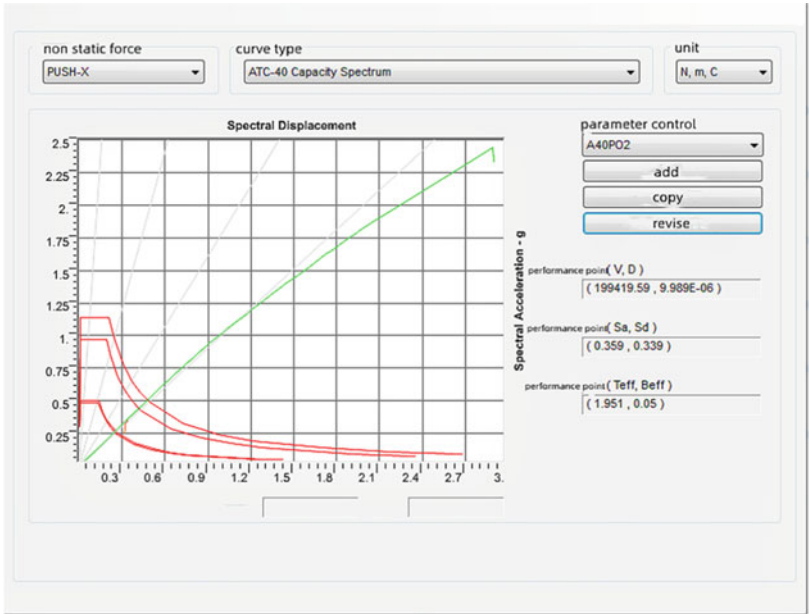
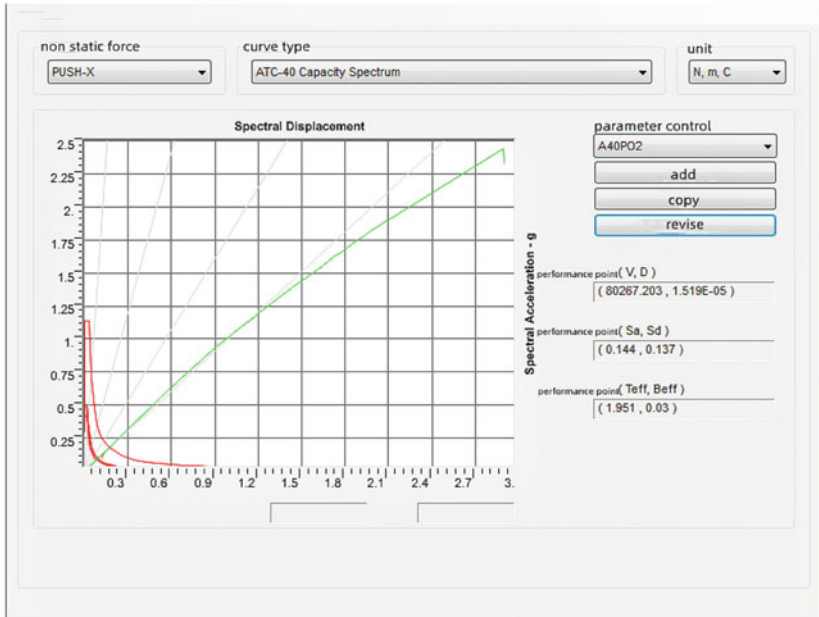


Fig. 2 Building vulnerability curve. *Note* 1 Fulnerability curve of multi-storey masonry houses. 2 Fulnerability curve of multi-storey reinforced concrete houses



1



2

Fig. 3 Building performance point curve. Note (1) Performance point curve of Xinchengzi 83 dormitory building. (2) Performance point curve of Xinchengzi Huamei Shopping Mall

Table 2 Vulnerability matrix of each building

Corpore	Destruction degree	Damage probability (%)
Xinchengzi No.83 middle school dormitory building	No damage	46.14
	Minor damage	53.21
Xinchengzi No.83 middle school dormitory building	Moderate damage	0.65
	Major damage	0
	Complete damage	0
Xinchengzi Huamei shopping mall	No damage	100
	Minor damage	0
	Moderate damage	0
	Major damage	0
	Complete damage	0

Table 3 VII degree seismic vulnerability matrix of four kinds of buildings in Xinchengzi community

Type	Basically intact (%)	Minor damage (%)	Moderate damage (%)	Serious damage (%)	Destroy (%)
Multi-storey masonry houses	59.74	34.08	6.18	0.00	0.00
Multistorey reinforced concrete house	100	0.00	0.00	0.00	0.00
Single floor workshop	56.79	42.04	1.17	0.00	0.00
Old house	0.00	0.00	58.78	41.22	0.00

vulnerability matrix of each building can be calculated according to Eq. (1), as shown in Table 2.

According to this method, the ten buildings in each of the four types of buildings in Xinchengzi community are selected for damage probability calculation. And the average value is taken to determine the earthquake damage matrix of the four types of the buildings, as shown in Table 3.

3 Conclusions

Based on seismic risk analysis, HAZUS and Pushover methods are used to analyze the vulnerability of community buildings and personnel. The results of risk analysis can be used as the basis of disaster prevention and mitigation decision of relevant administrative departments, and the evaluation of emergency preparedness ability

can effectively improve the ability and level of earthquake emergency management. The comprehensive analysis results of the two can help local governments grasp the current situation of emergency preparedness capacity, find the gap between ideal capacity and realistic demand, and provide direction and overall target for government departments to improve countermeasures.

Acknowledgements This work has been supported by Social Science Planning Fund of Liaoning Province (Key Project) under Grant L21ATJ012.

References

1. Hongmei G, Zhen Z, Ying Z, Juncheng K (2021) A method of earthquake disaster risk assessment suitable for mountain areas—takes Baoxing County, Sichuan Province as an example. *Disaster Sci* 36(3):147–152
2. Cheng Q, Xu Z, Gu D et al (2019) Risk assessment of building earthquakes in major cities based on urban seismic elasto-plastic analysis. *J Seismic Eng* 41(2):299–306
3. Jing W (2014) (Master's thesis). Dalian University of Technology, Dalian
4. Shao Y, Xu J (2015) Urban resilience: a conceptual analysis based on an international literature review. *Int Urban Plan* 30(2):48–54
5. Zhao JJ (2009) Research on emergency response mechanism under earthquake disaster (Master's thesis). Southwest Jiaotong University, Chengdu
6. The Ministry of Housing and Urban-Rural Development, PRC (2021) GB 55007-2021 General specification for masonry structure. China Standards Press, Beijing, pp 7–15
7. The Ministry of Housing and Urban-Rural Development, PRC (2010) GB 50010-2010 Code for concrete design. China Standards Press, Beijing, pp 5–13

Open Access This chapter is licensed under the terms of the Creative Commons Attribution 4.0 International License (<http://creativecommons.org/licenses/by/4.0/>), which permits use, sharing, adaptation, distribution and reproduction in any medium or format, as long as you give appropriate credit to the original author(s) and the source, provide a link to the Creative Commons license and indicate if changes were made.

The images or other third party material in this chapter are included in the chapter's Creative Commons license, unless indicated otherwise in a credit line to the material. If material is not included in the chapter's Creative Commons license and your intended use is not permitted by statutory regulation or exceeds the permitted use, you will need to obtain permission directly from the copyright holder.



Research on Deformation Characteristics of SCP Foundation for HKZM Bridge



Bin Li, Jiaying Zhang, Xuelei Zhang, and Zhongke Tian

Abstract To further determine the bearing capacity of sand compaction pile (SCP) composite foundation in the West artificial island of Hong Kong-Zhuhai-Macao (HKZM) Bridge, a large-scale in-situ load test system was designed to study the mechanical and deformation characteristic of SCP foundation. The test adopts the anchor pile method, the results show that the stress sharing ratio of the underwater SCP foundation under the same replacement rate is closely related to the load and time. With the increase of load level, the curve of stress sharing ratio decreases first and then increases. Under the same load level, the ratio decreases gradually with time and finally approaches a certain value. Based on the analysis of site monitoring data, the settlement law of SCP is clear, and the error of the empirical formula is found. The stress reduction ratio and empirical coefficient are proposed to correct the original formula. The research results in this paper can be used to guide the design and construction of SCP foundation of cross-sea project.

Keywords Load test · Bearing capacity · Monitoring data · Settlement · Formula

1 Introduction

SCP has been applied earlier and more widely in treating soft soil foundations along the coast of Japan. Since 1996, China has begun to explore the application technology of SCP in port engineering. The HKZM Bridge adopts the bridge-island-tunnel combination scheme, in which the foundations of the island-tunnel are mostly covered with deep soft clay, and the bearing capacity is very low. SCP foundation

B. Li (✉) · J. Zhang · X. Zhang · Z. Tian
Tianjin Port Engineering Institute Co., Ltd. of CCCC First Harbor Engineering Co., Ltd.,
Tianjin 300222, China
e-mail: lee_binbin@163.com

Key Laboratory of Port Geotechnical Engineering, Ministry of Communications, PRC,
Tianjin 300222, China

Key Laboratory of Tianjin Port Geotechnical Engineering, Tianjin 300222, China

CCCC First Harbor Engineering Company Ltd., Tianjin, China

© Crown 2023

Y. Yang (ed.), *Advances in Frontier Research on Engineering Structures*, Lecture Notes in Civil Engineering 286, https://doi.org/10.1007/978-981-19-8657-4_39

435

is adopted in the island wall and transition section, with relatively high replacement rate. Because there is very little research on the high-replacement rate SCP foundation in China, the in-site load plate test is used to study the deformation and bearing capacity of the high-replacement SCP.

Through field tests, Yea and Kim [1] pointed out that the replacement rate of SCP was the main factor determining the undrained shear strength and consolidation characteristics of Marine sedimentary clay in Busan New port. Zhang and Wang [2] and Wang [3] pointed out that consolidation settlement of SCP with large diameter and high replacement rate mainly occurred in the early loading stage, while the average settlement and residual settlement of SCP were smaller than those areas of low replacement rate. Heo et al. [4] specially studied the combined influence of replacement rate and penetration ratio of SCP on the foundation reinforcement effect through centrifuge test. According to previous studies, most of the researches on SCP mainly focus on the low replacement rate (30–50%), and few researches focus on the bearing capacity of high replacement rate (50–80%).

Most of the existing methods for calculating the bearing capacity of SCP are based on the failure form of single pile swelling, and there is a large error when applied to the high displacement rate. At present, there are few researches on failure mode of high-displacement.

In this paper, the settlement and deformation of high displacement rate SCP are analyzed by in-situ test data and post-construction settlement monitoring data, and the deep-water and in-situ load test methods and modified settlement calculation formula are obtained, which can be used to guide the design and construction of SCP foundation.

2 Project Overview

In the main structure island tunnel project of the HKZM Bridge, SCPs are used as the foundation treatment technology on a large-scale [5, 6], and different compacted sand pile replacement rates are used in different areas. Among them, the SCP is adopted at the rescue wharf side which diameter is 1.6 m, arrangement is square layout, spacing is 1.8 m, and with 62% replacement rate. Based on the previous engineering experience, it is necessary to carry out large-scale underwater load test, to study the consolidation settlement, deformation modulus, stress sharing ratio and soil index change of SCP foundation comprehensively.

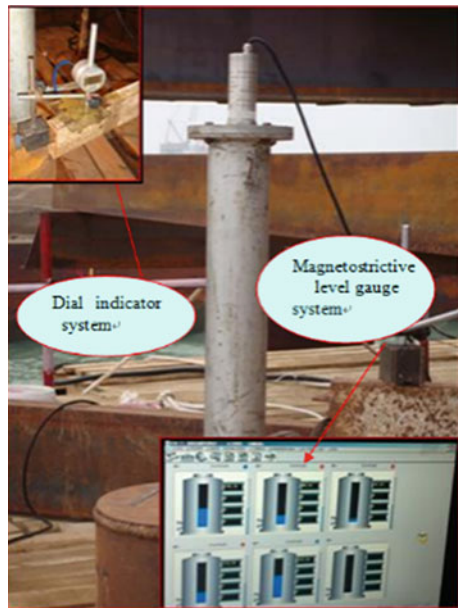
3 Experiment

3.1 Experiment Design

The anchor pile method is used to carry out the load test of the underwater SCP foundation. The bearing plate size is 5.4 m × 5.4 m. Anchor piles are made of steel piles with diameter of 1.2 m, wall thickness of 16 mm; there are four piles in total. The layout is a square with a spacing of 9.4 m. The benchmark piles are also steel piles and the layout is the square with a spacing of 14 m.

The underwater SCP foundation load test platform is mainly composed of a reaction force system, a loading system, a measurement system, and a limit device. The offshore test platform is always in a low-frequency vibration state under the influence of strong wind and ocean currents. Therefore, on the underwater load board set up a set of high-precision static leveling system for settlement observation, as shown in Fig. 1. After improvement, the system has good sealing performance and can be applied to deep underwater measurement [7, 8]. The measurement accuracy of this system is ± 0.4 mm, and the range is 400 mm. The loading mode adopted two-cycle loading. When the settlement increases sharply, or the cumulative settlement is greater than 6% of the width of the load plate; or the settlement is greater than twice the previous level of load, and has not stabilized after 24 h, the test will be terminated.

Fig. 1 Test settlement measurement system



3.2 Analysis of Test Results

The p-s curve of settlement under various loads is shown in Fig. 2. In the first loading cycle of the test, the settlement amount was 53.69 mm, the settlement after unloading was 48.18 mm, and the rebound value was 5.51 mm. In the second cycle, the settlement is 124.29 mm, and the settlement after unloading to 274.35 kPa and maintaining the load for 50 days is 148.51 mm. The settlement after unloading is 136.82 mm, and the rebound value is 11.69 mm. This test did not reach failure, so the ultimate bearing capacity should be greater than 340 kPa.

Pile-soil stress analysis

There is gravel cushion between the bearing plate and the SCP foundation. It is necessary to calculate the stress on the top surface of the sand pile. The stress on the top surface of the sand pile caused by the floating bulk density of the gravel cushion is 11 kPa. The stress diffusion angle of crushed stone is set as 38°. According to the calculation results, the relationship between the calculated average stress and load on the top surface of the SCP is shown in Fig. 3.

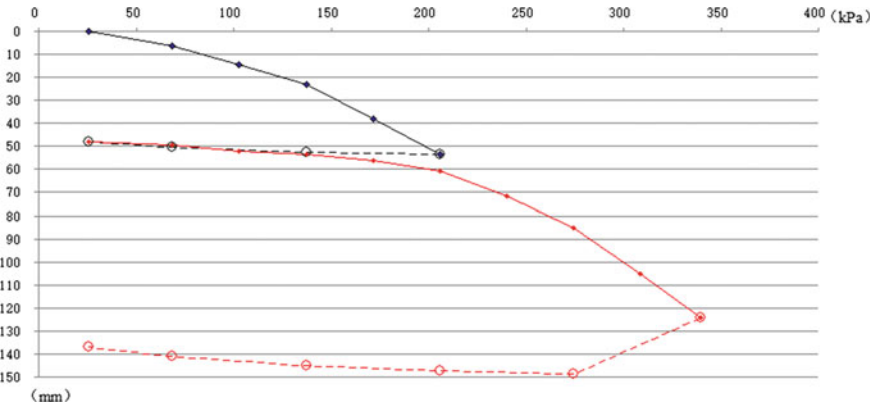


Fig. 2 The curve of load and stress

Fig. 3 The relationship between the calculated average stress and load

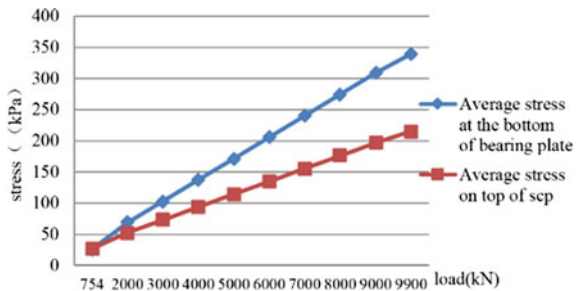
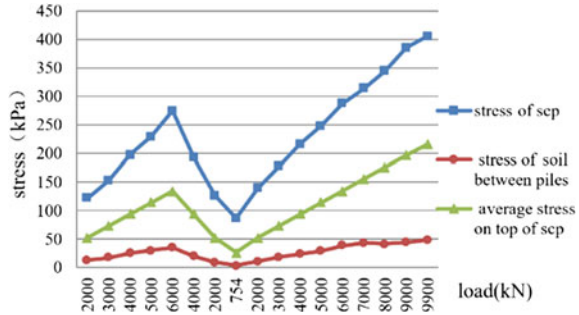


Fig. 4 The relationship between the load and the average stress



During the load maintenance period, the relationship between the load and the average stress on the top surface of the sand pile, the stress of the sand pile and the stress of the soil between the piles is shown in Fig. 4.

Figure 5 is the pile-soil stress ratio which is measured during the maintenance load. The replacement rate of the sand piles in the test area is measured to be 59.14%. It can be inferred that the load borne by the sand piles is 7700.75 kN, It is estimated that the stress on the top surface of sand piles could be 268 kPa, and the stress of soil between the piles could be 42 kPa. Therefore, the revised pile-soil stress ratio should be 6.3 actually.

It can be concluded that as time goes by, the stress of sand piles and the pile-soil stress ratio decrease. When the stress redistribution is basically completed and the stress redistribution phenomenon no longer occurs, the calculated pile-soil stress ratio reflects the real situation.

Deformation modulus

The deformation modulus E_0 of foundation is an important parameter to evaluate the deformation characteristics. This research assumes that the deformation modulus remains unchanged before and after the foundation reinforcement. According to the definition of the deformation modulus [9, 10]:

Fig. 5 Pile-soil stress ratio during maintenance load



Table 1 Deformation modulus values of reinforced composite ground

The stress level (kPa)	p/s	Deformation modulus/MPa
0–102.9	5.310	23.12
102.9–205.8	2.542	11.07
205.8–308.6	2.279	9.92

$$E_{sp} = I_0(1 - \mu^2) \frac{P_{sp}\alpha}{s} \tag{1}$$

where, E_{sp} is the deformation modulus of composite foundation respectively (MPa); P_s, P_{sp} is the load borne by the soil between the piles and the foundation (kPa); I_0 is the shape coefficient of pressure bearing plate, and the square plate is taken as 0.886; μ is the Poisson’s ratio of soil, 0.30 for sand; s is the settlement corresponding to p (mm).

According to Eq. 1, the deformation modulus of compacted sand piles composite foundation in each stage is calculated as shown in Table 1 [11]. Therefore, the deformation modulus of the composite foundation under the load of 100–200 kPa is 11.07 MPa, and that of the natural foundation before reinforcement is 1.03 Mpa. The effect of foundation reinforcement is obvious.

Bearing capacity of SCP

At present, the calculation of composite foundation bearing capacity is usually obtained by combining the bearing capacity of the pile body and the soil between the piles according to a certain principle, and the calculation formula is:

$$f_{spk} = mf_{pk} + (1 - m)f_{sk} \tag{2}$$

where f_{pk} and f_{sk} are the ultimate bearing capacity of the pile and the soil between the piles, respectively.

The ultimate bearing capacity of discrete material piles mainly depends on the maximum confining force σ_{ru} that the soil at the side of the pile can provide. The ultimate bearing capacity of discrete material pile can be calculated according to the passive earth pressure method [12]:

$$f_{pk} = \sigma_{ru}K_p \tag{3}$$

where, σ_{ru} is the lateral ultimate stress; K_p is the passive earth pressure coefficient of the pile material.

There are many methods to calculate the maximum lateral limit stress, such as BRauns formula, Wong formula, Hughes & withers formula, and passive soil pressure method [8, 11–15]. In this paper, the ultimate bearing capacity of the discrete material pile is calculated according to above-mentioned theories. The calculation results are compared with the standard penetration test results and load test results in Table 2.

Table 2 Calculated and measured ultimate bearing capacity of composite ground

Parameter	Ultimate bearing capacity of single pile f_{pk}/kPa	Ultimate bearing capacity of soil between piles f_{sk}/kPa	Ultimate bearing capacity of composite foundation f_{spk}/kPa
Brauns formula	278.4	96.6	209.3
Wong H.Y formula	148.6	96.6	128.8
Hughes and Withers formula	329.9	96.6	241.2
Passive earth pressure method	323.3	96.6	237.2
Standard penetration test estimate	372	96.6	267.3
Load test			> 340

The ultimate bearing capacity of the foundation is greater than 340 kPa. The foundation bearing capacity obtained by the passive earth pressure method and the Hughes and Withers calculation formula is close to the test results.

4 Monitoring Data Analysis

With various replacement rates, the settlement of the relevant area of West island transition section is reduced from 314–401 mm to about 28–50 mm, and the settlement is reduced to about 8.9–23.2% than the original foundation.

In West island, three types of replacement rate of SCP are adopted. As shown in Table 4, it can be found that with the increase of replacement rate from 42 to 55%, the settlement of foundation decreases significantly. However, when the replacement rate increases from 55 to 70%, the average settlement of foundation does not decrease significantly.

In East island, the upper part and the lower part of SCP have different replacement rates. The settlement is reduced from 108.4–926.7 mm to 42.6–214.3 mm and it is reduced to 11.2–50.7%.

In fact, the settlement of SCP foundation consists of settlement of reinforcement zone and settlement of underlying layer. A site in Hong Kong, Zhuhai-Macao is selected for specific analysis, whose upper part is clay layer and the lower part is the medium sand layer, this is a typical double-sided drainage foundation. The consolidation characteristics of this layer of soil should be considered when the total settlement of clay layer under preloading is calculated. According to the geological survey report, clay layer is over consolidated soil and the over consolidation ratio average is 1.49. Therefore, the influence of soil stress history should be fully considered when calculating the total settlement. According to the calculation, the stratum

stress at the top of the underlying is 226.2 kPa, which is greater than the consolidation pressure in the earlier stage.

Thus, the final settlement of the underlying layer at this point under preloading is 43.9 mm, and the consolidation degree within 4 months of full load during preloading is 47%. The settlement of the underlying layer at this point during preloading is 20.7 mm. As the measured settlement of this point during preloading period is 64.1 mm, so the settlement of the underlying layer accounts for about 32% of the overall settlement.

5 Conclusion

As it is difficult to accurately evaluate the bearing characteristic of underwater SCP foundation, large-scale in-situ load tests and deformation characteristic tests were carried out based on the Hong Kong-Zhuhai-Macao Bridge project. The stress sharing ratio of underwater SCP composite foundation with the same replacement rate is closely related to the load level and time, and the stress sharing ratio decreases with the increase of the load level. The bearing capacity of single pile of SCP is calculated according to the passive earth pressure method, which is close to the load test results. The calculation needs to consider the influence of the underlying clay layer on the overall settlement.

- (1) The underwater static leveling measurement system proposed in this test project can obtain more realistic and stable settlement data.
- (2) The pile-soil stress ratio is 6.3, the deformation modulus is about 8 kPa, and the rebound and compression modulus is 32.65 kPa.
- (3) The ultimate bearing capacity of SCP composite foundation is greater than 340 kPa.
- (4) The settlement of West island transition section relevant area is reduced from 314–401 mm to about 28–50 mm, and the settlement is reduced to about 8.9–23.2% than the original foundation. The settlement of East island was reduced from 108.4–926.7 mm to 42.6–214.3 mm, and it is reduced to 11.2–50.7%.

Acknowledgements The writers wish to acknowledge the support of Shenzhen Science and Technology Planning Project No.JCYJ20210324121402008 on “Study on stability of large diameter steel cylinder foundation in composite seabed foundation.”

References

1. Yea GG, Kim TH (2010) Evaluation of undrained shear strength and consolidation characteristics of disturbed marine sedimentary clay due to SCP installation. *Mar Georesour Geotechnol* 28(1):76–90
2. Zhang YG, Wang J (2015) Monitoring and analysis of underwater preloading reinforcement effect of offshore compacted sand pile composite foundation. *China Harbour Constr* 35(11):20–24
3. Wang YN (2018) Design and test verification of foundation treatment for the transition section between submerged tunnel and island. *J Rock Mech Eng* 37(S2):4297–4307
4. Heo Y, Jeong GC, Bae WS (2015) Evaluation of the effect of penetration ratios on composite grounds improved with sand compaction piles. *Mar Georesour Geotechnol* 33(3):253–263
5. Lin M, Liang H (2012) Method for construction of offshore SCPs and its application for island and tunnel project for HKZM Bridge. *China Harbour Eng* 21(4):72–77
6. Mo JY, Huang JS (2007) Application of sand compacted pile for ground treatment of oceanic shore protection engineering works. *Port Waterw Eng* 31(11):123–128
7. Gong XN (2007) Composite foundation theory and engineering application, 2nd edn. China Architecture & Building Press, Beijing
8. China Construction Research Institute (2009) Code for investigation of geotechnical engineering, GB50021–2001
9. Gao DZ (1998) Soil mechanics and basic engineering, 1st edn. China Architecture & Building Press, Beijing
10. Qian JH, Yin ZZ (1995) Geotechnical principles and calculations, 2nd edn. China Water & Power Press, Beijing
11. Jiang MJ, Shen ZJ (1997) On expansion of cylindrical cavity with linear softening and shear dilatation behavior. *Chin J Rock Mech Eng* 16(6):550–557
12. Zhao MH, Zhang L (2007) Bearing capacity calculating method of discrete material pile composite foundation. *J Cent S Univ (Sci Technol)* 6:555–560
13. Chen CF, Xiao SJ (2007) Bearing capacity of aggregate pile with different ratio of tension modulus to compression modulus based on unified strength theory. *Eng Mech* 10:105–111
14. Zhao MH, Yang MH (2006) The calculation of bearing capacity of composite foundation on discrete material pile. *J Huazhong Univ Sci Technol (Nat Sci Ed)* 34(3):91–93
15. Yu MH, He LN (1991) A new model and theory on yield and failure of materials under complex stress state, 6th edn. Pergamon Press, Oxford, Oxford

Open Access This chapter is licensed under the terms of the Creative Commons Attribution 4.0 International License (<http://creativecommons.org/licenses/by/4.0/>), which permits use, sharing, adaptation, distribution and reproduction in any medium or format, as long as you give appropriate credit to the original author(s) and the source, provide a link to the Creative Commons license and indicate if changes were made.

The images or other third party material in this chapter are included in the chapter's Creative Commons license, unless indicated otherwise in a credit line to the material. If material is not included in the chapter's Creative Commons license and your intended use is not permitted by statutory regulation or exceeds the permitted use, you will need to obtain permission directly from the copyright holder.



Research on Vibration Design of Large Compressor Foundation



Xiaoshuai Qiao, Chao Sun, Yanzheng Hu, and Congbin Jiang

Abstract The safe operation of a compressor machine heavily relies on the proper design of its foundation. The frame-type supporting foundation is usually adopted in engineering. This paper studies the vibration design of the compressor's foundation. Two types of finite element model for the foundation are considered, which are beam-slab element model and solid element model. By the comparative analysis of vibration mode shape and time-history dynamic calculation, it is concluded that the commonly used beam-slab element model could be unsafe for a design purpose. In contrast, the solid element model is more reliable. Then, the solid element model was used to study the influence of structural arrangement parameters on vibration response, including roof thickness, column's section size, eccentric unit arrangement and plate cantilever length. It is concluded that the thickness of the top plate has the most significant influence on the vibration response compared to other factors.

Keywords Compressor foundation · Beam-slab element · Solid finite element · Dynamic analysis

1 Introduction

The column-plate foundation is usually used as the supporting structure of the compressor machine unit. Its dynamic characteristics have an important impact on the vibration of the entire unit, which is directly related to the safe operation of the air separation plant. With the continuous expansion of the production scale of air separation, the foundation scale of compressors has become larger, and the types of foundation have become more complex. However, the content of the simplified model of dynamic calculation and construction requirements in the current relevant standards [1, 2] are based on the previous engineering examples or experience with small-scale and simple foundation form. In this paper, more advanced finite element software is used to calculate and analyze the compressor foundation vibration to

X. Qiao (✉) · C. Sun · Y. Hu · C. Jiang
Changzheng Engineering Co., Ltd., Beijing 101111, China
e-mail: qiaoxiaoshuai@china-ceco.com

verify the applicability of the existing standard to the large and complex compressor foundation design. And the factors that affect the vibration are summarised through analysis, which can provide a reference for future design. Therefore, firstly, dynamic calculation and comparative analysis are carried out through two models of different finite element unit types to verify the applicability of the model. Then the solid element model is used to study the influence of structural arrangement parameters on vibration, including roof thickness, column's section size, eccentric unit arrangement and plate cantilever length.

2 Engineering Overview

Taking an engineering project of a turbo compressor foundation as an example, the plane size of the foundation's roof is 32 m by 19 m, its thickness is 2000 mm, the lateral clear span is 9.2 m, the longitudinal maximum clear span is 7.95 m, and the maximum cantilever is 4 m. The column's section is 1800 by 1800 mm, and the net height of the column is 10.3 m. The plane size of the bottom plate is 34.7 m by 21 m and its thickness is 3000 mm. See Fig. 1. Table 1 show the parameters of the main components of the unit, which are provided by the manufacturer.

3 Comparison of Computational Models of Two Different Finite Element Types

3.1 Build the Model

The dynamic calculation method of the current standard [1, 2] recommends to use a frame calculation model, and the mass points in the model are arranged according to the distribution of disturbance force and the span and stiffness of longitudinal and transverse beams. For large compressor foundations, due to the huge scale of the roof structure (the thickness of the plate is up to 2 m) and the long overhangs around it (up to 4 m), it remains to be verified whether the accuracy of the simplified calculation model in the specification meets the requirements. Therefore, two models are first established [3–5]: Model 1 (M1)—beam-slab element model, this model uses conventional beam-slab finite elements for modelling. It is noted that conventional design software usually does not consider the deduction of the mass of the overlapping part of the beam and the floor, which will increase the mass of the roof by 40%. So this model adopts the method of setting the material bulk density of the beam element to 0 to eliminate this effect. Model 2 (M2)—three-dimensional solid finite element model, all components of this model use three-dimensional solid elements, and through fine mesh division, it can better reflect the overall stiffness of the foundation structure, to be closer to the real situation of the foundation. In both models, in order to more

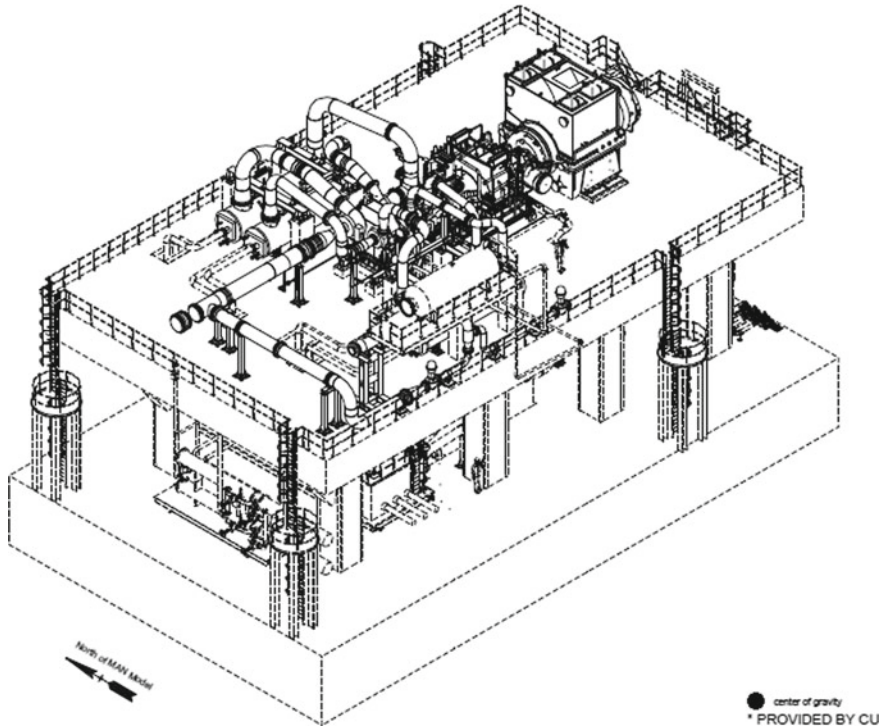


Fig. 1 Compressor foundation layout

Table 1 Parameters of the main components of the unit

Component name	Steam turbine (ST)	Multistage air compressor (MAC)	Booster air compressor (BAC)
Total weight of the unit (t)	115	195	43
Rotor weight (t)	10.6	11.74	1.47
Maximum speed (1/min)	4421	4421	4421
Minimum speed (1/min)	4126	4126	4126
Running speed (1/min)	4210	4210	4210
Dynamic load (KN)	29.2	32.3	4

accurately simulate the influence of the rotor centroid position on the vibration of the foundation, a node is established at the centroid position of the rotor of each equipment, The node and the foundation are formed as a rigid body, and the dynamic load is applied to this node [6, 7]. The base plate of the foundation has sufficient rigidity to meet the condition of the column bottom embedded, so the rigid connection boundary condition is adopted for the column foot in the model.

When modeling, the large-scale finite element software Midas-GEN and the commonly used design software PKPM are used to establish finite element models respectively. After the static calculation of both softwares is checked and correct, the Midas-GEN software is used for the dynamic calculation. The calculation model is shown in Figs. 2 and 3.

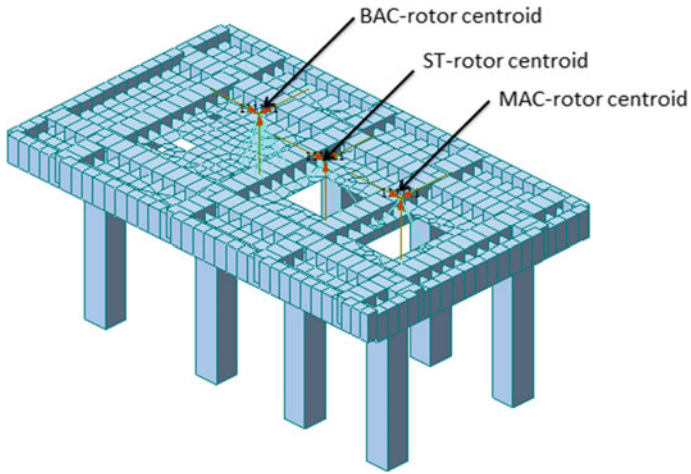


Fig. 2 M1—beam-slab element

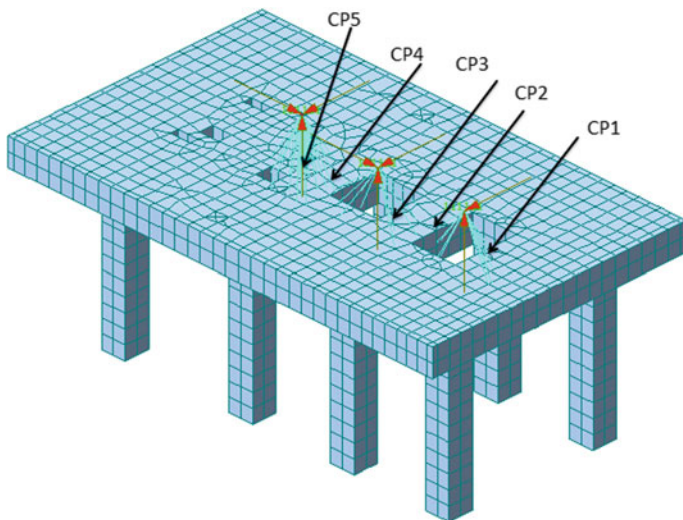


Fig. 3 M2—solid element

3.2 Mode Shape Comparative Analysis

The mode shape can reflect the vibration characteristics of the structure. Figure 4 lists the first 6-order mode shapes and their periods of the two models (M1—beam-slab element, M2—solid element). It can be seen from the mode shape diagram that the mode shapes of the two models have obvious similarities, and there are differences too. The similarities are: the first four modes have the same shape, and the first three modes of the two models are the overall translational vibration of the structure, with a period ranging from 0.27 to 0.37 s. The modes after the third order are all roof bending vibrations, and the mode period is less than 0.061 s, which is significantly smaller than the first three modes. The differences are: after the fourth order, the mode shapes of the two models are no longer the same. It can be seen from the resonance principle that a lower load frequency is required to excite the horizontal vibration of the roof, while load of higher frequency is required to excite the vertical vibration of the roof. According to the equipment manufacturer's information, the equipment's rotating speed during normal operation is 4210 rounds per minute, the rotation period is 0.0143 s, and the frequency is about 70.333 Hz, which is equivalent to the 40th order mode period of the structure. The high-frequency mode shape after that is a key factor affecting the vertical vibration of the structural roof, so it can be inferred that there may be significant differences in the vertical vibration of the two models.

Figure 5 shows the first 50 orders of vibration periods and frequencies of the two models. It can be seen from the figure that the period of the first 5 modes of M1 is higher than that of M2; the period of the two models of the 5th to 13th modes is relatively close; while the period of the higher mode of M2 (after the 13th) is significantly higher than that of M1, and the higher-order mode shape period is denser. This shows that by using solid elements, the translational stiffness of the top plate is improved, while the vertical stiffness of the top plate is decreased.

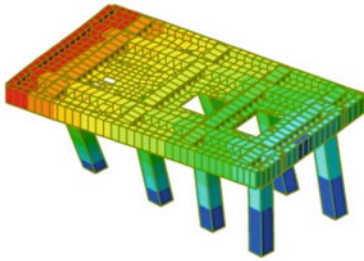
3.3 Comparative Analysis of Vibration Velocity Response

In order to verify the findings in the previous section, five control points (CP1–CP5) were selected on the top plate (see Fig. 3), and the vibration velocity responses of the two models at these control points were compared and analyzed.

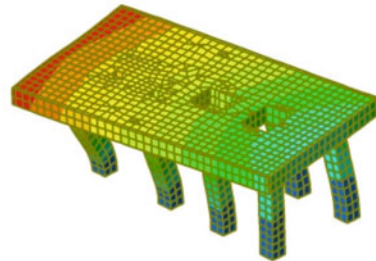
In addition, according to the standard [1, 2], the frequency sweep calculation should be performed within the range of $\pm 20\%$ of the machine speed. Therefore, the frequency sweep calculation in the range of 0–90 Hz is carried out for the two models respectively. That is, taking each mode frequency below 90 Hz as a working condition, the corresponding disturbance force [8, 9] is calculated according to formula 1, and the maximum vibration velocity under all working conditions is taken for comparative analysis.

$$F = 0.2 \text{ mg} \frac{n}{3000} \tag{1}$$

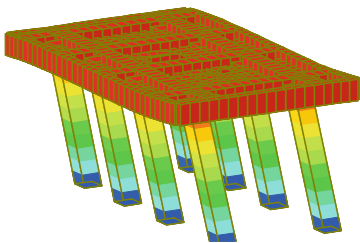
Figure 6 shows the maximum vibration velocity at the control point of the two models under normal operating conditions. All results meet the requirement [10]. It can be seen from the figure that, except for individual vibration speeds (Y direction



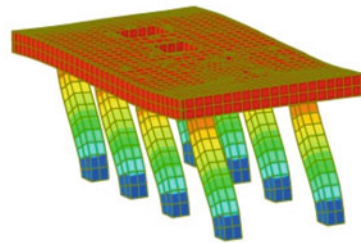
Mode 1 $T=0.374\text{s}$
X-direction translation



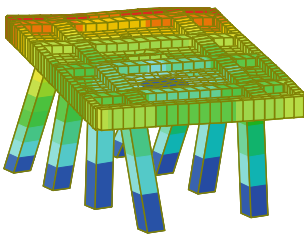
Mode 1 $T=0.328\text{s}$
X-direction translation



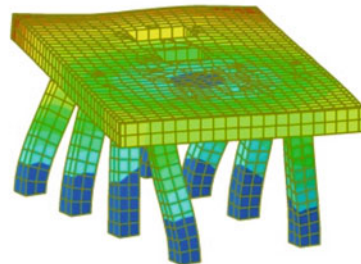
Mode 2 $T=0.352\text{s}$
Y-direction translation



Mode 2 $T=0.306\text{s}$
Y-direction translation

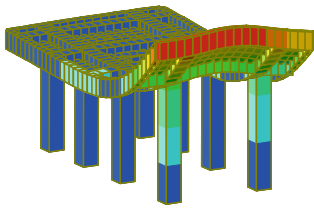


Mode 3 $T=0.318\text{s}$
Overall twist



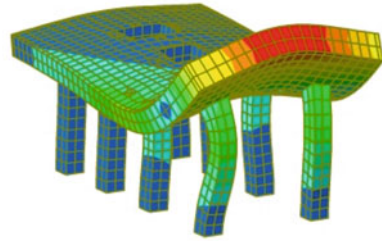
Mode 3 $T=0.276\text{s}$
Overall twist

Fig. 4 The mode shapes



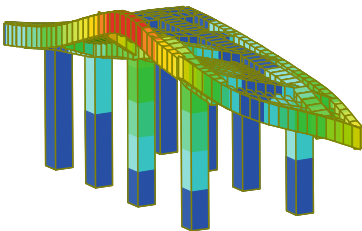
Mode 4 $T=0.061s$

Warping of the end cantilever plate



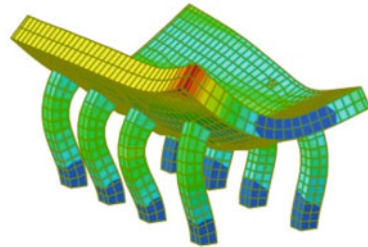
Mode 4 $T=0.059s$

Warping of the end cantilever plate



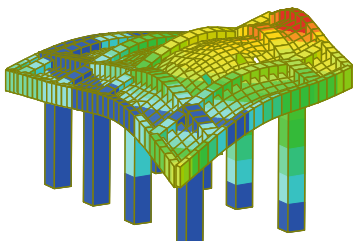
Mode 5 $T=0.059s$

Bending of the roof



Mode 5 $T=0.057s$

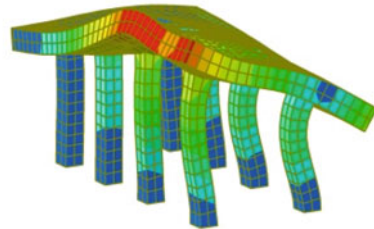
Bending of the roof



Mode 6 $T=0.057s$

Bending of the roof

$M1$ —beam-slab element



Mode 6 $T=0.056s$

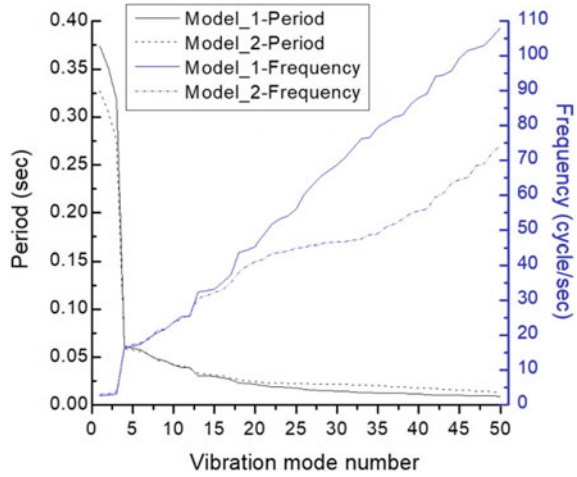
Bending of the roof

$M2$ —solid element

Fig. 4 (continued)

of CP2 and X direction of CP3), the values of other speed M2 are larger than those of M1, and most of them are about two times. This shows that the calculated value of the model using the beam-slab element is too small and unsafe. This also verifies the findings in the mode shape analysis in the previous section. In the high-order mode

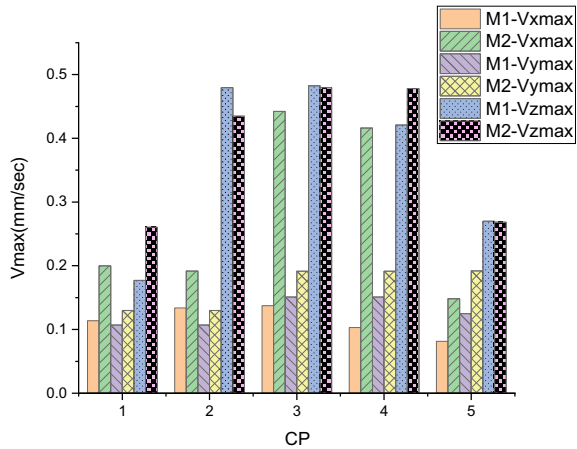
Fig. 5 Natural vibration periods and frequencies



stage, the M2 of solid element model has a lower frequency than the M1 of beam-plate element, and the dynamic load of the equipment that excites the foundation vibration belongs to the high-frequency range, thus resulted in the M2 has a larger speed response than M1.

Figure 7 shows the time-history curve of the vibration velocity of M2 at CP3, and other control points are the same as this rule. It can be seen from the curve that the vibration velocity response becomes a simple harmonic periodic vibration characteristic after the vibration velocity response is stable. At the same time, it also shows that the high-order mode shape is the main factor causing the structural vibration, which cannot be ignored in the design.

Fig. 6 Maximum vibration velocity



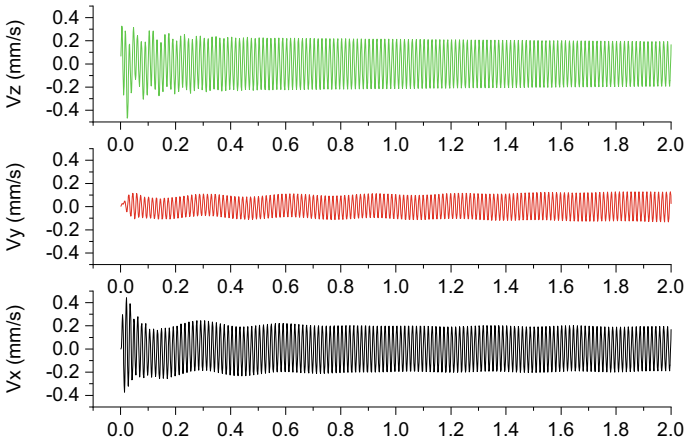


Fig. 7 The time-history curve of vibration velocity

4 Influence of Structural Arrangement on Vibration

In this section, the solid finite element model will be used to study the influence of structural arrangement parameters on vibration, including roof thickness, column’s section size, eccentric arrangement of units and plate overhang length.

4.1 Influence of Roof Thickness on Vibration

According to the requirements of the codes the ratio between the clear span of the roof and its thickness should not be greater than 4 in the transverse direction, and 4–5 in the longitudinal direction. In order to study the influence of different roof plate thicknesses on vibration, five models with plate thickness h of 1600, 1800, 2000 mm (used in actual engineering), 2200 and 2400 mm were set up for calculation and analysis. The vibration velocities of the five control points in three directions are shown in Fig. 8. It can be seen from the figure that the Y direction is parallel to the axis, and the vibration velocity is the smallest, so it is no longer analyzed. An obvious trend can be seen in the X and Z directions, that is, with the increase of the plate thickness, the vibration speed decreases, especially in the Z axis direction, and the vibration speed difference is up to 7 times. This shows that the thickness of the top plate is the main factor affecting the vibration.

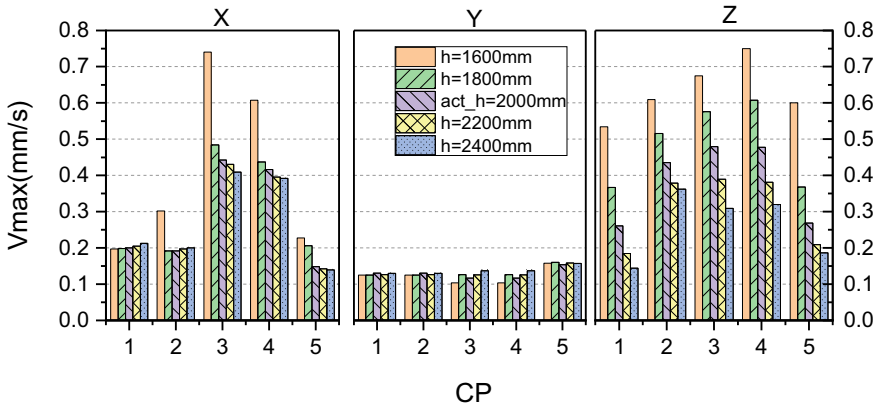


Fig. 8 Influence of roof thickness on vibration

4.2 Influence of Column’s Section on Vibration

According to the requirements of the specification, the minimum width of the column’s section should be 1/10–1/12 of its net height. The net height of the column in this project is 10.3 m, and the column width should be 858–1030 mm according to this calculation. In order to study the influence of different column’s sections on vibration, five models with column’s sections of 1200, 1500, 1800 mm (used in actual engineering), 2100, and 2400 mm were set up for calculation and analysis. The vibration velocity of each control point in three directions is shown in Fig. 9. It can be seen from the figure that the overall impact of the column’s section size on the vibration is not obvious, but there is one thing that needs special attention: with the increase of the column’s section, the vibration speed not only does not weaken, but has a tendency to increase as a whole. Therefore, the designer should pay special attention to this law, and cannot blindly increase the size of the column’s section in the design.

4.3 Influence of Equipment Axis and Foundation Eccentricity on Vibration

According to the requirements of the specification, the arrangement of foundation beams and columns should be symmetrical to the main axis (longitudinal axis) of the machine, and the load should be arranged on the centerline of the member. In fact, due to the layout requirements of the process piping, the main axis of the machine and the central axis of the foundation are not on the same line in many cases, so five models with eccentricity e of 0, 200, 400, 600, and 800 mm are set for calculation and analysis. The vibration velocities in three directions are shown in Fig. 10. As

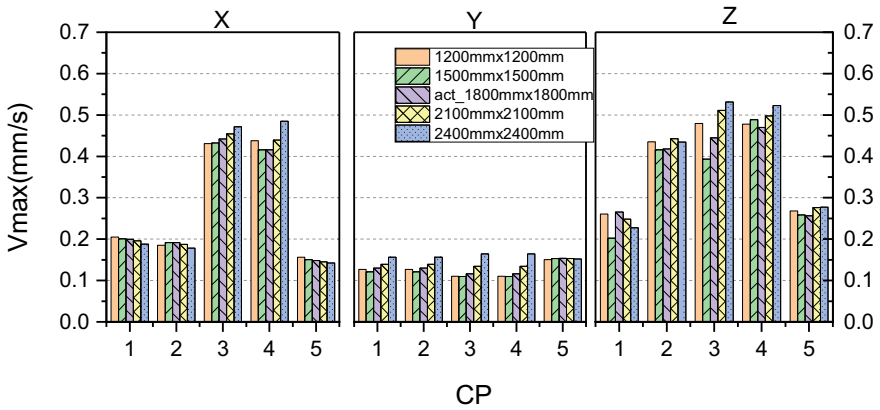


Fig. 9 Influence of column's section on vibration

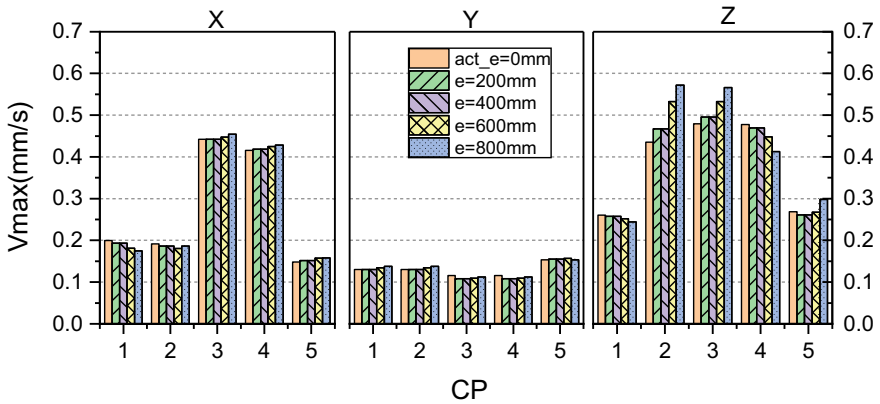


Fig. 10 Influence of equipment axis and foundation eccentricity on vibration

can be seen from the figure, the overall effect of the eccentricity e on the vibration is not very obvious. In the design, the eccentric distance should be minimized, but there is no need to strictly require the coincidence of the two axes.

4.4 Influence of Roof Overhang Length on Vibration

Figures 11 and 12 show the vibration velocity response of each control point under different cantilever lengths L in the Y and X directions, respectively. It can be seen from the figure that the influence of the overhang length of the top plate in the Y direction on the vibration velocity of each control point is not obvious. However, the

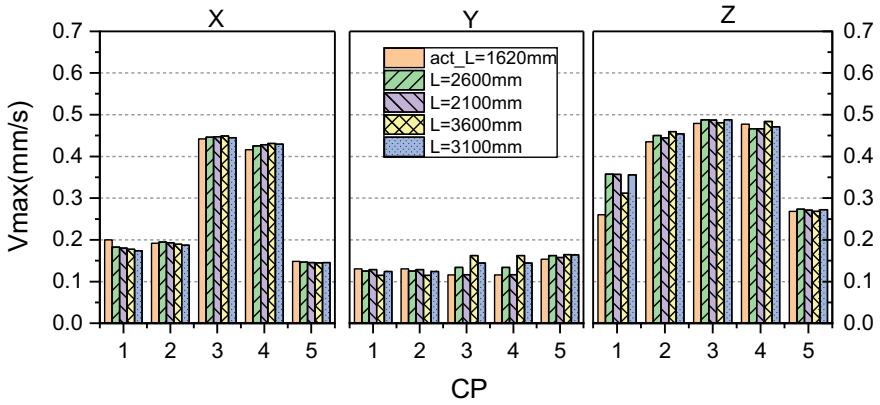


Fig. 11 Influence of roof y-direction overhang length on vibratio

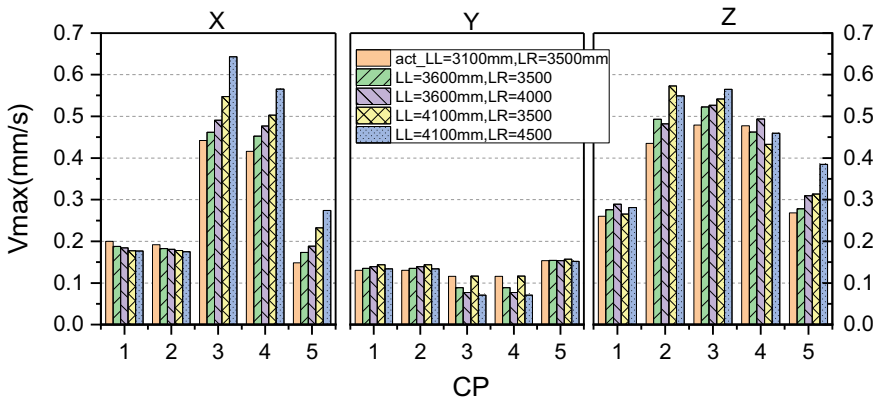


Fig. 12 Influence of roof x-direction overhang length on vibration

effect of the X direction still requires attention. With the increase of the cantilever length, the vibration speed of the Z-direction also increases.

5 Conclusion

The following points are highlighted in this paper:

1. Through the dynamic calculation and analysis of two models with different finite element types, namely M1 of beam-slab element model and M2 of solid element model, it is concluded that by using solid elements, the translational stiffness of

the top plate is improved, while its vertical stiffness is decreased. The velocity responses of both models are quite different, and the beam-slab model is unsafe.

2. The solid element model is used to study the influence of structural arrangement parameters on vibration, including roof thickness, column's section size, eccentric unit arrangement and plate cantilever length. It is concluded that the thickness of the top plate has the most obvious influence on the vibration, and the vibration decreases with the increase of the plate thickness. The influence of other factors on the vibration is not very obvious. It should be noted that with the increase of the column's section, the vibration is possibly not weakened, but has a tendency to increase as a whole. Special attention should be paid to this point that the size of the column's section cannot be overlarged in the design.

References

1. GB 50040-2020, Standard for design of dynamic machine foundation
2. SH/T 3091-2012, Design specification for compressor foundation in petrochemical industry
3. Wang Z (2005) Modal analysis for a 1:10 model of turbine-dynamotor frame foundation. *Earthq Eng Vib* 25(1)
4. Kang l (2008) Experimental research and analysis on dynamic characters of turbine-generator unit frame foundation. *J Build Struct* (S1):20–26
5. De-qing MEI (2001) Research on dynamic behavior of frame foundation for large-scale steam turbine-generator set. *Power Eng* 21(1):1014–1018
6. Guoliang H (2011) Dynamic analysis of frame foundation for compressor based on finite element method. *Chin J Turbomach* 03:15–19
7. Wen H (2016) Dynamic characteristics analysis of turbine compressor foundation based on ANSYS. *Build Struct* 46(S1)
8. Wang D, Zhou Y (2022) Comparative analysis of dynamic response of large steam turbine elastic foundation based on Chinese, American and Germany standards. *Build Struct* 52(5):93–98,62
9. Li X, Zhou D (2006) Comparison between DIN standards and GB standards for steam turbine-generator foundations. *Eng J Wuhan Univ* 39(S):142–145
10. GB 50868-2013, Standard for allowable vibration of building engineering

Open Access This chapter is licensed under the terms of the Creative Commons Attribution 4.0 International License (<http://creativecommons.org/licenses/by/4.0/>), which permits use, sharing, adaptation, distribution and reproduction in any medium or format, as long as you give appropriate credit to the original author(s) and the source, provide a link to the Creative Commons license and indicate if changes were made.

The images or other third party material in this chapter are included in the chapter's Creative Commons license, unless indicated otherwise in a credit line to the material. If material is not included in the chapter's Creative Commons license and your intended use is not permitted by statutory regulation or exceeds the permitted use, you will need to obtain permission directly from the copyright holder.



Analysis of the Impact of Earthquakes on the Stability of Overlying Fill Slopes



Bin li and Wensheng Hou

Abstract Earthquakes are one of the main factors causing landslides. In this paper, the author conducted a numerical simulation of an overlying fill slope in Guangxi, the subject, with Midas GTS under the vibration conditions of magnitude 6, 6.5, 7, 7.5, and 8 earthquakes and obtained the total, horizontal and vertical displacement of the slope and its stability coefficient. The results showed that the displacement of the slope increased with the increase of the seismic acceleration; its maximum displacement occurred in the middle of the slope (fill); the difference of the maximum horizontal displacement from the total displacement and vertical displacement was that as the seismic acceleration increased, the maximum horizontal displacement occurred not only in the middle of the slope (fill), but also at the top and on the middle and upper surfaces; the vertical displacement was most susceptible, while the horizontal displacement was least susceptible; as the magnitude increased, the stability coefficient of the slope also decreased significantly; and, vegetation planting on the slope and the setup of a retaining wall at the foot could improve its stability coefficient effectively. Therefore, it was necessary to plant vegetation on a slope and set up a retaining wall at the foot.

Keywords Earthquakes · Stability analysis · Slope · Midas GTS · Numerical simulation

B. li (✉)

Tianjin Port Engineering Institute Co., Ltd. of CCCC First Harbor Engineering Co., Ltd.,
Tianjin 300222, China
e-mail: lee_binbin@163.com

Key Laboratory of Port Geotechnical Engineering, Ministry of Communications, PRC,
Tianjin 300222, China

Key Laboratory of Tianjin Port Geotechnical Engineering, Tianjin 300222, China

CCCC First Harbor Engineering Company Ltd., Tianjin, China

W. Hou

Jiangsu Weihua Ocean Heavy Industry Co., Ltd., Changyuan County, China

© Crown 2023

Y. Yang (ed.), *Advances in Frontier Research on Engineering Structures*, Lecture Notes in Civil Engineering 286, https://doi.org/10.1007/978-981-19-8657-4_41

1 Introduction

China has a vast territory, a large proportion of which is taken up by mountainous areas. Natural slopes are widely distributed throughout the country. Many artificial slopes have been built to ensure the safety of railways and highways during their construction and use. China located in an earthquake-prone area is characterized by frequent earthquakes, high magnitude, and wide distribution [1]. Almost all magnitude 8 earthquakes and 80–90% of strong earthquakes of magnitude 7 and above in mainland China occurred in the boundary zone of active tectonic blocks, indicating that China is a country with frequent earthquakes [2]. Slope instability (collapses and landslides, etc.) induced by earthquakes is often the main factor causing casualties and property losses in earthquakes [3]. The total number of landslides collapses and debris flows triggered by the 2008 Wenchuan earthquake was up to 30,000–50,000, including more than 12,600 sites with hidden hazards that directly threatened the safety and temporary resettlement of people after the earthquake (according to the statistics of 39 worst hit counties in Sichuan Province), of which there were dozens of giant landslides with a scale over $1000 \times 104 \text{ m}^3$ [4]. The 2010 earthquake in Port-au-Prince, Haiti triggered about 30,000 landslides [5]. The disasters caused by slope instability are shocking. The analysis of the seismic stability of slopes has become one of the important topics in geotechnical engineering and seismic engineering fields [6]. In China, studies on the dynamic stability of slopes were mostly conducted based on the dynamic stability coefficient. The research methods can be roughly divided into the quasi-static method [7], dynamic time-history method [8] and dynamic strength reduction method [9]. In this paper, the slope was simulated with the finite element method through modeling with Midas-GTS to study the law and characteristics of the stability of the overlying fill slope under seismic conditions.

2 Determination of Model Dimensions and Parameters

2.1 Slope Dimensions

The subject, an overlying fill slope in Guangxi, was covered with vegetation on the surface and provided with a retaining wall at the foot. Figure 1 shows the geometric dimensions of the slope. Mechanical parameters of slope rocks and soil masses.

Mechanical parameters of slope rocks and soil masses are shown in Table 1. The slope surface was covered with vegetation and the plant roots could greatly improve the shear strength of soils [10]. With the increase of the root length density and surface area density, the internal friction angle (φ) of soil increased logarithmically and its cohesion (c) increased linearly and significantly [11]. Therefore, the internal friction angle and cohesion of soil on the slope surface were increased appropriately in this paper.

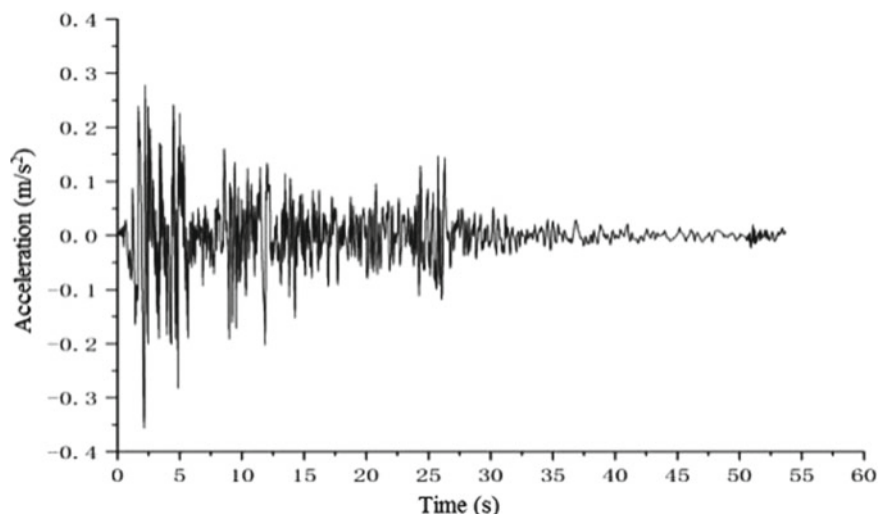


Fig. 1 Seismic acceleration time history

Table 1 Basic parameters of slope rocks and soil masses

Soil layer	Soil mass	Unit weight γ (KN/m ³)	Internal friction angle φ ($^{\circ}$)	Cohesion c (MPa)	Initial void ratio e	Poisson's ratio ν	Elastic modulus E (GPa)
Soil layer 1	Moderately weathered slate	24	55	85	0.5	0.25	25
Soil layer 2	Strongly weathered slate	22	28	66	1	0.2	16
Soil layer 3	Silty clay	18.5	15	30	1	0.3	0.03
Topsoil	Root soil	18.5	25	36	1	0.3	0.03

2.2 Boundary Conditions

Dynamic wave reflection would exist on the boundary during dynamic calculation, which would affect the dynamic calculation results to some extent. Therefore, Midas-GTS provided two boundaries in the dynamic calculation, namely static boundary, and free field boundary. Input wave reflection at the boundary of the model could be reduced through the designation of different boundary conditions. The free field boundary was selected as the boundary condition in the dynamic calculation based on the actual conditions of the model slope. Due to the large modulus of the model material, the input wave could be applied directly to the bottom of the model as an

acceleration time-history curve or velocity time-history curve, and it was unnecessary to apply a static boundary to the bottom [12].

3 Design of Seismic Conditions

The slope stability under the conditions of magnitude 6, 6.5, 7, 7.5, and 8 earthquakes was studied. Peak acceleration is 0.05, 0.075, 0.1, 0.15, and 0.2 g according to the Code for Seismic Design of Buildings [13].

The acceleration time-history curve is shown in Fig. 1:

4 Analysis of Slope Stability Under Seismic Conditions

4.1 Displacement

(1) Total displacement

The total displacement of the slope under the conditions of seismic acceleration of 0.05, 0.075, 0.1, 0.15, and 0.2 g were get from computing.

A line chart of the maximum total displacement under the conditions of different seismic acceleration was drawn based on the total displacement diagrams under the five different conditions above, as shown in Fig. 2.

According to the analysis from the perspective of total displacement, the maximum total displacement under the five different conditions was 0.023 m, 0.035 m, 0.0407 m, 0.061 m, 0.0813 m,

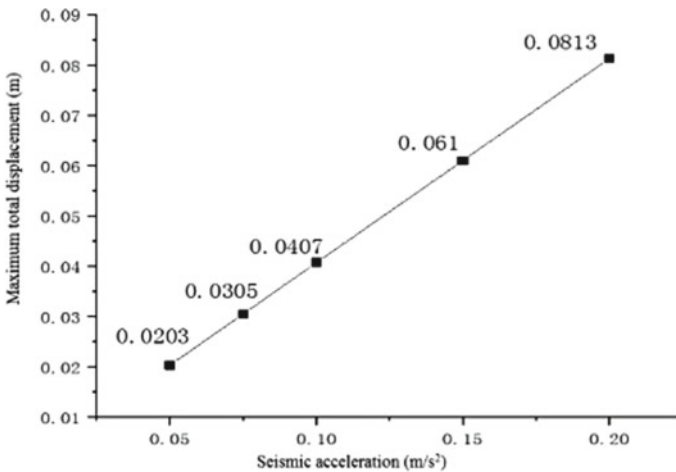


Fig. 2 Maximum displacement

0.061 m, and 0.081 m, respectively. The maximum displacement mainly occurred at the soil layer 3 (fill) because the shear strength of the slope was less than the total stress on it under the combined action of seismic stress and the gravity stress of the slope due to the low strength and stability of the soil layer 3 (fill). The corresponding displacement also increased with the increase of seismic acceleration. However, the total displacement at the slope bottom was almost zero because the retaining wall offset the landslide thrust of soil through the friction resistance generated by its gravity which improved its anti-sliding and anti-overturning abilities.

(2) horizontal displacement

The horizontal displacement of the slope under the conditions of seismic acceleration of 0.05, 0.075, 0.1, 0.15, and 0.2 g were get from computing. A line chart of the maximum horizontal displacement under the conditions of different seismic acceleration was drawn based on the horizontal displacement diagrams under the five different conditions above, as shown in Fig. 3.

The horizontal displacement was the smallest, which was 0.0040 m, 0.0061 m, 0.0399 m, 0.0599 m, and 0.0799 m under the five different conditions of 0.05 g, 0.075 g, 0.15 g, 0.1 g, and 0.2 g, respectively. The maximum displacement occurred at the top and on the middle and upper surfaces of the slope. What differs from the total displacement and vertical displacement was that the maximum displacement in the horizontal direction occurred not only at the soil layer 3 (fill), but also at the top and on the middle and upper surfaces of the slope, while there was hardly any displacement at the bottom of the slope.

(3) Vertical displacement

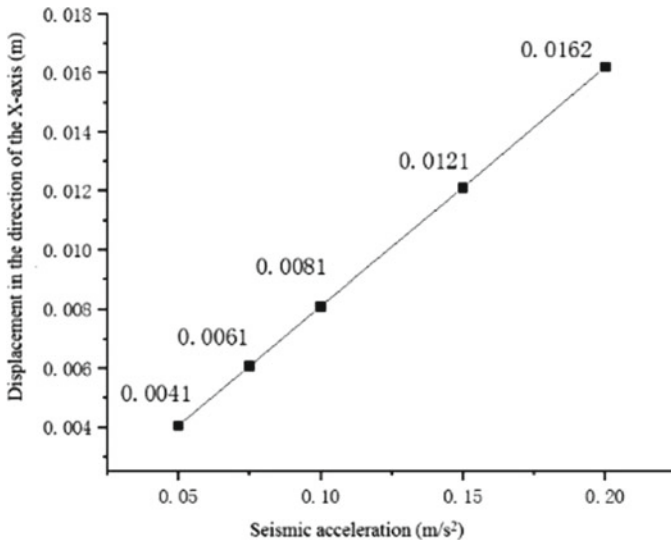


Fig. 3 Horizontal displacement

The vertical displacement of the slope under five conditions was get from computing. A line chart of the maximum vertical displacement under the conditions of different seismic acceleration was drawn.

The vertical displacement was relatively large, which was 0.0200 m, 0.0300 m, 0.0399 m, 0.0599 m, and 0.0799 m under the five different conditions of 0.05 g, 0.075 g, 0.1 g, 0.15 g, and 0.2 g, respectively. In general, the displacement mainly occurred at the soil layer 3 (fill) and decreased gradually from the middle to the foot and top of the slope.

It can be seen from the nephograms and line charts of the horizontal, vertical, and total displacement distribution under five different conditions that the maximum displacement mainly occurred at soil layer 3 (fill) for the reason that the shear strength of the slope was less than the total stress on it under the conditions of different seismic acceleration under the combined action of seismic stress and the gravity stress of the slope due to the low strength and stability of the soil layer 3 (fill), resulting in plastic fracture at different levels; however, the total displacement at the slope bottom was almost zero for the reason that the retaining wall offset the landslide thrust of soil through the friction resistance generated by its gravity which improved its anti-sliding and anti-overturning abilities.

4.2 Stability Coefficient

An analysis was conducted on the stability coefficient under the conditions of seismic acceleration of 0.05, 0.075, 0.1, 0.15, and 0.2 g and four different conditions (no vegetation or retaining wall; vegetation planting but no retaining wall; retaining wall setup but no vegetation; both vegetation planting and retaining wall setup) to analyze the stability of the slope with different reinforcement methods under different seismic acceleration conditions.

According to the results, the stability coefficient of the slope was 1.135, 1.117, 1.096, 1.048, and 0.986 respectively under the conditions of seismic acceleration 0.05, 0.075, 0.1, 0.15, and 0.2 g and different reinforcement measures. The energy released by an earthquake and its dynamic load increased geometrically with the increase of earthquake magnitude and acceleration, so the slope stability coefficient decreased greatly. The stability coefficient was only 0.986 under the condition of seismic acceleration of 0.2 g, in which case the slope became unstable and damaged. This shows the importance of the aseismic design of a slope. According to Table 3, the setup of a retaining wall at the foot of the slope could improve its stability coefficient. The stability coefficient of the slope was greatly improved under the condition of vegetation planting. Deep and thick roots had an anchoring effect, and shallow and thin roots had a reinforcing effect [14], which could improve the shear strength of soil masses [10] and thus the stability of the slope.

According to the comprehensive analysis above, the greatest damage to the slope occurred almost all in its middle part, indicating that the middle part was prone to

deformation and damage. Therefore, it was quite necessary to reinforce the slope by vegetation planting on the surface and setting up a retaining wall at the foot.

5 Conclusions

This paper mainly studied the impact of five different earthquake magnitudes (different earthquake acceleration) on slope stability and discussed the stability of the slope under seismic conditions from the perspectives of slope displacement and stability coefficient. The following conclusions were drawn:

1. Seen from the displacement nephograms, the maximum displacement occurred at soil layer 3 (fill). The corresponding displacement increased with the increase of the seismic acceleration. What differs from the total displacement and vertical displacement was that the maximum displacement in the horizontal direction occurred not only at the soil layer 3 (fill), but also at the top and on the middle and upper surfaces of the slope. According to the analysis of displacement susceptibility in each direction, the vertical displacement was the largest while the horizontal displacement was the smallest.
2. The slope stability coefficient decreased significantly with the increase of the earthquake magnitude. Planting vegetation on the slope and setting up a retaining wall at the foot could improve the stability coefficient of the slope effectively. Therefore, it was quite necessary to plant vegetation and set up a retaining wall for slopes with a low stability coefficient.

References

1. Zhang XD, Wang YY, He XJ (2022) Seismic hazards and earthquake prevention and mitigation. *China Insur* 02:35–39
2. Zhang PZ, Deng QD, Zhang GM, Ma J, Gan WJ, Min W, Mao FY, Wang Q (2003) Strong earthquakes and active blocks in mainland China. *Sci China (Ser D: Earth Sci)* S1:12–20
3. Keefer DK (1984) Landslides caused by earthquakes. *Geol Soc Am Bull* 95(4):406–421
4. Huang RQ (2009) Mechanism of landslide disasters triggered by Wenchuan M8.0 earthquake and its geomechanical model. *Chin J Rock Mech Eng* 28(06):1239–1249
5. Hough SE, Altidor JR, Anglade D et al (2010) Localized damage caused by topographic amplification during the 2010 M7.0 Haiti earthquake. *Nat Geoence* 3(11):778–782
6. Li HB, Jiang HJ, Zhao J, Huang LX, Li JR (2003) Several problems of rock mass engineering safety under dynamic load. *Chin J Rock Mechan Eng* 11:1887–1891
7. Li N, Cheng GD, Xie DY (2001) Rock mechanics problems in China's western development. *Chin J Geotech Eng* 03:268–272
8. Liu X, Tang HM, Hu XL, Wang LQ, Liao SB, Zou ZX (2012) Formation mechanism and dynamic stability of long-distance landslide on Jingu expressway. *Chin J Rock Mechan Eng* 31(12):2527–2537
9. Dai ML, Li TC (2007) Safety evaluation and analysis of dynamic stability of complex rock slopes based on numerical calculation with strength reduction method. *Chin J Rock Mechan Eng* S1:2749–2754

10. Jiang F, Zhang JY (2008) Study on mechanical properties between plant roots and slope soil masses. *J Geol Hazards Environ Preserv* 01:57–61
11. Li JX, He BH, Chen Y, Huang R, Tao J, Tian TQ (2013) Root distribution characteristics of different herbs for slope protection and their effects on soil shear strength. *Trans Chin Soc Agric Eng* 29(10):144–152
12. Du XM (2020) Study on slope stability under the combined action of rainfall and earthquake based on Midas-GTS. Chongqing Jiaotong University, Chongqing
13. GB 50011-2010 (2010) Code for seismic design of buildings
14. Jiang ZQ, Sun SL, Cheng LF (2005) Analysis of soil consolidation by roots and stability of plant slopes. *Site Invest Sci Technol* 04:12–14

Open Access This chapter is licensed under the terms of the Creative Commons Attribution 4.0 International License (<http://creativecommons.org/licenses/by/4.0/>), which permits use, sharing, adaptation, distribution and reproduction in any medium or format, as long as you give appropriate credit to the original author(s) and the source, provide a link to the Creative Commons license and indicate if changes were made.

The images or other third party material in this chapter are included in the chapter's Creative Commons license, unless indicated otherwise in a credit line to the material. If material is not included in the chapter's Creative Commons license and your intended use is not permitted by statutory regulation or exceeds the permitted use, you will need to obtain permission directly from the copyright holder.



Theoretical Study of the Reinforcement of Pre-stressed Concrete Cylinder Pipes with External Pre-stressed Strands



Lijun Zhao and Tiesheng Dou

Abstract Reinforcement of the pre-stressed concrete cylinder pipes with external pre-stressed strands is an effective way to enhance a prestressed concrete cylinder pipe's ability to bear the design hydraulic pressure. A theoretical derivation is studied, and this formula derivation could be used to determine the cross-sectional area per unit length. This derivation determine the cross-sectional area and target tensile strength of steel strands in order to meet the requirements of ultimate limit states, serviceability limit states, and quasi-permanent limit states. The theoretical results agree well with the experimental results. This paper could provide technical supports for the application of the external reinforcement of PCCPs with strands.

Keywords Pre-stressed concrete cylinder pipe · External pre-stressed strands · Theoretical study · Breaking wires

1 Introduction

The pre-stressed concrete cylinder pipe (PCCP) has strong bearing capacity and it is economically affordable because of the efficiencies in construction and reductions in fabrication costs. However, it is necessary to reinforce the deteriorate pipe because the wire-breakage may lead to the rupture of the pipe. This study introduced the theoretical derivation and determined the pre-stress loss of steel strands hooped on PCCPs. To estimate pre-stress losses, the normal stress between the strands and the pipe was considered as a trigonometric distribution instead of uniformly. The cross-sectional area per unit length of the pre-stressed strands was determined to meet the requests of ultimate limit states, serviceability limit states, and quasi-permanent

L. Zhao (✉) · T. Dou

Earthquake Engineering Research Center, China Institute of Water Resources and Hydropower Research (IWRH), Beijing 100038, China
e-mail: zhaolj@iwhr.com

T. Dou

Division of Materials, China Institute of Water Resources and Hydropower Research (IWRH), Beijing 100038, China

This is a U.S. government work and not under copyright protection in the U.S.; foreign copyright protection may apply 2023

Y. Yang (ed.), *Advances in Frontier Research on Engineering Structures*, Lecture Notes in Civil Engineering 286, https://doi.org/10.1007/978-981-19-8657-4_42

limit states. The load response of the deteriorate pipe during the whole procedure was analyzed.

2 Theoretical Research

2.1 Determination of Pre-stress Loss, $\sigma_{st,l}$

The pre-stress loss contains two parts, which is instantaneous loss and long-term loss [1–3]. Instantaneous loss exists during the tensioning operation and long-term loss exists after the tensioning procedure. Long-term pre-stress losses included pre-stress losses [1, 4] including shrinkage and creep losses of concrete, and long-term relaxation losses of pre-stressed steel strands. This part gives out the calculation method of the friction resistance between the surface of the pipe and the pre-stressed strands.

The retraction length, l_{re} , and its corresponding angle, θ_{re} , can be given $l_{re} = \sqrt{\frac{\Delta l_{re} E_{st} r_{st}}{\mu \sigma_{st}}}$, where E_{st} is the elastic modulus of the pre-stressed strand (N/mm²), σ_{st} is the tension stress of the strand (N/mm²), r_{st} is the calculated radius of the strand hooped on the pipe (m) and μ is the average friction coefficient between the pre-stressed strands and the outer surface of the PCCP. The value of Δl_{re} differed with the type of anchor.

The pre-stress loss caused by the friction resistance, σ_{11} , was induced by bending and deviation. The radial compressive stress, σ_r , was caused by pre-stressed strands which located between the strand and the pipe. And the extrusion friction occurred. The bending loss accounted for a large proportion of the total friction loss.

Based on the assumption of a rigid body, we assumed that the pressure between the pre-stressed strand and the PCCP would not show uniform distribution [5]. It was not accurate enough to consider the contact stress as uniformly distributed under normal contact pressure. And when the two elastic bodies began to contact each other, elastic deformation occurs.

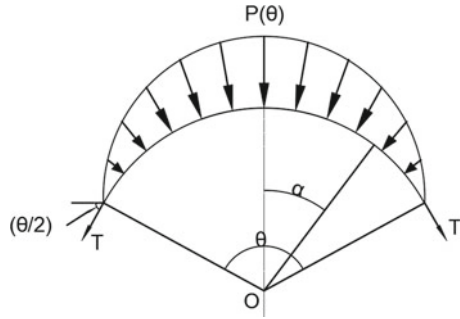
The scope of the bending loss was relevant to the retraction length, l_{re} . The assumption was made that the normal stress between the strands and the PCCP would show a trigonometric distribution [6] (Fig. 1).

The equation is given as $p_{(\alpha)} = p_0 \cos^2\left(\frac{\pi}{\theta}\alpha\right)$,

where $\cos^2\left(\frac{\pi}{\theta}\alpha\right) = \begin{cases} 0 & \alpha = \frac{\theta}{2} \\ 1 & \alpha = 0 \\ 0 & \alpha = -\frac{\theta}{2} \end{cases}$.

A forces in the z-direction could reach a balance (Eqs. 1 and 2). Therefore, the normal stress was calculated by Eq. 3.

Fig. 1 Distribution of the normal stress



$$T \cdot \sin\left(\frac{\theta}{2}\right) + (T + dT) \cdot \sin\left(\frac{\theta}{2}\right) + 2 \int_0^{\frac{\theta}{2}} p(\alpha) \cdot \cos \alpha \, dl = 0 \tag{1}$$

$$p_0 = \frac{\sin \frac{\theta}{2}}{\int_0^{\frac{\theta}{2}} \cos^2\left(\frac{\pi}{\theta}\alpha\right) \cos \alpha \, d\alpha} \times \frac{T}{R} \tag{2}$$

in which $\int_0^{\frac{\theta}{2}} \cos^2\left(\frac{\pi}{\theta}\alpha\right) \cos \alpha \, d\alpha = \left(\cos^2\left(\frac{\pi}{\theta}\alpha\right) \sin \alpha\right)\Big|_0^{\frac{\theta}{2}} + \frac{\pi}{\theta} \int_0^{\frac{\theta}{2}} \sin \alpha \sin\left(\frac{2\pi}{\theta}\alpha\right) d\alpha$

$$p(\alpha) = \left(2 - \frac{\theta^2}{2\pi^2}\right) \cdot \cos^2\left(\frac{\pi}{\theta}\alpha\right) \cdot \frac{\sigma_0}{R} \tag{3}$$

The pre-stress loss which was related to the bending loss, F , during the tensioning procedure is depicted in Eq. 4.

$$F = 2 \int_0^{\frac{\theta}{2}} \mu p(\theta) \cdot dl = \mu \theta \sigma_0 \left(1 - \frac{\theta^2}{4\pi^2}\right) \tag{4}$$

Errors in the positioning and installation of the pipe induced the friction between the force rib and the pipe material. And the contact friction formed. The deviation loss was related to the contact friction. In comparison to the bending loss, the deviation loss owned a small proportion of the total friction loss. The total pre-stress loss caused by the friction resistance was calculated as $\sigma_{l1} = c_1 F$, where c_1 is the correction coefficient, usually in the range of [1, 1.3] [7].

2.2 Calculation of Area of Pre-stressed Steel Strands

The cracking of PCCPs under combined loads mainly occurs at three dangerous sections [8–10] (1) the 6-o'clock orientation of the inner surface of the concrete core, (2) the 12-o'clock orientation of the inner surface of the concrete core, and (3) the 3-o'clock or 9-o'clock orientation of the outer surface of the concrete core. The cross-sectional area per unit length of the pre-stressed steel strands can be determined under the assumption of a complete loss of pre-stress of pre-stressing wires.

The combined loads acting on the pipe included the vertical earth pressure at the 12 o'clock orientation of the pipe, $F_{sv,k}$, lateral earth pressure, $F_{ep,k}$, ground pile load, the weight of the pipe, G_{1k} , the weight of fluid in the pipe, G_{wk} and variable load.

The value of $F_{sv,k}$ and $F_{ep,k}$ is calculated according to Marston theory and Rankine's earth pressure theory [11], separately. The variable load can be regarded as the ground stacking load and its standard value is defined as $q_{mk} = 10$ kN/m. $G_{1k} = \pi r_G (D_i + h_c) h_c$, where D_i is the inner diameter of the pipe (m); h_c is the thickness of concrete core (m), r_G is the gravity density of the pipe (kN/m³). G_{wk} , can be calculated by $G_{wk} = \frac{r_w \pi D_i^2}{4}$, where r_w is the gravity density of the fluid in the pipe (kN/m³).

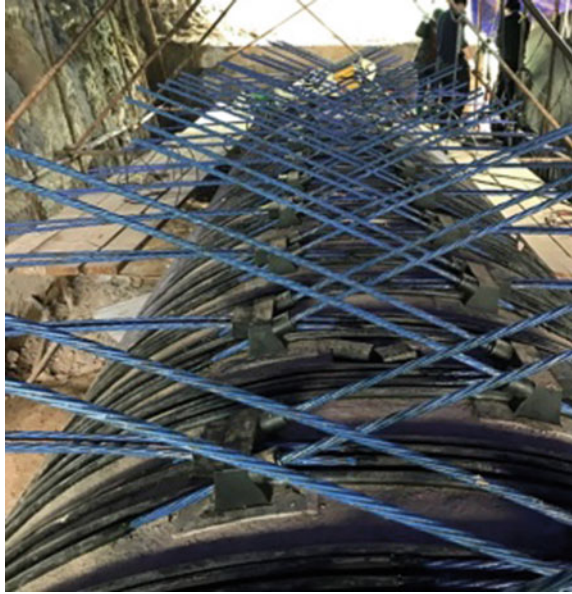
The design requests for calculation of ultimate limit states under the external soil load, the weight of pipe, the weight of the fluid, and other variable loads were carried out [12, 13]. The area of the pre-stressed strands of ultimate limit states should be calculated by $A_{st} \geq \frac{\lambda_y}{f_{pyk}} \left(N^1 + \frac{M_{max}^1}{d_0} - A_{sc} f'_{yy} \right)$, where λ_y is the comprehensive adjustment factor of the PCCP. f_{pyk} is the design strength of pre-stressed strands (N/mm²). Therefore, the area of pre-stressed strands should be calculated by $A_{st} \geq (\sigma_{ss} - K \gamma f_{ty}) \frac{A_p}{\sigma_{st}^1}$, where σ_{ss} is the maximum tensile stress at the edge of the pipe at the bottom. Meanwhile, checking calculation of mortar at the 3 or 9 o'clock orientation of the pipe should be conducted under different limit states.

3 Applications

Parameters of the design and materials were given in the former article [14]. $\Delta l_{re} = 6$ mm (Obtained from the full-scale test). Given $\mu = 0.1$, the calculated radius of the strand hooped outside the pipe, r_{st} , and l_{re} , is $r_{st} = 1.1726$ m and $l_{re} = 3.61$ m, respectively. The corresponding angle of the retraction length, θ_{re} , is π , which is in accordance with the value of θ . The correction coefficient is 1.01 and the pre-stress loss caused by friction resistance, σ_{l1} , can be calculated as $\sigma_{l1} = 278.860$ N/mm². The total pre-stress loss of pre-stressed wire is 490.74 N/mm².

According to the Marston theory, the vertical earth pressure at the top of the pipe, $F_{sv,k} = 164.245$ kN/m. And the lateral earth pressure is calculated based on the Rankine's earth pressure theory, $F_{ep,k} = 25.026$ kN/m. Weight of the pipe, $G_{1k} = 29.157$ kN/m. Weight of water in the pipe, $G_{wk} = 31.416$ kN/m.

Fig. 2 The strengthened pipe after tensioning



The area of pre-stressed strands should meet the requirement of $A_{st} \geq (\sigma_{ss} - K\gamma f_{iy}) \frac{A_p}{\sigma_{st}} = 2257.64 \text{ mm}^2/\text{m}$. The area of pre-stressed strands is $A_{st} = 2258 \text{ mm}^2/\text{m}$.

$(\alpha_m \varepsilon_{mt} E_m = 17.44 \text{ N/mm}^2) > (\sigma_{ss}^l = 9.57 \text{ N/mm}^2)$, indicating that the area of pre-stressed strands can reach the tensile request of the mortar coating under the states of serviceability limit.

$(\alpha'_m \varepsilon_{mt} E_m = 13.95 \text{ N/mm}^2) > (\sigma_{ss}^l = 8.31 \text{ N/mm}^2)$, indicating that the area of pre-stressed strands can reach the tensile request of the mortar coating under the states of quasi-permanent limit.

Above all, it is reasonable of the calculation result of the area of pre-stressed strands, which is $A_{st} = 2258 \text{ mm}^2/\text{m}$. The predictions of the results by the equations agrees well with the test results [14]. The strengthened pipe with external strands was capable of sustaining the design internal hydraulic pressure and the pipe do not leak (Fig. 2). The rationality of the theory in this study was testified by the effective reinforcement effect with external pre-stressed strands.

4 Conclusion

A theoretical research was studied aiming at the determination of the appropriate cross-sectional area per unit length of pre-stressed strands in this paper.

- (1) The pre-stress loss of pre-stressed strands contains several types. The formula derivation in this study provides a reliable method to determine the effective pre-stress of the strands.
- (2) The stress of the concrete core under different limit states was calculated. And the condition of the mortar coating under different limit states is then verified, and the appropriate cross-sectional area per unit length of pre-stressed strands is finally determined.

References

1. Cao G, Hu J, Kai Z (2016) Coupling model for calculating prestress loss caused by relaxation loss, shrinkage, and creep of concrete. *23(2):470–478*
2. Cao G, Zhang W, Hu J et al (2018) Experimental study on the long-term behaviour of RBPC t-beams. *Int J Civ Eng 16(8):887–895*
3. Baolin K (2002) The estimating of the external prestressing loss in the bridge strengthen system. *J Hebei Inst Architect Sci Technol 19(3):27–29*
4. Zhang J, Pan J, Dong H (2012) Analysis of prestressing loss on construction of external prestressed wooden buildings. *Adv Mater Res. Trans Tech Publications, Switzerland*
5. Zhang S, Zhang K, Xie B et al (2013) Research on the mechanism of pre-stressed loss for curving hole of pre-stressed concrete structure caused by frictional resistance. *Appl Mech Mater. Trans Tech Publications, Switzerland*
6. Gao A (2016) Research on pre-stress loss based on friction, retraction and natural frequency. *Southeast University, Nanjing*
7. Hu Z, Hu Z (2006) Practical estimation method for pre-stress loss of externally pre-stressed structures. *Bridge Constr 1:73–75*
8. Erbay OO, Zarghamee MS, Ojdrovic RP (2007) Failure risk analysis of lined cylinder pipes with broken wires and corroded cylinder
9. Zarghamee MS, Fok K, Sikiotis ES (1990) Limit states design of pre-stressed concrete pipe II: procedure. *J Struct Eng 116(8):2105–2126*
10. Zarghamee MS, Fok K (1990) Analysis of pre-stressed concrete pipe under combined loads. *J Struct Eng 116(7):2022–2039*
11. Concrete pressure pipe: M9 (2008). American Water Works Association
12. CECS 140:2011 (2011) Specification for structural design of buried pre-stressed concrete pipeline and pre-stressed concrete cylinder pipeline of water supply and sewerage engineering. Beijing
13. GB 50332 (2002) Structural design code for pipelines of water supply and waste water engineering. Beijing
14. Zhao L, Dou T, Cheng B et al (2019) Experimental study on the reinforcement of pre-stressed concrete cylinder pipes with external pre-stressed steel strands. *Appl Sci 9(1):149*

Open Access This chapter is licensed under the terms of the Creative Commons Attribution 4.0 International License (<http://creativecommons.org/licenses/by/4.0/>), which permits use, sharing, adaptation, distribution and reproduction in any medium or format, as long as you give appropriate credit to the original author(s) and the source, provide a link to the Creative Commons license and indicate if changes were made.

The images or other third party material in this chapter are included in the chapter's Creative Commons license, unless indicated otherwise in a credit line to the material. If material is not included in the chapter's Creative Commons license and your intended use is not permitted by statutory regulation or exceeds the permitted use, you will need to obtain permission directly from the copyright holder.



Structural Seismic Performance of Prefabricated Steel Plate Shear Wall with High Energy Dissipation



Xiaofei Ma, Yinquan Yu, and Zhe Wang

Abstract China is located at the intersection of the Pacific Rim seismic belt and the Alpine Mountain-Himalayan seismic belt. Earthquakes occur frequently and with high intensity in China, and the structural damage caused by earthquakes leads to huge casualties and serious economic losses. Steel plate shear wall exhibits satisfying seismic performance which is the key to its application in high-rise buildings and high intensity areas. Meanwhile, the industrialization of new construction requires prefabricated steel plate shear wall structure. In this paper, a kind of prefabricated steel plate shear wall with high energy dissipation is proposed. The finite element study on the seismic performance of the prefabricated steel plate shear wall under low cyclic load was carried out by varying the width-to-thickness ratio of steel connecting plate belt and width-to-thickness ratio of ring damper. The failure modes, hysteresis curves, skeleton curves, stiffness degradation, energy dissipation and displacement ductility coefficients were analyzed. The results showed that the hysteretic curves of the prefabricated steel plate shear wall are relatively full under low cyclic load, and the displacement ductility coefficients are above 8. It is noted that the seismic performance of the prefabricated steel plate shear wall is advantageous. It is suggested that width-to-thickness ratio of the steel connecting plate belt and the width-to-thickness ratio of the ring damper are 3.75 for engineering practice.

Keywords Prefabricated · Steel plate shear wall · High energy dissipation · Seismic performance · Finite element study

1 Introduction

More than 80% of new buildings in China each year are high-energy buildings, and the energy consumption for unit area is more than twice that of the developed countries. At the same time, nearly 1.5 billion tons of construction waste is generated annually, and construction and construction waste transportation are the main sources

X. Ma (✉) · Y. Yu · Z. Wang
China Institute of Building Standard and Research, Beijing 100048, China
e-mail: maxf@cbs.com.cn

of urban pollution. China is the country with the largest construction scale and steel output in the world. However, steel structure construction area in China only accounts for 5–7% of the total construction area, and the development of the steel structure construction lags behind seriously.

The urbanization in China has entered a stage of high-quality development from high-speed development, which requires steel structure and other prefabricated buildings to change the construction mode, promote industrial transformation and upgrading, and realize high precision construction and industrialization of construction [1, 2]. Steel plate shear wall structure has been widely used for its high strength, light weight, satisfying energy dissipation, satisfying ductility, high lateral displacement resistance and high construction efficiency.

The seismic performance of steel plate shear wall has been studied by many scholars. Hitaka et al. [3] proposed the shear-wall with vertical slits and conducted an in-depth study on the seismic performance of the shear wall with slits. The results showed that the seismic performance of the shear wall with slits is satisfying. Cortes and Liu [4] and Chen [5] studied the seismic performance of the steel plate shear wall with multilayer slits and obtained good results. In order to meet the purpose of building function and improve the seismic performance of steel plate shear wall, Robert and Sabouri-ghomi [6], Alavi and Nateghi [7], Matteis et al. [8] and Phillips and Eatherton [9] studied the seismic performance of the steel plate shear wall with holes. Valizadeh et al. [10] proposed a kind of prefabricated steel plate shear wall with butterfly connecting rods, and investigated its seismic performance. The results showed that the prefabricated steel plate shear wall can effectively reduce the out-of-plane buckling, improve the shrinkage of hysteretic curve, and enhance the energy dissipation capacity.

This paper presents a kind of prefabricated steel plate shear wall with high energy dissipation. The prefabricated steel plate shear wall has the characteristics of advantaged energy dissipation and ductility, light weight, convenient transportation and efficient construction, which can adapt to the large-scale, high-rise and diversified development of modern structure and meet the needs of building safety, aesthetics and space use. The finite element analysis of seismic performance of the prefabricated steel plate shear wall under low cyclic load was carried out, and the influence of the width of the steel connecting plate belt and the width of the ring damper on its hysteretic performance was analyzed.

2 Fabricated Steel Plate Shear Wall with High Energy Dissipation

The fabricated steel plate shear wall with high energy dissipation is composed of inner panel and steel–concrete constrained composite plate, as shown in Fig. 1. Under the effective restraint of steel–concrete composite plate, the inner panel with ring metal

damper provides lateral force resistance and high energy dissipation under the action of horizontal load.

The inner panel consists of ring dampers, steel connecting plate belts and boundary connecting plate belts. The ring dampers are arranged alternately with the steel connecting plate belts. And they were placed diagonally across the horizontal direction at 45° , and then connected by the boundary connecting plate belts to form the inner panel. The boundary connecting belts acts as a moment frame and can withstand vertical load.

The steel–concrete constrained composite plate is composed of outer steel plate and inner filled concrete. The outer steel plate is in the shape of a cap, and the concave part of the cap is filled with plain concrete to form an out-of-plane constrained composite plate. In this way, the steel plate shear wall does not need to consider the requirements of reinforcements, reducing the thickness of the out-of-plane constrained composite plate, which is convenient for transportation and installation. The out-of-plane constrained composite plate covers the inner panel using concrete face, which can effectively prevent the plain concrete from being damaged, so that the out-of-plane constrained composite plate can be reused after earthquake. The purpose of repairing and using can be achieved only by rapidly replacing the damaged inner panel after earthquake.

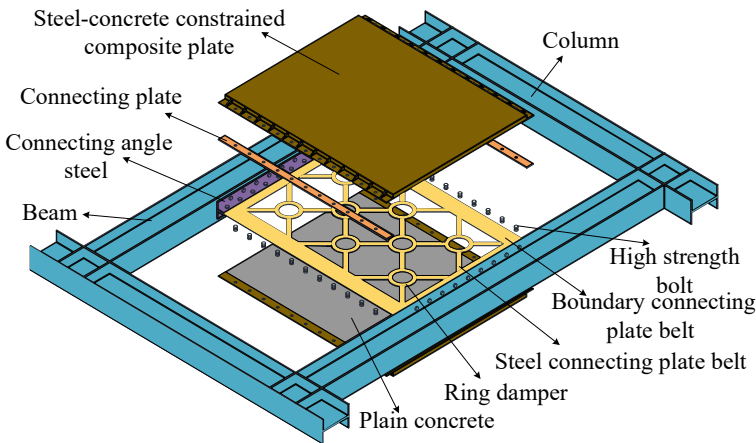


Fig. 1 Prefabricated steel plate shear wall with high dissipation

3 Finite Element Analysis

3.1 Finite Element Model

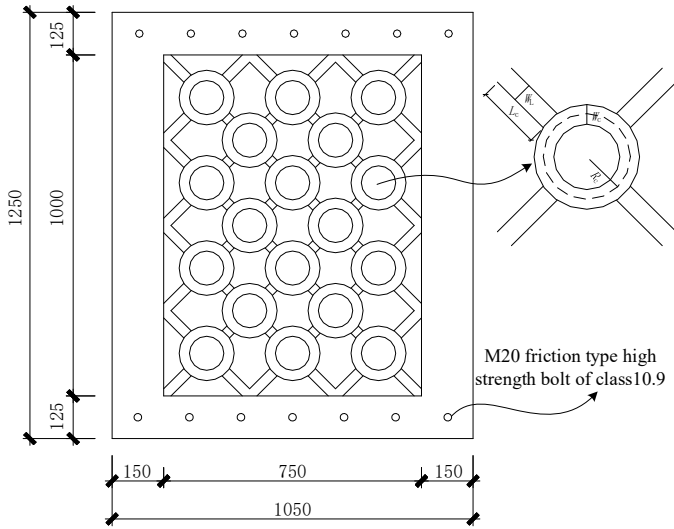
The scale ratio between the finite element model and the actual structure was about 1:3. The finite element model size was 1250 mm × 1050 mm (length × width), and the thickness of the inner panel was 8 mm. The steel connecting plate belt of w_1 were 30 mm, 50 mm, 70 mm, respectively. The ring damper of w_c were 20 mm, 30 mm, 40 mm, respectively. The radius of R_c was 65 mm. The shear wall was connected to the upper and lower I-beams through angle steels and high strength bolts, and the high strength bolt was friction type of class 10.9 M20. The specific size of the model is shown in Fig. 2a.

The finite element model is shown in Fig. 2b. Finite element software ABAQUS was used to simulate the seismic performance of the prefabricated steel plate shear wall with high energy dissipation, and the hysteretic performance was analyzed through varying parameters. The 8-node C3D8R element was used for the inner panel, out-of-plane constrained composite plates and high-strength bolts. The friction contact was used between the high-strength bolts and the connecting angle steels, the high-strength bolts and the inner panel, the connecting angle steels and the inner panel, the inner panel and the outer constraint plates, and the out-of-plane constraint plate and the high-strength bolts.

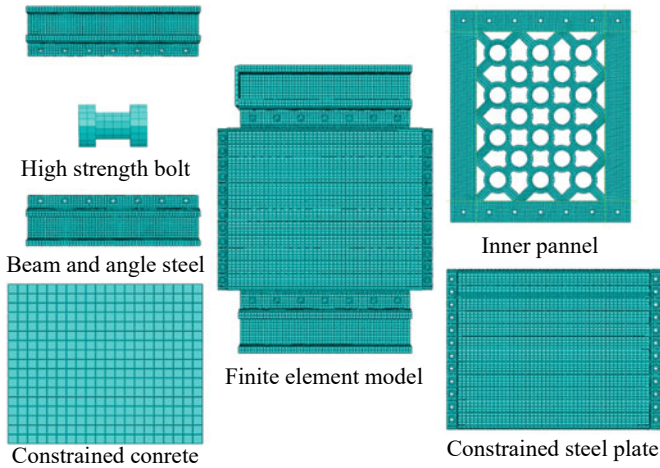
The steel class of Q355B was used for the inner panel, out-of-plane restrained steel plates, connecting angle steels and I-beams, and the constitutive relationship was presented by a double line model. The C30 concrete was adopted, and the plastic damage of the concrete was considered.

3.2 Model Parameter and Cyclic Loading Procedure

The width-to-thickness ratio of the steel connecting plate belt and width-to-thickness ratio of the ring damper are selected as varying parameters, as shown in Table 1. The horizontal low cyclic loading procedure of the finite element model was controlled by displacement, which was transformed from storey drift. The storey drift was 0.00375, 0.005, 0.0075, 0.01, 0.015, 0.02, 0.03, 0.04, respectively, and each storey drift was cyclic loaded twice. The limit of the elastic–plastic storey drift of the multi-storey and high-rise steel structures is 0.02, and the storey drift of the finite element model is 2 times of that.



(a) Model dimension



(b) Finite element model

Fig. 2 Finite element model and dimension

4 Result Analysis

4.1 Failure Mode

The panel failure mode of the finite element model of the prefabricated energy dissipation steel plate shear wall is shown in Fig. 3. Under the action of horizontal low

Table 1 Parameter variation

Model	Width-to-thickness ratio of steel connecting plate belt	Width-to-thickness ratio of ring damper
M-1	3.75	3.75
M-2	6.25	3.75
M-3	8.75	3.75
M-4	6.25	2.50
M-5	6.25	5.00

cyclic load, the ring dampers and boundary connecting plate belts yielded and formed plastic hinges.

4.2 Hysteretic Curve

The hysteretic curves of the calculation model of prefabricated energy dissipation steel plate shear wall are shown in Fig. 4. The hysteretic curves experienced elasticity, yield and ultimate stages. In addition, the hysteretic curves are full, and this indicates that the prefabricated energy dissipation steel plate shear wall exhibits a satisfying energy dissipation performance.

4.3 Skeleton Curve

The model skeleton curves of the prefabricated energy dissipation steel plate shear wall are shown in Fig. 5a. The carrying capacity of the model M-1 is the largest, while that of the model M-4 is the smallest.

The characteristic value points of the models are shown in Table 2. It can be seen from the table that as the width-to-thickness ratio of the steel connecting plate belt increases from 2.50 to 8.75, the yield capacity of the model increases, while the ultimate bearing capacity and failure capacity decrease first and then increase. The yield capacity, ultimate capacity and failure capacity of the model increase with the increase of the ring damper width-to-thickness ratio from 2.50 to 5.00.

4.4 Stiffness Degradation

Stiffness degradation of the model of the prefabricated energy dissipation steel plate shear wall is shown in Fig. 5b. As can be seen from the figure, the lateral stiffness

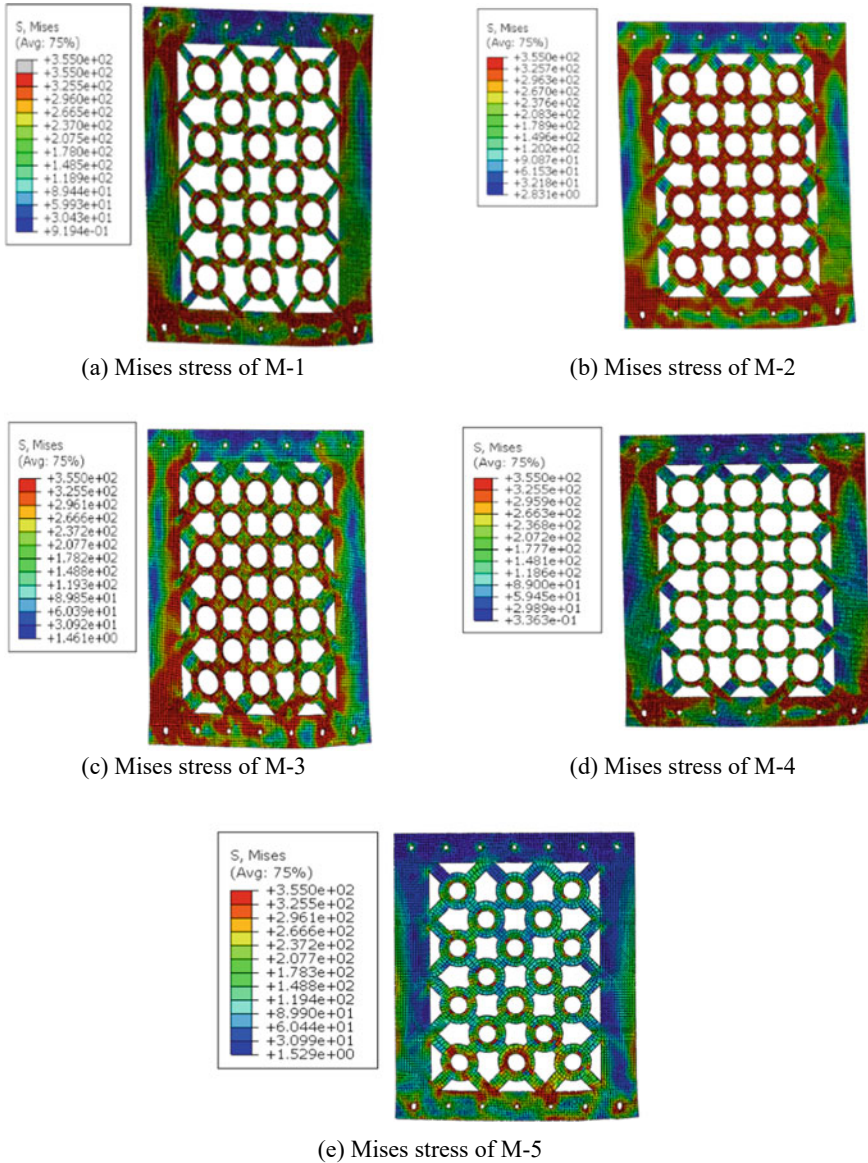
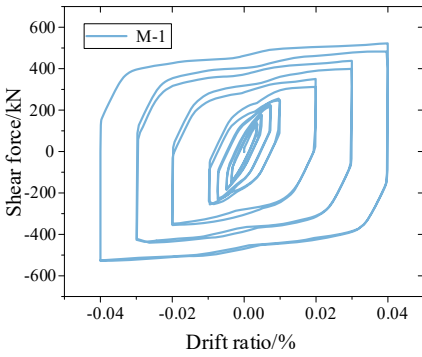


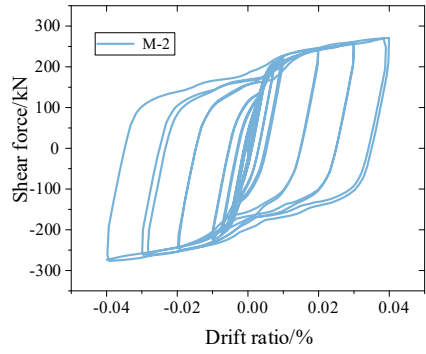
Fig. 3 Mises stress of panels

of the models decrease with the increase of horizontal loading displacement, and the stiffness degrade rapidly within the storey drift of 0.01, but slowly after that.

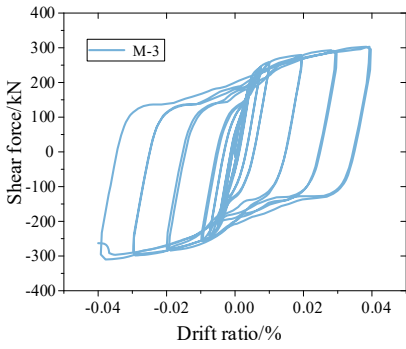
The initial stiffness of each model is shown in Table 2. It can be seen from the table that the initial stiffness of the model M-5 is the maximum and that of the model M-4 is the minimum. With the increase of the width-thickness ratio from 2.50 to 8.75,



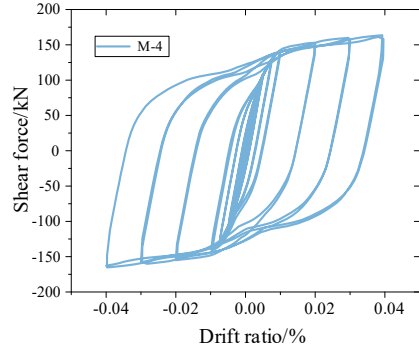
(a) hysteretic curve of M-1



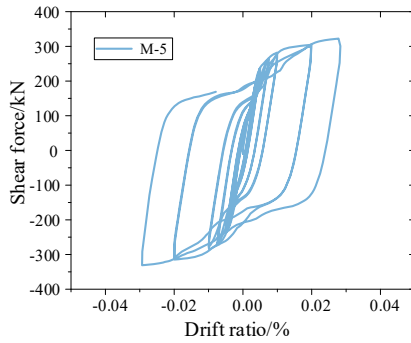
(b) hysteretic curve of M-2



(c) hysteretic curve of M-3



(d) hysteretic curve of M-4



(e) hysteretic curve of M-5

Fig. 4 Hysteretic curves of models

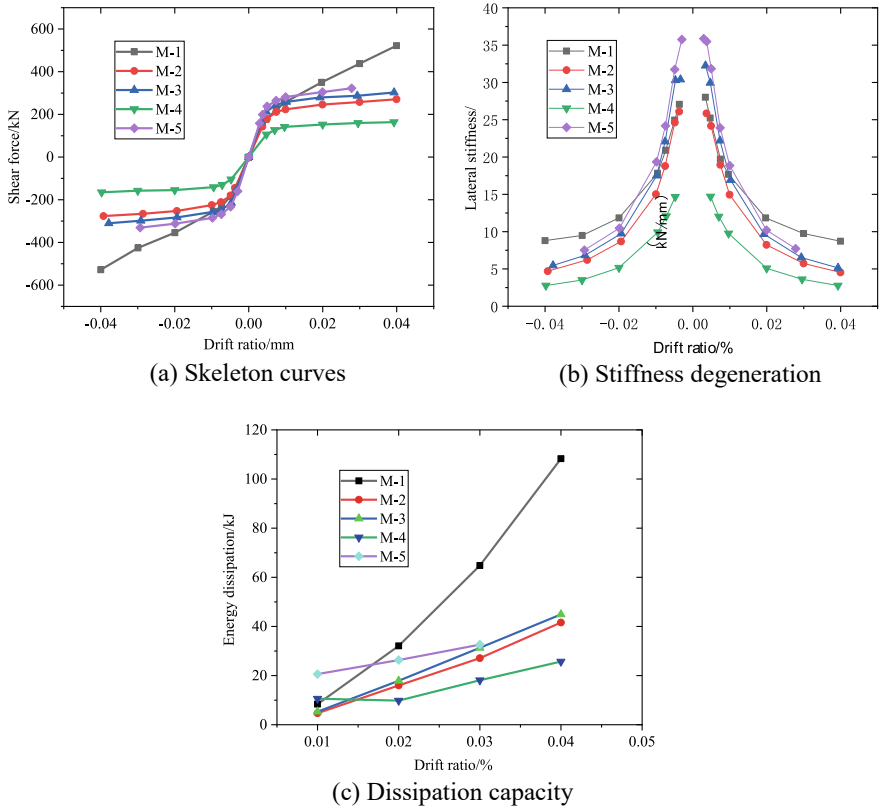


Fig. 5 Skeleton curves, stiffness degeneration and dissipation capacity

Table 2 Characteristic values of models

Model	Yield capacity/kN	Ultimate capacity/kN	Failure capacity/kN	Initial stiffness/(kN/mm)	Displacement ductility coefficient/ μ
M-1	142.5	522.1	522.1	28.0	8.5
M-2	178.6	271.0	271.0	25.9	8.1
M-3	212.5	302.8	302.8	32.2	8.3
M-4	105.8	163.6	163.6	14.7	8.2
M-5	237.8	322.3	322.3	35.9	5.6

Note As the loading displacement reaches 0.04 drift, the model carrying capacities did not decrease, so the failure capacity is selected in accordance to the final loading displacement value point

the initial stiffness of the model decreases first and then increase. With the increase of the ring damper width-to-thickness ratio from 2.50 to 5.00, the initial stiffness of the model increases.

4.5 Displacement Ductility

The displacement ductility coefficient μ of the model is the ratio of failure displacement to yield displacement, and the displacement ductility coefficients of the models are shown in Table 2. The displacement ductility coefficient of the model decreases first and then increases with the increase of the width-thickness ratio of the steel connecting plate belt from 2.50 to 8.75. As the width-to-thickness ratio of the ring damper increases from 2.50 to 5.00, the displacement ductility coefficient decreases. Among them, the displacement ductility coefficient of the model M-1 is the largest, and that of the model M-5 is the smallest. This is because the model calculation was terminated when the loading displacement of the model M-5 reaches 0.03 drift due to divergence of calculation, so the displacement ductility coefficient is smaller. Above all, the displacement ductility coefficients of the prefabricated steel plate shear wall are above 8.0 except for the model M-5.

4.6 Energy Dissipation Performance

The energy dissipation performance of the model is represented by the hysteretic energy dissipation (E) under the loading cycle of each stage, as shown in Fig. 5c. As can be seen from the figure, the hysteretic energy dissipation E of each model increases gradually with the horizontal displacement increase, and the hysteretic energy dissipation E of the model M-1 is the largest, while that of the model M-4 is the smallest.

The hysteretic energy dissipation of the models decrease first and then increase with the increase of the width-to-thickness ratio from 2.50 to 8.75. The hysteretic energy dissipation of the models increase with the increase of the width-to-thickness ratio of the ring damper from 2.50 to 5.00.

5 Conclusions

Industrialization of new construction and multi-earthquake-happening area in China require prefabricated steel plate shear wall with satisfying seismic performance. Through the finite element study of seismic performance of the prefabricated steel plate shear wall with high energy dissipation, the hysteretic curves and failure modes

of the shear wall were obtained, and then the carrying capacity, stiffness degradation, displacement ductility and energy dissipation performance were analyzed. The conclusions are as follows:

- (1) The seismic performance of prefabricated steel plate shear wall with high energy dissipation is advantageous. The hysteretic curve of the steel plate shear wall is relatively full, and the displacement ductility coefficient is above 8.0.
- (2) The failure mode of the prefabricated steel plate shear wall is that the ring dampers and the boundary connecting plate belts yield and fail under the action of horizontal load.
- (3) When the width-to-thickness ratio of the steel connecting plate belt is 2.5 and the width-to-thickness ratio of the ring damper is 3.75, the ductility and energy dissipation performance of the prefabricated steel plate shear wall with high energy dissipation are the best.
- (4) The test investigation should be conducted on the basis of the finite element study.

Acknowledgements The authors wish to thank the China institute of building standard and research for financially supporting the research in the paper through the Grant No. 2021104.

References

1. Yu Y, Zhu F, Wang Z (2020) Review of the promotion and application of steel structures in construction. *China Constr Metal Struct* 35(01):59–69
2. Zhang A (2020) Accelerate the industrialization of steel structure building products for epidemic prevention and disaster relief with full bolt site quick assembly. *China Constr Metal Struct* (03):40–44
3. Hitaka T, Matsui C, Sakai J (2007) Cyclic tests on steel and concrete-filled tube frames with slit walls. *Earthq Eng Struct Dyn* 36(6):707–727
4. Cortes G, Liu J (2011) Experimental evaluation of steel slit panel–frames for seismic resistance. *J Constr Steel Res* 67(2):181–191
5. Chen Y, Ning Y, Lu J (2012) Experimental study on seismic behavior of frame-steel plate shear wall with slits. *J Build Struct* 33(07):133–139
6. Robert TM, Sabouri-ghomi S (1992) Hysteretic characteristics of unstiffened perforated steel plate shear panels. *Thin-Walled Struct* 14:139–151
7. Alavi E, Nateghi F (2013) Experimental study on diagonally stiffened steel plate shear walls with central perforation. *J Constr Steel Res* 89:9–20
8. Matteis DG, Sarracco G, Brando G (2016) Experimental tests and optimization rules for steel perforated shear panels. *J Constr Steel Res* 123:41–52
9. Phillips AR, Eatherton MR (2018) Large-scale experimental study of ring shaped-steel plate shear walls. *J Struct Eng* 144(8):04018106
10. Valizadeh H, Veladi H, Azar BF, Sheidaei MR (2020) The cyclic behavior of butterfly-shaped link steel plate shear walls with and without buckling-restrainers. *Structures* 27:607–625

Open Access This chapter is licensed under the terms of the Creative Commons Attribution 4.0 International License (<http://creativecommons.org/licenses/by/4.0/>), which permits use, sharing, adaptation, distribution and reproduction in any medium or format, as long as you give appropriate credit to the original author(s) and the source, provide a link to the Creative Commons license and indicate if changes were made.

The images or other third party material in this chapter are included in the chapter's Creative Commons license, unless indicated otherwise in a credit line to the material. If material is not included in the chapter's Creative Commons license and your intended use is not permitted by statutory regulation or exceeds the permitted use, you will need to obtain permission directly from the copyright holder.



Sensor Fault Diagnosis Method of Bridge Monitoring System Based on FS-LSTM



Lili Li, Hao Luo, He Qi, and Feiyu Wang

Abstract An improved long-short-term memory neural network (FS-LSTM) fault diagnosis method is proposed based on the problems of damage false alarm, data of health monitoring system incorrect caused by sensor fault in bridge structure health monitoring system. The method is verified by simulating three-span continuous beams to install several sensors and considering the five failures of one sensor, the faults such as: constant, gain, bias, gain linearity bias, and noise. At first, several pieces of white noise data are randomly generated, and each piece of white noise data is applied as a ground pulsation excitation to the structure support, and the acceleration response of the structure at the sensor location is calculated. Simultaneously, each structural response record of each sensor adds white noise with the same signal-to-noise ratio to obtain the test value of each sensor; Secondly, in order to study the generality, except for the five types of faulty sensors in sequence, one sensor is randomly selected from each of the remaining spans, to verify whether there will be a situation where an intact sensor is misdiagnosed as a faulty sensor; Finally, the FS-LSTM network is constructed through the training set to predict the acceleration data, determine the sensor fault threshold, and compare the residual sequence with the fault threshold to diagnose whether the sensor is faulty. The case research of a three-span continuous beam shows that when the above-mentioned five types of faults occur in the sensor, the proposed method can correctly determine whether the sensor is faulty, and it will not be misdiagnosed, which can be used for daily bridge

L. Li (✉) · H. Luo · H. Qi · F. Wang
China Construction Science and Technology Group Co., Ltd., Shenzhen 408317, China
e-mail: li.lili@cscec.com

H. Luo
e-mail: luohao@cscec.com

H. Qi
e-mail: qihe@cscec.com

F. Wang
e-mail: Feiyu@cscec.com

L. Li
School of Civil and Environmental Engineering, Harbin Institute of Technology, Shenzhen,
Shenzhen 518055, China

health monitoring. Furthermore, it provides a new method for the maintenance of the bridge health monitoring system.

Keywords Bridge engineering · Sensor fault · LSTM · Three-span continuous beam

1 Introduction

With the constantly increasing trend of our infrastructure construction, the world bridge center has been transferred gradually from developed countries like America, Japan to China. At the same time, since the bridge construction in our country is experiencing the process of large span, high technology along with high difficulties, more and more bridges start to apply the SHM (structural health monitoring) system in case of assuring the structure operation safety [1–4].

The sensors in SHM systems usually have a short-term limit of life scale because of the complex operation environment as well as the improper use, which also makes it difficult to match the sensors have short-term life with those built structures that can last hundreds of years. What's worse, the data distortion caused by the failure of the sensors will also lead to the high false alarm rate, which can pose a certain threat to the operation of the expensive health monitoring system. In this case, it is urgent to carry out related researches on self-diagnosis of sensor faults.

Self-diagnosis of sensor faults can be divided into two types [5]. One is based on models, the other is focused on the data. The model-based type can estimate the system output by forming observers with precise mathematical models or finite element models and then compare the output data with actual measured values to obtain details of faults [6]. The model-based type takes the advantage of high efficiency and good effect, which also shows its terrific adaption to those sensor systems with accurate linear models. However, the development of model-based method has been restricted when considering the difficulties of establishing precise non-linear mathematical models on structural engineering with large complex nonlinear system [7, 8].

The data-based method is to process the output data obtained by the sensor measurement, and diagnose the sensor faults based on the analysis results [9, 10]. One outstanding advantage of this method over model-based method is that it does not require precise mathematical models and rich prior knowledge.

The neural network method is widely used in the field of fault diagnosis because of its fast response, good fault tolerance, strong learning ability, excellent adaptive performance, and high degree of nonlinear approximation. Deep learning has undergone structural changes based on neural networks, which not only overcomes the shortcomings of traditional neural networks, but also makes the new round of deep learning methods more widely used. The main feature of this method is that it can do adaptive feature learning and strengthen the extraction and combination of abstract fault features which realizes artificial intelligence in the true sense [11].

In the field of bridge SHM, research based on deep learning has initially realized structural damage identification and location, abnormal data diagnosis and classification [12–15]. It is shown that although deep learning method has already carried out some researches in the field of bridge SHM, they mainly focus on the detection and identification of bridge apparent disease, and the routine fault diagnosis of sensors. In another word, researches on sensor fault self-diagnosis are still in the initial stage, few theoretical results have been obtained and therefore it is necessary to study many basic problems systematically and deeply.

In this case, the FS-LSTM sensor fault diagnosis method is proposed when considering problems of sensor fault diagnosis in the bridge SHM system, with the law of data produced by sensors in abnormal working conditions and the principle of deep learning. Based on the traditional LSTM neural network, the prediction ability and robustness of the network are improved by constructing a new fully connected layer and state memory unit, thereby improving the recognition rate of sensor faults, and reducing the occurrence of false alarms.

2 Mathematical Model of Sensor Faults

Acceleration sensors with different test principles often have different failures, and acceleration sensors with the same test principle may also have different types of failures [16]. Therefore, difference can appear in sensors faults' causes, locations, and forms. In a word, these faults can be generalized into the following five types according to the statistical law of the distorted data output by the fault sensor.

2.1 Constant

When internal coil of the sensor has been broken, its sensitivity will decrease and output constant, this kind of fault can be defined as the constant fault.

$$x_{out}(t) \equiv c \quad (1)$$

As is shown in formula (1), where c stands for a constant, $x_{out}(t)$ represents the output signal of sensor. Since noise is inevitably introduced in the process of data collection and transmission, when the sensor has a stuck fault, the collected signal closer to the true value can be expressed as

$$x_{out}(t) \equiv c + \delta \quad (2)$$

where δ represents white noise.

2.2 Gain

When the internal spring of the sensor undergoes plastic deformation, the output signal of the sensor can be several times of the real signal. This type of fault is defined as the sensor gain fault, and the mathematical model is shown as follows

$$x_{out}(t) = \beta x(t) + \delta \quad (3)$$

where $x(t)$, β stands for real signal and gain coefficient respectively, the size of the gain is different at each moment and the gain coefficient is proportional to the signal variance.

2.3 Bias

When the sensor base is loose or the sensitive components creep, the sensor will appear as a deviation fault. Its mathematical model is expressed as follows:

$$x_{out} = x(t) + d + \delta \quad (4)$$

where d represents the degree of Bias.

2.4 Gain and Linear Drift

When the transmission cable is artificially bent and rubbed on the ground, there exist a gain and linear drift change in the response of the fault sensor over time. The mathematical model can be expressed as

$$x_{out} = \beta_1 x(t) + a + b \cdot t + \delta \quad (5)$$

where β_1 , a , b , t represents constant term, linear offset monomial term and time variable respectively.

2.5 Noise

When the sensor is subject to external electromagnetic interference. Its mathematical model is expressed as follows:

$$x_{out} = K \quad (6)$$

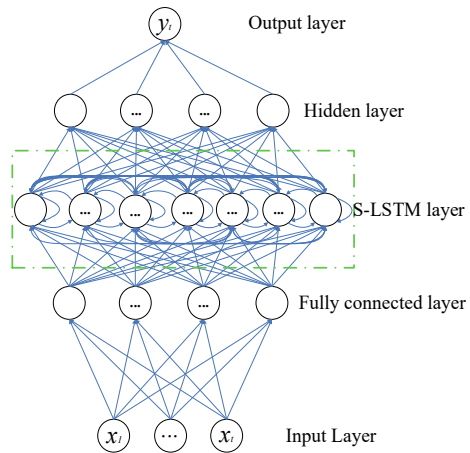
where, K stands for a random signal with unknown mean and variance. However, in a lot of cases white noise is usually used to represent this kind of signal.

3 Fault Diagnosis Method of FS-LSTM

In order to deal with the long-term or short-term time dependence of the time series data in the bridge structure, while considering that the bridge structure is exposed to humidity, high temperature and complex external environment for a long time. The acceleration response of the bridge structure is determined by both time dependence and environmental factors. Two improvements have been made to the acceleration response characteristics of the bridge structure, which are carried out based on the neural network basic architecture shown in literature [17] as well as lots of real bridge acceleration data. As is demonstrated in Fig. 1, the first improvement is to introduce a fully connected layer between the input layer and the LSTM layer and the second one is to add a full training sample (epoch) state memory unit to the LSTM layer, instead of only performing state memory on each training sample batch.

The first improvement is considered because the acceleration response of the bridge structure is a time series output. The acceleration response at the current time point is similar to the data at the historical time point within a certain range, and will be affected by the temperature, air humidity, air humidity and external factors such as rain and snow. As is shown in Fig. 2, taking the 10 s' data of the same sensor from a real bridge in different seasons and months, it can be found that the data amplitude of each season is obviously different. Therefore, in order to make a reasonable prediction of the acceleration response. It is necessary to fully consider the influence of external factors and the acceleration at all time.

Fig. 1 FS-LSTM neural network simple architecture



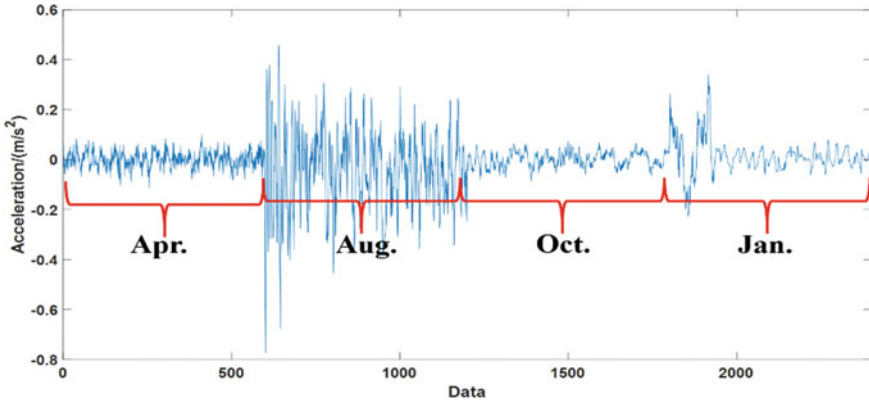


Fig. 2 Four season data of a real bridge accelerometer

The reason for proposing the second improvement is that considering the current network has poor robustness by setting the memory state on the grouped data, and the memory state unit is added through all training samples to improve its robustness. As is shown in Fig. 3, in the improved model, when constructing the LSTM layer, the inherent state parameter must be set to true. It is not necessary to specify the input size, and encoding the number of samples, along with the time step and the feature number in time step must through setting batch input shape. What's more, by adding Stateful unit to LSTM layer under the Keras frame, the LSTM network can get more refined control. At the same time, the same batch size is used when evaluating the model and making predictions. Usually, after training a group each time, the state in the network is reset and the model is fitted, and the model is called to predict or evaluate the model each time. These all allow the new model to establish a state throughout the training sequence and even maintain that state when it needs to make predictions.

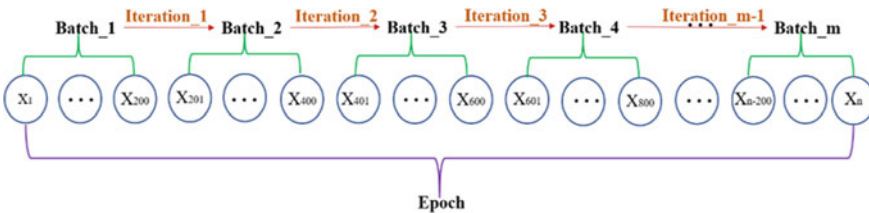


Fig. 3 Full training sample to add a structure diagram of the memory state unit

3.1 Update and Forecasting Process

(1) Network Update Process

FS-LSTM has two improvements in the network structure. Compared with the LSTM network, in the update process of network weights and deviations, there are extra weight and deviation vector \mathbf{W}^{out} , \mathbf{b}^{out} and full training sample state vector output by the fully connected layer. The forward calculation is mainly reflected in the input gate, as is shown in formula (7), (8), and the other steps are the same as the forward calculation of LSTM in literature [17].

$$f(\mathbf{u}_i^t) = f[\mathbf{W}\mathbf{X}^t \ \mathbf{W}^n \mathbf{r}^t] + [\mathbf{b} \ \mathbf{b}^n] \quad (7)$$

$$f(\mathbf{u}_{i,F}^t) = f(\mathbf{W}^{\text{out}} f \mathbf{u}_i^t + \mathbf{b}^{\text{out}}) \quad (8)$$

\mathbf{W} and \mathbf{b} represent the weight and deviation vector of the input samples, \mathbf{W}^n and \mathbf{b}^n stand for weight and deviation vector of full training sample, \mathbf{W}^{out} and \mathbf{b}^{out} are weight and deviation vector of fully-connected layer, \mathbf{u}_i^t and $\mathbf{u}_{i,F}^t$ represent the output of the inactive layer input and the output of the fully connected layer.

Backpropagation is mainly to obtain the weight \mathbf{W}^{out} , the deviation \mathbf{b}^{out} , and the update process of the triple gate weight and deviation parameters of the fully connected layer output after adding the full training sample state vector \mathbf{r}^t . The gradient calculation of the entire backpropagation process of the algorithm is shown as follows (9)–(19).

$$\delta_{w,k}^t = (\mathbf{W}^{\text{out}} \mathbf{W})^T \delta_k^t f'(\mathbf{u}_i^t) \mathbf{h}(S_k^t) f'(\mathbf{u}_{w,k}^t) \quad (9)$$

$$\delta_{\phi,k}^t = (\mathbf{W}^{\text{out}} \mathbf{W})^T \delta_k^t f'(\mathbf{u}_i^t) \mathbf{h}(S_k^t) f'(\mathbf{u}_{w,k}^t) S_{k-1}^t f(\mathbf{u}_{w,k}^t) \quad (10)$$

$$\delta_{l,k}^t = (\mathbf{W}^{\text{out}} \mathbf{W})^T \delta_k^t f'(\mathbf{u}_i^t) \mathbf{h}'(S_k^t) f'(\mathbf{u}_{l,k}^t) S_{k-1}^t f(\mathbf{u}_{w,k}^t) \quad (11)$$

$$\delta_{c,k}^t = (\mathbf{W}^{\text{out}} \mathbf{W})^T \delta_k^t f'(\mathbf{u}_i^t) \mathbf{h}'(S_k^t) \mathbf{h}'(\mathbf{u}_{c,k}^t) b_{kl}^t f(\mathbf{u}_{w,k}^t) \quad (12)$$

$$\frac{\partial L_N}{\partial \mathbf{W}^{\text{out}}} = \sum_{t=1}^N \delta_k^t (f(\mathbf{u}_i^t))^T \quad (13)$$

$$\frac{\partial L_N}{\partial \mathbf{b}^{\text{out}}} = \sum_{t=1}^N \delta_k^t \quad (14)$$

$$\frac{\partial L_N}{\partial \mathbf{W}} = \sum_{t=1}^N (\mathbf{W}^{\text{out}})^T \delta_k^t f'(\mathbf{u}_i^t) (\mathbf{X}^t)^T \quad (15)$$

$$\frac{\partial L_N}{\partial \mathbf{W}^n} = \sum_{t=1}^N (\mathbf{W}^{out})^T \delta_k^t f'(u_t^t) (r^t)^T \quad (16)$$

$$\frac{\partial L_N}{\partial \mathbf{b}} = \sum_{t=1}^N (\mathbf{W}^{out})^T \delta_k^t f'(u_t^t) \quad (17)$$

$$\frac{\partial L_N}{\partial \mathbf{b}^n} = \sum_{t=1}^N (\mathbf{W}^{out})^T \delta_k^t f'(u_t^t) \quad (18)$$

$$\left\{ \begin{array}{l} \frac{\partial L_N}{\partial \mathbf{W}^{x\tau}} = \sum_{t=1}^N \delta_{\tau,k}^t (X^t)^T \\ \frac{\partial L_N}{\partial \mathbf{W}^{h\tau}} = \sum_{t=1}^N \delta_{\tau,k}^t (\mathbf{h}_{k-1}^t)^T, \tau \in \{c, l, \phi, w\} \\ \frac{\partial L_N}{\partial \mathbf{b}^{\tau}} = \sum_{t=1}^N \delta_{\tau,k}^t \end{array} \right. \quad (19)$$

The above is all the gradient solving process in FS-LSTM, and all weights and deviation coefficients in the network can be updated by using the above gradients. from the back propagation process shown in formula (9)–(19), δ represents the reciprocal of the weight, \mathbf{N} is the total time step, \mathbf{L} represents the loss function, \mathbf{k} represents the last time step, $\mathbf{W}^{x\tau}$ represents the state corresponding to the input value, the weight parameters of input gate, forget gate and output gate, $\mathbf{W}^{h\tau}$ represents the corresponding state, input gate, forget gate and output gate weight parameter of the output at the previous moment, \mathbf{b}^{τ} is the corresponding deviation with state, input gate, forget gate and output gate.

(2) Network Forecasting Process

In the improved FS-LSTM network for fault diagnosis of the bridge structure acceleration sensor, suppose there are m samples, the i -th sample is the time series data of length t , where t represents the time step of the sequence, that is, use data from t time points to predict the data at the next time point.

The number of nodes in the input layer and output layer of the network is determined by the characteristics of the network task and the sample. In the prediction process, acceleration data with a specific time lag is grouped into input (represented by the dotted rectangle) and prediction (represented by the solid rectangle), as shown in Fig. 4.

The predicted value $\hat{y}^{(i)}$ is generated through the constructed FS-LSTM network model. The loss function is selected to minimize the sum of square errors and the L2 regularization of the model, as shown in formula (20). Subsequently, the mini-batch gradient descent optimization method is used for weight correction and model training to make it approach the target value. The bridge structure acceleration time series prediction model uses a small batch of samples to calculate the gradient loss in each iteration of the gradient descent.

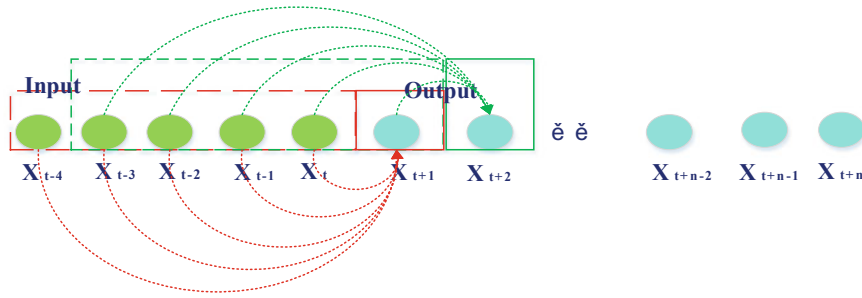


Fig. 4 Network prediction process

$$Loss(\hat{y}, y) = \frac{1}{2} \sum_{j=1}^m (y^{(j)} - \hat{y}^{(j)})^2 + \frac{1}{2} \lambda \sum \theta^2 \tag{20}$$

where, $y^{(i)}$ stands for the true value of the i -th sample. λ represents the regularization parameter, and θ is the model parameter.

At the same time, in order to prevent the local explosion of gradient and the robustness of model training, the method of gradient truncation is introduced. The principle of gradient truncation is to determine whether the L2 norm of the gradient loss generated by the model during backpropagation exceeds the preset gradient threshold. If it exceeds, the gradient is truncated by using formula (21).

$$\hat{g} = \frac{threshold}{\|\hat{g}\|^2} \hat{g} \tag{21}$$

where, \hat{g} represents the gradient loss, $\|\cdot\|^2$ represents the L2 norm, and threshold represents the threshold set in advance. At the same time, in order to prevent network overfitting, the dropout parameter is used to reduce the complexity of the model.

3.2 Determine Network Structure Hyper Parameters

In the FS-LSTM bridge acceleration time series model, the main hyper parameters include the number of output layer nodes, the number of input layer nodes, the time step of time series data, the number of neurons in the fully connected layer, the number of LSTM units in the hidden layer, the loss of the model threshold, number of sample training mini-batch, and initial learning rate. The K-fold cross-validation algorithm in literature [18] is used to determine the hyper parameters of the network in the improved LSTM bridge acceleration time series prediction model. FS-LSTM neural network structure network model parameter settings are shown in Table 1.

Table 1 FS-LSTM neural network parameter list

Parameters	Values
Number of input layer nodes	5
Number of output layer nodes	1
Number of neurons in the fully connected layer	126
Number of neurons in the feedforward hidden layer	128
Number of FS-LSTM units	256
Threshold of model loss	5
The number of small batches during sample training	200
Initial learning rate	0.001
Model evaluation index	RMSE
The maximum number of iterations	1000
Epoch	40
The value of dropout	0.3

Note Table 1 is the optimal parameter combination after applying the K-fold cross-validation algorithm

3.3 Fault Threshold

When the sensor is healthy and the structure is intact, the established FS-LSTM NN is used to calculate its predicted value, and the residual \mathbf{R}_e of the true value and the predicted value is used as an indicator for diagnosing sensor faults. Residual error calculation is shown in formula (22).

$$\mathbf{R}_e = \|\hat{y} - y\|^2 \tag{22}$$

According to the parameter confidence interval setting in statistics, the mean and variance of the residual series are calculated by Eqs. (23) and (24).

$$\mu(\mathbf{R}_e) = \frac{1}{n} \sum_{i=1}^n R_{ei} \tag{23}$$

$$\sigma^2(\mathbf{R}_e) = \frac{1}{n-1} \sum_{i=1}^n [R_{ei} - \mu(\mathbf{R}_e)]^2 \tag{24}$$

where R_{ei} is the residual value corresponding to different moments. The confidence interval with a confidence level of α can be expressed as:

$$P(\mu - Z_{\frac{\alpha}{2}}\sigma, \mu + Z_{\frac{\alpha}{2}}\sigma) = 1 - \alpha \tag{25}$$

where α is the confidence level; Z is the coefficient related to confidence level and it is set as 3, and the confidence level is 99.74%. Therefore, the threshold can be

derived from the 3σ criteria:

$$\lambda = \mu(\mathbf{R}_e) + 3\sigma^2(\mathbf{R}_e) \tag{26}$$

The λ value is the fault threshold for judging whether the sensor is faulty or not. When $R_{ei} > \lambda$ the sensor is faulty, and vice versa.

4 Numerical Example

Using ANSYS finite element software to build a three-span continuous beam model, elastic modulus $E = 3 \times 10^{10} \text{ N/m}^2$, Poisson’s ratio $\mu = 0.3$, density $\rho = 2500 \text{ kg/m}^3$. The beam length is 40 m, the rectangular section is $0.25 \text{ m} \times 0.6 \text{ m}$, and the beam is equally divided into 200 units, as shown in Fig. 5. Random white noise pulsation is selected to excite of the continuous beam, without considering the influence of damping, and the acceleration time history response is calculated by the Newmark- β method [19]. The placement position of the 10 acceleration sensors on the beam is shown in Fig. 5, and they are numbered S1–S10 sensors from left to right. Where the S1 sensor marked by the red solid circle is an analog fault sensor, and the S6 and S8 marked by the green dashed circle are randomly selected health sensors for each span, and they are supposed to verify whether there will be a second type of error in the fault diagnosis (the sensor health is misdiagnosed as a fault).

Randomly generate 400 pieces of white noise data, each piece of white noise data contains 120 data points, assuming that each data point has an interval of 0.01 s. Apply each piece of white noise data as ground pulsation excitation to the structure support, and calculate the acceleration response $y_{i,j}^*(t)$ of the structure where the sensor is installed. The subscript i represents the sensor number, $i = 1, 2, \dots, 10$; j represents the number of white noise excitation, $j = 1, 2, \dots, 400$; t represents the time step, $t = 1, 2, \dots, 120$. In order to avoid the non-stationary acceleration response of the structure at the initial stage of excitation, the first 20 data points of all the structure acceleration response records $y_{i,j}^*(t)$ are discarded, that is, each acceleration response data contains only 100-time steps. Then, for each structural response record of each sensor, white noise with a signal-to-noise ratio (SNR) of 20 is added to obtain the test value $y_{i,j}^*(t)$ of each sensor.

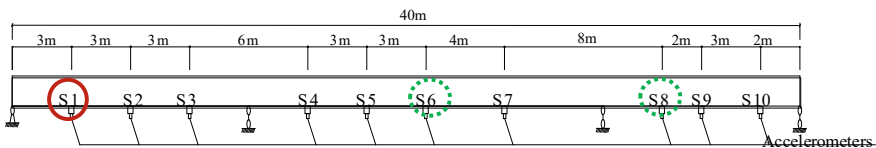


Fig. 5 Three-span continuous beam model

Table 2 Sensor fault thresholds

Sensor number	Mean $\mu(\mathbf{R}_e)$	Variance $\sigma^2(\mathbf{R}_e)$	Threshold λ
S1	0.0180	0.0092	0.0455
S6	0.0607	0.0693	0.2685
S8	0.0339	0.0331	0.1310

Assuming that the S1 sensor has constant fault, gain fault, bias fault, gain and linear drift fault, noise fault in sequence and these five operating conditions plus its own health conditions, a total of six operating conditions have been studied. Failure simulation can be found through formula (2)–(6), the fault parameters are selected by interpolation operation to obtain the optimal parameter combination. Each sensor response sample data consists of 40,000 time points. In order to study without loss of generality, randomly select a sensor from each remaining span as the research object (S6 and S8 sensors) to verify whether there will be a second type of fault diagnosis error (the intact sensor is misdiagnosed as a faulty sensor). The training set data ($40,000 \times 68\%$) and Eqs. (22)–(26) are used to calculate the fault thresholds of the three selected sensors. The calculation results are shown in Table 2.

The fault diagnosis result of the S1 sensor is shown in Fig. 6. The diagnosis result shows that under the above five fault conditions when the sensor has stuck faults, gain faults, deviation faults, gain linear drift faults, and noise faults in sequence, its residual values will greatly exceed the failure threshold obtained when they are healthy. From this, it can be determined that when the above five types of faults occur in the sensor, the proposed methods can work effectively.

In order to compare the diagnostic effects of the traditional LSTM and the improved FS-LSTM network, Figs. 7 and 8 show the fault diagnosis results of the S6 and S8 health sensors in different networks, as can be seen from Fig. 7a and b when the sensor does not fail, the residual values are all less than the set threshold. Although there are four test points in Fig. 7b (marked by the circle in Fig. 7b) that exceed the set threshold, they are in the allowable range ($40,000 \times 32\% \times 0.26\% \approx 33$) of the 3σ Guidelines, so the sensor is considered healthy. Compared with the FS-LSTM network diagnosis result, the LSTM network diagnosis result shows that many test points exceed the threshold, far exceeding the number allowed by the 3σ criteria. Therefore, if the traditional LSTM network is used to diagnose the fault of the sensor, its diagnosis result does not match the actual sensor fault condition, and a misdiagnosis will occur.

5 Conclusion

Based on the traditional long and short-term memory neural network, a new type of deep learning network is constructed by introducing fully connected layers and epoch state memory units. The parameter update, prediction process and the design

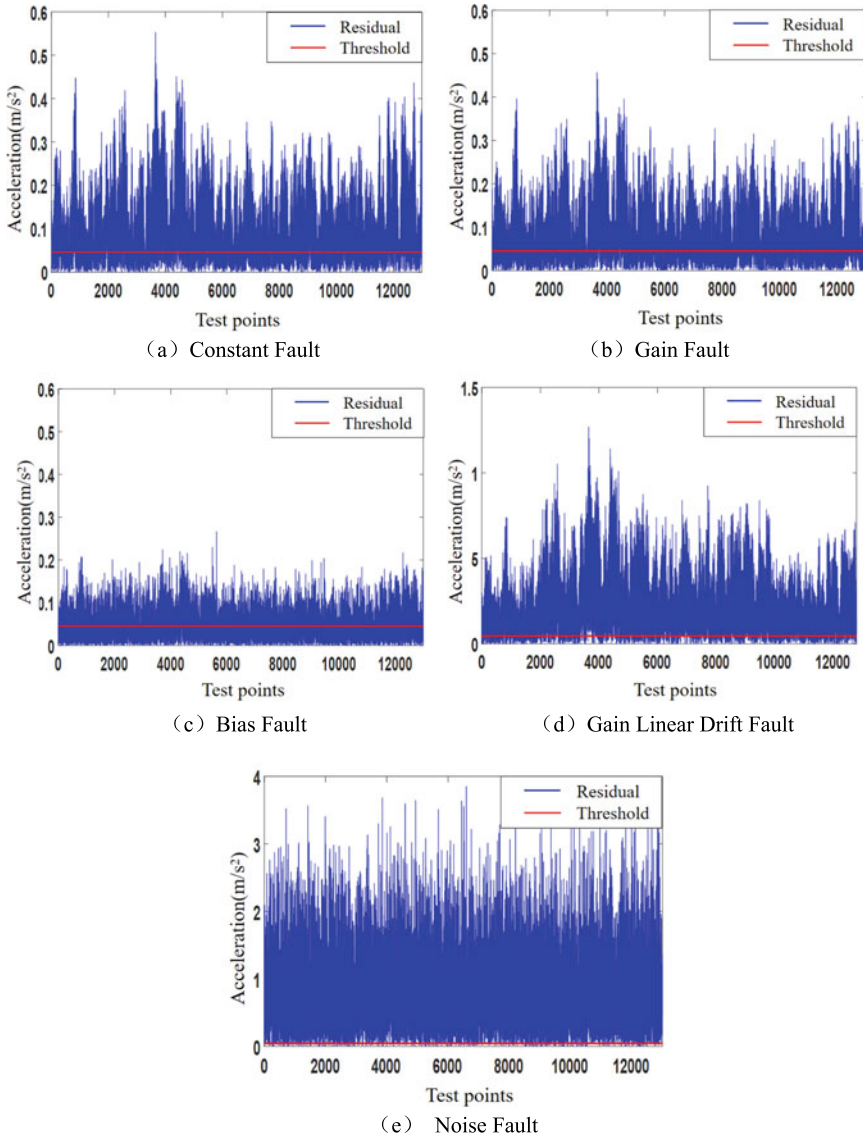


Fig. 6 Five fault detection results of the S1 sensor

of hyper parameters of the new network, have been described in detail. By setting a reasonable fault threshold, a new method of sensor fault diagnosis in the bridge health monitoring system is proposed. Numerical example studies show that when the sensor has stuck faults, gain faults, deviation faults, gain linear drift faults, and noise faults in sequence, the proposed FS-LSTM fault diagnosis method can correctly distinguish whether the faults in the bridge monitoring system are faulty or not.; At

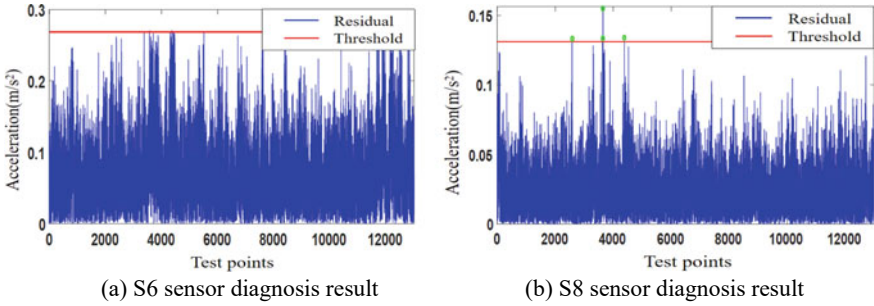


Fig. 7 Fault detection results for health sensors under FS-LSTM

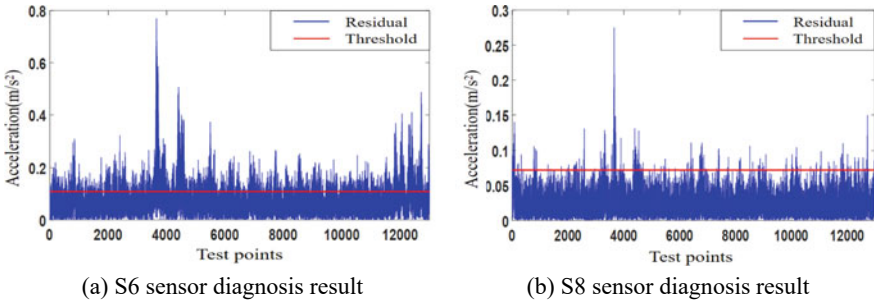


Fig. 8 Fault detection results of health sensors under LSTM

the same time, by randomly selecting the health sensor for each span, it is verified that the proposed method will not cause the second type of fault diagnosis error that misdiagnoses the health sensor as a fault sensor. The above research results are mainly based on the structural response of the finite element simulation for sensor fault diagnosis. In the future, the applicability of the proposed method can be further explored through the actual response of the real bridge.

Acknowledgements This work was financially supported by the China Post-doctoral Science Foundation (Grant Nos.2021M690838).

References

1. Hernandez GM, Masri SF (2008) Multivariate statistical analysis for detection and identification of fault sensors using latent variable methods. *Adv Sci Technol* 56(4):501–507
2. Zhang W, Cai CS, Pan F (2008) Nonlinear fatigue damage assessment of existing bridges considering progressively deteriorated road conditions. *Eng Struct* 56(6):1922–1932
3. Yi TH, Li HN, Sun HM (2013) Multi-stage structural damage diagnosis method based on “energy-damage” theory. *Smart Struct Syst* 12(3–4):345–361

4. Huang HB, Yi TH, Li HN (2016) Canonical correlation analysis based fault diagnosis method for structural monitoring sensor networks. *Smart Struct Syst* 17(6):1031–1105
5. Thomas P (2002) Fault detection and diagnosis in engineering systems: Janos J. Gertler; Marcel Dekker Inc., New York, 1998. *Control Eng Pract* 10(9):1037–1038. ISBN: 0-8247-9427-3
6. Shao JY, Xu Mq, Wang RX (2008) Model-based fault diagnosis system for spacecraft propulsion system. *Gas Turbine Exp Res* 22(003):47–49
7. Olivier A, Smyth AW (2017) Particle filtering and marginalization for parameter identification in structural systems. *Struct Control Health Monit* 24(3):e1874
8. Wan Z, Wang T, Li S (2018) A modified particle filter for parameter identification with unknown inputs. 25:e2268
9. Hung HB, Yi TH, Li HN (2017) Bayesian combination of weighted principal-component analysis for diagnosing sensor faults in structural monitoring systems. *J Eng Mech* 143(9)
10. Li LL, Liu G, Zhang LL (2019) Sensor fault detection with generalized likelihood ratio and correlation coefficient for bridge SHM. *J Sound Vib* 442:445–458
11. Ren H, Qu Jf, Chai Y, Tang Q, Ye X (2017) Deep learning for fault diagnosis: the state of the art and challenge. *Control Decis* 32(8):1345–1358
12. Cha YJ, Choi W, Büyüköztürk O (2017) Deep learning-based crack damage detection using convolutional neural networks. *Comput-Aided Civ Infrastruct Eng* 32(5):361–378
13. Lin Y, Nie Z, Ma H (2017) Structural damage detection with automatic feature-extraction through deep learning. *Comput-Aided Civ Infrastruct Eng* 32(12):1025–1046
14. Bao YQ, Tang ZY, Li HN (2019) Computer vision and deep learning-based data anomaly detection method for structural health monitoring. *Struct Health Monit* 18(2):401–421
15. Bao YQ, Chen Z, Wei S (2019) The state of the art of data science and engineering in structural health monitoring. *Engineering* 5(2):234–242
16. Salmasi FRA (2017) Self-healing induction motor drive with model free sensor tampering and sensor fault detection, isolation, and compensation. *Trans Ind Electron* 64(1):6105–6115
17. Malhotra P, Vig L, Shroff G, Agarwal P (2008) Long short term memory networks for anomaly detection in time series. In: *European symposium on artificial neural networks*, vol 23
18. Nam JS (2018) Injection-moulded lens form error prediction using cavity pressure and temperature signals based on k-fold cross validation. *Proc Inst Mech Eng B* 232:928–934
19. Zhang XS, Zhu YS, Gu H (1996) Study on the technology for transducer fault detection based on signal processing. *J Electron Meas Instrument* 4:1–5

Open Access This chapter is licensed under the terms of the Creative Commons Attribution 4.0 International License (<http://creativecommons.org/licenses/by/4.0/>), which permits use, sharing, adaptation, distribution and reproduction in any medium or format, as long as you give appropriate credit to the original author(s) and the source, provide a link to the Creative Commons license and indicate if changes were made.

The images or other third party material in this chapter are included in the chapter's Creative Commons license, unless indicated otherwise in a credit line to the material. If material is not included in the chapter's Creative Commons license and your intended use is not permitted by statutory regulation or exceeds the permitted use, you will need to obtain permission directly from the copyright holder.



Experimental Study on Inclination Test of Fiber Bragg Grating



Kang Tan, Ping Dong, Wanchun Gou, Qi Guo, and Yi Li

Abstract Deep displacement monitoring is an important means to monitor the deformation of slope, landslide and deep foundation pit. Traditional deep displacement monitoring uses manual inclinometer, which is time-consuming and laborious, and has large manual operation error, so it is impossible to realize automatic monitoring. It is urgent to adopt new technical means to make up for these shortcomings. Based on fiber Bragg grating sensing technology and beam bending theory, this paper establishes the calculation formula of fiber Bragg grating deep inclinometer, which can calculate the deep displacement curve of inclinometer through the change of fiber Bragg grating center wavelength; The strain sensitivity coefficient of fiber Bragg grating is calibrated by indoor calibration test. The experimental results show that the center wavelength of fiber Bragg grating has a high correlation with strain, and the relationship is linear. The strain and displacement of inclinometer tube are monitored and compared by indoor model test. The test results show that the displacement error calculated by fiber Bragg grating is 2% ~ 12%, which can meet the needs of deep displacement monitoring. The relevant conclusions provide a certain reference for the research of fiber Bragg grating deep displacement monitoring.

Keywords Fiber Bragg grating · Inclination · Deep displacement monitoring · Difference algorithm · Strain sensitivity coefficient

K. Tan (✉) · W. Gou · Q. Guo · Y. Li

Technology Innovation Center of Geohazards Automatic Monitoring, Ministry of Natural Resources (Chongqing Institute of Geology and Mineral Resources), Chongqing 401120, China
e-mail: tankangmove@163.com

Chongqing Engineering Research Center of Automatic Monitoring for Geological Hazards (Chongqing Institute of Geology and Mineral Resources), Chongqing 401120, China

P. Dong

Zhong'an Mutual Inductance (Chongqing) Intelligent Technology Co., Ltd., Chongqing 401120, China

1 Introduction

With the increase of human engineering activities, artificial slopes and deep foundation pits are increasing, and slope instability and deep foundation pit collapse occur from time to time. In addition, the range of human activities is also expanding to landslides and other geological disasters prone areas. In order to ensure the safety of human life and property, it is necessary to monitor the deformation of artificial slopes, deep foundation pits and natural landslides. Deep displacement monitoring can directly and effectively reflect the deformation and development law of rock and soil, and is an important means of deformation monitoring [1].

Traditional deep displacement monitoring mainly uses manual inclinometer, which is easy to operate, but it has high labor intensity, long time consumption, low automation degree and large errors caused by manual operation. Optical fiber has the characteristics of high sensitivity, anti-electromagnetic interference and strong automatic real-time, and has been well used in power communication [2], petrochemical industry [3], aerospace [4, 5], building structure monitoring [6–8], medical equipment [9] and other fields.

Some scholars have also applied optical fiber sensing technology to the field of geotechnical inclination measurement. Pei et al. [10] used fiber Bragg grating sensing technology to monitor the slope of an expressway for a long time. Chen et al. [11] used fiber Bragg grating sensors to monitor the landslide of a pipeline. Bims et al. [12] applied fiber Bragg grating sensing technology to deformation monitoring of slope indoor model. Jia et al. [13] developed a fiber Bragg grating test system for geotechnical centrifuge, which can monitor soil displacement in real time. Peng et al. [14] used fiber Bragg grating to monitor the deep displacement of a landslide, and analyzed the position and deformation mode of its main sliding surface.

At present, although there are some application examples of fiber Bragg grating inclinometer, the monitoring effect is only verified by deformation trend analysis. Fiber Bragg grating inclinometer, as a new monitoring technology, involves a wide range of theoretical knowledge and professional technology, so it is still necessary to study its inclinometer principle and effect through indoor experiments. In this paper, the calculation formula of fiber Bragg grating inclination is established firstly, and then the strain sensitivity coefficient and strain characteristics of fiber Bragg grating are studied by laboratory calibration test. Then, through model test, the effectiveness of fiber Bragg grating inclinometer technology is studied.

2 Principle of Fiber Bragg Grating Inclination Test

2.1 Characteristics of Fiber Bragg Grating

As shown in Fig. 1, when light waves are incident into the fiber, the grating will reflect light waves of a specific wavelength, which meets the following specific conditions:

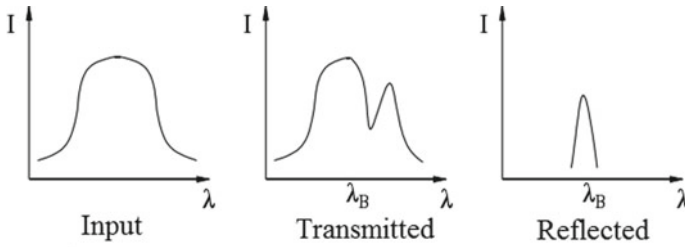


Fig. 1 Light wave propagation diagram of fiber Bragg grating

$$\lambda_B = 2n_{eff}\Lambda \tag{1}$$

where λ_B represents the central wavelength of reflected light; n_{eff} represents the effective refractive index of optical fiber; Λ represents the pitch of the fiber Bragg grating.

The relationship between λ_B and ambient temperature T and strain ε is as follows:

$$\frac{\Delta\lambda_B}{\lambda_{B0}} = (\alpha + \xi)\Delta T + (1 - p^{eff})\Delta\varepsilon \tag{2}$$

where $\Delta\lambda_B$ represents the change of the central wavelength; λ_{B0} is the initial center wavelength of the grating at 0 °C without external force; $\Delta\varepsilon$ and ΔT represent the strain and temperature changes of fiber Bragg grating respectively. α , ξ and p^{eff} represent the thermal expansion coefficient, thermo-optical coefficient and photoelastic coefficient of optical fiber, respectively.

Equation (2) can be rewritten as:

$$\Delta\lambda_B = c_\varepsilon\lambda_{B0}\Delta\varepsilon + c_T\lambda_{B0}\Delta T \tag{3}$$

where: $c_\varepsilon = 1 - p^{eff}$, $c_T = \alpha + \xi$.

2.2 Principle of Fiber Bragg Grating Inclination Measurement

It is generally necessary to install an inclinometer tube with fiber Bragg grating in the monitoring position, collect the reflection center wavelength of fiber Bragg grating by fiber demodulator, and calculate the deep displacement of rock and soil by analyzing the wavelength change.

In order to accurately measure the strain of the inclinometer tube, it is necessary to eliminate the influence of temperature on the wavelength, and the temperature compensation can be carried out by pasting fiber Bragg grating on both symmetrical

sides of the inclinometer tube. When the inclinometer tube is deformed, the wavelength changes of the reflection center of the symmetrical grating on both sides are as follows:

$$\Delta\lambda_{B1} = c_{\varepsilon 1}\lambda_{B10}\Delta\varepsilon_1 + c_{T1}\lambda_{B10}\Delta T_1 \quad (4)$$

$$\Delta\lambda_{B2} = c_{\varepsilon 1}\lambda_{B20}\Delta\varepsilon_2 + c_{T1}\lambda_{B20}\Delta T_2 \quad (5)$$

Fiber Bragg gratings of the same batch are used on symmetrical sides of inclinometer tubes, $c_{\varepsilon 1} \approx c_{\varepsilon 2}$, $\lambda_{B10} \approx \lambda_{B20}$, $c_{T1} \approx c_{T2}$. The temperature changes of symmetrical gratings on both sides are equal, namely $\Delta T_1 = \Delta T_2$. Therefore, the following formula can be obtained by (4) and (5):

$$\Delta\varepsilon_1 - \Delta\varepsilon_2 = \frac{\Delta\lambda_{B1} - \Delta\lambda_{B2}}{\lambda_{B0}c_{\varepsilon}} \quad (6)$$

From Eq. (6), it can be seen that temperature compensation can be realized by symmetrical double grating structure.

According to the beam bending theory, the deflection of the inclinometer tube is calculated from the strain of the inclinometer tube as follows:

$$S(z) = \int_L^z \int_L^z \frac{\Delta\varepsilon_1(z) - \Delta\varepsilon_2(z)}{2R} dz dz \quad (7)$$

where: L represents the length of the inclinometer, z represents the depth, and R represents the radius of the inclinometer.

The following formula can be obtained by substituting Eq. (6) into Eq. (7):

$$S(z) = \frac{1}{2Rc_{\varepsilon}\lambda_{B0}} \int_L^z \int_L^z [\Delta\lambda_{B1}(z) - \Delta\lambda_{B2}(z)] dz dz \quad (8)$$

After the change of reflection center wavelength of grating point is collected in the field, Eq. (8) can be solved by difference method.

3 Fiber Bragg Grating Calibration Test

The strain sensitivity coefficient of fiber Bragg grating is affected by the type of fiber and grating writing process. In order to ensure the accuracy of monitoring results, it is necessary to calibrate the strain sensitivity coefficient before using fiber Bragg grating to measure inclination.

3.1 Experimental Steps

- (1) Fix the two slides to the 32a channel steel base respectively, and then paste the two ends of the 3-m-long optical fiber to the two slides respectively with 502 glue (see Fig. 2) to ensure that the stretched part of the optical fiber has three grating areas.
- (2) Lock one sliding table to ensure that it cannot move, rotate the handwheel of the other sliding table to pre-tighten the optical fiber, measure the length of the optical fiber at this time with a steel tape measure, install a dial indicator on the movable sliding table and adjust it to zero, and then use an optical fiber demodulator to read the initial value of the central wavelength of three grating points in the tension area.
- (3) Turn the handwheel of the movable sliding table to stretch the optical fiber, control the amount of optical fiber stretching according to the reading of the dial indicator, test the stretching of 1 mm in each stage, and read the grating center wavelength after stretching in each stage (see Fig. 3a).
- (4) Stretch until the point wavelength of the grating is abnormal, then move the slider in the opposite direction to shrink the fiber, shrink 1 mm in each stage, continue to the initial pre-tightening length in step 2, and read the center wavelength of the grating after shrinking in each stage (see Fig. 3b).

Fig. 2 Calibration test device





Fig. 3 Calibration test readings

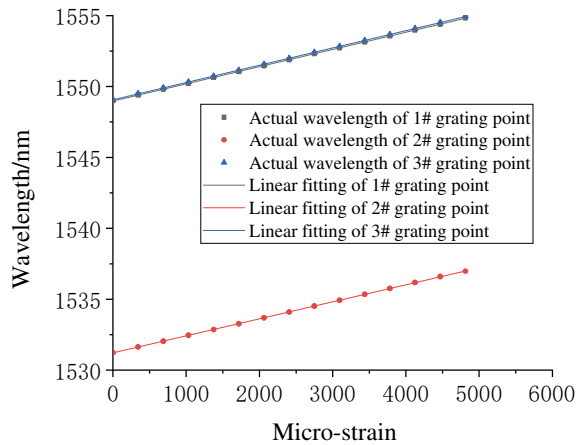
3.2 Test Results and Analysis

The relationship between the measured strain and the central wavelength is shown in Fig. 4.

The following results can be obtained from Fig. 4 and linear fitting results:

- (1) The correlation coefficient R^2 of the three grating points is greater than 0.999, the correlation between the center wavelength and strain is very high, and the fitting relationship is linear.
- (2) The relationship between strain and wavelength of 1# grating point is: $\lambda = 0.00121\mu\varepsilon + 1548.975$, the relationship between strain and wavelength of 2# grating point is: $\lambda = 0.0012\mu\varepsilon + 1531.220$, the relationship between strain and wavelength of 3# grating point is: $\lambda = 0.00122\mu\varepsilon + 1549.063$, and the average strain sensitivity coefficient $c_\varepsilon\lambda_{B0}$ of three grating points is 0.00121.

Fig. 4 Relationship between grating point strain and center wavelength



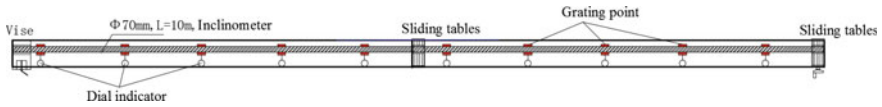


Fig. 5 Schematic diagram of test device

- (3) The central wavelength in the stretching process and the central wavelength in the shrinking process basically coincide, which shows that the relationship between the strain and the central wavelength of the fiber has good repeatability and no fatigue phenomenon.
- (4) The length of the fiber is 2909 mm. When the fiber is stretched 15 mm, that is, the strain reaches $5156\mu\epsilon$, the wavelength data is lost, which shows that the limit micro-strain of the fiber Bragg grating used in the test is about $5156\mu\epsilon$.

4 Indoor Model Test

In order to analyze the error of inclinometer formula and verify the validity of inclinometer with fiber Bragg grating, indoor model test is needed.

4.1 Test Ideas

Channel steel is used as the base, a vise is installed at the tail of the base, and a sliding table is installed at the middle and end parts respectively. The inclinometer tube attached with fiber Bragg grating and strain gauge is placed on the vise and sliding table, and the sliding table at the end is moved to make the inclinometer tube displacement. The strain of the inclinometer tube is measured by fiber demodulator and strain gauge, and then the displacement of the inclinometer tube is solved, and the actual displacement of the inclinometer tube is measured at the same time. See Fig. 5 for the schematic diagram of the test device.

4.2 Experimental Steps

- (1) Calibration of grating point position. The point spacing of the fiber Bragg grating used this time is 1 m. The manufacturer has marked the point position of the purchased fiber Bragg grating, but there may be some deviation in the point position of the grating due to machining error, so it is necessary to recalibrate the point position of the grating. It is preferred to use an optical fiber fusion splicer to fusion the armored lead cable with the optical fiber, and then connect the optical fiber to the optical fiber demodulator, slightly stretch at the raster points

Fig. 6 Calibration of grating point position



marked by the manufacturer, If the demodulated wavelength increases sharply, the position of the grating point is accurate. If the demodulated wavelength does not change, stretch near the position of the grating point calibrated by the manufacturer until the position where the demodulated wavelength increases sharply is found, which is the accurate position of the grating point. After calibration, mark the position of the grating point with a marker pen, as shown in Fig. 6.

- (2) Fabrication of fiber Bragg grating inclinometer. This time, the length of a single section of aluminum alloy inclinometer pipe is 2 m, and five inclinometer pipes are connected by casing. Four rows of casing joints are drilled with six holes in each row, and then rivets are used for anchoring to ensure that the inclinometer pipes are firmly connected. According to the calibrated grating point position, mark the grating point sticking position on both symmetrical sides of the inclinometer tube with a marker pen. The fiber Bragg grating is arranged in U-shaped loop at the end of inclinometer tube, In order to make the grating closely fit with the surface of the inclinometer tube, And better coupled together, Use sandpaper to polish around the sticking point, After the surface is rough and scratched, use cotton swabs dipped in alcohol to wipe off dust, oil stains and other pollutants on the surface of the inclinometer tube, Align the center of the grating point with the marked point, paste one end of the grating area on the inclinometer tube with 502 glue, then pretighten the fiber Bragg grating, paste the other end of the grating area on the inclinometer tube with 502 glue, and then apply epoxy resin glue to the grating point area, so that the grating point and the inclinometer tube are completely glued together. See Fig. 7 for the schematic diagram of the fabricated fiber Bragg grating inclinometer tube.
- (3) Installation of strain gauge. A resistance strain gauge is pasted on the symmetrical side of the protrusion of the inclinometer tube for comparative monitoring, as shown in Fig. 7. Before mounting, the mounting part of the inclinometer tube is polished with fine sandpaper, Remove the oxide layer, the grinding direction is about 45° with the wire grid direction of the strain gauge, then wipe the patch with cotton swab dipped in absolute alcohol, then drop 502 glue on the strain

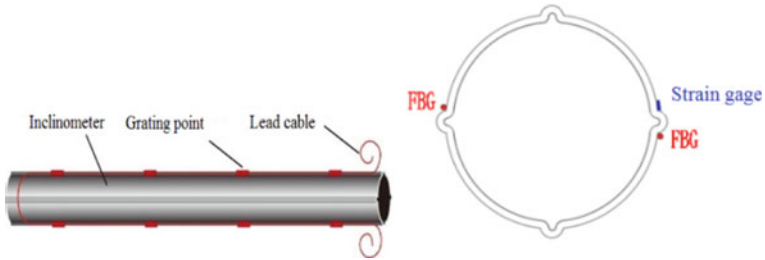


Fig. 7 Schematic diagram of fiber Bragg grating inclinometer

Fig. 8 Inclinometer model test device



gauge, and then paste it to the patch position. During the pasting process, roll it evenly with fingers to ensure that the excess glue is extruded out, so that the bonding place is uniform and free of bubbles.

- (4) Installation of test device. 5 sections of 2 m long 32a channel steel are assembled into a 10 m long base. A vise is fixed at the tail of the channel steel for clamping the fixed simulated fixed end at the tail of the inclinometer pipe. Sliding tables are respectively installed at the end and middle of the channel steel, and the end sliding tables can be moved left and right by shaking the handwheel to make

the end of the inclinometer pipe displacement. The middle sliding table can slide freely, which is used to prevent the inclinometer tube from drooping and contacting the channel steel base from affecting the test results Fig. 8.

- (5) Fiber Bragg grating inclinometer installation. Three days after the fiber Bragg grating is attached to the inclinometer tube, the epoxy resin glue is completely cured. Install the inclinometer tube on the test device, and make the vise clamp the tail of the inclinometer tube. Starting from the tail of the inclinometer, a dial indicator is installed at each grating point and zeroed, with a total of 6 indicators installed. Because the displacement of the end is larger than the measuring range of the dial gauge during the test, the displacement of the remaining four grating points at the end is calculated by marking the channel steel base with a line.
- (6) Data measurement. Connecting the optical fiber demodulator with the optical fiber Bragg grating to read the initial wavelength of each grating point; Connect the strain gauge to the strain gauge and zero it. This test is divided into three times of loading, that is, moving the end sliding table three times, reading the wavelength of each grating point after displacement by optical fiber demodulator, and reading the strain value at the grating point after displacement by strain gauge.

4.3 Experimental Results and Analysis

- (1) Comparative analysis of fiber Bragg grating strain and strain gauge strain.

As can be seen from Fig. 9:

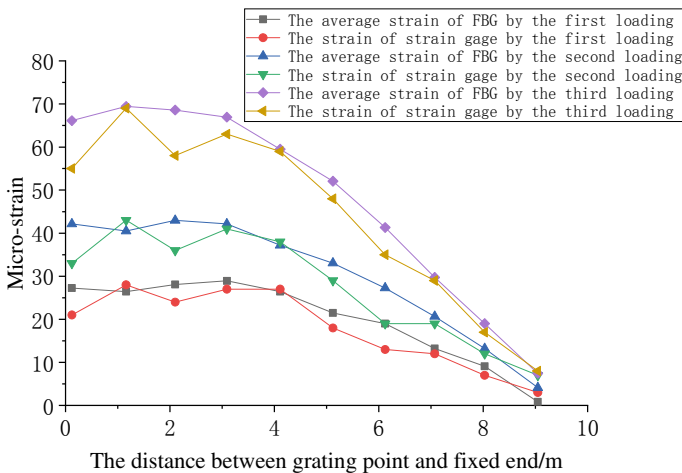
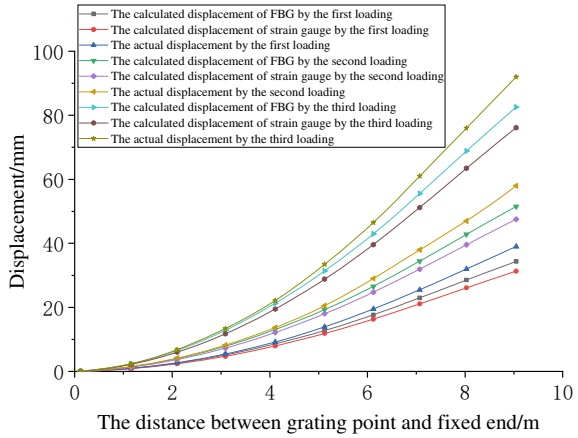


Fig. 9 Strain comparison analysis diagram

Fig. 10 Displacement comparison analysis diagram



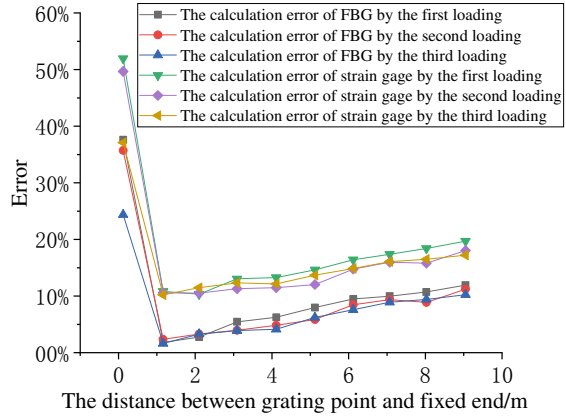
- ① In the three tests, the strain calculated by fiber Bragg grating and the strain measured by strain gauge are basically the same, and the strain gradually decreases from the tail to the end of the inclinometer tube, which accords with the strain change law of cantilever beam.
 - ② On the whole, the strain curve measured by strain gauge has larger twists and turns, while the strain curve calculated by fiber Bragg grating has smaller twists and turns, and the curve is more uniform and smooth.
- (2) Comparative analysis of displacement calculated by fiber Bragg grating, displacement calculated by strain gauge and actual displacement.

It can be seen from Fig. 10: ① In the three tests, the displacement law calculated by fiber Bragg grating and strain gauge is the same, and the displacement from the tail to the end of inclinometer gradually increases, which accords with the displacement change law of cantilever beam. ② The calculated displacement of fiber Bragg grating and strain gauge are smaller than the actual displacement, and the calculated displacement of fiber Bragg grating is closer to the actual displacement.

It can be seen from Fig. 11: ① With the increase of end displacement (loading amount), the calculation displacement error of fiber Bragg grating and strain gauge decreases continuously. The error of the first point at the tail of the inclinometer is large, mainly because the actual displacement of this point is small, while the dial indicator can only be accurate to 0.01 mm. ② The error of displacement ratio calculated by fiber Bragg grating is 2% ~ 12%.

The calculated displacement of fiber Bragg grating is smaller than the actual displacement, which may be caused by the following reasons: ① The deformation of inclinometer tube is transmitted to fiber Bragg grating through glue, and there is a certain transmissibility. ② There is casing joint in inclinometer pipe. Although the joint is connected by rivets, there will be some gap looseness.

Fig. 11 Error between calculated and actual displacement



5 Conclusion

- (1) Based on fiber Bragg grating sensing technology and beam bending theory, the calculation formula of fiber Bragg grating inclination measurement is established.
- (2) The correlation between the center wavelength of fiber Bragg grating and the strain measured by indoor calibration test is very high, and the fitting relationship is linear. The average strain sensitivity coefficient of grating points is 0.00121, and the limit micro-strain of fiber Bragg grating is about 5156 μm .
- (3) The displacement calculated by using fiber Bragg grating is closer to the actual displacement than that calculated by using strain gauge. The displacement error calculated by fiber Bragg grating is 2% ~ 12%, which can meet the needs of deep displacement monitoring.

Acknowledgements Fund project, supported by scientific research project of Chongqing Municipal Planning and Natural Resources Bureau (No.KJ-2020008, No.KJ-2020009).

References

1. Ding Y, Wang QC (2009) Remediation and analysis of kinematic behavior of roadway landslide in the upper Minjiang River, Southwest China. *Environ Geol* 58(7):1521–1532
2. Bjerkan L (2000) Application of fiber-optic Bragg grating sensors in monitoring environmental loads of overhead power transmission lines. *Appl Opt* 39(4):554–560
3. Spirin VV, Shlyagin MG, Miridonov SV et al (1999) Fiber Bragg grating sensor for petroleum hydrocarbon leak detection. *Opt Laser Eng* 32(5):497–503
4. Di SR (2015) Fibre optic sensors for structural health monitoring of aircraft composite structures: recent advances and applications. *Sensors* 15(8):18666–18713
5. Li P, Liu YJ, Leng JS (2014) A new deformation monitoring method for a flexible variable camber wing based on fiber Bragg grating sensors. *J Intell Mater Syst Struct* 25(13):1644–1653

6. Majumder M, Gangopadhyay TK, Chakraborty AK et al (2008) Fibre Bragg gratings in structural health monitoring-present status and applications. *J Lightwave Technol* 35(18):150–164
7. Zhu HH, Yin JH, Jin W et al (2010) Health monitoring of foundations using fiber Bragg grating sensing technology. *Chin Civil Eng J* 43(6):109–115
8. Ou JP, Zhou Z, Wu ZJ et al (2004) Intelligent monitoring of Heilongjiang Hulan River bridge based on FBGs. *Chin Civil Eng J* 37(1):45–49
9. Mishra V, Singh N, Tiwari U et al (2011) Fiber Bragg grating sensors in medicine: current and emerging applications. *Sens Actuators* 167(2):279–290
10. Pei HF, Yin JH, Zhu HH et al (2010) In-situ monitoring of displacements and stability evaluation of slope based on fiber Bragg grating sensing technology. *Chin J Rock Mechan Eng* 29(8):1570–1576
11. Chen PC, Li J, Liu JP et al (2010) Monitoring technology of pipelines using fiber Bragg grating and its application in landslide areas. *Chin J Rock Mechan Eng* 32(6):897–902
12. Bimis A, Karalekas D, Bouropoulos N et al (2016) Monitoring of hardening and hygroscopic induced strains in a calcium phosphate bone cement using FBG sensor. *J Mech Behav Biomed Mater* 60:195–202
13. Jia LX, Shi B, Wei GQ et al (2017) Fiber Bragg grating test system and model tests based on geotechnical centrifuge. *Chin J Geotech Eng* 39(5):896–905
14. Peng HY, Chen BL, Dong P et al (2020) Application of FBG sensing technology to internal deformation monitoring of landslide. *Adv Civ Eng Article ID 1328945*

Open Access This chapter is licensed under the terms of the Creative Commons Attribution 4.0 International License (<http://creativecommons.org/licenses/by/4.0/>), which permits use, sharing, adaptation, distribution and reproduction in any medium or format, as long as you give appropriate credit to the original author(s) and the source, provide a link to the Creative Commons license and indicate if changes were made.

The images or other third party material in this chapter are included in the chapter's Creative Commons license, unless indicated otherwise in a credit line to the material. If material is not included in the chapter's Creative Commons license and your intended use is not permitted by statutory regulation or exceeds the permitted use, you will need to obtain permission directly from the copyright holder.



The External Prestress Effect of Curved Tendons on the Natural Vibration Characteristics of Steel Beams



Zhi-wei Xu, Li-xia Lin, Nan-hong Ding, and Lei Chen

Abstract In order to explore the external prestress effect of the curved tendons on the stiffness and natural vibration characteristics of the steel beam, this paper deduced the calculation equation of the natural frequency on the external prestressed simply supported steel beam of the curved arrangement, which was based on the Hamilton principle. The natural frequency is calculated by combining the example of I-shaped simply supported steel beam, which was analyzed and verified by establishing the finite element model. The results show that: the calculation of the equation is well demonstrated by the finite element results, and the validity of model equation was verified. When the applied prestress increases, the natural vibration frequency decreases and the change range is not large, which indicates that the magnitude of the prestress has little effect on the natural frequency of simply supported steel beams.

Keywords Simple supported beam · External prestress · Curved tendons · Natural frequency

1 Introduction

Prestress can affect the dynamic characteristics of the beam to a certain degree. When the anchoring methods of prestressed reinforcement and the beam are determined, the influencing factors mainly include the types of tendons, the magnitude of prestress and so on. There are three types of external prestressing tendons: straight-line tendons, broken line tendons and curve tendons. The convenient construction makes the first two more common, while the curve tendons help the components obtain more ideal stress distribution.

In summary, there is little research on the external prestress effect of the curved tendons on the natural vibration characteristics of the steel beam, and it is necessary to analyze and verify the characteristics by using different theories and research methods. Based on the Classical Dynamic theory, the authors apply the Hamilton

Z. Xu · L. Lin (✉) · N. Ding · L. Chen
School of Civil Engineering, Lanzhou Jiaotong University, Lanzhou 730070, Gansu, China
e-mail: linlixia@126.com

principle to the calculation of natural vibration characteristics of the external prestressed simply supported steel beam of the curved arrangement for the first time. Then the vertical bending vibration differential equation of the beam is established by variational method, and the analytical expressions of its natural frequency and vibration shape are solved; Taking the curved externally prestressed I-shaped simply supported steel beam as an example and combining with the finite element calculation results, this paper analyzes the external prestress effect of the curved tendons on the natural vibration characteristics of the simply supported steel beam.

2 Establishment of the Vibration Equation Based on the Hamilton Principle

Hamilton principle:

$$\int_{t_1}^{t_2} \delta(T - V)dt + \int_{t_1}^{t_2} \delta W_{nc}dt = 0 \quad (1)$$

Kinetic energy generated by the beam during vibration:

$$T = \int_0^1 \frac{1}{2} m \dot{y}^2 dx \quad (2)$$

m —mass per unit length; \dot{y} — the first derivative of the dynamic deflection y of the beam with respect to time t .

The potential energy generated by the beam during vibration is divided into three parts:

One is the bending strain energy of the beam:

$$V_1 = \int_0^1 \frac{1}{2} E_c I_c (y'')^2 dx \quad (3)$$

where: $E_c I_c$ denotes the bending stiffness of simply supported beam itself; (y'') ² means the second derivative of the dynamic deflection y of the beam to the spatial coordinate x .

The second one is the strain energy of prestressed reinforcement:

$$V_2 = \int_0^l \frac{1}{2} E_p A_p (y'')^2 h dx \tag{4}$$

According to Reference [1], $h = \int_0^l ((e(x))^2 (\cos \theta)^2 \cdot 10^{-3}) dx$ can be induced; Where, $\theta = de(x)/dx$; $e(x) = C_1 x^2 + C_2 x + C_3$; x represents the distance from the coordinate origin to the calculated section along the beam axis; E_p indicates elastic modulus of prestressed reinforcement; A_p refers to section area of prestressed reinforcement; $e(x)$ is the eccentricity of prestressed reinforcement; θ means included angle between prestressed reinforcement and beam axis.

The third is the tensile and compressive strain energy of the beam:

$$V_3 = \int_0^l \frac{1}{2} E_c A_c r_q^2 h dx \tag{5}$$

where, $r_q = I_p y''$; $I_p = (E_p A_p) / (E_c A_c)$ represents the converted reinforcement ratio of externally prestressed tendons; E_c represents elastic modulus of beam; A_c means cross sectional area of beam body.

Therefore, the total potential energy is:

$$V = V_1 + V_2 + V_3 \tag{6}$$

When the beam vibrates, the work done by the non-conservative force is:

$$W_{nc} = \int_0^l \frac{1}{2} N_{p\theta} \cos \theta_0 (y')^2 dx \tag{7}$$

where, $N_{p\theta} \cos \theta_0$ stands for the horizontal component of initial prestress value; y' is the first derivative of dynamic deflection y to space coordinate t .

Variation of kinetic energy:

$$\int_{t_1}^{t_2} \delta T dt = - \int_{t_1}^{t_2} \int_0^l m \ddot{y} \delta y dx dt \tag{8}$$

Variation of bending strain energy:

$$\begin{aligned}
 \int_{t_1}^{t_2} \delta V_1 dx dt &= \delta \int_{t_1}^{t_2} \int_0^l \frac{1}{2} E_c I_c (y'')^2 dx dt = \int_{t_1}^{t_2} \int_0^l \frac{1}{2} E_c I_c y^{(4)} \delta y dx dt \\
 &+ \int_{t_1}^{t_2} E_c I_c y_l'' \delta y_l' dt - \int_{t_1}^{t_2} E_c I_c y_0'' \delta y_0' dt \\
 &- \int_{t_1}^{t_2} E_c I_c y_l^{(3)} \delta y_l dt + \int_{t_1}^{t_2} E_c I_c y_0^{(3)} \delta y_0 dt
 \end{aligned} \tag{9}$$

Variation of strain energy of prestressed reinforcement:

$$\begin{aligned}
 \int_{t_1}^{t_2} \delta V_2 dx dt &= \delta \int_{t_1}^{t_2} \int_0^l \frac{1}{2} E_p A_p (y'')^2 h dx dt = \int_{t_1}^{t_2} \int_0^l \frac{1}{2} E_p A_p h y^{(4)} \delta y dx dt \\
 &+ \int_{t_1}^{t_2} E_p A_p h y_l'' \delta y_l' dt - \int_{t_1}^{t_2} E_p A_p h y_0'' \delta y_0' dt \\
 &- \int_{t_1}^{t_2} E_p A_p h y_l^{(3)} \delta y_l dt + \int_{t_1}^{t_2} E_p A_p h y_0^{(3)} \delta y_0 dt
 \end{aligned} \tag{10}$$

Variation of beam tensile and compressive strain energy:

$$\begin{aligned}
 \int_{t_1}^{t_2} \delta V_3 dx dt &= \delta \int_{t_1}^{t_2} \int_0^l \frac{1}{2} E_c A_c (I_p y'')^2 h dx dt = \int_{t_1}^{t_2} \int_0^l \frac{1}{2} E_c A_c I_p^2 h y^{(4)} \delta y dx dt \\
 &+ \int_{t_1}^{t_2} E_c A_c I_p^2 h y_l'' \delta y_l' dt - \int_{t_1}^{t_2} E_c A_c I_p^2 h y_0'' \delta y_0' dt \\
 &- \int_{t_1}^{t_2} E_c A_c I_p^2 h y_l^{(3)} \delta y_l dt + \int_{t_1}^{t_2} E_c A_c I_p h y_0^{(3)} \delta y_0 dt
 \end{aligned} \tag{11}$$

Variation of total potential energy:

$$\int_{t_1}^{t_2} \delta V dt = \int_{t_1}^{t_2} \int_0^l D y^{(4)} \delta y dx dt + \int_{t_1}^{t_2} D y_l'' \delta y_l' dt$$

$$- \int_{t_1}^{t_2} D y_0'' \delta y_0' dt - \int_{t_1}^{t_2} D y_l^{(3)} \delta y_l dt + \int_{t_1}^{t_2} D y_0^{(3)} \delta y_0 dt \quad (12)$$

where:

$$D = E_c I_c + E_p A_p h + E_c A_c I_p^2 h = E_c I_c + E_p A_p h \left(1 + \frac{E_p A_p}{E_c A_c} \right) \quad (13)$$

Variation of non-conservative work:

$$\begin{aligned} \delta \int_{t_1}^{t_2} W_{nc} = \delta \int_{t_1}^{t_2} \int_0^l \frac{1}{2} N_{p\theta} \cos \theta_o (y')^2 dx dt = - \int_{t_1}^{t_2} \int_0^l N_{p\theta} \cos \theta_o y'' \delta y dx dt \\ \int_{t_1}^{t_2} N_{p\theta} \cos \theta_0 y_l' \delta y_l dt - \int_{t_1}^{t_2} N_{p\theta} \cos \theta_0 y_0' \delta y_0 dt \end{aligned} \quad (14)$$

Through integrating Eqs. (12) and (14), the following can be obtained:

$$\begin{aligned} \int_{t_1}^{t_2} \int_0^l (-m \ddot{y} - D - N_{p\theta} \cos \theta_o y'') \delta y dx dt - \int_{t_1}^{t_2} D y_l'' \delta y_l' dt + \int_{t_1}^{t_2} D y_0'' \delta y_0' dt \\ + \int_{t_1}^{t_2} (D y_l^{(3)} + N_{p\theta} \cos \theta_0 y_l') \delta y_l dt - \int_{t_1}^{t_2} (D y_0^{(3)} + N_{p\theta} \cos \theta_0 y_0') \delta y_0 dt = 0 \end{aligned} \quad (15)$$

According to the variational calculation, the variation is equal to zero on the boundary displacement condition, and the variation in the domain is arbitrary, then:

$$m \ddot{y} + D + N_{p\theta} \cos \theta_0 y'' = 0 \quad (16)$$

Therefore, Eq. (16) is the bending vibration equation of simply supported beam. From the solution of higher-order differential equation, the following can be obtained:

$$\begin{aligned} \omega_n = \left(\frac{n\pi}{l} \right)^2 \sqrt{\frac{E_c I_c}{m}} \sqrt{1 - \frac{N_{p\theta} \cos \theta_0}{\left(\frac{n\pi}{l} \right)^2 E_c I_c}} \\ \sqrt{1 + \frac{E_p A_p h}{E_c I_c \left(1 - \frac{N_{p\theta} \cos \theta_0}{\left(\frac{n\pi}{l} \right)^2 E_c I_c} \right)} (1 + I_p)} (n = 1, 2, \dots, \infty) \end{aligned} \quad (17)$$

where: ω_n is the n -th natural vibration circle frequency; the fourth item is the correction item of natural frequency of simply supported beam after prestressing.

According to the relationship between natural circular frequency and natural frequency, the natural frequency of external prestressed simply supported beam is:

$$f_n = \frac{\omega_n}{2\pi} = \frac{n^2\pi}{2l^2} \sqrt{\frac{E_c I_c}{m}} \sqrt{1 - \frac{N_{p\theta} \cos \theta_0}{\left(\frac{n\pi}{l}\right)^2 E_c I_c}} \sqrt{1 + \frac{E_p A_p h}{E_c I_c \left(1 - \frac{N_{p\theta} \cos \theta_0}{\left(\frac{n\pi}{l}\right)^2 E_c I_c}\right)}} (1 + I_p) (n = 1, 2, \dots, \infty) \tag{18}$$

The vibration shape function: $\varphi(x) = A_3 \sin \frac{n\pi x}{l}$. Where, the magnitude of A_3 does not affect the variation law of vibration shape function.

3 Reliability Verification of Vibration Equation

Equation (17) can be simplified to $\omega_n = \left(\frac{n\pi}{l}\right)^2 \sqrt{\frac{E_c I_c}{m}}$ ($n = 1, 2, \dots, \infty$) without the effect of curve prestress, while in Reference [2], the natural vibration circle frequency is $\omega_n = n^2 \pi^2 \sqrt{\frac{EI}{mL^4}}$ ($n = 1, 2, \dots, \infty$) without considering the moment of inertia and shear deformation, so the two equations are consistent. Equation (17) can be simplified as $\omega_n = \left(\frac{n\pi}{l}\right)^2 \sqrt{\frac{E_c I_c}{m}} \sqrt{1 - \frac{N_{p\theta} \cos \theta_0}{\left(\frac{n\pi}{l}\right)^2 E_c I_c}}$ ($n = 1, 2, \dots, \infty$) without the action of eccentricity of curved prestressing bar, while in Reference [2], the natural circular frequency of the beam under axial force is $\omega_n = n^2 \pi^2 \sqrt{1 - \frac{NL^2}{n^2 \pi^2 EI}} \sqrt{\frac{EI}{mL^4}}$ ($n = 1, 2, \dots, \infty$), so the two equations are consistent. After replacing the curve eccentricity influence coefficient h with linear eccentricity e_p^2 , Eq. (17) can be simplified as

$$\omega_n = \left(\frac{n\pi}{l}\right)^2 \sqrt{\frac{E_c I_c}{m}} \sqrt{1 - \frac{N_{p\theta} \cos \theta_0}{\left(\frac{n\pi}{l}\right)^2 E_c I_c}} \sqrt{1 + \frac{E_p A_p e_p^2}{E_c I_c \left(1 - \frac{N_{p\theta} \cos \theta_0}{\left(\frac{n\pi}{l}\right)^2 E_c I_c}\right)}} (1 + I_p) (n = 1, 2, \dots, \infty),$$

while in reference [3], the natural circular frequency of external prestressed simply supported beams with eccentric linear reinforcement is

$$\omega_n = \left(\frac{n\pi}{l}\right)^2 \sqrt{\frac{E_c I_c}{m}} \sqrt{1 + \frac{E_p A_p e_p^2}{E_c I_c \left(1 - \frac{N_{p0} \cos \theta_0}{\left(\frac{n\pi}{l}\right)^2 E_c I_c}\right)}} (1 + I_p) - \frac{N_{p0} l^2}{n^2 \pi^2 E_c I_c} (n = 1, 2, \dots, \infty),$$

so, the two equations consistent. By comparing the above equations with the equation in the special case of the existing reference, it can be seen that the equation established in this paper is more general.

4 Finite Element Verification

4.1 Influence of Prestress Value on Natural Frequency

The cross-sectional area of prestressed cable is 139 mm², and the range of prestress value is 0–200 kn. The comparison between the calculated value of natural vibration frequency of simply supported beam and the finite element simulation value is shown in Table 1. It can be seen that under different prestress, the analytical solution of the first-order natural frequency of simply supported steel beam is very close to the finite element calculation results, the variation trend is consistent, and the maximum error is no more than 2%. It verifies the reasonableness of the calculation methods in this paper; The calculation error of the second-order natural frequency is relatively large, which is the result of the large degree of freedom of the finite element solution. The displacement element solution will lead to the small overall stiffness, and the larger solution order means the larger finite element calculation error, so it is reasonable to make the calculation result of the second-order frequency small [3].

In order to further verify the correctness of the equations established in this paper, the vibration shape calculation solution derived in this paper is compared with the vibration shape finite element solution calculated by ANSYS. The comparison results of the first-order vibration shape and the second one are shown in Fig. 1.

As can be seen from Fig. 1, the calculation results in this paper are in good agreement with the finite element simulation results, especially the first-order vibration shape, and the second-order vibration modes can basically coincide. The result further shows that the calculation method of the external prestressed simply supported steel beam of the curved arrangement in this paper is correct and reliable.

Table 1 The first two-order natural frequency and error with different preloads

Prestress (kN)	First-order frequency (Hz)			Prestress (kN)	Second-order frequency (Hz)		
	Calculated value	Finite element value	Error (%)		Calculated value	Finite element value	Error (%)
0	48.056	48.627	-1.20	0	192.225	174.486	9.23
50	47.477	46.682	1.67	50	191.859	173.904	9.36
100	46.819	46.140	1.45	100	191.235	173.423	9.31
150	46.152	45.591	1.22	150	190.561	172.839	9.30
200	45.474	45.034	0.97	200	189.908	172.353	9.24

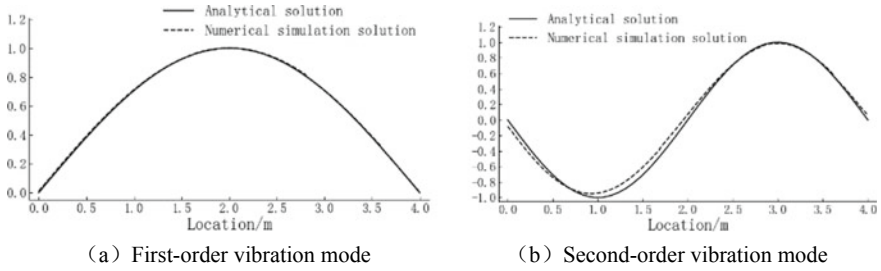


Fig. 1 Vibration shape comparison chart

Table 2 The first-order natural frequency and error with different cross-sectional areas of tendons

Cross-sectional area (mm ²)	The first-order natural frequency (Hz)		
	Calculated value	Finite element value	Calculated value
54.8	44.568	54.8	44.568
98.7	45.130	98.7	45.130
139	45.474	139	45.474
191	45.716	191	45.716
285	45.996	285	45.996

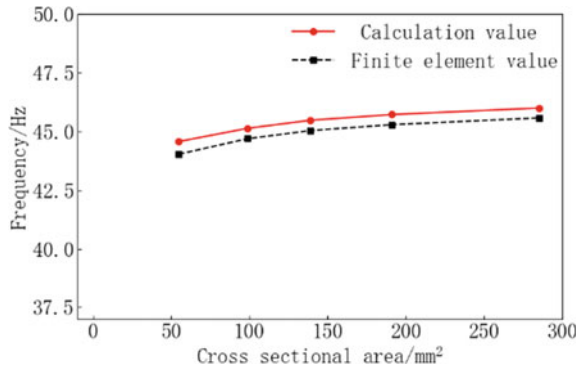
4.2 Influence of Prestressed Cable Section Area on Natural Frequency

By using different specifications of steel strands, the cross-sectional areas of prestressed cables are changed and the variation law of natural frequency is analyzed. If the prestress value is 200 kN, the comparison between the calculated value of the first-order natural frequency of the simply supported beam and the finite element simulation value can be seen in Table 2. As the cross-sectional area of prestressed cable gradually increases, the natural frequency of simply supported steel beam gradually increases (as shown in Fig. 2).

5 Conclusions

- (1) In this paper, based on Hamilton energy variational principle, this paper established the bending vibration differential equation of external prestressed simply supported steel beams with curved tendons for the first time, and then obtained the solution of the analytical expression of natural vibration frequency and the vibration shape function; The accuracy of the equation is verified by the comparative analysis of the equation and the finite element calculation results.

Fig. 2 Frequency comparison chart



- (2) With the gradual increase of prestress, the natural frequency of simply supported steel beam decreases gradually, but the change range is small and less than 5%, indicating that the applied prestress has little effect on the natural frequency of simply supported steel beam; With the increasing cross-sectional area of prestressed cable, the natural frequency of simply supported steel beam increases gradually.
- (3) The equations established in this paper are suitable for external prestressed simply supported steel beams with curved tendons. The adopted methods and the deduced equations carry a certain reference value for the calculation and analysis of prestressed concrete beams with unbonded [4] curved tendons.

References

1. Xiao J-t, Wu H-l (2010) Prestress force effect on natural frequencies of simply supported beams. *Sci Technol Eng* 10(12):2029–2912, 2919
2. Liu J, Du X (2005) *Structural dynamics*, vol 1(2019,1 reprint). China Machine Press, Beijing, pp 163–167
3. Zhong C-l, Liang D, Zhang Y-l et al (2020) Calculation of natural vibration frequency of external prestressed steel-concrete composite simply supported beams. *J Jilin Univ (Eng Technol Ed)* 50(06):2159–2166
4. Hamed E, Frostig Y (2006) Natural frequencies of bonded and unbonded prestressed beams—prestress force effects. *J Sound Vibr* 295(1–2):28–39

Open Access This chapter is licensed under the terms of the Creative Commons Attribution 4.0 International License (<http://creativecommons.org/licenses/by/4.0/>), which permits use, sharing, adaptation, distribution and reproduction in any medium or format, as long as you give appropriate credit to the original author(s) and the source, provide a link to the Creative Commons license and indicate if changes were made.

The images or other third party material in this chapter are included in the chapter's Creative Commons license, unless indicated otherwise in a credit line to the material. If material is not included in the chapter's Creative Commons license and your intended use is not permitted by statutory regulation or exceeds the permitted use, you will need to obtain permission directly from the copyright holder.



Transverse Vibration Characteristics of Clamped-Elastic Pinned Beam Under Compressive Axial Loads



Jianxun Zhang, Pengchong Zhang, Huicun Song, and Lei Zhu

Abstract Based on the Bernoulli–Euler theory, the vibration characteristics of a clamped-elastic pinned beam under the elastic constraint and the compressive axial loads are derived and verified by finite element method. The results of examples show that the natural frequency of the beam decreases with loads increase and the frequency increases with the increase of the elastic constraint stiffness. When the constraint stiffness increases from 10^4 to 10^8 N/m, the first-order natural frequency becomes 4.24 times, the second-order natural frequency becomes 2.19 times, and the third-order natural frequency becomes 1.57 times; when the constraint is weak, the loads change is mainly reflected in the first mode shape. When the constraint stiffness is 10^4 N/m, the first-order natural frequency decreases by 20%, the second-order modal natural frequency changes by 3%, and the third-order natural frequency changes by less than 1%. The range of the elastic constraints with significant changes in the natural frequencies of the higher-order modes is larger. When the first-order frequency is taken to $100EI/l^3$, the change tends to be flat, the second-order frequency is about five times that of the first-order, and the range of the third-order frequency is 15 times or more.

Keywords Clamped-elastic pinned beam · Compressive axial loads · Elastic constraint · Natural frequency · Mode · Finite element analysis

J. Zhang · P. Zhang · L. Zhu (✉)

School of Civil and Transportation Engineering, Beijing Key Laboratory of Functional Materials for Building Structure and Environment Remediation, Beijing Advanced Innovation Center for Future Urban Design, Beijing Higher Institution Engineering Research Center of Structural Engineering and New Materials, Beijing University of Civil Engineering and Architecture, Beijing 100044, China
e-mail: zhulei@bucea.edu.cn

H. Song

Culture Development Research Institute/School of Humanities, Beijing University of Civil Engineering and Architecture, Beijing 100044, China

© Crown 2023

Y. Yang (ed.), *Advances in Frontier Research on Engineering Structures*, Lecture Notes in Civil Engineering 286, https://doi.org/10.1007/978-981-19-8657-4_47

527

1 Introduction

A great deal of research work has been done on the natural vibration characteristics of beams under simple working conditions. In recent years, the research on beam structures under complex working conditions such as elastic restraint or axial load has been increasing gradually.

Clough and Penzien [1] gave the expressions of natural frequencies and mode functions of beams under various simple working conditions by solving the free vibration equation of transverse bending. Bokaian [2] proposed the natural frequencies and modes of beams under general boundary conditions under axial compression by solving analytical or semi-analytical solutions. Banerjee and Ananthapuvirajah [3] and Lee et al. [4] focused on the model itself and used different methods to analyze the free vibration of tapered beams. Murtagh et al. [5] simplified the research model into a beam structure, and numerically simulated the vibration characteristics of the structure by finite element method. Hu et al. [6] discussed the influence of axial pressure on the natural frequency of classical boundary beam structure and verified it by finite element method. Jafari et al. [7] analyzed the free vibration of Timoshenko beam by combining theory with finite element method. Chang et al. [8] studied the vibration characteristics of axially moving beams with fixed boundary conditions. Li [9] and Lin et al. [10] used the improved Fourier series method to study the free vibration of beams with general boundary conditions and elastic constraint boundary conditions. Zhao et al. [11] used the improved Fourier series method to study the influence of elastic constraint and axial load on the vibration characteristics of beams. Bao et al. [12] and Yang et al. [13] gave semi-analytical solutions of vertically elastically restrained beams for different models. The former considers the influence of variable cross-section, while the latter discusses the influence of constraint order. Wang [14] considered the influence of prestress effect on the natural frequency of beams. Zhang [15] and others simplified the wind turbine into a beam model and analyzed the theoretical solution and the finite element solution based on the beam element.

Considering that there is little research on the vibration characteristics of beams under the combined action of elastic constraint and external load, this paper analyzes the first three natural frequencies and corresponding vibration modes of beams by theoretical derivation and discusses the influence of constraint stiffness and axial compression load on the natural vibration characteristics of beams, which is verified by finite element method.

2 Theoretical Derivation

Figure 1 is a schematic diagram of the clamped-elastic pinned beam system, where EI is the equivalent bending stiffness of the beam ($\text{N} \times \text{m}^2$), m is the distributed mass of the beam (kg), k is the elastic constraint stiffness (N/m) in the y direction of the

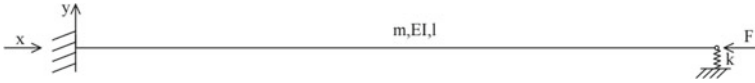


Fig. 1 Clamped-elastic pinned beam system

hinge end, and the compressive axial loads F moves with the end, keeps horizontal and always acts on the geometric center line of the beam.

With Euler–Bernoulli beam model, it can be known that the transverse free vibration equation of the beam is a partial differential equation [1]:

$$m(x) \frac{\delta^2 y(x, t)}{\delta t^2} + F \frac{\delta^2 y(x, t)}{\delta x^2} + \frac{\delta^2}{\delta x^2} \left[EI(x) \frac{\delta^2 y(x, t)}{\delta x^2} \right] = 0 \tag{1}$$

With the method of separating variables, the general solution of the equation is [1]:

$$y(x) = A \sin \delta x + B \cos \delta x + C \sinh \varepsilon x + D \cosh \varepsilon x \tag{2}$$

where A, B, C and D are constant coefficients, and δ and ε are defined as [1]:

$$\begin{aligned} \delta &= \left\{ [(m\omega^2/EI) + (F/2EI)^2]^{1/2} + (F/2EI) \right\}^{1/2} \\ \varepsilon &= \left\{ [(m\omega^2/EI) + (F/2EI)^2]^{1/2} - (F/2EI) \right\}^{1/2} \end{aligned} \tag{3}$$

The deformation of the system belongs to linear elastic small deformation motion, and the boundary condition of the fixed end is:

$$\begin{aligned} [y(x, t)]_{x=0} &= 0; \\ \left[\frac{\partial y(x, t)}{\partial x} \right]_{x=0} &= 0 \end{aligned} \tag{4}$$

Considering the influence of forces generated by rotation angle and displacement at the elastic hinge supporting end, the boundary condition is:

$$\begin{aligned} \left[\frac{\partial^2 y(x, t)}{\partial x^2} \right]_{x=l} &= 0; \\ \left[\frac{\partial^3 y(x, t)}{\partial x^3} + (F/EI) \frac{\partial y(x, t)}{\partial x} \right]_{x=l} &= [-(k/EI)y(x, t)]_{x=l} \end{aligned} \tag{5}$$

Substituting formula (4) into formula (2), we obtained the following equations:

$$\begin{aligned}
 [y(x, t)]_{x=0} &= B + D = 0; \\
 \left[\frac{\partial y(x, t)}{\partial x} \right]_{x=0} &= \delta A + \varepsilon C = 0
 \end{aligned}
 \tag{6}$$

Substituting formula (5) into formula (2), we obtained the following equations:

$$\begin{aligned}
 \left[\frac{\partial^2 y(x, t)}{\partial x^2} \right]_{x=l} &= -A\delta^2 \sin \delta l - B\delta^2 \cos \delta l \\
 &+ C\varepsilon^2 \sinh \varepsilon l + D\varepsilon^2 \cosh \varepsilon l = 0; \\
 \left[\frac{\partial^3 y(x, t)}{\partial x^3} + (F/EI) \frac{\partial y(x, t)}{\partial x} + (k/EI)y(x, t) \right]_{x=l} &= -A\delta^3 \cos \delta l + B\delta^3 \sin \delta l + C\varepsilon^3 \cosh \varepsilon l + D\varepsilon^3 \sinh \varepsilon l \\
 &+ (F/EI)(A\delta \cos \delta l - B\delta \sin \delta l + C\varepsilon \cosh \varepsilon l + D\varepsilon \sinh \varepsilon l) \\
 &+ (k/EI)(A \sin \delta l + B \cos \delta l + C \sinh \varepsilon l + D \cosh \varepsilon l) = 0
 \end{aligned}
 \tag{7}$$

Then substitute formula (6) into formula (7), and keep A and B to get:

$$\begin{aligned}
 A(-\delta^2 \sin \delta l - \delta\varepsilon \sinh \varepsilon l) + B(-\delta^2 \cos \delta l - \varepsilon^2 \cosh \varepsilon l) &= 0 \\
 A[-\delta^3 \cos \delta l - \delta\varepsilon^2 \cosh \varepsilon l + (F/EI)(\delta \cos \delta l - \delta \cosh \varepsilon l) \\
 + (k/EI)(\sin \delta l - \delta/\varepsilon \sinh \varepsilon l)] + B[\delta^3 \sin \delta l - \varepsilon^3 \sinh \varepsilon l \\
 + (F/EI)(-\delta \sin \delta l - \varepsilon \sinh \varepsilon l) + (k/EI)(\cos \delta l - \cosh \varepsilon l)] &= 0
 \end{aligned}
 \tag{8}$$

Equation (8) should have a non-zero solution, therefore, it is impossible for both A and B to be 0, then the corresponding determinant is 0, which can be solved as:

$$\begin{aligned}
 \delta\varepsilon[2\delta^2\varepsilon^2 - \delta\varepsilon(\delta^2 - \varepsilon^2) \sin \delta l \sinh \varepsilon l + (\delta^4 + \varepsilon^4) \cos \delta l \cosh \varepsilon l] \\
 + k/EI(\delta^2 + \varepsilon^2)(\varepsilon \sin \delta l \cosh \varepsilon l - \delta \cos \delta l \sinh \varepsilon l) &= 0
 \end{aligned}
 \tag{9a}$$

If we introduce the definitions of $U = N/(2EI)$ and $\Omega = \omega (m/EI)^{1/2}$, there are:

$$\delta^4 + \varepsilon^4 = 4U^2 + 2\Omega^2; \delta^2 - \varepsilon^2 = 2U; \delta\varepsilon = \Omega
 \tag{10}$$

The formula (9a) can be reduced to:

$$\begin{aligned}
 2\delta\varepsilon[\Omega^2 - U\Omega \sin \delta l \sinh \varepsilon l + (2U^2 + \Omega^2) \cos \delta l \cosh \varepsilon l] \\
 + k/EI(\delta^2 + \varepsilon^2)(\varepsilon \sin \delta l \cosh \varepsilon l - \delta \cos \delta l \sinh \varepsilon l) &= 0
 \end{aligned}
 \tag{9b}$$

When k approaches 0, the system becomes a cantilever beam system under compressive axial loads, and the natural frequency characteristic equation is equivalent to:

$$\Omega^2 - U\Omega \sin \delta l \sinh \varepsilon l + (2U^2 + \Omega^2) \cos \delta l \cosh \varepsilon l = 0 \quad (11)$$

The formula is the same as that of the cantilever beam frequency equation in reference [3].

When k tends to infinity, the system becomes a clamped-elastic pinned beam system under compressive axial loads, and the natural frequency characteristic equation is equivalent to:

$$\varepsilon \sin \delta l \cosh \varepsilon l - \delta \cos \delta l \sinh \varepsilon l = 0 \quad (12)$$

The formula is the same as the result given in reference [5].

The frequency characteristic Eq. (9a) is a transcendental equation, and only its numerical solution can be obtained instead of analytical solution. After obtaining the natural frequency, we can obtain the mode function by formula (8).

We may as well set $C = 1$, and we can get from the first equation in Eqs. (6) and (8):

$$\begin{aligned} A &= -\varepsilon/\delta; B = \frac{\delta\varepsilon \sin \delta l + \varepsilon^2 \sinh \varepsilon l}{\delta^2 \cos \delta + \varepsilon^2 \cosh \varepsilon}; \\ C &= 1; D = -\frac{\delta\varepsilon \sin \delta l + \varepsilon^2 \sinh \varepsilon l}{\delta^2 \cos \delta + \varepsilon^2 \cosh \varepsilon}; \end{aligned} \quad (13)$$

The coefficients in the formula do not include k , and the influence of elastic constraint stiffness on the mode shape is reflected by the natural frequency value. These coefficients can also be deduced from the second equation in Eq. (8), and although they are expressed in different forms, their values are the same.

3 Verification

3.1 Model Establishment

In order to verify the reliability of the theoretical derivation in this paper, the finite element method is used to carry out numerical calculation, and the model data of different scales are compared. A 137-m-high circular section tower was selected as the analysis object, and the general finite element software ABAQUS was used for analysis. In engineering analysis, the model can be simplified into a beam model, where the outer diameter and inner diameter of the tower are 4.28 and 4.23 m, the material is steel, the elastic modulus is 2.1×10^{11} N/m², the Poisson's ratio is 0.3, the density is 7850 kg/m³, and the critical load of Euler under cantilever state is about 2.05×10^7 N.

The B21 Euler beam element was chosen to establish the beam model, and the effects of shear deformation and moment of inertia were ignored. The whole beam



Fig. 2 Finite element model of beam

was divided into 20 elements and a total of 21 nodes. Considering the request of modal number was limited, the subspace iteration method was used to solve the natural frequency. The finite element model is shown in Fig. 2.

3.2 Calculation of Natural Frequency

Considering that in practical engineering, the structure may be unstable if the axial load reaches the critical load, the range of compressive axial loads variation is set as 0 N to 2.05×10^7 N, and the maximum value corresponds to the Euler critical load of the first mode shapes of the cantilever beam. The comparison of natural frequencies obtained from different elastic constraint stiffness values and compressive axial loads values is shown in Table 1.

As can be seen from Table 1, the natural frequency value derived by the method in this paper is very close to the value obtained by the finite element method, with an error of less than 1%, which verifies the theoretical solution.

The data in Table 1 show that the natural frequency values corresponding to the first three modes of the structure decrease with the increase of the compressive axial loads under these constraints. The higher the order corresponding to the natural frequency is, the smaller the influence brought by the axial loads is. When the compressive axial loads change from 0 to half of Euler critical load, the maximum range of first-order frequency can reach 25.96%, the maximum value of second-order frequency is 4.20%, and the third-order frequency is 1.26%. At the same time, it can be seen that the stronger the top elastic constraint is, the smaller the influence of compressive axial loads with the same amplitude will be. When the constraint is raised from 10^4 to 10^8 N/m, the variation range of the first-order frequency is reduced to 2.95%, and the variation range of the second-order and third-order frequency is less than 1%.

The influence of compressive axial loads and elastic constraint on natural frequency is further discussed below, and only the first order frequency with obvious change is concerned. Figure 3 shows the change trend of natural frequency with the increase of restraint stiffness when the compressive axial loads is set. It can be seen that with the increase of the elastic restraint stiffness, the natural frequency also rises, but the rising rate gradually slows down.

Figure 4 shows the variation trend of natural frequency with the increase of compressive axial loads when the constraint stiffness is fixed. It can be seen that the natural frequency decreases with the increase of compressive axial loads, and the rate of decline gradually accelerates, which is consistent with the conclusion in

Table 1 Comparison of finite element method and equations

Rigidity k/(N/m)	Axial loads F/(N/m)	First order natural frequency			Second order natural frequency			Third order natural frequency		
		Natural frequency/Hz	FEA	Relative error (%)	Natural frequency/Hz	FEA	Relative error (%)	Natural frequency/Hz	FEA	Relative error (%)
10 ⁴	0	1.4977	1.4977	-0.002	9.1517	9.1515	0.003	25.6099	25.6103	-0.001
	1.02E + 07	1.1089	1.1089	-0.002	8.7677	8.7676	0.002	25.2884	25.2886	-0.001
	2.05E + 07	0.3508	0.3511	-0.098	8.3605	8.3604	0.001	24.9596	24.9600	-0.001
10 ⁵	0	1.8023	1.8023	0.002	9.2082	9.2080	0.002	25.6300	25.6297	0.001
	1.02E + 07	1.5101	1.5102	-0.004	8.8255	8.8254	0.002	25.3086	25.3087	0.000
	2.05E + 07	1.1087	1.1088	-0.008	8.4195	8.4195	0.000	24.9798	24.9801	-0.001
10 ⁶	0	3.4259	3.4259	0.000	9.8068	9.8068	0.000	25.8349	25.8352	-0.001
	1.02E + 07	3.3265	3.3265	0.000	9.4463	9.4461	0.002	25.5147	25.5148	0.000
	2.05E + 07	3.2210	3.2209	0.002	9.0632	9.0635	-0.003	25.1871	25.1874	-0.001
10 ⁷	0	5.8388	5.8387	0.001	14.8719	14.8717	0.002	28.2447	28.2448	0.000
	1.02E + 07	5.7045	5.7044	0.001	14.7077	14.7077	0.000	27.9592	27.9595	-0.001
	2.05E + 07	5.5610	5.5609	0.001	14.5407	14.5405	0.001	27.6672	27.6674	-0.001
10 ⁸	0	6.3428	6.3429	-0.001	20.0786	20.0785	0.000	40.0798	40.0811	-0.003
	1.02E + 07	6.1559	6.1558	0.002	19.8803	19.8800	0.002	39.8939	39.8951	-0.003
	2.05E + 07	5.9601	5.9600	0.001	19.6775	19.6777	-0.001	39.7048	39.7060	-0.003

Fig. 3 Relationship between constraint stiffness and natural frequency

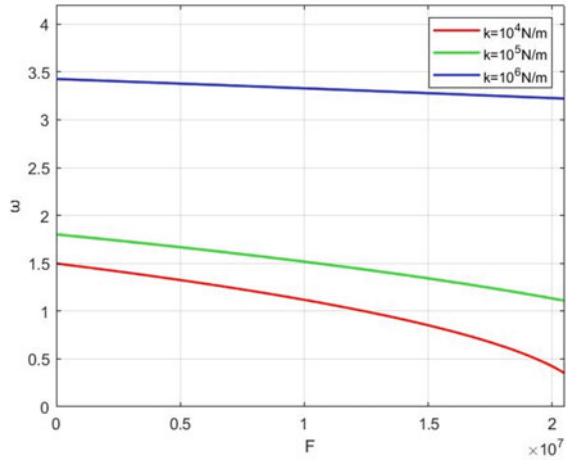
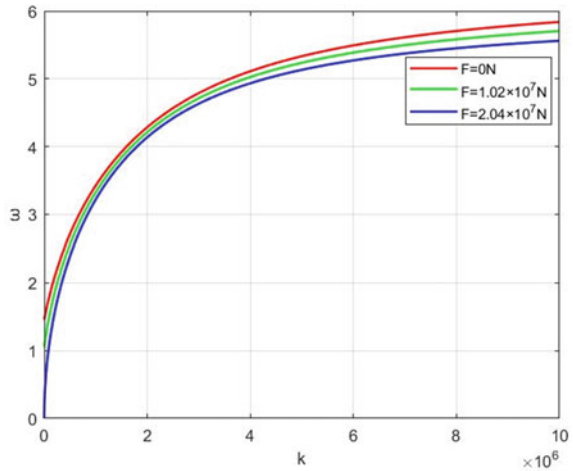


Fig. 4 Relationship between axial load stiffness and natural frequency



reference [2]. At the same time, it can be noticed that when the elastic constraint takes a small value, the decline rate is faster; when the value is larger, the decline rate is relatively slower, which is consistent with the change trend shown in Table 1.

3.3 Modes Analysis

The transverse bending mode shapes of the tower are obtained by modal analysis in ABAQUS. In order to study the influence of the number of divided elements on the results, the displacement of the node of the beam divided into 5 elements is used. Compared with the results of 20 elements, the maximum error of the natural

frequency value is 1.02%. Compared with the theoretical results obtained in Eqs. (2), (3) and (13), the first three bending modes are shown in Figs. 5 and 6.

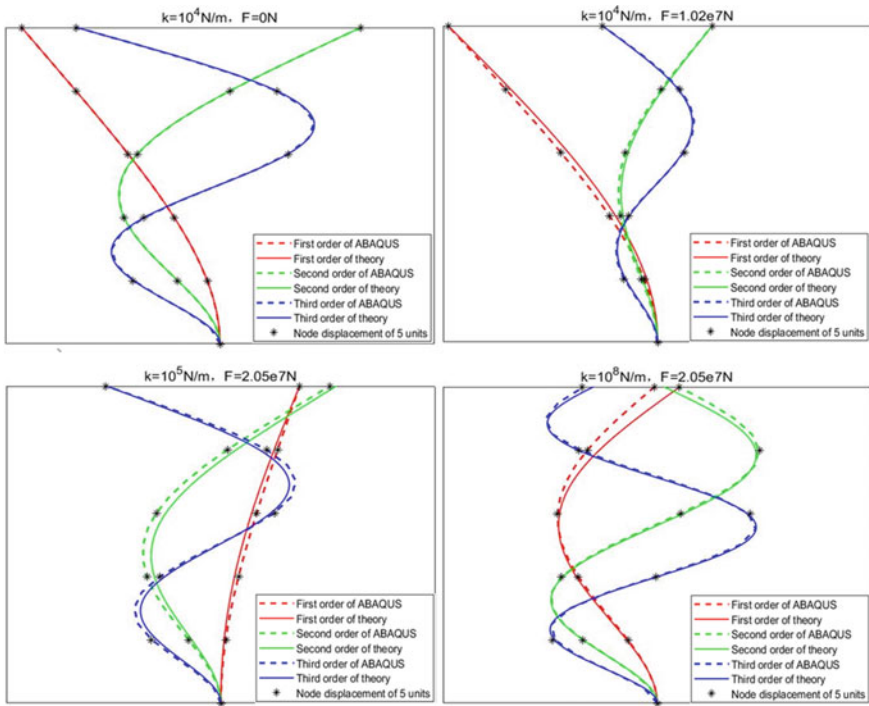


Fig. 5 Comparison of the first three modes of finite element and theoretical solution

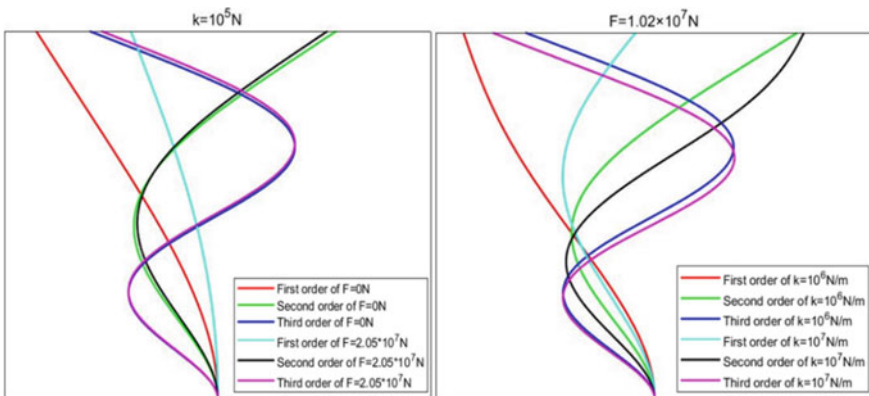


Fig. 6 Comparison of the first three modes derived from theory

It can be seen that the influence of compressive axial loads on the first mode is more significant than that on the higher mode, and the elastic constraint also has a more obvious influence on the higher mode.

3.4 Influence of Coupling of Constrained Stiffness and Compressive Axial Loads on Natural Frequency

As can be seen from the above results, the degree of influence of axial pressure on structural vibration characteristics decreases significantly with the increase of constraint stiffness, and the higher order mode is not sensitive to the change of axial pressure. This may be due to the different critical loads corresponding to the different modes of the calculation model. The larger the critical load is, the smaller the modal change caused by compressive axial loads with the same change amplitude is. Considering that the parameters of different beams are different, the constraints stiffness, axial pressure and natural frequency are dimensionlessly processed in the following analysis. Each parameter is written as:

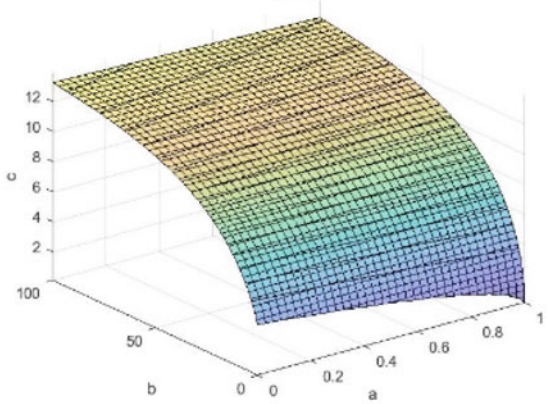
$$F = aP_{cr} \quad k = b\frac{EI}{l^3} \quad \omega = c\sqrt{\frac{EI}{ml^4}} \quad (14)$$

In the formula, a is a constant with a value between 0 and 1, and P_{cr} is the first order Euler critical load of the structure under the cantilever beam condition; b and c are constants with values greater than 0.

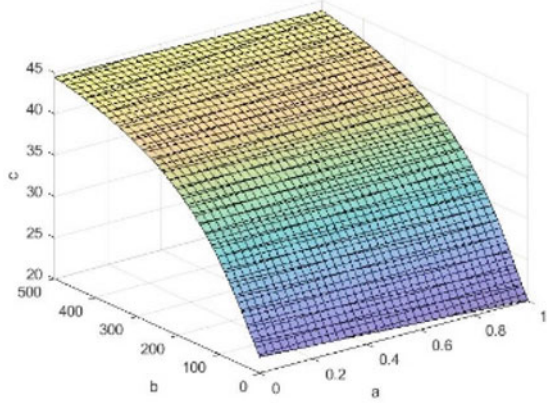
The influence of the constraint stiffness and the compressive axial loads on the natural frequencies of the beam is as follows:

As can be seen from Fig. 7, compared with the low-order modes, the elastic constraint value range of the natural frequency of the high-order modes with significant changes is larger. When the first order frequency reaches $100EI/l^3$, the change tends to be gentle; when the second order frequency reaches $500EI/l^3$, the change tends to be gentle; and the third order frequency will gradually gentle when it reaches over $1500EI/l^3$. Theoretically speaking, the natural frequency will not increase infinitely with the increase of constraint stiffness. Finally, when the constraint stiffness is large, the elastic end displacement is small, and the structure can be approximated as a clamped-elastic pinned beam. In addition, it can be seen from the figure that when the axial compression is not greater than the first-order Euler critical load, its influence on the natural frequency of the structure is mainly reflected in the first-order modes, but it is not obvious in the higher-order modes, and the natural frequency of the second and third order modes decreases by no more than 10%.

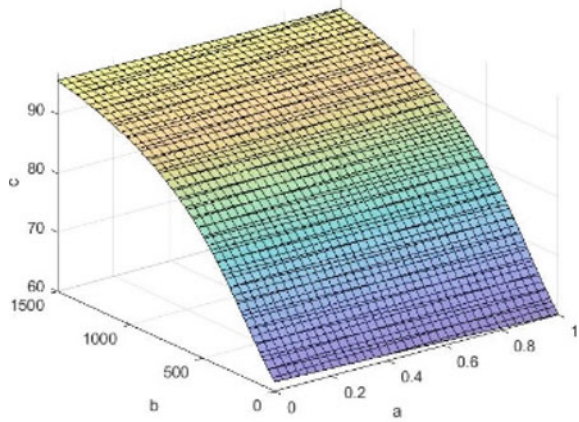
Fig. 7 Influence of coupling of axial pressure and constraint stiffness on the first three modes



The first order mode



The second order mode



The third order mode

4 Conclusions

In this paper, theoretical derivation and finite element method are used to study the vibration characteristics of clamped-elastic pinned beams, and the following conclusions are drawn:

- (1) Based on the Euler beam theory, the natural frequency characteristic equation and mode shape expression of the clamped-elastic pinned beam are obtained and verified by finite element analysis.
- (2) When the compressive axial load on the beam increases, the beam's natural frequency decreases, and the first-order frequency decreases from 2.95 to 25.96% corresponding to 0–50% Euler critical load under different elastic restraint stiffness. When the lateral elastic restraint stiffness of the elastic end of the beam increases, the natural frequency increases. When the restraint stiffness increases from 10^4 to 10^8 N/m, the first natural frequency becomes 4.24 times, the second natural frequency becomes 2.19 times and the third natural frequency becomes 1.57 times.
- (3) When the elastic end constraint of the beam is strong, the change of axial compression in a certain range will not have great influence on the vibration characteristics. When the constraint stiffness is 10^8 N/m, the influence of 50% Euler critical load on the first-order frequency is less than 3%, and the high-order frequency is less than 1%. When the constraint of the elastic end of the beam is weak, the influence of the change of axial pressure is mainly reflected in the first mode shape. When the constraint stiffness is 10^4 N/m, the influence of the variation amplitude of the axial compression can reach more than 20%, while the influence of the variation amplitude of the higher order mode is small. The variation of the natural frequency of the second order mode is about 3%, and the variation amplitude of the third order mode is less than 1%.
- (4) The elastic constraint value range with significant change in the natural frequency of the higher order mode is larger. When the first order frequency reaches $100EI/l^3$, the change tends to be flat, the second order frequency is about five times than that of the first order, and the third order frequency value range is 15 times or more.

Acknowledgements The authors gratefully acknowledge the financial supported by the National Natural Science Foundation of China (Grant No.51778035), Beijing Advanced Innovation Center for Future Urban Design (No. UDC2016030200) and The Fundamental Research Funds for Beijing University of Civil Engineering and Architecture (X19038), as well as Beijing Cooperative Innovation Research Center on Energy Saving and Emission Reduction.

References

1. Clough RW, Penzien J (1975) Dynamics of structures. McGraw-Hill
2. Bokaian A (1988) Natural frequencies of beams under compressive axial loads. *J Sound Vib* 126(1):49–65
3. Banerjee JR, Ananthapuvirajah A (2019) Free flexural vibration of tapered beams. *Comput Struct* 224(Nov):106106.1–106106.6
4. Lee JW, Lee JY (2016) Free vibration analysis using the transfer-matrix method on a tapered beam. *Comput Struct* 164(FEB):75–82
5. Murtagh PJ, Basu B, Broderick BM (2004) Simple models for natural frequencies and mode shapes of towers supporting utilities. *Comput Struct* 82(20/21):1745–1750
6. Hu Z, Gao Q, Wang R et al (2014) Influence of axial load on natural vibration frequency of structure. *Low Temp Architect Technol* 36(012):75–78 (in Chinese)
7. Jafari A, Ezzati M, Atai AA (2018) Static and free vibration analysis of Timoshenko beam based on combined peridynamic-classical theory besides FEM formulation. *Comput Struct* 213
8. Chang JR, Lin RJ, Huang RJ et al (2010) Vibration and stability of an axially moving rayleigh beam. *Appl Math Model* 34(6):1482–1497
9. Li WL (2000) Free vibrations of beams with general boundary conditions. *J Sound Vib* 237(4):709–725
10. Lin LB, Wan YL, Jun D et al (2011) Vibration analysis of beams with arbitrary elastic boundary conditions. *Appl Mech Mater* 1326
11. Zhao Y, Du J, Xu D (2020) Vibration characteristics analysis for an axially loaded beam with elastic boundary restraints. *J Vibr Shock* 39(15):109–117 (in Chinese)
12. Bao S, Zhou J, Cao J, Shen F (2020) Free vibration analysis of foundation-beams with variable cross section and arbitrary elastic end-constraints. *Chin J Appl Mech* 37(05):2228–2234 + 2335–2336 (in Chinese)
13. Yang S, Wang T (2011) Nature frequency analysis of a cantilever beam with elastic restraint in vertical direction. *J Tianjin Univ (Sci Technol)* 44(001):18–22 (in Chinese)
14. Wang L (2013) Analysis of prestressing effect on nature frequency for simply supported beam. Jilin University (in Chinese)
15. Zhang Y, Lou M (2010) The modal characteristics analysis of wind turbine. *Chin J Appl Mech* (03):626–629 (in Chinese)

Open Access This chapter is licensed under the terms of the Creative Commons Attribution 4.0 International License (<http://creativecommons.org/licenses/by/4.0/>), which permits use, sharing, adaptation, distribution and reproduction in any medium or format, as long as you give appropriate credit to the original author(s) and the source, provide a link to the Creative Commons license and indicate if changes were made.

The images or other third party material in this chapter are included in the chapter's Creative Commons license, unless indicated otherwise in a credit line to the material. If material is not included in the chapter's Creative Commons license and your intended use is not permitted by statutory regulation or exceeds the permitted use, you will need to obtain permission directly from the copyright holder.



Correction to: Experimental Study on the Self-Repair Properties of Shape Memory Alloy Concrete Beam



Yue Zhang and Xian Cui

Correction to:
**Chapter “Experimental Study on the Self-Repair Properties
of Shape Memory Alloy Concrete Beam” in: Y. Yang (ed.),
Advances in Frontier Research on Engineering Structures,
Lecture Notes in Civil Engineering 286,
https://doi.org/10.1007/978-981-19-8657-4_36**

In the original version of the chapter, the following correction has been incorporated:
The author Xian Cui now has been changed as corresponding author.

The correction chapter and the book have been updated with the changes.

The updated version of this chapter can be found at
https://doi.org/10.1007/978-981-19-8657-4_36